LINKING HYDROLOGICAL AND BIOGEOCHEMICAL PROCESSES IN RIPARIAN CORRIDORS

EDITED BY: Dipankar Dwivedi, Sarah E. Godsey and Tim Scheibe
PUBLISHED IN: Frontiers in Water

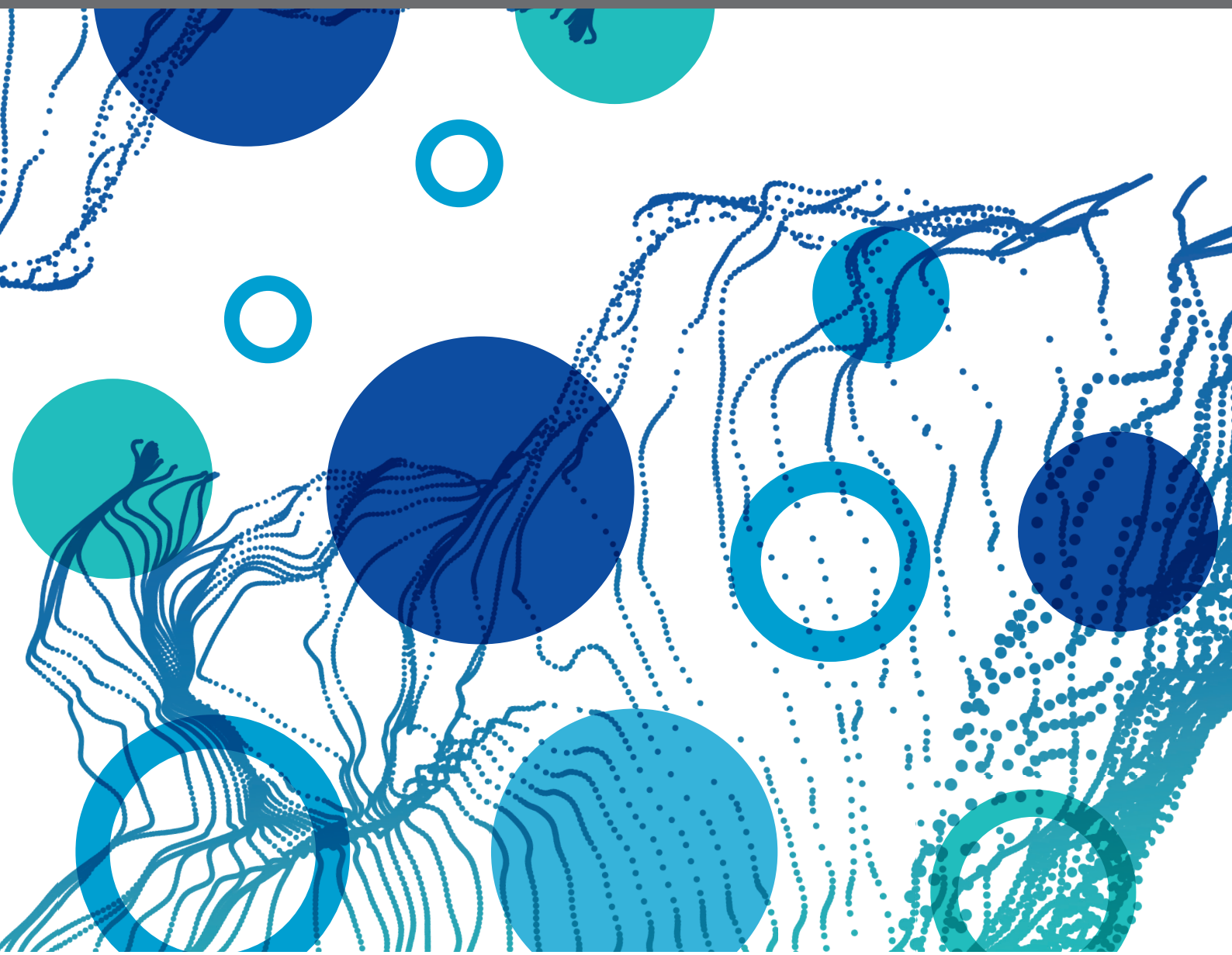

frontiers Research Topics

ISSN 1664-8714
ISBN 978-2-88971-074-4
DOI 10.3389/978-2-88971-074-4

About Frontiers

Frontiers is more than just an open-access publisher of scholarly articles: it is a pioneering approach to the world of academia, radically improving the way scholarly research is managed. The grand vision of Frontiers is a world where all people have an equal opportunity to seek, share and generate knowledge. Frontiers provides immediate and permanent online open access to all its publications, but this alone is not enough to realize our grand goals.

Frontiers Journal Series

The Frontiers Journal Series is a multi-tier and interdisciplinary set of open-access, online journals, promising a paradigm shift from the current review, selection and dissemination processes in academic publishing. All Frontiers journals are driven by researchers for researchers; therefore, they constitute a service to the scholarly community. At the same time, the Frontiers Journal Series operates on a revolutionary invention, the tiered publishing system, initially addressing specific communities of scholars, and gradually climbing up to broader public understanding, thus serving the interests of the lay society, too.

Dedication to Quality

Each Frontiers article is a landmark of the highest quality, thanks to genuinely collaborative interactions between authors and review editors, who include some of the world's best academicians. Research must be certified by peers before entering a stream of knowledge that may eventually reach the public - and shape society; therefore, Frontiers only applies the most rigorous and unbiased reviews.
Frontiers revolutionizes research publishing by freely delivering the most outstanding research, evaluated with no bias from both the academic and social point of view. By applying the most advanced information technologies, Frontiers is catapulting scholarly publishing into a new generation.

What are Frontiers Research Topics?

Frontiers Research Topics are very popular trademarks of the Frontiers Journals Series: they are collections of at least ten articles, all centered on a particular subject. With their unique mix of varied contributions from Original Research to Review Articles, Frontiers Research Topics unify the most influential researchers, the latest key findings and historical advances in a hot research area! Find out more on how to host your own Frontiers Research Topic or contribute to one as an author by contacting the Frontiers Editorial Office: frontiersin.org/about/contact

LINKING HYDROLOGICAL AND BIOGEOCHEMICAL PROCESSES IN RIPARIAN CORRIDORS

Topic Editors:
Dipankar Dwivedi, Lawrence Berkeley National Laboratory, United States
Sarah E. Godsey, Idaho State University, United States
Tim Scheibe, Pacific Northwest National Laboratory (DOE), United States

Citation: Dwivedi, D., Godsey, S. E., Scheibe, T., eds. (2021). Linking Hydrological and Biogeochemical Processes in Riparian Corridors. Lausanne: Frontiers Media SA. doi: 10.3389/978-2-88971-074-4

Table of Contents

frontiers in Water

EDITORIAL
published: 26 May 2021
doi: 10.3389/frwa.2021.693763

Editorial: Linking Hydrological and Biogeochemical Processes in Riparian Corridors

Dipankar Dwivedi[1]*, *Sarah E. Godsey*[2] *and Timothy D. Scheibe*[3]

[1] *Lawrence Berkeley National Laboratory, Berkeley, CA, United States,* [2] *Department of Geosciences, Idaho State University, Pocatello, ID, United States,* [3] *Pacific Northwest National Laboratory, Richland, WA, United States*

Keywords: riparian corridors, hydrobiogeochemical process, hydrologic connectivity, hydrologic exchange flows, C-Q hysteresis loops

Editorial on the Research Topic

Linking Hydrological and Biogeochemical Processes in Riparian Corridors

The riparian corridor is a key component of the critical zone and an essential component of watershed systems. According to Merriam-Webster Dictionary, the word riparian is derived from the Latin word *riparius*, meaning "existing alongside a river." Riparian corridors typically extend from a few meters to hundreds of meters adjacent to a river and are marked by rich biodiversity, vegetation, and intense biogeochemical activity. They act as integrators of watershed processes and constitute the primary pathways for the subsurface geochemical exports from the watershed. Although riparian corridors comprise only 2–10% of a watershed's area, as much as 90–98% of biogeochemical processing in watersheds occurs in this region, thereby affecting the subsurface geochemical exports and downstream river water quality. Indeed, the riparian corridor is a good example of the Pareto principle (e.g., Dwivedi et al., 2018a; McClain et al., 2003; Bernhardt et al., 2017). This outsized contribution occurs at the interface between aquatic (river) and terrestrial (land) environments, where interactions between hydrologic and biogeochemical processes are intensified. Variations in the river corridor over time can thus also have outsize impacts. Therefore, it is important to understand the hydrological and biogeochemical linkages in riparian corridors to determine water availability and quality for sustainable management.

Riparian corridors include various subsystems, such as hyporheic zones, meanders, wetlands, and lagoons, all of which impact river water quality (**Figure 1**). These subsystems demonstrate distinct biogeochemical potential depending upon their hydrologic connectivity to the main channel. However, several hurdles must be overcome to improve the predictive capability of riparian corridor processes across scales. This Research Topic aimed to enhance our understanding and predictive capability related to linked hydrological and biogeochemical processes in riparian corridors. We received contributions across a wide spectrum of topics, including hydrologic exchange and river connectivity as well as geochemical exports of carbon, nitrogen, colloids, and microbial dynamics (**Figure 2**). These topics also involved novel method development, new observational networks, advanced mechanistic modeling, and the use of artificial intelligence and machine learning approaches. Below, we briefly synthesize these contributions under two groups focused on dynamic hydrologic connectivity and microbial and physical controls on spatial patterns in river corridors.

OPEN ACCESS

Edited and reviewed by:
Carl I. Steefel, Lawrence Berkeley National Laboratory, United States

***Correspondence:**
Dipankar Dwivedi
ddwivedi@lbl.gov

Specialty section:
This article was submitted to Water and Critical Zone, a section of the journal Frontiers in Water

Received: *12 April 2021*
Accepted: *03 May 2021*
Published: *26 May 2021*

Citation:
Dwivedi D, Godsey SE and Scheibe TD (2021) Editorial: Linking Hydrological and Biogeochemical Processes in Riparian Corridors. Front. Water 3:693763. doi: 10.3389/frwa.2021.693763

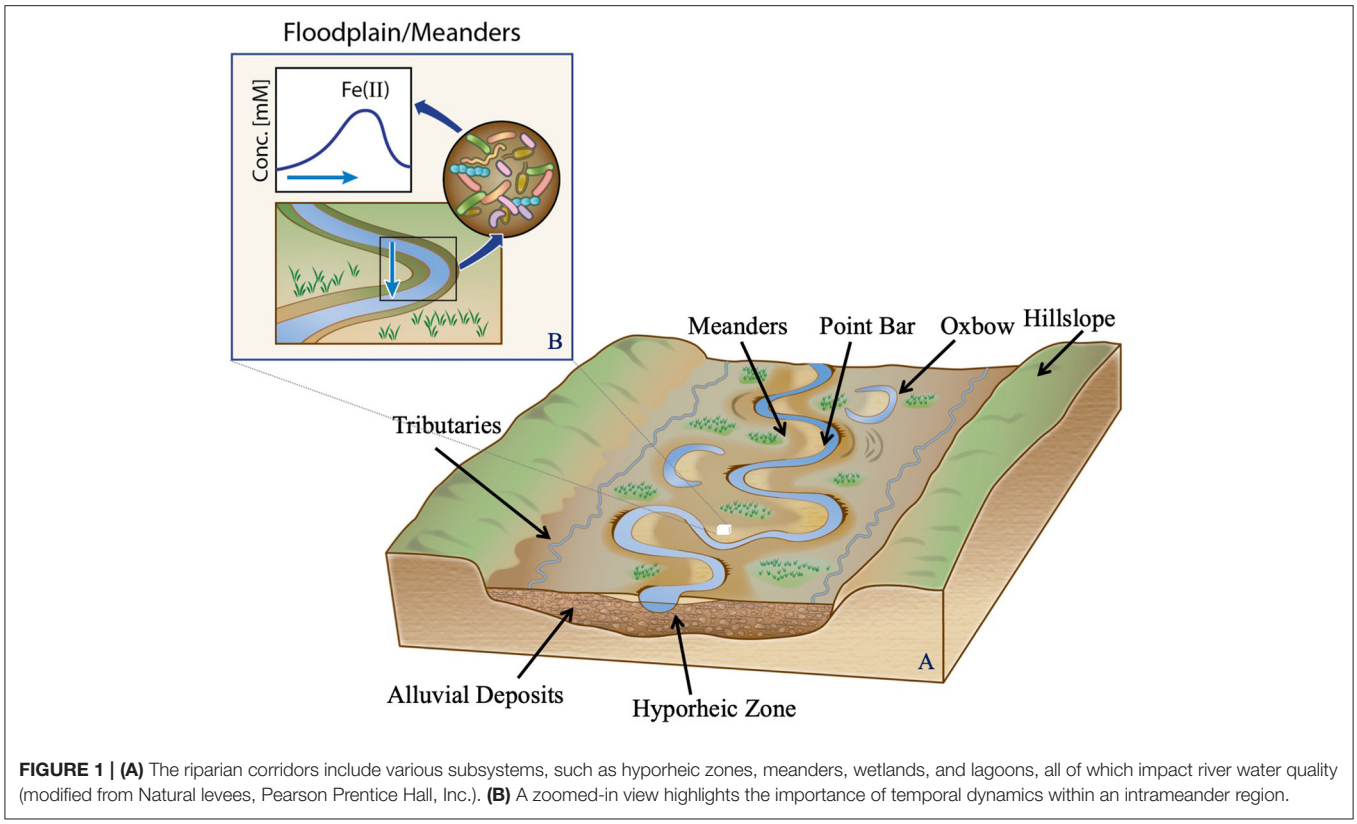

FIGURE 1 | (A) The riparian corridors include various subsystems, such as hyporheic zones, meanders, wetlands, and lagoons, all of which impact river water quality (modified from Natural levees, Pearson Prentice Hall, Inc.). **(B)** A zoomed-in view highlights the importance of temporal dynamics within an intrameander region.

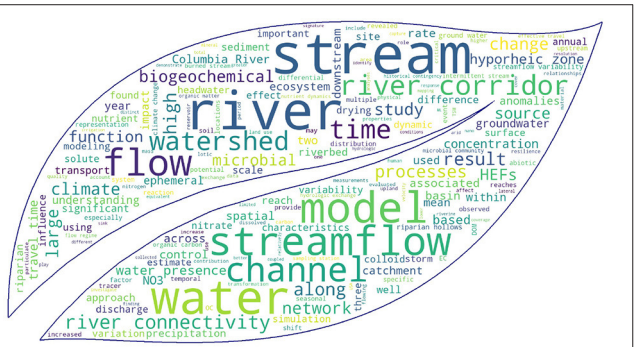

FIGURE 2 | Linking hydrological and biogeochemical processes in riparian corridors include a wide spectrum of topics, such as hydrologic exchange and river connectivity, geochemical exports, and microbial dynamics addressing critical gaps in our understanding of changes in river corridors over different spatial and temporal scales.

1. DYNAMIC HYDROLOGIC CONNECTIVITY

Hydrologic connectivity is a primary factor leading to high biogeochemical activity in riparian corridors. River water and its chemical and biological constituents are critical to the growth and metabolic function of plants, microbes, and other organisms.

One important aspect of hydrologic connectivity relates to intermittent and ephemeral streams, which exhibit disconnected surface flows during drought periods as sections of a river network dry up. Based on a statistical analysis of gauge data and a reduced-complexity heuristic model parameterized using data readily available in unstudied catchments, Ward et al. quantified the impacts of climate change on river channel connectivity in a mountainous fifth-order river basin in the United States (U.S.) Pacific Northwest. They found that not only are headwater streamflows generally decreasing, especially during low-flow periods, but river connectivity is also being reduced through decreases in flow permanence. They noted that increasing flow impermanence under climate change affects connectivity and associated biogeochemical functions as well as regulatory protections that may be afforded only to permanent streams. Temporal patterns of surface water and soil moisture, along with the related hydrologic connectivity, also vary across spatial gradients in climate, but there may be limits to past categorization of streamflow patterns as "perennial" and "non-perennial" (Busch et al., 2020). Gallo et al. combined electrical resistivity sensors with available stream gauge data to identify five distinct flow regimes in southern Arizona streams: (1) dry ephemeral, (2) wet ephemeral, (3) dry intermittent, (4) wet intermittent, and (5) seasonally intermittent. This new classification approach was based not only on streamflow, but also on water presence in ponds or soils, which may be needed to better predict ecological function in dryland systems. Nutrient cycling is one such function of riparian ecosystems; Lohse et al. investigated the impact of climate change and fluctuating streamflow regimes on litter decomposition and subsequent

nutrient dynamics in ephemeral and intermittent streams. They found that climatic conditions do not affect litter decay rates in upland and riparian positions and that flow duration is a better indicator of ephemeral and intermittent stream function than streamflow alone. MacNeille et al. considered the compounding effects of wildfire and stream drying in intermittent stream networks. In spatiotemporal studies of two catchments that experienced partial drying of the stream networks, one of which had been burned, they observed similar temporal patterns in hydrologic and biogeochemical processes, with the primary difference being a sharp decrease in total nitrogen in the burned catchment streams during the drying period.

On the other end of the spectrum from drying streams is the role of lentic (ponded) water bodies in expanding the riparian corridor. Harvey and Schmadel used a new high-resolution conterminous U.S. (CONUS)-wide dataset to investigate the relative contribution of lotic (flowing) and lentic (ponded) waters to river networks at continental scales. They found that the character of river corridors has varied widely over four centuries of human disturbance, including reservoir construction and beaver extirpation, which have led to a two to four times increase in water residence times in the 20th century, which in turn can affect water quality. Konrad et al. demonstrated that it is also necessary to account for the temporal variability of streamflow when estimating residence or travel times through the stream network. They developed a statistical approach to quantify flowpath travel times to steams and inferred that streamflow variability is the main control of regional- to continental-scale variation in stream travel times.

One key reason that accounting for streamflow variability is important is hydrologic exchange flows (HEFs), which are the dynamic two-way exchanges of water between the flowing river channel and subsurface and other relatively slow-moving environments. HEFs affect residence times and biogeochemical reactions that control how nutrients, including carbon and nitrogen, are retained, released, and transformed within the riparian corridor. HEFs vary significantly in space and time depending on several factors, such as river-stage, riverbed morphology, and hydraulic conductivity. However, measurements of HEFs at the watershed scale are non-trivial; they can be indirectly measured using high-frequency temperature and electrical conductivity along the bed of the river (Conner et al.). Alternatively, high-resolution, three-dimensional reactive transport models can be advantageous for accurately quantifying HEFs but require detailed parameterization of spatially heterogeneous properties. Although sediment grain-size distribution can be used as a proxy to derive the spatial distribution of hydraulic properties, sediment grain-size measurements are typically spatially sparse. Ren et al. developed a novel method using machine learning (ML) to categorize and map the spatial distributions of riverbed substrate grain size in the Hanford Reach located in the Columbia River Basin. Representing the effects of spatial heterogeneity of physical properties along a river enables high-resolution numerical models to appropriately capture residence times and HEFs. However, such models may currently be computationally prohibitive over large spatial domains. Fang et al. compared a surrogate model (transient storage model) with high-resolution simulations of reactive transport in a 20-kilometer reach of the mainstem Columbia River and identified strengths and weaknesses of the surrogate approach.

Painter studied two alternative representations of HEFs and solute transport: (1) a stochastic Lagrangian travel time model of advective pumping and (2) a multirate diffusive exchange model. Although both representations produced comparable results for conservative tracers, they predicted significantly different results for reactive species. The multirate diffusive exchange model assumes that each transient storage zone is connected with the channel and well-mixed. Consequently, transient storage zones do not undergo anoxic conditions and fail to represent redox zonation adequately. The advective pumping model representing only one-dimensional flowpaths through the hyporheic zone is not suitable for complex geometries. Painter suggested combining diffusion- and advection-based conceptualization to accurately capture multiscale reactive transport in river corridors.

2. HYDROLOGICAL AND MICROBIAL CONTROLS ON SPATIAL PATTERNS IN RIVER CORRIDORS

Efforts to understand riparian connectivity and associated ecological function, such as those described above, are aimed at significantly advancing the predictive understanding of geochemical exports at watershed and basin scales. These depend strongly on the biogeochemical processes that are tightly related to hydrologic connectivity. For example, Bicknell et al. demonstrated that hydrologic connectivity-in this case, between a stream and its tributaries along with man-made delivery and drain canals-could be exploited to mitigate nutrient loads. Different connected channels seasonally act as either nutrient sources or sinks, so they can be managed to meet societal needs and reduce nutrient loads. Both connected channels and microtopographic features, such as riparian hollows, located along the sides of a river, can act as a source or sink of reactive chemical species and have an outsized impact on river chemistry. Working in the mountainous headwater East River Colorado watershed, Rogers et al. explored the effects of riparian hollows as N-cycling hotspots and as critical small-scale controls on watershed-scale trends. Indeed they found that groundwater upwelling limits N transformations which suggests that even though riparian hollows are key nitrate sources, they are also the main inhibitors of nitrate delivery at the watershed scale. For the same watershed, Arora et al. developed a differential C-Q approach to characterize spatial variability in solute behavior across stations, as well as investigate their controls, by following a different spatial scheme and organizing the river into multiple sections. Using water quality data collected over four water years (2015–2018) in the East River in Colorado, they compared traditional and differential C-Q relationships in predicting solute behavior among three sampling stations distributed throughout the river. The new differential C-Q approach performed just as well as the traditional approach but allowed for source

apportionment and the identification of critical stream segments that assimilate chemicals like nitrate and phosphate.

Source apportionment, which is important for advancing the predictive understanding of geochemical exports across the spatial scale, is a complex mechanism comprising several factors. For instance, biotic (e.g., microbial dynamics) and abiotic (e.g., mineral association, sunlight) processes exert significant controls on solute transport and transformation within multiple reaches in a river corridor. Furthermore, storm and peak discharge events introduce notable spatio-temporal variability in solute concentrations. Using storm-induced variations of biomarkers at three sampling stations, Kim et al. characterized particulate organic carbon sources in Clear Creek in Iowa. They found that fatty acid-rich organic matter mobilizes algal mats in the stream channel at the storm's early stage when water velocities begin to increase and that understanding complex, storm-driven transport requires high-resolution tracer information in both space and time. Rod et al. compared the coupled relationships between soil organic matter and minerals using batch and column leaching experiments under aerobic and anaerobic conditions and applying multiple imaging and analytical techniques. Using two riparian sediments—namely, Columbia River in Washington and Tims Branch in South Carolina—they characterized natural organic carbon fraction associated with mineral nano-colloids (1–100nm), small colloids (<450nm), and other particles (<1,000nm) and found that the dispersible colloids facilitate the release of organic carbon.

Although organic carbon drives redox processes in the riparian corridors, accounting for the biotic and abiotic chemical transformation of organic matter is equally important to enhance predictive understanding of watershed processes. For example, Fudyma et al. characterized organic matter in the hyporheic zone of the Columbia River using high-resolution Fourier-transform ion cyclotron resonance mass spectrometry. They inferred that the abiotic degradation of organic matter, potentially driven by sunlight, can increase dissolved organic matter's availability to the hyporheic zone, which should be represented in predictive models to account for microbial activity adequately and enhance understanding of watershed dynamics. Furthermore, they concluded that the hyporheic zone is metabolically active irrespective of the river-stage. However, riverine microbial communities are shaped by the local environment, including climate, geomorphology, land cover, and anthropogenic activities in a watershed, and can help monitor relevant upstream characteristics. Song et al. linked the history of river-stage or groundwater fluctuations (or historical contingency) with the shifts in microbial community and, thereby, with specific microbial activity. They further demonstrated that the historical contingency was more pronounced for specialized functions associated with individual species than the community functions (i.e., functional redundancy) where one species could substitute for another. URycki et al. exploited knowledge of the evolution of riverine microbial communities and their relationship with upstream macroscale conditions and hydrology. They assessed the correlation between microbial community composition and 40 basin characteristics reflecting the geomorphology, climate, land cover, and level of human development in stream catchments. They found differing degrees of correlation with basin size, suggesting opportunities still remain to better understand the heterogeneity of river corridor microbial communities and their impact on water quality.

3. CONCLUDING REMARKS

Over the past several decades, the complexity of rivers and their adjacent environments and the important roles that they play in watershed function have been increasingly recognized (Harvey and Gooseff, 2015; Chen et al., 2020; Dwivedi et al., 2018b). The large number of contributions to this Research Topic reflect continued high interest in understanding and quantifying the interactions between hydrological, microbial, and biogeochemical processes that underlie ecological health and water quality in these critical systems across spatiotemporal scales. It is particularly encouraging to see that hydrological connectivity has received considerable attention in this Research Topic to unravel the conundrum of high biogeochemical activity in riparian corridors. However, it is important to realize that there is no consensus about the definition of hydrological connectivity across fields (e.g., Wohl et al., 2019; Bracken et al., 2015; Wainwright et al., 2011; Singh and Sinha, 2019). Further, we need to acknowledge the wide range of complexity of dynamic hydrological connectivity appropriately to enhance process understanding of riparian corridors. Finally, we expect that emerging technologies, radical collaboration, new constructs, and open science principles (e.g., Hubbard et al., 2020; Arora et al., 2019) will keep transforming predictive capabilities of hydrobiogeochemical behavior of riparian corridors.

AUTHOR CONTRIBUTIONS

All authors listed have made a substantial, direct and intellectual contribution to the work, and approved it for publication.

FUNDING

DD was supported in part by the Watershed Function Science Focus Area and ExaSheds projects at Lawrence Berkeley National Laboratory funded by the U.S. Department of Energy, Office of Science, and Biological and Environmental Research under Contract No. DE-AC02-05CH11231. SG was supported in part by NSF EAR 1653998 and RC CZO Coop Agreement EAR 1331872. TS was supported by the River Corridor Science Focus Area project at Pacific Northwest National Laboratory funded by the U.S. Department of Energy, Office of Biological and Environmental Research, and Environmental System Science program.

ACKNOWLEDGMENTS

We thank Diana Swantek of Berkeley Lab for assistance with preparing **Figure 1**.

REFERENCES

Arora, B., Dwivedi, D., Faybishenko, B., Jana, R. B., and Wainwright, H. M. (2019). Understanding and predicting vadose zone processes. *Rev. Mineral. Geochem.* 85, 303–328. doi: 10.2138/mg.2019.85.10

Bernhardt, E. S., Blaszczak, J. R., Ficken, C. D., Fork, M. L., Kaiser, K. E., and Seybold, E. C. (2017). Control points in ecosystems: moving beyond the hot spot hot moment concept. *Ecosystems* 20, 665–682. doi: 10.1007/s10021-016-0103-y

Bracken, L. J., Turnbull, L., Wainwright, J., and Bogaart, P. (2015). Sediment connectivity: a framework for understanding sediment transfer at multiple scales. *Earth Surf. Process. Landf.* 40, 177–188. doi: 10.1002/esp.3635

Busch, M. H., Costigan, K. H., Fritz, K. M., Datry, T., Krabbenhoft, C. A., Hammond, J. C., et al. (2020). What's in a name? Patterns, trends, and suggestions for defining non-perennial rivers and streams. *Water* 12:1980. doi: 10.3390/w12071980

Chen, X., Lee, R. M., Dwivedi, D., Son, K., Fang, Y., Zhang, X., et al. (2020). Integrating field observations and process-based modeling to predict watershed water quality under environmental perturbations. *J. Hydrol.* 125762. doi: 10.1016/j.jhydrol.2020.125762

Dwivedi, D., Arora, B., Steefel, C. I., Dafflon, B., and Versteeg, R. (2018a). Hot spots and hot moments of nitrogen in a riparian corridor. *Water Resour. Res.* 54, 205–222. doi: 10.1002/2017WR022346

Dwivedi, D., Steefel, C. I., Arora, B., Newcomer, M., Moulton, J. D., Dafflon, B., et al. (2018b). Geochemical exports to river from the intrameander hyporheic zone under transient hydrologic conditions: East River Mountainous Watershed, Colorado. *Water Resour. Res.* 54, 8456–8477. doi: 10.1029/2018WR023377

Harvey, J., and Gooseff, M. (2015). River corridor science: hydrologic exchange and ecological consequences from bedforms to basins. *Water Resour. Res.* 51, 6893–6922. doi: 10.1002/2015WR017617

Hubbard, S. S., Varadharajan, C., Wu, Y., Wainwright, H., and Dwivedi, D. (2020). Emerging technologies and radical collaboration to advance predictive understanding of watershed hydrobiogeochemistry. *Hydrol. Process.* 34, 3175–3182. doi: 10.1002/hyp.13807

McClain, M. E., Boyer, E. W., Dent, C. L., Gergel, S. E., Grimm, N. B., Groffman, P. M., et al. (2003). Biogeochemical hot spots and hot moments at the interface of terrestrial and aquatic ecosystems. *Ecosystems* 6, 301–312. doi: 10.1007/s10021-003-0161-9

Singh, M., and Sinha, R. (2019). Evaluating dynamic hydrological connectivity of a floodplain wetland in north Bihar, India using geostatistical methods. *Sci. Total Environ.* 651, 2473–2488. doi: 10.1016/j.scitotenv.2018.10.139

Wainwright, J., Turnbull, L., Ibrahim, T. G., Lexartza-Artza, I., Thornton, S. F., and Brazier, R. E. (2011). Linking environmental regimes, space and time: Interpretations of structural and functional connectivity. *Geomorphology* 126, 387–404. doi: 10.1016/j.geomorph.2010.07.027

Wohl, E., Brierley, G., Cadol, D., Coulthard, T. J., Covino, T., Fryirs, K. A., et al. (2019). Connectivity as an emergent property of geomorphic systems. *Earth Surf. Process. Landf.* 44, 4–26. doi: 10.1002/esp.4434

Conflict of Interest: The authors declare that the research was conducted in the absence of any commercial or financial relationships that could be construed as a potential conflict of interest.

frontiers in Water

ORIGINAL RESEARCH
published: 23 April 2020
doi: 10.3389/frwa.2020.00007

Climate Change Causes River Network Contraction and Disconnection in the H.J. Andrews Experimental Forest, Oregon, USA

Adam S. Ward[1]*, *Steven M. Wondzell*[2], *Noah M. Schmadel*[3] and *Skuyler P. Herzog*[1]

[1] O'Neill School of Public and Environmental Affairs, Indiana University, Bloomington, IN, United States, [2] Pacific Northwest Research Station, U. S. Forest Service, Corvallis, OR, United States, [3] U.S. Geological Survey, Reston, VA, United States

Headwater streams account for more than 89% of global river networks and provide numerous ecosystem services that benefit downstream ecosystems and human water uses. It has been established that changes in climate have shifted the timing and magnitude of observed precipitation, which, at specific gages, have been directly linked to long-term reductions in large river discharge. However, climate impacts on ungaged headwater streams, where ecosystem function is tightly coupled to flow permanence along the river corridor, remain unknown due to the lack of data sets and ability to model and predict flow permanence. We analyzed a network of 10 gages with 38–69 years of records across a 5th-order river basin in the U.S. Pacific Northwest, finding increasing frequency of lower low-flow conditions across the basin. Next, we simulated river network expansion and contraction for a 65-year period of record, revealing 24% and 9% declines in flowing and contiguous network length, respectively, during the driest months of the year. This study is the first to mechanistically simulate network expansion and contraction at the scale of a large river basin, informing if and how climate change is altering connectivity along river networks. While the heuristic model presented here yields basin-specific conclusions, this approach is generalizable and transferable to the study of other large river basins. Finally, we interpret our model results in the context of regulations based on flow permanence, demonstrating the complications of static regulatory definitions in the face of non-stationary climate.

Keywords: river corridor, river network, intermittent, ephemeral, stream, hyporheic, climate

OPEN ACCESS

Edited by:
Dipankar Dwivedi, Lawrence Berkeley National Laboratory, United States

Reviewed by:
Heather E. Golden, United States Environmental Protection Agency, United States
Zexuan Xu, Lawrence Berkeley National Laboratory, United States

***Correspondence:**
Adam S. Ward
adamward@indiana.edu

Specialty section:
This article was submitted to Water and Critical Zone, a section of the journal Frontiers in Water

Received: *02 January 2020*
Accepted: *20 March 2020*
Published: *23 April 2020*

Citation:
Ward AS, Wondzell SM, Schmadel NM and Herzog SP (2020) Climate Change Causes River Network Contraction and Disconnection in the H.J. Andrews Experimental Forest, Oregon, USA. Front. Water 2:7. doi: 10.3389/frwa.2020.00007

INTRODUCTION

More than 89% of the global river network is headwaters (Downing et al., 2012; Allen et al., 2018), supporting ecosystem services and the health of downstream waters (Alexander et al., 2007; US EPA, 2015). These services are associated with the frequency with which streams have surface flow (hereafter "flow permanence"), and any declines in flow permanence will effectively disconnect larger rivers from their headwaters and their functions. Flow generated in headwater streams is highly sensitive to changes in precipitation timing, magnitude, and duration based on a small

number of empirical studies over short timescales (Godsey and Kirchner, 2014; Jensen et al., 2017; Zimmer and McGlynn, 2017; Prancevic and Kirchner, 2019). However, no observational studies have covered a sufficient period of record to evaluate if and how changing climate has altered flow permanence across river networks. Consequently, numerical simulations parameterized with readily available data are needed to fill this knowledge gap (Gallart et al., 2016; Ward et al., 2018a).

Changes in flow permanence can alter the transport and transformation of water, energy, dissolved and suspended materials, and organisms throughout the river network (Larned et al., 2010; Gallart et al., 2012; Steward et al., 2012; Datry et al., 2016, 2017; Raymond et al., 2016). Evaluating how flow permanence has changed requires quantification of both the temporal variation (i.e., the frequency a given segment has surface flow) and spatial variation (i.e., the spatial connectivity of surface flow) (Covino, 2017; Wohl, 2017; Wohl et al., 2017). In headwater streams, flow permanence is controlled by the dynamic interaction of geologic setting with hydrologic forcing (Costigan et al., 2016; Prancevic and Kirchner, 2019). Climate change is primarily associated with changes to hydrologic forcing, such as altering the spatial distribution and within-year timing of precipitation. Geologic setting—such as valley width and slope, sinuosity, and hydraulic conductivity—will remain relatively static compared to the pace of climate change.

Changes in flow permanence complicate management and protection of headwater streams. Regulatory protections in the U.S. and E.U. are traditionally focused on perennially flowing waters, with emerging attention paid to temporarily flowing waters (US DoD, 1986; Nikolaidis et al., 2013; US DoD EPA, 2015; Fritz et al., 2018; US DoD US EPA, 2018; Walsh and Ward, 2019). Further complicating management, data on headwater streams, and particularly intermittent and ephemeral streams, are lacking. For example, only 3% of the rivers gaged in the U.S. are headwater streams, as gages are heavily biased toward larger rivers (Poff et al., 2006; Eng and Milly, 2007). A proposed rule would revise protected status to waters with contiguous surface flow in a "typical" 30-year period in the U.S., but does not address systematic changes in flow permanence (US DoD US EPA, 2018). The time-variable definition of the 30-year window does not consider the role of climate change and shifting norms, despite clear evidence that non-stationarity is prevalent in hydrologic systems (Milly et al., 2008). For example, systematic declines in streamflow, and particularly lower low-flows, have been observed across the U.S. Pacific Northwest (Luce and Holden, 2009). Subsequent study revealed that slowing westerlies during winter months reduced the orographic enhancement of precipitation in the region, changing both the amount of precipitation reaching the landscape and the timing for storage vs. export from catchments (Luce et al., 2013). A more recent example paints another dire picture for the future of streamflow in the Southwestern U.S. in response to shifting precipitation and temperature (Milly and Dunne, 2020).

Here we assess whether flow permanence in headwater streams has shifted over the past 65 years from the mid twentieth century baseline in response to observed changes in climate-driven hydrologic forcing. We investigate how timing and magnitude of discharge have shifted over a 65-yr period of record and yielded changes in flow permanence along mountain stream networks. Finally, we consider how our findings may inform current and future protections for streams under the proposed Waters of the U.S. (WOTUS) Rule (US DoD US EPA, 2018) and subsequently finalized in the Navigable Waters Protection Rule (US DoD US EPA, 2019). We selected the 5th-order Lookout Creek basin (Western Cascade Mountains, Oregon, USA) because of the extensive and long-term network of gages on low-order streams (**Table S2**). Furthermore, this basin is representative of the broader Pacific Northwest where climate change impacts on the timing and magnitude of moisture delivery to high elevation watersheds are known to cause declines in large rivers (Luce and Holden, 2009; Luce et al., 2013). Thus, reduced orographic enhancement of precipitation due to climate change is projected at the field site. This study considers the cascading impact of this change on stream discharge, and how discharge changes in headwaters may change flow permanence and connectivity in a river network.

METHODS

Site Description and Available Data

The study was conducted at the H.J. Andrews Experimental Forest (HJA), a 5th-order basin in the Western Cascades, Oregon, USA (site map in **Figure S1**). The basin drains about 6,400 ha of forested landscape, with elevations ranging from about 410–1,630 m a.m.s.l, making it an ideal place to evaluate the impact of a changing climate on river networks of the broader Pacific Northwest. The basin has been a long-term study site for ecological and forest management research for more than 70 years and is relatively pristine with no urban land use, no dams or reservoirs, and minimal logging during the period of this study. At the longest currently operating meteorological station (CS2MET, elev. 485 m a.m.s.l.) annual precipitation averages 2,345 mm and average annual air temperature is 9.2 deg. C. Additional summaries of temperature and precipitation including trends for the period of record for each station are summarized in **Table S1** and **Figures S2–S15**). In general, significant trends in monthly precipitation and air temperature are infrequently detected, due largely to the short observational records at the local meteorological network (**Table S1**). Further details about the local climate, morphology, geology, and ecology are comprehensively described elsewhere (Dyrness, 1969; Swanson and James, 1975; Swanson and Jones, 2001; Jefferson et al., 2004; Cashman et al., 2009; Deligne et al., 2017).

The HJA includes a network of 10 stream gages with drainage areas ranging from 8.5 to 6,241.9 ha, with records of 38–69 years of data across the gage network (**Table S2**). Additionally, a high quality digital elevation model derived from an airborne LiDAR survey is available for the entire basin, which has been reliably processed to extract topographic metrics including valley width, valley slope, and stream sinuosity (after Corson-Rikert et al., 2016; Schmadel et al., 2017; Ward et al., 2018a,b). For each gage we also calculated annual summary metrics of discharge including annual minimum discharge, mean discharge, maximum discharge, exceedance discharges (1, 5, 10, 25, 50, 75,

90, 95, 99th percentiles), total annual discharge, and the days elapsed to various cumulative fractions of discharge (1, 5, 10, 25, 50, 75, 90, 95, 99%).

Finally, an extensive data collection effort spanning the stream orders and lithologic regions of the basin was completed in 2015, providing a database of stream and valley morphologies and hydraulic conductivities to inform network-scale model parameterization (Ward et al., 2019b).

Simulation of the River Network

Simulation of network expansion and contraction followed the methods, data sources, and implementation described by Ward et al. (2018a). Briefly, the approach conceptualizes the river corridor in 1-D along the valley, with domains representing the surface stream and down-valley flow in the valley bottom. Critically, the down-valley subsurface flow (or "underflow") is filled first, with surface flow representing only the volumetric flow in excess of what the valley bottom can transmit downstream (**Figure 1**). Put another way, surface flow occurs only when the valley's subsurface cannot accommodate all of the down-valley discharge.

Ward et al. (2018a) validated the model in a 2nd order catchment within our study basin, concluding the model was appropriate to represent network expansion and contraction based on correct prediction of flowing or dry streambed conditions for more than 95% of over 3.2 million observations. We proceed with implementation of this model across a 5th order basin on the basis of Ward's et al. (2018a) success within our study basin, particularly given the accuracy in representing network expansion and contraction in response to diurnal fluctuations driven by evapotranspiration, storms, and seasonal baseflow.

The model was intentionally derived and constructed to require geomorphic and hydrologic data that are readily estimated for unstudied catchments (Ward et al., 2018a), consistent with our application in this study. Valley width, valley slope, along-stream slope, sinuosity, and the lateral contributing area for each 10-m segment of the valley bottom were extracted from the LiDAR data using a modified version of the TopoToolbox (Schwanghart and Kuhn, 2010; Schwanghart and Scherler, 2014; Schmadel et al., 2017). Stream width at each location was estimated using a power-law regression of 62 observations collected in August 2015 (Ward et al., 2019b) as:

$$b = 0.003926^{*} UAA^{0.4488}$$

where b is the width of the channel (m) and UAA is the total drainage area (ha), and the best-fit relationship had a coefficient of determination of 0.84. We assigned a uniform Manning's n of 0.045 along the entire network based on visual inspection while working in the basin. Ward et al. (2018a) identified hydraulic conductivity as the largest source of uncertainty in the model. In response, we measured hydraulic conductivity of the streambed at 57 sites in August 2015 (Ward et al., 2019b) and assigned the geometric mean, 1.53×10^{-4} m s^{-1}, across the network. Porosity was assigned as 0.3 at all locations, the midpoint of past studies (Dyrness, 1969; Kasahara and Wondzell, 2003; Wondzell et al., 2009; Ward et al., 2017) and the same value used in model validation (Ward et al., 2018a). We set valley colluvium depth to a minimum value of 1-m (Gooseff et al., 2006; Ward et al., 2018a),

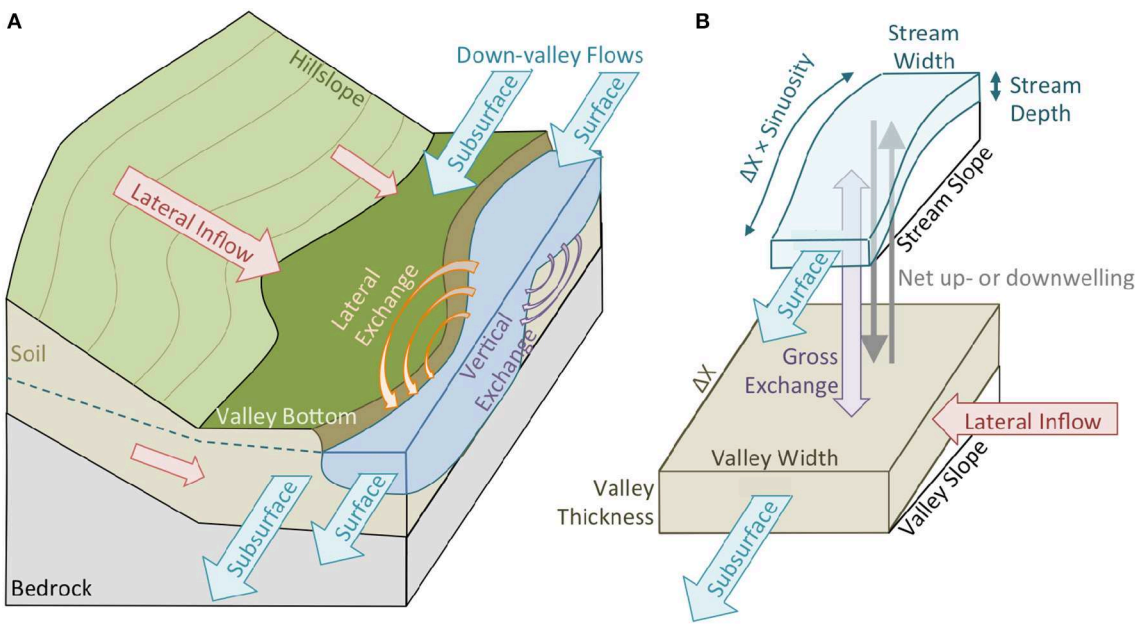

FIGURE 1 | (A) Perceptual model of river corridor exchange showing the inflows and outflows considered in the model. **(B)** Representation of stores, fluxes, and key variables used in the model implementation. The key advance of this model is the representation of the river corridor as parallel transport in the subsurface and surface domains, with surface flow only activating when the subsurface cannot accommodate all down-valley flow. Reprinted with permission from Ward et al. (2018a).

increasing as:

$$h = 1 + 0.01w$$

where h is colluvium depth (m) and w is valley width (m). This functional form was selected to reflect the limited measurements of subsurface colluvium depth that are available, including geophysical observations at several headwater locations (Crook et al., 2008; Ward et al., 2012) and along the 5th order reach of Lookout Creek (*Wondzell*, personal communication, and unpublished data).

To parameterize the total down-valley discharge at the upstream end of each 1st order segment, we calculated a unique power-law regression for the gage discharge and drainage area for each 15-min timestep simulated, and defined the discharge based on *UAA*. Thus, all available gage data, and their time variation, informed the upstream boundaries for model headwaters. Lateral inflows for each segment were estimated using the same power-law regression, where the change in UAA between the up- and downstream end of each segment was used to calculate the associated change in discharge attributed to the lateral area (Schmadel et al., 2017; Ward et al., 2018a,b). Finally, we used the threshold of at least 2.21×10^{-4} m^3 s^{-1} to differentiate surface flow from dry streambeds after past studies in the basin (Ward et al., 2018a).

Consistent with Ward et al. (2018a), we underscore that reduced complexity models are intended to represent the dominant mechanisms and interactions in a system of interest. This necessarily comes at the expense of representation of complexity and heterogeneity within the system. While our model has been derived and validated for headwaters within the study basin, the parameterization detailed above requires simplifications. To that end, this model is most appropriately viewed as heuristic, consistent with common practice in the study of river corridors (e.g., Gooseff et al., 2006; Cardenas and Wilson, 2007; Trauth et al., 2013; Irvine and Lautz, 2015; Schmadel et al., 2016, 2017). At the scale of river networks, comparable models have been applied to study patterns and trends at large spatial scales at the expense of site-specific localized predictions (e.g., Gomez-Velez and Harvey, 2014; Kiel and Cardenas, 2014; Gomez-Velez et al., 2015; Schmadel et al., 2018). Thus, given the model's strong performance at the reach-scale within our study basin (Ward et al., 2018a), explicit design as a heuristic that can be implemented at minimally studied sites, the wealth of data available across our network, and the tradition of heuristic models to test hypotheses in river corridor science, we proceed with this approach.

Statistical Tests

All between-group differences were tested using one-way ANOVA, Kruskal-Wallis, and Mann-Whitney-Wilcoxson U tests. We report differences as significant only if $p < 0.05$ for all three tests.

For all trends in discharge metrics, flowing frequency, contiguous frequency, flowing length, and contiguous length, we used Mann-Kendall tests and Sen's slopes to define the significance and direction of trends. Decreasing trends are reported for $p < 0.05$ for the Mann-Kendall tests and a Sen's slope of < 0. Increasing trends are reported for $p < 0.05$ for the Mann-Kendall tests and a Sen's slope > 0. We report no significant trend for a Mann-Kendall test with $p > 0.05$ or if Sen's slope is zero.

Analysis of trends may be sensitive to the length of the data set and which years or timesteps are included (i.e., different starting or ending dates, or different trend lengths). Consequently, we analyzed trends for every moving window of 10 or more years for every metric considered in the study, including those related to discharge at gages as well as flowing and contiguous lengths. In the body of manuscript we report significance and direction based on overall trends for each analysis. In the supplemental information we also tabulate how many of the moving windows agree with the overall trends, the length of the single longest trend that opposes the overall trend, and the length of the single longest period with no significant trend. We also tabulated the mean, median, maximum, and minimum Sen's Slope for every analysis, and the number of trends that are increasing, decreasing, or exhibit no significant trend (see **Table S4** for robustness of discharge trends, **Table S5** for robustness of flowing length and connected length trends, and **Figures S29, S30** for visualization of the annual flowing length and connected length trends).

RESULTS AND DISCUSSION

Headwater Stream Discharge Is Declining During the Dry Season

Discharge is predominantly decreasing across all gages in the basin over a 65-year period of record (**Figure 2**). For example, the Lookout Creek gage at the basin outlet has decreasing discharge for 81% of the year (about 300 days), steady discharge for 4% of the year (about 15 days), and increasing discharge for 15% of the year (about 55 days) (**Figure 2C**; remaining sites in **Figures S16–S24**; **Tables S2, S3**). The largest and most consistently decreasing trends are during the summer season when discharge is lowest. We found no increasing discharge for the driest 7-months of the year (April through October; **Figure 2D**).

Across the gage network, we find significant inter- and intra-annual changes in the timing and magnitude of discharge. Annual mean, median, and total discharge are all decreasing for 9 of 10 gages across their periods of record. We also found decreasing annual minimum and maximum discharges for 7 of 10 stream gages, declining annual low-flows (75–99% exceedance flows) at all gages, and declining annual high-flows (1–25% exceedance flows) at 7 of 10 gages (**Table S3**). Conceptually, the changes in moisture delivery is causing an increased export of water during winter months (Luce et al., 2013; **Table S3**), as evidenced by the more rapid time to export the first 10% of streamflow each year. Consequently, less water is stored during the rainy season, resulting in decreased dry-season baseflow, and extended times to export the last 10% of annual discharge.

Decreased Flow Permanence Has Reduced River Network Connectivity

Using the stream gage data, topographic analysis, and published data collected in the basin, we simulated dynamic expansion and contraction of the network (**Figure 3** and **Figure S25**) (Ward

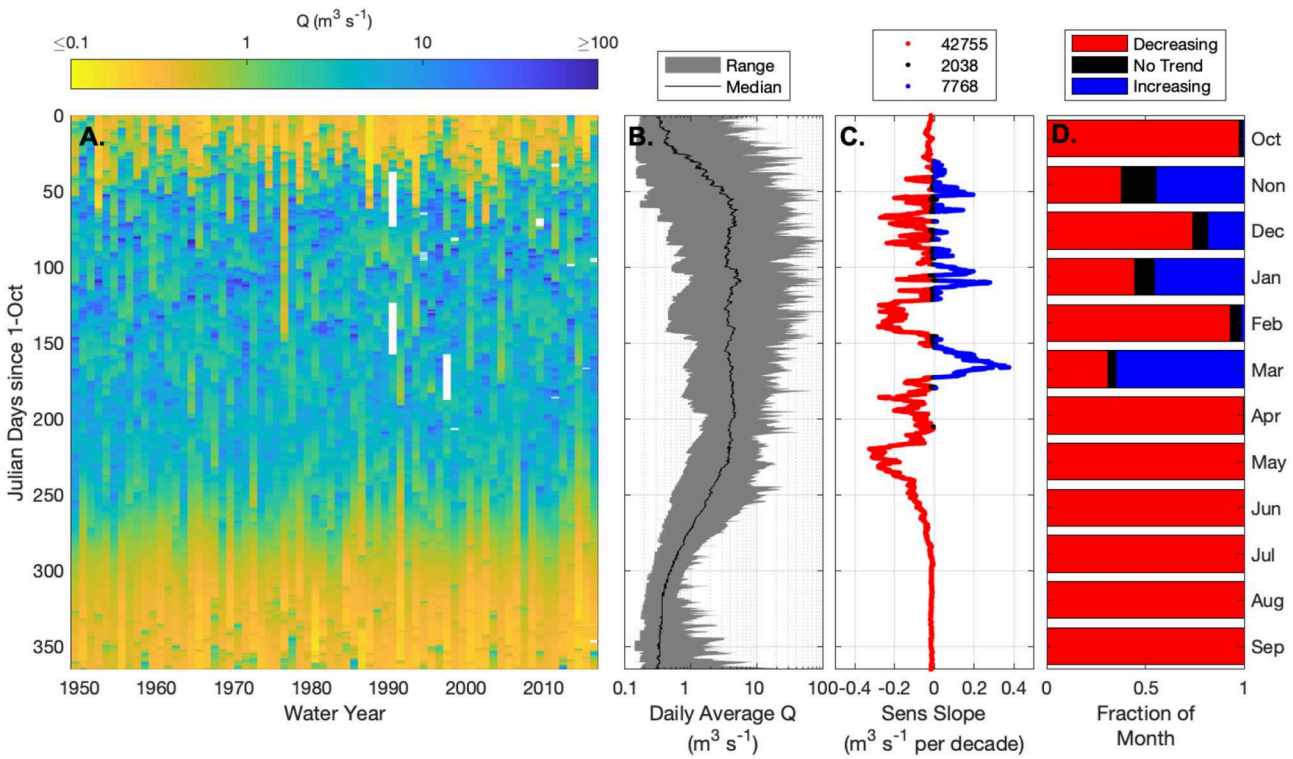

FIGURE 2 | Ten minute discharge analysis for Lookout Creek gage near the outlet of the basin. **(A)** Discharge for every day, every year of record (white indicates missing data). **(B)** Range of discharges from the period of record. The median discharge for each 10-min is timestep displayed atop the range. **(C)** Sen's slope for each 10-min period. Color indicates trend is significantly decreasing (red; 81% of the year; $n = 42{,}755$; $p < 0.05$), not changing (black; 4% of the year; $n = 2{,}038$), or significantly increasing (blue; 15% of the year; $n = 7{,}768$; $p < 0.05$). **(D)** Fraction of each month with decreasing, no, or increasing discharge trends for the period of record. See **Figures S6–S24** for comparable plots of all gages in this study.

et al., 2018a). For the 65-year simulation period, declining discharge, and increasing early season export of water within the basin result in an overall contraction of the flowing network (**Figure 3**). We found the flowing network reaches a maximum length of about 40-km during the wet winter months and contracts to as short as 15-km during the driest periods of record (**Figure 3B** and **Figure S25**). Flowing network length is a useful proxy for connectivity along the river corridor, where longer flowing lengths allow more rapid connection of hillslopes to downstream water and promote rapid export of energy and materials rather than internal transformation (van Meerveld et al., 2019).

Next, we found the connected network length plateaus at about 21-km during the wet winter months and contracts to as small as about 5-km under the lowest discharge conditions (**Figure S10**). The connected network represents an average of 57.4% of the flowing network across the entire simulation (median 55.9%; range 8.9–79.8%). The connected network defines the migration corridor through which aquatic organisms may travel upstream from the basin outlet without encountering a dry streambed location.

We found significant declines in flowing length for 75.7% of the year (about 276 days) compared to 23.6% of the year with no-trend (about 86 days), and < 1% of the year (about 3 days) with increasing flowing length (**Figure 3C**). The decreasing trends are common throughout much of the year except for the highest discharge conditions associated with spring storms and snowmelt runoff (April through June) when the network length is more steady. Connected length exhibits similar trends, declining for 66.7% of the year (about 243 days), no trend for 33.1% of the year (about 121 days) and increasing trends for < 1% of the year (about 2 days; **Figure S25**).

Decreasing flowing and connected lengths are not distributed evenly through the year. Flowing length declines by a long-term average rate of 21.0 m yr^{-1} (median 2.3 m yr^{-1} contraction; range 124.3 m yr^{-1} contraction to 1.1 m yr^{-1} expansion) and connected length declines by an average of 4.7 m yr^{-1} (median 0.6 m yr^{-1} decline; range 44.1 m yr^{-1} decline to 0.40 m yr^{-1} expansion). The largest average rate of flowing length decline, 94.2 m yr^{-1}, is in September. Average September flowing length is 24.1% shorter in 2009–2018 than 1953–1962. Similarly, connected length averages a loss of 21.4 m/yr in August, and is 9.2% shorter in 2009–2018 than the 1953–1962 August average.

Network expansion and contraction exhibit threshold behavior, generally consistent with past studies (Ward et al., 2018a; Prancevic and Kirchner, 2019). When discharge at the Lookout Creek gage is greater than about 1 m^3 s^{-1}, the flowing and connected lengths are nearly constant at their plateau values (**Figure 3B** and **Figure S27**). Under these wet-season, high discharge conditions, the flowing length maximum reflects a

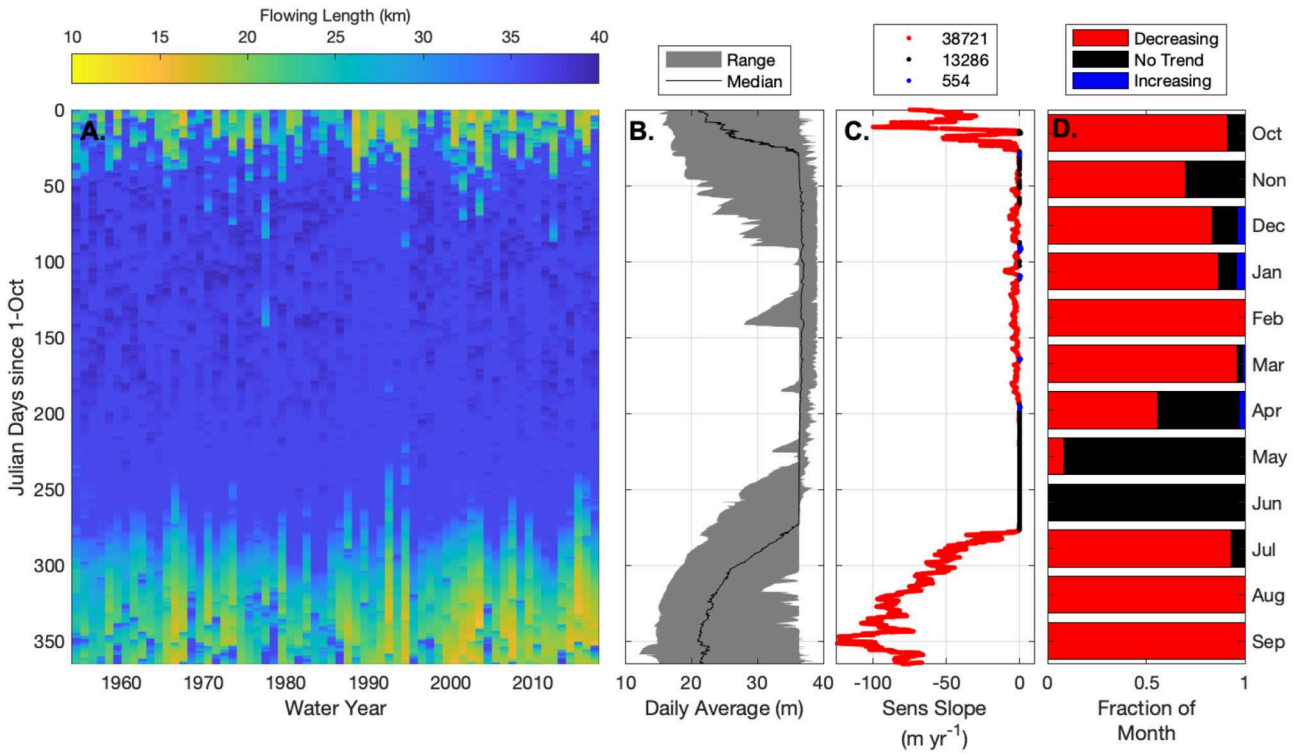

FIGURE 3 | Summary of flowing lengths for the simulation period, including: **(A)** Flowing length for every 10-min period for water years 1953 through 2017; **(B)** annual flowing lengths; **(C)** Sen's slope for the period of record, calculated for every 10-min period of the year; and **(D)** fraction of each month that length is decreasing, increasing, or has no significant trend. A comparable plot of contiguously flowing length is provided in **Figure S25**.

geologic limitation on network expansion where the drainage network is sufficiently dense to drain additional precipitation from the landscape without developing additional channels. As discharge drops below 1 m^3 s^{-1}, the network dynamically expands and contracts in response to precipitation. Under these dynamic conditions, the capacity of the valley bottom is comparable to the down-valley discharge, resulting in the large variation in flowing length in response to minor fluctuations in discharge (Ward et al., 2018a).

Headwater Streams In Steeper and/or Wider Valleys Are the Most Sensitive to Climate Change

About 41% of the headwater stream network exhibits a decreasing surface flow frequency, with the remaining 59% exhibiting no change (**Figure 4A**). No location had increasing frequency of surface flow. Similarly, 27% of locations decrease in frequency of connected flow, 73% have no change, and no sites are more frequently connected across the period of record (**Figure S11**).

Declining trends in flowing and connected frequency are not evenly distributed through the year. Instead, we found few significant trends for any segment during the wet season (November through June) because maximum network extent is controlled by basin morphology and drainage density (**Figure 4B**). During the dry season (July–October) we found declining frequency of surface flow and contiguous flow in many network segments, due to declining discharge during this period. Similarly, trends in flowing and connected frequency are not evenly distributed in space. The reaches with the largest declines in flowing and connected frequency have significantly smaller drainage areas, steeper valley slopes, and/or wider valleys compared to locations with no trend (**Figure S28**), consistent with past findings in smaller catchments and the conceptual model (Costigan et al., 2015; Ward et al., 2018a; Prancevic and Kirchner, 2019). Decreasing trends in both flowing and connected frequency are most prevalent at the most upstream extents of the network, making the lowest-order streams "canaries in the coal mine" to first detect the impacts of climate change on flow permanence.

Changing Flow Permanence Challenges Current Regulatory Strategies

Non-stationarity is now the dominant paradigm in water resources (Milly et al., 2008). In our study system, the peak and average connected lengths are significantly larger in the first 30 years than the last 30 years. From a practical perspective, some waters that would have been federally jurisdictional (herafter "jurisdictional") in 1982 (based on the period 1953–1982) may not be jurisdictional in 2018 (based on the period 1989–2018).

The revised definition for Waters of the United States, which defines the basis for a water receiving federal protections under

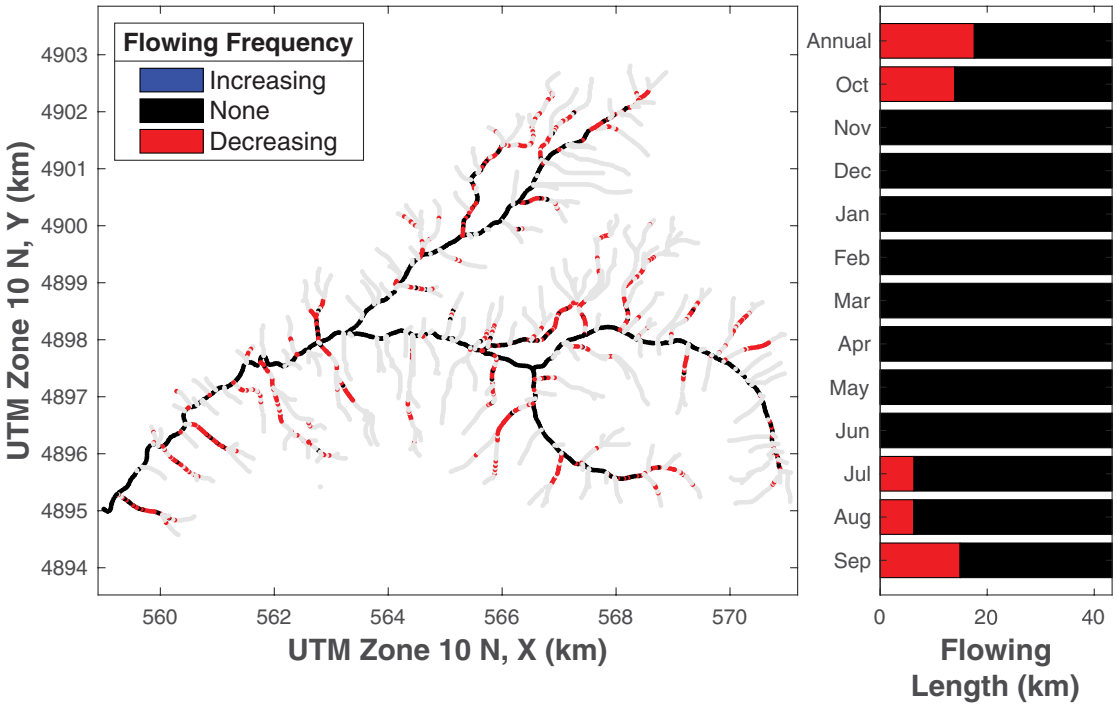

FIGURE 4 | (**A**, left) Annual trends in flowing days for each segment. (**B**, right) Annual and monthly summary of model segments exhibiting increasing, decreasing, or no trends in flowing frequency. Panel B presents data discretized in space, while **Figure 3D** presents data lumped in time. A comparable plot for trends in contiguously flowing status is presented in **Figure S26**.

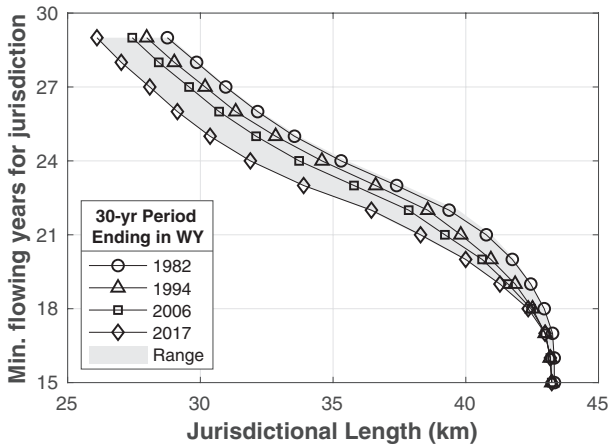

FIGURE 5 | Federal jurisdictional length (x-axis) as a function of the minimum number of flowing years to establish jurisdiction (y-axis) and final year of rolling 30-year period. The horizontal range between the lines is the change in jurisdictional length for a fixed definition of "typical year" (e.g., must flow 25 of 30 years to be jurisdictional). The vertical range between lines is the reduction in threshold that would be required to protect the same length of stream.

the federal Clean Water Act, focuses on the frequency of surface flow (US DoD US EPA, 2018). The definition would establish jurisdiction over streams with surface water flow in a "typical year" based on precipitation during a rolling 30-year window absent extreme flood and drought events. Thus, flow permanence is a de facto standard for protection, but its systematic changes with climate are not accounted for in regulations. For example, if jurisdictional status is defined as flow during 29 of 30 years, jurisdictional network length would decline from about 29-km in 1982 to about 26-km in 2017 (horizontal range at Y = 29-year; **Figure 5**). As the minimum number of flowing years for regulatory protection decreases, changes due to climate become negligible (e.g., horizontal range at Y = 15-year; **Figure 5**). In contrast, if the Navigable Waters Protection Rule was intended to provide a constant-in-time determination, it must explicitly adjust the definition of "typical year" with climate. The systematic contraction in our study system, and thereby loss of federal protections for streams and their nearby wetlands, is only one response to changes in climate. In a landscape where flow permanence increases due to changing climate, federal jurisdictional scope could increase. Our critique here is consistent with draft comments from the US EPA's Science Advisory Board (Honeycutt and Board, 2019).

CONCLUSIONS

While past studies have explored the reduction in discharge at downstream gages on large rivers (Luce and Holden, 2009), this study is the first to examine how known changes in

precipitation (Luce et al., 2013) and discharge translate into changes in connectivity between mountain hillslopes and their headwaters. Compared to their 1953–1962 averages, the 2009–2018 network has contracted by 24.1% and 9.2% in flowing and connected length, respectively, during the driest months. The dynamic connections along the network underpin a host of ecosystem services that we expect to also vary with flowing frequency. The loss of ecological function of such streams could be irreversible, and time-variable jurisdictional protections complicate the protection of these important resources. These losses are relative to a mid twentieth century baseline, and while some function will be lost as flow permeance decreases, other functions could be amplified as a result of increased duration or frequency of non-flowing conditions. Decreases in streamflow during periods when water resources are in highest demand, as was recently observed across the western U.S. (e.g., Milly and Dunne, 2020), further highlights the need for the extending the approaches presented here to more river basins.

Simulations predict that reaches with smaller drainage areas and larger subsurface flow capacity are the most likely to change in their flowing and connected frequencies in response to climate change. Thus headwater locations with steep valley gradients, larger valley widths, and/or disproportionately high hydraulic conductivity (Wondzell, 2006; Ward et al., 2019a) should be closely monitored to assess catchment response to climate change. Importantly, there are a small number of critical locations within a valley that can cutoff entire upstream reaches from the contiguous network—one location with a wider- or steeper-than-average morphology can transition to entirely subsurface flow. We observed this threshold disconnection when the Lookout Creek gage discharge dropped below about 1 m^3 s^{-1}. While this threshold is the result of local geologic setting, we expect other systems will exhibit similar threshold behavior as a function of subsurface flow capacity and discharge. Finally, we underscore that current regulations are not designed with climate change-induced shifts in flowing and connected frequency, which will complicate policy enforcement for protection of headwater streams. The conclusions presented here are specific to one river basin in the Pacific Northwest, but the modeling approach and interpretation were intentionally designed to be transferable to other river networks, enabling extended analysis with modest, commonly-available data.

DATA AVAILABILITY STATEMENT

Topographic data and stream discharge data are available from the H.J. Andrews Experimental Forrest LTER database (https://andrewsforest.oregonstate.edu/data) as data sets GI010 and HF004, respectively. Valley and stream geometries derived from the LiDAR are publicly available (Ward et al., 2019b). Model outputs including timeseries of flowing length, contiguous length, and flowing frequency for each modeled segment are archived in CUAHSI's HydroShare at: http://www.hydroshare.org/resource/2f9643bb5d85436ba997a466ba8ed653.

AUTHOR CONTRIBUTIONS

AW conceived of the study and led the modeling, analysis, and writing. NS completed the topographic analyses and contributed to conceptual and numerical model development. AW and SW secured funding to support the research. AW, SH, SW, and NS participated in the data analysis and writing of the study.

FUNDING

This research was funded in part, by the National Science Foundation under Grant No. DEB-1440409. Additional support to individual authors is acknowledged from National Science Foundation (NSF) awards EAR 1652293, EAR 1417603, and EAR 1446328, Department of Energy award DE-SC0019377, and the Burnell and Barbara Fischer Faculty Fellowship at Indiana University. This research was sponsored by the Office of Biological and Environmental Research within the Office of Science of the U. S. Department of Energy (DOE), as part of the Mercury Science Focus Area project at Oak Ridge National Laboratory (ORNL), which is managed by UT-Battelle, LLC under Contract no. DE-AC05-00OR22725 with the DOE. NS was supported by the USGS Water Mission Area Mendenhall postdoctoral fellowship (NMS).

ACKNOWLEDGMENTS

Data and facilities were provided by the H.J. Andrews Experimental Forest and Long Term Ecological Research program, administered cooperatively by the USDA Forest Service Pacific Northwest Research Station, Oregon State University, and the Willamette National Forest. The authors acknowledge this would not have been possible without support from their home institutions. Any use of trade, firm, or product names is for descriptive purposes only and does not imply endorsement by the U.S. Government nor the authors' institutions.

SUPPLEMENTARY MATERIAL

The Supplementary Material for this article can be found online at: https://www.frontiersin.org/articles/10.3389/frwa.2020.00007/full#supplementary-material

REFERENCES

Alexander, R. B., Boyer, E. W., Smith, R. A., Schwarz, G. E., and Moore, R. B. (2007). The role of headwater streams in downstream water quality. *JAWRA*. 43, 41–59. doi: 10.1111/j.1752-1688.2007.00005.x

Allen, G. H., Pavelsky, T. M., Barefoot, E. A., Lamb, M. P., Butman, D., Tashie, A., et al. (2018). Similarity of stream width distributions across headwater systems. *Nat. Commun.* 9:610. doi: 10.1038/s41467-018-02991-w

Cardenas, M. B., and Wilson, J. L. (2007). Exchange across a sediment-water interface with ambient groundwater

discharge. *J Hydrol.* 346, 69–80. doi: 10.1016/j.jhydrol.2007.08.019

Cashman, K. V., Deligne, N. I., Gannett, M. W., Grant, G. E., and Jefferson, A. (2009). Fire and water: volcanology, geomorphology, and hydrogeology of the cascade range, central oregon. *Field Guide.* 15, 539–582. doi: 10.1130/2009.fld015(26)

Corson-Rikert, H. A., Wondzell, S. M., Haggerty, R., and Santelmann, M. V. (2016). Carbon dynamics in the hyporheic zone of a headwater mountain streamin the Cascade Mountains, Oregon. *Water Resour. Res.* 52, 7556–7576. doi: 10.1002/2016WR019303

Costigan, K. H., Daniels, M. D., and Dodds, W. K. (2015). Fundamental spatial and temporal disconnections in the hydrology of an intermittent prairie headwater network. *J. Hydrol.* 522, 305–316. doi: 10.1016/j.jhydrol.2014.12.031

Costigan, K. H., Jaeger, K. L., Goss, C. W., Fritz, K. M., and Goebel, P. C. (2016). Understanding controls on flow permanence in intermittent rivers to aid ecological research: integrating meteorology, geology and land cover. *Ecohydrology*. 9, 1141–1153. doi: 10.1002/eco.1712

Covino, T. (2017). Hydrologic connectivity as a framework for understanding biogeochemical flux through watersheds and along fluvial networks. *Geomorphology*. 277, 133–144. doi: 10.1016/j.geomorph.2016.09.030

Crook, N., Binley, A. M., Knight, R., Robinson, D. A., Zarnetske, J. P., and Haggerty, R. (2008). Electrical resistivity imaging of the architecture of substream sediments. *Water Resour. Res.* 44:W00D13. doi: 10.1029/2008WR006968

Datry, T., Bonda, N., and Boulton, A. J. (Eds.). (2017). *Intermittent Rivers and Ephemeral Streams : Ecology and Management*, 1st ed. London: Academic Press.

Datry, T., Pella, H., Leigh, C., Bonada, N., and Hugueny, B. (2016). A landscape approach to advance intermittent river ecology. *Freshw. Biol.* 61, 1200–1213. doi: 10.1111/fwb.12645

Deligne, N. I., Mckay, D., Conrey, R. M., Grant, G. E., Johnson, E. R., O'Connor, J., et al. (2017). *Field-Trip Guide to Mafic Volcanism of the Cascade Range in Central Oregon - A Volcanic, Tectonic, Hydrologic, and Geomorphic Journey*. U. S. Geological Survey Scientific Investigations Report 2017-5022-H. 94. doi: 10.3133/sir20175022H

Downing, J. A., Cole, J. J., Duarte, C. M., Middelburg, J. J., Melack, J. M., Prairie, Y. T., et al. Tranvik, L. J. (2012). Global abundance and size distribution of streams and rivers. *Inland Waters*. 2, 229–236. doi: 10.5268/IW-2.4.502

Dyrness, C. T. (1969). *Hydrologic Properties of Soils on Three Small Watersheds in the Western Cascades of Oregon*. USDA Forest Serv. Res. Note Pnw-111.

Eng, K., and Milly, P. C. D. (2007). Relating low-flow characteristics to the base flow recession time constant at partial record stream gauges. *Water Resour. Res.*, 43, 1–8. doi: 10.1029/2006WR005293

Fritz, K. M., Schofield, K. A., Alexander, L. C., McManus, M. G., Golden, H. E., Lane, C. R., et al. (2018). Physical and chemical connectivity of streams and riparian wetlands to downstream waters: a synthesis. *J. Am. Water Resour. Assoc.* 54, 323–345. doi: 10.1111/1752-1688.12632

Gallart, F., Llorens, P., Latron, J., Cid, N., Rieradevall, M., and Prat, N. (2016). Validating alternative methodologies to estimate the regime of temporary rivers when flow data are unavailable. *Sci. Total Environ.* 565, 1001–1010. doi: 10.1016/j.scitotenv.2016.05.116

Gallart, F., Prat, N., Garca-Roger, E. M., Latron, J., Rieradevall, M., Llorens, P., et al. Froebrich, J. (2012). A novel approach to analysing the regimes of temporary streams in relation to their controls on the composition and structure of aquatic biota. *Hydrol. Earth Syst. Sci.* 16, 3165–3182. doi: 10.5194/hess-16-3165-2012

Godsey, S. E., and Kirchner, J. W. (2014). Dynamic, discontinuous stream networks: Hydrologically driven variations in active drainage density, flowing channels and stream order. *Hydrol. Process.* 28, 5791–5803. doi: 10.1002/hyp.10310

Gomez-Velez, J. D., and Harvey, J. W. (2014). A hydrogeomorphic river network model predicts where and why hyporheic exchange is important in large basins. *Geophys. Res. Lett.* 41, 6403–6412. doi: 10.1002/2014GL061099

Gomez-Velez, J. D., Harvey, J. W., Cardenas, M. B., and Kiel, B. (2015). Denitrification in the Mississippi River network controlled by flow through river bedforms. *Nat. Geosci.* 8, 1–8. doi: 10.1038/ngeo2567

Gooseff, M. N., Anderson, J. K., Wondzell, S. M., LaNier, J., and Haggerty, R. (2006). A modelling study of hyporheic exchange pattern and the sequence, size, and spacing of stream bedforms in mountain stream networks, Oregon, USA. *Hydrol. Process.* 20, 2443–2457. doi: 10.1002/hyp.6349

Honeycutt, M., and Board, U. E. S. A. (2019). *Draft Commentary on the Proposed Rule Defining the Scope of Waters Federally Regulated Under the Clean*. Water Act.

Irvine, D. J., and Lautz, L. K. (2015). High resolution mapping of hyporheic fluxes using streambed temperatures: Recommendations and limitations. *J. Hydrol.* 524, 137–146. doi: 10.1016/j.jhydrol.2015.02.030

Jefferson, A., Grant, G. E., and Lewis, S. L. (2004). "A river runs underneath it: geological control of spring and channel systems and management implications, cascade range, Oregon," in *Advancing the Fundamental Sciences Proceedings of the Forest Service: Proceedings of the Forest Service National Earth Sciences Conference, 1*(October 2004), 18–22.

Jensen, C. K., McGuire, K. J., and Prince, P. S. (2017). Headwater stream length dynamics across four physiographic provinces of the Appalachian Highlands. *Hydrol. Process.* 31, 3350–3363. doi: 10.1002/hyp.11259

Kasahara, T., and Wondzell, S. M. (2003). Geomorphic controls on hyporheic exchange flow in mountain streams. *Water Resour. Res.* 39:1005. doi: 10.1029/2002WR001386

Kiel, B., and Cardenas, M. (2014). Lateral hyporheic exchange throughout the Mississippi River network. *Nat. Geosci.* 7, 413–417. doi: 10.1038/ngeo2157

Larned, S. T., Datry, T., Arscott, D. B., and Tockner, K. (2010). Emerging concepts in temporary-river ecology. *Freshw. Biol.* 55, 717–738. doi: 10.1111/j.1365-2427.2009.02322.x

Luce, C. H., Abatzoglou, J., and Holden, Z. A. (2013). The missing mountain water: slower westerlies decrease orographic enhancement in the Pacific Northwest USA. *Science*. 1360, 1360–1365. doi: 10.1126/science.1242335

Luce, C. H., and Holden, Z. A. (2009). Declining annual streamflow distributions in the Pacific Northwest United States, 1948-2006. *Geophys. Res. Lett.* 36, 2–7. doi: 10.1029/2009GL039407

Milly, P. C. D., Bentacourt, J., Falkenmark, M., Robert, M., Hirsch, R. M., Kundzewicz, Z. W., et al. (2008). Stationarity is dead: Whither water management? *Science*. 319, 573–574. doi: 10.1126/science.1151915

Milly, P. C. D., and Dunne, K. A. (2020). Colorado River flow dwindles as warming-driven loss of reflective snow energizes evaporation. *Science*. 9187:eaay9187. doi: 10.1126/science.aay9187

Nikolaidis, N. P., Demetropoulou, L., Froebrich, J., Jacobs, C., Gallart, F., Prat, N., et al. (2013). Towards sustainable management of Mediterranean river basins: policy recommendations on management aspects of temporary streams. *Water Policy*. 15, 830–849. doi: 10.2166/wp.2013.158

Poff, L. N., Bledsoe, B. P., and Cuhaciyan, C. O. (2006). Hydrologic variation with land use across the contiguous United States: geomorphic and ecological consequences for stream ecosystems. *Geomorphology*. 79, 264–285. doi: 10.1016/j.geomorph.2006.06.032

Prancevic, J. P., and Kirchner, J. W. (2019). Topographic controls on the extension and retraction of flowing streams. *Geophys. Res. Lett.* 46, 2084–2092. doi: 10.1029/2018GL081799

Raymond, P. A., Saiers, J. E., and Sobczak, W. V. (2016). Hydrological and biogeochemical controls on watershed dissolved organic matter transport: pulse- shunt concept. *Ecology*. 97, 5–16. doi: 10.1890/14-1684.1

Schmadel, N. M., Harvey, J. W., Alexander, R. B., Schwarz, G. E., Moore, R. B., Eng, K., et al. (2018). Thresholds of lake and reservoir connectivity in river networks control nitrogen removal. *Nat. Commun.* 9:2779. doi: 10.1038/s41467-018-05156-x

Schmadel, N. M., Ward, A. S., Lowry, C. S., and Malzone, J. M. (2016). Hyporheic exchange controlled by dynamic hydrologic boundary conditions. *Geophys. Res. Lett.* 43, 4408–4417. doi: 10.1002/2016GL068286

Schmadel, N. M., Ward, A. S., and Wondzell, S. M. (2017). Hydrologic controls on hyporheic exchange in a headwater mountain stream. *Water Resour. Res.* 53, 6260–6278. doi: 10.1002/2017WR020576

Schwanghart, W., and Kuhn, N. J. (2010). TopoToolbox: a set of Matlab functions for topographic analysis. *Environ. Model. Softw.* 25, 770–781. doi: 10.1016/j.envsoft.2009.12.002

Schwanghart, W., and Scherler, D. (2014). Short communication: topoToolbox 2 - MATLAB-based software for topographic analysis and modeling in Earth surface sciences. *Earth Surface Dyn.* 2, 1–7. doi: 10.5194/esurf-2-1-2014

Steward, A. L., Von Schiller, D., Tockner, K., Marshall, J. C., and Bunn, S. E. (2012). When the river runs dry: human and ecological values of dry riverbeds. *Front. Ecol. Environ.* 10, 202–209. doi: 10.1890/110136

Swanson, F. J., and James, M. E. (1975). *Geology and geomorphology of the H.J.* Andrews Experimental Forest, western Cascades, Oregon. Portland, OR.

Swanson, F. J., and Jones, J. A. (2001). Geomorphology and Hydrology of the H.J. Andrews Experimental Forest, Blue River, Oregon. 1–5.

Trauth, N., Schmidt, C., Maier, U., Vieweg, M., and Fleckenstein, J. H. (2013). Coupled 3-D stream flow and hyporheic flow model under varying stream and ambient groundwater flow conditions in a pool-riffle system. *Water Resour. Res.* 49, 5834–5850. doi: 10.1002/wrcr.20442

US DoD (1986). Final rule for regulatory programs of the corps of engineers. *Fed. Regist.* 51, 41206–41260.

US DoD and EPA (2015). Clean water rule: definition of "Waters of the United States." *Fed. Regist.* 80, 37054–37127.

US DoD and US EPA (2018). *Revised definition of "Waters of the United States" (pp. 253 pp. EPA-HQ-OW-2018-0149).* pp. 253 pp. EPA-HQ-OW-2018-0149.

US DoD and US EPA (2019). *Definition of '"Waters of the United States"'-Recodification of Pre-Existing Rules* (Vol. *84)*.

US EPA (2015). *Connectivity of Streams and Wetlands to Downstream Waters: A Review and Synthesis of the Scientific Evidence (Final Report).*

van Meerveld, H. J. I., Kirchner, J. W., Vis, M. J. P., Assendelft, R. S., and Seibert, J. (2019). Expansion and contraction of the flowing stream network changes hillslope flowpath lengths and the shape of the travel time distribution. *Hydrol. Earth System Sci. Discuss.* 2006(September 2006), 1–18. doi: 10.5194/hess-2019-218

Walsh, R., and Ward, A. S. (2019). Redefining clean water regulations reduces protections for wetlands and jurisdictional uncertainty. *Front. Water* 1:1. doi: 10.3389/frwa.2019.00001

Ward, A. S., Fitzgerald, M., Gooseff, M. N., Voltz, T. J., Binley, A. M., and Singha, K. (2012). Hydrologic and geomorphic controls on hyporheic exchange during base flow recession in a headwater mountain stream. *Water Resour. Res.* 48:W04513. doi: 10.1029/2011WR011461

Ward, A. S., Schmadel, N. M., and Wondzell, S. M. (2018a). Simulation of dynamic expansion, contraction, and connectivity in a mountain stream network. *Adv. Water Resour.* 114, 64–82. doi: 10.1016/j.advwatres.2018.01.018

Ward, A. S., Schmadel, N. M., and Wondzell, S. M. (2018b). Time-variable transit time distributions in the hyporheic zone of a headwater mountain stream. *Water Resour. Res.* 54, 2017–2036. doi: 10.1002/2017WR021502

Ward, A. S., Schmadel, N. M., Wondzell, S. M., Gooseff, M. N., and Singha, K. (2017). Dynamic hyporheic and riparian flow path geometry through base flow recession in two headwater mountain streamcorridors. *Water Resour. Res.* 53, 3988–4003. doi: 10.1002/2016WR019875

Ward, A. S., Wondzell, S. M., Schmadel, N. M., Herzog, S., Zarnetske, J. P., Baranov, V., et al. (2019a). Spatial and temporal variation in river corridor exchange across a 5th order mountain stream network. *Hydrol. Earth Syst. Sci.* 23, 5199–5225. doi: 10.5194/hess-23-5199-2019

Ward, A. S., Zarnetske, J. P., Baranov, V., Blaen, P. J., Brekenfeld, N., Chu, R., et al. (2019b). Co-located contemporaneous mapping of morphological, hydrological, chemical, and biological conditions in a 5th order mountain stream network, Oregon, USA. *Earth Syst. Sci. Data Discuss.* 11, 1567–1581. doi: 10.5194/essd-11-1567-2019

Wohl, E. (2017). Connectivity in rivers. *Progress Phys. Geogr.* 41, 345–362. doi: 10.1177/0309133317714972

Wohl, E., Magilligan, F. J., and Rathburn, S. L. (2017). Introduction to the special issue: connectivity in Geomorphology. *Geomorphology.* 277, 1–5. doi: 10.1016/j.geomorph.2016.11.005

Wondzell, S. M. (2006). Effect of morphology and discharge on hyporheic exchange flows in two small streams in the Cascade Mountains of Oregon, USA. *Hydrol. Process.* 20, 267–287. doi: 10.1002/hyp.5902

Wondzell, S. M., LaNier, J., and Haggerty, R. (2009). Evaluation of alternative groundwater flow models for simulating hyporheic exchange in a small mountain stream. *J. Hydrol.* 364, 142-151. doi: 10.1016/j.jhydrol.2008.10.011

Zimmer, M. A., and McGlynn, B. L. (2017). Ephemeral and intermittent runoff generation processes in a low relief, highly weathered catchment. *Water Resour. Res.* 53, 7055–7077. doi: 10.1002/2016WR019742

Conflict of Interest: The authors declare that the research was conducted in the absence of any commercial or financial relationships that could be construed as a potential conflict of interest.

frontiers in Water

ORIGINAL RESEARCH
published: 19 August 2020
doi: 10.3389/frwa.2020.00024

Differential C-Q Analysis: A New Approach to Inferring Lateral Transport and Hydrologic Transients Within Multiple Reaches of a Mountainous Headwater Catchment

Bhavna Arora[1], Madison Burrus[1], Michelle Newcomer[1], Carl I. Steefel[1], Rosemary W. H. Carroll[2], Dipankar Dwivedi[1], Wenming Dong[1], Kenneth H. Williams[1,3] and Susan S. Hubbard[1]*

[1] Lawrence Berkeley National Laboratory, Berkeley, CA, United States, [2] Desert Research Institute, Reno, NV, United States, [3] Rocky Mountain Biological Laboratory, Gothic, CO, United States

Concentration-discharge (C-Q) relationships have been widely used as "hydrochemical tracers" to determine the variability in riverine solute exports across event, seasonal, annual, and decadal time scales. However, these C-Q relationships are limited to investigating solute transport dynamics at individual sampling stations, such that they create an incomplete understanding of the solute behavior upstream or downstream of the sampling station. Therefore, the objective of this study is to develop, apply and assess a differential C-Q approach that can characterize spatial variability in solute behavior across stations, as well as investigate their controls, by following a different spatial scheme and organizing the river into multiple sections. The differential C-Q approach captures the difference in concentration in a river segment over the difference in discharge, thereby accounting for gains, losses or fractional solute turnover between sampling stations. Using water quality data collected over four water years (2015–2018) in a mountainous headwater catchment of the East River, Colorado, this study compares traditional and differential C-Q relationships in predicting solute behavior between three sampling stations distributed throughout the river. Results from the differential C-Q analysis demonstrate significant differences in solute behavior within upstream vs. downstream reaches of the East River watershed. In particular, the meandering downstream section is marked by significant gains in both groundwater and solute concentrations as opposed to the dilution and the declining trends observed in the high-relief, steep terrain upstream reach. Shale mineralogy was determined to have a major influence on in-stream concentrations pertaining to Ca, DIC, DOC, Mg, Mo, NO_3, and SO_4. The analyses further revealed that total P concentration in the downstream reach exceeded the U.S. Environmental Protection Agency's desired goal for control of eutrophication (110 ppb). Overall, differential C-Q metrics yield a better understanding of the lateral storage and interactions within catchments than traditional analyses, and holds potential for aiding water quality managers in the identification of critical stream reaches that assimilate harmful chemicals.

Keywords: streamflow, spatial variability, temporal variability, field observations, phosphorus, nitrate, concentration-discharge, shale mineralogy

OPEN ACCESS

Edited by:
Michael Bliss Singer, Cardiff University, United Kingdom

Reviewed by:
Scott W. Bailey, United States Forest Service (USDA), United States
Lucy Rose, University of Minnesota Twin Cities, United States

****Correspondence:***
Bhavna Arora
barora@lbl.gov

Specialty section:
This article was submitted to Water and Critical Zone, a section of the journal Frontiers in Water

Received: *30 March 2020*
Accepted: *14 July 2020*
Published: *19 August 2020*

Citation:
Arora B, Burrus M, Newcomer M, Steefel CI, Carroll RWH, Dwivedi D, Dong W, Williams KH and Hubbard SS (2020) Differential C-Q Analysis: A New Approach to Inferring Lateral Transport and Hydrologic Transients Within Multiple Reaches of a Mountainous Headwater Catchment. Front. Water 2:24. doi: 10.3389/frwa.2020.00024

INTRODUCTION

Mountainous headwater catchments are highly vulnerable to perturbations, such as those caused by changes in weather, land use, vegetation cover, and snowmelt timing, and these perturbations can greatly impact downstream water quality. The sensitivity of riverine freshwater is due to the many hydrological and biogeochemical reactions that take place in catchments across distinct topographic settings. The resulting geochemical species are laterally transported to the river, through surface runoff, preferential transport, interflow, groundwater exchange and terrestrial-aquatic flow paths (Pearce et al., 1986; Sklash et al., 1986; McDonnell, 1990). Solutes including pesticides, radionuclides and trace metals migrate and transform as they move through the terrestrial landscape and aggregate in river waters determining its quality. Understanding what controls the lateral water flux and solute transport from landscapes to surface waters is key to fully understanding the biogeochemistry of riverine freshwaters, particularly so in mountainous catchments where lateral fluxes are likely to be significant.

Hydrologists typically monitor the interaction between riverine solute concentration, water, and the surrounding landscape via concentration-discharge (C-Q) analyses (Hall, 1970; Gwenzi et al., 2017; Hoagland et al., 2017). Using simultaneous measurements of river discharge and solute concentrations, C-Q analyses can ascertain how source/end-member waters mix, provide insights on relative locations of mixing sources, and can make simplistic predictions about the transport of solutes in river water (Godsey et al., 2009; Winnick et al., 2017). These predictions are typically based on assumptions about the timing and volume of mixing as well as the constant composition of each end-member (e.g., Chanat et al., 2002; Bernal et al., 2006). Even with these assumptions, the traditional C-Q method offers a limited view of river-solute interactions in the sense that it is unclear how solutes behave beyond the single sampling location. The observations and inferences made at each sampling location therefore present an incomplete or isolated picture because some fundamental hydrogeochemical processes occurring between sampling locations such as lateral transport, solute transformation and non-uniform mixing may not be accounted for (Hall, 1970; Hornberger et al., 2001). For example, the spatial variability of runoff, reaction rates, and lithologic characteristics, which is known to be significant at catchment scales, is not considered in C-Q analyses (Rodríguez-Iturbe et al., 1992; McDonnell et al., 2007). Further, the straightforward C-Q method does not yield the quality of information (e.g., transient behavior, varying end-member compositions) that is required to estimate hydrogeochemical response in the presence of perturbations (Anderson et al., 1997; Milly et al., 2008; Milne et al., 2009; Arora et al., 2019b).

Although catchment processes are difficult to quantify and model, C-Q observations are becoming easier to collect at multiple spatial and temporal resolutions. It is important therefore to develop tools that can probe these growing spatio-temporal datasets to improve our understanding of the heterogeneity and complexity of catchments, especially its response to recent climatic and anthropogenic changes. This study presents a modified C-Q approach, herein defined as the differential C-Q analysis (described in more detail below), that can examine the spatial processes causing any increase, decrease, or stationary response of solute concentrations across multiple sampling locations. We develop the differential C-Q approach and apply it to 14 different solutes at three sampling stations within a mountainous headwater catchment located in the East River Basin in Colorado. Analyzed solutes include elements typically associated with geochemical weathering (e.g., Ca, Mg and Si); redox-sensitive elements (e.g., Fe, K and Mo); and elements associated with other factors (e.g., atmospheric deposition, land use) such as DIC, NO_3, and P. The specific objectives of this study are to (a) examine solute behavior using traditional C-Q metrics (i.e., shapes of actual and log-transformed C-Q curves), (b) determine if the differential C-Q approach provides insights on solute behavior beyond the traditional analyses, and (c) examine controls on solute transport and transformation within multiple reaches of a headwater catchment.

The remainder of the paper is organized as follows. Theoretical Background section describes the main concepts of the differential C-Q technique and presents a comparison with the more traditional approaches. Field Site and Datasets section describes the field site and datasets, as well as a guide to interpreting solute characteristics based on the different C-Q approaches. Results and Discussion section presents the results for C-Q behavior and patterns obtained through different metrics. A summary of the important findings is provided in Summary and Conclusions section.

THEORETICAL BACKGROUND

The differential C-Q relationship was derived on the basis of the advective-dispersive equation (ADE), which is typically used to solve for solute concentration:

$$\frac{\partial c}{\partial t} = \frac{\partial}{\partial x}\left(D\frac{\partial c}{\partial x}\right) - \frac{\partial vc}{\partial x} + R \tag{1}$$

where, t is time [T], x is the space coordinate [L], c is the solute concentration in water [ML^{-3}], D is the dispersion coefficient [L^2T^{-1}], v is velocity [LT^{-1}], and R is the reaction term. In an advection-dominated system at steady-state, this equation reduces to:

$$R = \frac{\partial vc}{\partial x} \tag{2}$$

Here, the right-hand side term represents concentration change across space (or multiple stations), which is the divergence of the advective flux. At steady state, the divergence of the flux is equal to the sum of the reactions or sources/sinks that can act to increase or decrease solute concentration. Building on this concept, we propose that capturing the change in concentration and discharge in relation to one another across multiple stations can provide a foundation for interpreting changes in lateral

inputs and biogeochemical processing within the river segment delineated by the corresponding sampling stations. To ensure a direct comparison of temporal changes in the hydrochemical functioning of the stream segment, annual discharge graphs were used to first assess the difference in time to peak across sampling stations that define the stream segment. This difference in time (Δt) was then incorporated into the differential analyses such that:

$$\Delta Q_t = Q_{upstream,t+\Delta t} - Q_{downstream,t} \quad (3)$$

$$\Delta C_t = C_{upstream,t+\Delta t} - C_{downstream,t} \quad (4)$$

where, ΔC [ML^{-3}] and ΔQ [L^3T^{-1}] represent the difference in concentration and discharge across upstream and downstream sampling stations, respectively. Interpretations of all possible combinations of ΔC- ΔQ relationships are provided in **Table 1**.

To further evaluate the advantages of using differential concentration-discharge (ΔC- ΔQ) relationship in comparison to other approaches, **Figure 1** depicts the characteristic features of traditional and differential C-Q relationships for a hypothetical solute sampled at an upstream station A and a downstream station B. **Figure 1A** demonstrates the seasonal variability in solute concentration and its corresponding relationship to stream discharge using the traditional C-Q analysis. Here, the direction of hysteresis loops can be used to infer the timing and mixing of various source waters (e.g., Evans and Davies, 1998; Carroll et al., 2007; Ward et al., 2013). For example, the hypothetical solute demonstrates negative counterclockwise hysteresis at station A implying that higher concentrations are observed on the falling than the rising limb at this location. In contrast, the hypothetical solute demonstrates a negative clockwise hysteresis at station B suggesting that that higher concentrations are observed on the rising than the falling limb at this location. When used in combination with hysteresis indices or mixing models, these C-Q hysteresis patterns can be further used to infer the relative contribution of different sources (e.g., Evans and Davies, 1998; Rose, 2003; Aich et al., 2014). In comparison, logarithmic C-Q analyses (**Figure 1B**) provide information about the overall variability in solute concentration (Godsey et al., 2009; Musolff et al., 2015; Bieroza et al., 2018). In particular, a slope essentially equal to 0 in log-log plot defines chemostatic behavior, or where concentration remains constant as discharge varies (Godsey et al., 2009; Wymore et al., 2017). In contrast, a negative (or positive) slope suggests a chemodynamic behavior corresponding to dilution (or concentration) of the solute at that location. The log-log plot here indicates that the hypothetical solute shows dilution with increasing discharge at both stations A and B, albeit to different degrees. Although recent availability of high-frequency data sets are expanding the scope and application of these techniques (e.g., Rose et al., 2018; Knapp et al., 2020), log-log plots are typically applied to long time-frame datasets and are used to compare solutes across different catchments, while standard C-Q relationships are typically used to study solutes intensively at one station with temporal differentiation. More importantly, both the standard and logarithmic C-Q relationships provide solute behavior characteristics at a single location within a stream.

In contrast, differential C-Q relationships can provide insights on temporal and spatial variability in solute concentration across river segments (as delineated by different sampling stations). In addition, it provides information on the change in concentration within a specific interval of the river system, and thus on the applicable source or sink term. This technique can be particularly useful in identifying stream sections that are hot spots of metals or harmful solutes as well as the timing of when these hot spots occur. For example, **Figure 1C** suggests that the difference between solute concentration at station B and station A is >0 during the rising limb period, while it is negative during the base flow period. This indicates that the solute accumulates within the segment between stations A and B during the rising limb period, while it is diluted during the base flow period. For a harmful chemical, the rising limb period would be the time where monitoring or best management practices may be needed to

TABLE 1 | Analysis and interpretation of differential concentration-discharge relationships.

Trend in ΔQ between stations	Trend in ΔC between stations	Component Source or Sink
No change	Gaining	Lateral inputs/interactions from the terrestrial environment between stations are a significant source of solute
No change	No change	Solute chemistry is maintained as water is neither lost nor gained from the system
No change	Losing	Removal of solute between stations by mineral sorption, re-precipitation, or increased microbial activity
Gaining	Gaining	New water added to the system, which acts as a significant source of the solute. This new water could be groundwater, precipitation runoff, or other lateral sources
Gaining	No change	Solute chemistry is maintained as new water is added to the system
Gaining	Losing	New water added to the system, which causes dilution and/or the region between stations acts as a sink via mineral sorption, re-precipitation, or increased microbial processing
Losing	Gaining	Removal of water from the system, which causes concentration and/or the region between stations acts as a significant source of solute.
Losing	No change	Solute chemistry is maintained as water is removed from the system
Losing	Losing	Removal of water from the system, which causes dilution and/or the region between stations acts as a sink via mineral sorption, re-precipitation, or increased microbial processing

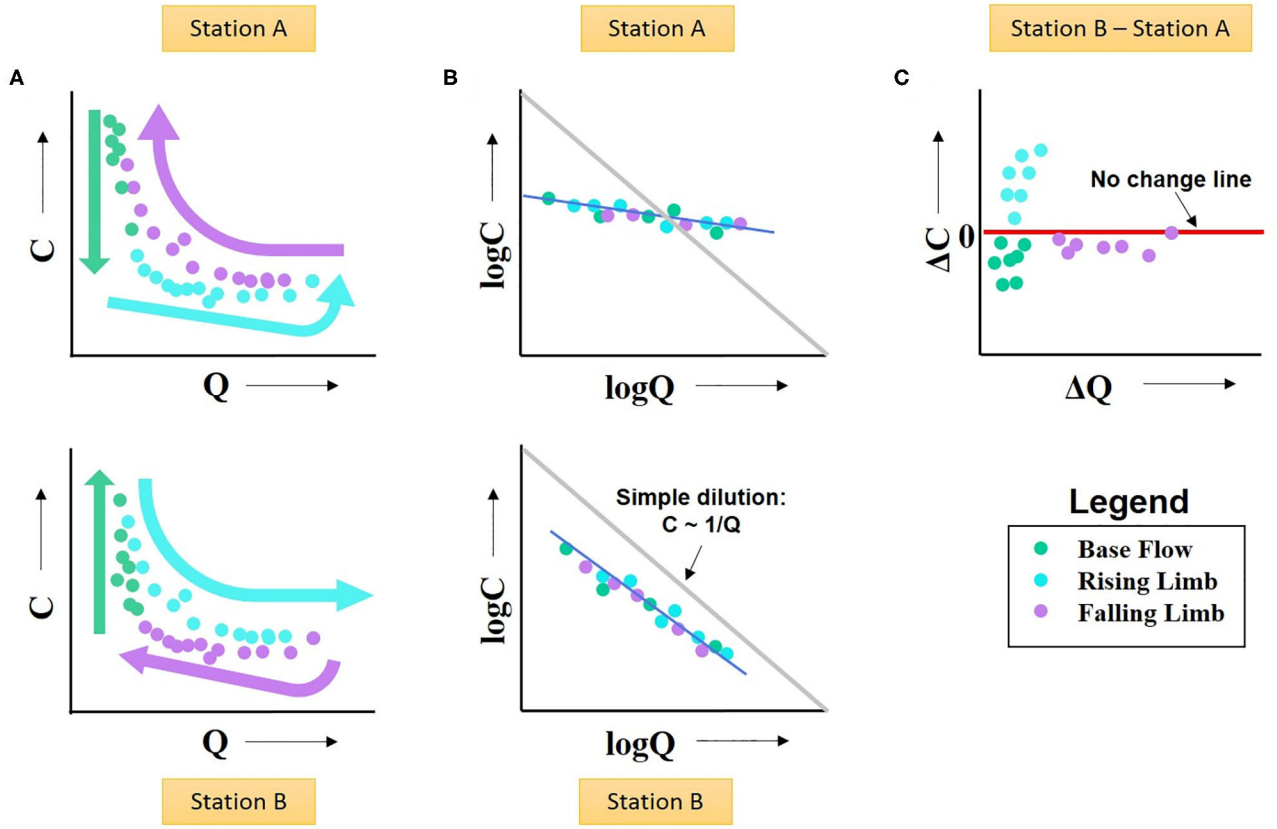

FIGURE 1 | Comparison of concentration-discharge analyses for a hypothetical solute at hypothetical stations A (upstream) and B (downstream) using **(A)** actual C-Q, **(B)** log C- log Q, and **(C)** ΔC- ΔQ. Arrows in **(A)** indicate direction through time; gray diagonal lines in **(B)** represent a log-log slope of −1 indicating dilution and blue lines show linear fits; a red "no change" line is shown in **(C)** demarcating gains from losses in solute turnover.

bring down the concentration to an acceptable level. A negative difference in concentration across stations during the falling limb period, which increases with increasing discharge, suggests that the solute concentration is decreasing due to reactions, sorption or other biogeochemical processes within the river segment during this time period.

FIELD SITE AND DATASETS

Study Site

To evaluate and compare differential C-Q approach with traditionally used approaches in understanding solute behavior, we focus on water quality data available for three sampling stations within the East River Catchment. The East River Catchment, described in detail in Hubbard et al. (2018), is located in Gunnison County near the town of Crested Butte, Colorado (**Figure 2**). The East River contributes approximately 25% of water to the Gunnison River, which is an important tributary of the Colorado River (Battaglin et al., 2012). Given that by mid-21st century the population utilizing this water is expected to increase by 50–100% while streamflow is expected to decrease by 20% (Udall and Overpeck, 2017), the East River flow and its runoff components are important to characterize and catalog for downstream users of the Colorado River.

The East River watershed covers an approximate area of 84 km^2 with an average elevation of 3,350 m (Winnick et al., 2017). The East River hydrologic cycle (**Figure 3**) is dominated by snowmelt in spring and early summer months, with monsoonal rain being significant in early-to-late summer months (Markstrom et al., 2012; Winnick et al., 2017). The geology of the watershed is comprised of a diverse collection of Paleozoic and Mesozoic sedimentary rocks intruded by Tertiary igneous laccoliths and ore-rich stocks (Dwivedi et al., 2018b; Hubbard et al., 2018). Cretaceous Mancos Shale forms the primary bedrock of the study site (**Figure 2**). Mancos Shale in this region is associated with elevated carbon, metal and pyrite content, and its weathering can thus significantly affect water quality (Morrison et al., 2012; Kenwell et al., 2016).

Climate at the East River is characterized by long, cold winters and short, cool summers (Hubbard et al., 2018). The mean annual air temperature and annual precipitation (1981-2017) at the site are 2.12°C and 673 mm, respectively. Precipitation occurs in the form of rainfall between July and September, with June being the driest month. Snow accounts for about 64% of the precipitation (Pribulick et al., 2016). Snowmelt typically

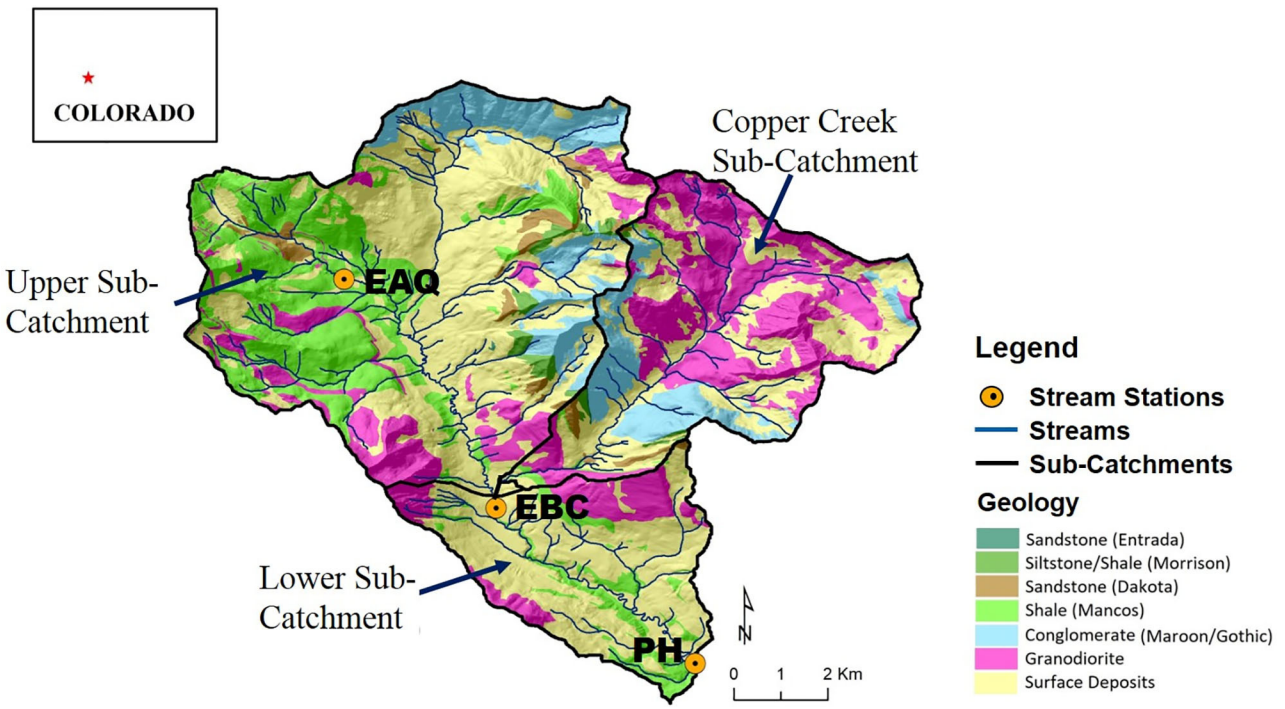

FIGURE 2 | Location of the East River Catchment, CO, USA overlain on a bedrock geology map showing the monitoring stations and the sub-catchments that are the focus of this study. The upstream reach is defined as the segment between EAQ and EBC, and the downstream reach is defined as the segment between EBC and PH. EAQ, East Above Quigley; EBC, East Below Copper; and PH, Pump House.

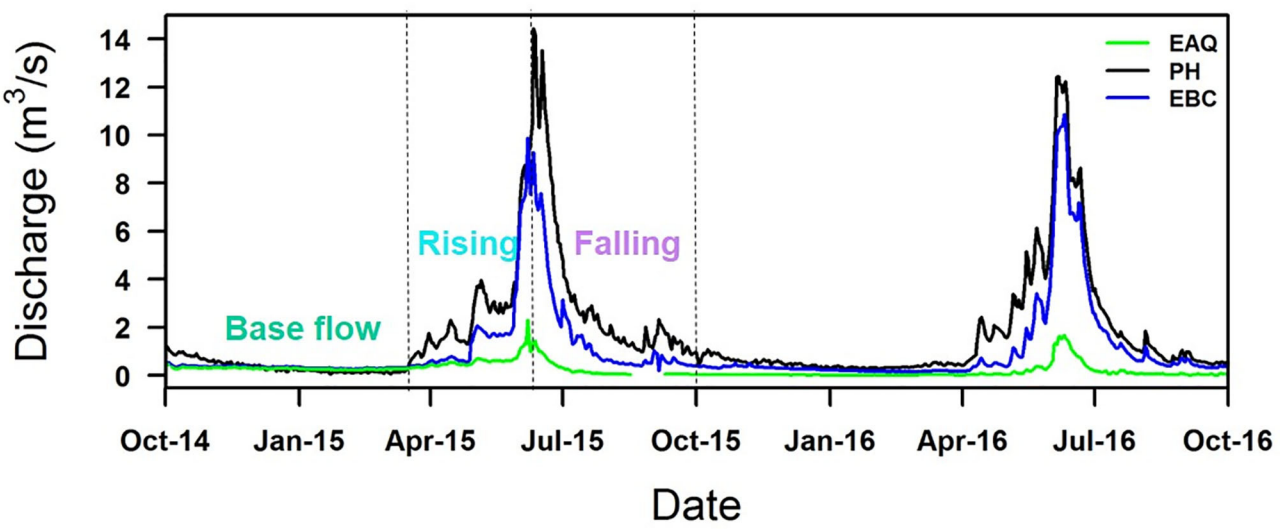

FIGURE 3 | Discharge rates measured at East Above Quigley (EAQ), Pump House (PH), and East Below Copper (EBC) stations for two consecutive water years. Discharge represents distinct seasonal trends, being higher in snowmelt-dominated spring months than in winter. Note that the C-Q relationships were analyzed on the basis of the discharge graph separation into base flow, rising and falling limb components as shown here.

begins in early April and freeze-up occurs in late November. Vegetation at the site consists primarily of four community types—sagebrush, spruce-fir, upland-herbaceous, and alpine (Zorio et al., 2016).

Streamflow Sampling and Chemical Analyses

Stream samples and discharge measurements were collected for multiple consecutive water years (2015–2018) at three

stream gauging stations—East Above Quigley (EAQ), East Below Copper (EBC), and Pump House (PH) (**Figure 2**). These data are available online at http://dx.doi.org/10.21952/WTR/1495380. Among these stations, EAQ drains water from a basin with medium elevation, medium relief and steep slopes, while EBC drains water from the entire upper basin with overall higher elevation and higher relief features (**Table 2**). An important difference between the stations is that streamflow at EAQ originates from the upper sub-catchment that is primarily underlain by Mancos Shale, while at EBC, a significant proportion of the flow originates within an igneous cirque composed of quartz monzonite and granodiorite from which it then traverses sedimentary strata. In comparison, PH is located in the low-relief meandering floodplain section of the East River that is eroding primarily into the Mancos shale. These three sampling stations were chosen for this study because they are representative of the topographically complex terrain of the East River catchment and reside directly along the main East River tributary.

At all sampling stations, instantaneous stream discharge measurements were made using SonTek Flow Tracker® acoustic Doppler velocimeter (Winnick et al., 2017; Carroll et al., 2018). The discharge characteristics for the entire duration of the study period are shown in **Figure 3**. The pattern of discharge is quite consistent from year to year, although the scale may vary from one year to the next. In particular, EAQ had the lowest discharge values, while EBC and PH had comparable values. In this study, discharge measurement collected with a paired geochemical data are only reported.

Geochemical analysis of all instream samples includes Ca, Cl, Cu, dissolved inorganic carbon (DIC), dissolved organic carbon (DOC), Fe, K, Mg, Mo, Na, NO_3, P, Si, and SO_4. Detection limits and estimated relative standard deviation for each solute is provided in **Table S1**. Instream samples for geochemical analysis were collected daily using automatic sampler (Model 3700; Teledyne ISCO, NE, USA) via a peristaltic pump at PH, while water samples were collected *in-situ* at EBC and EAQ stations at bi-weekly to monthly frequencies. All samples were filtered in the field using 0.45 μm Millipore filters. Anion samples were collected in no-headspace 2 mL polypropylene vials. DIC/DOC samples were collected in no-headspace 40 mL glass vials with polypropylene open-top caps and butyl rubber septa (VWR® TraceClean®). Cations samples were collected in high-density polyethlene 20 mL vials and acidified to 2% nitric acid with ultra-pure concentrated nitric acid. The samples were transported to the laboratory on ice and stored in 4°C refrigerator until analysis. Anion concentrations were measured using a Dionex ICS-2100 Ion Chromatography (IC) system (Thermo Scientific, USA), while cation concentrations were analyzed using an inductively coupled plasma mass spectrometry (ICP-MS) (Elan DRC II, PerkinElmer SCIEX, USA) (Carroll et al., 2018). DIC and DOC concentrations were measured using a TOC-VCPH analyzer (Shimadzu Corporation, Japan). DOC was analyzed as non-purgeable organic carbon (NPOC) by purging acidified samples with carbon-free air to remove DIC prior to measurement. Further details on sampling and measurement methods are described in detail elsewhere (Williams et al., 2011; Dong et al., 2017).

Note that paired upstream C-Q and downstream C-Q data are needed for differential C-Q analysis. Therefore, the requirement of data for ΔC-ΔQ is much larger than traditional analyses. Because sampling frequency differed by station type, sample size varied between 234 and 1,164 observations with lowest frequencies associated with solutes at EAQ. Even with these limited data, the results of this study highlight the value of using differential C-Q analysis in spatially characterizing solute behavior within a watershed. Moreover, the sampling spanned over 90% of the flow regime, indicating good representation of flow conditions.

Concentration-Discharge Metrics

We compared the differential C-Q technique with commonly used C-Q metrics to identify what new information, if any, can be obtained from the new differential technique that is not apparent from these metrics with respect to lateral transport, mixing and reaction processes. For this purpose, concentration-discharge relationships were assessed using three metrics: (1) logarithmic concentration- logarithmic discharge (log-log), (2) actual concentration -discharge (C-Q), and (3) differential concentration-differential discharge (ΔC- ΔQ).

First, we plotted the concentrations of each of the major solutes against discharge on logarithmic axes of equal units. Assuming a power law relationship of the form $C = aQ^b$, the best-fit slope b of the log-log plot was used to describe chemostatic or chemodynamic behavior (Godsey et al., 2009). As

TABLE 2 | Characteristics of sub-catchments in the East River Watershed relevant to this study (modified from Carroll et al., 2018).

	Upper sub-catchment draining to EAQ	Copper sub-catchment	Upper + Copper sub-catchment draining to EBC	Lower sub-catchment draining to PH
Drainage Area, km^2	5.27	23.67	69.81	84.73
Mean Elevation, m	3349	3528	3421	3346
Mean slope, %	24	25	22	21
Mancos Shale cover mapped at surface, %	70	1	18	18
Barren land cover*, %	21	50	31	26
Conifer and aspen tree cover*, %	61	46.9	53.1	57.4

**Grasslands, shrubs, riparian and other (developed and open water) represent the remaining land cover.*

suggested above, a slope of 0 indicates chemostatic behavior—i.e., the solute remains at a constant concentration despite changes in discharge—and therefore, discharge is not considered to be the dominant control. A slope of −1 indicates solute concentration dilutes with discharge and a slope of +1 indicates solute concentration increases with discharge; both of these relationships are dependent on river discharge and demonstrate chemodynamic behavior. Student's *t*-test was further used to determine whether the best-fit slopes were significantly similar to reference slopes of 1, 0, or −1 (Godsey et al., 2009; Wymore et al., 2017). However, C-Q patterns can be more complex and need not adhere to these simple slopes of 1, 0, or −1. To identify such solutes, we examined residual data points about the best-fit line; those with large ranges in concentration and low coefficients of determination (R^2) do not have a power law relationship and are classified as such (Thompson et al., 2011; Moatar et al., 2017; Bieroza et al., 2018).

Second, we used plots of solute concentration vs. discharge to determine hysteresis patterns and seasonal trends. Hysteresis patterns signify the difference in solute concentration on the falling and rising limb of the C-Q plot at the same value of discharge (Williams, 1989; Gellis, 2013). The extent and degree of hysteresis depends on different catchment pathways activated and the mixing of different source waters. An examination of the hysteresis patterns can therefore provide information regarding different transit times and the differing contribution of solutes to the stream from various water sources (Evans and Davies, 1998; Lloyd et al., 2016). In this study, hysteresis categories were based on Hamshaw et al. (2018), who expanded on the original classes proposed by Williams (1989). Four hysteresis patterns were found to commonly persist: (1) clockwise hysteresis with higher concentrations on the rising than the falling limb, (2) counterclockwise hysteresis with higher concentrations on the falling than the rising limb, (3) figure-eight configuration with higher concentrations on the rising than the falling limb for a certain range of Q values and lesser concentrations for other Q values, and (4) type-1 where C/Q ratio on the falling and rising limbs fall on a single-valued line. Additionally, a distinction is made with the figure-eight configuration that typically follows a counterclockwise pattern first and then becomes clockwise. In contrast, a figure-then-counterclockwise hysteresis pattern occurs when an initial solute concentration is followed by a delayed release (Gellis, 2013). Furthermore, each of these C-Q plots can be used to determine if solute concentration is consistently higher at base flow than at other times, or if rising or falling limb concentrations are greater than base flow concentration. In this study, the variable source contributions were interpreted based on the framework proposed by Evans and Davies (1998). Evans and Davies (1998) in a benchmark paper presented a unique relationship between the form of C-Q hysteresis loops and variable contributions of two- and three-component mixtures. Here, a three-component mixing model comprised of ground water (GW), soil water (SW), and event water (SO) was deemed appropriate based on prior work (Carroll et al., 2018). These hysteresis patterns thus provide important information regarding the prevalence of event, soil and ground water, and dynamic watershed interactions at different times.

Lastly, ΔC- ΔQ was obtained as the difference in concentration in a river segment over the difference in discharge across the same segment over the same time period (adjusted by the time to peak at individual stations). As shown in **Figure 3**, the hydrograph peaks were coincidental for EAQ and EBC stations, while the difference in hydrograph peak at PH was 1 day. These plots were interpreted according to **Table 1**.

TABLE 3 | Log- log relationship for solutes at all three stations of the East River watershed.

	EAQ		EBC		PH	
Solute	**Slope**	**Classification**	**Slope**	**Classification**	**Slope**	**Classification**
Ca	−0.040*	Chemostatic	−0.160†	Chemodynamic[a]	−0.141†	Chemodynamic[b]
Cl	0.005	Not power law	−0.132†	Not power law	−0.056†	Not power law
Cu	0.349*	Not power law	0.034	Not power law	0.255†	Not power law
DIC	−0.054†	Chemostatic	−0.087†	Chemostatic	−0.078†	Chemostatic
Fe	0.114	Not power law	0.019	Not power law	0.025	Not power law
K	−0.059†	Chemostatic	−0.066†	Chemostatic	−0.063†	Chemostatic
Mg	−0.099†	Chemostatic	−0.190†	Chemodynamic[a]	−0.117†	Chemodynamic[b]
Mo	−0.047†	Chemostatic	−0.146†	Chemodynamic[a]	−0.148†	Chemodynamic[b]
Na	−0.062*	Chemostatic	−0.204†	Chemodynamic[a]	−0.202†	Chemodynamic[b]
NO_3	0.118	Not power law	0.074*	Not power law	0.095*	Not power law
DOC	0.039	Not power law	0.265†	Not power law	0.433†	Not power law
P	−0.203*	Not power law	−0.181†	Not power law	−0.196†	Not power law
Si	0.002	Chemostatic	−0.099†	Chemostatic	−0.055†	Chemostatic
SO_4	−0.110†	Chemodynamic[c]	−0.273†	Chemodynamic[c]	−0.221†	Chemodynamic[b]

*Slopes of the log-log relationship are given. Slopes that are significant at 0.05 level are marked with * and those at 0.0001 level are shown with†. Three archetype patterns for chemodynamic solutes are observed here: [a]Dilution at low flow and constant at high flow, [b]Constant at low flow and dilution at high flow, and [c]Dilution throughout the flow range.*

RESULTS AND DISCUSSION

Analysis of Log-Log Relationships

Table 3 displays the log-log trends for all solutes at EAQ, EBC, and PH stations. In this table, each geochemical species is assigned a chemostatic/chemodynamic classification and a slope based on where the data points lie within the logarithmic space. As described in the previous section, logarithmic C-Q slopes can be defined if the relationship between the solute and river discharge at the target location is linear, i.e., if a power-law relationship exists, and these linear slopes can be positive, negative, or neutral. For power-law relationships with significant variability in concentration values such that the |slope| is > 0.1, solutes are considered to be chemodynamic (Godsey et al., 2009; Bieroza et al., 2018).

For a majority of the solutes in this study (24 out of 42), logarithmic concentration-discharge relationships are linear, suggesting that a power-law relationship exists between concentration and discharge at these sampling stations. For these

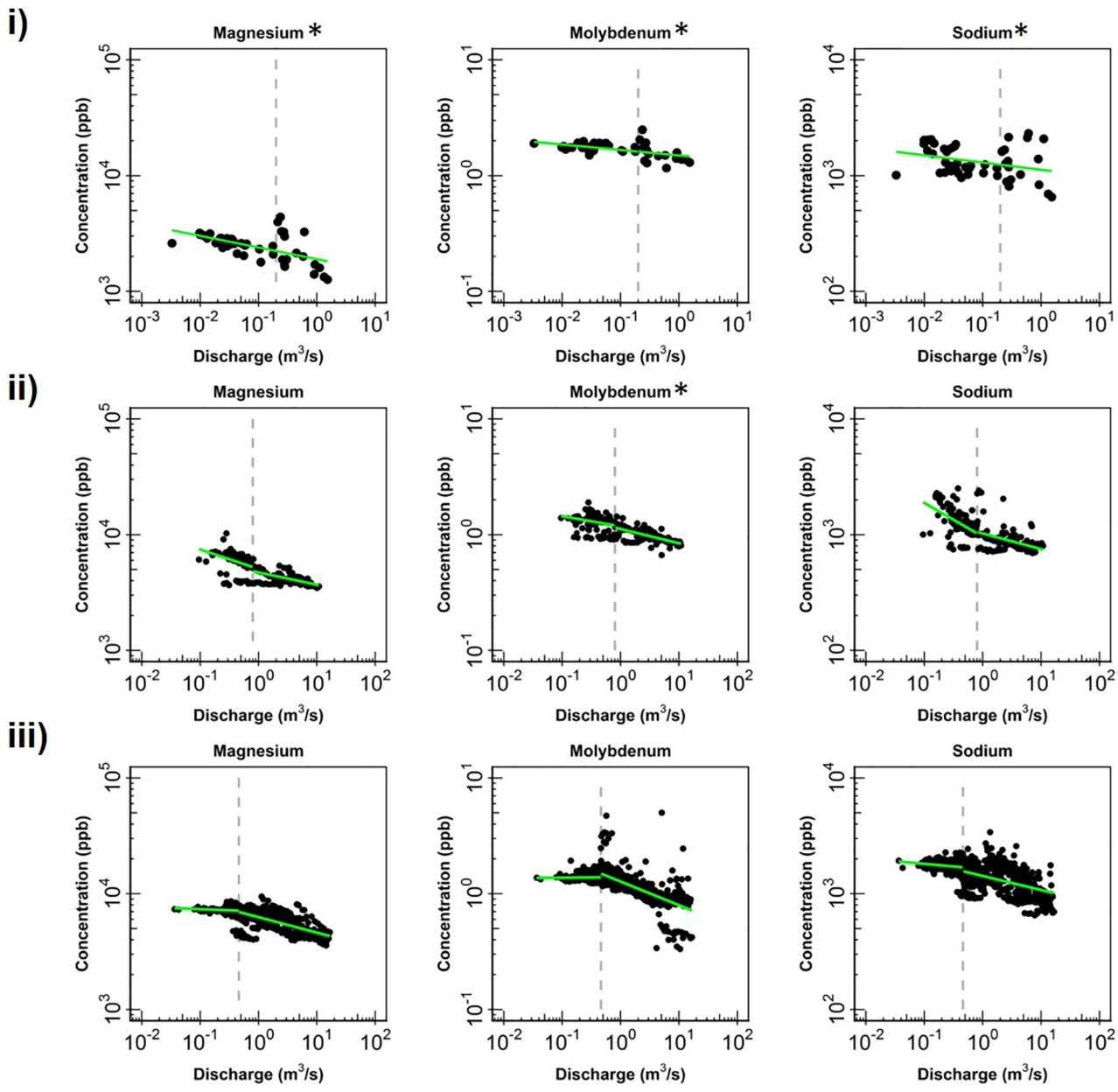

FIGURE 4 | Change in log-log relationships for Mg, Mo and Na at (i) EAQ, (ii) EBC, and (iii) PH when segmenting the hydrograph at the median discharge (dashed gray line). Low flows indicate values below the median discharge and high flows indicate values above the median discharge. Green lines represent segmented linear fits to the data, and * indicates if slopes at low and high flows are significantly similar to each other at 0.10 level.

solutes, the slope parameter ranged between −0.273 and 0.002 across all sites and solutes. This indicates that most of these solutes have a constant or negative relationship with discharge. Further, a *p*-value of 0.05 and 0.0001 is used to signify the strength of this relationship. In contrast, certain solutes Cl, Cu, Fe, NO_3, DOC, and P, have a wide range in concentration with most residual data points lying well outside the best-fit slopes of either 1, 0, or −1. Moreover, the coefficient of variation ratios (CV_C/CV_Q) for these six solutes ranged from 0.61 to 3.73, while the corresponding values for Ca, Mg and Na ranged from 0.06 to 0.28. Therefore, the higher ratios and lower R^2-values ($\leq$ 0.28) suggest that the power law equation alone is insufficient to describe the C-Q relationship for these six solutes. It is interesting to note that a few of these non-conforming solutes (Cu, Fe, NO_3, DOC) showed a positive slope indicating enrichment of these solutes with increasing discharge.

Table 3 further shows that three solutes (DIC, K and Si) consistently demonstrated chemostatic behavior (|slope|<0.1) across all stations. This implies that these solutes either have a uniform distribution within the catchment or that changes in hydrologic connectivity and flow paths within the catchment do not affect the concentration or production of these solutes (Godsey et al., 2009; Moatar et al., 2017). With the exception of these three, all other solutes showed chemodynamic behavior at the Pumphouse (PH). Among these, solutes that conformed to the power-law relationship demonstrated stable patterns at low flow conditions and dilution during high flows (**Figures 4**, **5**). These solutes are considered to be source-limited since delivery to the stream network is controlled by their rate of production as opposed to transport-limitation (Meybeck and Moatar, 2012; Bieroza et al., 2018). Both redox-sensitive solutes (e.g., Mo, SO_4) as well as weathering-related solutes (e.g., Ca, Mg, Na) demonstrated source-limitation at PH. While chemodynamic behavior of redox-sensitive and biogeochemically active solutes is commonly observed, chemodynamic behavior of weathering-based ions has also been reported in some carbonate-dominated catchments (e.g., Sullivan et al., 2018). This is usually attributed to spatial heterogeneity, activation of different flow paths and/or mineral control (Koger et al., 2018; Rose et al., 2018; Molins et al., 2019; Knapp et al., 2020). At PH, sulfuric acid weathering is estimated to account for 35–75% carbonate dissolution (Winnick et al., 2017), thus resulting in source-limitation of weathering solutes at this location.

Apart from the commonalities described above, most of the solutes at EAQ demonstrated chemostatic behavior. These include Mo as well as weathering-related solutes such as Ca, Mg and Na. Only SO_4 showed chemodynamic behavior, with a negative slope parameter indicating dilution throughout the flow range (**Figure 5**).

At EBC, all solutes exhibited the same chemostatic and chemodynamic relationship as observed at the PH station. However, a major difference between the chemodynamic relationship at PH and EBC is that solutes at EBC showed dilution at low flow conditions and stabilization under high flow conditions (**Figure 4**). This was consistent for weathering-related solutes like Ca, Mg and Na as well as redox-sensitive species like Mo. Therefore, these solutes exhibited more variability in concentration at low flows at EBC, while at PH, these solutes demonstrated more variability at high flows. Furthermore, SO_4 patterns at EBC showed dilution throughout the whole flow

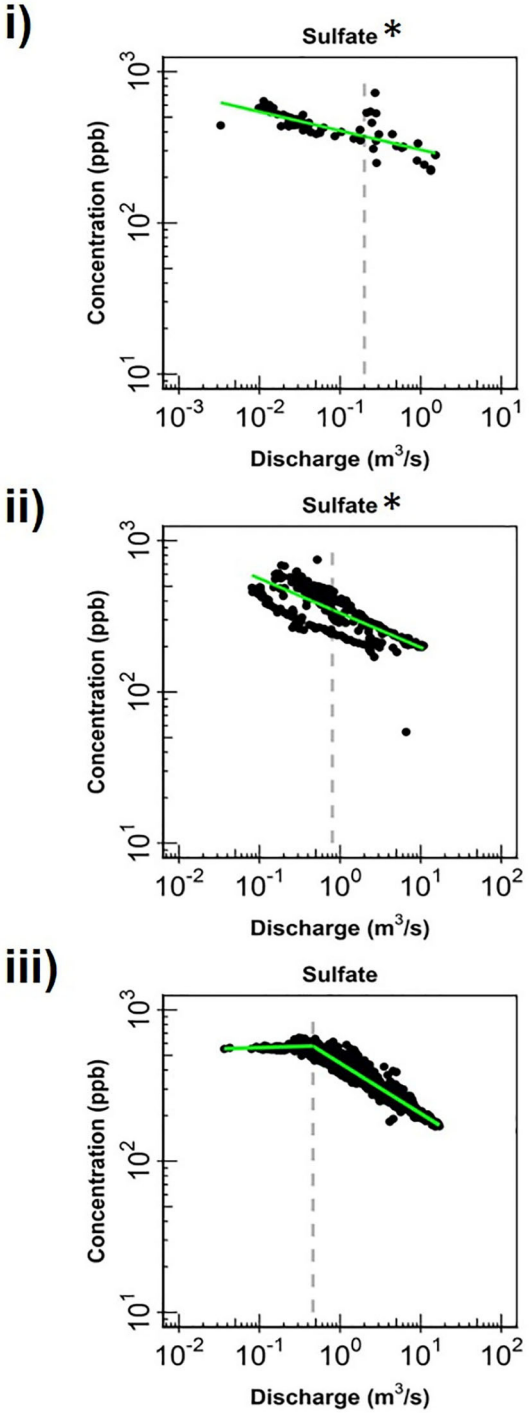

FIGURE 5 | Change in log-log relationships for SO_4 at (i) EAQ, (ii) EBC, and (iii) PH when segmenting the hydrograph at the median discharge (dashed gray line). Green lines represent segmented linear fits to the data, and * indicates if slopes at low and high flows are significantly similar to each other at 0.10 level.

range, while SO_4 at PH showed stabilization at low flow conditions (**Figure 5**).

Even though all three stations lie within the East River catchment, variability was observed in solute concentrations as well as their log-log behavior. In particular, weathering-related solutes showed chemostatic behavior at EAQ, and chemodynamic behavior at EBC and PH. These differences in the nature of C-Q relationship can be attributed to seasonal shifts in flow paths and variability in the fraction of base flow contribution that interacts with the weathered profile and ends up in the stream. Note that the fraction of groundwater contribution to the EAQ station varied by only 0.15 throughout the flow regime, while the variation for EBC and PH was much higher at 0.25 (Carroll et al., 2018).

Analysis of C-Q Hysteresis Patterns

Within the East River, discharge is highest during the spring months (the rising limb) and lowest during the winter months (base flow), as is typical for Rocky Mountain headwaters (**Figure 3**). These seasonal discharge patterns can cause hysteresis and influence solute concentrations. Solute concentrations across all stations were analyzed for three portions of the hydrograph: (1) base flow, (2) rising limb, and (3) falling limb. Hysteresis differences in solute concentrations between the rising and falling limb were also analyzed as shown in **Table 4**.

Table 4 indicates that most of the solutes (25 out of 42) exhibited clockwise (CW) hysteresis, where higher solute concentrations occur on the rising limb of the hydrograph and lower concentrations occur on the recessional limb (Wood, 1977; Williams, 1989; Gellis, 2013; Gwenzi et al., 2017). Causes for this hysteresis pattern have been explained primarily by an initial "flushing" of the solute and relative depletion during the falling limb. **Table 4** further indicates that significant subcategories of the CW loop were obtained by discriminating between the loop direction. These subcategories can provide important insights about how transport mechanisms vary between solutes and through time. CW loops were observed in solutes across all stations. In contrast, only a small number of solutes (8 out of 42) showed counterclockwise (CCW) behavior (**Table 4**). CCW behavior has been explained by a solute peak arriving later than the discharge peak, such that there is a delayed source or lagged "through-flow" response contributing to higher concentration on the falling than the rising limb of the hydrograph. For the CCW loops, all except one were sampled at EAQ. **Table 4** further indicates that all CCW loops had a negative trend.

Both EBC and PH featured significant diversity in hysteresis types, including occurrences of figure-eight and figure-then-counterclockwise patterns. Figure-eight hysteresis is observed when C/Q ratios on the rising limb for some discharge values are greater than those on the falling limb for the same discharge values. In the latter, C/Q ratios on the rising limb for some discharge values are smaller than those on the falling limb for the same discharge values, with the distinction that the initial solute concentration is followed by a delayed release. Both figure-eight

TABLE 4 | Classes of hysteresis in concentration-discharge plots for solutes at all three stations of the East River watershed.

Solute	EAQ			EBC			PH		
	Hysteresis Type	**Trend**	**Cause of hysteresis shape**	**Hysteresis Type**	**Trend**	**Cause of hysteresis shape**	**Hysteresis Type**	**Trend**	**Cause of hysteresis shape**
Ca	CCW	Negative	GW>SO>SE	CW	Negative	GW > SE>SO	Figure-eight	–	GW > SE&SO
Cl	CW	Convex	SE > GW>SO	CW	Convex	SE > GW>SO	CW	Convex	SE > GW>SO
Cu	CW	L-Shaped	Solute peaks before peak discharge	CW	L-Shaped	Solute peaks before peak discharge	CW	L-Shaped	Solute peaks before peak discharge
DIC	CW	Negative	GW > SE>SO	CW	Negative	GW > SE>SO	CW	Negative	GW > SE>SO
Fe	CW	L-Shaped	Solute peaks before peak discharge	CW	L-Shaped	Solute peaks before peak discharge	CW	L-Shaped	Solute peaks before peak discharge
K	CW	Negative	GW > SE>SO	Figure-then-CCW	–	SO > GW & SE	CCW*	Negative	GW > SO>SE
Mg	CCW	Negative	GW>SO>SE	CW	Negative	GW > SE>SO	Figure-eight	–	GW > SE&SO
Mo	CCW	Negative	GW>SO>SE	Figure-then-CCW	–	SO > GW & SE	CCW	Negative	GW>SO>SE
Na	CCW	Negative	GW>SO>SE	CW	Negative	GW > SE>SO	Figure-eight	–	GW > SE&SO
NO_3	CW	L-Shaped	Solute peaks before peak discharge	CW	L-Shaped	Solute peaks before peak discharge	CW	L-Shaped	Solute peaks before peak discharge
DOC	CW	Delayed source	SE >SO> GW	CW	Delayed source	SE >SO> GW	CW	Delayed source	SE >SO> GW
P	CCW	Negative	GW>SO>SE	Type 1	–	GW > SE&SO	CW	Negative	GW > SE>SO
Si	CCW	Negative	GW>SO>SE	CW	Negative	GW > SE>SO	Figure-eight	–	SE > GW&SO
SO_4	CCW	Negative	GW>SO>SE	Type 1	–	GW > SE&SO	Figure-eight	–	GW > SE&SO

Hysteresis types are summarized as counterclockwise (CCW), clockwise (CW), figure-eight, figure-then-counterclockwise, and Type I. GW, ground water; SO, soil water; SE, event water.
**Trend for 2016 only. For all other years, a negative CW pattern was observed.*

and figure-then-counterclockwise hysteresis loops are indicative of distinct solute sources that become activated at different times during the year (Megnounif et al., 2013).

Patterns exhibiting no hysteresis (Type 1) were also observed, although these occurred relatively infrequently (2 out of 42) and were noted only at EBC. Type 1 patterns occur when there is a systematic variation in solute concentrations with discharge (Murphy et al., 2014). We demonstrate the different C-Q patterns observed within the East River watershed using specific examples from the sampling stations (**Figure 6**).

At EAQ, seven solutes (Cl, Cu, DIC, DOC, Fe, K, and NO_3) exhibited clockwise hysteresis and an equal number of solutes (Ca, Mg, Mo, Na, P, Si, and SO_4) exhibited counterclockwise hysteresis. As suggested above, only negative counterclockwise loops were observed. This implies that for these solutes, groundwater contributions were greatest at this location, followed by soil water contributions, and then surface runoff. For the clockwise loops, trends at EAQ varied significantly between solutes. DIC and K had negative clockwise hysteresis, such that groundwater contributions still dominated the C-Q behavior, but event water contributions were greater than soil water contributions. In contrast, DOC exhibited a clockwise loop with an irregular pattern. This loop is characterized by an early, rapid increase in DOC concentration during the rising limb, followed by a delayed, second pulse of DOC concentrations. The second pulse is typically attributed to a slow contributing source or late activation of certain flow paths. At the East River, these pulses can be attributed to shallow soil horizon DOC concentrations that are rapidly mobilized by spring snowmelt, and deeper groundwater DOC contributions that are lagged because of the progressive infiltration of snowmelt. This loop is similar to Type 2E reported in Hamshaw et al. (2018). Unique C-Q relationships were also demonstrated by Cu, Fe, and NO_3, which showed an L-shaped clockwise hysteresis. This implies that a peak in solute concentration occurred before the peak in discharge. This can potentially occur due to fast release or flushing of old water with high solute concentration. Such loops were characterized as Type 2D by Hamshaw et al. (2018) and were most frequently observed in the rainier summer and early Autumn months. Here, significant concentration of these metals and nitrate are attributed to the underlying Mancos Shale (Deacon and Driver, 1999; Morrison et al., 2012).

Unlike EAQ, half of the solutes at PH exhibited clockwise hysteresis (7 out of 14), five solutes showed a figure-eight configuration, and two exhibited counterclockwise hysteresis. Except P, all solutes that showed clockwise hysteresis (Cl, Cu, DIC, DOC, Fe, and NO_3) at PH had trends that mirrored those observed at EAQ. P was found to demonstrate consistently different patterns across stations. However, it is notable that groundwater contributions were greatest for P across stations, while soil water and event water contributions varied. At PH, the figure-eight loops were specifically observed for Ca, Mg, Na, DIC, Si, and SO_4. As suggested above, this could be related to a variety of factors such as variable source area contributions or the relative difference between concentration and discharge peaks. One notable exception to the clockwise and figure-eight loops observed at PH was Mo, which showed a counterclockwise hysteresis loop. However, similar to EAQ, it had a negative trend such that groundwater contributions were greatest, followed by soil water, and then event water contributions. Mo deposits are also attributed to the underlying geology at this site (Deacon and Driver, 1999; U.S. Department of Energy, 2011). Note that K is the only element that displayed different hysteretic patterns for 2016 at PH than other years and shows a CCW trend as opposed to the typically observed CW pattern. This suggests that in a typical year, snowmelt event water is the secondary source of K to the stream, but in 2016 subsurface soil water was the secondary source of K. This seems reasonable because 2016 had lower than average precipitation.

Across all stations, only six solutes showed consistent behavior in their C-Q patterns. These include Cl, Cu, DIC, Fe, NO_3, and DOC, all of which exhibit clockwise hysteresis. Two other solutes with clockwise hysteresis—Mo and K—displayed similar behavior across EAQ and PH, but different from those observed at EBC. Interestingly, weathering-related solutes and P showed consistently different patterns across all stations. At EBC, weathering-related solutes including Ca, Mg, and Na showed a negative clockwise hysteresis. As suggested above, this implies that groundwater contributions were greatest, followed by surface runoff, and then soil water. Two notable exceptions observed at EBC were the Type 1 pattern shown by P and SO_4, and the figure- then-counterclockwise hysteresis exhibited by K and Mo. While Type 1 is indicative of a consistent source or source area contributions to the solute concentrations sampled at EBC, the figure-then-counterclockwise hysteresis is typically a result of distinct sources or variable source area contributions. The steep slopes, high relief and convergent topographic features of EBC can result in an uninterrupted supply of certain solutes such as P and SO_4. Carroll et al. (2019) also noted that recharge in the Copper Creek sub-catchment appears to be decoupled from annual climate variability, resulting in a steady supply of certain solutes.

Analysis of ΔC- ΔQ Patterns

Solute data in the upstream and downstream reaches of the East River watershed were analyzed through ΔC- ΔQ analysis to evaluate storage mechanisms and lateral connectivity. The increase in discharge was on average 0.22% of the absolute discharge (range 0.01 to 2.06%) between EAQ and EBC (i.e., the upstream reach) and at 0.12% (range −0.07 to 0.92%) between EBC and PH (i.e., the downstream reach). Because EBC is a tributary junction (see **Figure 2**), larger increases in discharge are observed in the upstream than the downstream reach. The range of discharge values further demonstrate that both upstream and downstream reaches were generally gaining during the study period. Only for a few times during the base flow period does the downstream reach become a losing stream (not shown here). The fraction of solute gained or lost within a given reach varied with change in discharge.

Figure 7 shows the ΔC- ΔQ relationships for a subset of solutes in the downstream reach for 2015 and 2016 water years. A complete description of the differential C-Q relationships for all years (2015–2018) is shown in **Table 5**. For ease of interpretation of results from **Figure 7**, we present an example

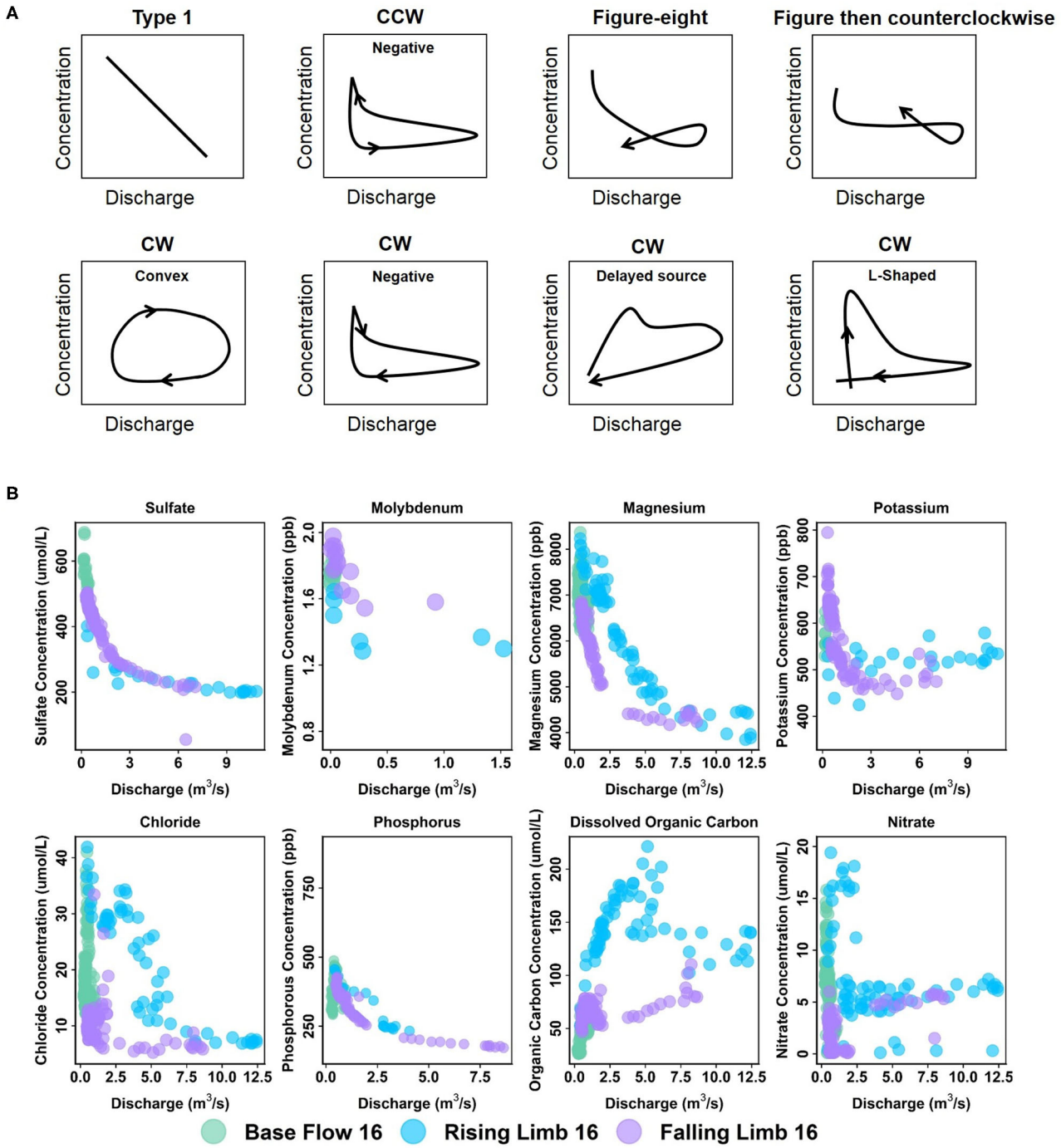

FIGURE 6 | (A) Types of C-Q patterns commonly observed at the East River Catchment, and **(B)** example of solutes from different stations demonstrating these patterns. Arrows in **(A)** indicate direction through time. C-Q plots of K and SO_4 correspond to EBC, Mo to EAQ, and the rest to PH.

wherein Ca is the solute of interest. We note that both gains and losses of Ca are obtained when the difference in discharge between stations is small (∼0). Although overall gains in discharge are small, the stream is not a pipe and significant stream water-groundwater interactions are expected within this focus floodplain section. Here, the downstream reach shows a loss (negative concentration) of Ca during the rising limb, while it shows a gain (positive concentration) for most of the falling limb, especially with higher ΔQ values. Spring snowmelt is an important contributor to the streamflow during the

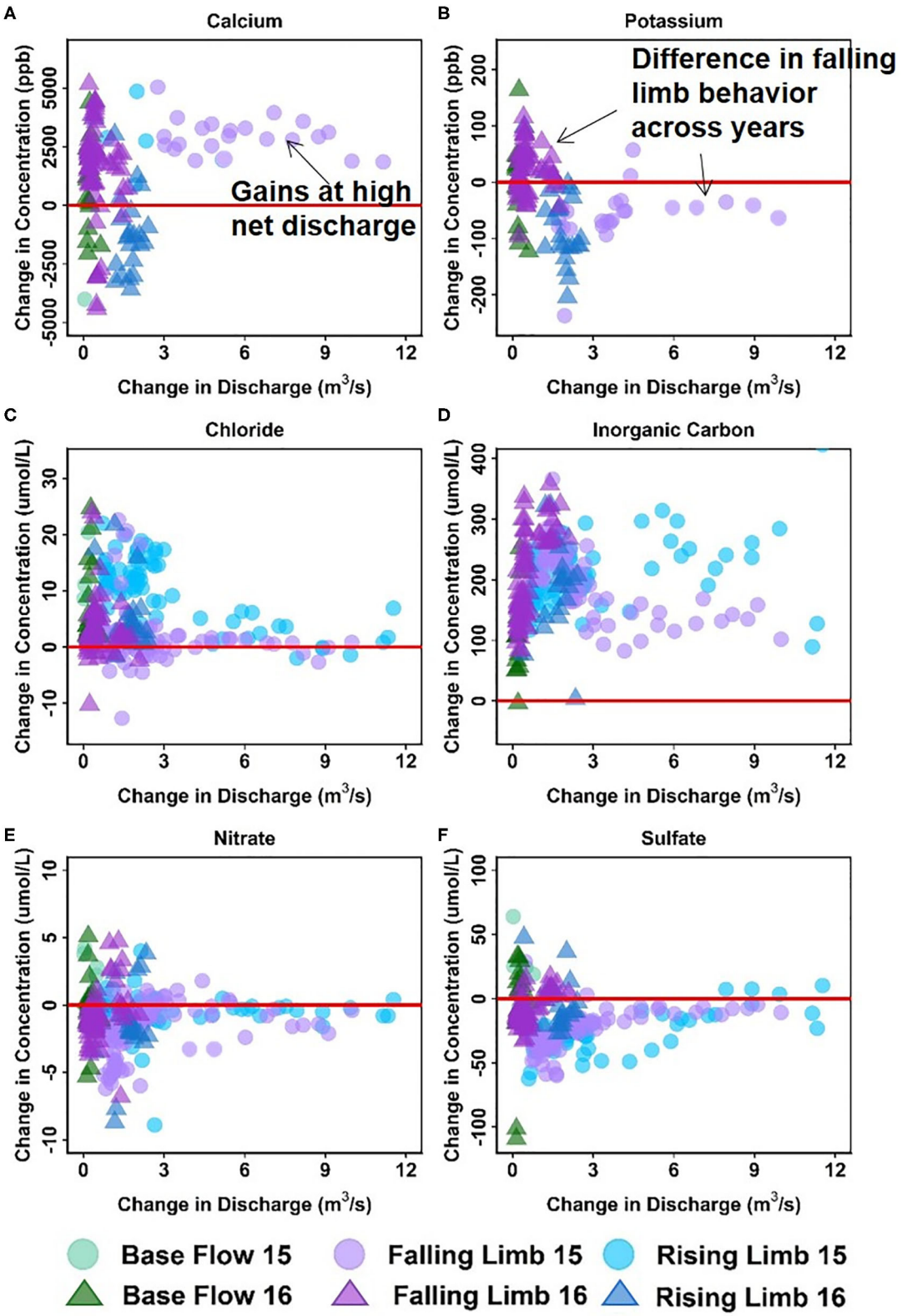

FIGURE 7 | Differential C-Q analyses for the downstream reach showing changes in concentrations of **(A)** Ca, **(B)** K, **(C)** Cl, **(D)** DIC, **(E)** NO_3, and **(F)** SO_4 relative to changes in flow. For clarity, gains and losses of solutes are demarcated relative to a solid red "no change" line.

TABLE 5 | Differential concentration-discharge relationship for solutes at the upstream and downstream reaches of the East River watershed.

	Upstream reach (EAQ to EBC)			Downstream reach (EBC to PH)		
Solute	**Low ΔQ**	**High ΔQ**	**Overall trend**	**Low ΔQ**	**High ΔQ**	**Overall trend**
Ca	Mostly losing†	Losing	Losing most of the time, while baseflow shows both losses and gains.	Both gaining and losing*[a]	Gaining	Gaining at high ΔQ
Cl	Mostly gaining†	Neither gaining nor losing	Gaining at low ΔQ	Mostly gaining†	Mostly gaining†	Gaining most of the time
Cu	Neither gaining nor losing	Neither gaining nor losing	Neither gaining nor losing	Both gaining and losing*[d]	Neither gaining nor losing	Neither gaining nor losing
DIC	Losing	Losing	Losing at all times	Gaining	Gaining	Gaining at all times
Fe	Both gaining and losing[d]	Neither gaining nor losing	Neither gaining nor losing	Both gaining and losing	Mostly gaining†	Gaining at high ΔQ, including during base flow and part of rising limb
K	Mostly gaining†	Both gaining and losing[b]	Gaining most of the time, including during base flow	Both gaining and losing*[a]	Mostly losing†	Losing at high ΔQ
Mg	Gaining	Gaining	Gaining at all times	Gaining	Gaining	Gaining at all times
Mo	Losing	Losing	Losing at all times	Both gaining and losing*[a]	Gaining	Gaining at high ΔQ
Na	Mostly gaining†	Neither gaining nor losing[b]	Gaining at low ΔQ including during base flow	Mostly losing†	Mostly gaining†	Losing at small discharge and gaining at high. Baseflow shows both losses and gains
NO_3	Mostly gaining†	Mostly gaining†	Gaining most of the time	Both gaining and losing*[d]	Mostly losing†	Losing at high ΔQ
DOC	Gaining	Gaining	Gaining at all times	Both gaining and losing[c]	Gaining	Gaining at high ΔQ but baseflow is losing
P	Both gaining and losing*[d]	Losing	Losing at high ΔQ	Both gaining and losing*[c]	Gaining	Gaining at high flow
Si	Both gaining and losing*	Losing	Losing at high ΔQ, including throughout falling limb	Both gaining and losing*[c]	Gaining	Gaining at high ΔQ
SO_4	Both gaining and losing*	Losing	Losing at high ΔQ, including throughout rising limb	Mostly losing†	Mostly losing†	Losing most of the time, while baseflow shows both losses and gains

Losing and gaining patterns at low and high gains in discharge as well as across recessional limbs are provided.
†80% samples or greater.
**Base flow acts as both a source and sink of solute.*
[a]Losing during rising limb, gaining during falling limb.
[b]Losing during falling limb, gaining during rising limb.
[c]Gaining during both falling and rising limbs.
[d]No clear pattern across recessional limbs.

rising limb and can dilute Ca concentration. Note that other processes may also contribute to a decline during the rising limb, such as gypsum precipitation or ion exchange. However, the effect of these processes may be small in comparison to the significant dilution obtained due to snowmelt. For the increase in concentration noted during the falling limb, it is possible that these sources were generated at the far end of the contributing area, and thus Ca reaches the stream mainly during the falling limb. Overall, the downstream reach between EBC and PH shows a net increase in Ca specifically during periods of high gains in discharge. This trend is noted in **Table 5** documenting Ca behavior at both low and high ΔQ values. It is interesting to note that Mo and K show a behavior similar to Ca, except that K shows net losses with higher ΔQ (**Table 5**). The main reason for this is that losses in K are observed during the falling limb of 2015, while gains are observed during the falling limb of 2016 (**Figure 7B**). This inconsistency is due to the fact that 2015 had greater total precipitation, which mainly came from a larger proportion of summer monsoon (30%) than observed in 2016 (26%). Because significant uptake of K can occur by plants, microbes or both, that

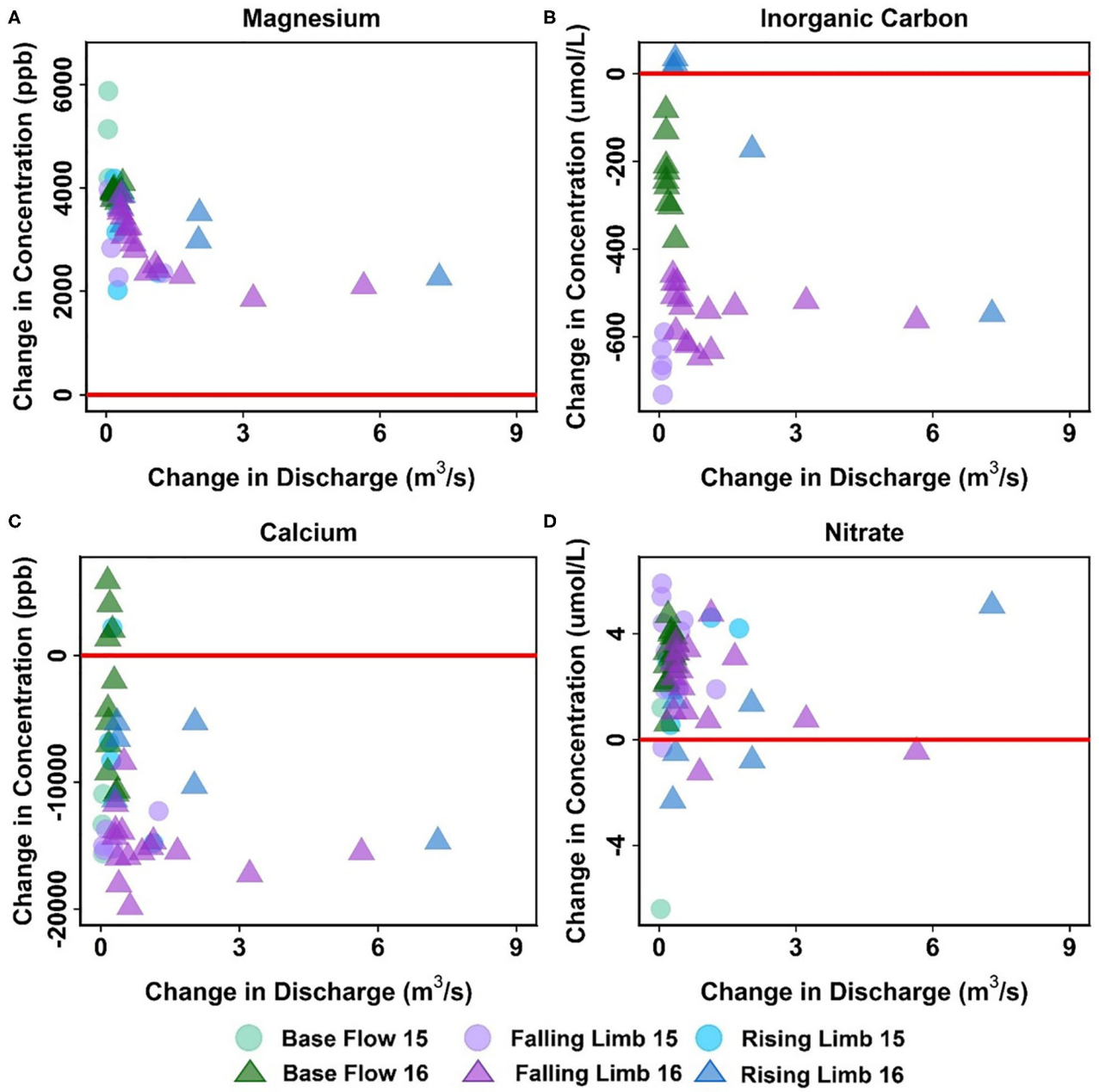

FIGURE 8 | Differential C-Q analyses for the upstream reach showing changes in concentrations of **(A)** Ca, **(B)** DIC, **(C)** Mg, and **(D)** NO_3 relative to changes in flow. For clarity, gains and losses of solutes are demarcated relative to a solid red "no change" line.

are typically triggered by moisture conditions, these monsoon events led to a noticeable decline in K during 2015, but not in 2016.

Table 5 further indicates that most solutes (9 out of 14) showed net gaining trends or increases in concentration in the downstream reach. This is reasonable given the low relief meandering nature of this section of the East River. Among these, Cl, DIC, and Mg showed a consistent increase in concentration throughout the hydrograph (see, for example, **Figures 7C,D**). This implies that lateral contributions are significant in this focus floodplain section and add to the stream concentrations of these solutes. Tokunaga et al. (2019) confirm that hillslope contributions to PH are significant and typically contribute to 54–57% of solute exports. In comparison to these solutes, DOC, P and Si showed a gain in concentration at all times except the base flow period. This suggests that base flow is not a significant source of these solutes or that surficial soils and shorter flow paths are important sources that are able to increase

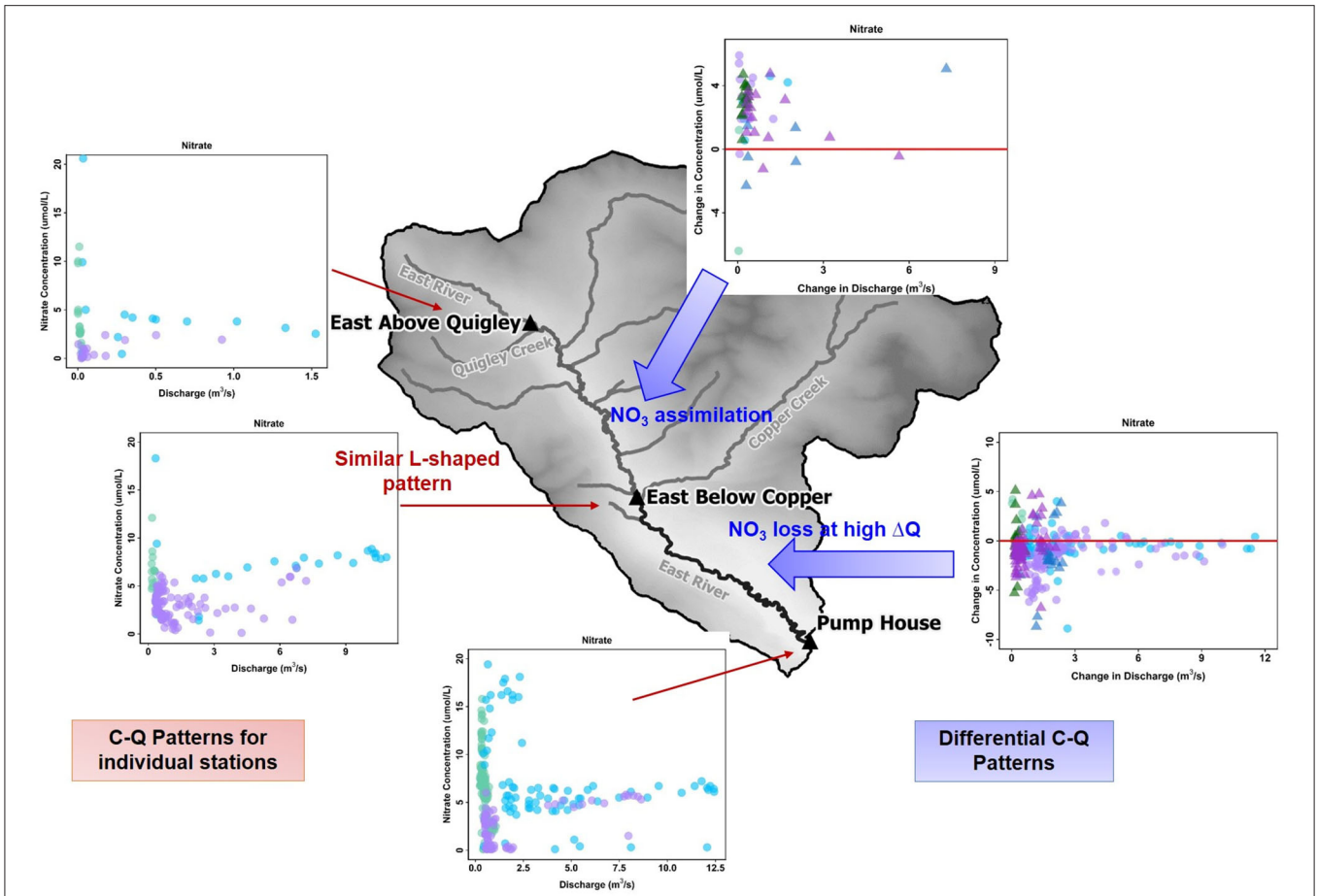

FIGURE 9 | A comparison of C-Q hysteresis patterns for NO_3 across individual stations and differential C-Q analyses across the upstream and downstream reaches encompassing those stations. The C-Q patterns show a consistent L-shaped pattern for NO_3 across all three stations of the East River Catchment. In comparison, differential C-Q metrics show gains in nitrate in the upstream reach and losses in the downstream reach during high gains in discharge.

or maintain their concentration in the stream. Last but not least, Fe showed a gaining trend within this reach, especially at high ΔQ values. At low ΔQ values, base flow and portions of rising limb showed gains in Fe, while the falling limb acts as both a source and sink of Fe. In their study, Wan et al. (2019) noted that water table fluctuations drive pyrite weathering in Mancos shale environments. Thus, gains in Fe are possibly associated with pyrite oxidation, while the losses during the falling limb may be attributed to chemolithoautotrophic microbial reactions, mineral precipitation or other processes that consume Fe (Arora et al., 2015, 2016).

Only three solutes showed a decline in concentration within this reach. In particular, SO_4 showed a consistent loss, while K and NO_3 showed losses at high ΔQ only. For both sulfate and nitrate, a gain in concentration was observed for most of the base flow period, while a loss was observed for most of the rising and falling limb (**Figures 7E,F**). This suggests that ground water is a significant source of sulfate and nitrate, while spring snowmelt and microbial reactions result in a decline of these concentrations. Cu and Na showed unique trends within this reach (**Table 5**). Na, in particular, showed losses at low ΔQ values and gains at high ΔQ. Further, gains in Na were only observed in 2015 and losses were limited to 2016. It is well known that rainfall is an important source of Na and Cl (Junge and Wurbe, 1958). Given that 2016 had lower than average rainfall while 2015 had a greater percentage of precipitation falling as summer rain, it is reasonable that we observed an increase in Na concentration only in 2015. Chloride concentrations, on the other hand, showed gains at both low and high ΔQ values. This is because deep groundwater is also a source of chloride in this segment of the river. In contrast to Na and Cl, Cu showed neither gains nor losses within this reach. A similar trend for Cu was also observed in the upstream reach.

Apart from Cu, Mg is the only other solute that showed consistent trends across the reaches (**Table 5**, **Figure 8A**). In fact, most solutes (7 out of 14) in the upstream reach showed trends opposite to those observed in the downstream reach. For example, DIC shows an overall losing trend within the upstream reach as opposed to an accumulation within the floodplain (**Figures 7D**, **8B**). Similar to DIC, solutes such as Ca, Mo, P,

and Si also switched from losing trends in the upstream reach to gaining trends in the downstream reach (see, for example, **Figure 8C**). Because EBC is a tributary junction assimilating flows from both EAQ and Copper Creek, the gross loss of a solute can imply that concentration at EAQ is higher than at Copper Creek or combined flow at EBC. Further note that EAQ captures the solute turnover from most of the upper catchments in the East River that have a higher fraction of basin area underlain by Mancos Shale (0.70) as compared to Copper Creek (0.01) (Carroll et al., 2018). Thus, most of the losing trends in the upstream reach are observed in geogenic elements associated with Mancos shale (e.g., DIC, Ca, Mo). In contrast, the downstream reach is defined by a low-energy meandering floodplain that is eroding primarily into the Mancos shale, which is composed of quartz, feldspar, interbedded clays, carbonates, and pyrite (Gaskill et al., 1991). Thus, gains in these geogenic solutes are observed in the downstream segment. **Table 5** further suggests that only K and NO_3 switched from gaining trends in the upstream section to losing trends in the downstream section (**Figures 7E**, **8D**). Given the ∼11 km long meanders in the downstream reach that offer significant area for lateral interactions and microbial uptake (Dwivedi et al., 2017, 2018b), it is reasonable that we observed a decline in reactive elements like K and NO_3. Taken together, most solutes (6 out of 14) showed losses within the upstream reach, with 50% of these solutes showing losses only at higher ΔQ values. In contrast, gains were limited to geogenic and runoff-derived solutes such as K, Mg, NO_3 and DOC. Sodium and chloride gains were limited to low ΔQ suggesting similar processes (e.g., rainfall) impacting their turnover. Only trace metals like Cu and Fe showed neither gains nor losses within this reach.

Comparison of ΔC-ΔQ to Other Studies and Implications

Capturing solute turnover across stream segments has important implications for water and land management applications such as nutrient transport, contaminant transport, and developing pollution prevention/intervention strategies. Previous studies have used transient storage models to simulate solute tracer movement, stream water-ground water exchange, and interpret downstream solute transport (Payn et al., 2009; Covino et al., 2011; Ward et al., 2013). While transient storage models have provided a useful context for quantifying stream water balance, these models are constrained by the use and interpretation of recovered tracer breakthrough curves. These models can therefore miss longer recovery times and underestimate lateral exchange from stream segments. Studies by Szeftel et al. (2011) and Ward et al. (2013) further suggest that discharge alone is a poor predictor of gross gains and losses across stream reaches and can complicate transient storage interpretations by adding uncertainty to model parameters. Work is still underway in developing new experimental techniques (e.g., heat tracing) and advanced process representation (e.g., reactive transport models) to improve mechanistic understanding of solute behavior at stream water-ground water interfaces (Krause et al., 2014; Dwivedi et al., 2018a; Arora et al., 2019a). In this regard, the differential C-Q analysis presented here provides an easy-to-use tool to investigate the fractional solute turnover as a function of water gains and losses over each stream segment. Although stream segments are defined by sampling locations, smart pairing of these locations for ΔC-ΔQ analyses can provide an integrated measure of lateral transport and biogeochemical processing across multiple segments. By following a different spatial scheme and organizing the river into multiple sections, ΔC-ΔQ can provide a rapid assessment of the proportional influences of hillslope contributions to stream water composition and aid in identifying stream segments that are vulnerable to change. Further, ΔC-ΔQ analysis can evaluate solute turnover at a range of flow conditions. At the East River site, smaller gains in solutes were typically confined to base flow conditions, while larger gains across upstream and downstream segments were associated with rising limb and snowmelt periods (e.g., **Figures 7**, **8**). Thus, this C-Q analysis is a valuable tool that can account for the specific sources, hillslope contributions and critical stream segments that can adversely impact instream concentrations.

SUMMARY AND CONCLUSIONS

Managing freshwater resources is proving difficult and exposes gaps in our scientific understanding of hydrological and biogeochemical processes controlling stream concentrations of solutes, trace metals and nutrients. To address this scientific and management need, we proposed a new differential C-Q analyses that identifies stream segments accumulating harmful chemicals under specific flow conditions. Hydrochemical data collected over 4 years in the headwaters of the Colorado River were analyzed through several C-Q metrics.

Log-log metrics demonstrated mostly negative relationships indicating that dilution is a primary mechanism controlling C-Q behavior within the ER watershed. Only a few solutes (DIC, K, Si) showed a discharge-invariant (chemostatic) behavior that was consistent across stations. Most solutes at EBC and PH showed chemodynamic behavior with two linear components at median Q values. Specifically, solutes at EBC showed more variance at low Q values and stability at higher flows, while solutes at PH showed greater variance at high flows and stability at low flows. In contrast, chemodynamic solutes at EAQ demonstrated highly linear trends and lacked the breakpoints or threshold behavior evident at other stations.

C-Q relationships showed that the most commonly observed hysteresis types were clockwise patterns indicative of a flushing behavior that causes a spike in solute concentration to occur before peak discharge. Counterclockwise patterns occurred less frequently and were more commonly observed at EAQ, indicative of distant sources or delayed mobilization. Hysteretic behavior suggestive of multiple sources and variable source area contributions was observed at both EBC and PH in the form of figure-eight and figure-then-counterclockwise patterns. Patterns exhibiting no hysteresis (Type 1) occurred relatively infrequently and only at EBC, suggesting a consistent supply of certain solutes like P and SO_4.

Differential C-Q metrics suggested that most solutes show a gaining behavior in the downstream reach of the East River, as opposed to the significant losing trend observed in the upstream reach. As much as 97% of the river discharge at EBC is from Copper Creek and only 3% is attributed to EAQ (Carroll et al., 2018). Given this hydrologic context, the larger inflows from Copper Creek caused attenuation of geogenic solutes tied to Mancos Shale at EBC. Gains in Mg, K, DOC, NO_3 loads at EBC can also be attributed to the topographic and lithologic characteristics of Copper Creek; however, most of these solutes are diminished in the downstream segment. In contrast, nearly 60% of the increase in discharge in the downstream reach is the result of lateral interactions in the low relief, meandering floodplain. Here, Mancos Shale is determined to be the primary source of Ca, DIC, DOC, Mg, Mo, NO_3, and SO_4 loads. Groundwater upwelling and surface runoff also contributed to concentrations of certain solutes such as Cl and P. Only Cu behaved conservatively across the upstream and downstream segments.

There are two interesting conclusions from the differential C-Q metrics applied here. First, differential C-Q metrics showed increasing concentration of trace metal (Fe and Mo) and nutrients (P and DOC) as the water flowed in the floodplain (downstream) section of the East River. Herein, median concentration of total P (446 ppb) was found to be higher when compared to other similar headwater streams (Spahr, 2000), and exceeding the state limit of 110 ppb (Colorado Water Quality Control Commission, 2012). Further increase in recreation activities and urbanization of these mountainous watersheds can significantly add to the concentrations of both P and N. However, the downstream reach seems to be adequate in reducing instream N concentration. In contrast, the upstream reach can absorb the increases in P and N concentrations to a certain limit. This demonstrates the impact of such C-Q analyses, which can clearly indicate when and where small increases in nutrients like P and N can be particularly concerning given the potential for algal growth and eutrophication (**Figure 9**). Second, differential C-Q analyses under the falling limb conditions of 2015 vs. 2016 provided greater understanding of the catchment processes that impact instream concentrations. Within the downstream section of the East River, certain solute concentrations responded to changes in hydrologic forcing, such as Na and K. However, other solutes showed minimal control of changing precipitation inputs. Such an understanding is essential as headwater catchments like the East River brace toward greater variability in precipitation form and inputs. This study suggests that the differential C-Q analysis is a valuable tool for assessing differences across stream reaches, comparing solute accumulation and mobilization within, and across reaches, and monitoring solute responses in the face of hydrologic and climatic perturbations. The spatial segmentation possible with this technique can aid watershed and land managers in identifying the stream segments that are essential to monitor, the long-term time series to continue monitoring (e.g., P in downstream reach), and designing intervention strategies (e.g., development of new ski resorts away from certain reaches).

DATA AVAILABILITY STATEMENT

Publicly available datasets were analyzed in this study. This data can be found here: http://dx.doi.org/10.21952/WTR/1495380.

AUTHOR CONTRIBUTIONS

BA and CS designed the study. MB, MN, and DD were in charge of the technical aspects of this work. KW collected samples and provided ancillary data. RC provided discharge data and WD performed geochemical analyses. BA and MB wrote the manuscript, with edits from CS, RC, DD, WD, and SH. All authors contributed to the article and approved the submitted version.

ACKNOWLEDGMENTS

This material is based on work supported as part of the Aggregated Watershed Component of the Watershed Function Scientific Focus Area funded by the U.S. Department of Energy, Office of Science, Office of Biological and Environmental Research under Award no. DE-AC02-05CH11231.

SUPPLEMENTARY MATERIAL

The Supplementary Material for this article can be found online at: https://www.frontiersin.org/articles/10.3389/frwa.2020.00024/full#supplementary-material

REFERENCES

Aich, V., Zimmermann, A., and Elsenbeer, H. (2014). Quantification and interpretation of suspended-sediment discharge hysteresis patterns: How much data do we need? *Catena* 122, 120–129. doi: 10.1016/j.catena.2014.06.020

Anderson, S. P., Dietrich, W. E., Torres, R., Montgomery, D. R., and Loague, K. (1997). Concentration-discharge relationships in runoff from a steep, unchanneled catchment. *Water Resour. Res.* 33, 211–225. doi: 10.1029/96WR02715

Arora, B., Dwivedi, D., Faybishenko, B., Jana, R. B., and Wainwright, H. M. (2019a). Understanding and predicting vadose zone processes. *Rev. Mineral. Geochemistry* 85, 303–328. doi: 10.2138/rmg.2019.85.10

Arora, B., Sengör, S. S., Spycher, N. F., and Steefel, C. I. (2015). A reactive transport benchmark on heavy metal cycling in lake sediments. *Comput. Geosci.* 19, 613–633. doi: 10.1007/s10596-014-9445-8

Arora, B., Spycher, N. F., Steefel, C. I., Molins, S., Bill, M., Conrad, M. E., et al. (2016). Influence of hydrological, biogeochemical and temperature transients on subsurface carbon fluxes in a flood plain environment. *Biogeochemistry*. 127, 367–396. doi: 10.1007/s10533-016-0186-8

Arora, B., Wainwright, H. M., Dwivedi, D., Vaughn, L. J., Curtis, J. B., Torn, M. S., et al. (2019b). Evaluating temporal controls on greenhouse gas (GHG) fluxes in an Arctic tundra environment: An entropy-based approach. *Sci. Total Environ.* 649, 284–299.

Battaglin, W. A., Hay, L. A., and Markstrom, S. L. (2012). *Watershed Scale Response to Climate Change—East River.* Basin: Colorado. doi: 10.3133/fs20113126

Bernal, S., Butturini, A., and Sabater, F. (2006). Inferring nitrate sources through end member mixing analysis in an intermittent Mediterranean stream. *Biogeochemistry* 81, 269–289. doi: 10.1007/s10533-006-9041-7

Bieroza, M. Z., Heathwaite, A. L., Bechmann, M., Kyllmar, K., and Jordan, P. (2018). The concentration-discharge slope as a tool for water quality management. *Sci. Total Environ*. 630, 738–749. doi: 10.1016/j.scitotenv.2018.02.256

Carroll, K. P., Rose, S., and Peters, N. E. (2007). *Concentration/Discharge Hysteresis Analysis of Storm Events at the Panola Mountain Research.* Watershed: Gerogia.

Carroll, R. W. H., Bearup, L. A., Brown, W., Dong, W., Bill, M., and Willlams, K. H. (2018). Factors controlling seasonal groundwater and solute flux from snow-dominated basins. *Hydrol. Process.* 32, 2187–2202. doi: 10.1002/hyp.13151

Carroll, R. W. H., Deems, J. S., Niswonger, R., Schumer, R., and Williams, K. H. (2019). The importance of interflow to groundwater recharge in a snowmelt-dominated headwater basin. *Geophys. Res. Lett*. 46, 5899–5908. doi: 10.1029/2019GL082447

Chanat, J. G., Rice, K. C., and Hornberger, G. M. (2002). Consistency of patterns in concentration-discharge plots. *Water Resour. Res.* 38, 22-1–22-10. doi: 10.1029/2001WR000971

Colorado Water Quality Control Commission (2012). *Regulation No. 85. Nutrients Management Control Regulation*. 5 CCR 1002-85.

Covino, T., McGlynn, B., and Mallard, J. (2011). Stream-groundwater exchange and hydrologic turnover at the network scale. *Water Resour. Res*. 47, 1–11. doi: 10.1029/2011WR010942

Deacon, J. R., and Driver, N. E. (1999). Distribution of trace elements in streambed sediment associated with mining activities in the upper colorado river basin, Colorado, USA, 1995–96. *Arch. Environ. Contam. Toxicol*. 37, 7–18. doi: 10.1007/s002449900484

Dong, W., Wan, J., Tokunaga, T. K., Gilbert, B., and Williams, K. H. (2017). Transport and humification of dissolved organic matter within a semi-arid floodplain. *J. Environ. Sci*. 57, 24–32. doi: 10.1016/j.jes.2016.12.011

Dwivedi, D., Arora, B., Steefel, C. I., Dafflon, B., and Versteeg, R. (2018a). Hot spots and hot moments of nitrogen in a riparian corridor. *Water Resour. Res.* 54, 205–222. doi: 10.1002/2017WR022346

Dwivedi, D., Steefel, C. I., Arora, B., Newcomer, M., Moulton, J. D., Dafflon, B., et al. (2018b). Geochemical exports to river from the intrameander hyporheic zone under transient hydrologic conditions: east river mountainous watershed, colorado. *Water Resour. Res*. 54, 8456–8477. doi: 10.1029/2018WR023377

Dwivedi, D., Steefel, I. C., Arora, B., and Bisht, G. (2017). Impact of intra-meander hyporheic flow on nitrogen cycling. *Procedia Earth Planet. Sci*. 17, 404–407. doi: 10.1016/j.proeps.2016.12.102

Evans, C., and Davies, T. D. (1998). Causes of concentration/discharge hysteresis and its potential as a tool for analysis of episode hydrochemistry. *Water Resour. Res*. 34, 129–137. doi: 10.1029/97WR01881

Gaskill, D. L., Mutschler, F. E., Kramer, J. H., Thomas, J. A., and Zahony, S. G. (1991). *Geologic Map of the Gothic Quadrangle, Gunnison County, Colorado*. Reston, VA: U.S. Geological Survey Map GQ-1969. U.S. Geological Survey.

Gellis, A. C. (2013). Factors influencing storm-generated suspended-sediment concentrations and loads in four basins of contrasting land use, humid-tropical Puerto Rico. *Catena*. 104, 39–57. doi: 10.1016/j.catena.2012.10.018

Godsey, S., Kirchner, J., and Clow, D. (2009). Concentration–discharge relationships reflect chemostatic characteristics of US catchments. *Hydrol. Process*. 23, 1844–1864. doi: 10.1002/hyp.7315

Gwenzi, W., Chinyama, S. R., and Togarepi, S. (2017). Concentration-discharge patterns in a small urban headwater stream in a seasonally dry water-limited tropical environment. *J. Hydrol*. 550, 12–25. doi: 10.1016/j.jhydrol.2017.04.029

Hall, F. R. (1970). Dissolved solids-discharge relationships: 1. Mixing Models. *Water Resour. Res*. 6, 845–850. doi: 10.1029/WR006i003p00845

Hamshaw, S. D., Dewoolkar, M. M., Schroth, A. W., Wemple, B. C., and Rizzo, D. M. (2018). A new machine-learning approach for classifying hysteresis in suspended-sediment discharge relationships using high-frequency monitoring data. *Water Resour. Res*. 54, 4040–4058. doi: 10.1029/2017WR022238

Hoagland, B., Russo, T. A., and Brantley, S. L. (2017). Relationships in a headwater sandstone stream. *Water Resour. Res.* 53, 4643–4667. doi: 10.1002/2016WR019717

Hornberger, G. M., Scanlon, T. M., and Raffensperger, J. P. (2001). Modelling transport of dissolved silica in a forested headwater catchment: the effect of hydrological and chemical time scales on hysteresis in the concentration-discharge relationship. *Hydrol. Process*. 15, 2029–2038. doi: 10.1002/hyp.254

Hubbard, S. S., Williams, K. H., Agarwal, D., Banfield, J., Beller, H., Bouskill, N., et al. (2018). The east river, colorado, watershed: a mountainous community testbed for improving predictive understanding of multiscale hydrological-biogeochemical dynamics. *Vadose Zo. J*. 17, 1–25. doi: 10.2136/vzj2018.03.0061

Junge, C. E., and Wurbe, R. T. (1958). The concentration of chloride, sodium, potassium and sulfate in rain water over the United States. J. *Meteorol*. 15, 417–425.

Kenwell, A., Navarre-Sitchler, A., Prugue, R., Spear, J. R., Hering, A. S., Maxwell, R. M., et al. (2016). Using geochemical indicators to distinguish high biogeochemical activity in floodplain soils and sediments. *Sci. Total Environ*. 563–564, 386–395. doi: 10.1016/j.scitotenv.2016.04.014

Knapp, J. L. A., von Freyberg, J., Studer, B., Kiewiet, L., and Kirchner, J. W. (2020). Concentration–discharge relationships vary among hydrological events, reflecting differences in event characteristics. *Hydrol. Earth Syst. Sci*. 24, 2561–2576. doi: 10.5194/hess-24-2561-2020

Koger, J. M., Newman, B. D., and Goering, T. J. (2018). Chemostatic behaviour of major ions and contaminants in a semiarid spring and stream system near Los Alamos, NM, USA. *Hydrol. Process*. 32, 1709–1716. doi: 10.1002/hyp.11624

Krause, S., Boano, F., Cuthbert, M. O., Fleckenstein, J. H., and Lewandowski, J. (2014). Understanding process dynamics at aquifer-surface water interfaces: an introduction to the special section on new modeling approaches and novel experimental technologies. *Water Resour. Res.* 50, 1847–1855. doi: 10.1002/2013WR014755

Lloyd, C. E. M., Freer, J. E., Johnes, P. J., and Collins, A. L. (2016). Using hysteresis analysis of high-resolution water quality monitoring data, including uncertainty, to infer controls on nutrient and sediment transfer in catchments. *Sci. Total Environ*. 543, 388–404. doi: 10.1016/j.scitotenv.2015.11.028

Markstrom, S. L., Hay, L. E., Ward-Garrison, C. D., Risley, J. C., Battaglin, W. A., Bjerklie, D. M., et al. (2012). *Integrated Watershed-Scale Response to Climate Change for Selected Basins Across the United States*. doi: 10.3133/sir20115077

McDonnell, J. J. (1990). A rationale for old water discharge through macropores in a steep, humid catchment. *Water Resour. Res*. 26, 2821–2832. doi: 10.1029/WR026i011p02821

McDonnell, J. J., Sivapalan, M., Vaché, K., Dunn, S., Grant, G., Haggerty, R., et al. (2007). Moving beyond heterogeneity and process complexity: a new vision for watershed hydrology. *Water Resour. Res*. 43, 1–6. doi: 10.1029/2006WR005467

Megnounif, A., Terfous, A., and Ouillon, S. (2013). A graphical method to study suspended sediment dynamics during flood events in the Wadi Sebdou, NW Algeria (1973–2004). *J. Hydrol*. 497, 24–36. doi: 10.1016/j.jhydrol.2013.05.029

Meybeck, M., and Moatar, F. (2012). Daily variability of river concentrations and fluxes: indicators based on the segmentation of the rating curve. *Hydrol. Process.* 26, 1188–1207. doi: 10.1002/hyp.8211

Milly, P. C. D., Betancourt, J., Falkenmark, M., Hirsch, R. M., Kundzewicz, Z. W., Lettenmaier, D. P., et al. (2008). Climate change. Stationarity is dead: whither water management? *Science* 319, 573–574. doi: 10.1126/science.1151915

Milne, A. E., Macleod, C. J. A., Haygarth, P. M., Hawkins, J. M. B., and Lark, R. M. (2009). The wavelet packet transform: a technique for investigating temporal variation of river water solutes. *J. Hydrol*. 379, 1–19. doi: 10.1016/j.jhydrol.2009.09.038

Moatar, F., Abbott, B. W., Minaudo, C., Curie, F., and Pinay, G. (2017). Elemental properties, hydrology, and biology interact to shape concentration-discharge curves for carbon, nutrients, sediment, and major ions. *Water Resour. Res*. 53, 1270–1287. doi: 10.1002/2016WR019635

Molins, S., Trebotich, D., Arora, B., Steefel, C. I. and Deng, H. (2019). Multi-scale model of reactive transport in fractured media: diffusion limitations on rates. *Transport in Porous Media*. 128, 701–721.

Morrison, S. J., Goodknight, C. S., Tigar, A. D., Bush, R. P., and Gil, A. (2012). Naturally occurring contamination in the mancos shale. *Environ. Sci. Technol*. 46, 1379–1387. doi: 10.1021/es203211z

Murphy, J. C., Hornberger, G. M., and Liddle, R. G. (2014). Concentration-discharge relationships in the coal mined region of the New River basin and Indian Fork sub-basin, Tennessee, USA. *Hydrol. Process*. 28, 718–728. doi: 10.1002/hyp.9603

Musolff, A., Schmidt, C., Selle, B., and Fleckenstein, J. H. (2015). Catchment controls on solute export. *Adv. Water Resour*. 86, 133–146. doi: 10.1016/j.advwatres.2015.09.026

Payn, R. A., Gooseff, M. N., McGlynn, B. L., Bencala, K. E., and Wondzell, S. M. (2009). Channel water balance and exchange with subsurface flow along a mountain headwater stream in Montana, United States. *Water Resour. Res.* 45, 1–14. doi: 10.1029/2008WR007644

Pearce, A. J., Stewart, M. K., and Sklash, M. G. (1986). Storm runoff generation in humid headwater catchments: 1. where does the water come from? *Water Resour. Res.* 22, 1263–1272. doi: 10.1029/WR022i008p01263

Pribulick, C. E., Foster, L. M., Bearup, L. A., Navarre-Sitchler, A. K., Williams, K. H., Carroll, R. W. H., et al. (2016). Contrasting the hydrologic response due to land cover and climate change in a mountain headwaters system. *Ecohydrology* 9, 1431–1438. doi: 10.1002/eco.1779

Rodríguez-Iturbe, I., Ijjász-Vásquez, E. J., Bras, R. L., and Tarboton, D. G. (1992). Power law distributions of discharge mass and energy in river basins. *Water Resour. Res.* 28, 1089–1093. doi: 10.1029/91WR03033

Rose, L. A., Karwan, D. L., and Godsey, S. E. (2018). Concentration-discharge relationships describe solute and sediment mobilization, reaction, and transport at event and longer timescales. *Hydrol. Process.* 32, 2829–2844. doi: 10.1002/hyp.13235

Rose, S. (2003). Comparative solute-discharge hysteresis analysis for an urbanized and a "control basin" in the Georgia (USA) Piedmont. *J. Hydrol.* 284, 45–56. doi: 10.1016/j.jhydrol.2003.07.001

Sklash, M. G., Stewart, M. K., and Pearce, A. J. (1986). Storm runoff generation in humid headwater catchments: 2. a case study of hillslope and low-order stream response. *Water Resour. Res.* 22, 1273–1282. doi: 10.1029/WR022i008p01273

Spahr, N. E. (2000). Water quality in the upper colorado river basin, colorado, 1996-98. *U.S. Dep. Interior, U.S. Geol. Survey Circular.* 1214. doi: 10.3133/cir1214

Sullivan, P. L., Stops, M. W., Macpherson, G. L., Li, L., Hirmas, D. R., and Dodds, W. K. (2018). How landscape heterogeneity governs stream water concentration-discharge behavior in carbonate terrains (Konza Prairie, USA). *Chem. Geol.* 527:118989. doi: 10.1016/j.chemgeo.2018.12.002

Szeftel, P., Moore, R. D., and Weiler, M. (2011). Influence of distributed flow losses and gains on the estimation of transient storage parameters from stream tracer experiments. *J. Hydrol.* 396, 277–291. doi: 10.1016/j.jhydrol.2010.11.018

Thompson, S. E., Basu, N. B., Lascurain, J., Aubeneau, A., and Rao, P. S. C. (2011). Relative dominance of hydrologic versus biogeochemical factors on solute export across impact gradients. *Water Resour. Res.* 47, 1–20. doi: 10.1029/2010WR009605

Tokunaga, T. K., Wan, J., Williams, K. H., Brown, W., Henderson, A., Kim, Y., et al. (2019). Depth- and time-resolved distributions of snowmelt-driven hillslope subsurface flow and transport and their contributions to surface waters. *Water Resour. Res.* 55, 9474–9499. doi: 10.1029/2019WR025093

U.S. Department of Energy (2011). *Natural Contamination from the Mancos Shale.*

Udall, B., and Overpeck, J. (2017). The twenty-first century Colorado River hot drought and implications for the future. *Water Resour. Res.* 53, 2404–2418. doi: 10.1002/2016WR019638

Wan, J., Tokunaga, T. K., Williams, K. H., Dong, W., Brown, W., Henderson, A. N., et al. (2019). Predicting sedimentary bedrock subsurface weathering fronts and weathering rates. *Sci. Rep.* 9:17198. doi: 10.1038/s41598-019-53205-2

Ward, A. S., Gooseff, M. N., Voltz, T. J., Fitzgerald, M., Singha, K., and Zarnetske, J. P. (2013). How does rapidly changing discharge during storm events affect transient storage and channel water balance in a headwater mountain stream? *Water Resour. Res.* 49, 5473–5486. doi: 10.1002/wrcr.20434

Williams, G. P. (1989). Sediment concentration versus water discharge during single hydrologic events in rivers. *J. Hydrol.* 111, 89–106. doi: 10.1016/0022-1694(89)90254-0

Williams, K. H., Long, P. E., Davis, J. A., Wilkins, M. J., N'Guessan, A. L., Steefel, C. I., et al. (2011). Acetate availability and its influence on sustainable bioremediation of uranium-contaminated groundwater. *Geomicrobiol. J.* 28, 519–539. doi: 10.1080/01490451.2010.520074

Winnick, M. J., Carroll, R. W. H., Williams, K. H., Maxwell, R. M., Dong, W., and Maher, K. (2017). Snowmelt controls on concentration-discharge relationships and the balance of oxidative and acid-base weathering fluxes in an alpine catchment, East River, Colorado. *Water Resour. Res.* 53, 2507–2523. doi: 10.1002/2016WR019724

Wood, P. A. (1977). Controls of variation in suspended sediment concentration in the River Rother, West Sussex, England. *Sedimentology* 24, 437–445. doi: 10.1111/j.1365-3091.1977.tb00131.x

Wymore, A. S., Brereton, R. L., Ibarra, D. E., Maher, K., and Mcdowell, W. H. (2017). Critical zone structure controls concentration-discharge relationships and solute generation in forested tropical montane watersheds. *Water* 53, 6279–6295. doi: 10.1002/2016WR020016

Zorio, S. D., Williams, C. F., and Aho, K. A. (2016). Sixty-five years of change in montane plant communities in Western Colorado, U.S.A. Arctic, Antarct. *Alp. Res.* 48, 703–722. doi: 10.1657/AAAR0016-011

Conflict of Interest: The authors declare that the research was conducted in the absence of any commercial or financial relationships that could be construed as a potential conflict of interest.

frontiers in Water

ORIGINAL RESEARCH
published: 20 August 2020
doi: 10.3389/frwa.2020.00022

Linking Hydrobiogeochemical Processes and Management Techniques to Close Nutrient Loops in an Arid River

Kelsey Bicknell[1], *Peter Regier*[1†], *David J. Van Horn*[2], *Kelli L. Feeser*[2] *and Ricardo González-Pinzón*[1*]

[1] Department of Civil, Construction and Environmental Engineering, University of New Mexico, Albuquerque, NM, United States, [2] Department of Biology, University of New Mexico, Albuquerque, NM, United States

In this study, we explored opportunities to optimize food-energy-water (FEW) resources by closing nutrient loops in aridland rivers. We evaluated source and sink behavior of nitrogen as nitrate (NO_3-N) in three connected channels associated with an irrigation network, i.e., man-made delivery and drain canals, and the main stem of the Rio Grande river near Albuquerque, New Mexico, USA. All three channels are located downstream of a large wastewater treatment plant that is the main contributor of nutrients to this reach of the Rio Grande. We used a mass balance approach paired with stable isotope analysis to link sources and processing of NO_3-N with reaction pathways within the channels over time (a year) and through space (along ∼14–53 km reaches). Results indicated that the growing season was an important period of net sink behavior for the delivery channel and the Rio Grande, but the drain channel was a year-round net source. Stable isotope analyses of ^{15}N and ^{18}O found a distinct nitrate signature in the drain associated with biological processing, as well as sites along the Rio Grande impacted by agricultural outflow, but no equivalent signature was present in the delivery channel. Based on our findings, we provide recommendations to help close nutrient loops in our study system and in analogous aridland irrigation networks by (1) minimizing loss during the transfer of nutrients from wastewater facilities to agricultural areas, and (2) minimizing enrichment to downstream aquatic ecosystems by sequestering nutrients that would otherwise escape the nutrient loop.

Keywords: nitrate dynamics, close nutrient loops, arid rivers, water management, hydrobiogeochemical processes, food-energy-water nexus

OPEN ACCESS

Edited by:
Dipankar Dwivedi, Lawrence Berkeley National Laboratory, United States

Reviewed by:
Clare Robinson, University of Western Ontario, Canada
Megan J. Klaar, University of Leeds, United Kingdom

***Correspondence:**
Ricardo González-Pinzón
gonzaric@unm.edu

***Present address:**
Peter Regier, Pacific Northwest National Laboratory, Richland, WA, United States

Specialty section:
This article was submitted to Water and Critical Zone, a section of the journal Frontiers in Water

Received: *30 March 2020*
Accepted: *07 July 2020*
Published: *20 August 2020*

Citation:
Bicknell K, Regier P, Van Horn DJ, Feeser KL and González-Pinzón R (2020) Linking Hydrobiogeochemical Processes and Management Techniques to Close Nutrient Loops in an Arid River. Front. Water 2:22. doi: 10.3389/frwa.2020.00022

INTRODUCTION

Nitrogen (N) and phosphorus (P) are limiting nutrients for plant growth (Chapin, 1980; Vitousek and Howarth, 1991), and current agricultural practices depend on addition of both N and P via fertilizers for crop production to keep pace with global food consumption (Gruber and Galloway, 2008). The majority of N and P fertilizers produced worldwide rely either on limited resources (i.e., phosphate mining) or energy-intensive, polluting processes (i.e., the Haber-Bosch process) (Erisman et al., 2008; Cordell et al., 2009). As global fertilizer production increases, higher demands on finite resources have motivated efforts to increase nutrient use efficiency through closing nutrient loops (Mortensen et al., 2016).

Holistic approaches to ecosystem management recognize that managing the food-energy-water (FEW) sectors in isolation is unsustainable and this has sparked the call for FEW nexus approaches toward environmental sustainability and resource security (FAO, 2014; NSF, 2014). Within this context, expanding wastewater reuse could help close nutrient loops through nutrient recycling and result in energy savings, including reduced fertilizer production and transportation, improving resource recovery and potentially environmental health (Hanjra et al., 2012). This approach is particularly relevant in arid regions because water is scarce and waste water treatment plant (WWTP) effluents are often the dominant source of bioavailable nutrients to streams and rivers, given that most of the population reside near large arid rivers (Caraco and Cole, 2001; Dumont et al., 2005; Harrison et al., 2005; Mortensen et al., 2016). For example, in the study region described here, 50% of New Mexicans live in the Albuquerque metropolitan area along the Rio Grande valley, and similar cases occur in Idaho along the Snake River, Arizona along the Gila River, multiple states along the Colorado River, Australia, western Spain, Mexico, and muliple countries in Africa along the Nile river.

Recent global estimates suggest that about 10 and 2 g/person/day of N and P, respectively, are available as nutrients in wastewater from human metabolism, representing magnitudes that are comparable to major components of nutrient cycles (Larsen et al., 2016). For example, the N available from the wastewater generated by nine billion people would be on the same order of magnitude as anthropogenic production through the energy-intensive Haber-Bosh fixation process (forecasted as ∼35 Mt of reactive N per year). Recent sustainability assessments suggest that an estimated 40% of nitrogen fertilizer is lost back to the environment rather than utilized by crops (Galloway et al., 2004), and increased nutrient recycling from wastewater effluents may provide a source to offset such losses (Childers et al., 2011; Larsen et al., 2016).

Recycling wastewater as a management technique to close nutrient loops relies on identifying nutrient sources and sinks in fluvial networks, particularly in large rivers. In aridlands, irrigation networks contain high densities of regulatory structures (e.g., dams and weirs), infrastructure (e.g., supply canals and drainage ditches), and intermittent flow paths (e.g., flood irrigation of fields) that enhance nutrient retention via increased residence times, uptake in biogeochemically heterogeneous channels, and uptake by channel vegetation and crops (Soana et al., 2011; Bartoli et al., 2012; Lassaletta et al., 2012; Mortensen et al., 2016). In these regions, water is withdrawn from large rivers at diversion dams, routed into canals that bifurcate until they form small channels, and is applied to fields through flood irrigation. This water then percolates through the soil column, enters the shallow alluvial aquifer, and flows via shallow groundwater flowpaths to low-lying agricultural return drains. These drains gather water from numerous subsurface outflows, coalesce to form larger channels, and eventually return to the river at outflow points. This complex system effectively turns the aridland river flood plains into systems that can be highly nutrient retentive (Caraco and Cole, 2001) and provide the potential to close nutrient loops by recycling the nutrients from wastewater effluent back into crops (Mortensen et al., 2016).

While there is a clear need to maximize water and nutrient recycling in aridland fluvial networks and an abundance of conveyance and water control structures exist that could be used to facilitate these goals, little is known about nutrient processing rates in the different compartments of these systems and how management can be structured to optimize nutrient reuse (Mortensen et al., 2016). In this study, we used rapid assessments (i.e., cross-sectional and longitudinal monitoring assessments taken at multiple sites within a day) over a year in three characteristic reaches of an aridland river-irrigation network in the Middle Rio Grande Basin to resolve spatiotemporal patterns of nutrient sources, processing, and reaction pathways. Based on our understanding of the system, we developed recommendations to (1) minimize loss during the transfer of nutrients from wastewater facilities to agricultural areas, and (2) minimize enrichment to downstream aquatic ecosystems by sequestering nutrients that would otherwise escape the nutrient loop.

METHODS

Site Description

This study took place in the Middle Rio Grande Basin in New Mexico, USA. This basin is the most agriculturally productive and densely populated area along the 3,000 km length of the Rio Grande river (**Figure 1**), and encompasses a reach ∼300 km long bounded by Cochiti Dam to the north and Elephant Butte Reservoir to the south. The Rio Grande is the main source of water for flood irrigation to over 4,000 km^2 of cropland, which consists primarily of alfalfa and pasture grass. The historic river floodplain contains a complex network of adjacent channels, summing to ∼2,100 km of delivery canals and acequias (small irrigation ditches) that carry water to croplands and drain ditches that return excess water back to the main river. This irrigation network is managed and maintained by the Middle Rio Grande Conservancy District (MRGCD).

We studied two major characteristic channels of this irrigation network, i.e., a delivery and a drain canal, and the main channel of the Rio Grande, to understand nutrient sources and sinks and the biogeochemical and hydrological processes occurring during the growing (March-October) and non-growing (November-February) seasons. In the area of the study sites, water is diverted from the Rio Grande at Isleta Diversion Dam into delivery canals and acequias (irrigation ditches) that supply agricultural users (**Figure 1**). At the start and end of the growing season, the delivery canals are flushed with high flows to remove debris from the channel. Return drains, which are dredged below the elevation of the water table, collect excess irrigation water, drainage from the agriculture fields, and lateral groundwater seepage from the river. The water in the drains is returned to the Rio Grande ∼50 km downstream of where it was diverted (Bartolino and Cole, 2002). The specific channels that we studied were the Peralta Main Canal and Lower Peralta Riverside Drain, hereafter referred to as the "Delivery" and the "Drain," respectively (**Figure 2**). These sites were selected for study

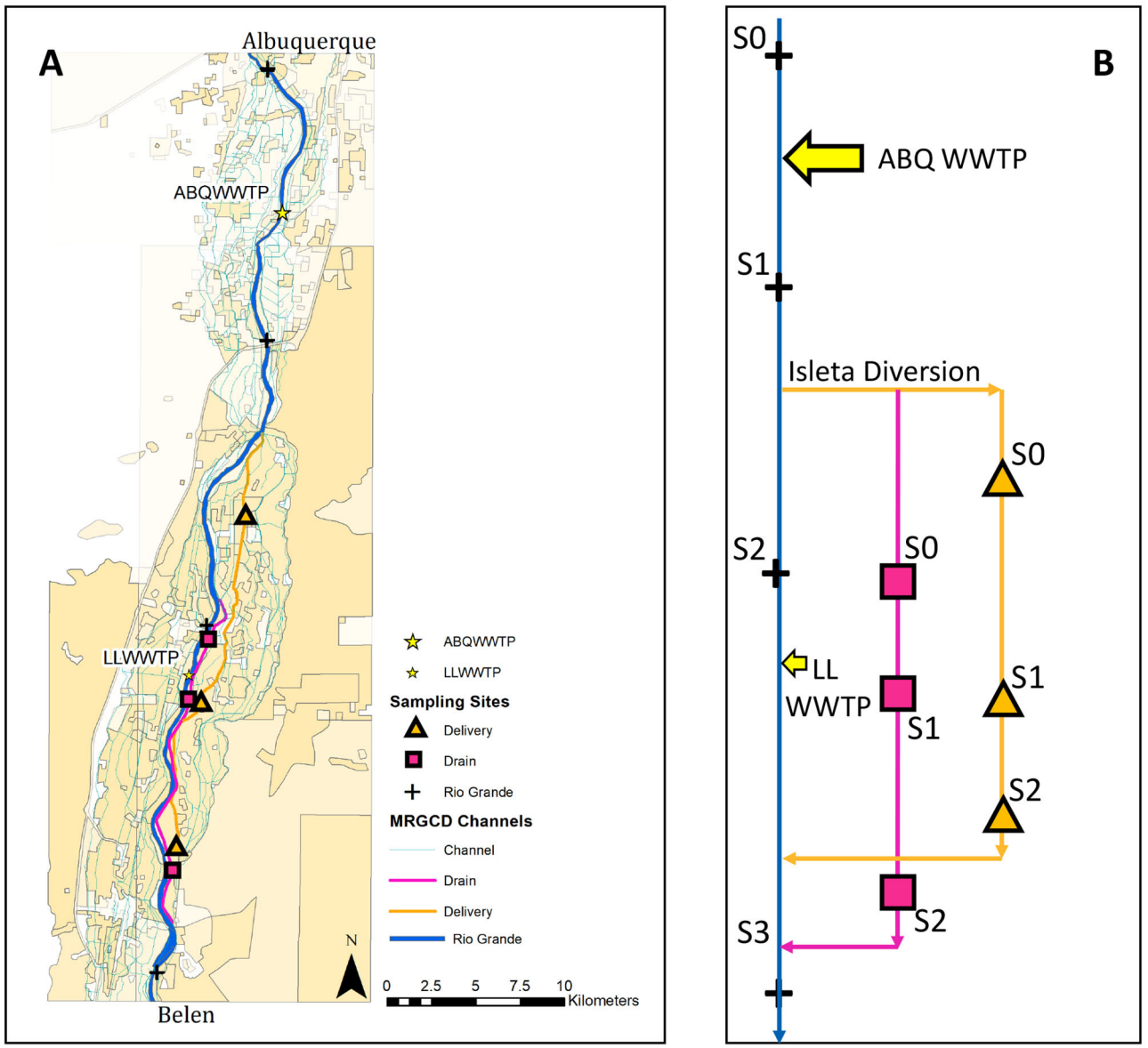

FIGURE 1 | (A) Study reaches: Rio Grande (blue), Drain (pink), and Delivery (orange) channels with sampling sites along each (black markers). The Albuquerque WWTP (ABQ WWTP) and the Los Lunas WWTP (LL WWTP) discharge into the Rio Grande, and are labeled in yellow. **(B)** Flow schematic using the same color scheme as **(A)** to show the location of sampling sites in **Table 1** in relation to various inputs.

based on accessibility and minimal cross connections between conveyance types.

Flows within the Delivery canal (~8 m top width) vary between 0.4 and 7 m^3/s from the point of diversion to the point of return to the Rio Grande during the growing season (the canal runs dry during the non-growing season). Turbidity (~300 NTU on average, with peaks of up to 5,000 NTU) and sediment texture (~99.8% of sediment particles are <10 mm, and ~4% are <0.1 mm) are similar to that of the Rio Grande (Fluke et al., 2019; Regier et al., 2020), and primary productivity is limited to the edge of the wetted channel and its surrounding banks. The discharge in the Drain (~6 m top width) varies between 0.4 and 2.5 m^3/s. Turbidity is low (~20 NTU on average) in this channel, with the bed of the channel covered in filamentous algae and emergent macrophytes. The banks of the Delivery canal and the Drain are lined with Coyote Willow (*Salix exigua*) and various species of grass (*Agrostis gigantea* and *Sporobolus wrightii*).

Within our study reach, the Rio Grande (~110 m top width) receives inputs from the Albuquerque WWTP (ABQ WWTP) and the Los Lunas WWTP (LL WWTP) (**Figure 1**). The ABQ WWTP releases ~2.5 m^3/s of water at concentrations between 3 and 5 mg/L of NO_3-N into the Rio Grande upstream of the Isleta Diversion Dam, thus water in the Delivery canal is a mix

FIGURE 2 | Sampling sites at the **(A)** Rio Grande (~110 m wide), **(B)** Delivery Canal (~8 m wide), and **(C)** Drain (~6 m wide).

of water from the Rio Grande and ABQ WWTP effluent. The LL WWTP releases ~0.05 m^3/s at concentrations ranging from 4 to 25 mg/L NO_3-N downstream of the Isleta Diversion Dam (Van Horn, 2010; Mortensen et al., 2016).

Data Collection

We took water samples every month along the study reaches between October 2017 and October 2018, for a total of 13 sampling campaigns. We identified three to four sampling sites along each reach to track the longitudinal change in NO_3-N loads (kg/day) and isotopic signals as water traveled through the system. The length between the first and last monitoring sites in the Delivery, Drain, and Rio Grande reaches were 21, 14, and 53 km, respectively (**Figure 1**, **Table 1**). Point sources (i.e., small drains discharging) to each reach were also sampled to calculate nutrient budgets. Sampling sites were chosen due to their proximity to a gauging station operated by either the USGS or MRGCD (**Table 1**) and point sources were visually identified in reconnaissance campaigns. At sites that were ungauged, discharge was measured using a SonTek FlowTracker handheld ADV (SonTek, San Diego, CA). The Delivery canal was not sampled during the non-growing season as it was dry. Grab samples of water were collected using 60 mL syringes, filtered using 0.45-μm nylon filters, transported to lab on ice in the dark, and stored frozen until analysis (Pfaff, 1996).

Solute Concentrations and Isotopic Analysis

We determined Cl and NO_3 concentrations from grab samples using a Dionex ICS-1000 Ion Chromatograph with AS23/AG23 analytical and guard columns. We employed dual nitrogen and oxygen isotopic analysis to determine potential nitrate sources and mechanisms of removal. For this, 20 mL aliquots from the samples collected were analyzed for ambient isotopes at the University of Washington IsoLab using a Gas Bench II coupled with a Finnigan Delta Plus Advantage mass spectrometer. Nitrate isotopes were determined using the denitrifier method (Sigman et al., 2001).

Values for ^{15}N and ^{18}O are reported in units of per-mil (‰), which is defined as the ratio of heavy to light isotope in the sample

TABLE 1 | Sampling sites and their distance from the Albuquerque WWTP.

Channel	Site name	Distance from ABQ WWTP (km)	Longest reach distance (km)	Source of discharge data
Delivery	Delivery S0	18	21	MRGCD
	Delivery S1	30		MRGCD
	Delivery S2	39		MRGCD
Drain	Drain S0	27	14	Manual
	Drain S1	31		Manual
	Drain S2	41		Manual
Rio Grande	Rio Grande S0	−9	53	USGS (08330000)
	Rio Grande S1	8		USGS (08330875)
	Rio Grande S2	26		USGS (08331160)
	Rio Grande S3	44		USGS (08331510)

MRGCD stands for Middle Rio Grande Conservancy District and USGS stands for United States Geological Survey.

(R_{sample}) vs. a standard ($R_{standard}$):

$$\delta\,(‰) = \left(\frac{R_{sample}}{R_{standard}} - 1\right) * 1000 \quad (1)$$

Measured values of ^{15}N and ^{18}O of NO_3 are compared to international standards USGS35, USGS34, USGS32, and IAEANO3 and are reported with respect to atmospheric-N_2 and the Vienna Standard Meteoric Ocean Water (VSMOW), respectively. Long-term precision for $\delta^{15}N$ and $\delta^{18}O$ is 0.3 and 0.5, respectively.

To evaluate potential sources of nitrate, we compared the $\delta^{15}N$ and $\delta^{18}O$ values of NO_3 samples collected at the Albuquerque and Los Lunas WWTPs during our sampling campaigns with previous measurements of precipitation and liquid fertilizer collected near the Rio Grande (Sanchez et al., 2017). The previous, geographically similar, measures of precipitation values, which are influenced by complex atmospheric processes including nitrate formation during thunderstorms and various photochemical reactions (Kendall, 1998; Xue et al., 2009), ranged from −4.7 to −2.1 and 36.6 to 44.9‰ for $\delta^{15}N$-NO_3 and $\delta^{18}O$-NO_3, respectively, during the monsoon season of 2014 (Sanchez et al., 2017). These values are comparable to measured values in precipitation from other areas, where $\delta^{15}N$-NO_3 and $\delta^{18}O$-NO_3 values ranged from −15 to +15‰ (Kendall, 1998; Jin et al., 2019) and from +25 to +75‰ (Voerkelius and Schmidt, 1990; Durka et al., 1994; Kendall, 1998; Jin et al., 2019), respectively. Additionally, Kendall (1998) reported an average value for $\delta^{18}O$-NO_3 in precipitation of 43.6 ± 14.6‰ ($n = 232$).

Similarly, the previous measurements of fertilizers from this area, which have predictable and distinctive $\delta^{15}N$-NO_3 and $\delta^{18}O$-NO_3 signatures due to the processes inherent to their formation (Flipse and Bonner, 1985) had values of $\delta^{15}N$-NO_3 ranging from −0.7 to 3.1‰ (Sanchez et al., 2017). These results are comparable to compiled values from studies measuring the $\delta^{15}N$-NO_3 of ammonium fertilizer ($n = 11$ studies), nitrate fertilizers ($n = 8$), and urea ($n = 9$), finding typical ranges of −6 to +6‰ (10 and 90th percentiles) (Xue et al., 2009). The synthetic nitrate in fertilizers also has a distinctive $\delta^{18}O$ signature of +17 to +25‰ because it is primarily derived from atmospheric O_2 (Amberger and Schmidt, 1987). These values are also in agreement with those from fertilizers applied locally as documented by Sanchez et al. (2017).

After establishing end-member values, we used a dual ^{15}N and ^{18}O isotope approach to evaluate the potential nitrate sources (i.e., WWTP effluent, precipitation, and synthetic fertilizers) of the samples collected in this study. We performed linear regression among these three end-members to create a mixing model to resolve the relative contributions of each source to nitrate in the reaches sampled. The position of samples along the regression (mixing) line with respect to end-members indicates the relative contribution of each end-member. Considering the associated standard deviations of ±2–3‰, we generalized the estimated relative contributions into bins with a range of 20% to encompass the inherent uncertainty and potential error.

When calculating the average end-member $\delta^{15}N$ and $\delta^{18}O$-NO_3 values, we excluded WWTP effluent samples that trended toward denitrification. The impact of microbial denitrification was also considered as it attenuates nitrate levels while simultaneously enriching the pool of residual nitrate isotopes (Kendall and Aravena, 2000; Kendall et al., 2007). The denitrification process can be identified by its unique signature of a 1:2 enrichment of $\delta^{15}N$:$\delta^{18}O$-NO_3 (Böttcher et al., 1990), and any samples plotting to the right of the mixing line among end-members are considered to be denitrified (Kendall et al., 2007; Sanchez et al., 2017). Thus, we plotted denitrification vectors extending from the mixing line with a slope of 0.5 to estimate nitrate source contributions while disentangling the effects of denitrification. A total of six parallel denitrification vectors were drawn to encompass the estimated contribution bins. Samples were then analyzed with respect to the denitrification vectors to distinguish nitrate source mixing from the timing of the denitrification process, as previously described in Kendall (1998).

Nutrient Budget

We developed a non-dimensional fraction change (F) metric to understand source/sink behaviors along the study reaches based on Zarnetske et al. (2012):

$$F = \frac{NO_3 - N_{dn}}{NO_3 - N_{up} + \sum NO_3 - N_{in}(\frac{l}{L})} \quad (2)$$

where $NO_3 - N_{up}$, $NO_3 - N_{dn}$, and $NO_3 - N_{in}$ represent the upstream, downstream, and lateral (external) loads in a given reach, l is the distance between a known lateral input and the downstream site, which is located a distance L from the upstream point. When $F > 1$, NO_3-N is being added to the system and that reach becomes a source. When $F < 1$, NO_3-N is being removed from the system and the reach becomes a sink.

Statistics

Statistics were calculated in R using a significance threshold of $p < 0.05$, although actual p-values are presented where possible so that the significance of individual test results can be directly

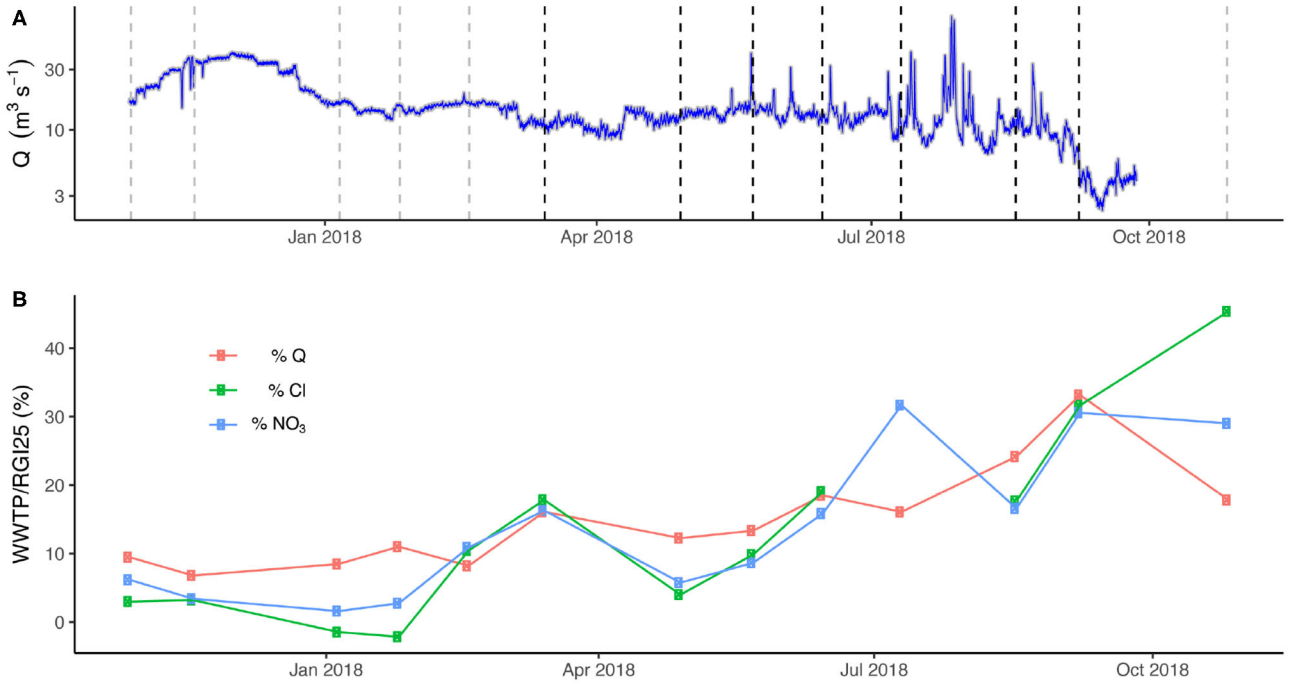

FIGURE 3 | (A) Hydrograph from the Rio Grande at Central Bridge in Albuquerque (Rio Grande S0) during the study period. Dashed lines show sampling dates (growing season in black, non-growing season in gray). **(B)** Influence of the ABQ WWTP on discharge (Q), Cl, and NO_3-N values observed in the Rio Grande at I-25 bridge, which is located ∼9 km downstream of WWTP.

compared. Due to the non-Gaussian distributions of *F*-values ($p < 0.0001$ for Shapiro-Wilk tests), we used Wilcoxon tests to compare groups.

RESULTS

Wastewater Influence

The Albuquerque WWTP is a major source of both water and nutrients to the Rio Grande, but its influence on the chemistry of the river depends on the seasonality of flow (**Figure 3A**). For example, during the period of highest flow in December 2017, the daily average discharge in the Rio Grande was 35.1 m^3/s at the Central Bridge USGS gauge (#08330000), and 36.7 m^3/s at the I-25 Bridge (#08330875), which are located upstream and downstream of the WWTP outfall, respectively (i.e., ∼1.0× or negligible discharge increase). For these same sampling locations, the NO_3-N load was 191 kg/day upstream of the WWTP, which contributed 630 kg/day to the Rio Grande, increasing its load downstream to 821 kg/day (i.e., ∼4.3× load increase). Conversely, during September of 2018, the daily average discharge of 6.3 m^3/s in the Rio Grande at Central Bridge was at the lowest during the study period, and increased to 8.6 m^3/s at I-25 Bridge (i.e., ∼1.4× discharge increase), whereas the associated NO_3-N load from the WWTP was 1,055 kg/day, increasing the NO_3-N load in the Rio Grande from 114 kg/day upstream to 1,169 kg/day downstream (i.e., ∼10.2× load increase). Based on the similar trends of both conservative (i.e., chloride) and non-conservative (i.e., nitrate) parameters sourced from the WWTP to the percentage of discharge sourced from the WWTP (**Figure 3B**), we observe that the ABQ WWTP strongly influences downstream hydrochemistry. Therefore, the dynamic mixing of the Rio Grande with ABQ WWTP effluent directly controls the water and nutrient budgets of the study reach of the Rio Grande as well as the Delivery channel, which receives river water diverted by the Isleta diversion dam (**Figure 1B**). The Drain channel, which receives water draining croplands (delivered by the Delivery canal) as well as intercepted groundwater, is also likely indirectly influenced by the ABQ WWTP.

General Source/Sink Behavior

Clear differences in nitrate concentrations and source/sink behavior were observed between seasons and between the channels examined for this study (**Figure 4**). Nitrate concentrations were significantly higher during the growing season ($p = 0.0018$, **Figure 4A**) and were associated with lower dilution of WWTP inputs (**Figure 3**). Such concentrations were also significantly lower in the Drain than either the Rio Grande or the Delivery ($p < 0.0001$ for both, **Figure 4B**).

Median F_{NO_3} values for the growing and non-growing seasons (0.495 and 1.207, respectively) indicate that the entire system functioned as a net sink for the majority of the growing season, but as a net source for the majority of the non-growing season (**Figure 4C**). This is supported by a strong significant difference

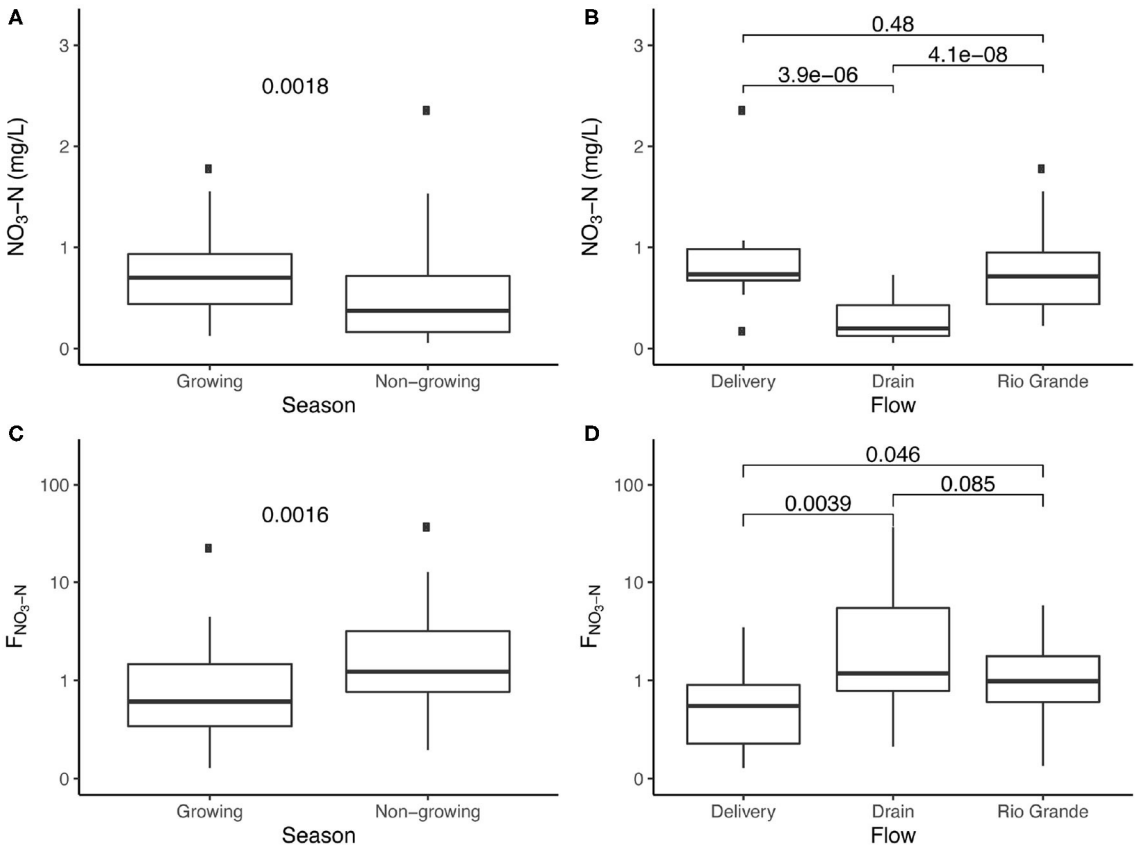

FIGURE 4 | Nitrate concentrations and *F*-values ($F_{NO_3} > 1$ and $F_{NO_3} < 1$ represent source and sink behaviors) divided by season **(A,C)** and flowpath **(B,D)**. Significance test results are presented as *p*-values above data.

in F_{NO_3} values between seasons ($p = 0.0016$). Median values by channel (**Figure 4D**) indicate that the Delivery channel primarily acts as a sink, with only 3 of 16 measurements (∼19%) indicating source behavior. Rio Grande F_{NO_3} values had a median of 0.948, with a slim majority of measurements (21 of 36, or ∼57%) >1, indicating that the Rio Grande is both a sink and a source along the study reach. Drain F_{NO_3} values were significantly higher than Delivery F_{NO_3} values ($p = 0.0039$), and both a median *F*-value > 1 (1.176) and a higher percentage of Drain samples with F_{NO_3} values > 1 (16 of 27, or ∼59%) indicate source behavior was more common than sink behavior. A significant difference ($p = 0.0460$) is present between the Rio Grande and Delivery *F*-values in **Figure 4D**, though this difference is less significant than the difference between Drain and Delivery *F*-values ($p = 0.0039$).

Spatiotemporal Patterns of Source/Sink Dynamics

Figure 5 displays the spatial (x-axis) and temporal (columns) variation in source/sink (y-axis) behavior for each channel (rows). In the Delivery channel, clear sink behavior ($F_{NO_3} < 1$) is present at S1 for both seasons, and at S2 during the growing season, with the strongest sink behavior (smallest F_{NO_3}) of any site at Delivery S2 (**Figure 5**). In the Drain, both seasons exhibit net source behavior ($F_{NO_3} > 1$ at S2). During the growing season, an apparent weak sink occurs at the Drain S1 site (**Figure 5**). During the non-growing season, source behavior increases downstream, with strongest source behavior (largest F_{NO_3}) of any site during any season observed at Drain S2 (median $F_{NO_3} = 10.2$). In the Rio Grande, sink behavior is evident at the lower two sites during the growing season, while apparent source behavior occurs at the most downstream site during the non-growing season. In general, a pattern of stronger sink behavior during the growing season is observed at Delivery S2, Drain S1, and Rio Grande S2 and S3 relative to the non-growing season.

Isotopes as Fingerprints

We used natural abundance N and O isotope analyses to explore potential NO_3-N sources and biological processing. $\delta^{15}N$ and $\delta^{18}O$-NO_3 values ranged from −4.1 to 20.5‰ and 0 to 36.5‰, respectively (**Figure 6A**, **Supplementary Table 1**). Average ± SD isotope values were enriched in the Drain samples ($\delta^{15}N$: 16.1 ± 4.5, $\delta^{18}O$: 4.9 ± 2.7 ‰) compared to the Rio Grande ($\delta^{15}N$: 12.1 ± 3.8, $\delta^{18}O$: −0.1 ± 3.6‰) and Delivery samples ($\delta^{15}N$: 13.5 ± 2.7, $\delta^{18}O$: −0.7 ± 2.9‰) (**Table 2**). We considered WWTPs, local fertilizers, and precipitation as potential sources of nitrate. Isotopes from WWTP effluent were measured in this study and combined with previously reported liquid fertilizer and precipitation measurements in the Rio Grande from Sanchez

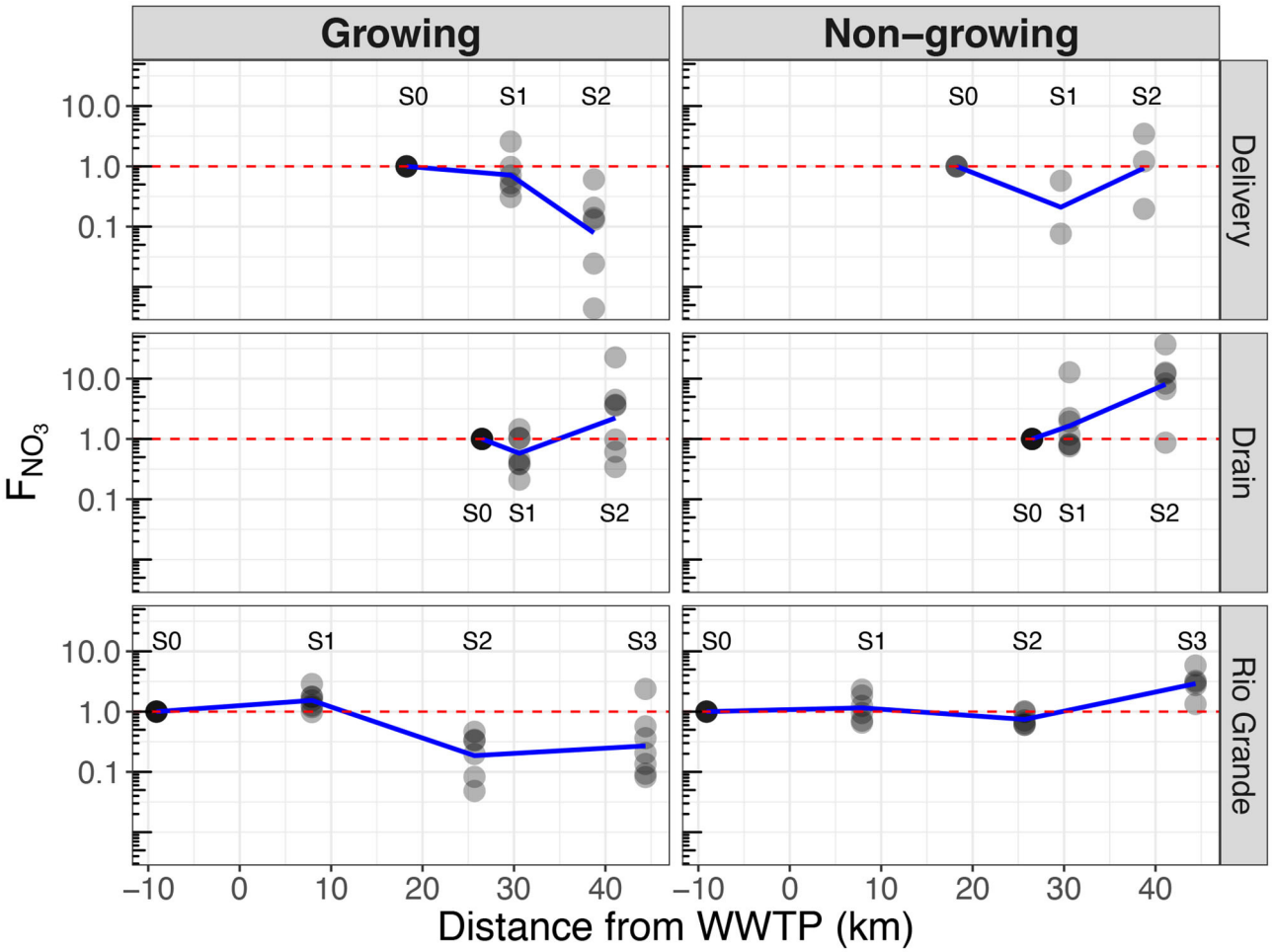

FIGURE 5 | Source ($F_{NO_3} > 1$) and sink ($F_{NO_3} < 1$) behavior across channels (rows) through space and season (columns). Blue lines are mean F_{NO_3} for all sampling events.

et al. (2017) (**Figure 6A**, **Supplementary Tables 1**, **3**). Of the potential nitrate sources, precipitation was the most depleted in $\delta^{15}N$ (average $= -3.2 \pm 1.3$‰) and most enriched in $\delta^{18}O$ (40.6 ± 3.0‰), WWTP effluent had the heaviest $\delta^{15}N$ values (8.1 ± 2.9‰) and the lightest $\delta^{18}O$ (-3.9 ± 1.5‰) (excluding samples that trended toward microbial denitrification), and liquid fertilizers had intermediate values ($\delta^{15}N$: 0.6 ± 1.7, $\delta^{18}O$: 18.3 ± 1.8‰). We performed linear regression among these three end-members (adjusted $R^2 = 0.82$, $p < 0.001$), creating a basis for a mixing model to resolve the relative contributions of each source to nitrate in the reaches sampled (**Figure 6A**). Drain and Delivery samples generally plotted between fertilizer and WWTP effluent, suggesting that most of the nitrate in the system is derived from these sources and that precipitation provides a negligible input. Due to this, the mixing model was simplified to the two isotopically distinct end-members (fertilizer and WWTP effluent; **Figure 6B**).

The impact of microbial denitrification was considered, as it can lead to significant increases in both $\delta^{15}N$- and $\delta^{18}O$-NO_3 values (Kendall, 1998; Kendall et al., 2007). Denitrification processes favor the uptake of lighter isotopes leaving the residual pool of nitrate enriched, typically at a rate of 1:2 ($\delta^{15}N$:$\delta^{18}O$-NO_3) (Kendall, 1998; Veale et al., 2019). Therefore, denitrification can be identified by a slope of 0.5 on N and O isotope biplots, and we found that many irrigation samples fell along denitrification vectors (**Figure 6B**). By analyzing the samples with respect to the parallel vectors, we removed the confounding effects of denitrification and used a two end-member mixing model based on the averages of fertilizer and WWTP effluent. Considering the associated standard deviations of ±2–3‰, we generalized the estimated relative contributions into bins with a range of 20%, finding that the majority of samples were comprised of nitrate derived primarily from WWTP effluent (**Figure 6B**). Furthermore, while many samples were affected by denitrification, Drain samples were most heavily impacted (**Figure 6B**).

DISCUSSION

Here, we summarize where nutrient sources and sinks occur throughout this system under the current management

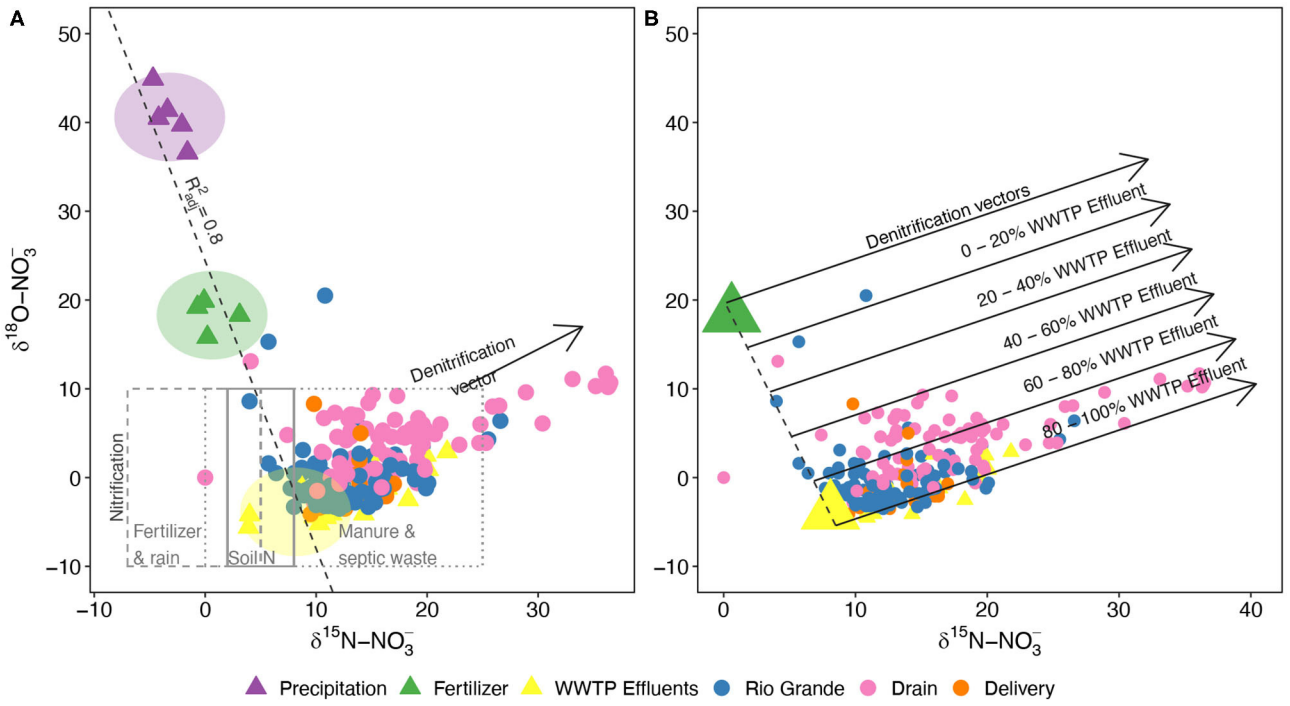

FIGURE 6 | (A) Isotope biplot of $\delta^{15}N$ and $\delta^{18}O$ of dissolved NO_3 within the Middle Rio Grande watershed. Triangles indicate the three main sources of measured NO_3: precipitation, liquid fertilizer (Sanchez et al., 2017), and WWTP effluents (this study). Typical ranges of isotope values of nitrate derived from the nitrification of ammonium in fertilizer and rain, soil, and organic waste are shown in the gray boxes [values based off Kendall (1998)]. Colored circles indicate the three main reaches studied. Shifts toward microbial denitrification are signified by the vector. The dotted line represents a linear regression ($R^2_{adj} = 0.82$) performed among the highlighted (in circles) main sources of nitrate, excluding WWTP effluents that trend toward denitrification. None of the samples plot near precipitation, indicating the end-member's negligible contribution to dissolved nitrate. **(B)** Estimation of the relative contributions of nitrate sources using $\delta^{15}N$ and $\delta^{18}O$. Precipitation had minimal influence on the isotopic signature of samples, and therefore a two-endmember mixing model was used to estimate the NO_3 contributions of liquid fertilizer and WWTP effluent. Large triangles indicate the averages of the two endmember sources and colored circles denote the watershed samples of the three main reaches of the Rio Grande. The effects of denitrification can be parsed by analyzing the samples with respect to the parallel vectors, e.g., samples that fall between the upper two vectors were derived from 0 to 20% WWTP effluent (and therefore 80–100% fertilizer), regardless of the timing of the denitrification reactions.

practices and make suggestions for optimizing the operation of such systems.

Wastewater Inputs

Our finding that the ABQ WWTP is the primary source of nutrients to the Middle Rio Grande is consistent with results from previous studies in this area (Oelsner et al., 2007; Mortensen et al., 2016). Similarly, in other arid regions, wastewater effluent provides a significant portion of river flow (Villarreal et al., 2012; Cooper et al., 2013), particularly during low-flow periods, accompanied by substantial nutrient loads. Thus, while in mesic regions agricultural inputs are the predominant source of nutrients to aquatic systems (Bouwman et al., 2005; Howarth, 2008), in aridlands urban wastewater inputs appear to be more important contributors (e.g., Regier et al., 2020). These conclusions are supported by the dual N and O isotope results that indicate that the majority (60–100%) of nitrate in the irrigation network is derived from WWTP effluent (**Figure 6B**) and only negligible amounts were derived from precipitation (**Figure 6A**). A small number of samples ($n = 3$) were impacted by local synthetic fertilizers with at least 60% of their nitrate from that source.

TABLE 2 | Average isotope values for the channels with ± one standard deviation.

Site or channel	$\delta^{15}N$ (‰)	$\delta^{18}O$ (‰)
WWTP	12.2 ± 2.7	−3.3 ± 1.0
Rio Grande	12.1 ± 3.8	−0.1 ± 3.6
Drain	16.1 ± 4.5	4.9 ± 2.7
Delivery	13.5 ± 2.7	−0.7 ± 2.9

Modern wastewater treatment facilities are designed to utilize tertiary (to reduce nutrient loads and disinfect) and quaternary treatment procedures (to remove pharmaceuticals and personal care products) (Sonune and Ghate, 2004; Carey and Migliaccio, 2009; Falk et al., 2013). Given that wastewater is the dominant source of nutrients to the Middle Rio Grande, some modifications could be employed to close nutrient loops and maximize recycling of this limited resource. For example, while within-wastewater treatment plant nutrient removal is typically deemed essential to prevent eutrophication of downstream aquatic environments in many areas, in aridlands, where wastewater-rich

river water is diverted for agricultural irrigation, these nutrient removal steps may be energetically expensive (Falk et al., 2013) and deplete valuable nutrient sources for crops. Accordingly, reducing the level of treatment to secondary treatment or excluding nutrient removal steps in tertiary treatment prior to delivery to the agricultural system would provide an opportunity to conserve both energy and nutrient resources. Also, rather than discharging wastewater directly to the river, where nutrients are diluted or lost via in-stream microbial uptake (Caraco and Cole, 2001; Mortensen et al., 2016), we suggest routing effluent through the existing irrigation channel network for direct delivery to crops. While this approach would require overcoming regulatory hurdles and issues of public perception, relevant examples of this approach are abundant. For example, in Sweden, the government set the goal of recovering and reusing 60% of all *P* in sewage (Cordell et al., 2009); in California, ∼61% (0.5×10^9 m^3/year) of the reused water is used for irrigation; and on a global scale, ∼1.7% (7.7×10^9 m^3/year) of the municipal wastewater is reused, mostly in irrigation (Jimenez and Asano, 2015).

Delivery Channels

The next link in the hydrologic network is the delivery channels that move water and effluent into the irrigation systems. Our finding that the delivery channels exhibited the strongest and most consistent sink behavior of the three flow paths suggests distinctive characteristics of this conveyance type that support nitrogen uptake. One of the most likely mechanisms for this uptake is removal in slow flowing areas. While the delivery conveyances are channelized and have high flow velocities along significant portions of their length, which would likely reduce nutrient uptake, there are frequent small dams that serve as control structures to divert water from the main conveyance into smaller irrigation channels. At these junctions, the water velocity is slowed, likely leading to nutrient uptake hotspots due to longer residence times in surface and subsurface flowpaths (Royer et al., 2004; Klocker et al., 2009; Powers et al., 2012).

In other stream systems, nutrient retention is considered to be a valuable ecosystem service and managers implement restoration measures to promote this capacity (Sweeney et al., 2004; Bukaveckas, 2007; Roberts et al., 2007). However, in the case of the delivery channels described in this study, nutrient retention in this portion of the hydrologic network is counterproductive as it decreases the potential to recycle nutrient resources through crop production and close loops, limiting offsets to the energy and financial costs of fertilizer use. Thus, we suggest employing management options that reduce this behavior in delivery channels. Potential options include lining slow flowing portions of the channel with concrete or another impervious layer, and periodically flushing or mechanical removal of deposited sediments from these areas, both of which would serve to limit water-sediment interactions and thus limit hotspots of nutrient removal.

Drains

Following delivery to crops in irrigated fields, excess water and associated nutrients seep into low-lying drains which eventually flow back into the mainstem of the river. The seasonal variations in source/sink behavior of the drains described here (i.e., sink patterns during the growing season but source behavior during non-growing season months) are likely due to the seasonally dynamic interactions between the channel and riparian vegetation, as well as to variations in microbial processing. Both of these interactions are dependent on temperature and light availability, which influence plant and microbial growth and metabolism [e.g., Vymazal et al. (2017)]. Thus, during warm months when riparian production and microbial metabolic rates are high, drains exhibit sink behavior, while during cooler months, nutrient inputs from seepage water appear to overwhelm the processing capacity of the system. Additionally, as our isotopic data indicates, the Drain was the conveyance type where the most denitrification occurred, suggesting that dissimilatory microbial processing may be an important control on nitrate transport in irrigation drain channels (Inwood et al., 2005; Mulholland et al., 2008).

From the perspective of closing nutrient loops, nutrients that reach the drains have effectively escaped the loop, and releasing these constituents to downstream receiving waters has the potential to cause eutrophication (Daniel et al., 1998; Boesch et al., 2001; Withers et al., 2014) and alterations to instream metabolic regimes (Bernhardt et al., 2018). Thus, in contrast to the delivery channels, we suggest that managers should apply approaches in this portion of the irrigation network that maximize nutrient retention and removal. Suggested interventions include traditional restoration techniques such as the addition of meanders to the currently uniformly straight channels, the installation of coarse woody debris, modification of the channel to increase the width-to-depth ratio, and the addition of flow control structures to decrease water velocity (Sweeney et al., 2004; Bukaveckas, 2007; Roberts et al., 2007). Each of these modifications would increase residence times and water-sediment interactions, promoting nutrient removal and retention.

CONCLUSIONS

The coupling between human and river systems affects nutrient budgets from reach to regional scales. In arid regions, WWTPs are major sources of both water and nutrients, and their interaction with downstream agricultural systems provides opportunities to close nutrient loops while optimizing FEW resources. Traditionally, reclamation and conservancy district stakeholders operate in isolation, seeking to maximize their agencies' goals (status quo), but our work demonstrates that there are multiple opportunities to coordinate efforts to benefit urban and agricultural societies relying on the river systems where they operate. Specifically, our findings using nutrient budgets and isotopic fingerprinting techniques demonstrate that characteristic river-irrigation systems in arid regions follow dynamic nutrient source/sink patterns controlled by WWTP discharges and agricultural activity. These patterns are predictable in space (i.e., location downstream of WWTP

discharge) and time (growing vs. non-growing seasons), and could be used to improve the management of FEW resources.

Although the source/sink nutrient budget could be managed following a variety of strategies (such as those described here), managing FEW resources holistically requires not only the implementation of new infrastructure and approaches but also a shift of paradigms to support the transformation of traditionally "linear" societies, which manage FEW resources in isolation of one another, into "recycling" societies capable of making productive gains (e.g., crop and biofuel production), while closing nutrient loops to minimize environmental pollution and energy consumption. Breaking from the status quo will require collaboration between farmers, municipalities, and state and federal governments to adopt approaches embracing FEW nexus philosophies. In arid human-river systems, the reward of such cooperation could introduce a way to close nutrient loops and reduce energy consumption in wastewater nutrient removal, and in fertilizer production, transportation, and application.

DATA AVAILABILITY STATEMENT

All datasets presented in this study are included in the article/**Supplementary Material**.

AUTHOR CONTRIBUTIONS

RG-P and DV secured funding and created the conceptual framework. KB and PR led the field experimental work. KB led the development of the manuscript with support from all authors.

FUNDING

The National Science Foundation provided funding support through grants CBET-1707042, HRD-1914490, and HRD-1345169.

ACKNOWLEDGMENTS

The authors want to thank the reviewers, Dr. Megan J. Klaar and Dr. Clare Robinson, as well as the editor, Dr. Dipankar Dwivedi, for providing insightful feedback on an early version of this manuscript.

SUPPLEMENTARY MATERIAL

The Supplementary Material for this article can be found online at: https://www.frontiersin.org/articles/10.3389/frwa.2020.00022/full#supplementary-material

REFERENCES

Amberger, A., and Schmidt, H. L. (1987). Natural isotope contents of nitrate as indicators for its origin. *Geochim. Cosmochim. Acta* 51, 2699–2705. doi: 10.1016/0016-7037(87)90150-5

Bartoli, M. E., Racchetti, C. A., Delconte, E., Sacchi, E., Soana, A., Laini, D., et al. (2012). Nitrogen balance and fate in a heavily impacted watershed (Oglio River, Northern Italy): in quest of the missing sources and sinks. *Biogeosciences* 9, 361–373. doi: 10.5194/bg-9-361-2012

Bartolino, J. R., and Cole, J. C. (2002). Ground-water resources of the middle rio grande basin. *U.S. Geol. Surv. Circ.* 1222, 71–86. doi: 10.3133/cir1222

Bernhardt, E. S., Heffernan, J. B., Grimm, N. B., Stanley, E. H., Harvey, J. W., Arroita, M., et al. (2018). The metabolic regimes of flowing waters. *Limnol. Oceanogr.* 63, S99–S118. doi: 10.1002/lno.10726

Boesch, D. F., Brinsfield, R. B., and Magnien, R. E. (2001). Chesapeake bay eutrophication. *J. Environ. Qual.* 30, 303–320. doi: 10.2134/jeq2001.302303x

Böttcher, J., Strebel, O., Voerkelius, S., and Schmidt, H. L. (1990). Using isotope fractionation of nitrate-nitrogen and nitrateoxygen for evaluation of microbial denitrification in a sandy aquifer. *J. Hydrol.* 114, 413–424. doi: 10.1016/0022-1694(90)90068-9

Bouwman, A. F., Van Drecht, G., Knoop, J. M., Beusen, A. H. W., and Meinardi, C. R. (2005). Exploring changes in river nitrogen export to the world's oceans. *Glob. Biogeochem. Cycles* 19:1002. doi: 10.1029/2004GB002314

Bukaveckas, P. A. (2007). Effects of channel restoration on water velocity, transient storage, and nutrient uptake in a channelized stream. *Environ. Sci. Technol.* 41, 1570–1576. doi: 10.1021/es061618x

Caraco, N. F., and Cole, J. J. (2001). Human influence on nitrogen export: a comparison of mesic and xeric catchments. *Mar. Freshwater Res.* 52, 119–125. doi: 10.1071/MF00083

Carey, R. O., and Migliaccio, K. W. (2009). Contribution of wastewater treatment plant effluents to nutrient dynamics in aquatic systems: a review. *Environ. Manag.* 44, 205–217. doi: 10.1007/s00267-009-9309-5

Chapin, F. S. (1980). The mineral nutrition of wild plants. *Ann. Rev. Ecol. Syst.* 11, 233–260. doi: 10.1146/annurev.es.11.110180.001313

Childers, D. L., Corman, J., Edwards, M., and Elser, J. J. (2011). Sustainability challenges of phosphorus and food: solutions from closing the human phosphorus cycle. *Bioscience* 61, 117–124. doi: 10.1525/bio.2011.61.2.6

Cooper, S. D., Lake, P. S., Sabater, S., Melack, J. M., and Sabo, J. L. (2013). The effects of land use changes on streams and rivers in mediterranean climates. *Hydrobiologia* 719, 383–425. doi: 10.1007/s10750-012-1333-4

Cordell, D., Drangert, J.-O., and White, S. (2009). The story of phosphorus: global food security and food for thought. *Global Environ. Change* 19, 292–305. doi: 10.1016/j.gloenvcha.2008.10.009

Daniel, T., Sharpley, A., and Lemunyon, J. (1998). Agricultural phosphorus and eutrophication: a symposium overview. *J. Environ. Qual.* 27, 251–257. doi: 10.2134/jeq1998.00472425002700020002x

Dumont, E., Harrison, J. A., Kroeze, C., Bakker, E. J., and Seitzinger, S. P. (2005). Global distribution and sources of dissolved inorganic nitrogen export to the coastal zone: results from a spatially explicit, global model. *Glob. Biogeochem. Cycles* 19. doi: 10.1029/2005GB002488

Durka, W., Schulze, E.-D., Gebauer, G., and Voerkelius, S. (1994). Effects of forest decline on uptake and leaching of deposited nitrate determined from ^{15}N and ^{18}O measurements. *Nature* 372, 765–767. doi: 10.1038/372765a0

Erisman, J. W., Sutton, M. A., Galloway, J., Klimont, Z., and Winiwarter, W. (2008). How a century of ammonia synthesis changed the world. *Nat. Geosci.* 1, 636–639. doi: 10.1038/ngeo325

Falk, M. W., Reardon, D. J., Neethling, J., Clark, D. L., and Pramanik, A. (2013). Striking the balance between nutrient removal, greenhouse gas emissions, receiving water quality, and costs. *Water Environ. Res.* 85, 2307–2316. doi: 10.2175/106143013X13807328848379

FAO (2014). *The Water-Energy-Food Nexus: A New Approach in Support of Food Security and Sustainable Agriculture*. Rome: The Food and Agriculture Organization of the United Nations.

Flipse, W. J. Jr., and Bonner, F. T. (1985). Nitrogen-isotope ratios of nitrate in ground water under fertilized fields, Long Island, New York. *Groundwater* 23, 59–67. doi: 10.1111/j.1745-6584.1985.tb02780.x

Fluke, J., González-Pinzón, R., and Thomson, B. (2019). Riverbed sentiments control the spatiotemporal variability of *E. coli* in a highly managed, arid river. *Front. Water* 1:4. doi: 10.3389/frwa.2019.00004

Galloway, J. N., Dentener, F. J., Capone, D. G., Boyer, E. W., Howarth, R. W., Seitzinger, S. P. et al. (2004). Nitrogen cycles: past, present, and future. *Biogeochemistry* 70, 153–226. doi: 10.1007/s10533-004-0370-0

Gruber, N., and Galloway, J. N. (2008). An earth-system perspective of the global nitrogen cycle. *Nature* 451, 293–296. doi: 10.1038/nature06592

Hanjra, M. A., Blackwell, J., Carr, G., Zhang, F., and Jackson, T. M. (2012). Wastewater irrigation and environmental health: implications for water governance and public policy. *Int. J. Hygiene Environ. Health* 215, 255–269. doi: 10.1016/j.ijheh.2011.10.003

Harrison, J. A., Seitzinger, S. P., Bouwman, A. F., Caraco, N. F., Beusen, A. H. W., and Vörösmarty, C. J. (2005). Dissolved inorganic phosphorus export to the coastal zone: results from a spatially explicit, global model. *Glob. Biogeochem. Cycles* 19:GB4S03. doi: 10.1029/2004GB002357

Howarth, R. W. (2008). Coastal nitrogen pollution: a review of sources and trends globally and regionally. *Harmful Algae* 8, 14–20. doi: 10.1016/j.hal.2008.08.015

Inwood, S. E., Tank, J. L., and Bernot, M. J. (2005). Patterns of denitrification associated with land use in 9 midwestern headwater streams. *J. North Am. Benthol. Soc.* 24, 227–245. doi: 10.1899/04-032.1

Jimenez, B., and Asano, T. (2015). Water reuse: an international survey of current practice, issues and needs. *Water Intell. Online* 7:9781780401881. doi: 10.2166/9781780401881

Jin, Z., Cen, J., Hu, Y., Li, L., Shi, Y., Fu, G., et al. (2019). Quantifying nitrate sources in a large reservoir for drinking water by using stable isotopes and a Bayesian isotope mixing model. *Environ. Sci. Pollut. Res.* 26, 20364–20376. doi: 10.1007/s11356-019-05296-7

Kendall, C. (1998). "Tracing nitrogen sources and cycling in catchments," in *Isotope Tracers in Catchment Hydrology* eds C. Kendall and J. McDonnell (New York, NY: Elsevier), 519–576. doi: 10.1016/B978-0-444-81546-0.50023-9

Kendall, C., and Aravena, R. (2000). "Nitrate isotopes in groundwater systems, Chapter 9," in *Environmental Tracers in Subsurface Hydrology*, eds P. Cook and A. L. Herczeg (New York, NY: Kluwer Academic Publishers), 261–297. doi: 10.1007/978-1-4615-4557-6_9

Kendall, C., Elliott, E. M., and Wankel, S. D. (2007). "Tracing anthropogenic inputs of nitrogen to ecosystems," in *Stable Isotopes in Ecology and Environmental Science, Vol. 2*, eds R. Michener and K. Lajtha (London: John Wiley & Sons Inc.), 375–449. doi: 10.1002/9780470691854.ch12

Klocker, C. A., Kaushal, S. S., Groffman, P. M., Mayer, P. M., and Morgan, R. P. (2009). Nitrogen uptake and denitrification in restored and unrestored streams in urban Maryland, USA. *Aquat. Sci.* 71, 411–424. doi: 10.1007/s00027-009-0118-y

Larsen, T. A., Hoffmann, S., LÃthi, C., Truffer, B., and Maurer, M. (2016). Emerging solutions to the water challenges of an urbanizing world. *Science* 352, 928–933. doi: 10.1126/science.aad8641

Lassaletta, L., Romero, E., Billen, G., Garnier, J., García-Gómez, H., and Rovira, J. V. (2012). Spatialized N budgets in a large agricultural Mediterranean watershed: high loading and low transfer. *Biogeosciences* 9, 57–70. doi: 10.5194/bg-9-57-2012

Mortensen, J. G., GonzÃlez-PinzÃn, R., Dahm, C. N., Wang, J., Zeglin, L. H., and Van Horn, D. J. (2016). Advancing the food-energy–water nexus: closing nutrient loops in arid river corridors. *Environ. Sci. Technol.* 50, 8485–8496. doi: 10.1021/acs.est.6b01351

Mulholland, P. J., Helton, A. M., Poole, G. C., Hall, R. O., Hamilton, S. K., Peterson, B. J., et al. (2008). Stream denitrification across biomes and its response to anthropogenic nitrate loading. *Nature* 452, 202–205. doi: 10.1038/nature06686

NSF (2014). *Food, Energy, and Water: Transformative Research Opportunities in the Mathematical and Physical Sciences.* National Science Foundation.

Oelsner, G. P., Brooks, P. D., and Hogan, J. F. (2007). Nitrogen sources and sinks within the middle Rio grande, New Mexico. *J. Am. Water Res. Assoc.* 43, 850–863. doi: 10.1111/j.1752-1688.2007.00071.x

Pfaff, J. D. (1996). "Determination of inorganic anions by ion chromatography," in *Methods for the Determination of Metals in Environmental Samples* (Westwood, NJ: Elsevier), 388–417. doi: 10.1016/B978-0-8155-1398-8.50022-7

Powers, S. M., Johnson, R. A., and Stanley, E. H. (2012). Nutrient retention and the problem of hydrologic disconnection in streams and wetlands. *Ecosystems* 15, 435–449. doi: 10.1007/s10021-012-9520-8

Regier, P., González-Pinzón, R., Van Horn, D. J., Reale, J., Nichols, J., and Khandelwal, A. (2020). Water quality impacts of urban and non-urban arid-land runoff on the Rio Grande. *Sci. Total Environ.* 729:138443. doi: 10.1016/j.scitotenv.2020.138443

Roberts, B. J., Mulholland, P. J., and Houser, J. N. (2007). Effects of upland disturbance and instream restoration on hydrodynamics and ammonium uptake in headwater streams. *J. North Am. Benthol. Soc.* 26, 38–53. doi: 10.1899/0887-3593(2007)26[38:EOUDAI]2.0.CO;2

Royer, T. V., Tank, J. L., and David, M. B. (2004). Transport and fate of nitrate in headwater agricultural streams in Illinois. *J. Environ. Qual.* 33, 1296–1304. doi: 10.2134/jeq2004.1296

Sanchez, D. A., Szynkiewicz, A., and Faiia, A. M. (2017). Determining sources of nitrate in the semi-arid Rio Grande using nitrogen and oxygen isotopes. *Appl. Geochem.* 86, 59–69. doi: 10.1016/j.apgeochem.2017.09.012

Sigman, D. M., Casciotti, K. L., Andreani, M., Barford, C., Galanter, M., and Böhlke, J. (2001). A bacterial method for the nitrogen isotopic analysis of nitrate in seawater and freshwater. *Anal. Chem.* 73, 4145–4153. doi: 10.1021/ac010088e

Soana, E., Racchetti, E., Laini, A., Bartoli, M., and Viaroli, P. (2011). Soil budget, net export, and potential sinks of nitrogen in the lower oglio river watershed (Northern Italy). *Clean Soil Air Water* 39, 956–965. doi: 10.1002/clen.201000454

Sonune, A., and Ghate, R. (2004). Developments in wastewater treatment methods. *Desalination* 167, 55–63. doi: 10.1016/j.desal.2004.06.113

Sweeney, B. W., Bott, T. L., Jackson, J. K., Kaplan, L. A., Newbold, J. D., Standley, L. J., et al. (2004). Riparian deforestation, stream narrowing, and the loss of stream ecosystem services. *Proc. Natl. Acad. Sci. U.S.A.* 101, 14132–14137. doi: 10.1073/pnas.0405895101

Van Horn, D. (2010). *Nutrient Cycling in Impacted Stream Ecosystems: From Microbes to Watersheds*. Available online at: https://digitalrepository.unm.edu/biol_etds/119 (accessed August 31, 2020).

Veale, N., Visser, A., Esser, B., Singleton, M. J., and Moran, J. E. (2019). Nitrogen cycle dynamics revealed through δ18O-NO3– analysis in California groundwater. *Geosciences* 9:95. doi: 10.3390/geosciences9020095

Villarreal, M., Drake, S., Marsh, S., and McCoy, A. (2012). The influence of wastewater subsidy, flood disturbance and neighbouring land use on current and historical patterns of riparian vegetation in a semi-arid watershed. *River Res. Appl.* 28, 1230–1245. doi: 10.1002/rra.1510

Vitousek, P. M., and Howarth, R. W. (1991). Nitrogen limitation on land and in the sea: how can it occur? *Biogeochemistry* 13, 87–115. doi: 10.1007/BF00002772

Voerkelius, S., and Schmidt, H.-L. (1990). Natural oxygen and nitrogen isotope abundance of compounds involved in denitrification. Mitteilungen der deut. *Bodenkundlichen Gesselschaft* 60, 364–366.

Vymazal, J., Brezinová, T. D., KoŽeluh, M., and Kule, L. (2017). Occurrence and removal of pharmaceuticals in four full-scale constructed wetlands in the Czech Republic–the first year of monitoring. *Ecol. Eng.* 98, 354–364. doi: 10.1016/j.ecoleng.2016.08.010

Withers, P. J., Neal, C., Jarvie, H. P., and Doody, D. G. (2014). Agriculture and eutrophication: where do we go from here? *Sustainability* 6, 5853–5875. doi: 10.3390/su6095853

Xue, D., Botte, J., De Baets, B., Accoe, F., Nestler, A., Taylor, P., et al. (2009). Present limitations and future prospects of stable isotope methods for nitrate source identification in surface-and groundwater. *Water Res.* 43, 1159–1170. doi: 10.1016/j.watres.2008.12.048

Zarnetske, J. P., Haggerty, R., Wondzell, S. M., Bokil, V. A., and González-Pinzón, R. (2012) Coupled transport and reaction kinetics control the nitrate source-sink function of hyporheic zones. *Water Resour. Res*. 48:12999. doi: 10.1029/2012WR011894

Conflict of Interest: The authors declare that the research was conducted in the absence of any commercial or financial relationships that could be construed as a potential conflict of interest.

frontiers in Water

ORIGINAL RESEARCH
published: 16 September 2020
doi: 10.3389/frwa.2020.00029

Accounting for Temporal Variability of Streamflow in Estimates of Travel Time

Christopher P. Konrad[1], Noah M. Schmadel[2], Judson W. Harvey[2], Gregory E. Schwarz[2], Jesus Gomez-Velez[3], Elizabeth W. Boyer[4] and Durelle Scott[5]*

[1] US Geological Survey, Tacoma, WA, United States, [2] US Geological Survey, Reston, VA, United States, [3] Department of Civil and Environmental Engineering, Vanderbilt University, Nashville, TN, United States, [4] Department of Ecosystem Science and Management, Pennsylvania State University, University Park, PA, United States, [5] Department of Biological Systems Engineering, Virginia Tech, Charlottesville, VA, United States

Retention, processing, and transport of solutes and particulates in stream corridors are influenced by the travel time of streamflow through stream channels, which varies dynamically with discharge. The effects of streamflow variability across sites and over time cannot be addressed by time-averaged models if parameters are based solely on the characteristics of mean streamflow. We develop methods to account for the effects of streamflow variability on travel time and compare our estimates to flow-weighted ("effective") travel time at 100 streams in the southeastern United States. Velocity time series were generated for each stream from multiple-year (median 15.5 years), high-frequency (15 min interval) records of instantaneous streamflow and field measurements of velocity and inverted to produce time series of specific travel time [T/L]. The effective travel times for streams are 60–90% of the specific travel time of mean streamflow because a large fraction of the total streamflow volume is discharged during higher flows with higher velocities. We find that adjusting the specific travel time of mean streamflow at a site by a factor of 0.81 generally accounts for the effect of a skewed streamflow distribution, but at-site estimates of the coefficient of variation of streamflow are necessary to resolve differences in streamflow variability between streams or changes in variability over time. For example, the effective travel time of urban streams is less than the effective travel of forested streams in the southeastern United States as a result of increased streamflow variability in urban streams. Effective travel time accounts for both the variation in velocity with streamflow and the large fraction of streamflow discharged during high flows in most streams and provides time-averaged models with limited capability to account for effects of streamflow variability that otherwise they lack. This capability is needed for continental-scale modeling where streamflow variability is not uniform because of heterogeneous surficial geology, hydro-climatology, and vegetation and for applications where streamflow variability is not stationary as a response to climate change or hydrologic alteration.

Keywords: streamflow, in-stream processes, travel time, hydrologic modification, urban

OPEN ACCESS

Edited by:
Dipankar Dwivedi, Lawrence Berkeley National Laboratory, United States

Reviewed by:
Reza Soltanian, University of Cincinnati, United States
Eve-Lyn S. Hinckley, University of Colorado Boulder, United States

****Correspondence:***
Christopher P. Konrad
cpkonrad@usgs.gov

Specialty section:
This article was submitted to Water and Critical Zone, a section of the journal Frontiers in Water

Received: *09 April 2020*
Accepted: *04 August 2020*
Published: *16 September 2020*

Citation:
Konrad CP, Schmadel NM, Harvey JW, Schwarz GE, Gomez-Velez J, Boyer EW and Scott D (2020) Accounting for Temporal Variability of Streamflow in Estimates of Travel Time. Front. Water 2:29. doi: 10.3389/frwa.2020.00029

INTRODUCTION

The velocity of streamflow has two fundamental but distinct roles on the processing of solutes and particulates in river corridors: it determines the rate of downstream advective transport of materials in a channel and it affects the "turnover length" of streamflow, which is the distance that streamflow must travel for complete exchange with water in transient storage zones in river corridors (e.g., hyporheic sediments, in-channel alcoves, off-channel sloughs, and floodplains) (Newbold et al., 1983; Meyer and Edwards, 1990; Mulholland et al., 1990; Stream Solute Workshop, 1990; Czuba and Foufoula-Georgiou, 2014; Harvey, 2016). The ratio of downstream advective transport to in-channel processing (e.g., settling velocity of particulates or uptake velocity of nutrients) limits the efficiency of in-channel retention of fine sediment in river channels (Konrad, 2009), filtration of organic particulates by invertebrates (Wallace et al., 1977), and nutrient uptake by photosynthetic organisms (Hall et al., 2002). Turnover lengths indicate hydrologic connectivity of streamflow (fraction exchanged) with hyporheic and other storage zones and its contact time with reactive sediments (Hein et al., 2004; Schmadel et al., 2016; Harvey et al., 2019; Findlay, 1995). Given these roles, streamflow velocity or, inversely, travel time is a lynch pin for accurate accounting of material processing and loads through river networks.

Large-scale synoptic investigations (Konrad and Gellis, 2018), remotely-acquired data (Konrad et al., 2008) and spatially-distributed models (Czuba et al., 2018) can address spatial variability in streamflow velocity, but high-frequency measurements and dynamic models are needed to account explicitly for the temporal variability of travel time forced by streamflow and its resulting effects on biophysical processing (Konrad, 2009; Botter et al., 2010; Basu et al., 2011; Ye et al., 2012). It is more often the case that time-averaged models of material transport and reactivity are applied to river networks (Boyer et al., 2006; Mulholland et al., 2008; Alexander et al., 2009; Helton et al., 2011; Czuba and Foufoula-Georgiou, 2014; Gomez-Velez et al., 2015). The temporal distributions of streamflow velocity and travel time remain a critical gap for river basin and larger scale biogeochemical modeling over seasonal and longer timescales (Wollheim et al., 2006; Bergstrom et al., 2016; Raymond et al., 2016). Since streamflow cannot be presumed to be steady over these time scales, effective values of velocity, and travel time are used in time-averaged models (Wolman and Miller, 1960; Doyle, 2005; Basso et al., 2015; Harvey and Gooseff, 2015). Application of such models to assess impacts of climate, land use, or water management in river corridors, however, requires adjustments to the effective values of velocity or travel time to account for changes in temporal variability of streamflow.

Time-averaged biogeochemical models of river networks typically use the velocity, travel time, or hydraulic load (product of velocity and depth divided by reach length) for mean streamflow (Behrendt and Opitz, 1999; Wollheim et al., 2006; Alexander et al., 2009; Helton et al., 2011). Mean streamflow, however, does not represent the variability of streamflow, which ranges across streams because of spatial heterogeneity in geology, soils, climate, watershed size, drainage density, and land cover (Carlston, 1963; Thomas and Benson, 1970; Poff and Ward, 1989; Dettinger and Diaz, 2000; Konrad et al., 2005; Pagano and Garen, 2005; Poff et al., 2007; Jiménez Cisneros et al., 2014; Basso et al., 2015). Without a way to represent differences in streamflow variability in space or over time, time-averaged models have limited capability to account for the effects of basin scale, climate, and hydrologic alteration by land and water uses (Ensign and Doyle, 2006; Wollheim et al., 2006; Hall et al., 2009; Basu et al., 2011; Raymond et al., 2016).

Urban development in particular increases streamflow variability as a result of reduced storage of water in soil and land surface depressions and shorter, less resistant pathways for water to flow through drainage systems into channels. These changes result in more rapid runoff and greater flow peaks for a given storm (Leopold, 1968; Konrad and Booth, 2005). Despite efforts to manage urban stormwater, modification of streamflow regimes persists in urban areas (Paul and Meyer, 2001; Konrad et al., 2005; Chang, 2007; Smith et al., 2013). While structural changes in stream channels (e.g., lining the channel with concrete, removing emergent vegetation) reduces flow resistance and travel time, shorter travel times in urban streams can be expected simply as a result of the re-distribution of runoff from lower-flow to higher-flow periods.

Our objective is to develop a method for estimating the effective travel time in stream channels that accounts for streamflow variability at and across sites and can conveniently be applied in time-averaged modeling stream transport and reaction of processes with first-order kinetics. The method is generalized by using the variance and skew of a streamflow distribution for the estimate without prejudice to why streamflow has a particular skew and variance. Thus, it is transferrable to infer effects on processing and retention for any factor that is known to influence the moments of a streamflow distribution. Potential applications extend to the evaluation of retention and processing of sediment and nutrients (1) at regional-scales because of heterogeneity in geology and hydro-climatology, (2) across large river basins because of downstream reduction in streamflow variability, and (3) in the context of climate and land use changes that affect streamflow variability. We demonstrate how differences in travel time at decadal time scales can be inferred from differences in streamflow distributions as a result of urban development in the southeastern United States.

METHODS AND MATERIALS

Effective Travel Time for First-Order Reaction Processes

For in-stream processes involving first-order kinetics of transformation or retention (e.g., nutrient uptake that is a constant fraction of nutrient concentration), the effective travel time of water through a reach, Tr_{ef} [T], can be derived by equating the mass flux calculated from a time-averaged model to the instantaneous mass flux integrated over time,

$$k\, Tr_{ef}\, \overline{C}\, \overline{Q} = \int_{t=0}^{T} kL\, \frac{1}{u_t}\, C_t\, Q_t\, dt \qquad (1)$$

where k is the reaction rate constant, L is reach length, $\overline{C}$ is mean concentration of the constituent of interest, $\overline{Q}$ is mean discharge, T is the total time for the period for interest, $C_t$is concentration at time t, Q_t is discharge at time t, and u_t is velocity at time t. By simplifying Equation (1), the effective travel time reduces to the flow- and concentration-weighted, mean travel time,

$$Tr_{ef} = \frac{L}{T}\int_{t=0}^{T}\frac{C_t}{\overline{C}}\frac{Q_t}{\overline{Q}}\frac{1}{u_t}dt \quad (2)$$

We limit the analysis to cases where temporal variation in streamflow is much greater than the variation in first-order reaction rates, k is constant, and variation in concentration using the approximations $\frac{C_t}{\overline{C}} \approx 1$. These approximations allows Tr_{ef} to be calculated simply as the flow-weighted mean travel time:

$$Tr_{ef} = \frac{L}{T}\int_{t=0}^{T}\frac{Q_t}{\overline{Q}}\frac{1}{u_t}dt \quad (3)$$

Based on Equation (3), flow-weighted travel times will generally be shorter than time-averaged travel time because velocity increases with streamflow. For cases where concentration and first-order reaction rates vary over time, the effective travel depends on the joint probability of travel time, concentration, and first-order reaction rate [see Doyle (2005) for an example of temporally variable streamflow and concentration]. When concentration increases with streamflow and first-order reaction rates decrease with concentration (e.g., a saturation effect), Equation (3) would provide a better estimate than the time-averaged travel time, but travel time would still be under-estimated.

Specific Travel Time

Calculation of effective travel time with Equation (3) requires time series of discharge and travel time. While discharge time series are available from gages and can be extrapolated over a reach without significant inflows and outflows or simulated using spatially-distributed hydrologic models, time series of travel time are only available at locations with velocity meters, hydraulic models, or where travel time has been measured over a range of streamflow (Hubbard et al., 1982; Bergstrom et al., 2016). For gaged streams with velocity data, a stage or discharge time series can be transformed into velocity time series (Jobson, 2000) and inverted to produce a time series of specific travel time, $\tau_t = 1/u_t$, [L/T] at the gage. The effective value (flow-weighted) of a distribution of specific travel times can be calculated from time series of discharge and velocity,

$$\tau_{ef} = \frac{1}{TS}\sum_{ts=1}^{TS}\frac{Q_{ts}}{\overline{Q}}\frac{1}{u_{ts}} \quad (4)$$

where ts represents an individual time step in each time series, TS is the total number of values in each time series, and τ_{ef} is the effective value of specific travel time at the gage and time series used with units of [T/L].

Equation (4) is used to demonstrate the effects of streamflow variability on velocity and specific travel time. The velocity at a gage is not necessarily representative of velocity averaged over a reach but it is useful as an index of variation of the reach-averaged mean velocity over time (Hubbard et al., 1982). Specific travel time at a gage is likely to biased downward in comparison to the travel time for a longer reach because gage locations are typically selected in narrower sections that maintain measurable, downstream velocity even during low flows. The bias is likely to diminish as streamflow increases and flow becomes more uniform through the reach (Hubbard et al., 1982). As a result, the effect of streamflow variability on specific travel time at a gage indicated by this analysis is likely to be less than its effect on travel time at the reach-scale.

Overview of Analysis and Streams

The analysis has three principal steps: (1) synthesize τ_{ef} distributions from multiple-year, instantaneous streamflow records and field-measured velocities for gaged streams spanning a range in streamflow variability; (2) apply and evaluate methods for estimating τ_{ef}; and (3) compare τ_t distributions characteristic of urban and undeveloped streams. We selected 100 gaged streams in the southeastern United States (**Figure 1**) from six Level III Ecoregions: Piedmont (76 streams), Blue Ridge (12 streams), Valley and Ridge (8 streams), Southeastern Plains (2 streams), North Piedmont (1 stream), and Southwestern Appalachians (1 stream) (Journey et al., 2015). The streams span a range of drainage areas (7–1000 km^2) and were selected to represent streamflow modification by reservoirs and land uses. Normal reservoir storage volume (US Army Corps of Engineers, 2010) in each stream basin divided by basin area ranged from 0 to more than 3 m (median value of 12 mm). Agricultural land cover ranged from 0 to 33% (median 6.5%) of stream basin area. Urban land cover ranged from <1 to 100% (median 22%). The values for each stream are available in Konrad (2020).

Stream size, land use, and streamflow regulation by reservoirs can all affect streamflow variability, so they are potential confounding factors when effects of urbanization on travel time. The coefficient of variation of streamflow distributions were examined in relation to drainage area, total agricultural and urban land cover in 2011 (Multi-Resolution Land Characteristics Consortium, 2019), and normal reservoir storage to identify domains where streamflow variability had little relation to each factor. These homoscedastic domains provided the basis for stratifying streams by size, land use, and regulation (**Table 1**).

Although streams are distributed over the ranges of these factors, not all combinations are well-represented. Streams with drainage areas outside of the range from 19 to 90 km^2, moderate development, mixed land use, or reservoirs providing more than 10 mm of storage over the stream's drainage area are excluded from the analysis of urbanization (step 3). Travel time is examined in streams where streamflow is regulated by reservoirs, but we do not test for effects because of differences in how reservoirs are operated among streams (e.g., power production, water supply, or flood control).

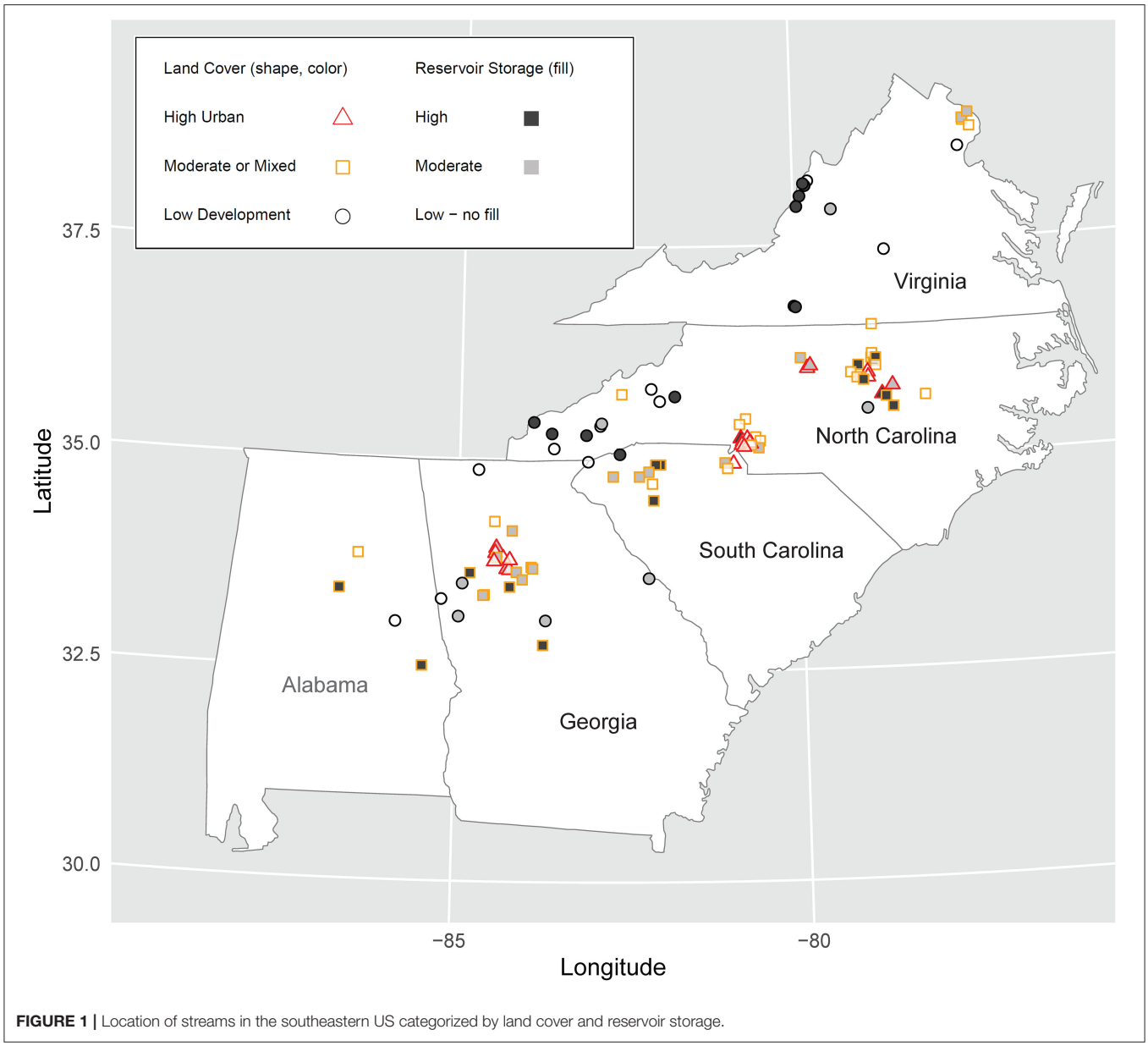

FIGURE 1 | Location of streams in the southeastern US categorized by land cover and reservoir storage.

Generating Specific Travel Time Distributions From Streamflow Time Series and Discrete Velocity Measurements

Available instantaneous streamflow records with a 15 min interval from 1 October 2000 to 30 September 2017 were retrieved from the National Water Information System (USGS, 2019). The length of the records ranged from 4 to 17 years among the streams with a median of 15.5 years. Field measurements of velocity and streamflow were retrieved for 1 October 2010 to 30 September 2017 at each site (Rantz, 1982; USGS, 2019). The period for field measurements relating measured velocity to discharge was limited to the most recent 7 years of the streamflow records to increase the likelihood that measurements were made at approximately the same section in each stream so that at-site variation in velocity is primarily due to variation in discharge rather than the location of the measurement section.

The measurement of stream velocity during unsteady flow may include a significant component of localized, flood-wave driven celerity that affects channel storage rather than contributing to the downstream advection of water. We eliminated measurements made during periods of unsteady flow by converting instantaneous stage measured at the gage during each measurement into values of hydraulic mean depth for the cross-section and eliminating those measurements when hydraulic mean depth changed by more than 10% during the measurement (USGS, 2019). After eliminating measurements made during unsteady flow, streams had between 26 and 96 remaining measurements (median of 52 measurements per

TABLE 1 | Number of streams stratified by reservoir storage and land cover.

Land cover	Reservoir storage normalized by drainage area		
	Low <10 mm	Medium 10–50 mm	High >50 mm
Low development: <15% total agriculture and <10% total urban	11 (5)	7 (1)	11 (1)
Moderate or mixed development: >15% total agriculture or 10–75% total urban	19 (11)	17 (8)	14 (3)
Urban: >75% total urban	14 (6)	5 (2)	2 (2)

Number of streams with drainage areas between 19 and 90 km in parentheses.

site) to define the relation between instantaneous streamflow and velocity.

Specific travel times, τ_t, [s/m] are synthesized for each stream by transforming instantaneous streamflow, Q_t, into instantaneous velocity, u_t, and inverting the velocities, $\tau_t = 1/u_t$. The transformation is based on linear regression of log of discrete streamflow measurements, Q_m, and log of mean cross-section velocity, u_m, for the measurements in a stream, s, using the function lm in R (R Core Team, 2019) to minimize the sum of the squared errors ε_m for each site,

$$\ln(u_m) = \beta_{0,s} + \beta_{1,s} \ln(Q_m) + \varepsilon_m \tag{5}$$

where $\beta_{0,s}$ is the intercept and $\beta_{1,s}$ is the slope for stream s assuming that the functional form is a power law, $u_m = \beta_0 Q_m^{\beta_1}$ (Rantz, 1982). The log of instantaneous travel time at time t, τ_t, is equal to the opposite of the velocity function applied to instantaneous streamflow,

$$\ln(\tau_t) = \ln\left(\frac{1}{u_t}\right) = -\left[\beta_{0,s} + \beta_{1,s} ln(Q_t)\right] \tag{6}$$

Methods for Estimating Effective Travel Time

Application of biogeochemical models across river networks requires spatially distributed estimates of effective travel time. While Equations (4)–(6) can be used at locations with measured velocities and streamflow time-series, we develop and evaluate three alternative methods for estimating τ_{ef} that could be applied more widely. Each method uses either a quantile or moment of a streamflow distribution, which could be calculated at gaged sites from streamflow records or, potentially, assigned to ungaged streams using a model. The overall purpose for the comparisons is to assess the viability of estimating τ_{ef} from an index streamflow rather than computing it directly from the τ_t distribution. The evaluation of the estimates with respect to streamflow variability is significant for both selecting the best method but also understanding the bias of using any of these method in comparisons across streams or scenarios where streamflow variability neither uniform in space or constant over time.

Direct calculation of τ_{ef} and all of the methods for estimating τ_{ef} depend on a known relation between discharge and travel time, which will be a primary source of uncertainty in any application. Estimation of τ_{ef} faces an additional issue of bias related to streamflow variability, which limits the utility of τ_{ef} estimates in comparative analyses across streams (e.g., in relation to basin size, climate, or land use) or over time (e.g., in relation to changes in climate, land use, or water management). Errors in estimates of τ_{ef} from each method are compared to the variance and higher moments of streamflow distributions to evaluate bias with streamflow variability.

The first method for estimating τ_{ef} uses the specific travel time for a fixed quantile of a streamflow distribution. This method accounts for the effect of streamflow variability on travel time generalized across sites but depends on a relatively consistent effect across sites for unbiased estimation. The effective discharge, Q_{ef}, that has a specific travel time equal to τ_{ef} is calculated by inverting Equation (6) and replacing τ_t with τ_{ef} for each stream,

$$Q_{ef,s} = \exp\left[\beta_{0,s} + \frac{\ln(\tau_{ef})}{-\beta_{1,s}}\right] \tag{7}$$

The quantiles representing Q_{ef} are compared to each of the first three linear (L-) moment ratios (Hosking and Wallis, 1997) of the observed streamflow distributions for the 100 streams:

$$\text{linear coefficient of variation, LCV} = \frac{\lambda_2}{\lambda_1}; \tag{8a}$$

$$\text{linear skew, LSK} = \frac{\lambda_3}{\lambda_2}; \text{ and} \tag{8b}$$

$$\text{linear kurtosis, LKU} = \frac{\lambda_4}{\lambda_2} \tag{8c}$$

where λ_i is the ith L-moment of the observed streamflow frequency distribution (Hosking, 2017). Systematic variation of the quantile for τ_{ef} with one or more of the L-moment ratios would indicate potential bias when using fixed quantile of streamflow distributions to estimate τ_{ef} among streams with differences in streamflow variability.

The second method for estimating τ_{ef} would adjust the travel time of mean streamflow for a stream, $\tau_{\overline{Q}}$, by a constant, $\tau^* = \tau_{ef}{:}\tau_{\overline{Q}}$ representing the ratio of effective travel time to the travel time of mean streamflow. The effective travel time, $\hat{\tau_{ef}}$, at a site is estimated as

$$\hat{\tau_{ef}} = \exp\left[-\beta_{0,s} - \beta_{1,s} \ln\left(\overline{Q}\right)\right] \tau^* \tag{9}$$

where $\tau_{\overline{Q}}$ is calculated by substituting $\overline{Q}$ for Q_t in Equation (6) using the regression coefficients $\beta_{0,s}$ and $\beta_{1,s}$ from Equation (5). The median cross-site ratio of $\tau_{ef}{:}\tau_{\overline{Q}}$ is used for τ^* in Equation (9).

We expect that τ^* will decrease with streamflow variability, so the third estimation method would adjust τ^* in Equation (9) based on a streamflow distribution's L-moment ratios. Our primary question is whether the *LCV* is adequate for adjusting τ^* to account for the effects of streamflow variability on τ_{ef} or higher-order moment ratios are necessary to prevent variability-biased estimation. The strength of the relation between the τ^* and each of the first three empirical L-moment ratios (Equations 8a,b,c) is tested using Kendall rank correlation coefficients. Finally, the L-moment ratio with the strongest correlation across sites is used to derive a power function for estimating τ^*:

$$\hat{\tau^*} = 1 - \left[\beta_2 \left(\frac{\lambda_j}{\lambda_i}\right)^{\beta_3}\right] \tag{10}$$

fit for the selected L-moment ratio, $\frac{\lambda_j}{\lambda_i}$, using non-linear least squares regression (R Core Team, 2019).

Effects of Urban Runoff on Travel Time

The effects of streamflow variability on travel time are demonstrated for the case of urban land development, which increases streamflow variability as a result of the re-distribution of water from flow paths slowed by interactions with hillslope storage (depression and soil) to overland flow and low-resistance flow through engineered drainage systems. Streamflow and specific travel time distributions for streams draining urbanized watersheds are compared to those distributions for streams draining watersheds with low development (**Table 1**).

The Wilcoxon rank-sum test is applied to identify significant differences in travel time, velocity, and effective discharge between low-development and urban streams with low reservoir storage. L-moment ratios were not correlated with drainage area for low development streams with drainage areas between 19 and 90 km^2, so the analysis of urbanization is limited to streams in this range of drainage areas to control for effects from basin scale.

Generalized effects of urban hydrologic alteration are synthesized by comparing travel time distributions generated from two theoretical streamflow distributions: one characteristic of a low-development stream and the other characteristic of an urban stream. There is no standard theoretical distribution used to represent instantaneous streamflow (Schaefli et al., 2013; Blum et al., 2017) so Generalized Extreme Value (GEV), 4-parameter Kappa, and Generalized Logistic distributions are evaluated as potential functional forms for the theoretical distributions. Each of the three theoretical distribution is fit to each site using the method of L-moments (Hosking and Wallis, 1997), such that the L-moments for the theoretical distribution matches the empirical L-moments of the instantaneous streamflow distributions to the extent possible.

The fit of each theoretical distribution is evaluated at each site using the one-sample Kolmogorov-Smirnov test (R Core Team, 2019) and a two-sided probability, $p < 0.05$ that the sample was drawn from the distribution. The theoretical distribution that is acceptable at the largest number of sites is selected as the functional form for the probability distributions of instantaneous streamflow. To verify that the theoretical streamflow distribution reproduces τ_{ef} at a site, cumulative distributions of specific travel time and τ_{ef} are calculated from Equations (4) and (6) using the theoretical streamflow distributions.

The characteristic parameters for a low-development stream and an urban stream are assigned using the median values of L-moment ratios for the five low-development streams and six urban streams with drainage areas between 19 and 90 km^2. The parameters of the velocity function are not correlated across sites (**Figure 2**), so the cross-site median values of all 11 streams ($\beta_0 = 0.27$, $\beta_1 = 0.48$) are used to calculate the specific travel times (Equation 6) characteristic of both the low-development stream and the urban stream. Using the same parameters in Equation (6) prevents differences related to channel hydraulics from affecting the travel time calculations.

RESULTS

Effective Travel Times in Relation to Streamflow Distributions

The effective (flow-weighted mean) value of specific travel time varies among the 100 streams from $\tau_{ef} = 0.88$–8.3 s/m (median of 3.1 s/m, **Table 2**). For streams with both low development and reservoir storage ($n = 11$, **Table 1**), τ_{ef} was negatively correlated with drainage area (Kendall rank correlation coefficient of -0.6, $p < 0.01$ that correlation coefficient is zero) indicating that smaller streams generally have longer travel times when compared to larger streams. The relation generally holds regardless of land use and regulation by reservoirs, but τ_{ef} still ranges widely among streams with approximately the same drainage area (**Figure 3A**).

Overall, τ_{ef} is poorly correlated with flow-weighted mean velocity (Kendall rank correlation of 0.1, $p = 0.13$ that correlation coefficient is zero) and, without exception, τ_{ef} is longer than the inverse of flow-weighted mean velocity in all streams (**Figure 3B**). The inverse relation between instantaneous velocity and specific travel time does not hold for their flow-weighted mean values because of the skew of the velocity distribution with respect to streamflow is inverted when its transformed into travel times using Equation (6): instantaneous velocities have larger deviations from their flow-weighted mean during high flows than low flows while, inversely, instantaneous travel times have larger absolute deviations from τ_{ef} during low flows than high flows. Flow-weighted mean velocity is influenced by both the velocity magnitude and volume of high flows. In contrast, τ_{ef} is sensitive to the long travel times during low flows despite their lower volumetric weighting. As a result, τ_{ef} cannot be estimated simply by inverting the flow-weighted mean velocity of a stream.

The quantile of a streamflow distribution that has a specific travel time equal to τ_{ef} is not consistent across sites: it ranges from the 0.52 (about median streamflow) to 0.97 (a relatively infrequent high flows) across streams (**Figure 4**). Across all sites, the quantile for τ_{ef} is <0.7 in only three streams–all with more than 50 mm of reservoir storage. The streamflow quantile corresponding to τ_{ef} is strongly correlated with both the linear skew (**Figure 4A**) and linear kurtosis of streamflow distributions (Kendall rank correlation coefficient >0.7, $p < 0.001$ that coefficient is zero for either). Variation in velocity

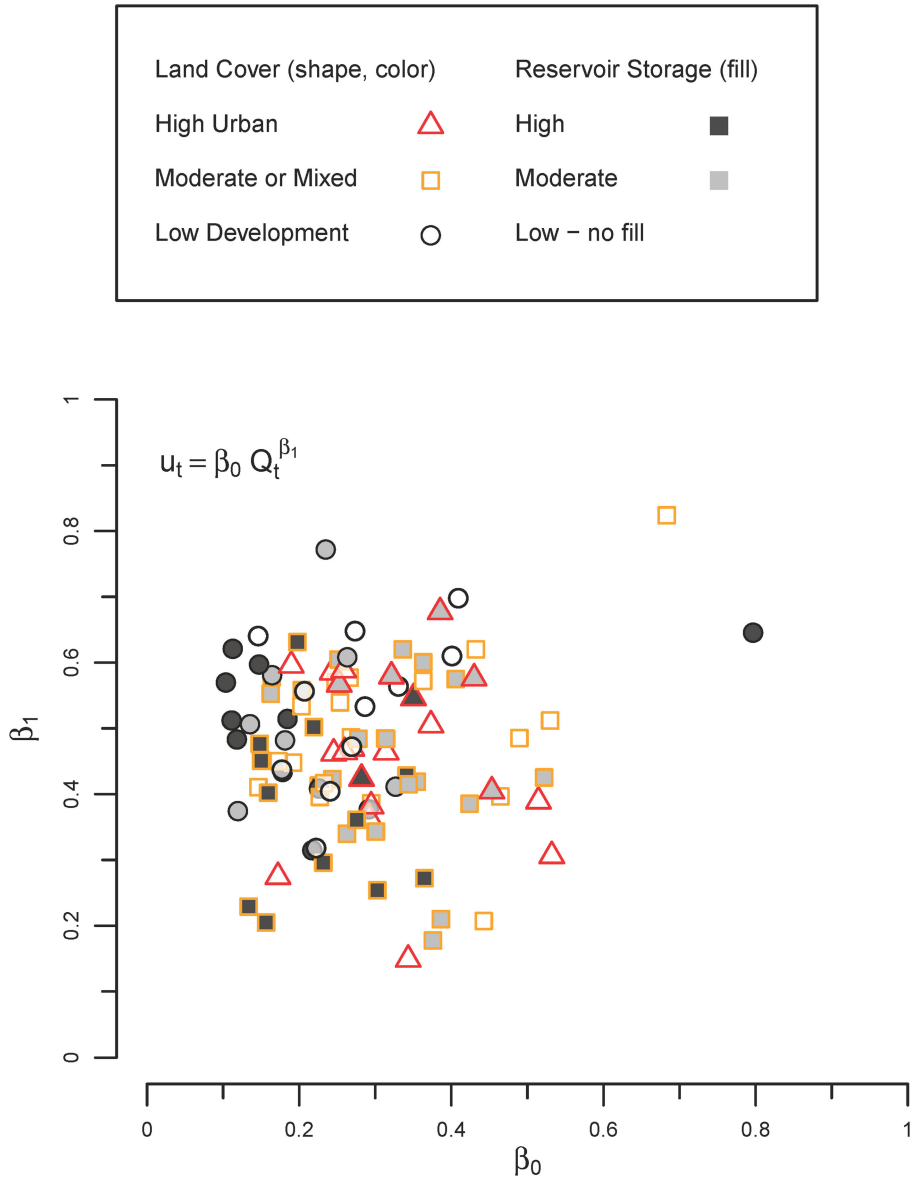

FIGURE 2 | Velocity function (Equation 5) parameters for 100 streams in the southeastern US.

with streamflow, which is indicated by the exponent, β_1, for the velocity function (Equation 6), does not account for much of the cross-site variation in the quantile of streamflow that has a specific travel time equal to τ_{ef} (**Figure 4B**).

Effects of Hydrologic Modification on Travel Time

The relation between streamflow variability and effective travel time leads to divergent responses of effective travel time to urbanization compared to reservoirs. Increased runoff from urbanized areas leads to higher variance and skew of instantaneous streamflow distributions (**Table 2**). As a result, a greater relative volume of streamflow has short travel times in urban streams compared to low-development streams (Wilcoxon rank sum test one-sided $p < 0.001$ that quantiles for τ_{ef} are equal for urban and low-development streams, **Table 2**). Channel modifications associated with urbanization (e.g., lining, straightening, removing obstruction, disconnection from overbank areas) typically increase the velocity of urban streams, but the re-distribution of runoff in response to urbanization (**Figure 4A**) rather than changes in channel hydraulics that affect either flow-weighted mean velocity (**Figure 3B**) or the variation of velocity with streamflow (**Figure 4B**) is likely the primary control on changes in the travel time for urban streams. In contrast, a reservoir that stores water during periods of high flow and releases it at lower flows reduces the skew

TABLE 2 | Cross-site median values of travel time and instantaneous streamflow distribution statistics for five strata of streams.

Strata	Effective travel time, τ_{ef} [s/m]	Ratio of τ_{ef} to specific travel time of mean streamflow	Linear coefficient of variation	Linear skewness
All streams ($n = 100$)	3.1	0.81	0.65	0.63
Low development, low regulation ($n = 11$)	2.3	0.9	0.48	0.51
Low development, low regulation, and drainage areas between 19–90 km^2 ($n = 5$)	5.2	0.87	0.57	0.55
Urban, low regulation ($n = 14$)	3.7	0.68	0.78	0.8
Urban, low regulation and drainage areas between 19–90 km^2 ($n = 6$)	3.1	0.74	0.73	0.79

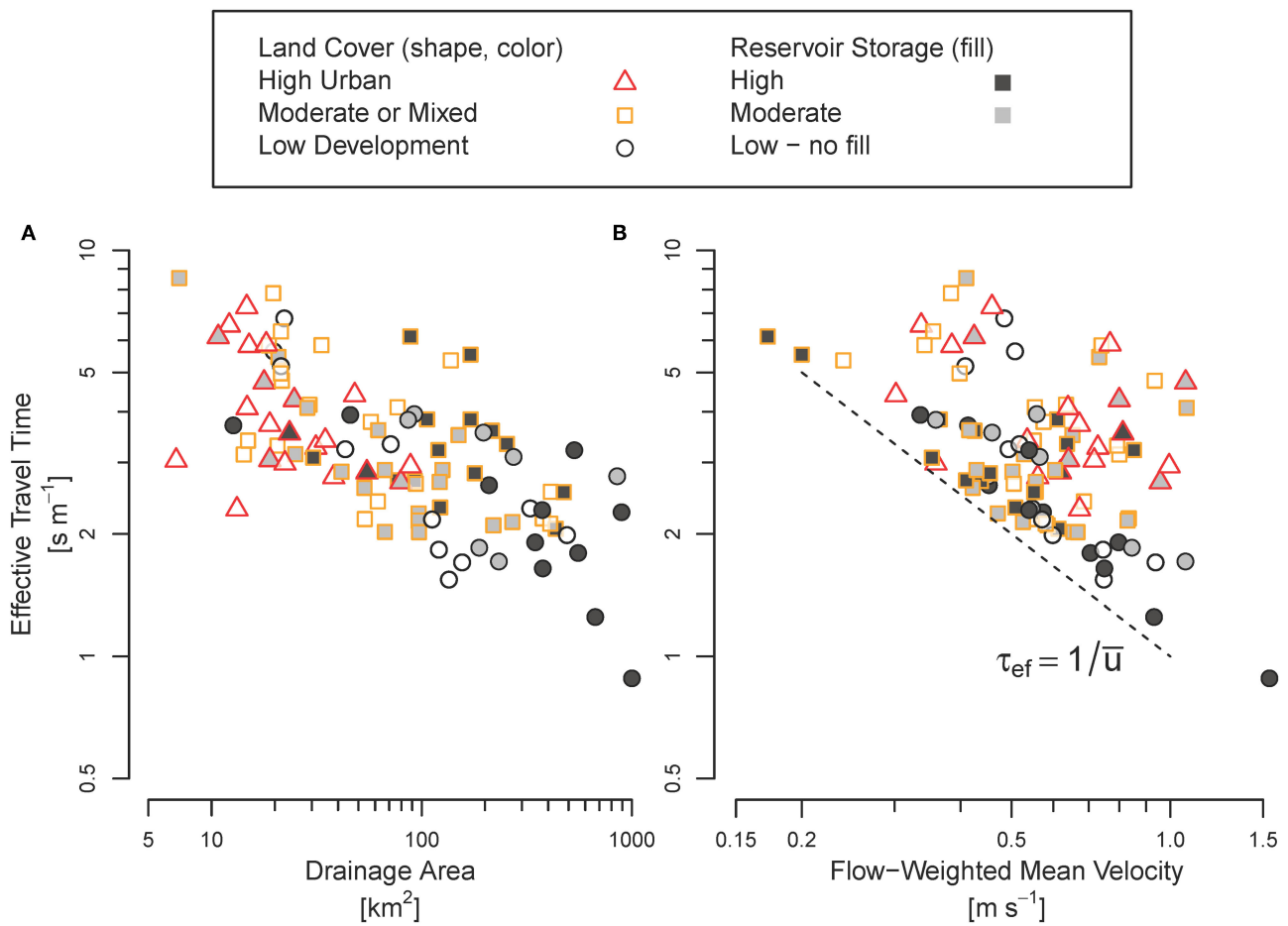

FIGURE 3 | Effective (flow-weighted mean) value of specific travel time for 100 streams in the southeastern US in relation to: **(A)** the drainage area of their watersheds; and **(B)** flow-weighted mean velocity, with a dashed line indicating where travel time would be equal to the inverse of flow-weighted mean velocity.

of a streamflow distribution, resulting in τ_{ef} that represents the specific travel time of a lower quantile of streamflow (**Figure 4A**). Not all reservoirs are operated in ways that reduce the skew of a streamflow distribution, so their effect on travel time is less consistent that the effect of urbanization (**Figure 4A**).

Comparison of Methods for Estimating τ_{ef}

Positively skewed, at-site streamflow distributions generally result in effective travel times that are less than the specific travel times of either median or mean streamflow (**Figures 4**, **5**). Using the specific travel time of the 0.89 quantile (the cross-site median value) of a streamflow distribution to estimate τ_{ef} at a site, the

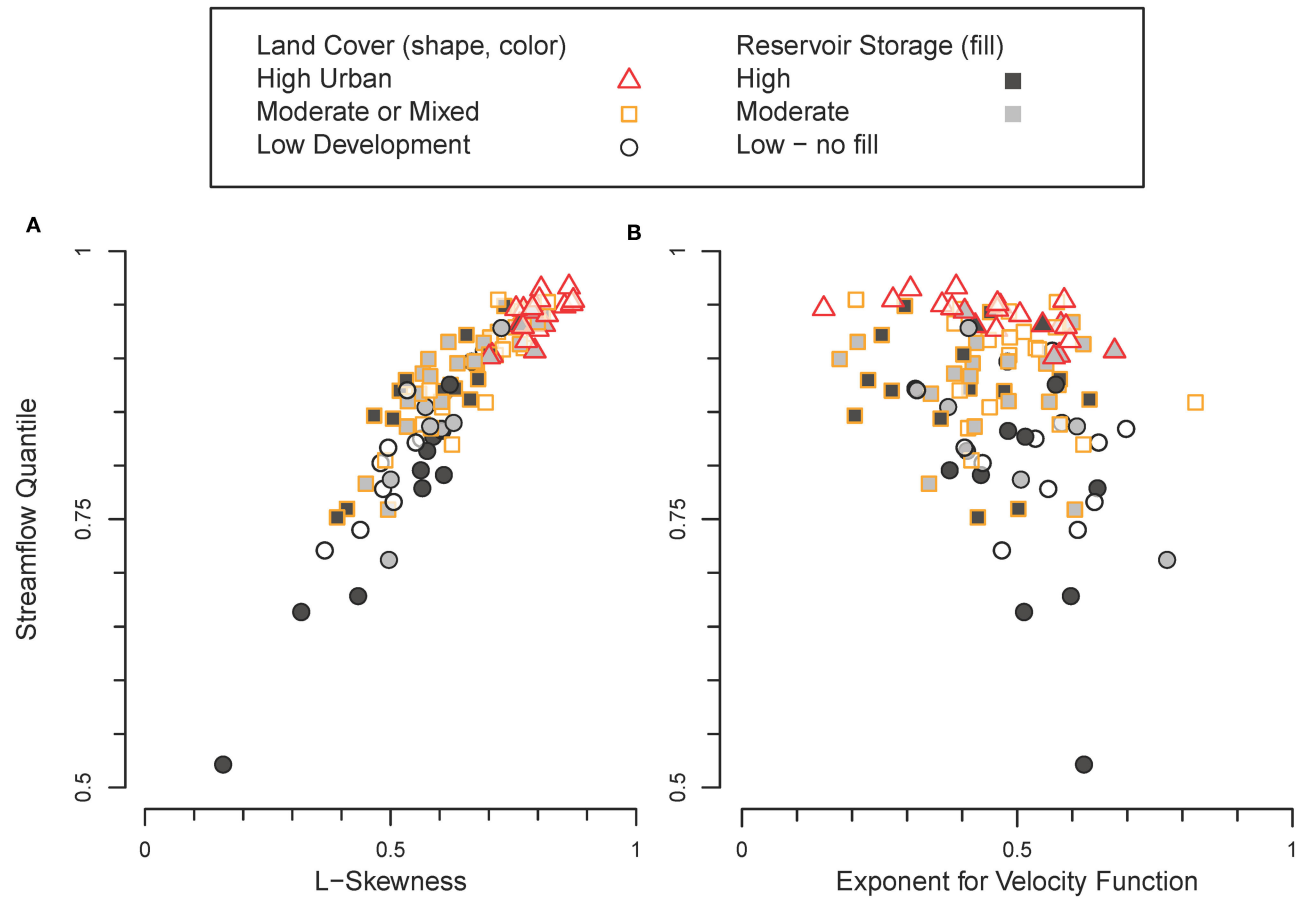

FIGURE 4 | The streamflow quantile with a specific travel time equal to the effective travel time in relation to **(A)** linear (L-) skewness of the streamflow distribution and **(B)** the exponent for the velocity-discharge function (Equation 5).

first estimation method had a RMSE of 1.2 s/m (**Table 3**). The second estimation method (Equation 9) adjusts the specific travel time of mean streamflow, $\tau_{\overline{Q}}$, (**Figure 5**) by the cross-site median ratio τ_{ef}:$\tau_{\overline{Q}}$, $\tau^* = 0.81$ and had a RMSE of 0.56 s/m.

The ratio indicates that τ_{ef} generally is about 20% shorter than $\tau_{\overline{Q}}$ and is needed to address this general bias from using mean streamflow to estimate τ_{ef}. Mean streamflow provides a better basis for estimating τ_{ef} (second method) than a fixed quantile (first method) because the mean value of a streamflow distribution is leveraged by the magnitude of high flows while a quantile reflects that time that streamflow is less than or equal a given magnitude without regard to how streamflow above or below the quantile is distributed.

The ratio of effective travel time in a stream to the specific travel time of its mean streamflow decreases as the variability of the stream's streamflow distribution increases (the inverse relation between τ^* and *LCV* in **Figure 6**). Thus, at-site estimation of τ_{ef} using the specific travel time of mean streamflow has increasing bias with streamflow variability. Urban streams, in particular, have highly variable and skewed streamflow distributions (**Figures 4A**, **6**, respectively) and, as a consequence, effective travel times are much shorter that the travel time of mean streamflow (median $\tau^* = 0.69$ for urban streams, **Table 2**) compared low-development streams (median $\tau^* = 0.9$, $p < 0.001$ that τ^* of urban streams are equal to or greater than τ^* of low-development/low-regulation streams, one-sided Wilcoxon test).

The third estimation method uses stream-specific values of τ^* based on the variability of the streamflow distribution for a stream to adjust the travel time of mean streamflow. Stream-specific values of τ^* vary inversely with the *LCV* of streamflow distributions (**Figure 6**) but can be estimated from *LCV* by the power function:

$$\hat{\tau^*} = 1 - 0.58\, LCV^{2.5} \tag{11}$$

Estimates of τ_{ef} from Equation (9) with τ^* calculated for each site from Equation (11) had a RMSE 0.1 s/m (**Table 3**). The bias of estimates from the third method is substantially lower than from the other two methods (**Table 2**) indicating how the increasing variance of a streamflow distribution scaled by its mean value reduces effective travel time τ_{ef}.

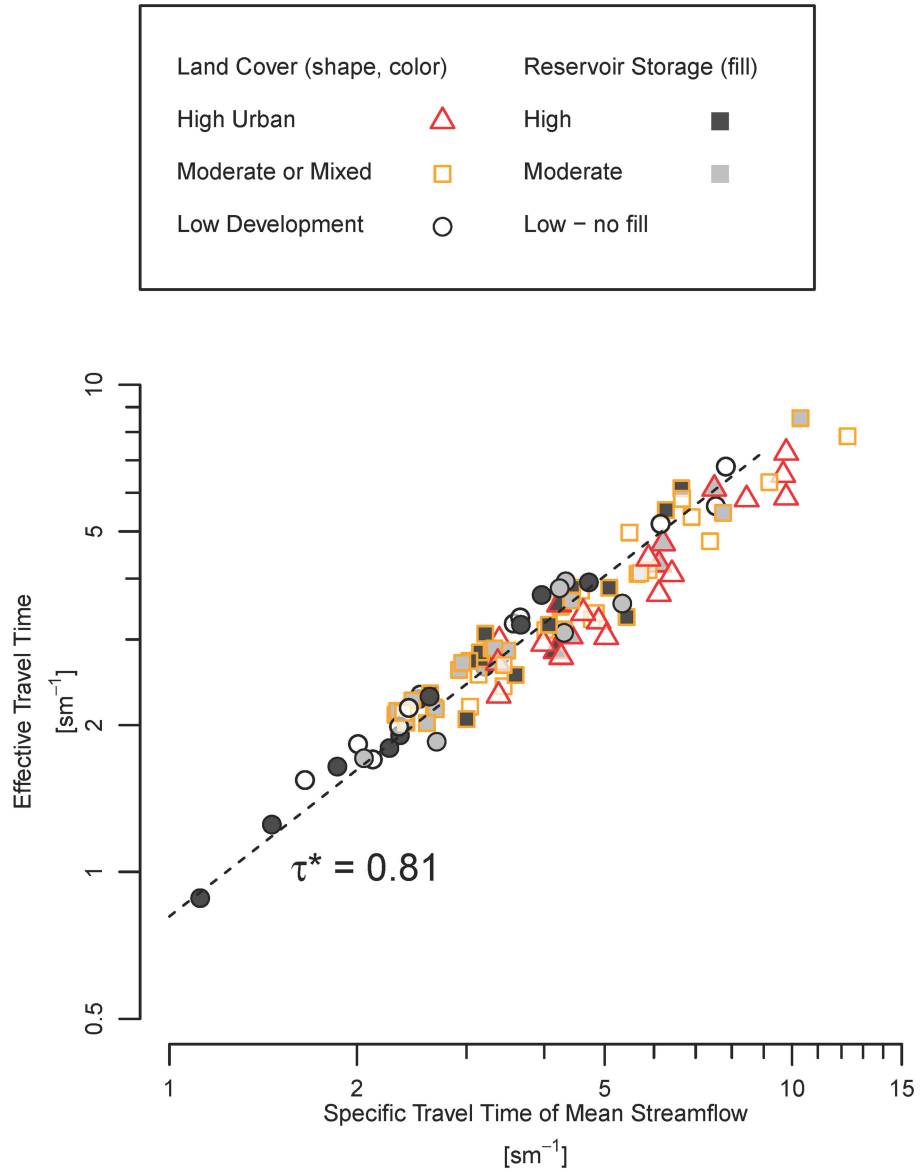

FIGURE 5 | Specific travel time of mean streamflow and effective travel time for 100 streams in the southeastern United States. The cross-site median ratio is $\tau^* = 0.81$.

TABLE 3 | Summary of methods for estimating effective travel time.

Method	Statistic providing basis for estimation	Statistic value	RMSE
1. Specific travel time of a specified streamflow quantile, Q^*	Median Q^* for all sites	0.88	1.2
2. Specific travel time of at-site mean streamflow adjusted by ratio of effective travel time to specific travel time of mean streamflow, τ^*	Median τ^* for all sites	0.81	0.56
3. Specific travel time of at-site mean streamflow adjusted by ratio of effective travel time to specific travel time of mean streamflow, τ^*	$\tau^* = 0.58\ LCV^{2.5}$ where LCV is at-site linear coefficient of variation of streamflow distribution	0.64–0.97	0.10

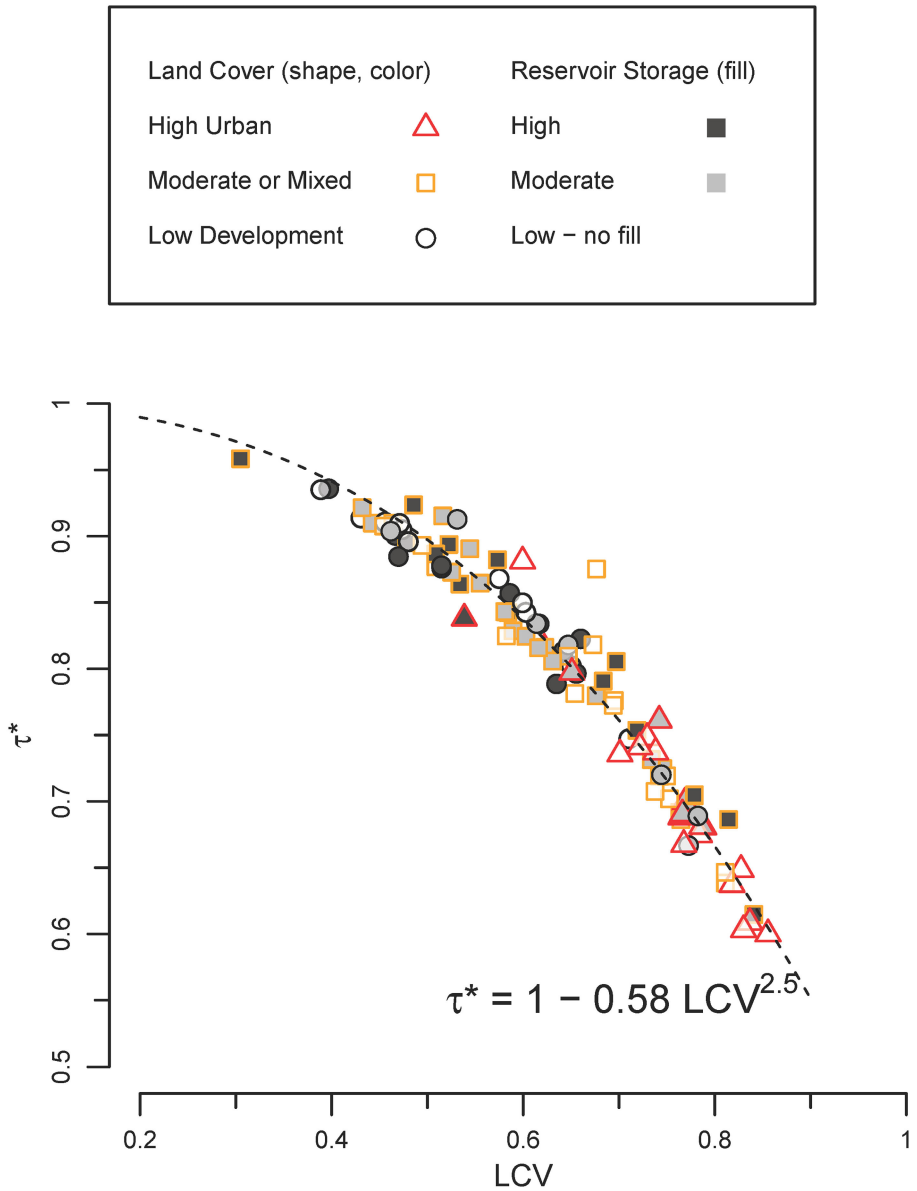

FIGURE 6 | Ratio of flow-weighted travel time to travel time of mean streamflow, τ^*, in relation to linear coefficient of variation, LCV. Dashed line is $\tau^* = 1–0.58\ LCV^{2.5}$.

Effect of Urbanization on Specific Travel Time

Streamflow distributions with variability characteristic of a low-development stream and an urban stream, respectively, were generated from a generalized extreme value (GEV). The GEV distribution provides a better approximation of instantaneous streamflow distributions than either the Kappa or Generalized Logistic distributions for all 100 streams but still could be rejected at 31 of them (two-sided $p < 0.05$ K-S test). Nonetheless, τ_{ef} calculated from Equation (6) using a GEV distribution fit to each stream to generate Q_t provides robust at-site estimates that closely matched τ_{ef} calculated from Equation (6) using observed streamflow values for Q_t (RMSE = 0.057 s/m; **Figure 7**).

The median values of GEV-distribution parameters for small, urban streams ($n = 6$) are distinct from those for small low-development streams ($n = 5$) and generally indicate the urban streams have higher variance and skew (**Figure 8**, **Table 4**). As a result, the travel time distribution for the characteristic urban stream generally shifts toward larger volumes of water with shorter travel times (**Figure 9**). The characteristic urban stream has an 19% increase in the volume of streamflow with relative short travel times (<1 s/m) and a 21% decrease in streamflow with travel times between 2 and 4 s/m compared to the characteristic low-development stream (**Figure 9A**). The re-distribution of streamflow to higher flows in the urban stream generally increases the volume of

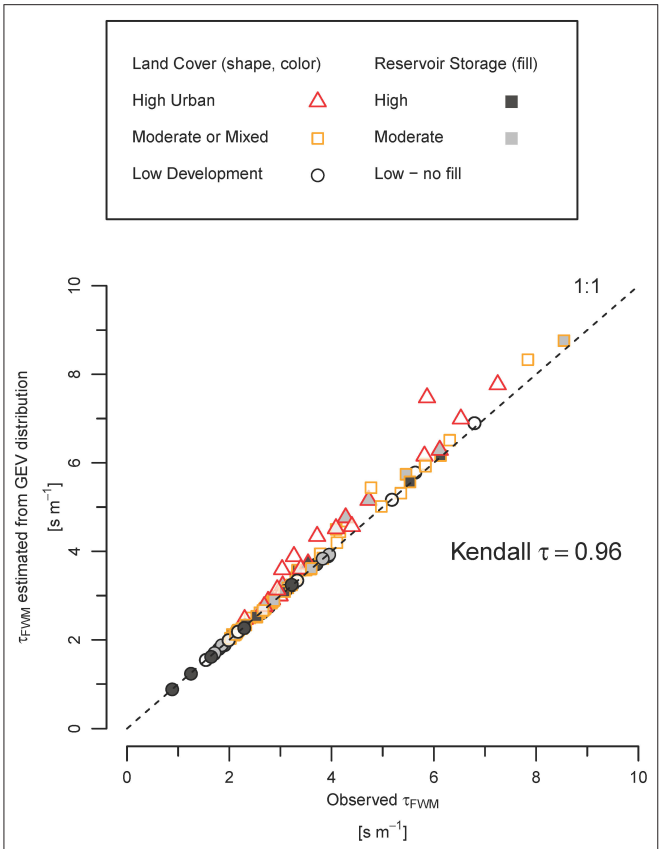

FIGURE 7 | Flow-weighted mean travel time (τ_{ef}) calculated from the observed streamflow distribution and a GEV distribution fit to each stream using L-moments.

urban streamflow with travel times < ~4 s/m (**Figure 9B**). The urban stream has slightly more streamflow with travel times >8 s/m (extremely low flow) than the low-development stream, but this represents a small portion (~2.5%) of total streamflow.

DISCUSSION

The specific travel time of mean streamflow is longer than the effective travel time of streamflow, τ_{ef}, over annual and longer time scales because streamflow distributions are positively skewed (Blum et al., 2017) with most of the total volume discharge during higher flows with shorter travel times (**Figure 5B**). The difference between τ_{ef} and the travel time of mean streamflow generally is about 20% (or equivalently $\tau^* \approx 0.8$). Streams with higher streamflow variability have a larger relative volume of high flows with short travel times and, thus, shorter effective travel times (**Figure 6**).

Flow-weighting of travel time in Equation (4) provides a physically based value of τ_{ef}, for modeling transport and processing at annual and longer time scales. Using τ_{ef}, rather than τ_{Qmean} in the empirical power-law expression for nitrogen removal proposed by Seitzinger et al. (2002), we would expect ~10% less nitrogen removal over a kilometer of channel. This is a significant difference in the mass of nitrogen retained, and it can have important cumulative effects for predictions at the river basin scale. While physically-based parameters have epistemic value for how processes scale over space and time and offer the promise of model parameterization from direct measurement, they do not necessarily improve model performance at calibration sites because of equifinality: parameters can compensate for each other's value resulting in comparable model performance for different parameter sets (Beven and Smith, 2015). Indeed, calibration of rate coefficients can offset the effect a particular travel time in a time-averaged biogeochemical model. Using the travel time of mean streamflow, however, will produce lower uptake velocities and deposition rates than models using τ_{ef}.

The primary reason for using effective travel times in time-average models is to increase the capability of such models to simulate the effects of streamflow variability. Simply using 80% of the travel time of mean streamflow (method 2), however, does not provide time-averaged models with capability to represent differences between streams as a result of streamflow variability. The third method we developed provides relatively accurate estimates of τ_{ef} (**Table 3**) but the at-site mean and variance of a streamflow distribution must be known to apply it. Low prediction skill of current models for the variance of streamflow (Farmer et al., 2014; Basso et al., 2015) is a crux for broader application of this estimation method to ungaged streams, but systematic variation in the *LCV* with land use (**Figure 8**) indicates the possibility for model-based estimation in some situations.

Effective travel time does not account for the dependencies of constituent concentrations on streamflow or first-order reaction rates on constituent concentrations. In cases where the temporal variability of concentrations and reaction rates are comparable to the variability of travel time, the joint distribution of streamflow, travel time, concentration, and first-order reaction rate is necessary to calculate an accurate, time-average mass flux for the process of interest (Doyle, 2005). If all such data were available, using a dynamic model would probably be preferable to a time-average model. Given that time series of velocity can be derived more widely (at streamflow gages with field measurements of velocity) than time series of concentration and reaction rate for any solute or particulate, adjustment of travel times is a pragmatic and broadly applicable approach to improve the capability of time-average river network models to represent effects of streamflow variability on biogeochemical processing in river networks.

For urban streams, a large fraction of the total runoff from the catchment is discharged during high-flow periods when streamflow has higher velocities in comparison to lower-flow periods. Even where stormwater detention controls peak flow rates, it has limited effectiveness reducing the volume of runoff during large storms (Booth et al., 2002; Hood et al., 2007; Smith et al., 2013). The volumetric differences between our characteristic undeveloped and urban streams are small for low flows longer travel time (e.g., >4 s/m), so substantial differences in processing would not be expected during low flow except for uptake or reactions with low mass-transfer coefficients.

Difference only emerges for high flows when a large fraction of streamflow has short travel times (e.g., <1 s/m) in urban stream (**Figure 7**).

The effect of urbanization on nitrogen retention during base flow conditions is equivocal. In the desert Southwest, Grimm et al. (2005) documented less retention (longer uptake lengths) of experimental NO_3- additions in urban streams but a strong effect from discharge. Using an expanded set of 72 streams, Hall et al. (2009) found uptake lengths varied with specific discharge (streamflow divided by width) streamflow at the time of the experiment ("stream size") but not land-use *per se*. Hall et al. (2009) recommended that hydrologic variability is critical for understanding differences in nitrogen retention at longer time scales. We propose streamflow variability is likely to reduce retention given the well-defined, inverse relation of effective travel time to streamflow variability (**Figure 6**), but verification would require high-flow experiments [e.g., Melis (2011)] and the integration of results for both low and high flows based on streamflow distributions.

Effects of streamflow variability on processing and retention in streams are important in the context of land use (Hall et al., 2009), variation between headwater streams and mainstem rivers (Gomez-Velez et al., 2015), and responses to climate change (Baron et al., 2013; Morse and Wollheim, 2014). Given the relation between effective travel time and variance of streamflow distributions (**Figure 6**), differences in travel time can be inferred broadly from the effects of drainage area (**Figure 2**)

TABLE 4 | Parameters used in the Generalized Extreme Value (GEV) distributions for characteristics streamflow distributions based on the median values for all streams, low-development streams with low reservoir storage and drainage areas between 19 and 90 km^2 (characteristic low-development stream), and urban streams with low reservoir storage and drainage areas between 19 and 90 km^2 (characteristic urban streams).

Parameter	All streams	Characteristic low-development stream	Characteristic urban stream
Location	0.31	0.39	0.22
Scale	0.33	0.37	0.19
Shape	−0.61	−0.52	−0.78

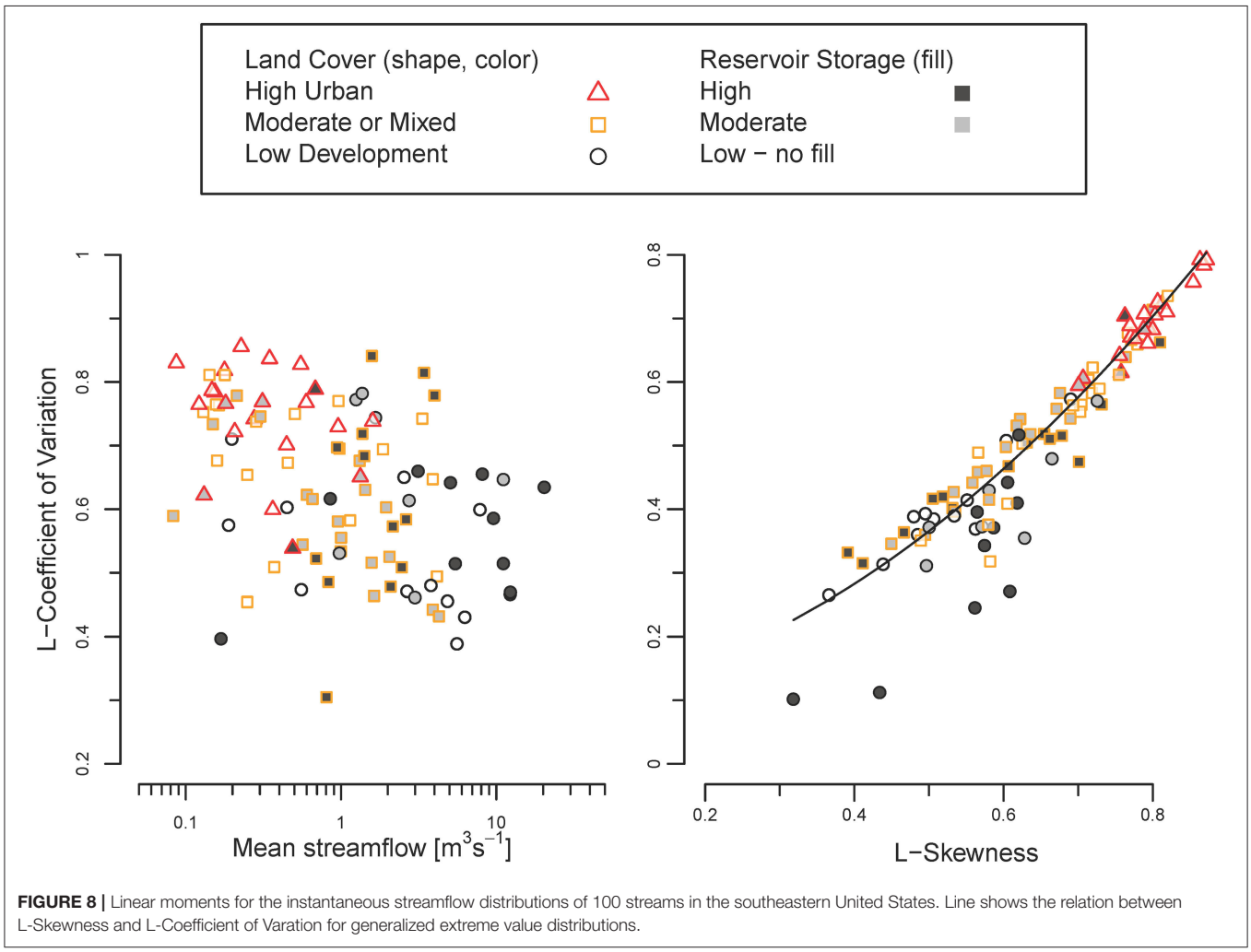

FIGURE 8 | Linear moments for the instantaneous streamflow distributions of 100 streams in the southeastern United States. Line shows the relation between L-Skewness and L-Coefficient of Varation for generalized extreme value distributions.

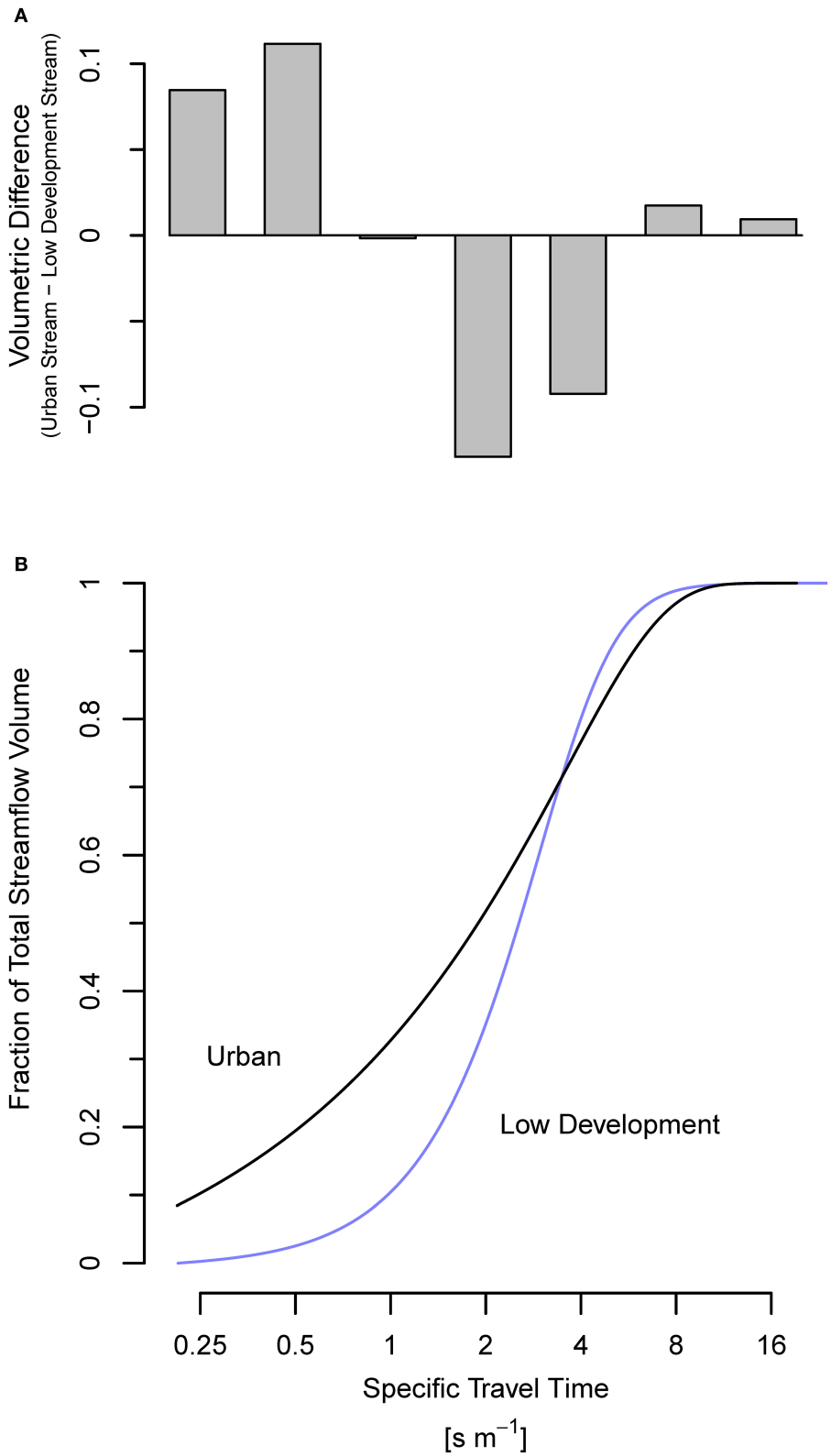

FIGURE 9 | Travel-time distributions for characteristic a low-development and urban stream reach with **(A)** the marginal difference between the urban and low-development streams in standardized volume [fraction of total] for seven bins of travel time and **(B)** the cumulative distribution of streamflow by volume for the range of travel times from 0.2 to 20 s/m. Fraction of streamflow volume with travel times <0.2 s/m is 0% for the low-development stream and 8% for the urban stream.

(Thomas and Benson, 1970; Dunne and Leopold, 1978), regional climate (Dettinger and Diaz, 2000), climate change (Pagano and Garen, 2005; Jiménez Cisneros et al., 2014), reservoirs (**Figure 2**) (Poff et al., 2007; Kroll et al., 2015), and engineered-drainage systems (King et al., 2015) on the variance of streamflow distributions. Globally, anthropogenic changes to streamflow continues to expand with more extensive drainage systems, river impoundments and diversions, and land cover conversion and changes in climate (Eng et al., 2013; Jiménez Cisneros et al., 2014; King et al., 2015; Kroll et al., 2015; Carlisle et al., 2019). As these factors affect streamflow variability, travel times in biogeochemical models need to be adjusted accordingly.

CONCLUSIONS

Streamflow variability forces dynamic processing and retention of materials in river networks. The effective (flow-weighted mean) travel time of streamflow generally is less than the travel time of mean streamflow over seasonal and longer time scales because a significant fraction of streamflow is discharged at high velocities during high flows in most streams. The effective travel time of streamflow is typically ∼80% of the travel time of mean streamflow for 100 streams in the southeastern United States and increases with streamflow variability. Application of the travel time of mean streamflow introduces a systematic bias in modeling of processing and retention where streamflow variability is neither uniform across streams nor constant over time. This bias limits the capability of time-averaged river-networks models to resolve differences between streams or changes over time. Time-average models can gain the capability to represent effects of streamflow variability by adjusting the travel time of mean streamflow using the at-site coefficient of variation of streamflow. This approach provides a pragmatic way to connect our understanding of spatial patterns in streamflow variability and its response to climate and land use change to processing and retention of transported materials (e.g., sediment, nutrients, contaminants) in river networks.

DATA AVAILABILITY STATEMENT

Publicly available datasets were analyzed in this study. This data can be found here: Instantaneous streamflow values and field measured velocity and streamflow are available from the US Geological Survey National Water Information System. Data derived in this investigation are available from US Geological Survey ScienceBase (https://doi.org/10.5066/P9665F6L).

AUTHOR CONTRIBUTIONS

CK proposed the objective and approach for this research during a workshop lead by JH, JG-V, EB, and DS. NS, GS, JH, and CK designed the analysis for general validity and broad relevance. CK compiled data, implemented the analysis, and drafted the initial manuscript. All of the authors were involved in preparing the final manuscript.

FUNDING

This research was supported by the US Geological Survey as part of the Regional Stream Quality Assessment and the River Corridor Working Group at the John Wesley Power Center for Analysis and Synthesis.

REFERENCES

Alexander, R. B., Böhlke, J. K., Boyer, E. W., David, M. B., Harvey, J. W., Mulholland, P. J., et al. (2009). Dynamic modeling of nitrogen losses in river networks unravels the coupled effects of hydrological and biogeochemical processes. *Biogeochemistry* 93, 91–116. doi: 10.1007/s10533-008-9274-8

Baron, J. S., Hall, E. K., Nolan, B. T., Finlay, J. C., Bernhardt, E. S., Harrison, J. A., et al. (2013). The interactive effects of excess reactive nitrogen and climate change on aquatic ecosystems and water resources of the United States. *Biogeochemistry* 114, 71–92. doi: 10.1007/s10533-012-9788-y

Basso, S., Frascati, A., Marani, M., Schirmer, M., and Botter, G. (2015). Climatic and landscape controls on effective discharge. *Geophys. Res. Lett.* 42, 8441–8447. doi: 10.1002/2015GL066014

Basu, N. B., Rao, P. S. C., Thompson, S. E., Loukinova, N. V., Donner, S. D., Ye, S., et al. (2011). Spatiotemporal averaging of in-stream solute removal dynamics. *Water Resour. Res.* 47:W00J06. doi: 10.1029/2010WR010196

Behrendt, H., and Opitz, D. (1999). Retention of nutrients in river systems: dependence on specific runoff and hydraulic load. *Hydrobiologia* 410, 111–122. doi: 10.1023/A:1003735225869

Bergstrom, A., McGlynn, B., Mallard, J., and Covino, T. (2016). Watershed structural influences on the distributions of stream network water and solute travel times under baseflow conditions. *Hydrol. Process.* 30, 2671–2685. doi: 10.1002/hyp.10792

Beven, K., and Smith, P. (2015). Concepts of information content and likelihood in parameter calibration for hydrological simulation models. *J. Hydrol. Eng.* 20:A4014010. doi: 10.1061/(ASCE)HE.1943-5584.0000991

Blum, A. G., Archfield, S. A., and Vogel, R. M. (2017). On the probability distribution of daily streamflow in the United States. *Hydrol. Earth Syst. Sci.* 21, 3093–3103. doi: 10.5194/hess-21-3093-2017

Booth, D. B., Hartley, D., and Jackson, R. (2002). Forest cover, impervious-surface area, and the mitigation of stormwater impacts. *J. Am. Water Resour. Assoc.* 38, 835–845. doi: 10.1111/j.1752-1688.2002.tb01000.x

Botter, G., Basu, N. B., Zanardo, S., Rao, P. S. C., and Rinaldo, A. (2010). Stochastic modeling of nutrient losses in streams: interactions of climatic, hydrologic, and biogeochemical controls. *Water Resour. Res.* 46:W08509. doi: 10.1029/2009WR008758

Boyer, E. W., Alexander, R. B., Parton, W. J., Li, C. S., Butterbach-Bahl, K., Donner, S. D., et al. (2006). Modeling denitrification in terrestrial and aquatic ecosystems at regional scales. *Ecol. Appl.* 16, 2123–2142. doi: 10.1890/1051-0761(2006)016[2123:MDITAA]2.0.CO;2

Carlisle, D. M., Wolock, D. M., Konrad, C. P., McCabe, G. J., Eng, K., Grantham, T. E., et al. (2019). *Flow Modification in the Nation's Streams and Rivers*. Technical Report, U.S. Geological Survey Circular 1461, Reston, VA. doi: 10.3133/cir1461

Carlston, C. W. (1963). *Drainage Density and Streamflow*. Technical Report, U.S. Geological Survey Prof. Paper 422–C, Washington, DC. doi: 10.3133/pp422C

Chang, H. (2007). Comparative streamflow characteristics in urbanizing basins in the Portland Metropolitan Area, Oregon, USA. *Hydrol. Process.* 21, 211–222. doi: 10.1002/hyp.6233

Czuba, C. R., Czuba, J. A., Magirl, C. S., Gendaszek, A. S., and Konrad, C. P. (2018). Effect of river confinement on depth and spatial extent of bed disturbance affecting salmon redds. *J. Ecohydraul.* 3, 4–17. doi: 10.1080/24705357.2018.1457986

Czuba, J. A., and Foufoula-Georgiou, E. (2014). A network-based framework for identifying potential synchronizations and amplifications of sediment delivery in river basins. *Water Resour. Res.* 50, 3826–3851. doi: 10.1002/2013WR014227

Dettinger, M. D., and Diaz, H. F. (2000). Global characteristics of stream flow seasonality and variability. *J. Hydrometeorol.* 1, 289–310. doi: 10.1175/1525-7541(2000)001<0289:GCOSFS>2.0.CO;2

Doyle, M. W. (2005). Incorporating hydrologic variability into nutrient spiraling. *J. Geophys. Res.* 110:G01003. doi: 10.1029/2005JG000015

Dunne, T., and Leopold, L. B. (1978). *Water in Environmental Planning*. New York, NY: W.H. Freeman and Company. 818.

Eng, K., Carlisle, D. M., Wolock, D. M., and Falcone, J. A. (2013). Predicting the likelihood of altered streamflows at ungauged rivers across the conterminous United States. *River Res. Appl.* 29, 781–791. doi: 10.1002/rra.2565

Ensign, S. H., and Doyle, M. W. (2006). Nutrient spiraling in streams and river networks. *J. Geophys. Res.* 111:G04009. doi: 10.1029/2005JG000114

Farmer, W. H., Archfield, S. A., Over, T. M., Hay, L. E., LaFontaine, J. H., and Kiang, J. E. (2014). *A Comparison of Methods to Predict Historical Daily Streamflow Time Series in the Southeastern United States*. Technical Report, U.S. Geological Survey Scientific Investigations Report 2014–5231, Reston, VA. doi: 10.3133/sir20145231

Findlay, S. (1995). Importance of surface-subsurface exchange in stream ecosystems: The hyporheic zone. *Limnol. Oceanogr.* 40, 159—64. doi: 10.4319/lo.1995.40.1.0159

Gomez-Velez, J., Harvey, J., Cardenas, M., and Kiel, B. (2015). Denitrification in the Mississippi River network controlled by flow through river bedforms. *Nature Geosci.* 8, 941–945. doi: 10.1038/ngeo2567

Grimm, N. B., Sheibley, R. W., Crenshaw, C. L., Dahm, C. N., Roach, W. J., and Zeglin, L. H. (2005). N retention and transformation in urban streams. *J. N. Am. Benthol. Soc.* 24, 626–642. doi: 10.1899/04-027.1

Hall, R. O. Jr., Bernhardt, E. S., and Likens, G.E. (2002). Relating nutrient uptake with transient storage in forested mountain streams. *Limnol. Oceanogr.* 47, 255–265. doi: 10.4319/lo.2002.47.1.0255

Hall, R. O. Jr., Tank, J. L., Sobota, D. J., Mulholland, P. J., O'Brien, J. M., Dodds, W. K., et al. (2009). Nitrate removal in stream ecosystems measured by 15N addition experiments: total uptake. *Limnol. Oceanogr.* 54, 653–665. doi: 10.4319/lo.2009.54.3.0653

Harvey, J., Gomez-Velez, J., Schmadel, N., Scott, D., Boyer, E., Alexander, R., et al. (2019). How hydrologic connectivity regulates water quality in river corridors. *J. Am. Water Resour. Assoc.* 55, 369–381. doi: 10.1111/1752-1688.12691

Harvey, J., and Gooseff, M. (2015). River corridor science: hydrologic exchange and ecological consequences from bed forms to basins. *Water Resour. Res.* 51, 6893–6692. doi: 10.1002/2015WR017617

Harvey, J. W. (2016). "Hydrologic exchange flows and their ecological consequences in river corridor in stream ecosystems in a changing environment," in *Stream Ecosystems in a Changing Environment*, eds J. B. Jones and E. M. Stanley (Amsterdam: Elsevier), 1–83. doi: 10.1016/B978-0-12-405890-3.00001-4

Hein, T., Baranyi, C., Reckendorfer, W., and Schiemer, F. (2004). The impact of surface water exchange on the nutrient and particle dynamics in side-arms along the River Danube, Austria. *Sci. Total Environ.* 328, 207–218. doi: 10.1016/j.scitotenv.2004.01.006

Helton, A. M., Poole, G. C., Meyer, J. L., Wollheim, W. M., Peterson, B. J., Mulholland, P. J., et al. (2011). Thinking outside the channel: modeling nitrogen cycling in networked river ecosystems. *Front. Ecol. Environ.* 9, 229–238. doi: 10.1890/080211

Hood, M. J., Clausen, J. C., and Warner, G. S. (2007). Comparison of stormwater lag times for low impact and traditional residential development. *J. Am. Water Resour. Assoc.* 43, 1036–1046. doi: 10.1111/j.1752-1688.2007.00085.x

Hosking, J., and Wallis, J. (1997). *Regional Frequency Analysis: An Approach Based on L-Moments*. Cambridge: Cambridge University Press. doi: 10.1017/CBO9780511529443

Hosking, J. R. M. (2017). *L-Moments, R package lmom, Version 2.8, 2019-03-11*. Available online at: https://cran.r-project.org (accessed May 20, 2020).

Hubbard, E. F., Kilpatrick, F. A., Martens, L. A., and Wilson, J. F. (1982). "Measurement of time of travel and dispersion in streams by dye tracing," in *Applications of Hydraulics, Book 3, Techniques of Water Resources Investigations of the United States Geological Survey, Chapter A9, version 1*. Available online at: https://pubs.usgs.gov/twri/twri3-a9/pdf/twri_3-a9_ver1.pdf (accessed May 30, 2020).

Jiménez Cisneros, B. E., Oki, T., Arnell, N. W., Benito, G., Cogley, J. G., Döll, P., et al. (2014). "Freshwater resources in climate change 2014: impacts, adaptation, and vulnerability. Part A: global and sectoral aspects," in *Contribution of Working Group II to the Fifth Assessment Report of the Intergovernmental Panel on Climate Change*, eds C. B. Field, V. R. Barros, D. J. Dokken, K. J. Mach, M. D. Mastrandrea, T. E. Bilir, et al. (Cambridge: Cambridge University Press), 229–269.

Jobson, H. E. (2000). *Estimating the Variation of Travel Time in River by Use of Wave Speed and Hydraulic Characteristics*. Technical Report, U.S. Geological Survey Water-Resources Investigations Report 00–4187, Reston, VA.

Journey, C. A., Van Metre, P. C., Bell, A. H., Garrett, J. D., Button, D. T., Nakagaki, N., et al. (2015). *Design and Methods of the Southeast Stream Quality Assessment (SESQA), 2014*. Technical Report, U.S. Geological Survey Open-File Report 2015–1095, Columbia, SC. doi: 10.3133/ofr20151095

King, K. W., Williams, M. R., and Fausey, N. R. (2015). Contributions of systematic tile drainage to watershed-scale phosphorus transport. *J. Environ. Qual.* 44, 486–494. doi: 10.2134/jeq2014.04.0149

Konrad, C., and Gellis, A. (2018). Factors influencing fine sediment on stream beds in the midwestern United States. *J. Environ. Qual.* 47, 1214–1222. doi: 10.2134/jeq2018.02.0060

Konrad, C. P. (2009). Simulating the recovery of suspended sediment transport and river bed stability in response to dam removal on the Elwha River, Washington. *Ecol. Eng.* 35, 1104–1115. doi: 10.1016/j.ecoleng.2009.03.018

Konrad, C. P. (2020). *Basin Characteristics and Travel Time Metrics for 100 Sites in the Southeastern United States*. USGS Data Release, Reston, VA. doi: 10.5066/P9665F6L

Konrad, C. P., Black, R. W., Voss, F., and Neale, C. M. U. (2008). Integrating remote sensing and field methods to assess effects of levee setbacks on riparian and aquatic habitats in glacial-melt water rivers. *River Res. Appl.* 24, 355–372. doi: 10.1002/rra.1070

Konrad, C. P., and Booth, D. B. (2005). "Hydrologic changes in urban streams and their ecological significance," in *Effects of Urbanization on Stream Ecosystems*, eds L. R. Brown, R. H. Gray, R. M. Hughes, and M. R. Meador (Bethesda, MD: American Fisheries Society), 157–177.

Konrad, C. P., Booth, D. B., and Burges, S. J. (2005). Effects of urban development in the Puget Lowland, Washington, on interannual streamflow patterns: consequences for channel form and streambed disturbance. *Water Resour. Res.* 41:W07009. doi: 10.1029/2005WR004097

Kroll, C. N., Croteau, K. E., and Vogel, R. M. (2015). Hypothesis tests for hydrologic alteration. *J. Hydrol.* 530, 117–126. doi: 10.1016/j.jhydrol.2015.09.057

Leopold, L. B. (1968). *Hydrology for Urban Land Planning: A Guidebook on the Hydrologic Effects of Urban Land Use*. Technical Report, U.S. Geological Survey Circular 554, Washington, DC. doi: 10.3133/cir554

Melis, T. S. (2011). *Effects of Three High-Flow Experiments on the Colorado River Ecosystem Downstream From Glen Canyon Dam, Arizona*. Technical Report, U.S. Geological Survey Circular 1366, Flagstaff, AZ. doi: 10.3133/cir1366

Meyer, J. L., and Edwards, R. T. (1990). Ecosystem metabolism and turnover of organic carbon along a blackwater river continuum. *Ecology* 71, 668–677. doi: 10.2307/1940321

Morse, N. B., and Wollheim, W. M. (2014). Climate variability masks the impacts of land use change on nutrient export in a suburbanizing watershed. *Biogeochemistry* 121, 45–59. doi: 10.1007/s10533-014-9998-6

Mulholland, P., Helton, A., Poole, G., Hall, R., Hamilton, S., Peterson, B., et al. (2008). Stream denitrification across biomes and its response to anthropogenic nitrate loading. *Nature* 452, 202–205. doi: 10.1038/nature06686

Mulholland, P. J., Steinman, A. D., and Elwood, J. W. (1990). Measurement of phosphorus uptake length in streams: comparison of radiotracer and sTable P04 releases. *Can. J. Fish. Aquat. Sci.* 47, 2351–2357. doi: 10.1139/f90-261 (accessed May 30, 2020).

Multi-Resolution Land Characteristics Consortium (2019). *National Land Cover Database 2011*. Available online at: https://www.mrlc.gov/data (accessed May 20, 2020).

Newbold, J. D., Elwood, J. W., O'Neill, R. V., and Sheldon, A. L. (1983). Phosphorus dynamics in a woodland stream ecosystem: a study of nutrient spiralling. *Ecology* 64, 1249–1265. doi: 10.2307/1937833

Pagano, T., and Garen, D. (2005). A recent increase in western U.S. streamflow variability and persistence. *J. Hydrometeor*. 6, 173–179. doi: 10.1175/JHM410.1

Paul, M. J., and Meyer, J. L. (2001). Streams in the urban landscape. *Annu. Rev. Ecol. Syst*. 32, 333–365. doi: 10.1146/annurev.ecolsys.32.081501.114040

Poff, N. L., Olden, J. D., Merritt, D. M., and Pepin, D. M. (2007). Homogenization of regional river dynamics by dams and global biodiversity implications. *Proc. Natl. Acad. Sci. U.S.A*. 104, 5732–5737. doi: 10.1073/pnas.0609812104

Poff, N. L., and Ward, J. V. (1989). Implications of streamflow variability and predictability for lotic community structure: a regional analysis of streamflow patterns. *Can. J. Fish. Aquat. Sci.* 46, 1805–1818. doi: 10.1139/f89-228 (accessed December 20, 2019).

R Core Team (2019). *R Base Package, Version 3.6.2.* The R Foundation for Statistical Computing. Available online at: https://cran.r-project.org/ (accessed December 20, 2019).

Rantz, S. E. (1982). *Measurement and Computation of Streamflow*. Technical Report, U.S. Geological Survey Water Supply Paper 2175, Washington, DC. doi: 10.3133/wsp2175

Raymond, P. A., Saiers, J. E., and Sobczak, W. V. (2016). Hydrological and biogeochemical controls on watershed dissolved organic matter transport: pulse-shunt concept. *Ecology* 97, 5–16. doi: 10.1890/14-1684.1

Schaefli, B., Rinaldo, A., and Botter, G. (2013). Analytic probability distributions for snow-dominated streamflow. *Water Resour. Res*. 49, 2701–2713. doi: 10.1002/wrcr.20234

Schmadel, N. M., Ward, A. S., Lowry, C. S., and Malzone, J. M. (2016). Hyporheic exchange controlled by dynamic hydrologic boundary conditions. *Geophys. Res. Lett*. 43, 4408–4417. doi: 10.1002/2016GL068286

Seitzinger, S. P., Styles, R. V., Boyer, E. W., Alexander, R. B., Billen, G., Howarth, R. W., et al. (2002). Nitrogen retention in rivers: model development and application to watersheds in the northeastern U.S.A. *Biogeochem*. 57, 199–237. doi: 10.1023/A:1015745629794

Smith, B. K., Smith, J. A., Baeck, M. L., Villarini, G., and Wright, D. B. (2013). Spectrum of storm event hydrologic response in urban watersheds. *Water Resour. Res*. 49, 2649–2663. doi: 10.1002/wrcr.20223

Stream Solute Workshop (1990). Concepts and methods for assessing solute dynamics in stream ecosystems. *J. North Am. Benthol. Soc.* 9, 95–119. doi: 10.2307/1467445

Thomas, D. M., and Benson, M. A. (1970). *Generalization of Streamflow Characteristics From Drainage-Basin Characteristics*. Technical Report, U.S. Geological Survey Water Supply Paper 1975, Washington, DC. doi: 10.3133/wsp1975

US Army Corps of Engineers (2010). *2009 National Inventory of Dams*. Available online at: http://nid.usace.army.mil/ (accessed May 30, 2020).

USGS (2019). *National Water Information System*. U.S. Geological Survey, Reston, VA. doi: 10.5066/F7P55KJN

Wallace, J. B., Webster, J. R., and Woodall, W. B. Jr. (1977). The role of filter feeders in stream ecosystems. *Arch. Hydrobiol.* 79, 506–532.

Wollheim, W. M., Vorosmarty, C. J., Peterson, B. J., Seitzinger, S. P., and Hopkinson, C. S. (2006). Relationship between river size and nutrient removal. *Geophys. Res. Lett*. 33:L06410. doi: 10.1029/2006GL025845

Wolman, M. G., and Miller, J. P. (1960). Magnitude and frequency of forces in geomorphic processes. *J. Geol.* 68, 54–74. doi: 10.1086/626637

Ye, S., Covino, T. P., Sivapalan, M., Basu, N. B., Li, H.-Y., and Wang, S.-W. (2012). Dissolved nutrient retention dynamics in river networks: a modeling investigation of transient flows and scale effects. *Water Resour. Res*. 48:W00J17. doi: 10.1029/2011WR010508

Conflict of Interest: The authors declare that the research was conducted in the absence of any commercial or financial relationships that could be construed as a potential conflict of interest.

Any use of trade, firm, or product names is for descriptive purposes only and does not imply endorsement by the U.S. Government.

frontiers in Water

ORIGINAL RESEARCH
published: 28 October 2020
doi: 10.3389/frwa.2020.578261

Storm-Induced Dynamics of Particulate Organic Carbon in Clear Creek, Iowa: An Intensively Managed Landscape Critical Zone Observatory Story

Jieun Kim[1], *Neal E. Blair*[1,2*], *Adam S. Ward*[3] *and Katie Goff*[4]

[1] *Department of Civil and Environmental Engineering, Northwestern University, Evanston, IL, United States,* [2] *Department of Earth and Planetary Sciences, Northwestern University, Evanston, IL, United States,* [3] *O'Neill School of Public and Environmental Affairs, Indiana University, Bloomington, IN, United States,* [4] *Department of Earth and Environmental Sciences, University of Iowa, Iowa City, IA, United States*

OPEN ACCESS

Edited by:
Tim Scheibe, Pacific Northwest National Laboratory (DOE), United States

Reviewed by:
Matthew Allen Ginder-Vogel, University of Wisconsin-Madison, United States
Hongyan Bao, Xiamen University, China

***Correspondence:**
Neal E. Blair
n-blair@northwestern.edu

Specialty section:
This article was submitted to Water and Critical Zone, a section of the journal Frontiers in Water

Received: *30 June 2020*
Accepted: *09 September 2020*
Published: *28 October 2020*

Citation:
Kim J, Blair NE, Ward AS and Goff K (2020) Storm-Induced Dynamics of Particulate Organic Carbon in Clear Creek, Iowa: An Intensively Managed Landscape Critical Zone Observatory Story. Front. Water 2:578261. doi: 10.3389/frwa.2020.578261

Rivers integrate and transport particulate organic carbon (POC) from multiple sources with varied diagenetic histories. A significant amount of POC is delivered to rivers during storm events, but the sources and fates of the mobilized material are often unclear. To gauge the variability of input sources, this study uses a biomarker approach that broadly characterizes organic matter at the molecular level. Suspended sediment was collected during a storm in October 2015 at three nested sampling locations along Clear Creek in Iowa, U.S.A. Supplemented with bulk elemental and C-isotopic measurements, biomarker analyses were obtained to identify changes in sources and the diagenetic state of the POC. Fatty acid-rich organic matter was attributed to the mobilization of algal mats in the stream channel at the early stage of the storm as precipitation initiated and water velocities began to increase. A significant contribution of lignin-rich material occurred at peak precipitation and elevated discharge signifying soil sources. Tracers for partially oxidized lignin and soil organic matter suggested that this was a partially time-resolved mixture of fresh and degraded material. Storm-induced variations of biomarkers were observed at the three sampling stations located throughout the watershed. The mixing patterns became more complex as the storm pulse moved downstream due to the additive contributions of multiple tributaries and the hypothesized increasing importance of alluvial bank erosion. This erosional increase is attributed to a systematic transition in basin geomorphology from a V-shape in the upper reach to a wider box-shaped valley in the lower reach. Even though biomarker concentration measurements revealed a diversity of sources over time, the complex mixture of POC associated with peak discharge dominated the flux of material downstream. This study highlights the complexity of storm-initiated C-transport and the need for high spaciotemporal resolution broad spectrum tracer studies in the future.

Keywords: organic carbon, streams, erosion, storms, biomarkers

INTRODUCTION

Streams and rivers integrate, transport, and transform organic carbon (OC) derived from multiple sources. Longitudinal transport flushes OC downstream while lateral transport exchanges OC with adjacent riparian zones (Wohl et al., 2015). In-channel spiraling of C facilitated by primary and secondary production contribute to the OC pool (Newbold et al., 1982; Griffiths et al., 2012). As a result, the OC in streams and rivers is complex in biogeochemical composition and diagenetic history. Understanding the spatiotemporal dynamics of the OC mixture is critical to identifying the role of streams and rivers in ecosystem processes and the C-cycle in general.

Storm events have a disproportionate impact on carbon mobilization and significantly influence the sources and fluxes of OC that are transported fluvially. Storm flows export >80% of particulate organic carbon (POC) and >70% of dissolved organic carbon (DOC) over time periods that constitute only 10–20% of the total year (Oeurng et al., 2011; Dhillon and Inamdar, 2014). Both dissolved and particulate forms of OC make comparable contributions to the total aquatic C pool (Meybeck, 1982; Cole et al., 2007) though their behaviors differ because of being either in suspension or dissolved (Alvarez-Cobelas et al., 2012; Jeong et al., 2012). Within storm events, the OC composition is expected to change due to the selective mobilization and transport of individual sources including terrestrial plant litter, in-channel production (algal biomass and invertebrates), and eroded soil organic matter (Blair and Leithold, 2013; Raymond et al., 2016). However, evidence for such changes is sparse, particularly for POC because of the challenge of performing detailed organic geochemical analyses with sufficient temporal resolution.

Investigations of storm event POC have typically suffered from two limitations. First, most studies have relied on carbon isotopes and elemental (C/N) ratios to resolve source inputs (Blair and Leithold, 2013; Blair et al., 2018). While valuable, interpretation of these measurements is limited due to non-unique signatures, which prevent specific source identification. In this study, a broad spectrum, compound-specific approach was used to complement stable isotope and elemental ratio information. The broad-spectrum biomarker scope enables observation of a wide range of compounds that can be source-specific, while at the same time providing a perspective that approaches that of the bulk sample because of the compound diversity (Le Meur et al., 2017).

Next, studies conducted at single stations within a river network do not reveal the systematic variation expected as POC moves from headwaters to downstream reaches (Blair et al., 2004; Aufdenkampe et al., 2007). The evolution of POC as it is transported downstream as a result of accumulated inputs, exchange with the riparian corridor and in-channel cycling is well-appreciated in large river systems and is thought to be highly dependent on watershed size (Aufdenkampe et al., 2007; Blair and Leithold, 2013; Leithold et al., 2016). The scale or nature of change in small tributaries is undocumented, however.

The transport of OC from agricultural landscapes, a global scale issue (Doetterl et al., 2016), is the specific focus of this study. Our objectives in this study were to, (1) identify temporal and spatial variations of POC sources by investigating the POC compositional changes, and (2) assess the quantity and composition of POC exported downstream within the watershed. To address these objectives, we collected samples at three stations within the small agricultural stream network of Clear Creek, Iowa with a multi-hour resolution sampling through a storm event. Such fine-resolution data has rarely been reported in previous studies, despite its importance to capture the rapid changes of POC export flux and composition during storm events. Moderate to high-frequency data improves POC flux estimates by allowing them to be parsed in terms of source and/or composition. The Clear Creek Watershed was part of NSF-supported Intensively Managed Landscape Critical Zone Observatory (IML-CZO) where the focus was to develop predictive capabilities of Critical Zone responses to future environmental change and land use.

MATERIALS AND METHODS

Study Site and Sample Collection

Clear Creek is a tributary of the Iowa River that drains a 270 km^2 watershed in east-central Iowa, USA (**Figure 1A**). It is an extensively studied field site that is part of the National Science Foundation's Intensively Managed Landscapes Critical Zone Observatory (IML-CZO) (Kumar et al., 2018; Wilson et al., 2018). Clear Creek dissects a pre-Illinoian glacial landscape (∼0.5–2.4 Ma), the Southern Iowa Drift Plain, that is mantled by loess and till (Prior, 1991). Till and paleosols are covered by a ∼15 m thick loess blanket that is moderate to highly erodible (Bettis et al., 2003). The rolling landscape is hydrologically well-integrated by numerous small streams, such as Clear Creek (Ruhe, 1969).

The warming climate following the last glaciation led to a succession of vegetation that culminated with a mosaic of prairie grasslands, wetlands and forested riparian corridors (Wilson et al., 2018). At the time of Euro-American settlement (∼1840), grasslands dominated whereas forests represented ∼10 % of the land cover. Deciduous angiosperms, primarily oaks (*Quercus sp.)*, were the forest species (Rayburn and Schulte, 2009a). Agricultural land use induced a further change in cover that is currently characterized by ∼56% row crop agriculture, 18% pasture, 10% woodland and 7% urban/suburban (**Table 1**, Rayburn and Schulte, 2009b). Forest species have shifted to the angiosperms *Acer saccharinum* L. (silver maple), *Salix nigra* Marsh (black willow), *Ulmus americana* L. (American elm), and *A. negundo* L. (box elder) (Rayburn and Schulte, 2009a). Row crops, while distributed through the watershed, are more concentrated in the headwater regions. Urban zones are localized in the lower reach (**Table 1**).

The soils in the region are legacies of the pre-settlement climate-ecosystem pairings. Prairie-derived Mollisols have thick, dark-colored and organic-rich top soils. Forest-derived Alfisols have thin, clay-leached, acidic top soils (Wilson et al., 2018). The advent of Euro-American agriculture on a loess-derived surface resulted in rapid loss of top soils and soil organic carbon (Papanicolaou et al., 2015; Yan et al., 2019). Periodic intense

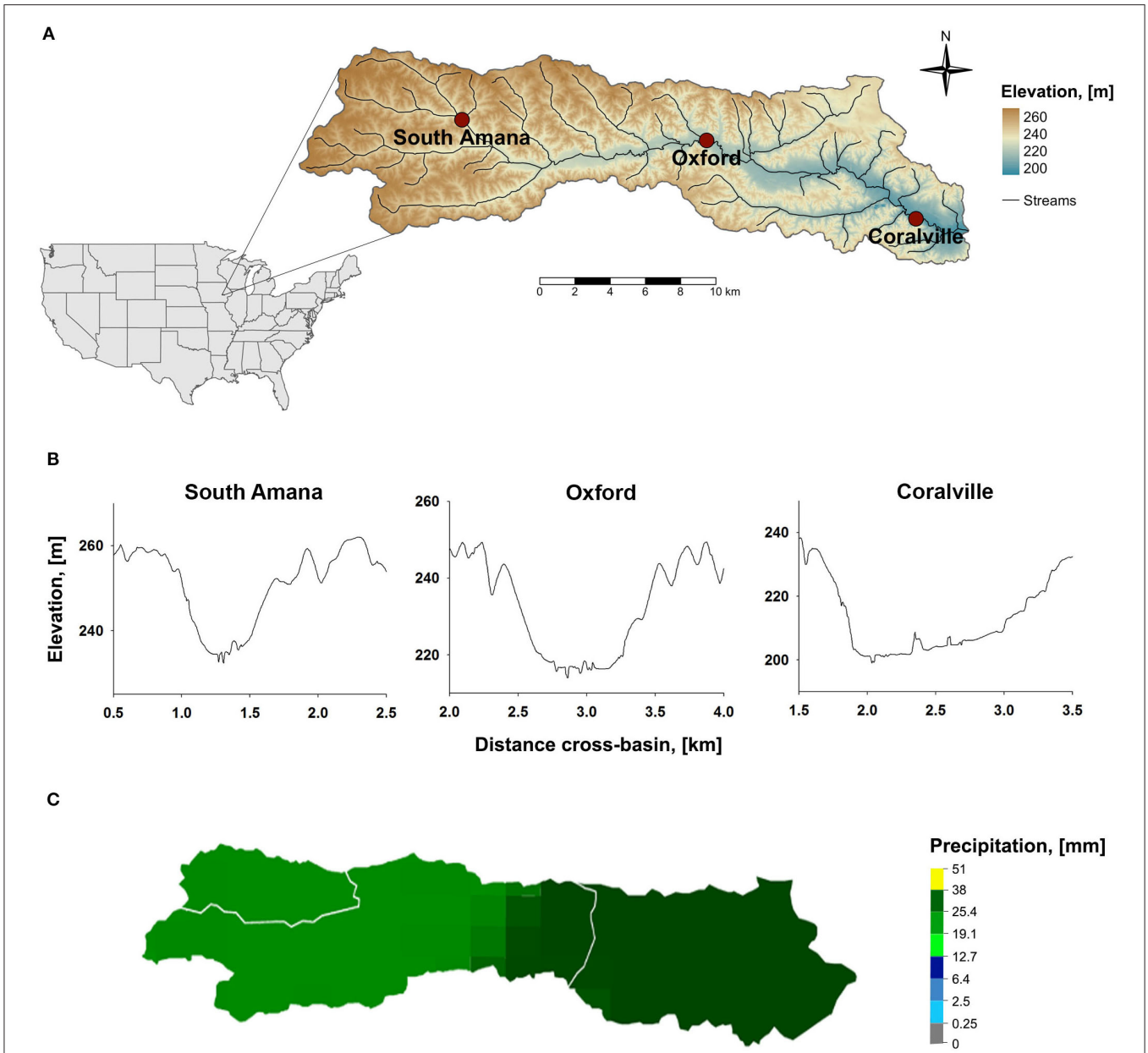

FIGURE 1 | (A) Map of Clear Creek watershed and locations of sampling stations; **(B)** Valley cross-sections at the sampling stations. Cross-section elevations were obtained from DEMs of the watershed using ArcGIS Pro.; **(C)** Precipitation estimates in Clear Creek for Oct 27 local time when ∼90% of the rain fell. Data were retrieved from The National Weather Service Advanced Hydrologic Prediction Service.

precipitation, about 75% of the annual precipitation (∼900 mm) occurs between April-June, contributes to high erosion rates (Wilson et al., 2012, 2018). Erosion has been attenuated by the adoption of soil conservation practices in the 1990's (Abaci and Papanicolaou, 2009; Papanicolaou et al., 2015). These include rotations of corn (*Zea mays* L.)—soybean (*Glycine max* L.) crops and no-till, spring shallow-till, fall deep-till practices. Contour tilling is commonly but not exclusively used. Grassed and forested riparian buffers between row crop fields and the stream channel are common but highly variable in width, ranging from almost non-existent to 10's of meters. Rills either terminate in the buffers or extend to the channel. In short, soil conservation practices are extensively, but not universally, practiced. The higher grass and forest cover of floodplains reflects the presence of the riparian buffers (**Table 1**).

Planting typically occurs in early May, weather permitting, thus rain during May-June creates the highest erosion rates due to the nearly bare ground and small plants (Wilson et al., 2012). Harvest occurs early October and fall tillage is performed in November. The storm event sampled in this study falls in the

TABLE 1 | Subbasin characteristics.

Sampling station	Sub-basin area [km^2]	Elevation [m]	Precipitation* [mm]	Vegetated land cover [%]**		
				Row crop	Grass	Forest
S. Amana	26.2	231–278	24	84 (78)	7 (17)	1 (0)
Oxford	157.5	213–278	25	67 (54)	20 (30)	3 (8)
Coralville	254.3	164–278	30	57 (44)	21 (26)	7 (11)

precipitation measured on 27–28 October, 2015.

***land cover in 2015 data derived from https://nassgeodata.gmu.edu/CropScape/. Values in parentheses are landcover percentages for the corresponding floodplains. Urban areas are not listed but are approximated by the difference between the vegetation totals and 100%.*

window when the surface was heavily littered with post-harvest crop debris before being tilled to the subsurface.

Tile drains are a substantial part of the agricultural landscape in the Clear Creek watershed. The tile drain contribution of water to nearby Iowa streams is substantial, with estimates ranging from 15% to over 50% (Schilling et al., 2012; Amado et al., 2017). Tile drain water inputs appear to be especially important at baseflow (Schilling and Helmers, 2008), however particulate fluxes are not a major source of POC to the channel (Blair et al., submitted).

Samples were collected at three sampling stations in the watershed (**Figure 1A**), near South Amana (upper subbasin), Oxford (middle subbasin), and Coralville (lower subbasin). The three locations provide a telescoping perspective in terms of the watershed area and topography integrated by Clear Creek. South Amana captures a predominantly headwater signature. The valley cross-section at that point is V-shaped (**Figure 1B**). Oxford represents an approximate mid-point and Coralville integrates almost the entire watershed (Davis et al., 2014). The valley cross-sections for these reaches are more U- or box-shaped (Yan et al., 2018). The field location at South Amana was maintained by the University of Iowa prior to becoming an IML-CZO site (Wilson et al., 2018). Discharge at South Amana was determined using a previously determined stage-discharge relationship (Abaci and Papanicolaou, 2009). The sampling stations in Oxford and Coralville were co-located with the USGS gaging stations (Station # 05454200 in Oxford and 05454300 in Coralville).

The stream water was collected at 3-hr intervals using ISCO autosamplers with 1-liter bottles throughout the storm event that occurred in late October 2015. The sampling interval was chosen to allow definition of the storm peak at three locations simultaneously while maintaining a feasible analytical workflow. Sampling was begun at the beginning of precipitation and ended as the hydrograph approached baseflow. The samples were transferred to the lab and kept frozen until analyzed.

Sediment, Bulk C, N Concentration, and Stable Isotope Analyses

Thawed samples were filtered on pre-combusted (at 500°C) and pre-weighed 47 mm o.d. glass fiber filters (0.7-micron nominal pore size, Millipore). The filter samples were lyophilized and weighed to determine sediment concentrations.

Samples for POC analyses were acidified with gaseous HCl for 1–4 days to eliminate the inorganic carbon (Harris et al., 2001), and the absence of carbonate in the samples were verified by monitoring a peak at 2513 cm^{-1} using a Bruker Tensor 37 FTIR (Vaculikova and Plevova, 2005). The sediment samples were analyzed for OC and total N contents along with $\delta^{13}C$ and $\delta^{15}N$ values using a Costech Elemental Analyzer-Conflo IV interface-Thermo Delta V plus isotope ratio mass spectrometer (IRMS). Isotope ratios are referenced to VPDB for C and air-N_2 for N (Coplen, 1995; Skrzypek, 2013) via the use of a calibrated acetanilide standard (Schimmelmann et al., 2009). The instrument precision was ∼0.2‰.

Broad Spectrum Biomarker Analyses

Thermochemolysis with tetramethyl ammonium hydroxide (Clifford et al., 1995; McKinney et al., 1995; Frazier et al., 2003) was employed to obtain a multi-biochemical class perspective of POC molecular composition on sediment samples from the filters. Approximately 50–100 mg of sediment was placed in a screw-top glass culture tube with 1 μg of methyl-D3-pentadecanoic acid (CAS 352431-40-4, Cambridge Isotope Laboratories, Inc.) and 150 μL of TMAH (25% in methanol, CAS 75-59-2, Sigma-Aldrich). Methyl-D3-pentadecanoic acid was added to monitor the reaction yield and the recovery of sample preparation. The amount of sample was varied to target a quantity of ∼0.5 mg of organic carbon. The methanol was removed via a vacuum concentrator. The tubes were sealed under N_2 with the Teflon-lined caps. The sample tubes were heated at 200°C for 3 h on a heating module (Reacti-Therm™ heating module, Thermo Scientific). After the reaction, the products were extracted with 3 mL of hexane and transferred in a 4 mL glass vial. Hexane was evaporated by purging with nitrogen gas. The residue was taken up with 100 μL of hexane. All glassware was pre-baked at 500°C for 8 h to remove any trace organic matter.

The prepared samples were analyzed using a Thermo Scientific Trace GC Ultra coupled with a DSQ II MS equipped with a Triplus auto-sampler and a TR-5MS column (L 30 m, I.D. 0.25 mm, film thickness 0.25 μm). Eluting peaks were identified by comparing their mass spectra with the NIST library and an in-house library. In order to resolve coeluting peaks and enhance the signal to noise, peak areas of compounds were measured after filtering the selective m/z for each compound. For compound quantification, authentic standards were analyzed using TMAH thermochemolysis under the identical experimental setup. Methyl-D3-pentadecanoic acid was used as the internal standard to calculate the Relative

TABLE 2 | Biomarkers quantified in this study.

Biomarker	Components	Main source	References
C12-34 FAs	Even numbered C12-34 saturated fatty acids	Short-chain saturated fatty acids (< C14) are high in microalgae, whereas long-chain saturated fatty acids (> C24) are only synthesized by vascular plants	Wakeham and Beier, 1991; Harvey, 1994; Canuel and Hardison, 2016
Anteiso-C15 FA	Anteiso-pentadecanoic acid	Bacteria	Cho and Salton, 1966; Cooper and Blumer, 1968; Derrien et al., 2017
USFAs	Unsaturated fatty acids including C16:1, C18:1, and C18:2 fatty acids	Mid-chain polyunsaturated fatty acids (C16-22) are high in microalgae	Kumari et al., 2013
Cutin acids	9,16-dihydroxyhexadecanoic acid, 10,16-dihydroxyhexadecanoic acid, and 9,10,16-trihydroxyoctadecanoic acid	Vascular plants (cutin, a major component of aerial surfaces of vascular plants called cuticle)	Del Rio and Hatcher, 1998; Filley et al., 2008
Phytosterols	Stigmasterol and β-sitosterol	Vascular plants	Li et al., 1995; Saliot et al., 2001
Bds	meta-hydroxybenzoic acid and 3,5-dihydroxybenzoic acid	Proteins and tannins (commonly associated with soil organic matter)	Otto and Simpson, 2006; Hatten et al., 2012
ΣLignin	Lignin phenols (Vanillyl phenols—vanillin, acetovanillone, and vanillic acid; Syringyl phenols—syringealdehyde, acetosyringone, and syringic acid; Cinnamyl phenols—cinnamic acid, p-coumaric acid, and ferulic acid)	Vascular plants	Clifford et al., 1995; Hatcher et al., 1995

Response Factors (RRF) for each compound. For compounds without authentic standards, the RRFs of nearby compounds in retention time and with similar compound structures were used for quantification. The calculated mass was then normalized to the quantity of organic carbon (in mg) in the sample. Quantified biomarkers and their main sources are listed in **Table 2**.

Analyses using the TMAH thermochemolysis method were performed on reference materials that represent major plant groups and provide a broad range of lignin phenol results. Plant samples include gymnosperms (Red Spruce, Eastern White Pine, Red Cedar), woody angiosperms (Oregon White Oak wood), and non-woody angiosperms (Oregon White Oak leaf, Red Alder, Smooth Cordgrass, Saltmarsh Hay, and Eel grass).

Precipitation Estimates

Hourly precipitation totals for the study period were obtained from the Iowa State University Environmental Mesonet (https://mesonet.agron.iastate.edu/request/download.phtml?network=IA_ASOS). The Iowa City (IOW) station was used. Data for the daily estimates in each of the Clear Creek subbasins were retrieved from The National Weather Service Advanced Hydrologic Prediction Service (https://water.weather.gov/precip/) (**Figure 1C**). The precipitation data were derived from radar and rain gauge estimates. The precipitation map products for each day were imported into ArcPro GIS software where the subbasin coverage was clipped and quantified.

Statistics

Correlation analysis was conducted between discharge (Q), hourly precipitation (P), and POC concentration to evaluate the strength of the C-Q or C-P relationships. The data matrix was computed using the "cor" function in R software for Pearson correlation analysis. The statistical significance of the correlation analysis was assessed with a 95% confidence interval.

RESULTS

Characteristics of the Storm

Samples analyzed in this study were collected between October 27–30, 2015 (ordinal days 300–303). Precipitation occurred primarily during October 27–28 (**Figure 2**). Weather radar estimates indicate that the storm passed over the entire watershed (**Figure 1C**, **Table 1**). Discharge measured in South Amana during the event peaked at ∼1,000 L/s. Clear Creek discharge measured at the USGS gaging stations in Oxford, IA (USGS gage no. 05454220) and Coralville, IA (USGS gage no. 05454300) during the event peaked at ∼6,000 L/s and ∼7,000 L/s, respectively. The peak discharge was ∼2.5 times greater than the mean discharge during the year (Oxford: 2,300 L/s and Coralville: 3,200 L/s, data available from March 8 to the end of the year), but smaller than the bankfull discharge estimated for Coralville (∼56,000 L/s) (Eash, 1993). This was a small discharge event with an approximate month return frequency. It followed another event 7 days prior of comparable duration and intensity. That storm followed a 2-month-long low-discharge period where discharge rarely exceeded half of the mean discharge of the year.

Bulk Composition of POC

Suspended sediment concentrations increased and then decreased in response to the passing storm event and change in discharge (**Figure 2**, **Table 3**). In response to changes in sediment load, POC concentrations (calculated as sediment concentration × %OC/100) ranged from 1.09 to 14.93 mg C/L. Percent POC and total N (%OC, %N) concentrations (both on a dry sediment weight basis) varied over the course of the storm with a range of

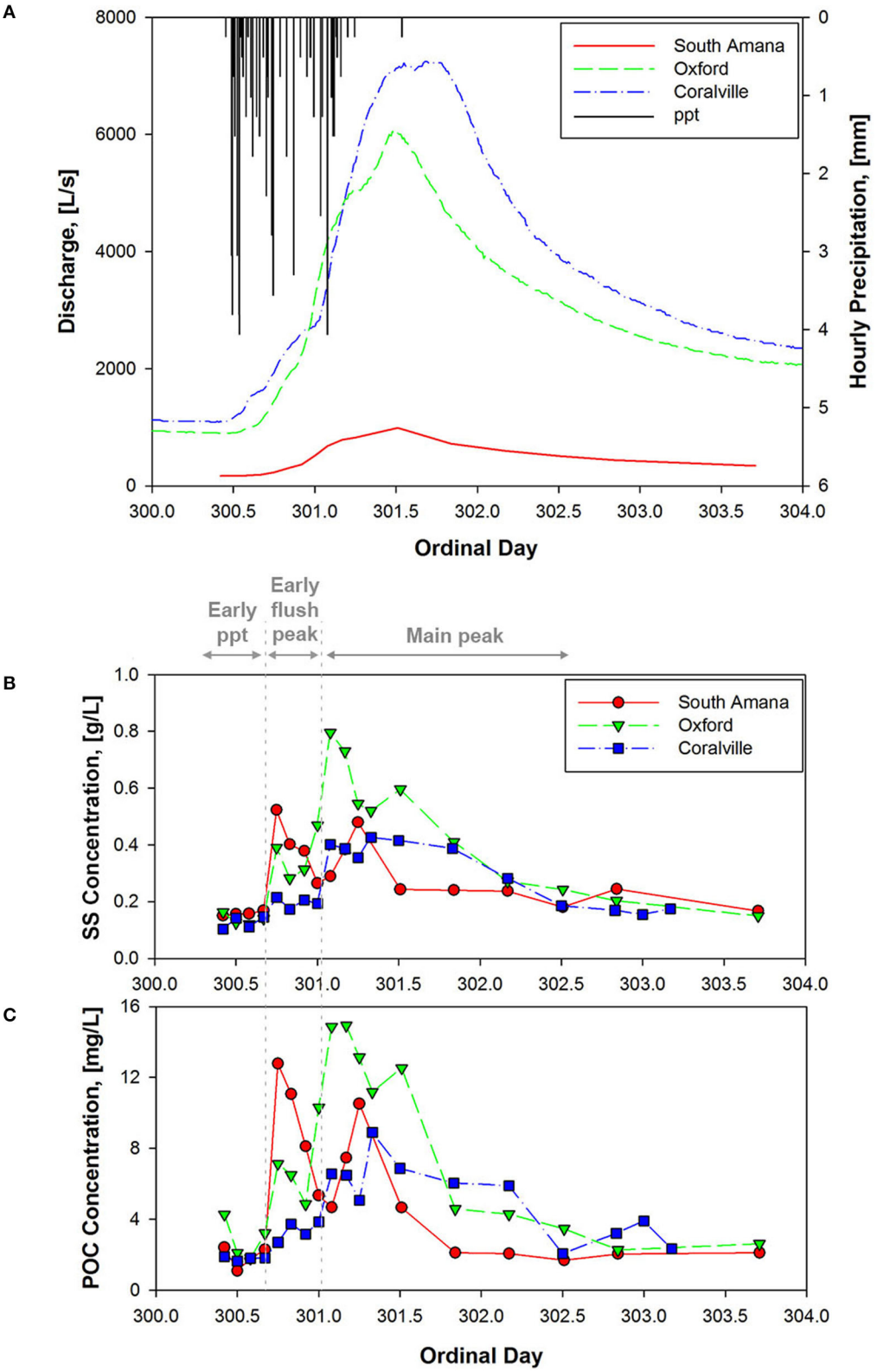

FIGURE 2 | (A) Hourly precipitation measured at near Iowa City and discharge at three sampling stations during 27–30 October 2015 storm; Temporal variation in the concentrations of **(B)** suspended sediment and **(C)** POC at three sampling stations. The early ppt phase refers to the period during the precipitation event before discharge rises rapidly. The early flush peak occurs on the rising limb of the hydrograph. The main peak correlates closely with discharge.

TABLE 3 | Storm characteristics, concentrations of sediment and POC, and bulk properties.

Ordinal day	Discharge [L/s]	Suspended sediments [g/L]	POC [mg/L]	%OC [wt%]	%N [wt%]	C:N [wt:wt]	$\delta^{13}C$ [‰]
South Amana							
300.42	169	0.15	2.41	1.61	0.14	11.67	−27.94
300.50	170	0.16	1.09	0.70	0.07	10.70	−36.94
300.58	177	0.16	1.79	1.14	0.11	10.81	−26.59
300.67	188	0.17	2.29	1.36	0.13	10.31	−24.04
300.75	232	0.52	12.77	2.44	0.24	10.03	−19.76
300.83	298	0.40	11.06	2.75	0.26	10.60	−20.41
300.92	364	0.38	8.12	2.15	0.20	10.86	−21.74
301.00	515	0.26	5.35	2.02	0.19	10.47	−21.79
301.08	683	0.29	4.67	1.61	0.15	10.42	−22.44
301.17	782	0.38	7.46	1.94	0.18	11.02	−21.28
301.25	824	0.48	10.51	2.19	0.22	9.86	−24.24
301.51	988	0.24	4.66	1.92	0.15	12.80	−22.55
301.84	721	0.24	2.12	0.88	0.08	11.00	−22.86
302.17	594	0.24	2.07	0.87	0.09	9.30	−23.16
302.51	510	0.18	1.70	0.94	0.09	10.44	−24.70
302.84	439	0.24	2.05	0.84	0.07	12.00	−22.02
303.71	342	0.17	2.12	1.27	0.13	10.05	−27.34
Oxford							
300.42	895	0.16	4.28	2.62	0.23	11.25	−28.67
300.50	909	0.13	2.11	1.69	0.13	12.82	−26.67
300.58	980	0.12	1.80	1.49	0.15	9.72	−25.88
300.67	1,110	0.14	3.23	2.30	0.21	11.15	MD*
300.75	1,447	0.39	7.13	1.83	0.18	10.28	−24.00
300.83	1,852	0.28	6.50	2.30	0.22	10.52	−24.05
300.92	2,251	0.31	4.86	1.55	0.15	10.24	−24.12
301.00	3,172	0.47	10.31	2.20	0.21	10.60	−17.63
301.08	4,191	0.80	14.86	1.87	0.19	9.79	−22.14
301.17	4,786	0.73	14.93	2.05	0.20	10.06	−20.99
301.25	5,041	0.54	13.13	2.41	0.23	10.30	−23.07
301.33	5,239	0.52	11.17	2.15	0.20	10.50	−21.83
301.51	6,032	0.60	12.52	2.10	0.21	9.81	−21.49
301.84	4,560	0.41	4.58	1.12	0.11	10.63	−22.42
302.17	3,653	0.27	4.29	1.58	0.15	10.26	−22.40
302.51	3,144	0.24	3.46	1.43	0.13	10.69	−24.74
302.84	2,713	0.20	2.27	1.12	0.11	10.00	−24.45
303.17	2,424	0.19	2.81	1.46	0.14	10.32	−24.15
303.71	2,121	0.15	2.62	1.76	0.19	9.03	−25.55
Coralville							
300.42	1,104	0.10	1.89	1.85	0.22	8.27	−29.26
300.50	1,164	0.14	1.64	1.16	0.12	9.89	−27.41
300.58	1,402	0.11	1.80	1.63	0.15	11.00	−27.45
300.67	1,631	0.15	1.83	1.25	0.13	9.94	−25.66
300.75	1,926	0.21	2.70	1.26	0.13	9.60	−25.76
300.83	2,325	0.17	3.73	2.16	0.19	11.44	−26.15
300.92	2,605	0.21	3.16	1.54	0.15	10.13	−26.65
301.00	2,722	0.19	3.86	2.00	0.19	10.78	−24.98
301.08	3,455	0.40	6.57	1.64	0.17	9.83	−25.09
301.17	4,673	0.39	6.49	1.68	0.17	10.05	−24.83
301.25	5,522	0.36	5.07	1.43	0.15	9.36	−24.51

(Continued)

TABLE 3 | Continued

Ordinal day	Discharge [L/s]	Suspended sediments [g/L]	POC [mg/L]	%OC [wt%]	%N [wt%]	C:N [wt:wt]	δ^{13}C [‰]
301.33	6,372	0.43	8.90	2.09	0.20	10.56	−24.14
301.50	7,137	0.42	6.87	1.65	0.18	9.37	−23.41
301.83	6,995	0.39	6.05	1.56	0.16	9.62	−22.48
302.17	5,041	0.28	5.90	2.09	0.23	9.19	−22.20
302.50	3,936	0.19	2.07	1.12	0.13	8.73	−23.81
302.83	3,342	0.17	3.22	1.90	0.19	10.00	−24.32
303.00	MD*	0.15	3.90	2.52	0.19	13.03	−25.81
303.17	2,917	0.17	2.35	1.35	0.13	10.08	−23.85

*missing data.

0.7–2.75 for %OC and 0.07 to 0.26 for %N (**Table 3**). A strong correlation ($r = 0.95$, $p < 0.05$) was observed between %OC and %N. We found %OC (or %N) and sediment concentrations were positively correlated at South Amana ($r = 0.91$ and 0.94 with %OC and %N, respectively), but not at the other stations. This conclusively demonstrates that changing OC mixtures moved downstream along the river network. C:N ratios varied in the range from 8.27 to 13.03 throughout the event. δ^{13}C values of POC ranged from −29.3 to −17.6‰, with one exceptionally negative value at South Amana (−36.9‰) that occurred during the early precipitation period (**Figure 3**). POC concentrations and δ^{13}C values are positively correlated ($r = 0.59$, $p < 0.05$), such that the source(s) contributing to the increase in POC was also relatively ^{13}C-enriched.

Broad Spectrum Biomarker Analyses

POC compositional changes were further investigated on the molecular level with TMAH-derived biomarker analyses (**Figure 4**, **Table 4**). The compounds identified included methylated derivatives of phenols derived from lignin (Clifford et al., 1995; Hatcher et al., 1995; McKinney et al., 1995), non-lignin hydroxy benzoic acids, alkyl (fatty) monocarboxylic acids, and sterols. The putative sources of these diagnostic compounds are listed in **Table 2**. The relative abundances of these compounds are dependent not only on their actual concentrations in samples but also the relative reactivities of the source materials toward the TMAH reagent, and the stabilities of the products. Thus, fatty acids often appear to be more abundant in samples than they are in the environment (e.g., relative to carbohydrates and proteins) because of the ease of formation and stability of the corresponding fatty acid methyl esters. Even so, changes in relative concentrations of detected compounds can be used as indicators of changes in sources (del Rio et al., 1998). Compound ratios within a biochemical class (e.g., lignin phenols, fatty acids) can also provide diagnostic information as to source (Bianchi et al., 2007).

The most abundant compounds from the TMAH thermochemolysis were lignin phenols, with totals ranging from 0.79 to 21.96 mg/100 mg OC. Insofar as lignin is the second or third most abundant biochemical on the planet and is an indicator of vascular plant OC (Hedges and Parker, 1976; Gordon and Goñi, 2003; Thevenot et al., 2010; Canuel and Hardison, 2016), this is not surprising in this setting. The phenols were followed in abundance by total saturated fatty acids (chain lengths 12–34 C's, or C12-C34) and unsaturated fatty acids (C16-C18), which ranged in concentration from 0.59 to 8.87 mg/100 mg OC and from 0.12 to 0.53 mg/100 mg OC, respectively. Among the saturated fatty acids, n-C16 and n-C18 fatty acids were the most dominant compounds reflecting their natural ubiquity in most organisms (Kvenvolden, 1967; Matsuda and Koyama, 1977; Behrens and Kyle, 1996). The yields of the other products while much less, exhibited varied responses to time (**Figure 4B**). Relatively short-chained (C12-14) saturated fatty acids and unsaturated fatty acids were more abundant during the early ppt period, whereas vascular plant-related biomarkers such as long-chain fatty acids (C26-34), cutin acids, and phytosterols were more abundant as precipitation and discharge increased. The hydroxy benzoic acids (Bds), which are thought to be soil indicators, spiked in concentration prior to the main peak in POC concentration (**Figure 4C**). In South Amana and Coralville, the Bd compounds spike a second time during the primary POC peak. In contrast, anteiso-C15 fatty acid, a bacterial lipid, is insensitive to the variations in discharge and time.

DISCUSSION

Hydrologic Controls on POC Dynamics

Storm events are "hot moments" in time when disproportionately high concentrations of POC in streams are observed during elevated discharge (McClain et al., 2003; Hatten et al., 2012; Caverly et al., 2013; Dhillon and Inamdar, 2013). However, there are only a few studies with high temporal resolution sampling and none with multiple sampling stations to permit observations of the evolving storm pulse (Jung et al., 2012, 2015; Dhillon and Inamdar, 2014). In this study, the sampling was carried out with a short time interval (3 h) in three sampling stations throughout the watershed, allowing us to capture the rapid changes in POC concentrations with the hydrograph and observe the POC storm peak development downstream.

The POC concentrations varied as functions of precipitation, discharge and location (**Figure 2**), driven by what appears to

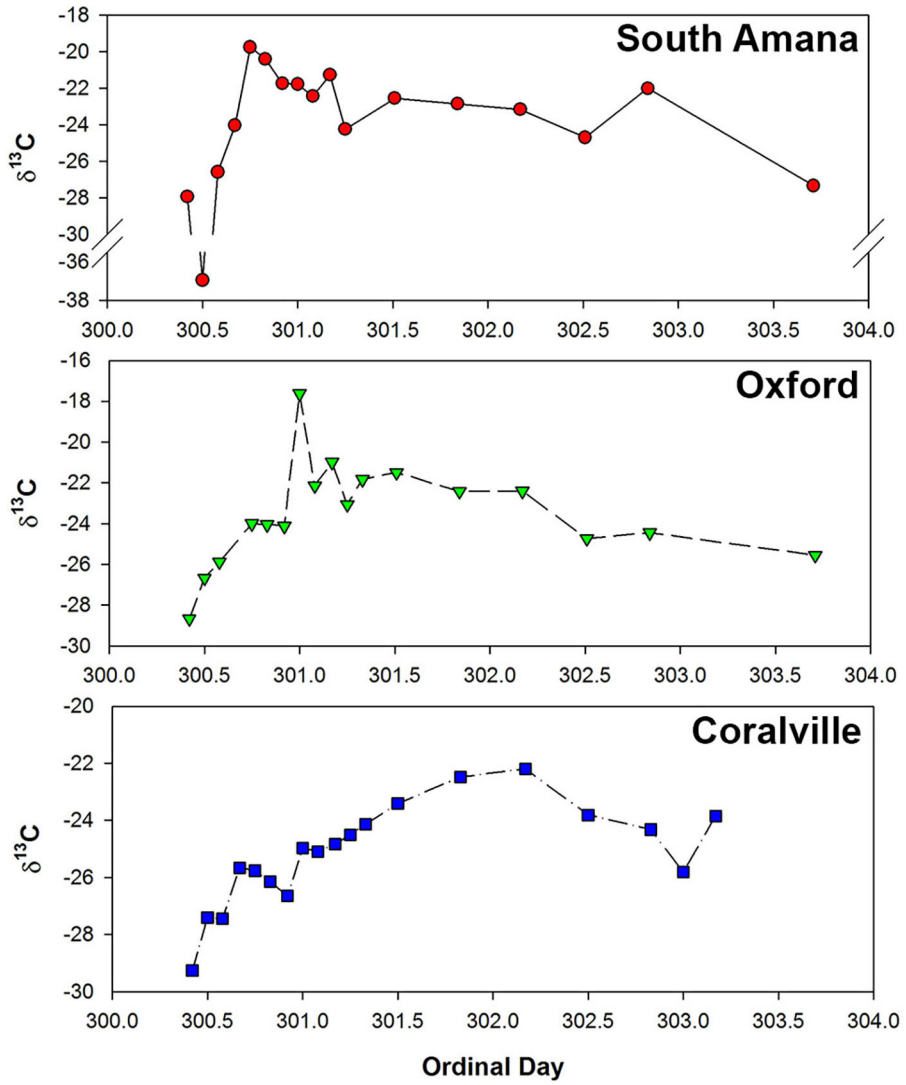

FIGURE 3 | Temporal variations in $\delta^{13}C$ of POC samples during the October, 2015 storm. From the upper panel on down, South Amana, Oxford, and Coralville.

be a sequence of processes. At the beginning of the storm—when the stream was still near baseflow—sediment and POC concentrations were low at all stations (**Figure 2**). Prominent early peaks in sediment and POC appeared at South Amana during the precipitation event. Similar but attenuated peaks were evident at the downstream locations. Peak discharge lagged precipitation as a result of hydrologic flow paths and the travel time of water to the channel (Howcroft and Willis, 1987; Haga et al., 2005). A later peak in sediment and POC correlated with the rise and fall of the discharge at all locations. The sequence marks the transition from a system that appears to be influenced initially by the precipitation itself, or is at least coeval with it, to one where discharge is the dominant control of POC transport.

Viewing the POC behavior as a function of discharge rather than time provides another perspective. Concentration-discharge (C-Q) relationships have been a useful tool to evaluate the overall processes and function of catchments (Williams, 1989; Picouet et al., 2001; Bieroza et al., 2018; Khanchoul et al., 2018), although less has been studied for particulate chemical species such as POC. The POC-Q relationship for the October 2015 storm displayed a clockwise hysteresis pattern for all three sampling stations (**Figure 5**). This is the most commonly observed C-Q relationship for sediment, where higher concentrations occur on the rising limb of the hydrograph and lower concentrations on the falling limb (Gellis, 2013; Cerro et al., 2014; Rose et al., 2018). This response has been attributed to inputs of easily mobilized sediment (or in this case POC) via the surface runoff from hillslopes and possibly resuspension of channel sediments (Wilson et al., 2012; Gellis, 2013). A similar observation for POC has been seen in agricultural watersheds (Oeurng et al., 2011; Caverly et al., 2013; Cerro et al., 2014), small forested watersheds (Dhillon and Inamdar, 2014; Johnson et al., 2018),

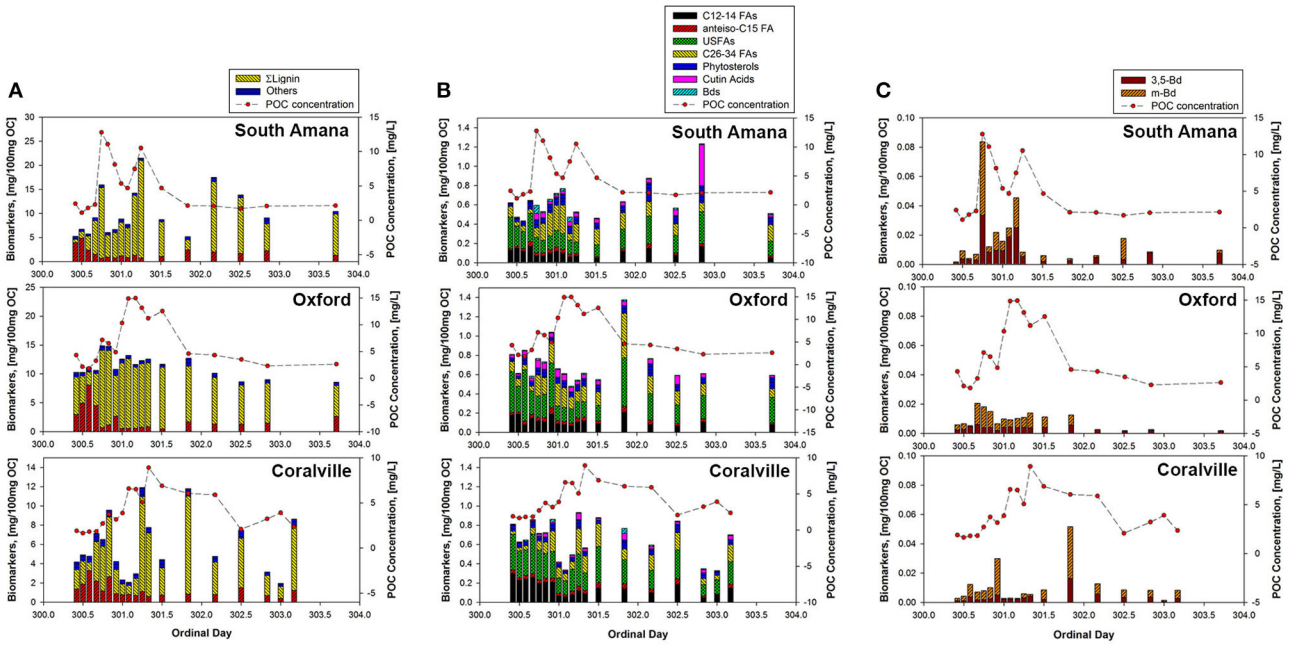

FIGURE 4 | Concentrations of biomarkers normalized to OC (mg/100 mg OC). **(A)** All biomarkers measured using TMAH thermochemolysis; **(B)** Biomarkers excluding C16-18 fatty acids and lignin phenols; **(C)** Concentrations of Bds. ΣLignin, Total lignin phenols; anteiso-C15 FA, anteiso-pentadecanoic acid; USFAs, unsaturated fatty acids (C16:1 FAs, C18:1 FAs, and C18:2 FA); Cutin acids, 9,16-dihydroxyhexadecanoic acid, 10,16-dihydroxyhexadecanoic acid, and 9,10,16-trihydroxyoctadecanoic acid; Bds, m-hydroxybenzoic acid and 3,5-dihydroxybenzoic acid; PSs, phytosterols (stigmasterol and β-sitosterol).

and steep-sloped forested watersheds (Hatten et al., 2012; Jung et al., 2012). As the rainfall ceased and the sediment sources were exhausted, the POC concentrations were reduced on the falling limb of the hydrograph. The increasing contribution of subsurface flow to the stream further diluted the POC concentrations on the falling limb.

Apart from the consistent clockwise direction of the hysteresis patterns, POC-Q relationships were station-dependent. While the POC concentrations for the two downstream stations strongly correlated with discharge ($r = 0.74$ for Oxford and 0.84 for Coralville, $p < 0.05$), a poor correlation existed ($p > 0.05$) for South Amana (**Table 5**). The slope of the rising limb of the POC-Q relationship also decreased in the downstream direction (**Figure 5**). The contrasting POC-Q relationships between South Amana and the two downstream stations are largely driven by the POC peaks that occurred in coincidence with the precipitation and the early rise in the hydrograph. These early flush peaks were most prominent at South Amana. Similar early flush peaks of sediment have been observed previously at South Amana and have been attributed to precipitation-driven erosion of surface soils based on ^{7}Be measurements (Wilson et al., 2012). The early flush peaks were responsible for 21–67% of the sediment load from the South Amana subbasin, the range being dependent on the availability of easily eroded soil (Wilson et al., 2012).

The differences in the responses at the three stations correlate with the local geomorphology and land use patterns within the basin. Storm trajectory is not thought to be a major factor in this case based on the modest increase in precipitation in the downstream direction from South Amana. The POC response to precipitation in South Amana is likely more dependent on the V-shaped morphology of the stream valley in the headwaters. The sediment delivery ratio (i.e., the fraction of mobilized soil delivered to the channel) approaches 0.9 for small areas (∼3 ha) of the South Amana subbasin and are close to 0.2 for the entire subbasin based on soil erosion model extrapolations (Abaci and Papanicolaou, 2009). Soil erodibility and delivery is enhanced further by agricultural activity (Abaci and Papanicolaou, 2009; Rose et al., 2018). During our study, the row crop fields were bare of vegetation after the autumn harvest with a substantial amount of organic matter in the form of crop residue left in the fields. In these conditions, surface soils are susceptible to erosion and runoff during a precipitation event (Abaci and Papanicolaou, 2009; Hou et al., 2018; Xu et al., 2019).

As the watershed widens to a U- or box-shape downstream of South Amana, the fraction of eroded surface soils intercepted by the lower gradient portion of the landscape before reaching the channel increases (Ferro and Minacapilli, 1995; Abaci and Papanicolaou, 2009). Sediment delivery ratios extrapolated from soil erosion model results based on basin area are ∼0.1, approximately half of what is estimated for South Amana (Abaci and Papanicolaou, 2009). The attenuation of local surface soil inputs is evident by the much smaller early flush peaks at Oxford and Coralville (**Figure 2C**, **Table 6**). Row crop cultivation also decreases from the upper to lower reach. Collectively

TABLE 4 | OC-normalized concentrations of TMAH products.

Ordinal day	Q [L/s]	TMAH products [mg/100 mg OC]											
		∑ LPs	C12-14 FAs	C16-18 FAs	C26-34 FAs	ai-C15 FA	USFAs	Cutin acids	Bds	PSs	S/V	C/V	$[Ad/Al]_v$
South Amana													
300.42	169	0.79	0.13	3.97	0.11	0.019	0.324	0.047	0.002	0.033	0.48	0.89	0.76
300.50	170	1.51	0.15	4.83	0.04	0.021	0.209	0.088	0.009	0.037	0.42	1.24	0.88
300.58	177	3.20	0.12	2.39	0.06	0.025	0.179	0.141	0.004	0.043	3.03	2.46	0.39
300.67	188	7.52	0.17	1.52	0.04	0.051	0.291	0.127	0.007	0.077	4.83	3.24	0.46
300.75	232	16.60	0.07	0.72	0.10	0.033	0.160	0.076	0.084	0.085	1.78	2.37	0.61
300.83	298	4.87	0.07	0.96	0.17	0.030	0.133	0.096	0.012	0.062	0.93	1.66	1.35
300.92	364	5.78	0.10	0.77	0.24	0.035	0.144	0.056	0.022	0.092	0.97	1.51	0.94
301.00	515	7.36	0.12	1.19	0.26	0.043	0.171	0.064	0.016	0.087	1.38	1.55	0.99
301.08	683	6.76	0.10	0.85	0.29	0.036	0.166	0.093	0.025	0.115	0.73	1.35	1.01
301.17	782	14.17	0.06	1.30	0.07	0.029	0.145	0.063	0.046	0.080	1.97	2.62	0.54
301.25	824	21.96	0.07	0.77	0.18	0.026	0.120	0.093	0.008	0.075	4.39	5.55	0.25
301.51	988	7.77	0.05	1.05	0.16	0.014	0.122	0.099	0.006	0.063	2.54	2.71	0.17
301.84	721	3.14	0.12	2.44	0.17	0.022	0.205	0.087	0.004	0.075	1.43	0.80	0.64
302.17	594	15.67	0.15	2.01	0.15	0.044	0.289	0.081	0.006	0.194	4.46	2.98	0.46
302.51	510	12.55	0.08	1.70	0.12	0.022	0.181	0.098	0.018	0.086	3.76	5.48	0.43
302.84	439	6.63	0.17	2.28	0.09	0.029	0.329	0.441	0.008	0.176	1.14	1.95	0.29
303.71	342	9.08	0.05	1.31	0.17	0.020	0.154	0.066	0.010	0.079	2.26	1.92	0.39
Oxford													
300.42	895	6.49	0.18	2.96	0.10	0.025	0.425	0.646	0.006	0.039	3.24	2.41	0.30
300.50	909	4.66	0.19	4.98	0.08	0.021	0.267	0.547	0.007	0.030	4.59	3.15	0.47
300.58	980	2.20	0.08	8.09	0.05	0.039	0.530	0.195	0.005	0.079	1.50	1.11	0.29
300.67	1,110	5.51	0.15	4.52	0.05	0.034	0.245	0.131	0.021	0.052	2.54	2.19	0.44
300.75	1,447	13.42	0.12	0.69	0.22	0.042	0.216	0.151	0.018	0.075	2.70	2.79	0.24
300.83	1,852	12.88	0.11	1.18	0.17	0.041	0.245	0.132	0.015	0.087	2.85	2.90	0.23
300.92	2,251	7.06	0.19	2.67	0.23	0.065	0.465	0.152	0.007	0.042	3.22	2.95	0.22
301.00	3,172	11.35	0.09	0.54	0.23	0.033	0.151	0.136	0.010	0.064	2.89	1.68	0.21
301.08	4,191	12.03	0.08	0.56	0.20	0.032	0.150	0.111	0.009	0.074	3.07	2.07	0.20
301.17	4,786	10.56	0.07	0.59	0.12	0.029	0.148	0.098	0.010	0.053	3.49	2.86	0.23
301.25	5,041	10.97	0.11	0.78	0.11	0.040	0.170	0.067	0.011	0.068	3.64	3.51	0.31
301.33	5,239	11.08	0.12	0.87	0.16	0.040	0.159	0.078	0.014	0.079	3.39	2.74	0.28
301.51	6,032	10.67	0.09	0.48	0.14	0.032	0.159	0.056	0.011	0.073	3.29	2.89	0.26
301.84	4,560	9.66	0.21	1.69	0.46	0.060	0.505	0.133	0.013	0.079	2.21	3.05	0.32
302.17	3,653	8.03	0.08	1.33	0.18	0.046	0.276	0.130	0.003	0.129	2.62	2.37	0.55
302.51	3,144	6.73	0.07	1.33	0.14	0.024	0.190	0.213	0.002	0.069	2.80	1.95	0.69
302.84	2,713	6.94	0.11	1.47	0.12	0.031	0.246	0.113	0.003	0.067	3.22	1.71	0.19
303.71	2,121	5.32	0.08	2.66	0.09	0.018	0.265	0.042	0.002	0.118	3.16	2.96	0.44
Coralville													
300.42	1,104	2.00	0.30	1.38	0.04	0.036	0.368	0.028	0.003	0.064	3.68	2.37	0.36
300.50	1,164	2.38	0.23	1.90	0.03	0.027	0.278	0.055	0.004	0.054	4.34	2.46	0.48
300.58	1,402	0.85	0.24	3.29	0.05	0.038	0.265	0.044	0.012	0.038	0.66	1.23	0.92
300.67	1,631	4.09	0.26	2.19	0.07	0.039	0.408	0.067	0.007	0.066	4.25	2.50	0.44
300.75	1,926	4.64	0.20	1.17	0.09	0.035	0.307	0.104	0.008	0.050	3.51	2.20	0.36
300.83	2,325	6.18	0.21	2.66	0.12	0.041	0.258	0.102	0.010	0.053	3.09	2.03	0.28
300.92	2,605	2.48	0.21	0.89	0.21	0.042	0.275	0.093	0.030	0.079	0.70	1.06	0.68
301.00	2,722	1.11	0.07	0.78	0.11	0.025	0.158	0.042	0.003	0.041	0.76	0.72	1.00
301.08	3,455	0.91	0.06	0.82	0.07	0.020	0.146	0.038	0.003	0.025	1.20	1.21	0.59
301.17	4,673	1.75	0.08	0.72	0.08	0.037	0.229	0.055	0.003	0.044	0.88	0.60	0.70
301.25	5,522	9.85	0.12	1.12	0.26	0.047	0.336	0.124	0.006	0.092	2.82	1.92	0.21
301.33	6,372	6.59	0.09	0.60	0.17	0.035	0.182	0.066	0.005	0.049	2.85	1.61	0.32

(Continued)

TABLE 4 | Continued

Ordinal day	Q [L/s]	TMAH products [mg/100 mg OC]											
		∑ LPs	C12-14 FAs	C16-18 FAs	C26-34 FAs	ai-C15 FA	USFAs	Cutin acids	Bds	PSs	S/V	C/V	$[Ad/Al]_v$
301.50	7,137	2.80	0.15	0.75	0.24	0.057	0.372	0.024	0.009	0.037	0.45	0.50	2.75
301.83	6,995	10.17	0.14	0.85	0.11	0.055	0.249	0.073	0.052	0.095	1.43	1.59	0.33
302.17	5,041	3.35	0.10	0.81	0.16	0.041	0.193	0.035	0.013	0.062	0.97	1.19	0.85
302.50	3,936	5.12	0.19	1.52	0.18	0.056	0.300	0.059	0.009	0.087	2.34	1.57	0.33
302.83	3,342	2.08	0.05	0.70	0.06	0.015	0.120	0.041	0.008	0.057	1.38	1.86	0.28
303.00	MD*	1.24	0.08	0.39	0.04	0.009	0.149	0.011	0.002	0.038	2.21	2.07	0.70
303.17	2,917	6.70	0.15	1.22	0.18	0.040	0.231	0.081	0.008	0.053	2.63	2.08	0.25

*missing data.

ΣLPs, total lignin phenols; ai-C15 FA, anteiso-pentadecanoic acid; USFAs, unsaturated fatty acids (C16:1 FAs, C18:1 FAs, and C18:2 FA); Cutin acids, 9,16-dihydroxyhexadecanoic acid, 10,16-dihydroxyhexadecanoic acid, and 9,10,16-trihydroxyoctadecanoic acid; Bds, m-hydroxybenzoic acid and 3,5-dihydroxybenzoic acid; PSs, phytosterols (stigmasterol and β-sitosterol).

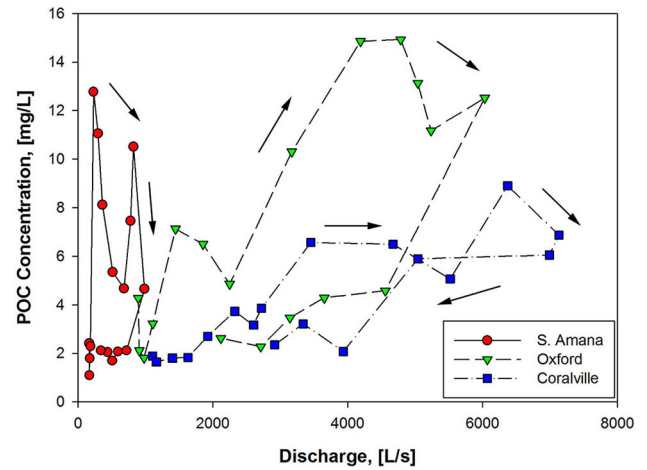

FIGURE 5 | POC concentrations as a function of discharge.

these factors contribute to the decrease in importance of local surface soil inputs relative to bank erosion and material exported from upstream at Oxford and Coralville (Sutarto et al., 2014; Papanicolaou et al., 2017). As a consequence, the precipitation dependence of POC concentration disappears and discharge assumes dominance as one moves from the upper to lower reach.

POC Compositional Changes

We observed temporal variations in the composition of the transported POC, consistent with selective mobilization of different sediment and POC sources observed in other catchments (Gellis, 2013; Koch et al., 2013; Smith et al., 2013). This was evident using both $^{13}C/^{12}C$ ratios and biomarker distributions (**Figures 3**, **4**). The C-isotopes are especially sensitive to source variations in an agricultural watershed where corn, a C4 plant, is a dominant row crop. The distinct ^{13}C-enrichment of corn ($\delta^{13}C \sim -10$ to -14‰) relative to more common terrestrial C3 plants (-25 to -29‰) and phytoplankton (-24 to -40‰) (Fry and Sherr, 1989; Thornton and McManus, 1994; Bianchi et al., 2007; Liu et al., 2018) allowed us to identify the input of corn-derived POC (Hou et al., 2018). Studies performed in the Clear Creek watershed indicate that surface soils and rain-drop liberated particulates from row crop fields have $\delta^{13}C$ values ranging from -16.6 ± 0.5 to -19.6 ± 1.3‰, which reflect varying corn OC inputs (Hou et al., 2018). In contrast, restored prairie soils and their rain-drop liberated particles have values of -27 ± 0.6‰ that record the predominantly C3 grass source (Hou et al., 2018). Whereas the bulk of the corn POC signal in the stream is anticipated to be associated with surface soil runoff, bank erosion may liberate ^{13}C-rich subsurface horizons as well. Rapid hillslope erosion and downslope deposition during the pre-conservation period buried and partially preserved agricultural top soils on the toes of hillslopes and the floodplain in at least one area within the South Amana subbasin (Yan et al., 2019). Floodplain deposition in general must be expected to contain ^{13}C-enriched C because the alluvia will be partially derived from eroded surface soils. Biomarker measurements complement those of the stable isotopes by providing additional dimensions to the source profiling. Specific to this project, lignin-derived phenols provide information concerning vascular plant inputs, and fatty acid distributions can provide clues concerning non-vascular plant sources (Hedges et al., 1986; Goñi and Thomas, 2000; Gordon and Goñi, 2003; Jung et al., 2015; Canuel and Hardison, 2016).

The time series of POC compositional changes during the storm were similar across all sampling stations. During the early ppt period, when both the POC concentrations and discharge were low, the most negative $\delta^{13}C$ values were observed. The most plausible explanation for the ^{13}C-depleted material given the timing is that it signals the contribution of in-channel algal production (Hatten et al., 2012). Algal productivity as a result of eutrophication under low flow conditions in summer and early fall is a major source of POC in agricultural streams (Griffiths et al., 2012; Dolph et al., 2017; Moatar et al., 2017). This has been verified by visual observations at Clear Creek and of filtered material from Clear Creek. This material should be the first to be mobilized as water velocities increase (Goñi et al., 1998; Ford and Fox, 2014). The biomarker composition of the POC samples is an

TABLE 5 | Correlation coefficients between hydrologic variables and POC concentrations.

Variable	Discharge			Precipitation		
Sampling station	**S. Amana**	**Oxford**	**Coralville**	**S. Amana**	**Oxford**	**Coralville**
Correlation Coefficient	NA $p > 0.05$	$r = 0.74$ $p < 0.05$	$r = 0.84$ $p < 0.05$	$r = 0.43$ $p < 0.05$	NA $p > 0.05$	$r = –0.018$ $p < 0.05$

TABLE 6 | POC loads per peak and event.

Sampling station	POC load [kg]				POC load during early ppt and early flush peak [%]
	Early ppt	Early flush peak	Main peak	Overall	
S. Amana	7	77	498	583	14.43
Oxford	53	215	5,917	6,185	4.33
Coralville	51	142	5,086	5,279	3.65

additional indicator of algal source. The early ppt POC samples had a greater abundance of short to medium-length (C12-18) saturated and medium-length (C16-18) monounsaturated fatty acids coupled with a lack of lignin phenols as would be expected for a non-vascular plant source. Although the C16 and C18 fatty acids are prevalent in most biogenic materials (Meyers et al., 1984), the extremely high concentrations of C16 and C18 fatty acids accompanied with short-chain fatty acids (C12-14) and C16-18 unsaturated fatty acids suggests a substantial contribution of algal or microbial biomass (Brooks et al., 1976; Kumari et al., 2013; Canuel and Hardison, 2016). Lower concentrations of vascular plant biomarkers (lignin, long-chain fatty acids (C26-34), phytosterols, and cutin acids) also support that in-stream production is the dominant source of POC. The anteiso-C15 fatty acid was examined to assess the contribution of bacteria-specific OC, but its profile did not show a consistent pattern with the hydrograph, possibly due to the ubiquity of bacteria and low concentration of bacteria-derived biomass in the stream (Goñi et al., 1998; Frazier et al., 2003; Cronan and Thomas, 2009; Canuel and Hardison, 2016).

The early flush peak and main storm peak in POC concentration exhibited major changes in $\delta^{13}C$ and the vascular plant biomarker concentrations (**Figures 3**, **4**). Lignin, in particular, increased in its concentration. The observed ^{13}C-enrichment reflects the input of corn-derived plant material. The dominance of vascular plant biomarkers, the diminished concentrations of algae-derived biomarkers, and the ^{13}C-enrichment supports our hypothesis that an important portion of POC introduced into the stream originated from eroded row crop soils. Non-lignin derived benzoic acids (3,5-dihydroxybenzoic acid and m-hydroxybenzoic acid), thought to be derived from proteins and tannins, are commonly associated with soil organic matter (Gordon and Goñi, 2003; Otto and Simpson, 2006; Hatten et al., 2012). These compounds paralleled the behavior of the vascular plant biomarkers (**Figure 4C**), showing a relatively high abundance during the early flush and main storm peaks.

The ratios of specific lignin phenols can provide more specificity in terms of plant type and plant tissue. Among major lignin monomers obtained from TMAH thermochemolysis, syringyl phenols (S) are uniquely synthesized by angiosperms, while vanillyl phenols (V) are found in all vascular plants. Cinnamyl phenols (C) are preferentially enriched in the non-woody tissues of vascular plants (Hedges and Mann, 1979). Therefore, higher S/V ratios can be a proxy for a higher contribution of angiosperms relative to gymnosperms and increased C/V ratios indicate a greater composition of non-woody derived OC (**Figure 6A**). The Clear Creek POC samples appear to lie along a mixing line between gymnosperms (woody and non-woody tissues are not well-resolved by the TMAH method) and non-woody angiosperms (**Figure 6A**). This is unexpected because the dominant vegetation in the watershed are non-woody angiosperms from the row crops and pastures, and woody angiosperms from forests (Nelson et al., 2016). Based on our GIS analysis of land cover in the watershed, gymnosperms appear to be << 1% of the vegetation. Some of the variation in lignin phenol ratios can be attributed to the large variability commonly seen within the non-woody angiosperm group (Goñi et al., 1998). Soils from corn-soybean cultivations differ from those of a restored prairie along a similar mixing line in the Clear Creek watershed where the prairie source is more gymnosperm-like (Hou et al., 2018).

There is also another potential explanation for the "gymnosperm" endmember signature that should not be discounted. Selective degradation of S and C phenols by fungi during diagenesis in soils can alter the S/V and C/V ratios to generate a more gymnosperm appearance (Hedges and Mann, 1979; Hedges et al., 1988; Goñi et al., 1993). The ratios of acids to aldehydes of V phenols and S phenols (e.g., $[Ad/Al]_v$ and $[Ad/Al]_s$) have been used as proxies of oxidative degradation of lignin (Vane et al., 2001; Klotzbücher et al., 2011). Increases in the ratios have been reported in laboratory experiments of fungal degradation of woods (Hedges et al., 1988; Goñi et al., 1993) and with sediment samples (Ertel and Hedges, 1985; Pautler et al., 2010). Our POC samples with lower S/V ratios showed higher $[Ad/Al]_v$, suggesting the preferential loss of S phenols is linked with the degradation state of lignin (**Figure 6B**). The same trend was observed for C/V ratios and ΣLignin with $[Ad/Al]_v$ further supporting the hypothesis that degradative processes are influencing lignin phenol ratios.

Both $[Ad/Al]_v$ and the hydroxy-benzoic acids (Bds) have been previously attributed to soil inputs to sediments. In Clear Creek, their appearances, while close in time, are not perfectly coincident (**Figure 7**). We hypothesize this reflects different soil inputs, further indicating the complexity of the POC mixtures

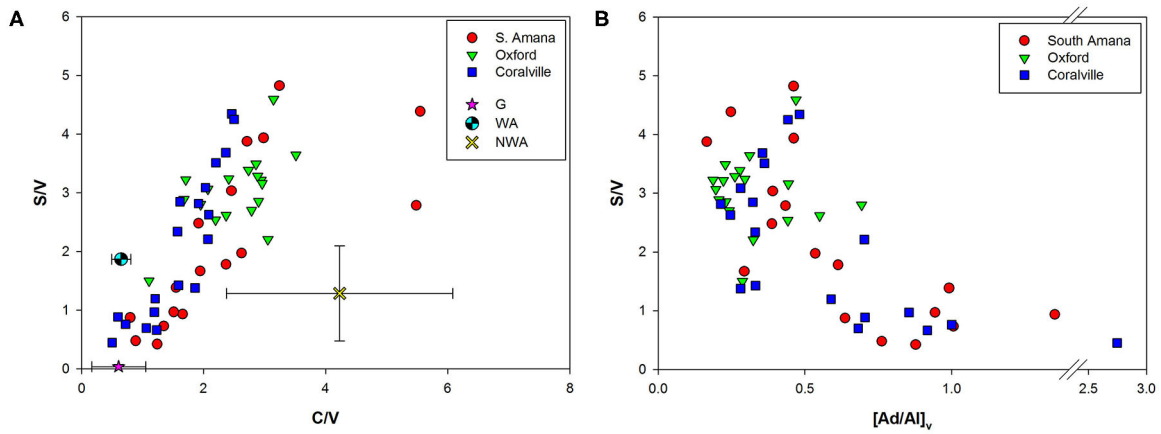

FIGURE 6 | (A) Lignin source identification biplot. Plant reference materials used include gymnosperms (G) (Red Spruce, Eastern White Pine, Red Cedar), woody angiosperms (WA) (Oregon White Oak wood), and non-woody angiosperms (NWA) (Oregon White Oak leaf, Red Alder, Smooth Cordgrass, Saltmarsh Hay, and Eel grass). **(B)** S/V and $[Ad/Al]_v$ biplot. Increases in $[Ad/Al]_v$ indicate oxidative degradation of lignin.

and the underlying mechanisms of delivery to the channel. The resolution of the sources also illustrates the importance of temporally frequent measurements through a storm event.

Landscape-Stream Connectivity and POC Export

Thus far, we have considered the concentrations and composition of POC from a static, or standing crop, perspective. This has provided information concerning the timing of inputs and the availability of OC for reaction and/or transport. Flux estimates on the other hand reveal the relative contributions of the different parcels of POC to downstream transport (**Figure 8**). The quantity of POC exported downstream for the sampling period was ∼580 kg C from South Amana, 6,200 kg C from Oxford, and 5,300 kg C from Coralville (**Table 6**). The ∼10-fold increase in POC loads between South Amana and Oxford reflects the integration of material from the multiple tributaries and the mainstem as the storm pulse travels downstream. The decrease in flux between Oxford and Coralville is less intuitive. While we must consider the possibility that the change is due to a bias in our single point sampling, it may also signal a loss of C via deposition as a result of lower water velocity in the flatter and wider channel. The POC fluxes due to the combined early ppt and early flush peaks represented 14.4, 4.3, and 3.7% of the total flux at South Amana, Oxford and Coralville, respectively. The bulk of the POC transport thus was accomplished via the peak that is most closely correlated with changes in discharge.

Whereas the POC in the early ppt and early flush peaks seems to be relatively simple in source, algal material and surface soils from row crops, the OC in the most important storm component in terms of export downstream is clearly more complicated in composition. This main peak appears to be an integrated mix of fresh and degraded vascular plant OC, likely derived from multiple yet to be identified soil sources.

A Conceptual Model for the Evolution of Storm-Pulse POC

The geochemistry has revealed both a temporal sequence of POC inputs and an evolution of the POC mixtures as they are transported downstream (**Figure 9**). Prior to the initiation of precipitation, the POC is dominated by in-channel sources. In the case of Clear Creek in autumn under low-flow conditions, algal production appeared to be the major source as is commonly seen in eutrophied agricultural streams (Dolph et al., 2017). Precipitation can trigger surface erosion and deliver POC to the channel. The magnitude of this input flux, which can be manifested as an early flush peak, is dependent on multiple factors. In Clear Creek and other agricultural settings, bare soils would be especially susceptible to erosion (Papanicolaou et al., 2015). Valley shape also influences sediment delivery ratios to the channel as illustrated by the attenuation of the early flush peak with valley widening downstream (**Figure 9**). The primary pulse of POC is correlated with the hydrograph. This complex mixture is derived from the accumulation of material from contributing tributaries and channel erosion. Bank erosion can contribute as much as 80% of sediment in agricultural catchments (Lamba et al., 2015). The broadening of this peak results from dispersion with transport (Romans et al., 2016) and an increase in complexity. This peak is not a homogeneous mixture in that it represents a partially resolved time series of inputs. Even though this conceptual model is based on the single Clear Creek event, aspects of it may be relevant to other events and systems. Specific details, such as the relative importance of the various components, will vary.

CONCLUSION

The results from this study provide a snapshot of the in-stream POC response to a storm in a small agricultural stream system. POC concentrations and compositions in Clear Creek responded to the passage of a storm event in October 2015.

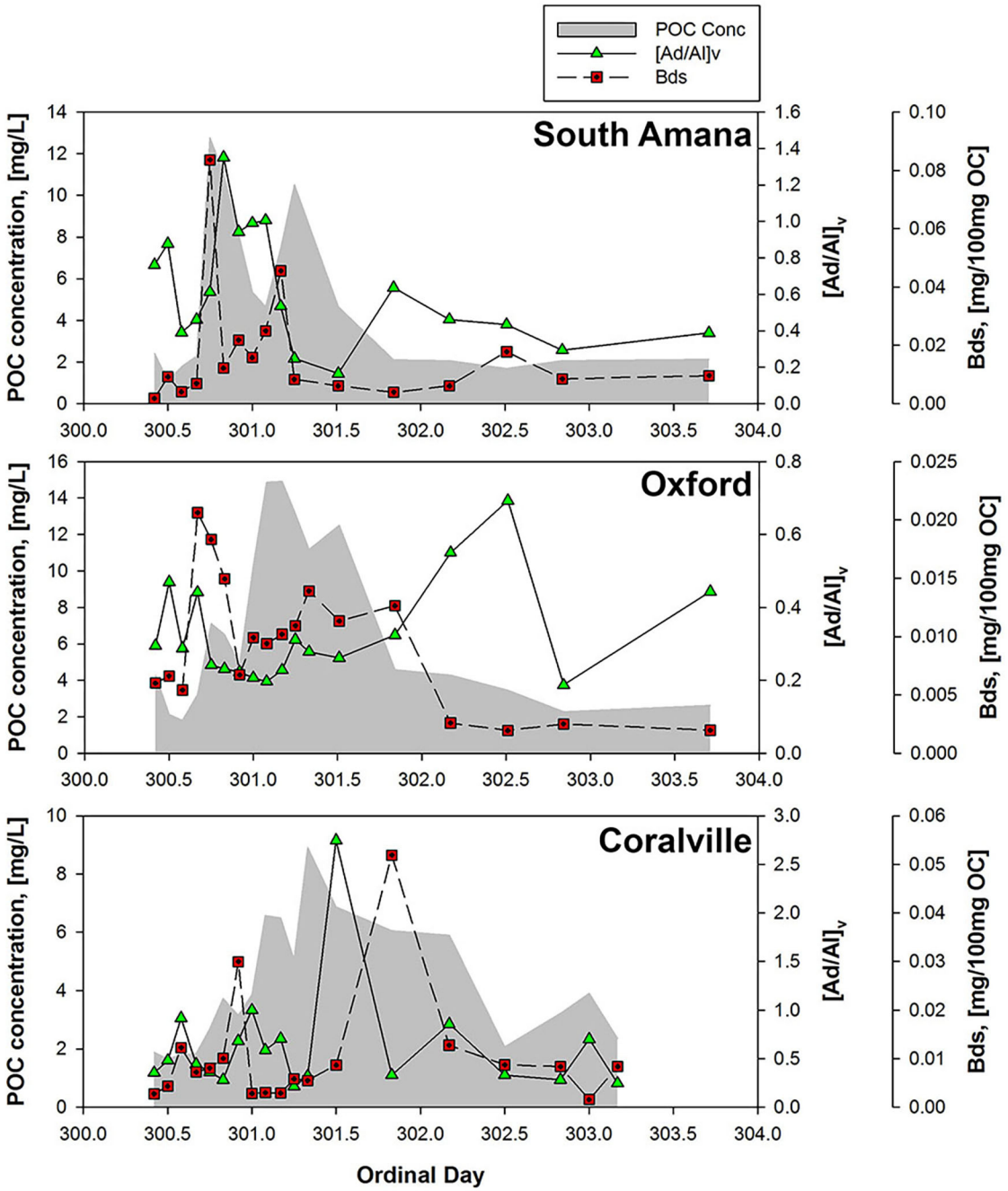

FIGURE 7 | POC concentrations and degradation tracers ($[Ad/Al]_v$ ratios and Bds concentrations). Increases in $[Ad/Al]_v$ or Bds indicate degradation of lignin or soil organic matter.

Broad spectrum biomarker analyses coupled with stable carbon isotope measurements revealed that the source of POC changed from in-stream sources prior to the storm event to surface soils with vascular plant debris mobilized by precipitation and stream discharge. POC concentrations rapidly increased with discharge with a clockwise C-Q hysteresis pattern. The hysteresis was driven by the generation of early flush peaks of POC. The early peaks occurred during peak precipitation, and based on isotopic and biomarker information, likely were derived from the erosion of bare post-harvest row crop soils. The precipitation dependence was most evident in the upper reach due to the steeper landscape that enabled more efficient erosion and sediment delivery to the channel.

Studies of both the spatial and temporal variability of fluvial POC have been done in the catchments of the Moselle in France (11,500 km^2, Le Meur et al., 2017) and the Amazon

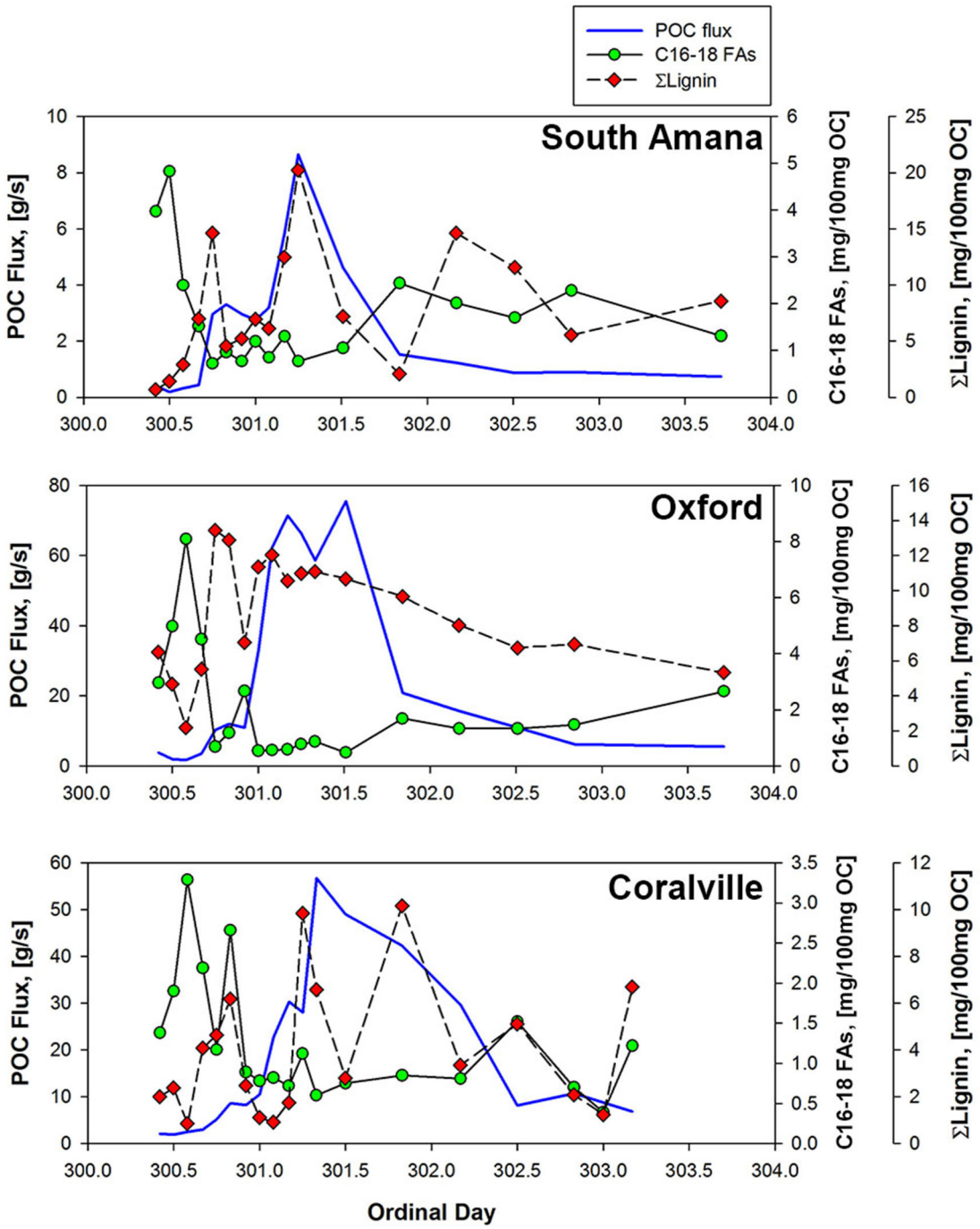

FIGURE 8 | POC fluxes and OC-normalized concentrations of lignin and C16-18 FAs at three sampling stations. From the upper panel on down, South Amana, Oxford, and Coralville.

(6,300,00 km^2, Aufdenkampe et al., 2007). It is apparent from these and other studies that the POC is a dynamic entity as it travels downstream. The size of the watershed seems to influence the turnover of bulk tracers such as radiocarbon but the impact on molecular biomarker compounds is unknown (Blair and Aller, 2012). Before this study, it was unclear if an interpretable behavior could be identified in a watershed as small as 280 km^2 in size during a storm event when transit times from source to export might be on the order of a day. As was discovered, temporal variations in such a system are obvious

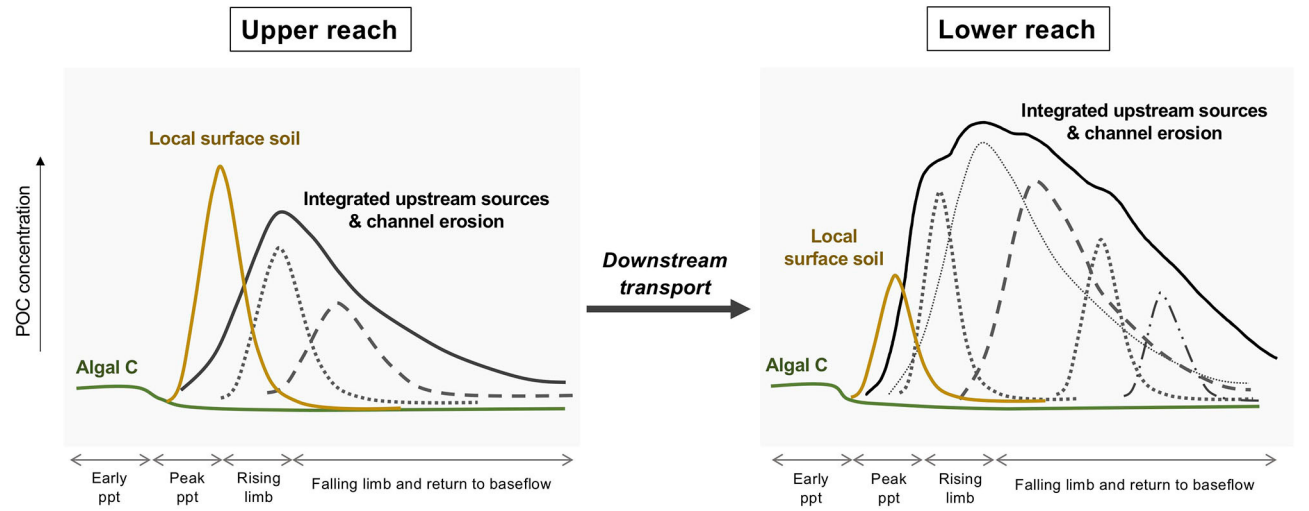

FIGURE 9 | Conceptual response of a small agricultural stream to a storm event in terms of sources of POC. During early ppt periods during the summer-early fall, algal growth dominates the POC pool. Heavy precipitation erodes surface soils from row crop fields, especially after harvest, and this material is delivered to the channel most efficiently in the upper reach. The dominant POC pool is a complex mixture that is an integration of upstream sources including bank erosion. Individual peaks under the larger umbrella curves represent hypothetical constituent sources that arrive at different times.

on timescales of hours, and probably shorter, and they appear to be linked to changes in precipitation and discharge, which in turn selectively trigger or initiate the delivery of different inputs. Changes in POC composition occur during transport over kilometer distances, primarily due to the integration of accumulating sources. The downstream evolution of valley cross-section morphology from a V- to U-shape appears to have an observable effect on the efficiency by which surface erosion reaches the channel. The C-isotopic contrast offered by the presence of a C4 plant species provided a clear tracer in this agricultural setting, thereby amplifying input signals. Given our observations, we conclude that it may be difficult to scale the magnitude of POC compositional change on the molecular level to the size of the watershed because of the rapidity by which changes occur. Local conditions other than size have control.

DATA AVAILABILITY STATEMENT

Original Clear Creek data are archived on the IML-CZO's Clowder database system. A spreadsheet can be downloaded from http://data.imlczo.org/clowder/datasets/5d922de44f0c55584a21a55b. The names of the repository/repositories and accession number(s) can be found in the article/**Supplementary Material**.

AUTHOR CONTRIBUTIONS

KG was responsible for sample collection. JK performed the biomarker analyses and led the manuscript preparation. NB and AW oversaw the project from proposal preparation to final report. All authors contributed to the article and approved the submitted version.

FUNDING

Financial support was provided by the U.S. National Science Foundation (NSF) Grant # EAR-1331906 for the Critical Zone Observatory for Intensively Managed Landscapes (IML-CZO), a multi-institutional collaborative effort. A portion of time for Ward was supported by NSF Grant EAR-1360276.

ACKNOWLEDGMENTS

Caroline Davis, Kara Prior, and Courtney Cappalli provided assistance with field sampling. Jessie Moravek, Paul Roots, Yue Zeng, Dana Cooperberg, and Koushik Dutta assisted with analyses. Special thanks to Art Bettis and Thanos Papanicolaou for their leadership at the Iowa field site, and to Praveen Kumar for his of the IML-CZO.

REFERENCES

Abaci, O., and Papanicolaou, A. N. T. (2009). Long-term effects of management practices on water-driven soil erosion in an intense agricultural sub-watershed: monitoring and modelling. *Hydrol. Process* 23, 2818–2837. doi: 10.1002/hyp.7380

Alvarez-Cobelas, M., Angeler, D., Sánchez-Carrillo, S., and Almendros, G. (2012). A worldwide view of organic carbon export from catchments. *Biogeochemistry* 107, 275–293. doi: 10.1007/s10533-010-9553-z

Amado, A. A., Schilling, K. E., Jones, C. S., Thomas, N., and Weber, L. J. (2017). Estimation of tile drainage contribution to streamflow and nutrient loads at the

watershed scale based on continuously monitored data. *Environ. Monit. Assess* 189:13. doi: 10.1007/s10661-017-6139-4

Aufdenkampe, A. K., Mayorga, E., Hedges, J. I., Llerena, C., Quay, P. D., Gudeman, J., et al. (2007). Organic matter in the Peruvian headwaters of the Amazon: compositional evolution from the Andes to the lowland Amazon mainstem. *Org. Geochem.* 38, 337–364. doi: 10.1016/j.orggeochem.2006.06.003

Behrens, P. W., and Kyle, D. J. (1996). Microalgae as a source of fatty acids. *J. Food Lipids* 3, 259–272. doi: 10.1111/j.1745-4522.1996.tb00073.x

Bettis, E. A., Muhs, D. R., Roberts, H. M., and Wintle, A. G. (2003). Last glacial loess in the conterminous USA. *Quat. Sci. Rev.* 22, 1907–1946. doi: 10.1016/S0277-3791(03)00169-0

Bianchi, T. S., Wysocki, L. A., Stewart, M., Filley, T. R., and McKee, B. A. (2007). Temporal variability in terrestrially-derived sources of particulate organic carbon in the lower Mississippi River and its upper tributaries. *Geochim. Cosmochim. Acta* 71, 4425–4437. doi: 10.1016/j.gca.2007.07.011

Bieroza, M. Z., Heathwaite, A. L., Bechmann, M., Kyllmar, K., and Jordan, P. (2018). The concentration-discharge slope as a tool for water quality management. *Sci. Total Environ.* 630, 738–749. doi: 10.1016/j.scitotenv.2018.02.256

Blair, N., and Leithold, E. (2013). "Impacts of watershed processes on exported riverine organic carbon," in *Biogeochemical Dynamics at Major River-Coastal Interfaces: Linkages With Global Change*, eds T. S. Blanchi, M. A. Allison, and W. J. Cai (Cambridge: Cambridge University Press), 174–199. doi: 10.1017/CBO9781139136853.011

Blair, N. E., and Aller, R. C. (2012). The fate of terrestrial organic carbon in the marine environment. *Ann. Rev. Mar. Sci.* 4, 401–423. doi: 10.1146/annurev-marine-120709-142717

Blair, N. E., Leithold, E. L., and Aller, R. C. (2004). From bedrock to burial: the evolution of particulate organic carbon across coupled watershed-continental margin systems. *Mar. Chem.* 92, 141–156. doi: 10.1016/j.marchem.2004.06.023

Blair, N. E., Leithold, E. L., Papanicolaou, A. T., Wilson, C. G., Keefer, L., Kirton, E., et al. (2018). The C-biogeochemistry of a Midwestern USA agricultural impoundment in context: Lake decatur in the intensively managed landscape critical zone observatory. *Biogeochemistry* 138, 171–195. doi: 10.1007/s10533-018-0439-9

Brooks, P., Eglinton, G., Gaskell, S., McHugh, D., Maxwell, J., and Philp, R. (1976). Lipids of recent sediments, Part I: straight-chain hydrocarbons and carboxylic acids of some temperate lacustrine and sub-tropical lagoonal/tidal flat sediments. *Chem. Geol.* 18, 21–38. doi: 10.1016/0009-2541(76)90058-9

Canuel, E. A., and Hardison, A. K. (2016). Sources, ages, and alteration of organic matter in estuaries. *Ann. Rev. Mar. Sci.* 8, 409–434. doi: 10.1146/annurev-marine-122414-034058

Caverly, E., Kaste, J. M., Hancock, G. S., and Chambers, R. M. (2013). Dissolved and particulate organic carbon fluxes from an agricultural watershed during consecutive tropical storms. *Geophys. Res. Lett.* 40, 5147–5152. doi: 10.1002/grl.50982

Cerro, I., Sanchez-Perez, J. M., Ruiz-Romera, E., and Antigüedad, I. (2014). Variability of particulate (SS, POC) and dissolved (DOC, NO3) matter during storm events in the Alegria agricultural watershed. *Hydrol. Process* 28, 2855–2867. doi: 10.1002/hyp.9850

Cho, K., and Salton, M. (1966). Fatty acid composition of bacterial membrane and wall lipids. *Biochim. Biophys. Acta.* 116, 73–79. doi: 10.1016/0005-2760(66)90093-2

Clifford, D. J., Carson, D. M., McKinney, D. E., Bortiatynski, J. M., and Hatcher, P. G. (1995). A new rapid technique for the characterization of lignin in vascular plants: thermochemolysis with tetramethylammonium hydroxide (TMAH). *Org. Geochem.* 23, 169–175. doi: 10.1016/0146-6380(94)00109-E

Cole, J. J., Prairie, Y. T., Caraco, N. F., McDowell, W. H., Tranvik, L. J., Striegl, R. G., et al. (2007). Plumbing the global carbon cycle: integrating inland waters into the terrestrial carbon budget. *Ecosystems* 10, 172–185. doi: 10.1007/s10021-006-9013-8

Cooper, W.J., and Blumer, M. (1968). Linear, iso and anteiso fatty acids in recent sediments of the North Atlantic. *Deep Sea Res. Oceanogr. Abstr.* 15, 535–540. doi: 10.1016/0011-7471(68)90062-4

Coplen, T. (1995). Reporting of stable hydrogen, carbon, and oxygen isotopic abundances. *Geothermics* 5, 707–712. doi: 10.1016/0375-6505(95)00024-0

Cronan, J. E., and Thomas, J. (2009). Bacterial fatty acid synthesis and its relationships with polyketide synthetic pathways. *Meth. Enzymol.* 459, 395–433. doi: 10.1016/S0076-6879(09)04617-5

Davis, C. A., Ward, A. S., Burgin, A. J., Loecke, T. D., Riveros-Iregui, D. A., Schnoebelen, D. J., et al. (2014). Antecedent moisture controls on stream nitrate flux in an agricultural watershed. *J. Environ. Qual.* 43, 1494–1503. doi: 10.2134/jeq2013.11.0438

Del Rio, J. C., and Hatcher, P. G. (1998). Analysis of aliphatic biopolymers using thermochemolysis with tetramethylammonium hydroxide (TMAH) and gas chromatography-mass spectrometry. *Org. Geochem.* 29, 1441–1451. doi: 10.1016/S0146-6380(98)00070-9

del Rio, J. C., McKinney, D. E., Knicker, H., Nanny, M. A., Minard, R. D., and Hatcher, P. G. (1998). Structural characterization of bio- and geo-macromolecules by off-line thermochemolysis with tetramethylammonium hydroxide. *J. Chromatogr. A* 823, 433–448. doi: 10.1016/S0021-9673(98)00268-4

Derrien, M., Yang, L., and Hur, J. (2017). Lipid biomarkers and spectroscopic indices for identifying organic matter sources in aquatic environments: a review. *Water Res.* 112, 58–71. doi: 10.1016/j.watres.2017.01.023

Dhillon, G. S., and Inamdar, S. (2013). Extreme storms and changes in particulate and dissolved organic carbon in runoff: entering uncharted waters? *Geophys. Res. Lett.* 40, 1322–1327. doi: 10.1002/grl.50306

Dhillon, G. S., and Inamdar, S. (2014). Storm event patterns of particulate organic carbon (POC) for large storms and differences with dissolved organic carbon (DOC). *Biogeochemistry* 118, 61–81. doi: 10.1007/s10533-013-9905-6

Doetterl, S., Berhe, A. A., Nadeu, E., Wang, Z., Sommer, M., and Fiener, P. (2016). Erosion, deposition and soil carbon: a review of process-level controls, experimental tools and models to address C cycling in dynamic landscapes. *Earth Sci. Rev.* 154, 102–122. doi: 10.1016/j.earscirev.2015.12.005

Dolph, C. L., Hansen, A. T., and Finlay, J. C. (2017). Flow-related dynamics in suspended algal biomass and its contribution to suspended particulate matter in an agricultural river network of the Minnesota River Basin, USA. *Hydrobiologia* 785, 127–147. doi: 10.1007/s10750-016-2911-7

Eash, D. A. (1993). *Estimating Design-Flood Discharges for Streams in Iowa Using Drainage-Basin and Channel-Geometry Characteristics*. Iowa City, IA: IAUS Geological Survey.

Ertel, J. R., and Hedges, J. I. (1985). Sources of sedimentary humic substances: vascular plant debris. *Geochim. Cosmochim. Acta* 49, 2097–2107. doi: 10.1016/0016-7037(85)90067-5

Ferro, V., and Minacapilli, M. (1995). Sediment delivery processes at basin scale. *Hydrol. Sci. J.* 40, 703–717. doi: 10.1080/02626669509491460

Filley, T. R., Boutton, T. W., Liao, J. D., Jastrow, J. D., and Gamblin, D. E. (2008). Chemical changes to nonaggregated particulate soil organic matter following grassland-to-woodland transition in a subtropical savanna. *J. Geophys. Res.* 113:564. doi: 10.1029/2007jg000564

Ford, W. I., and Fox, J. F. (2014). Model of particulate organic carbon transport in an agriculturally impacted stream. *Hydrol. Process* 28, 662–675. doi: 10.1002/hyp.9569

Frazier, S. W., Nowack, K. O., Goins, K. M., Cannon, F. S., Kaplan, L. A., and Hatcher, P. G. (2003). Characterization of organic matter from natural waters using tetramethylammonium hydroxide thermochemolysis GC-MS. *J. Anal. Appl. Pyrolysis* 70, 99–128. doi: 10.1016/S0165-2370(02)00098-0

Fry, B., and Sherr E. B. (1989). "δ13C measurements as indicators of carbon flow in marine and freshwater ecosystems," in Stable Isotopes in Ecological Research. Ecological Studies (Analysis and Synthesis), Vol. 68, eds P. W. Rundel, J. R. Ehleringer, and K. A. Nagy (New York, NY: Springer). doi: 10.1007/978-1-4612-3498-2_12

Gellis, A. C. (2013). Factors influencing storm-generated suspended-sediment concentrations and loads in four basins of contrasting land use, humid-tropical Puerto Rico. *Catena* 104, 39–57. doi: 10.1016/j.catena.2012.10.018

Goñi, M. A., Nelson, B., Blanchette, R. A., and Hedges, J. I. (1993). Fungal degradation of wood lignins: geochemical perspectives from CuO-derived phenolic dimers and monomers. *Geochim. Cosmochim. Acta* 57, 3985–4002. doi: 10.1016/0016-7037(93)90348-Z

Goñi, M. A., Ruttenberg, K. C., and Eglinton, T. I. (1998). A reassessment of the sources and importance of land-derived organic matter in surface sediments from the Gulf of Mexico. *Geochim. Cosmochim. Acta* 62, 3055–3075. doi: 10.1016/S0016-7037(98)00217-8

Goñi, M. A., and Thomas, K. A. (2000). Sources and transformations of organic matter in surface soils and sediments from a tidal estuary (North Inlet, South Carolina, USA). *Estuaries* 23, 548–564. doi: 10.2307/1353145

Gordon, E. S., and Goñi, M. A. (2003). Sources and distribution of terrigenous organic matter delivered by the Atchafalaya River to sediments in the northern Gulf of Mexico. *Geochim. Cosmochim. Acta* 67, 2359–2375. doi: 10.1016/S0016-7037(02)01412-6

Griffiths, N. A., Tank, J. L., Royer, T. V., Warrner, T. J., Frauendorf, T. C., Rosi-Marshall, E. J., et al. (2012). Temporal variation in organic carbon spiraling in Midwestern agricultural streams. *Biogeochemistry* 108, 149–169. doi: 10.1007/s10533-011-9585-z

Haga, H., Matsumoto, Y., Matsutani, J., Fujita, M., Nishida, K., and Sakamoto, Y. (2005). Flow paths, rainfall properties, and antecedent soil moisture controlling lags to peak discharge in a granitic unchanneled catchment. *Water Resour. Res.* 41:W12410. doi: 10.1029/2005WR004236

Harris, D., Horwáth, W. R., and Van Kessel, C. (2001). Acid fumigation of soils to remove carbonates prior to total organic carbon or carbon-13 isotopic analysis. *Soil Sci. Soc. Am. J.* 65, 1853–1856. doi: 10.2136/sssaj2001.1853

Harvey, H. R. (1994). Fatty acids and sterols as source markers of organic matter in sediments of the North Carolina continental slope. *Deep Sea Res Part II Top. Stud. Oceanogr.* 41, 783–796. doi: 10.1016/0967-0645(94)90048-5

Hatcher, P. G., Nanny, M. A., Minard, R. D., Dible, S. D., and Carson, D. M. (1995). Comparison of two thermochemolytic methods for the analysis of lignin in decomposing gymnosperm wood: the CuO oxidation method and the method of thermochemolysis with tetramethylammonium hydroxide (TMAH). *Org. Geochem.* 23, 881–888. doi: 10.1016/0146-6380(95)00087-9

Hatten, J. A., Goñi, M. A., and Wheatcroft, R. A. (2012). Chemical characteristics of particulate organic matter from a small, mountainous river system in the Oregon Coast Range, USA. *Biogeochemistry* 107, 43–66. doi: 10.1007/s10533-010-9529-z

Hedges, J. I., Blanchette, R. A., Weliky, K., and Devol, A. H. (1988). Effects of fungal degradation on the CuO oxidation products of lignin: a controlled laboratory study. *Geochim. Cosmochim. Acta* 52, 2717–2726. doi: 10.1016/0016-7037(88)90040-3

Hedges, J. I., Clark, W. A., Quay, P. D., Richey, J. E., Devol, A. H., and Santos, M. (1986). Compositions and fluxes of particulate organic material in the Amazon River 1. *Limnol. Oceanogr.* 31, 717–738. doi: 10.4319/lo.1986.31.4.0717

Hedges, J. I., and Mann, D. C. (1979). The characterization of plant tissues by their lignin oxidation products. *Geochim. Cosmochim. Acta* 43, 1803–1807. doi: 10.1016/0016-7037(79)90028-0

Hedges, J. I., and Parker, P. L. (1976). Land-derived organic matter in surface sediments from the Gulf of Mexico. *Geochim. Cosmochim. Acta* 40, 1019–1029. doi: 10.1016/0016-7037(76)90044-2

Hou, T., Berry, T. D., Singh, S., Hughes, M. N., Tong, Y., Papanicolaou, A. T., et al. (2018). Control of tillage disturbance on the chemistry and proportion of raindrop-liberated particles from soil aggregates. *Geoderma* 330, 19–29. doi: 10.1016/j.geoderma.2018.05.013

Howcroft, H., and Willis, A. (1987). The rainfall-runoff relationship in a small catchment. *Field Stud.* 6, 619–655.

Jeong, J.-J., Bartsch, S., Fleckenstein, J. H., Matzner, E., Tenhunen, J. D., Lee, S. D., et al. (2012). Differential storm responses of dissolved and particulate organic carbon in a mountainous headwater stream, investigated by high-frequency, in situ optical measurements. *J. Geophys. Res.* 117:G03013. doi: 10.1029/2012JG001999

Johnson, E. R., Inamdar, S., Kan, J., and Vargas, R. (2018). Particulate organic matter composition in stream runoff following large storms: role of POM sources, particle size, and event characteristics. *J. Geophys. Res. Biogeosci.* 23, 660–675. doi: 10.1002/2017JG004249

Jung, B. J., Jeanneau, L., Alewell, C., Kim, B., and Park, J. H. (2015). Downstream alteration of the composition and biodegradability of particulate organic carbon in a mountainous, mixed land-use watershed. *Biogeochemistry* 122, 79–99. doi: 10.1007/s10533-014-0032-9

Jung, B. J., Lee, H. J., Jeong, J. J., Owen, J., Kim, B., Meusburger, K., et al. (2012). Storm pulses and varying sources of hydrologic carbon export from a mountainous watershed. *J. Hydrol.* 440, 90–101. doi: 10.1016/j.jhydrol.2012.03.030

Khanchoul, K., Saaidia, B., and Altschu, R. (2018). Variation in sediment concentration and water disharge during storm eevents in two catchments, Northeast of Algeria. *Earth Sci. Malaysia (ESMY)* 2, 1–9. doi: 10.26480/esmy.02.2018.01.09

Klotzbücher, T., Filley, T. R., Kaiser, K., and Kalbitz, K. (2011). A study of lignin degradation in leaf and needle litter using 13C-labelled tetramethylammonium hydroxide (TMAH) thermochemolysis: comparison with CuO oxidation and van soest methods. *Org. Geochem.* 42, 1271–1278. doi: 10.1016/j.orggeochem.2011.07.007

Koch, J. C., Runkel, R. L., Striegl, R., and McKnight, D. M. (2013). Hydrologic controls on the transport and cycling of carbon and nitrogen in a boreal catchment underlain by continuous permafrost. *J. Geophys. Res. Biogeosci.* 118, 698–712. doi: 10.1002/jgrg.20058

Kumar, P., Le, P. V. V., Papanicolaou, A. N. T., Rhoads, B. L., Anders, A. M., Stumpf, A., et al. (2018). Critical transition in critical zone of intensively managed landscapes. *Anthropocene* 22, 10–19. doi: 10.1016/j.ancene.2018.04.002

Kumari, P., Kumar, M., Reddy, C. R. K., and Jha, B. (2013). "Algal lipids, fatty acids and sterols," in *Functional Ingredients From Algae for Foods and Nutraceuticals*, ed H. Domínguez (Cambridge: Woodhead Publishing), 87–134. doi: 10.1533/9780857098689.1.87

Kvenvolden, K. A. (1967). Normal fatty acids in sediments. *J. Am. Oil Chem. Soc.* 44, 628–636. doi: 10.1007/BF02680031

Lamba, J., Karthikeyan, K. G., and Thompson, A. M. (2015). Apportionment of suspended sediment sources in an agricultural watershed using sediment fingerprinting. *Geoderma* 239, 25–33. doi: 10.1016/j.geoderma.2014.09.024

Le Meur, M., Mansuy-Huault, L., Lorgeoux, C., Bauer, A., Gley, R., Vantelon, D., et al. (2017). Spatial and temporal variations of particulate organic matter from Moselle River and tributaries: a multimolecular investigation. *Org. Geochem.* 110, 45–56. doi: 10.1016/j.orggeochem.2017.04.003

Leithold, E. L., Blair, N. E., and Wegmann, K. W. (2016). Source-to-sink sedimentary systems and global carbon burial: a river runs through it. *Earth Sci. Rev.*153, 30–42. doi: 10.1016/j.earscirev.2015.10.011

Li, W., Dagaut, J., and Saliot, A. (1995). The application of sterol biomarkers to the study of the sources of particulate organic matter in the Solo River system and and Serayu River, Java, Indonesia. *Biogeochemistry* 31, 139–154. doi: 10.1007/BF00004046

Liu, W., Li, X., Wang, Z., Wang, H., Liu, H., Zhang, B., et al. (2018). Carbon isotope and environmental changes in lakes in arid Northwest China. *Sci. China Earth Sci.* 62, 1193–1209. doi: 10.1007/s11430-018-9232-4

Matsuda, H., and Koyama, T. (1977). Early diagenesis of fatty acids in lacustrine sediments—I. Identification and distribution of fatty acids in recent sediment from a freshwater lake. *Geochim. Cosmochim. Acta* 41, 777–783. doi: 10.1016/0016-7037(77)90048-5

McClain, M. E., Boyer, E. W., Dent, C. L., Gergel, S. E., Grimm, N. B., Groffman, P. M., et al. (2003). Biogeochemical hot spots and hot moments at the interface of terrestrial and aquatic ecosystems. *Ecosystems* 301–312. doi: 10.1007/s10021-003-0161-9

McKinney, D. E., Carson, D. M., Clifford, D. J., Minard, R. D., and Hatcher, P. G. (1995). Off-line thermochemolysis versus flash pyrolysis for the *in situ* methylation of lignin: is pyrolysis necessary? *J. Anal. Appl. Pyrolysis* 34, 41–46. doi: 10.1016/0165-2370(94)00865-X

Meybeck, M. (1982). Carbon, nitrogen, and phosphorus transport by world rivers. *Am. J. Sci.* 282, 401–450. doi: 10.2475/ajs.282.4.401

Meyers, P. A., Kawka, O. E., and Whitehead, D. R. (1984). Geolipid, pollen and diaton stratigraphy in postglacial lacustrine sediments. *Org. Geochem.* 6, 727–732. doi: 10.1016/0146-6380(84)90093-7

Moatar, F., Abbott, B. W., Minaudo, C., Curie, F., and Pinay, G. (2017). Elemental properties, hydrology, and biology interact to shape concentration-discharge curves for carbon, nutrients, sediment, and major ions. *Water Resour. Res.* 53, 1270–1287. doi: 10.1002/2016WR019635

Nelson, M. D., Barnett, C. J., Brewer, M., Butler, B. J., Crocker, S. J., Domke, G. M., et al. (2016). Iowa forests, 2013. *Resour. Bull.* 2013:124. doi: 10.2737/NRS-RB-102

Newbold, J., Mulholland, P., Elwood, J., and O'neill, R. (1982). Organic carbon spiralling in stream ecosystems. *Oikos* 266–272. doi: 10.2307/3544663

Oeurng, C., Sauvage, S., Coynel, A., Maneux, E., Etcheber, H., and Sánchez-Pérez, J. M. (2011). Fluvial transport of suspended sediment and organic carbon during flood events in a large agricultural catchment in southwest France. *Hydrol. Process* 25, 2365–2378. doi: 10.1002/hyp.7999

Otto, A., and Simpson, M. J. (2006). Evaluation of CuO oxidation parameters for determining the source and stage of lignin degradation in soil. *Biogeochemistry* 80, 121–142. doi: 10.1007/s10533-006-9014-x

Papanicolaou, A. N., Wacha, K. M., Abban, B. K., Wilson, C. G., Hatfield, J. L., Stanier, C. O., et al. (2015). From soilscapes to landscapes: a landscape-oriented approach to simulate soil organic carbon dynamics in intensively managed landscapes. *J. Geophys. Res. Biogeosci.* 120, 2375–2401. doi: 10.1002/2015JG003078

Papanicolaou, A. T., Wilson, C. G., Tsakiris, A. G., Sutarto, T. E., Bertrand, F., Rinaldi, M., et al. (2017). Understanding mass fluvial erosion along a bank profile: using PEEP technology for quantifying retreat lengths and identifying event timing. *Earth Surf. Process Landf.* 42, 1717–1732. doi: 10.1002/esp.4138

Pautler, B. G., Austin, J., Otto, A., Stewart, K., Lamoureux, S. F., and Simpson, M. J. (2010). Biomarker assessment of organic matter sources and degradation in Canadian high arctic littoral sediments. *Biogeochemistry* 100, 75–87. doi: 10.1007/s10533-009-9405-x

Picouet, C., Hingray, B., and Olivry, J. (2001). Empirical and conceptual modelling of the suspended sediment dynamics in a large tropical African river: the Upper Niger river basin. *J. Hydrol.* 250, 19–39. doi: 10.1016/S0022-1694(01)00407-3

Prior, J. C. (1991). *Landforms of Iowa*. Iowa City, IA: University of Iowa Press.

Rayburn, A. P., and Schulte, L. A. (2009a). Integrating historic and contemporary data to delineate potential remnant natural woodlands within midwestern agricultural landscapes. *Nat. Areas J.* 29, 4–14. doi: 10.3375/043.029.0102

Rayburn, A. P., and Schulte, L. A. (2009b). Landscape change in an agricultural watershed in the US Midwest. *Landsc. Urban Plan.* 93, 132–141. doi: 10.1016/j.landurbplan.2009.06.014

Raymond, P. A., Saiers, J. E., and Sobczak, W. V. (2016). Hydrological and biogeochemical controls on watershed dissolved organic matter transport: Pulse-shunt concept. *Ecology* 97, 5–16. doi: 10.1890/14-1684.1

Romans, B. W., Castelltort, S., Covault, J. A., Fildani, A., and Walsh, J. P. (2016). Environmental signal propagation in sedimentary systems across timescales. *Earth Sci. Rev.* 153, 7–29. doi: 10.1016/j.earscirev.2015.07.012

Rose, L. A., Karwan, D. L., and Godsey, S. E. (2018). Concentration–discharge relationships describe solute and sediment mobilization, reaction, and transport at event and longer timescales. *Hydrol. Process* 32, 2829–2844. doi: 10.1002/hyp.13235

Ruhe, R. V. (1969). *Quaternary Landscapes in Iowa*. Ames, IA: Iowa State University Press.

Saliot, A., Mejanelle, L., Scribe, P., Fillaux, J., Pepe, C., Jabaud, A., et al. (2001). Particulate organic carbon, sterols, fatty acids and pigments in the Amazon River system. *Biogeochemistry* 53, 79–103. doi: 10.1023/A:1010754022594

Schilling, K. E., and Helmers, M. (2008). Effects of subsurface drainage tiles on streamflow in Iowa agricultural watersheds: exploratory hydrograph analysis. *Hydrol. Process* 22, 4497–4506. doi: 10.1002/hyp.7052

Schilling, K. E., Jindal, P., Basu, N. B., and Helmers, M. J. (2012). Impact of artificial subsurface drainage on groundwater travel times and baseflow discharge in an agricultural watershed, Iowa (USA). *Hydrol. Process* 26, 3092–3100. doi: 10.1002/hyp.8337

Schimmelmann, A., Albertino, A., Sauer, P. E., Qi, H., Molinie, R., and Mesnard, F. (2009). Nicotine, acetanilide and urea multi-level 2H-, 13C- and 15N-abundance reference materials for continuous-flow isotope ratio mass spectrometry. *Rapid Commun. Mass Spectrom.* 23, 3513–3521. doi: 10.1002/rcm.4277

Skrzypek, G. (2013). Normalization procedures and reference material selection in stable HCNOS isotope analyses: an overview. *Anal. Bioanal. Chem.* 405, 2815–2823. doi: 10.1007/s00216-012-6517-2

Smith, J. C., Galy, A., Hovius, N., Tye, A. M., Turowski, J. M., and Schleppi, P. (2013). Runoff-driven export of particulate organic carbon from soil in temperate forested uplands. *Earth Planet. Sci. Lett.* 365, 198–208. doi: 10.1016/j.epsl.2013.01.027

Sutarto, T., Papanicolaou, A., Wilson, C., and Langendoen, E. (2014). Stability analysis of semicohesive streambanks with CONCEPTS: coupling field and laboratory investigations to quantify the onset of fluvial erosion and mass failure. *J. Hydraul. Eng.* 140:04014041. doi: 10.1061/(ASCE)HY.1943-7900.0000899

Thevenot, M., Dignac, M. F., and Rumpel, C. (2010). Fate of lignins in soils: a review. *Soil Biol. Biochem.* 42, 1200–1211. doi: 10.1016/j.soilbio.2010.03.017

Thornton, S., and McManus, J. (1994). Application of organic carbon and nitrogen stable isotope and C/N ratios as source indicators of organic matter provenance in estuarine systems: evidence from the Tay Estuary, Scotland. *Estuar. Coast. Shelf Sci.* 38, 219–233. doi: 10.1006/ecss.1994.1015

Vaculikova, L., and Plevova, E. (2005). Identification of clay minerals and micas in sedimentary rocks. *Acta Geodynam. Geomater.* 2:163.

Vane, C. H., Abbott, G. D., and Head, I. M. (2001). The effect of fungal decay (*Agaricus bisporus*) on wheat straw lignin using pyrolysis–GC–MS in the presence of tetramethylammonium hydroxide (TMAH). *J. Anal. Appl. Pyrolysis* 60, 69–78. doi: 10.1016/S0165-2370(00)00156-X

Wakeham, S. G., and Beier, J. A. (1991). Fatty acid and sterol biomarkers as indicators of particulate matter source and alteration processes in the Black Sea. *Deep Sea Res. A Oceanogr. Res. Papers* 38, S943–S968. doi: 10.1016/S0198-0149(10)80018-4

Williams, G. P. (1989). Sediment concentration versus water discharge during single hydrologic events in rivers. *J. Hydrol.* 111, 89–106. doi: 10.1016/0022-1694(89)90254-0

Wilson, C. G., Abban, B., Keefer, L. L., Wacha, K., Dermisis, D., Giannopoulos, C., et al. (2018). The intensively managed landscape critical zone observatory: a scientific testbed for understanding critical zone processes in agroecosystems. *Vadose Zone J.* 17, 1–21. doi: 10.2136/vzj2018.04.0088

Wilson, C. G., Papanicolaou, A. N. T., and Denn, K. D. (2012). Partitioning fine sediment loads in a headwater system with intensive agriculture. *J. Soils Sediments* 12, 966–981. doi: 10.1007/s11368-012-0504-2

Wohl, E., Bledsoe, B. P., Jacobson, R. B., Poff, N. L., Rathburn, S. L., Walters, D. M., et al. (2015). The natural sediment regime in rivers: broadening the foundation for ecosystem management. *Bioscience* 65, 358–371. doi: 10.1093/biosci/biv002

Xu, C., Yang, Z., Qian, W., Chen, S., Liu, X., Lin, W., et al. (2019). Runoff and soil erosion responses to rainfall and vegetation cover under various afforestation management regimes in subtropical montane forest. *Land Degrad. Dev.* 30, 1711–1724. doi: 10.1002/ldr.3377

Yan, Q. N., Iwasaki, T., Stumpf, A., Belmont, P., Parker, G., and Kumar, P. (2018). Hydrogeomorphological differentiation between floodplains and terraces. *Earth Surf. Process. Landf.* 43, 218–228. doi: 10.1002/esp.4234

Yan, Q. N., Le, P. V. V., Woo, D. K., Hou, T. Y., Filley, T., and Kumar, P. (2019). Three-dimensional modeling of the coevolution of landscape and soil organic carbon. *Water Resour. Res.* 55, 1218–1241. doi: 10.1029/2018WR023634

Conflict of Interest: The authors declare that the research was conducted in the absence of any commercial or financial relationships that could be construed as a potential conflict of interest.

frontiers in Water

ORIGINAL RESEARCH
published: 28 October 2020
doi: 10.3389/frwa.2020.571044

Influence of Climate and Duration of Stream Water Presence on Rates of Litter Decomposition and Nutrient Dynamics in Temporary Streams and Surrounding Environments of Southwestern USA

Kathleen A. Lohse[1]*, *Erika L. Gallo*[1,2] and *Thomas Meixner*[1]

[1] Department of Biological Sciences, Idaho State University, Pocatello, ID, United States, [2] Department of Hydrology and Atmospheric Sciences, University of Arizona, Tucson, AZ, United States

OPEN ACCESS

Edited by:
Dipankar Dwivedi,
Lawrence Berkeley National Laboratory, United States

Reviewed by:
Joel Rowland,
Los Alamos National Laboratory (DOE), United States
Pin Shuai,
Pacific Northwest National Laboratory (DOE), United States

***Correspondence:**
Kathleen A. Lohse
klohse@isu.edu

Specialty section:
This article was submitted to Water and Critical Zone, a section of the journal Frontiers in Water

Received: 09 June 2020
Accepted: 04 September 2020
Published: 28 October 2020

Citation:
Lohse KA, Gallo EL and Meixner T (2020) Influence of Climate and Duration of Stream Water Presence on Rates of Litter Decomposition and Nutrient Dynamics in Temporary Streams and Surrounding Environments of Southwestern USA. Front. Water 2:571044. doi: 10.3389/frwa.2020.571044

Ephemeral and intermittent streams are increasing with climate and land use changes, and alteration in stream water presence or flow duration will likely affect litter decomposition and nutrient dynamics in channel and riparian zones more than uplands. To investigate the influence of varying climate and streamflow regimes on rates of decomposition and associated nutrient dynamics, we used a space-for-time substitution design in which we deployed a common leaf litter across a range of ephemeral to seasonally- intermittent stream reaches (10) and landscape positions (channel, riparian, upland) in Arizona, USA over an 18-month period. We also measured soil physio-chemical properties and nutrient dynamics associated with these reaches and positions. Consistent with expectations, rates of litter decomposition (*k*) decreased significantly in the channels as cumulative percentage (%) of water presence decreased below 40%. Indeed, differences in cumulative duration of water presence as well as channel bed material silt content explained 80% of the variation in *k* across flow regimes. In contrast, decay rates of the common litter across sites were surprisingly similar in upland and riparian positions despite large differences in climate, specifically precipitation (160–516 mm). Relatively similar litter nitrogen immobilization and soil moisture in upland and riparian environments helped to explain the lack of difference in *k* and soil nutrient dynamics in these environments. Collectively, our findings indicate that stream water presence may be a more important indicator of ephemeral and intermittent stream function than streamflow alone and that riparian zones in these dryland regions may be less responsive to changes in climate and associated subsidies of streamflow.

Keywords: temporary streams, decomposition, thresholds, climate change, ephemeral stream flow, intermittent stream flow

INTRODUCTION

Ephemeral and intermittent streamflow are the dominant flow regimes in dryland regions—hyper-arid, arid, semi-arid, and dry sub-humid areas that together encompass >40% of the terrestrial land surface (Reynolds et al., 2007). The occurrence of ephemeral and intermittent streamflow, flow only during and immediately after a rainfall event or flow for short duration, respectively, is likely to increase in distribution and extent with climate change (Seager et al., 2007; Larned et al., 2010; Döll and Schmied, 2012) as well as human water appropriation (Postel et al., 1996; Alley et al., 2002; Larned et al., 2010). In the Southwestern United States (US) (Arizona, New Mexico, Nevada, Utah, Colorado and California), for example, over 81% of streams are classified as ephemeral and/or intermittent (U.S. Geological Survey, 2008; Levick et al., 2008). By 2050, it is projected that regime shifts from perennial to intermittent and ephemeral streamflow will increase by 5.4–7.0% globally under low to high emissions climate change scenarios, mostly in semi-arid regions (Döll and Schmied, 2012).

Intermittent and ephemeral streams have been identified as providing key hydrologic functions and services; they supply water to plants, animals, and drinking water systems in otherwise dry landscapes (Levick et al., 2008). They store and exchange surface and subsurface water (Lane, 1983; Goodrich et al., 1997, 2004), provide hydrologic connectivity and continuity for habitat (Jaeger and Olden, 2012; Jaeger et al., 2014), and recharge and discharge groundwater (Scanlon and Goldsmith, 1997; Scanlon et al., 1999; Heilweil et al., 2004). Despite their broad geographic significance and hydrologic importance, however, key ecological functions in ephemeral and intermittent streams remain poorly understood and characterized (Stanley et al., 1997; Levick et al., 2008; Larned et al., 2010; Datry et al., 2011, 2014). In particular, little is known about how changes in the frequency and duration of streamflow or water presence associated with ephemeral and intermittent streams will alter organic matter and nutrient dynamics and their controls. The few studies conducted have been associated with one or two intermittent streams (Schade and Fisher, 1997; Anderson and Nelson, 2006; Langhans and Tockner, 2006; Sangiorgio et al., 2007; Corman et al., 2016) or lab incubations that show the importance of frequency and duration of wetting of litter and sediment in releasing of carbon dioxide (CO_2) and nutrients (Gallo et al., 2014; Datry et al., 2018; Shumilova et al., 2019; Correa-Araneda et al., 2020). Direct measurements of streamflow duration, water presence, and decomposition rates across a strong climate gradient remain lacking. Moreover, linkages among uplands, floodplain or riparian zones and these temporary stream environments remain poorly characterized owing to the complexity and episodic nature of these interactions (Belnap et al., 2005; Welter et al., 2005).

Transitions from perennial to intermittent or ephemeral flow regimes in streams will introduce an ecologically significant terrestrial phase in the stream channel and the surrounding environment (Arce et al., 2019). In perennial streams, the chemical and physical properties of the organic matter (litter quality), detritivores present including invertebrates and fungal biofilms, stream temperature, and water column nutrients are considered to be the primary controls on decomposition (e.g., see Webster and Benfield, 1986; Tank et al., 2010). With transitions to intermittent and ephemeral flow, abiotic processes such as the frequency and duration of streamflow and soil drying and wetting cycles (Datry et al., 2018) as well as soil coverage and UV radiation may become more important factors controlling decomposition rates. These last factors are similar to those identified in the upland dryland literature (Austin and Vivanco, 2006; Throop and Archer, 2007; Barnes et al., 2012, 2015). Thus, it is likely that the relative importance of abiotic and biotic controls on decomposition and nutrient dynamics will teeter back and forth with changes in the terrestrial and aquatic phases associated with different flow regimes in intermittent to ephemeral streams.

Here we examine litter decomposition rates and nutrient dynamics in 10 ephemeral-to- seasonally-intermittent streams in Arizona, USA over an 18-month period. We used a space-for-time substitution and held litter quality constant across sites by deploying oak (*Quercus grisea*) leaf litterbags, sourced from the wettest site, to investigate the influence of varying climate and associated streamflow conditions on decomposition and nutrient dynamics. At each study site, we deployed litterbags along three cross-sectional transects in upland, riparian, and channel positions to evaluate the role of landscape position in determining decomposition and nutrient dynamics. We also characterized the soil physical and biogeochemical characteristics of the sites, monitored streamflow and water presence using electrical resistance (ER) sensors, and measured seasonal soil moisture and nutrient dynamics across sites and positions to evaluate possible controls on litter decomposition. We hypothesized that decomposition would be more rapid in channels with seasonally-intermittent flow compared to ephemeral flow, and expected that abiotic factors such as longer duration of streamflow and water presence and associated soil moisture would have a stronger influence on rates of decomposition than biotic processes such as nutrient availability and cycling rates. We also expected rates of decomposition to be more rapid in channels and riparian zones compared to upland environments, and differences in climate and subsidies of streamflow and/or soil-water moisture to control organic and nutrient release.

MATERIALS AND METHODS

Study Sites and Design

All study sites were located on military installations or near them as a part of a program to understand and manage ephemeral and intermittent streams on military lands. We initially selected 13 temporary stream channels or washes in southern Arizona (**Figure 1**) that spanned a climate gradient, with mean annual precipitation ranging from 160 to 750 mm, and a range of geomorphic conditions. Precipitation across the region is bimodal: summertime convective rainfall (the North American Monsoon) is intense, of short duration, spatially heterogeneous and lasts from mid-late June to mid-late September. A second precipitation period is observed primarily between December and March with rainfall of lower intensity and longer duration arising from widespread storm systems. The most arid study

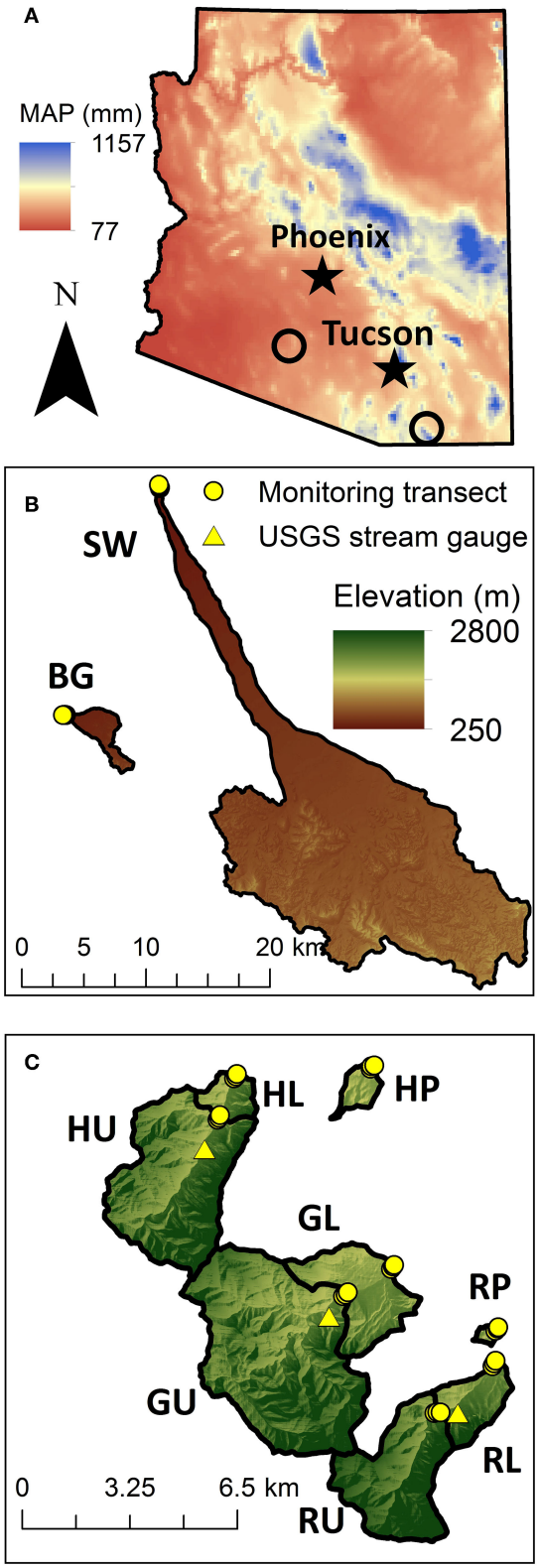

FIGURE 1 | (A) Location of two main study areas in Arizona along a climate gradient with black open circles showing locations of Barry Goldwater and *(Continued)*

FIGURE 1 | Fort Huachuca military installations. **(B)** Black Gap (BG) and Sauceda Wash (SW) are located in Barry Goldwater military installation. **(C)** Huachuca Piedmont (HP), Huachuca Lower Canyon (HL), and Huachuca Upper Canyon (GU) as well as Garden Piedmont (GP), Garden Lower (GL), and Garden Upper (GU) Canyon are located in the Fort Huachuca military installation. Ramsey Piedmont, Lower (RL), and Upper Ramsey (RU) Canyon are located in the Nature Preserve.

sites were located within the Barry M. Goldwater Air Force Base near Gila Bend, Arizona in the Lower Gila River Basin (Sauceda Wash, SW; and Black Gap, BG; **Figure 1B**), on semi-consolidated alluvial basin fans (200–300 m elevation). The catchment upstream of the BG reach is 10.2 km^2 and ranges in elevation from 324 to 676. The catchment upstream of the SW reach is the largest of our study sites, 326.4 km^2, and ranges in elevation from 258 to 1114 m. The 30-year mean annual precipitation (MAP_{30}) at these sites ranges between 160 mm at the lower elevations and 250 mm at the higher elevations. Mean annual temperature (MAT) is 23°C and can range between 5°C to 43°C (US Climate Data; http://www.ncdc.noaa.gov/).

Two semi-arid study washes were located on the Santa Rita Experimental Range near Sahuarita, Arizona in the Santa Cruz River Basin (SS and SR). These were center-of-basin braided unconsolidated sandy channels at 947 and 952 m in elevation. The catchment upstream of SS was 1.7 km^2 and ranged in elevation from 947 to 1,105 m, while the catchment upstream of SR was 18.0 km^2 and ranged in elevation from 952 to 1,748 m. The MAP_{30} ranges between 350 mm at the lower elevations and 570 mm at the higher elevations (PRISM Climate Group, 2013); while MAT is 22°C and can range between 6 and 38°C. These sites were later dropped from litter decomposition and nutrient analyses because these sites were established later and hence timing of litter deployment was offset from the rest of the sites, although soil and nutrient data are available in Lohse et al. (2020b). These two sites will not be discussed hereafter.

Nine other study sites were located on the Huachuca Mountains at the Fort Huachuca Army Post and Nature Conservancy Ramsey Canyon Preserve near Sierra Vista, Arizona; these catchments drain into the San Pedro River Basin. The study sites were located in three canyons at three distinct elevations in each canyon: Huachuca Canyon (H), Garden Canyons (G), and Ramsey Canyon (R; **Figure 1C**). The lowest elevation monitoring sites (HP, RP, GP) located at 1,400–1,500 m elevation are piedmont (P), semi-consolidated alluvial channels, and receive 430 to 580 mm MAP. The HP, GP, and RP catchments are the smallest (1.3, 0.5, and 0.3 km^2, respectively), and have stream channel densities similar to those of the alluvial basin sites with values ranging between 2.4 and 6.3 km km^{-2}. GP site was later dropped from the analysis after a fire swept through and burned the study area and litterbags, reducing the total site number to ten. Three lower (L) canyon sites (HL, GL, RL; **Figure 1C**), located at 1,500–1,600 m elevation, are incised streams with non-cohesive alluvial banks; MAP_{30} ranges between 520 and 650 mm. Finally, three upper (U)

canyon sites (HU, GU, RU; **Figure 1C**) are located at 1,600–1,700 m elevation on cohesive bedrock with moderate alluvium present. These upper sites have MAP_{30} ranging from 590 to 750 mm and temperature ranges from 1 to 34°C, with MAT of 17°C.

At each of the study sites, we selected a monitoring stream reach of 200 m in length (**Figure 2**). The catchment upstream of each monitoring stream reach was delineated and characterized using ArcMap 10.2 (ESRI, Redlands, CA). At each reach, we established three cross-sectional transects 100 m apart (0, 100, 200 m) and characterized the channel geometry (Gallo et al., 2020). We established sampling locations at channel, riparian, and upland positions along each of the three transects for measurement of site physical and chemical characteristics, litter decomposition and soil moisture and nutrient dynamics.

Site Physical and Chemical Characteristics

The physical and chemical properties of the <2 mm soils or sediments at all positions were characterized ($n = 99$ total). In brief, we cored soils (0–5 cm depth) in the field, brought them back to the lab, air dried and passed them through a 2 mm sieve. We determined particle size distributions (% sand, % silt, and % clay) and soil texture using a modified pipette method (Gee and Bauder, 1986). We determined water holding capacity (WHC) following methods by Dane et al. (2002). We made a 2:1 water to soil paste and determined soil pH with a probe calibrated using pH 10.01, 7.00, and 4.01 buffer solutions (Thomas, 1996). We measured soil C and N and isotopes of C and N on an Elemental Combustion System 4010 (Costech Analytical Tech, Inc, USA) attached to a Delta V Advantage Mass Spectrometer (Thermo Scientific, Germany) at the Center for Archaeology, Materials, and Applied Spectroscopy at Idaho State University, Pocatello, Idaho. In brief, we dried soils at 55°C for 24–48 h prior to grinding soil. We placed a 20 g soil subsample, which had been picked for roots, into a ball mill grinder and ground the soils until a fine powder was attained. We removed soil inorganic carbon by acid fumigation prior to analysis and then packed samples into 5 × 9 mm tin capsules. We report values for $\delta^{15}N$ in parts per thousand (‰) relative to atmospheric N_2 using the equation: δ (‰) = $[(R_{sample}/R_{std}) - 1] \times 1{,}000$ where R_{sample} = - ratio heavy to light isotope ($^{15}N/^{14}N$) of a sample. We are report values for $\delta^{13}C$ in parts per thousand (‰) relative to the Vienna PeeDee Belemnite standard. Both $\delta^{15}N$ and $\delta^{13}C$ values had an analytical precision of ≤0.2 that was determined from repeated analyses of standard materials. We also collected a separate set of soils from all sites and locations to determine soil bulk density (g cm^{-3}) using a modified version of the excavation method (Grossman and Reinsch, 2002; Gallo et al., 2014). In brief, we excavated the soil mass of an 8 cm diameter circle to 10 cm depth with a trowel. We determined the volume of the void by lining it with a plastic bag and filling it with water. We sieved the soils (<2 mm) collected from this void, dried them for soil moisture, and then weighed them for mass to determine the fraction of fine earth <2 mm. Particle density was assumed to be 2.65 g/cm^3. Fine and coarse fractions were determined from bulk density sampling.

Precipitation and Streamflow and Water Presence

To classify site climatic and flow conditions, we measured precipitation using the nearest, established tipping bucket rainfall gauges, streamflow presence using an electrical resistance (ER) sensor method described by Jaeger and Olden (2012) and determined soil-water presence using an ER sensor method by Gallo et al. (2020). In brief, we installed electrical resistance sensors (TidbiT v2 UTBI-001 data logger, Onset Corporation, Bourne, MA) at the thalweg of each cross-sectional transect to identify surface water presence frequency and duration. The ER sensors were modified as outlined in Blasch et al. (2002), with 2 electrical leads exposed to identify the onset and cessation of runoff, where the onset of runoff was marked by the sudden and rapid increase in the relative electrical conductivity (EC) signal to a less negative or a positive number. The termination of streamflow was marked by a similarly sudden shift in the EC signal back to a more negative signal. In contrast to the streamflow presence signal, the surface water presence signal had a distinct inflection point that marked a shift from a steep EC signal recession to a less steep EC signal recession. Because it was difficult to distinguish EC signals indicating water ponding versus soil moisture presence, we defined all EC signals indicative of water presence, including streamflow, as "water presence." Given that we were interested in identifying maximum length of time that water might be present in the stream either as ponded water, shallow soil water or streamflow available for biological activity, we used the maximum percent (%) water $presence_{transect}$ observed at each monitoring reach as the reach % water presence. We identified five distinct streamflow regime classes: dry-ephemeral, wet-ephemeral, dry-intermittent, wet-intermittent, and seasonally-intermittent groups (Gallo et al., 2020). Here we report cumulative precipitation, and monthly and cumulative streamflow and water-presence associated with date of litterbag collection; data are available in Lohse et al. (2020a).

Litter Decomposition

To test the influence of climatic and flow variables on decomposition, litter quality and quantity was held constant across sites. Given that streams are transitioning from wetter to drier flow regimes, we collected litter at the wettest site, upper Ramsey Canyon (RU) and deployed them at each site across all positions. At RU, we collected senesced oak (*Quercus grisea*) leaves as oak woodlands with conifers dominate the upper canyons in this region (Stromberg et al., 2015; Corman et al., 2016); we also collected a smaller subset of senesced Arizona sycamore (*Platanus wrightii)* leaves. Litter was collected in separate plastic bags, brought back to the lab, and dried at 40°C to obtain a constant water weight prior to packing. We note that mean average summer temperatures ranged from 32–42°C across sites so that drying at 40°C was not outside of the extremes. Nylon mesh litterbags (10 × 15 cm, 1 mm nylon mesh) were packed with 4 g dried leaf material. Every 35th bag was packed and then transferred to a pre-dried envelope for

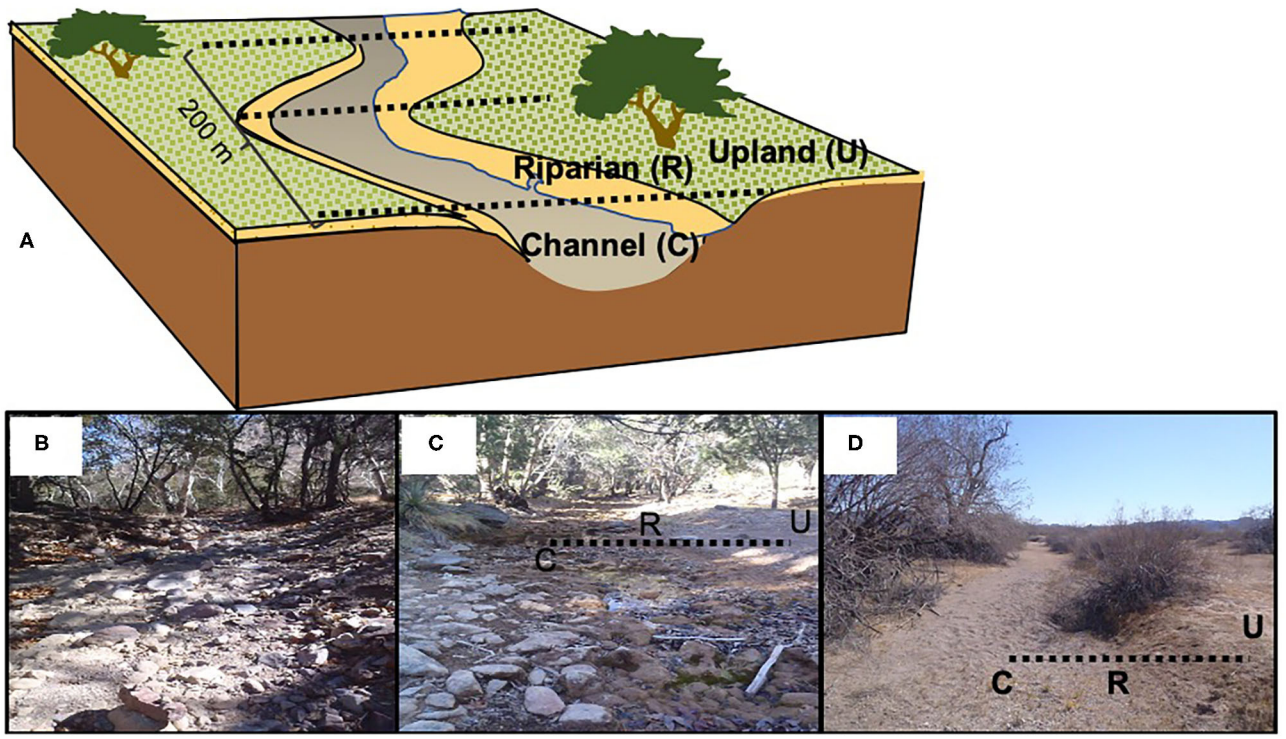

FIGURE 2 | (A) Study site design with location of monitoring stream transects and associated channel, riparian, and upland position. Examples of channel, riparian and upland positions at **(B)** HU, Huachuca Upper Canyon; **(C)** GL, Garden Lower; and **(D)** BG, Barry Goldwater.

wet-dry correction and initial chemical analysis where samples were dried to 55°C. Initial carbon (C) and nitrogen (N) contents were determined on a Fisons NA-1500 elemental analyzer (Fison Instruments, Milan, Italy). Initial litter C:*N*-values for oak were 32.2 ± 0.55 and for sycamore 85.7 ± 9.4 (mean ± standard error (SE).

On 10 January 2010, we placed nine randomly selected oak litterbags in each position x transect x site combination (upland, riparian, and channel positions, 3 transects, 10 sites for 810 total). Only one replicate per site for sycamore was deployed due to limited litter material (nine litter bags per landscape position, 27 per site, 288 total). We do not focus on this litter type hereafter except to note that decomposition rates of sycamore were slightly lower than oak but did not differ significantly within the channels (Stromberg et al., 2015). All litterbags were collected at time 0, 1 day, 4 weeks, 3, 6, 12, and 18 months. Following collection from the field, litter was cleaned to remove residual soil, dried at 55°C for 12–24 h and then weighed. Litter samples were ground to a fine powder (pass through no. 40 sieve) and stored in vials. Ash free dry mass (AFDM) was determined on 1.0 g of homogenized subsample by combusting it at 450°C for four hours and reweighing the mass after combustion. Another subsample of the ground litter was analyzed for C and N content by packing 6.0 mg of ground litter into tin capsules and analyzing it on the elemental analyzer. Oak and sycamore litter data are available in Lohse et al. (2020a).

Soil Moisture and Nutrient Dynamics

To evaluate possible moisture and biological controls on rates of decomposition, we monitored seasonal soil moisture and soil exchangeable mineral N pools and transformation rates using both soil extractions and incubations, wet up experiments, as well as *in-situ* ion exchange resins bags. Specifically, surface soils from each position were collected from 0–5 cm depth during winter/spring (January–March), pre-monsoon (May–June) and post-monsoon (August–September) seasons from June 2010 to September 2012, periods that maximized thermal and hydrologic contrasts (99 samples *per season*). Soils were collected with a core sampler, stored in plastic bags in coolers, returned to the laboratory, and subsampled for analyses. In the lab, we sieved the soils to <2 mm, and then dried one 25 g soil subsample at 105°C to determine gravimetric soil moisture. To determine exchangeable mineral N pools, we extracted a 10 g subsample with 50 ml of 2N potassium chloride (KCl), ammonium (NH_4^+) and nitrate (NO_3^-). To determine rates of net mineralization and nitrification, we incubated another soil subsample under aerobic conditions for 7 days in the dark and estimated rates based on difference between initial and 7-day exchangeable mineral N pools, NH_4^+ plus NO_3^-, and NO_3^- only, respectively (Hart et al., 1994). Finally, we performed wet-up experiments on pre-monsoon dry soils to evaluate the potential rates of nutrient release after monsoon wetting. In brief, we wet soils with 18.2 mOhm water to 60 % WHC moisture conditions, incubated these soils for 7 days in the dark,

extracted them, and analyzed them for exchangeable mineral N pools.

To assess *in-situ* nutrient availability and release in response to seasonal dynamics, we utilized exchange resin bags, which have been shown to be a useful integrator of chemical flux over time (Binkley and Matson, 1983). We deployed two sets of exchange resin bags, one for cations (Dowex 50W−8X; H^+form) and one for anions (Dowex 1–8X; $C1^-$ form). Bags (6 × 5 cm) were constructed on inert silk screen mesh-monopolyester, #85 and filled with 3.0 +/− 0.05 g resin and charged overnight in 2M sodium chloride (NaCl) for anion and 2 M Hydrochloric acid (HCl) for cation bags. One cation and anion exchange resin bag each was placed in the soil at a depth of 3–5-cm along the three transects at each site at the three landscape positions. Resin bags were deployed in upland, riparian and channel positions during the seasonal periods, winter/spring (January–March), pre-monsoon (May–June) and monsoon/post-monsoon (August–September) to contrast thermal and hydrologic contrasts as above. Bags were retrieved at the end of each period, and new bags of both cation and anion exchange resins were deployed in the same positions. In the lab, resin bags were washed free of soil using 18.2 mOhm water. The resins were then placed in centrifuge tubes for extraction in 0.5 M NaCl (40 ml) for anions and 2 M NaCl in 0.1 M HCl for cations. Extracts for NH_4^+ and NO_3^- in associated matrices (KCl, NaCl, NaCl in HCl) were analyzed on a SmartChem discrete autospectrophotometer (DA) (Unity Scientific Instruments, Inc., Brookfield, CT) at Idaho State University. We used a salicylate method (AMM-003-A) to analyze for NH_4^+ as N (hereafter referred to as NH_4^+) and a nitrate reduction method with a cadmium metal column (NO3-001-A) to analyze for NO_3^- as N (hereafter referred to as NO_3^-). We also report resin and soil soluble reactive phosphorus data in Lohse et al. (2020b).

Statistical Analyses

Statistical analyses were performed in JMP 11 (SAS, Carey, NJ). Changes in mass remaining, where litter AFDM at time (t) (M_t) is divided by the initial AFDM (M_0) (M_t/M_0), litter N remaining as percent, soil moisture, and nutrient dynamics were analyzed using repeated measures ANOVA. Loss of litterbags downstream in several channel positions (HU, GU) resulted in an unbalanced design and precluded statistical comparisons among sites and locations on 18-month time periods so that analyses for litter were performed up to 12 months. Flow regime (F) and landscape position (P) were considered main effects with interaction terms. Welch's ANOVA were used for main effects tests where variances were unequal. *Post-hoc* Tukey tests were performed to determine significant differences among flow regimes. Decay constants (k) were generated from regressions where the natural log transformation of M_t/M_0 was plotted against time since deployment (up to 18 months). Step-wise multiple linear regression models were performed to evaluate possible climate, streamflow condition, and nutrient availability controls on the decay rates (k, d^{-1}), in the absence of variation in litter quality and quantity as a common litter from the wettest site (RU) was deployed across

TABLE 1 | Soil physiochemical characteristics including soil bulk density (BD) (<2 mm), percent (%) sand, silt, and clay %, water holding capacity (WHC) as %, and soil carbon (C) and nitrogen (N) %, and C/N of channel, riparian, and upland positions across flow regimes.

Flow regime	Position	Soil BD (g/cm^3)	% Sand	% Silt	% Clay	Soil pH	WHC (%)	Soil C (%)	Soil N (%)	Soil C/N
Dry-ephemeral	Channel	2.00 ± 0.16^{a}	93.10 ± 1.3^{a}	4.5 ± 0.7^{d}	2.4 ± 0.7^{c}	8.20 ± 0.12^{a}	20.5 ± 1.0^{d}	0.34 ± 0.12^{e}	0.04 ± 0.01^{c}	7.0 ± 1.31
(BG, SW, HP)	Riparian	1.27 ± 0.05^{b}	75.4 ± 2.8^{cd}	19.8 ± 2.4^{ab}	4.8 ± 1.0^{abc}	7.64 ± 0.20^{ab}	26.6 ± 1.5^{cd}	0.91 ± 0.07^{de}	0.08 ± 0.01^{c}	10.7 ± 0.5
	Upland	1.24 ± 0.06^{b}	70.5 ± 1.9^{d}	23.3 ± 1.8^{a}	6.2 ± 1.2^{abc}	7.42 ± 0.25^{ab}	29.4 ± 2.0^{bcd}	1.04 ± 0.26^{de}	0.09 ± 0.01^{c}	11.0 ± 0.7
Wet-ephemeral	Channel	1.40 ± 0.12^{b}	90.3 ± 5.0^{abc}	8.1 ± 5.1^{bcd}	1.6 ± 0.2^{bc}	7.27 ± 0.37^{ab}	30.3 ± 5.3^{bcd}	1.19 ± 0.49^{de}	0.07 ± 0.02^{bc}	13.4 ± 5.7
(RL, RP)	Riparian	1.02 ± 0.08^{b}	76.6 ± 2.9^{bcd}	17.6 ± 1.7^{abc}	5.8 ± 1.2^{abc}	6.89 ± 0.39^{b}	45.9 ± 11.1^{abc}	3.13 ± 2.04^{bcde}	0.22 ± 0.07^{bc}	14.1 ± 1.4
	Upland	1.16 ± 0.10^{b}	76.7 ± 2.5^{bcd}	18.1 ± 2.1^{abc}	5.2 ± 0.6^{abc}	6.94 ± 0.31^{b}	39.7 ± 8.5^{abcd}	4.19 ± 3.28^{bcde}	0.25 ± 0.11^{bc}	14.2 ± 1.8
Dry-intermittent	Channel	1.48 ± 0.09^{ab}	93.4 ± 1.4^{ab}	5.0 ± 0.3^{cd}	1.7 ± 0.2^{abc}	8.43 ± 0.10^{a}	23.8 ± 1.3^{cd}	1.23 ± 0.70^{cde}	0.03 ± 0.00^{c}	34.7 ± 16.8
(GL, HU)	Riparian	1.03 ± 0.07^{b}	66.7 ± 6.5^{d}	25.6 ± 5.3^{a}	7.8 ± 1.2^{ab}	7.83 ± 0.16^{ab}	44.3 ± 5.0^{abc}	5.22 ± 0.37^{abcd}	0.25 ± 0.08^{bc}	27.1 ± 5.6
	Upland	1.16 ± 0.09^{b}	68.2 ± 6.0^{d}	23.8 ± 4.5^{a}	8.0 ± 1.7^{a}	7.68 ± 0.28^{ab}	42.5 ± 5.3^{abc}	5.77 ± 0.48^{abc}	0.32 ± 0.07^{ab}	18.3 ± 3.4
Wet-intermittent	Channel	1.27 ± 0.20^{b}	90.2 ± 1.9^{abc}	7.1 ± 1.5^{bcd}	2.8 ± 0.5^{abc}	8.56 ± 0.11^{a}	30.9 ± 4.0^{bcd}	1.88 ± 1.07^{cde}	0.04 ± 0.01^{c}	47.6 ± 18.1
(HL, GU)	Riparian	0.97 ± 0.10^{b}	70.5 ± 3.2^{d}	22.3 ± 2.7^{ab}	7.2 ± 0.9^{abc}	7.94 ± 0.13^{ab}	48.0 ± 5.7^{ab}	8.12 ± 2.21^{ab}	0.32 ± 0.10^{ab}	23.6 ± 0.2
	Upland	0.98 ± 0.12^{b}	73.1 ± 4.9^{cd}	19.8 ± 3.5^{abc}	7.1 ± 1.5^{abc}	7.49 ± 0.32^{ab}	58.0 ± 6.5^{a}	10.17 ± 2.14^{a}	0.52 ± 0.05^{a}	19.1 ± 2.9
Seasonally-intermittent	Channel	1.2 ± 0.2^{b}	88.4 ± 6.0^{abcd}	9.3 ± 5.8^{abcd}	2.3 ± 0.3^{abc}	8.02 ± 0.09^{ab}	36.3 ± 2.2^{abcd}	6.29 ± 1.68^{abcd}	0.37 ± 0.12^{ab}	17.9 ± 5.0
RU	Riparian	0.86 ± 0.10^{b}	66.1 ± 4.8^{d}	25.2 ± 4.1^{ab}	8.7 ± 0.7^{abc}	7.38 ± 0.23^{ab}	61.5 ± 2.1^{a}	2.22 ± 1.91^{bcde}	0.11 ± 0.08^{bc}	13.21 ± 4.0
	Upland	1.08 ± 0.24^{b}	73.5 ± 2.1^{abcd}	19.9 ± 2.2^{abcd}	6.6 ± 0.2^{abc}	7.28 ± 0.26^{ab}	52.2 ± 9.1^{abc}	5.80 ± 2.29^{abcde}	0.37 ± 0.14^{ab}	15.73 ± 4.0

Lowercase letters indicate significant differences based on ANOVA tests ($p < 0.05$).

sites. Transformations were performed to meet assumptions of normality and homoscedascity.

RESULTS

Soil Physical and Chemical Characteristics

Soil physio-chemical characteristics varied significantly with flow regimes and positions (**Table 1**). Soil bulk density (<2 mm fraction) was significantly higher in the dry-ephemeral washes (1.99 ± 0.15 g/cm^3) compared to other positions and flow regimes (range: 0.85–1.64 g/cm^3) ($p < 0.05$). Average sand content was high across sites, ranging from 70 to 94% whereas silt and clay made up a smaller and more variable percentage, 2–26% silt and 1.5–8.7% clay. Percent soil organic carbon (C) was significantly lower in channels than in other positions, and tended to be more similar in riparian and upland positions. Across flow regimes, soil C was lowest in the dry-ephemeral channels and increased substantially in the wet-intermittent to seasonally-perennial channels, 0.3–6.3%. Sediment nitrogen (N) was very low in most of the channel positions (0.03–0.07%) except in the seasonally-perennial channels, where % N was higher, 0.37 %. The upland and riparian soil carbon to nitrogen ratios (C:N) were generally higher than channel sediments, particularly under dry and wet-intermittent conditions where ratios were >40.

Precipitation and Streamflow and Water Presence

Precipitation was bimodal across all sites with higher precipitation with cumulative precipitation ranging from 111 mm at the dry-ephemeral to 516 mm at seasonally-intermittent site over the 18-month (January 2011–June 2012) litter deployment [**Supplementary Figure 1**; also see Gallo et al. (2020) for mean monthly distribution]. All but one group, the seasonally-intermittent flow regime, exhibited a bimodal streamflow similar to that of the regional rainfall (**Figures 3A,B**). Cumulative streamflow days varied dramatically from <1 to 434 days across the sites over the 18-month deployment, representing 0.2–85% of available days (**Figure 3C**). Cumulative daily stream water presence varied from 11 to 433 days, 2.5–85.5 % as annual water presence (**Figure 3D**). The most responsive sites to rainfall in terms of soil-water presence were the dry- and wet-ephemeral sites and had higher observed water presence relative to streamflow compared to the other sites (**Figure 3D**).

Decomposition Dynamics

Litter mass of oak decreased significantly with time across all sites, with landscape position exerting a significant influence on rates of decomposition across sites (**Figure 3**; RMANOVA: flow regime: $F_{4, 75} = 9.28$, $p < 0.0001$; position: $F_{2, 75}$ 74.45, $p < 0.0001$; flow regime*position: $F_{8, 75}$ 9.96, $p < 0.0001$; time: $F_{3, 73}$ 182.28; time*flow regime: $F_{12, 193}$ 3.85, $p < 0.0001$; time*position $F_{6, 146}$ 21.17, $p < 0.0001$ time*position*flow regime; $F_{24, 212} = 3.82$, $p < 0.0001$). Oak litter in upland and riparian positions had >50 % of mass remaining as ash free dry mass at the end of the 18th month deployment and did not differ significantly across sites and flow regimes (**Figures 4A,B**). In contrast, mass loss in the channels differed significantly across sites and flow regimes (**Figure 4C**). Indeed, these differences among flow regime in channels emerged as early as 4 weeks after deployment based on univariate ANOVA and *post-hoc* Tukey tests (**Figure 4C**). In seasonally- and wet-intermittent channels, <20 % of the oak litter mass remained after 18 months compared to other flow regimes that had >50 % remaining, percentages similar to those observed in the upland and riparian positions across sites (**Figure 4C**).

A single exponential decay model fit the oak litter data well (mean r^2 0.9, median 0.94). Oak leaf decay rates (k) ranged from 0.0003 to 0.0054 d^{-1}, and ANOVA and *post-hoc* Tukey tests conducted on channel locations showed that decay rates were significantly higher in channels with seasonally-intermittent compared to dry- and wet-intermittent streamflow and significantly higher than those with ephemeral flow (Welch's ANOVA $F_{4, 9.45}$ 38.17, $p < 0.0001$; **Figure 4D**).

Oak litter N dynamics as measured by percent N remaining varied significantly with flow regime and interactions with time and generally showed net gains of N mass in upland and riparian positions whereas litter in channel positions showed net losses of N mass (**Figure 4**) (RMANOVA: flow regime: $F_{5, 78} = 3.79$, $p = 0.004$; position; $F_{2, 78} = 2.05$, $p = 0.1344$, flow regime*position $F_{10, 78} = 0.56$, $p = 0.84$; time: $F_{3, 76} = 2.49$, $p = 0.06$; time*flow regime; $F_{15, 210} = 2.1$, $p = 0.01$). Specifically, oak litter % N mass remaining increased as much as 20–40% from the initial value of 1.5 ± 0.04% N in the riparian and upland positions, respectively, especially at the wetter sites (**Figures 4E,F**). The exception was the dry-ephemeral sites that showed declines in litter N in the uplands and to a lesser extent, riparian positions. In the channels, the % oak N remaining generally decreased across all flow regimes (**Figure 4G**).

Over the 18-month study period, correlations between % mass remaining and % N remaining differed across landscape positions and were highly variable especially in upland and riparian zones. Litter in upland and riparian positions lost proportionally less N than total mass and yielded weak relationships with slopes less than 1, 0.45 ± 0.35 for the upland and 0.74 ± 0.56 for the riparian position. In contrast, % N remaining was proportional to mass loss in the channel (**Figure 4H**), with a slope of 1.03 ± 0.37.

Environmental Controls on Decomposition in Channels

Given no significant differences in k in riparian and upland positions, a stepwise multiple linear regression was conducted to elucidate environmental controls on the k in channels across flow regimes, and only significant factors with $p < 0.05$ were retained in the model. Results showed that cumulative days of water presence and % silt of the channel bed material explained 80% of the variation in the k in channels across flow regimes (Whole model, $F_{2, 16}$ 28.39, $r^2 = 0.80$, $r^2_{adj} = 0.77$, RMSE = 0.0007, p <0.0001; **Figure 5A**). Log transformed cumulative days of streamflow and water presence days were highly correlated ($r = 0.95$; **Figure 5B**) and the correlation indicated that these terms could possibly be used interchangeably. However, there were more days of water presence compared to streamflow

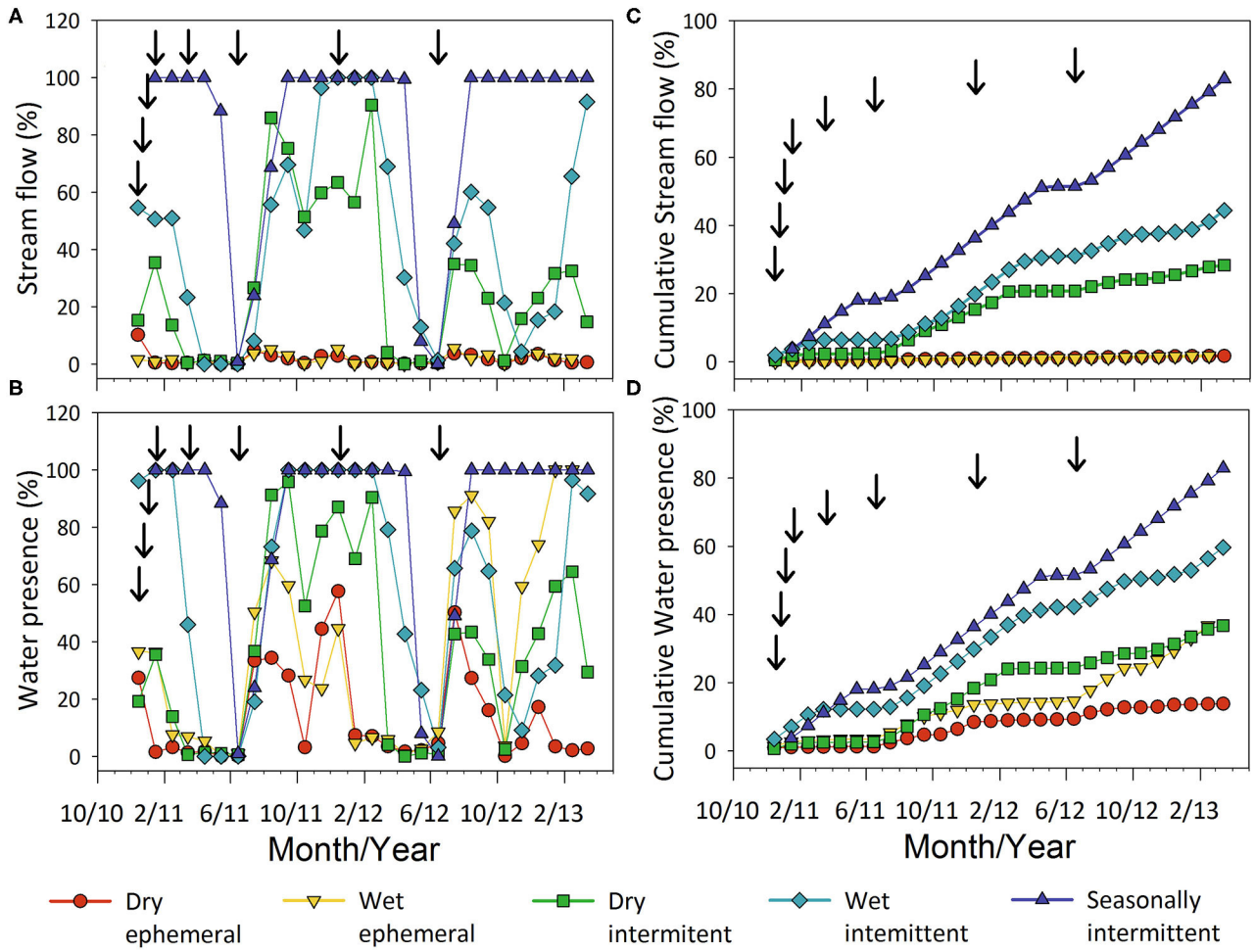

FIGURE 3 | Monthly percent of sites with streamflow and stream water presence at dry-ephemeral (BG, SW, HP, GP), wetephemeral (RP, RL), dry-intermittent (HU, GL), wet-intermittent (HL, GU), seasonally-intermittent (RU) locations. Mean monthly values for each flow regime category are shown in **(A,B)**. Arrows indicate litterbag collections. Cumulative streamflow and water presence percentages as a fraction of the total days over a monitoring periods are show in **(C,D)**.

detected at the dry end of the spectrum of flow regimes (i.e., DE regime), a range of 86 compared to 8.75 days, and therefore cumulative days of water presence was selected as a potentially more sensitive measure of water availability in these systems. Cumulative days of water presence was more normal distributed and thus reduced heteroscedascity in the multiple regression. Cumulative days of water presence alone explained 74% of the variation in decay rates (**Figure 5C**). Cumulative days of stream water presence and streamflow were also modestly correlated to cumulative precipitation (r = 0.62–0.78), but cumulative precipitation did not load in the model. Other biophysical variables considered such as % N remaining, pH, water holding capacity, litter % N, C:N, soil C and N, and soil C:N did not load into the stepwise regression model as significant factors. Lignin and other litter quality characteristics were held constant across all sites because of the common litter source and therefore not considered. Finally, soil temperature was not considered as a main factor in the regression models because site/position specific data were not available.

Soil Moisture and Nutrient Dynamics

Soil moisture dynamics followed stream and soil water presence patterns and varied significantly with flow regime, position, and season (RMANOVA: flow regime: $F_{4, 89} = 35.52$, $p < 0.0001$; position: $F_{2, 84}$ 26.92, $p < 0.0001$; flow regime*position: $F_{8, 89}$ 8.21, $p < 0.0001$; time: $F_{5, 85}$ 37.89, $p < 0.0001$; time*flow regime: $F_{20, 282}$ 6.11, $p < 0.0001$; time*position $F_{10, 170}$ 2.34, $p = 0.003$; time*position*flow regime; $F_{40, 373} = 3.73$, $p < 0.0001$; **Figures 6A–C**). *In-situ* gravimetric soil moisture was 2–6 times higher in the seasonally-intermittent compared to the dry-intermittent to ephemeral stream channels (**Figure 6A**). Soil moisture dynamics were more muted and less variable in the riparian and upland positions but peaked following the

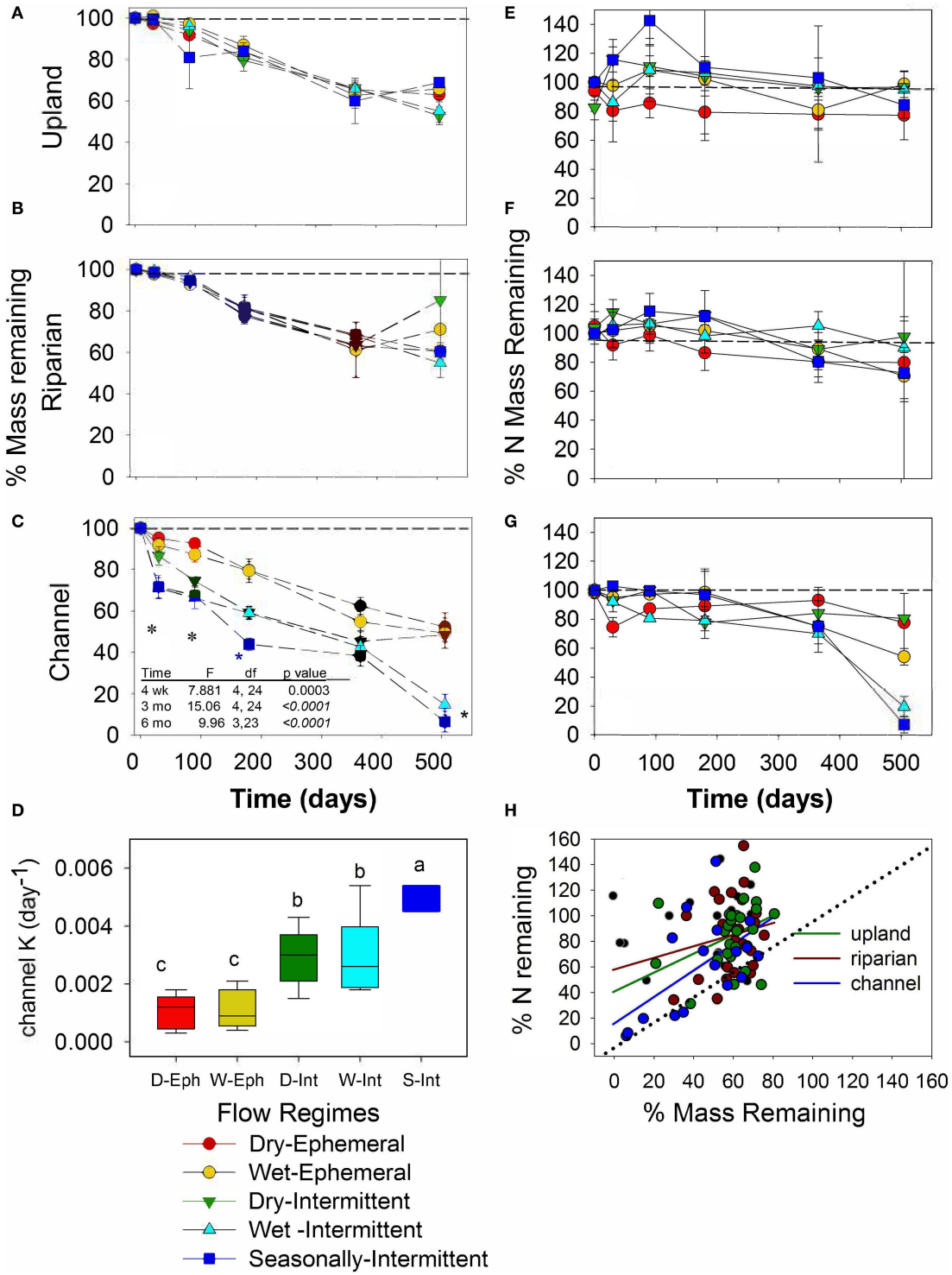

FIGURE 4 | Mass remaining as percent (%) of initial oak litter mass over time (days since deployment) for 10 study sites in the **(A)** upland, **(B)** riparian and **(C)** channel positions, and **(D)** oak leaf decay (*k*) rates shown for the channel position by flow regime (D-Eph, Dry-ephemeral; W-Eph, Wet-Ephemeral; D-Int, Dry-intermittent; W-Int, Wet-Intermittent; and S-Int, Seasonally-Intermittent). Asterisks in **(C)** indicate significant differences in mass loss among sites at different time points as tested with ANOVA and *post-hoc* Tukey tests ($p < 0.05$). Different letters in **(D)** indicate significant differences in decay rate among flow regimes ($p < 0.05$). Mass is expressed in ash free dry mass. Percent N mass remaining of initial oak litter N over time (day since deployment) for the different flow regimes in the **(E)** upland, **(F)** riparian, and **(G)** channel positions. **(H)** Relationship between %N remaining and % mass remaining shows that upland and riparian locations showed net gain while N loss in channel positions was proportional to mass loss.

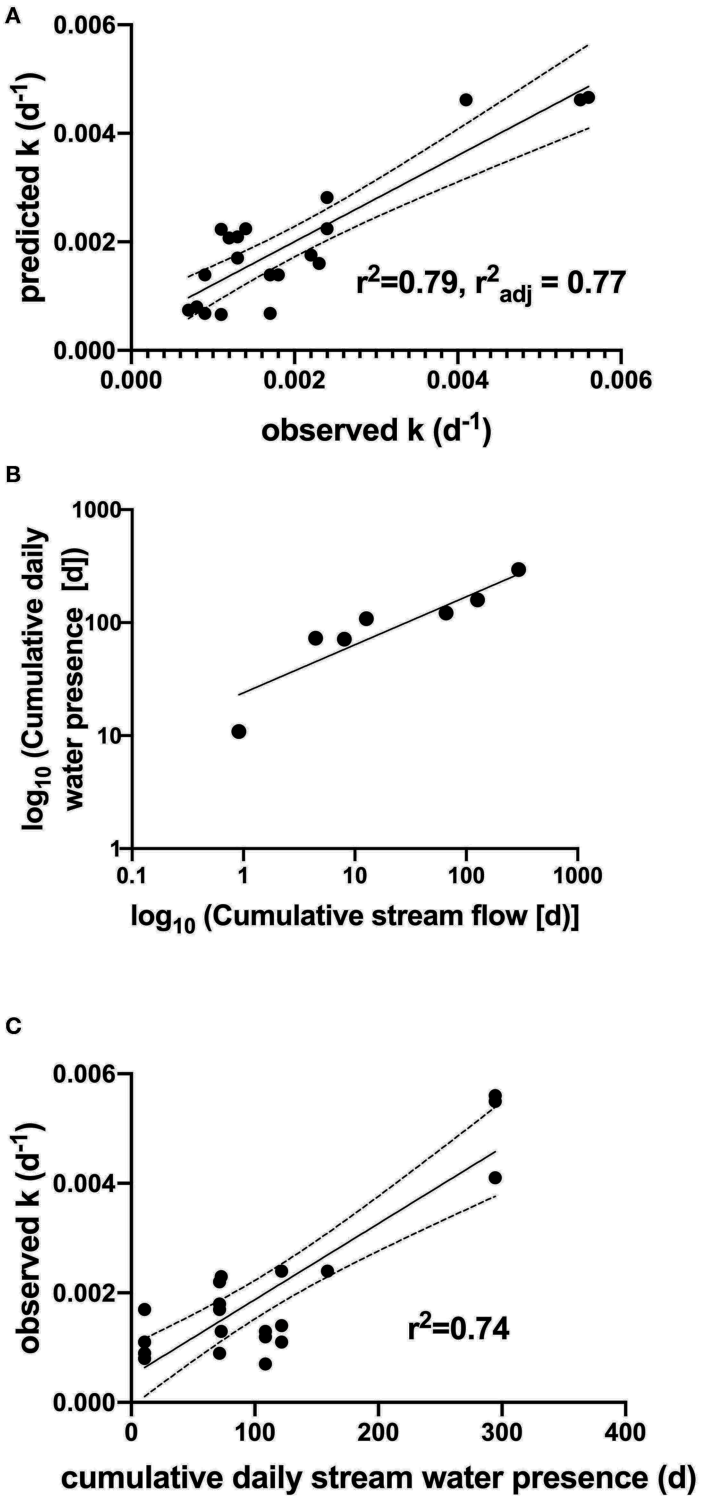

FIGURE 5 | (A) Cumulative daily stream water presence and % silt explain 79% of variation in decomposition rates (d^{-1}) in channels across flow regimes, **(B)** Log transformed cumulative daily stream presence is highly correlated to log transformed cumulative stream water flow days but detects water availability at lower flow conditions, **(C)** cumulative daily stream presence explain 74% of total variation in decomposition rates (*k*).

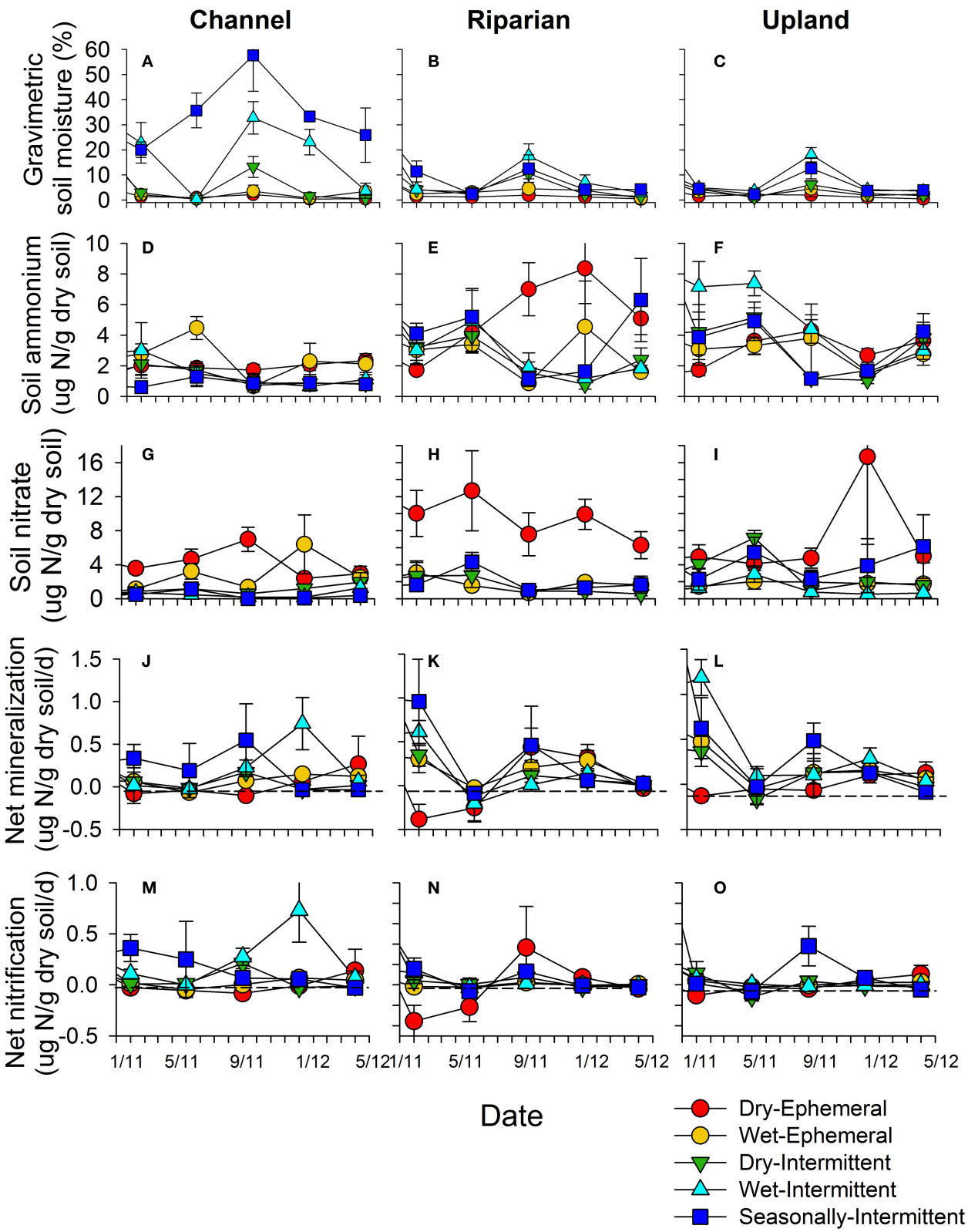

FIGURE 6 | Soil moisture **(A–C)**, ammonium **(D–F)**, and nitrate **(G–I)** pools, and *in-situ* net mineralization **(J–L)** and net nitrification rates **(M–O)** associated with different flow regimes and positions (channel, riparian, and upland) over the course of the decomposition experiment.

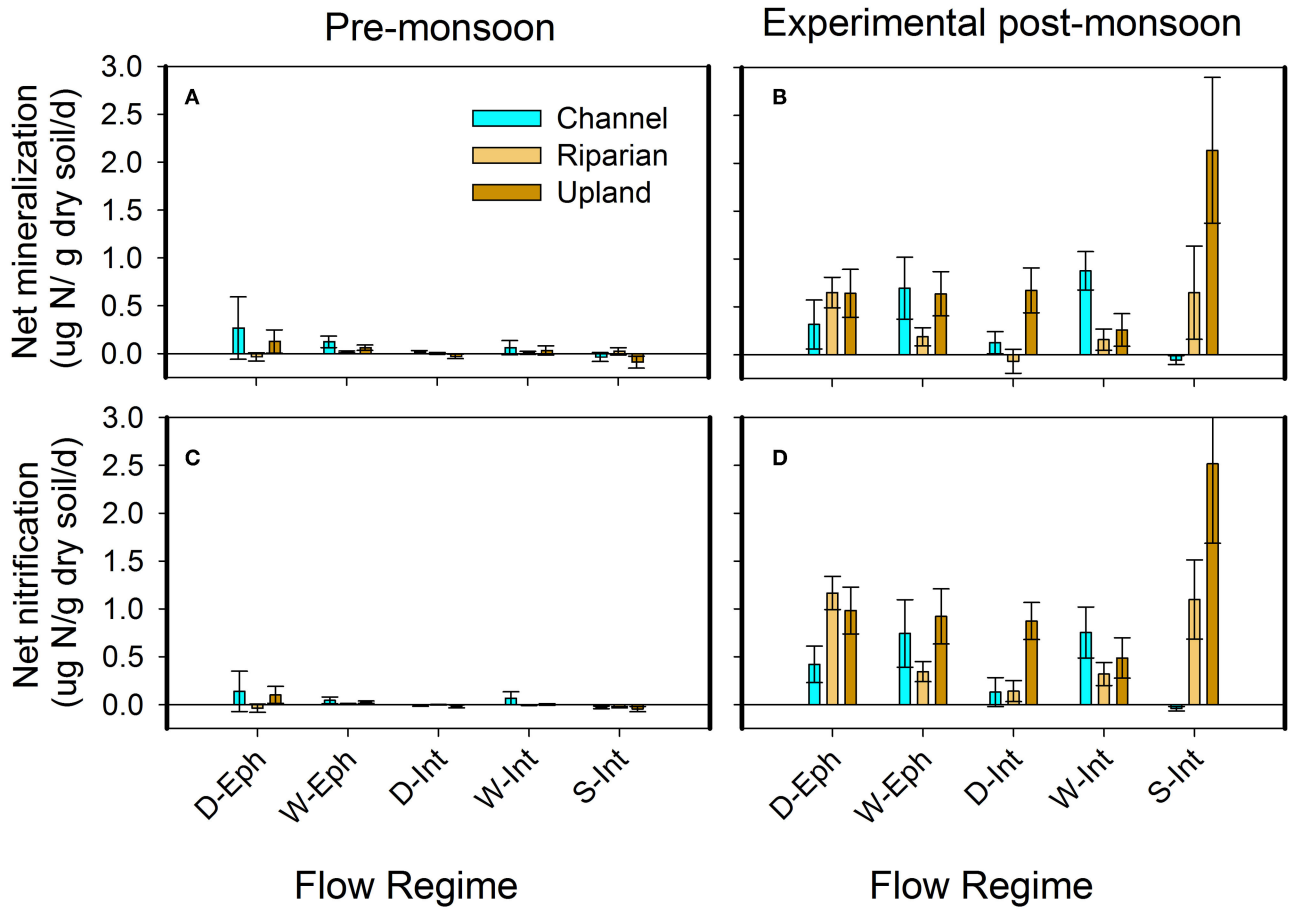

FIGURE 7 | Pre-monsoon rates of net mineralization **(A)**, potential rates of net mineralization in response to experimental wetting **(B)**, pre-monsoon rates of net nitrification **(C)**, and potential rates of net nitrification in response to experimental wetting **(D)** across flow regimes, D-Eph, Dry ephemeral; W-Eph, Wet-ephemeral; D-Int, Dry-intermittent; W-Int, Wet-Intermittent; and S-Int, Seasonally-Intermittent and positions.

monsoon season, especially under seasonally-intermittent and wet-intermittent flow conditions (**Figures 6B,C**).

Soil nitrogen pools and processes also varied significantly with flow regime, position, and season. Soil exchangeable NH_4^+ concentrations varied significantly with time and interactions with flow regime and position (RMANOVA: flow regime: $F_{4, 88} = 0.71$, $p = 0.587$; position: $F_{2, 88}$ 14.59, $p < 0.0001$; flow regime*position: $F_{8, 88}$ 2.425, $p = 0.02$; time: $F_{5, 84}$ 11.09, $p < 0.0001$; time*flow regime: $F_{20, 279}$ 4.05, $p < 0.0001$; time*position $F_{10, 168}$ 2.79, $p = 0.003$; time*position*flow regime; $F_{40, 368} = 1.44$, $p = 0.04$; **Figures 6D–F**). *Post-hoc* ANOVA tests showed that upland and riparian positions were significantly elevated in NH_4^+ compared to channel positions (Welch test: $F_{2, 428}$ 48.75 $p < 0.0001$). In contrast, only flow regime had a significant main effect on soil exchangeable NO_3^- concentrations (RMANOVA: flow regime: $F_{4, 89} = 7.76$, $p < 0.0001$; position: $F_{2, 89}$ 1.08, $p = 0.34$; flow regime*position: $F_{8, 89}$ 0.87, $p = 0.54$; time: $F_{5, 85}$ 1.38, $p = 0.23$). In particular, soil exchangeable NO_3^- was consistently and significantly elevated (4–8 times higher) under dry-ephemeral stream conditions relative to other flow regimes (Welch $F_{4, 254}$ 21.36, $p < 0.0001$; **Figures 6G–I**).

Rates of net mineralization and nitrification were much more variable across space and time, though they were generally positive under seasonally-intermittent flow conditions relative to others indicating nutrient release rather than immobilization (**Figures 6J–L**). In contrast to these field dynamics, controlled laboratory wetting experiments of pre-monsoon soils showed more consistent patterns in rates of N cycling. Indeed, experimental wetting of pre-monsoon soils resulted in 2–5 times higher potential rates of net mineralization and nitrification than pre-monsoon rates across flow regimes (**Figure 7**). The exception to this pattern was the seasonally-intermittent channel sites where rates of potential net mineralization and nitrification were comparable to pre-monsoon conditions (**Figures 6**, **7**).

Nutrient availability and potential loss as measured by resin bags during the monsoon season showed similar patterns as wet up experiments (**Figure 8**). Resin NH_4^+ and NO_3^- concentrations were similarly high across flow regimes in upland and riparian positions following monsoon events. Similar to field data (**Figure 6**), resin NO_3^- was higher in the channel positions in the dry ephemeral sites compared to the wet intermittent and seasonally intermittent sites. Notably,

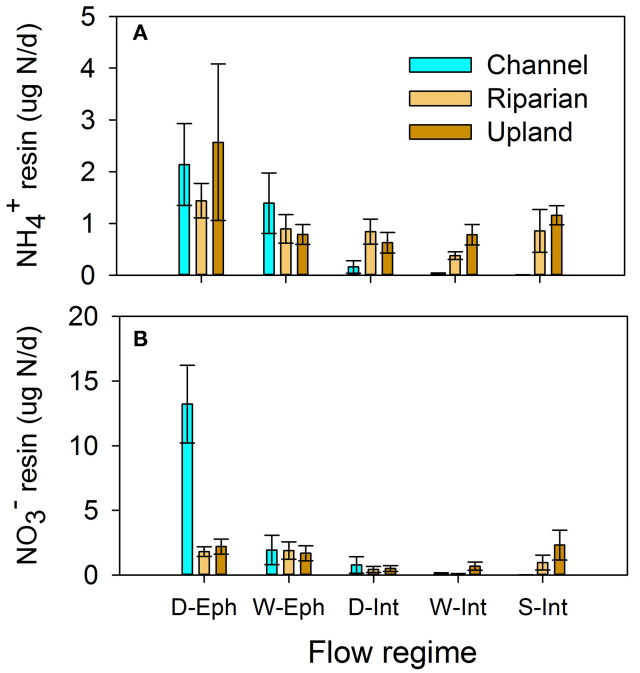

FIGURE 8 | (A) Ammonium and **(B)** nitrate availability as measured by resin bags and normalized by total days deployed during the monsoon across flow regimes, Dry ephemeral (D-Eph), Wet-ephemeral (W-Eph), Dry-intermittent (D-Int), Wet-Intermittent (W-Int), and Seasonally-Intermittent (S-Int), and positions (channel, riparian, and upland).

channel sediments in the wetter sites were low in nutrient availability (**Figure 8**).

DISCUSSION

Higher decomposition rates observed in the seasonally- and wet-intermittent channels were consistent with expectations that mass loss would be higher under more permanent flow regime conditions compared to more temporary flow conditions. Rates of decomposition decreased by a factor of 3–6 with the transition from seasonally- and wet-intermittent to dry-intermittent and ephemeral flow regimes (**Figure 4D**). The few decomposition studies conducted in intermittent or drought-influenced streams have typically focused on one stream and shown similar decreases in rates of decomposition (Anderson and Nelson, 2006; Langhans and Tockner, 2006; Sangiorgio et al., 2007). Sangiorgio et al. (2007), for example, conducted their study in Mediterranean stream channels experiencing drought conditions and showed lower rates of leaf decay in dry compared to wet sites (0.003 compared to 0.006 d^{-1}), rates which are comparable to those reported in this study (range: 0.001 to 0.0054 d^{-1}). Results from our study contrasts with two studies focused in Arizona, USA on short-term decomposition rates of different litter in the aquatic phase of intermittent streams. Specifically, Schade and Fisher (1997) showed faster rates of decomposition (0.017–0.005 d^{-1}) compared to this study, with the lowest rates of decomposition observed in sycamore leaves (0.005 d^{-1}) relative to the ash, cottonwood, and willow leaves. Corman et al. (2016) showed similarly high rates of decomposition of maple (*Acer grandidentatum*) leaves, 0.016–0.003 d^{-1}) in the wet-to seasonally intermittent sites in the Fort Huachuca. These differences among studies may indicate that short-term decomposition studies in temporary streams, particularly intermittent, and ephemeral streams, may overestimate organic matter dynamics and decay rates if only conducted during the aquatic phase. Difference in *k* across studies may also be explained owing to differences in litter type/quality, though a limited subset of sycamore leaves decomposed across these same sites in this study showed no substantial differences in *k* from oak leaves (**Figure 5**, Lohse et al., 2020a).

Faster rates of leaf decay have been typically observed in channels compared to other floodplain positions in perennial streams, similar to our findings. However, these effects often only emerged after 12–18 months (Gurtz and Tate, 1988; Anderson and Nelson, 2006; Langhans and Tockner, 2006; Langhans et al., 2008). In our study, differences in decomposition emerged among positions as early as 4 weeks after deployment and may possibly be explained based on differences in controls on decomposition in intermittent to ephemeral streams. Other global and regional analyses of organic matter and nutrient dynamics in intermittent streams have typically conducted lab incubations and pointed to the importance of rewetting and duration of wetting of litter and sediment in releasing of carbon dioxide (CO_2) and nutrients (Gallo et al., 2014; Datry et al., 2018; Shumilova et al., 2019; Correa-Araneda et al., 2020). These studies have pointed to the need to measure *in situ* decomposition rates and measure the resumption of flow and quantifying different flow regime (Datry et al., 2018). Though limited in scope to dryland regions (MAP, 111–750 mm), we directly measured streamflow duration, water presence, and decomposition rates across a strong climate gradient and held litter quality constant to evaluate these hydroclimatic controls. We found that cumulative days of stream channel water presence and channel bed sediment texture explained 79 % of the variation in *k* across all sites (**Figure 5**). Proportional loss of mass and N (**Figure 4D**) in the channels indicated that physical fragmentation from cumulative duration of streamflow could likely explain much of this variation, but that water presence contributed to explaining slightly more variation in decomposition rates, especially on the dry end of the spectrum. Collectively, our findings indicate that stream water presence may be a more important indicator of ephemeral and intermittent stream function than streamflow alone. This finding warrants further investigation and consideration in other studies.

Our findings that differences in rates of mass loss were only associated with the channel positions, not the upland and riparian positions, were surprising given the wide range of actual precipitation received across flow regimes, 111–516 mm annual precipitation (**Figures 4A–C**). Many upland studies show climate and litter quality as the main factors controlling decomposition rates (e.g., Hobbie, 1992; Couteaux et al., 1995; Aerts, 1997). In this study, we held litter quality constant by transplanting the wettest site litter material across sites. Seminal decomposition studies comparing *k* in different litter types in upland areas show

substantial differences in *k* associated with similar magnitude change in precipitation (∼400 mm) (Melillo et al., 1982). Our results indicate that the subsidy of water in the channels as streamflow and/or soil-water is the main factor driving the increase in rates of decomposition in the seasonally- and wet-intermittent channel sites compared to the dry-intermittent and ephemeral flow regimes rather than climate differences alone. If climate factors were the main factor driving these differences, significantly higher rates of decomposition would have been observed in the riparian and upland positions at the seasonally- and wet-intermittent sites. The lack of difference in *k* in the riparian and upland position despite differences in precipitation could be explained by the comparable soil moisture dynamics observed in the upland and riparian position across flow regimes (**Figure 6**). High sand and silt content across riparian and upland sites (>91 %) and relatively similar water holding capacity (**Table 1**) could also help to explain similar soil moisture dynamics despite differences in precipitation across flow regimes. Finally, similar effective precipitation, the amount of water actually added and stored in the soil, due to significant increases in vegetation volume and richness in the riparian and upland environments with decreasing aridity as shown by Stromberg et al. (2017) may also help to explain lack of difference in soil moisture dynamics. Collectively these findings indicate that rates of decomposition in the terrestrial portions of these landscapes may be less sensitive than channels to declines in precipitation and associated increases in temperature.

Litter quality such as % N and C:N did not emerge as a major factor explaining rates of decomposition. Indeed, the lack of difference in total mass loss among flow regimes in the upland and riparian positions may be explained by net gains of N being immobilized from the surrounding environment (**Figure 4**) indicating possible nutrient limitation to decomposition in these upland environments (Hobbie and Vitousek, 2000). In contrast, channels showed N loss varying in proportion to mass loss indicating that differences in water presence and the physical breakdown or physical abrasion of litter by water were the main factors contributing to differences in rates of decomposition in the channels. As the duration of streamflow decreased from intermittent to ephemeral flow, the importance of the terrestrial phase of the channel increased and N loss decreased such that N loss in ephemeral channels mirrored patterns of N loss in upland and riparian positions (**Figure 4**). Corman et al. (2016) suggested that phosphorus (P) availability may limit decomposition in the same wet-intermittent to seasonally intermittent reaches that we studied where calcium carbonate deposition occurs. However, we observed higher decomposition rates in these sites with low P availability compared to the drier reaches with higher P availability.

Other abiotic factors such as soil coverage/sediment burial (Fritz et al., 2006; Barnes et al., 2012, 2015) and UV degradation (Austin and Vivanco, 2006; Throop and Archer, 2007), as well as biotic factors such as invertebrates (Anderson and Nelson, 2006) and microbial communities associated with the litter (Kaiser et al., 2014) may need further consideration to be able to explain the remaining variation in decomposition rates observed, particularly in the uplands. As mentioned above, lignin was not evaluated because litter quality was held constant in this study, though sycamore leaves decomposed at the same rate as oak leaves in channels suggesting that physical controls were more important than litter quality in these dryland regions. Furthermore, studies have indicated in the past that lignin is not likely associated with inhibiting effects in desert environments (Schaefer et al., 1985). Mesh size (1 mm) in our study likely limited invertebrates attack and therefore breakdown of litter. The role of invertebrates and microbial films/consortium in driving decomposition was beyond the scope of this study and merits further consideration as these processes have been shown to be important in driving decomposition in both the aquatic (Langhans et al., 2008; McCluney and Sabo, 2009; Allen et al., 2014) and terrestrial (Barnes et al., 2012) portions of landscapes. Finally, sediment burial has also been found to slow decomposition rates in intermittent coastal plain streams (Fritz et al., 2006) as well as in dryland upland environments (Barnes et al., 2012, 2015) and may help to explain further variation in decomposition rates given that some of channel litterbags were buried in sediment during the monsoon season.

Soil nutrient dynamics were more variable in space and time across this climate gradient, although patterns emerged especially in the dry ephemeral streams. Specifically, experimental wetting and *in-situ* wetting following monsoon rains resulted in elevated soil nitrate concentrations as extractable nitrate and in resin bags in ephemeral channels. Previous work in ephemeral washes has shown large release of nutrient and gas fluxes following wetting and controlled by sediment texture and associated properties (Gallo et al., 2014). High soil nitrate concentrations observed in our dry ephemeral washes after *in-situ* and experimental wetting were similar to those observed in the sand washes (6.8 ug N/g dry soil) in Gallo et al. (2014). These findings suggest that soil nitrate concentrations and its accumulation may be a good indicator of streams transitioning from intermittent to ephemeral ones. They also point to rapid and large release of trace gases and nutrients following wetting that may not have been previously appreciated from dryland rivers (Marcé et al., 2019) and warrants further study in both natural and urban systems (Gallo et al., 2014).

Collectively, findings from this study indicate that decomposition and nutrient release in stream channels are tightly coupled to streamflow and water presence, and controls on these processes will reach a tipping point (Scheffer et al., 2009) as streams move from perennial to intermittent and ephemeral conditions with climate and/or land use change. Our data indicate that transitions to more temporary flow regimes (<40% streamflow) in this region and other dryland regions will result in a regime shift and rapid declines in organic matter processing (**Figure 4**) as well as gradual declines in soil stores of carbon and nutrients (**Table 1**). As such, changes in streamflow permanence associated with climate change may tip the relative importance of controls on decomposition and nutrient dynamics toward terrestrial compared to aquatic ones.

DATA AVAILABILITY STATEMENT

The datasets presented in this study can be found in online repositories. The names of the repository/repositories

and accession number(s) can be found below: Boise State University ScholarWorks doi: 10.18122/boisestate/reynoldscreek/17, doi: 10.18122/boisestate/reynoldscreek/18, doi: 10.18122/reynoldscreek/19.

AUTHOR CONTRIBUTIONS

KL and TM conceived and designed the study. KL performed the research. KL and EG analyzed the data. EG and TM contributed new methods to the paper and KL wrote the paper. All authors reviewed the manuscript.

FUNDING

This study was funded by the Department of Defense Strategic Environmental Research and Development Program (SERDP) project number RC-1726. Partial support to Gallo for analysis and writing was supported by NSF EPSCOR IIA-1301792 and to Lohse by NSF EAR 1331872.

ACKNOWLEDGMENTS

We acknowledge the contributions of Julie Stromberg at Arizona State University who conceived the overall project, assisted with design of the study, and compiled the final report to SERDP (Stromberg et al., 2015). We thank Elizabeth Hatton, Stacy Schwabedissen, Noelle Guernsey at ISU with soil and litter collection and analyses and Hilary Nicholas and Jeff Silvertooth at UA for assistance with soil and hydrology analyses, and Barry M. Goldwater Air Force Base, Fort Huachuca Army Post, and Nature Conservancy Ramsey Canyon Preserve for access to sites.

SUPPLEMENTARY MATERIAL

The Supplementary Material for this article can be found online at: https://www.frontiersin.org/articles/10.3389/frwa.2020.571044/full#supplementary-material

Supplementary Figure 1 | Cumulative precipitation dry-ephemeral [DE] sites (BG, SW, HP, GP), wet-ephemeral (WE) sites (RP, RL), dry-intermittent (DI) sites, (HU, GL), wetintermittent sites (WE) (HL, GU), and seasonally-intermittent (SI) sites (RU) locations since time of litterbag deployment.

REFERENCES

Aerts, R. (1997). Climate, leaf litter chemistry and leaf litter decomposition in terrestrial ecosystems: a triangular relationship. *Oikos* 79, 439–449. doi: 10.2307/3546886

Allen, D. C., McCluney, K. E., Elser, S. R., and Sabo, J. L. (2014). Water as a trophic currency in dryland food webs. *Front. Ecol. Environ.* 12, 156–160. doi: 10.1890/130160

Alley, W. M., Healy, R. W., LaBaugh, J. W., and Reilly, T. E. (2002). Flow and storage in groundwater systems. *Science* 296, 1985–1990. doi: 10.1126/science.1067123

Anderson, D. C., and Nelson, S. M. (2006). Flood pattern and weather determine populus leaf litter breakdown and nitrogen dynamics on a cold desert floodplain. *J. Arid Environ.* 64, 626–650. doi: 10.1016/j.jaridenv.2005.06.022

Arce, M. I., Mendoza-Lera, C., Almagro, M., Catalán, N., Romaní, A. M., Martí, E., et al. (2019). A conceptual framework for understanding the biogeochemistry of dry riverbeds through the lens of soil science. *Earth Sci. Rev.* 188, 441–453. doi: 10.1016/j.earscirev.2018.12.001

Austin, A. T., and Vivanco, L. (2006). Plant litter decomposition in a semi-arid ecosystem controlled by photodegradation. *Nature* 442, 555–558. doi: 10.1038/nature05038

Barnes, P. W., Throop, H. L., Archer, S. R., Breshears, D. D., McCulley, R. L., and Tobler, M. A. (2015). Sunlight and soil–litter mixing: drivers of litter decomposition in drylands. *Prog. Bot.* 76, 273–302. doi: 10.1007/978-3-319-08807-5_11

Barnes, P. W., Throop, H. L., Hewins, D. B., Abbene, M. L., and Archer, S. R. (2012). Soil coverage reduces photodegradation and promotes the development of soil-microbial films on dryland leaf litter. *Ecosystems* 15, 311–321. doi: 10.1007/s10021-011-9511-1

Belnap, J., Welter, J. R., Grimm, N. B., Barger, N., and Ludwig, J. A. (2005). Linkages between microbial and hydrologic processes in arid and semiarid watersheds. *Ecology* 86, 298–307. doi: 10.1890/03-0567

Binkley, D., and Matson, P. (1983). Ion exchange resin bag method for assessing forest soil nitrogen availability. *Soil Sci. Soc. Am. J.* 47, 1050–1052.

Blasch, K. W., Ferre, T. P. A., Christensen, A. H., and Hoffmann, J. P. (2002). New field method to determine streamflow timing using electrical resistance sensors. *Vadose Zone J.* 1, 289–299. doi: 10.2136/vzj2002.2890

Corman, J. R., Moody, E. K., and Elser, J. J. (2016). Calcium carbonate deposition drives nutrient cycling in a calcareous headwater stream. *Ecol. Monogr.* 86, 448–461. doi: 10.1002/ecm.1229

Correa-Araneda, F., Tonin, A. M., Pérez, J., Álvarez, K., López-Rojo, N., Díaz, A., et al. (2020). Extreme climate events can slow down litter breakdown in streams. *Aquat. Sci.* 82:25. doi: 10.1007/s00027-020-0701-9

Couteaux, M. M., Bottner, P., and Berg, B. (1995). Litter decomposition, climate and litter quality. *Trends Ecol. Evol.* 10, 63–66. doi: 10.1016/S0169-5347(00)88978-8

Dane, J. H., Topp, G. C., and Campbell, G. S. (2002). *Methods of Soil Analysis: Physical Methods.* (Madison, WI: SSSA), 721–738.

Datry, T., Corti, R., Claret, C., and Phillippe, M. (2011). Intermittence controls leaf litter breakdown in a French temporary alluvial river: the "drying memory". *Aquat. Sci.* 73, 471–483. doi: 10.1007/s00027-011-0193-8

Datry, T., Foulquier, A., Corti, R., von Schiller, D., Tockner, K., Mendoza-Lera, C., et al. (2018). A global analysis of terrestrial plant litter dynamics in non-perennial waterways. *Nat. Geosci.* 11, 497–503. doi: 10.1038/s41561-018-0134-4

Datry, T., Larned, S. T., and Tockner, K. (2014). Intermittent rivers: a challenge for freshwater ecology. *Bioscience* 64, 229–235. doi: 10.1093/biosci/bit027

Döll, P., and Schmied, H. M. (2012). How is the impact of climate change on river flow regimes related to the impact on mean annual runoff? A global scale analysis. *Environ. Res. Lett.* 7, 14–37. doi: 10.1088/1748-9326/7/1/014037

Fritz, K. M., Feminella, J. W., Colson, C., Lockaby, B. G., Governo, R., and Rummer, R. B. (2006). Biomass and decay rates of roots and detritus in sediments of intermittent Coastal Plain streams. *Hydrobiologia* 556, 265–277. doi: 10.1007/s10750-005-1154-9

Gallo, E. L., Lohse, K. A., Brooks, P. D., Ferlin, C., and Meixner, T. (2014). Physical and biological controls on trace gas fluxes in semi-arid urban ephemeral waterways. *Biogeochemistry* 121, 189–207. doi: 10.1007/s10533-013-9927-0

[Dataset] Gallo, E. L., Meixner, T., Lohse, K. A., and Nicholas, H. (2020). *Dataset for Estimating Surface Water Presence and Streamflow of Ephemeral and Intermittent Streams in Southwest US.* doi: 10.18122/reynoldscreek/19/boisestate

Gee, G. W., and Bauder, J. W. (1986). "Particle-size analysis" in *Methods of Soil Analysis. Part 1 - Physical and Mineralogical Properties*, ed A. Klute (Madison, WI: Soil Science Society of America), 383–411.

Goodrich, D. C., Lane, L. J., Shillito, R. M., Miller, S. N., Syed, K. H., and Woolhiser, D. A. (1997). Linearity of basin response as a function of scale in a semiarid watershed. *Water Resour. Res.* 33, 2951–2965. doi: 10.1029/97WR01422

Goodrich, D. C., Williams, D. G., Unkrich, C. L., Hogan, J. F., Scott, R. L., Hultine, K. R., et al. (2004). "Comparison of methods to estimate ephemeral channel recharge, Walnut Gulch, San Pedro River Basin, Arizona," in *Groundwater Recharge in a Desert Environment: The Southwestern United States*, eds J. F. Hogan, F. M. Phillips, and B. R. Scanlon (New York, NY: Water and Science Application 9, American Geophysical Union), 77–99.

Grossman, R. B., and Reinsch, T. G. (2002). "Bulk density and linear extensibility," in *Methods of Soil Analysis. Part 4. Physical Methods.* eds J.H. Dane, and C. Topp (Madison, WI: Soil Science Society of America), 201–225.

Gurtz, M. E., and Tate, C. M. (1988). Hydrologic influences on leaf decomposition in a channel and adjacent bank of a gallery forest stream. *Am. Midland Nat.* 120, 11–21. doi: 10.2307/2425882

Hart, S. C., Stark, J. M., Davidson, E. A., and Firestone, M. K. (1994). "Nitrogen mineralization, immobilization, and nitrification," in *Methods of Soil Analyses: Biochemical and Microbiological Properties*, ed R. E. A. Weaver (Madison, WI: Soil Science Society of America), 985–1018.

Heilweil, V. M., Solomon, D. K., Perkins, K. S., and Ellett, K. M. (2004). Gas-partitioning tracer test to quantify trapped gas during recharge. *Ground Water* 42, 589–600. doi: 10.1111/j.1745-6584.2004.tb02627.x

Hobbie, S. E. (1992). Effects of plant species on nutrient cycling. *Trends Ecol. Evol.* 7, 336–339. doi: 10.1016/0169-5347(92)90126-V

Hobbie, S. E., and Vitousek, P. M. (2000). Nutrient limitation of decomposition in Hawaiian forests. *Ecology* 81, 1867–1877. doi: 10.1890/0012-9658(2000)081(1867:NLODIH)2.0.CO;2

Jaeger, K. L., and Olden, J. D. (2012). Electrical resistance sensor arrays as a means to quantify longitudinal connectivity of rivers. *River Res. Appl.* 28, 1843–1852. doi: 10.1002/rra.1554

Jaeger, K. L., Olden, J. D., and Pelland, N. A. (2014). Climate change poised to threaten hydrologic connectivity and endemic fishes in dryland streams. *Proc. Natl. Acad. Sci. U.S.A.* 111, 13894–13899. doi: 10.1073/pnas.1320890111

Kaiser, C., Franklin, O., Dieckmann, U., and Richter, A. (2014). Microbial community dynamics alleviate stoichiometric constraints during litter decay. *Ecol. Lett.* 17, 680–690. doi: 10.1111/ele.12269

Lane, L. J. (1983). "Chapter 19: transmission losses," in *SCS National Engineering Handbook*. (Washington, DC: US Gov. Printing Office), 19.11–19.21.

Langhans, S. D., Tiegs, S. D., Gessner, M. O., and Tockner, K. (2008). Leaf-decomposition heterogeneity across a riverine floodplain mosaic. *Aquat. Sci.* 70, 337–346. doi: 10.1007/s00027-008-8062-9

Langhans, S. D., and Tockner, K. (2006). The role of timing, duration, and frequency of inundation in controlling leaf litter decomposition in a river-floodplain ecosystem (Tagliamento, Northeastern Italy). *Oecologia* 147, 501–509. doi: 10.1007/s00442-005-0282-2

Larned, S. T., Datry, T., Arscott, D. B., and Tockner, K. (2010). Emerging concepts in temporary-river ecology. *Freshw. Biol.* 55, 717–738. doi: 10.1111/j.1365-2427.2009.02322.x

Levick, L., Fonseca, J., Goodrich, D., Hernandez, M., Semmens, D., Stromberg, J., et al. (2008). *The Ecological and Hydrological Significance of Ephemeral and Intermittent Streams in the Arid and Semi-arid American Southwest*. Tucson, AZ: US Environmental Protection Agency and USDA/ARS Southwest Watershed Research Center.

Lohse, K. A., Gallo, E. L., and Meixner, T. (2020a). *Dataset on Rates of in-situ Litter Decomposition Across a Range of Ephemeral to Seasonally-Intermittent Stream Reaches and Landscape Positions in Arizona, USA*. Boise, ID: Boise State University Scholarworks.

Lohse, K. A., Gallo, E. L., and Meixner, T. (2020b). *Dataset on Soil Physio-Chemical Properties and Seasonal Moisture and Nutrient Dynamics in Temporary Stream Channels and Contributing Uplands in Arizona, USA*. Boise, ID: Boise State University ScholarWorks.

Marcé, R., Obrador, B., Gómez-Gener, L., Catalán, N., Koschorreck, M., Arce, M. I., et al. (2019). Emissions from dry inland waters are a blind spot in the global carbon cycle. *Earth Sci. Rev.* 188, 240–248. doi: 10.1016/j.earscirev.2018.11.012

McCluney, K. E., and Sabo, J. L. (2009). Water availability directly determines per capita consumption at two trophic levels. *Ecology* 90, 1463–1469. doi: 10.1890/08-1626.1

Melillo, J. M., Aber, J. D., and Muratore, J. F. (1982). Nitrogen and lignin control of hardwood leaf litter decomposition dynamics. *Ecology* 63, 621–626. doi: 10.2307/1936780

Postel, S. L., Daily, G. C., and Ehrlich, P. R. (1996). Human appropriate of renewable fresh water. *Science* 271, 785–787. doi: 10.1126/science.271.5250.785

PRISM Climate Group (2013). *PRISM Climate Data*. Oregon State University. Available online at: http://prism.oregonstate.edu

Reynolds, J. F., Maestre, F. T., Kemp, P. R., Stafford- Smith, D. M., and Lambin, E. (2007). "Natural and human dimensions of land degradation in drylands: causes and consequences," in *Errestrial Ecosystems in a Changing World,* eds *D.P. J. Canadell, L. F. Pitelka* (Berlin*: Springer)*, 247–258.

Sangiorgio, F., Fonnesu, A., and Mancinelli, G. (2007). Effect of drought frequency and other reach characteristics on invertebrate communities and litter breakdown in the intermittent Mediterranean river Pula (Sardinia, Italy). *Int. Rev. Hydrobiol.* 92, 156–172. doi: 10.1002/iroh.200510953

Scanlon, B. R., and Goldsmith, R. S. (1997). Field study of spatial variability in unsaturated flow beneath and adjacent to playas. *Water Resour. Res.* 33, 2239–2252. doi: 10.1029/97WR01332

Scanlon, B. R., Langford, R. P., and Goldsmith, R. S. (1999). Relationship between geomorphic settings and unsaturated flow in an arid setting. *Water Resour. Res.* 35, 983–999. doi: 10.1029/98WR02769

Schade, J., and Fisher, S. G. (1997). Leaf litter in a sonoran desert stream ecosystem. *J. North Am. Benthol. Soc.* 16, 612–626. doi: 10.2307/1468148

Schaefer, D., Steinberger, Y., and Whitford, W. G. (1985). The failure of nitrogen and lignin control of decomposition in a North American desert. *Oecologia* 65, 382–386. doi: 10.1007/BF00378913

Scheffer, M., Bascompte, J., Brock, W. A., Brovkin, V., Carpenter, S. R., Dakos, V., et al. (2009). Early-warning signals for critical transitions. *Nature* 461, 53–59. doi: 10.1038/nature08227

Seager, R., Ting, M. F., Held, I., Kushnir, Y., Lu, J., Vecchi, G., et al. (2007). Model projections of an imminent transition to a more arid climate in southwestern North America. *Science* 316, 1181–1184. doi: 10.1126/science.1139601

Shumilova, O., Zak, D., Datry, T., von Schiller, D., Corti, R., Foulquier, A., et al. (2019). Simulating rewetting events in intermittent rivers and ephemeral streams: a global analysis of leached nutrients and organic matter. *Glob. Chang. Biol.* 25, 1591–1611. doi: 10.1111/gcb.14537

Stanley, E. H., Fisher, S. G., and Grimm, N. B. (1997). Ecosystem expansion and contraction in streams. *Bioscience* 47, 427–435. doi: 10.2307/1313058

Stromberg, J., Gallo, E., Lohse, K., Meixner, T., Moody, E., Sabo, J., et al. (2015). "Structure and function of ephemeral streams in the arid and semiarid Southwest: implications for conservation and management," in *Department of Defense, Strategic Environmental Research and Development Program* (Alexandria, VA).

Stromberg, J., Setaroa, D., Gallo, E., Lohse, K., and Meixner, T. (2017). Riparian vegetation of ephemeral streams. *J. Arid Environ.* 138, 27–37. doi: 10.1016/j.jaridenv.2016.12.004

Tank, J. L., Rosi-Marshall, E. J., Griffiths, N. A., Entrekin, A. A., and Stephen, M. L. (2010). A review of allochthonous organic matter dynamics and metabolism in streams. *J. North Am. Benthol. Soc.* 29, 118–146. doi: 10.1899/08-170.1

Thomas, G. W. (1996). "Soil pH and soil acidity," in *Methods of Soil Analysis-Part 3 Chemical Methods*, eds D. L. Sparks, A. L. Page, P. A. Helmeke, R. H. Loeppert, P. N. Soltanpour, M. A. Tabatabai, C. T. Johnston, and M. E. Summer (Madison, WI: SSSA), 475–490.

Throop, H. L., and Archer, S. R. (2007). Interrelationships among shrub encroachment, land management and leaf litter decomposition in a semi-desert grassland. *Ecol. Appl.* 17, 1809–1823. doi: 10.1890/06-0889.1

U.S. Geological Survey (2008). *National Hydrography Dataset (ver. 2 USGS National Hydrography Dataset)*. Available online at: https://www.usgs.gov/core-science-systems/ngp/national-hydrography/access-national-hydrography-products

Webster, J. R., and Benfield, E. F. (1986). Vascular plant breakdown in freshwater ecosystems. *Annu. Rev. Ecol. Syst.* 17, 567–594. doi: 10.1146/annurev.es.17.110186.003031

Welter, J. R., Fisher, S. G., and Grimm, N. B. (2005). Nitrogen transport and retention in an arid land watershed: influence of storm characteristics on terrestrial-aquatic linkages. *Biogeochemistry* 76, 421–440. doi: 10.1007/s10533-005-6997-7

Conflict of Interest: The authors declare that the research was conducted in the absence of any commercial or financial relationships that could be construed as a potential conflict of interest.

frontiers in Water

ORIGINAL RESEARCH
published: 19 November 2020
doi: 10.3389/frwa.2020.574728

River Microbiome Composition Reflects Macroscale Climatic and Geomorphic Differences in Headwater Streams

Dawn R. URycki[1], Stephen P. Good[1], Byron C. Crump[2], Jessica Chadwick[1] and Gerrad D. Jones[1]*

[1] Department of Biological and Ecological Engineering, Oregon State University, Corvallis, OR, United States, [2] College of Earth, Ocean, and Atmospheric Sciences, Oregon State University, Corvallis, OR, United States

Maintaining the quality and quantity of water resources in light of complex changes in climate, human land use, and ecosystem composition requires detailed understanding of ecohydrologic function within catchments, yet monitoring relevant upstream characteristics can be challenging. In this study, we investigate how variability in riverine microbial communities can be used to monitor the climate, geomorphology, land-cover, and human development of watersheds. We collected streamwater DNA fragments and used 16S rRNA sequencing to profile microbiomes from headwaters to outlets of the Willamette and Deschutes basins, two large watersheds prototypical of the U.S. Pacific Northwest region. In the temperate, north-south oriented Willamette basin, microbial community composition correlated most strongly with geomorphic characteristics (mean Mantel test statistic $r = 0.19$). Percentage of forest and shrublands ($r = 0.34$) and latitude ($r = 0.41$) were among the strongest correlates with microbial community composition. In the arid Deschutes basin, however, climatic characteristics were the most strongly correlated to microbial community composition (e.g., $r = 0.11$). In headwater sub-catchments of both watersheds, microbial community assemblages correlated with catchment-scale climate, geomorphology, and land-cover ($r = 0.46$, 0.38, and 0.28, respectively), but these relationships were weaker downstream. Development-related characteristics were not correlated with microbial community composition in either watershed or in small or large sub-catchments. Our results build on previous work relating streamwater microbiomes to hydrologic regime and demonstrate that microbial DNA in headwater streams additionally reflects the structural configuration of landscapes as well as other natural and anthropogenic processes upstream. Our results offer an encouraging indication that streamwater microbiomes not only carry information about microbial ecology, but also can be useful tools for monitoring multiple upstream watershed characteristics.

Keywords: catchment hydrology, ungauged basins, watershed monitoring, 16S rRNA, microbial diversity, Pacific Northwest, ecohydrology

OPEN ACCESS

Edited by:
Tim Scheibe, Pacific Northwest National Laboratory (DOE), United States

Reviewed by:
Christopher L. Jerde, University of California, Santa Barbara, United States
Raven L. Bier, University of Georgia, United States

****Correspondence:***
Dawn R. URycki
uryckid@oregonstate.edu

Specialty section:
This article was submitted to Water and Critical Zone, a section of the journal Frontiers in Water

Received: *21 June 2020*
Accepted: *08 October 2020*
Published: *19 November 2020*

Citation:
URycki DR, Good SP, Crump BC, Chadwick J and Jones GD (2020) River Microbiome Composition Reflects Macroscale Climatic and Geomorphic Differences in Headwater Streams. Front. Water 2:574728. doi: 10.3389/frwa.2020.574728

INTRODUCTION

Water quality and availability depends on the integrity of water resource systems, which are sensitive to changes in climate (Jiménez Cisneros et al., 2014), human land use (Foley et al., 2005), and ecosystem composition. Climate change is projected to increase drought frequency and reduce surface and groundwater availability in arid regions, and to negatively impact freshwater ecosystems and reduce surface water quality (Delpla et al., 2009; Jiménez Cisneros et al., 2014). It is well-understood that human development and land-use change results in increased surface runoff, eventually leading to larger flooding events and reduced groundwater recharge (e.g., Carter, 1961; Moscrip and Montgomery, 1997; Gregory et al., 2006; Wheater and Evans, 2009). Interactions among these factors exacerbate impacts to water resources (e.g., Feddema et al., 2005; IPCC, 2019), and better tools are needed to diagnose these effects on catchment ecohydrology at local scales.

In watershed catchments lacking sufficient hydrologic data, Seibert and McDonnell (2015) found that key pieces of data collected on short field campaigns (i.e., "soft data") can prove useful for understanding catchment function. Leveraging a source of information-rich soft data could thus prove especially powerful in characterizing ungauged basins. DNA is gaining traction as a valuable source of data across research disciplines. One of the appeals of genetic data is the vast quantity of information (thousands of features or more) that can be extracted with relative ease from a single sample. In addition to falling costs, improved methods of DNA extraction and sequencing, resulting in higher-quality data (Li et al., 2015), have increased the appeal of genetic data for a wider range of applications, including hydrological studies. For instance, Mächler et al. (2019) used environmental DNA (eDNA) released from macro organisms to characterize hydrologic flow paths in an Alpine catchment in Switzerland. Analysis of aquatic DNA in boreal forests has been indicative of key gradients in catchment condition similar to morphologically derived stream macroinvertebrate metrics (Emilson et al., 2017), while similar DNA information has also been used to map landscape-level terrestrial biodiversity (Sales et al., 2020). Sugiyama et al. (2018) found that microbial DNA analysis, coupled with general information about optimal growth conditions of certain microbial groups, revealed information about groundwater flow paths that was not captured with chemical analyses. Microbial communities, or "microbiomes," with their high biodiversity, are hypothesized to hold new clues that traditional hydrologic tracers have not been able to elucidate.

Streamwater microbiomes respond to conditions that are also likely related to biogeochemical cycling and streamflow including nutrient concentrations, pH, and temperature (Fortunato et al., 2013; Read et al., 2015; Savio et al., 2015; Doherty et al., 2017). Given that streamwater microbiomes are composed primarily of microbes that originate in upslope soil and groundwater environments (Crump et al., 2007, 2012; Sorensen et al., 2013; but see Hermans et al., 2019), it follows that these microbiomes could be rich sources of data about hydrologic function and upslope catchment conditions. Beyond potential source variation, the characteristics of how genetic material is transported, retained, and resuspended has been examined for environmental DNA fragments (Jerde et al., 2016; Shogren et al., 2017) as well as for microorganisms themselves (Droppo et al., 2009; Newby et al., 2009), wherein stream water microbial composition is influenced by both abiotic factors (e.g., flow rate, mixing with sediment waters) and biotic factors such as predation, intrinsic cell mobility, and reproduction. Read et al. (2015) found that stream microbiomes were related to upstream hydrology, and Good et al. (2018) employed microbial community composition to characterize flow regimes in a set of large Arctic rivers. Savio et al. (2015) found that stream microbiomes were more strongly correlated with macroscale properties related to catchment hydrology, such as stream length and catchment size, than with water temperature or pH along the length of the Danube River. It is unclear, however, whether and to what extent other macroscale catchment factors may shape the microbial community. Our overarching objective is to employ stream microbiomes to gain insight about watershed conditions and catchment function and how they shape downstream water quality and availability. The first step toward this goal is to understand how watersheds may influence streamwater microbial community composition. In this study, we explored how streamwater microbial community composition, characterized with aquatic DNA fragments, correlates with upstream catchment properties. 16S rRNA gene fragments have been used in microbiology since the 1980s to classify bacterial taxonomy (Kolbert and Persing, 1999), and the 16S rRNA gene is the most widely used phylogenetic marker gene for assessing prokaryotic microbiomes (Goodrich et al., 2014). We isolated and sequenced 16S rRNA collected from streamwater and examined how differences between microbial (bacteria and archaea) communities among catchments were related to differences in catchment characteristics across major watersheds and across spatial scales.

MATERIALS AND METHODS

Watershed and Sub-catchment Characteristics

The Willamette and Deschutes basins, two similarly sized large (Willamette = 29,000 km^2; Deschutes = 27,700 km^2), adjacent watersheds separated by the Cascade Mountains in Oregon, USA were surveyed for variability in streamwater microbial communities. Mean elevation is 560 m in the Willamette Basin and 1,230 m in the Deschutes Basin. The Willamette Basin, on the windward side of the Cascades, receives a mean annual precipitation of 1,640 mm, but the Deschutes Basin on the leeward side receives a mean of just 530 mm annually. Mean annual discharge of the Willamette River (933 m^3/s) is thus much greater than the Deschutes River (165 m^3/s; U.S. Geological Survey, 2016a) at their respective outlets draining into the Columbia River at Oregon's northern border. Temperatures are comparable between the basins (mean annual minimum and maximum temperatures are 4 and 15°C in the Willamette Basin and 0 and 14°C in the Deschutes Basin, respectively). Both basins

exhibit a range of land use, including minimally disturbed upper elevation headwater streams, crop and livestock agriculture, and highly developed urban areas; however the Willamette Basin is more developed overall, with greater percentages of impervious area and low-, medium-, and high-intensity development (**Supplementary Table 1**).

Sub-catchment characteristics for areas upstream of DNA sample collection points throughout the Willamette and Deschutes watersheds were obtained using the StreamStats tool developed by the United States Geological Survey (Ries et al., 2008; U.S. Geological Survey, 2016b). StreamStats is a national map-based web application that allows users to obtain basin boundaries, basin characteristics, and streamflow statistic estimates for gauged or ungauged user-specified sites. StreamStats employs a wide array of digital geospatial raster data layers which are processed through an online geographic information system to define drainage basin characteristics for any location (although available information varies by state). A script was developed using the Python programming language (www.python.org) to obtain all available StreamStats basin characteristics for each of our 61 sampling sites distributed throughout the two watersheds (URycki and Good, 2020a). The program queries the StreamStats Service API for a list of available basin characteristics for a specified state (OR) and the values for those characteristics given the latitude and longitude for each sample location retrieved from an input spreadsheet. The StreamStats Service API outputs a JSON file with the requested data, which our Python script decodes and writes to a csv file containing the list of sites and associated drainage basin characteristics. For this analysis, StreamStats quantities reported in English units were converted to metric.

Our analysis considered 42 macroscale sub-catchment characteristics for a relationship with streamwater microbial communities (**Table 1**). In addition to the StreamStats characteristics, we calculated topographic index and added latitudinal and longitudinal coordinates. From an initial suite of 46 available characteristics for each sample point, we then eliminated all but one of any redundant variables and summed three StreamStats characteristics "MINOR ROADS," "STATE HIGHWAY ROADS," and "MAJOR ROADS" into a new variable "ALL ROADS" (**Supplementary Table 1**). We then grouped remaining variables into four categories: climatic, geomorphic, land-cover, and development characteristics.

DNA Collection and Sequencing

We collected streamwater DNA from a set of 61 sites in the summer of 2017. We sampled 40 sites in the Willamette watershed (25 July−8 August) and 21 sites in the Deschutes watershed (2–4 August; **Figure 1**). Sample sites spanned headwaters and tributaries to the main stem outlet at the bottom of the watershed. Sites were selected to capture the range of land cover, land use, and level of disturbance in each sub-catchment.

Prior to sample collection each day, the plastic collection bucket was washed with antimicrobial soap, soaked for several minutes in a 10% hydrochloric acid bath, and triple rinsed with ultrapure water. Other reusable field equipment, such as collection tubing, was sterilized in an autoclave. Equipment was sample-rinsed prior to each collection and then triple-rinsed with deionized water following each collection.

Streamwater was collected from the approximate center of the waterway. Most samples were collected using a clean 2-gallon bucket lowered with a rope from a bridge. Although it was difficult to standardize collection depth, samples were collected near the surface and care was taken not to disturb the streambed. At very small streams, such as those in HJ Andrews Experimental Forest, samples were collected into a bucket as water exited flumes. At the few sites where either a flume or bridge were not available, a rope and bucket were tossed from the riverbank to the approximate center of the stream and pulled back to shore, again taking care not to disturb the streambed.

DNA samples were filtered and extracted from collected streamwater as described in Crump et al. (2003). Briefly, streamwater was pumped through a 0.2 μm Sterivex-GP filter (Millipore, Billerica, MA, USA) with a peristaltic pump (Geotech Environmental Equipment, Denver, CO, USA) until the filter clogged. DNA preservation/extraction buffer (100 mM Tris, 100 mM NaEDTA, 100 mM phosphate buffer, 1.5 M NaCl, 1% CTAB) was added to the filter with a syringe, and then filters were sealed and stored on dry ice until transferred to a −80°C freezer the same day, where samples were stored until further processing. DNA was isolated using phenol-chloroform extraction and isopropanol precipitation (Zhou et al., 1996; Crump et al., 2003; Amaral-Zettler et al., 2009) and stored at −20°C until amplification.

16S rRNA genes were PCR-amplified with dual-barcoded primers targeting the V4 region (515f GTGCCAGCMGCCGCG GTAA, 806r GGACTACHVGGGTWTCTAAT; Caporaso et al., 2011) that were linked to barcodes and Illumina adapters following Kozich et al. (2013). PCRs of DNA samples and no-template negative controls were run with HotStarTaq DNA Polymerase Master Mix (Qiagen) and thermocycler conditions: 3 min at 94°C followed by 30 cycles of 94°C 45 s, 50°C for 60 s, and 72°C for 90 s, followed by 10 min at 72°C (Caporaso et al., 2012). PCR products were purified and normalized with SequalPrep Normalization Plates (Thermo-Fisher), and sequenced with Illumina Miseq V.2 paired end 250 bp sequencing. Sequences were denoised using DADA2 (Callahan et al., 2016) implemented in QIIME2 (Bolyen et al., 2019) using default settings to prepare an abundance table of unique amplified sequences variants (ASVs). Sequences were taxonomically classified with the SILVA 16S rRNA gene database v.132 (Quast et al., 2013), and ASVs were removed if they were classified as chloroplasts or mitochondria, or if they were not classified to the domains Bacteria and Archaea. The dataset was then rarefied to 1,164 sequences per sample prior to calculation of biodiversity metrics. Rarefaction to 1,164 samples resulted in undersampling of some communities, which is not unusual in microbial studies, but allowed for retention of the most samples for the analysis (**Supplementary Figure 1**). Sequences from no-template PCR controls that passed DADA2 quality control represented 6 ASVs that did not appear in the rarefied ASV dataset. In total, DNA was sequenced from 38 samples within the Willamette watershed and 17 from the Deschutes watershed. DNA sequence data is archived under BioProject

TABLE 1 | Mean, standard deviation (SD), and correlation with microbial community similarity (Mantel statistic [*r*]) for statistically significant StreamStats macroscale basin characteristics by watershed and in small (Sm) and large (Lg) sub-catchments across the Willamette (Wil) and Deschutes (Des) watersheds, Oregon, USA.

Characteristic	Wil mean (SD)	Wil r	Des mean (SD)	Des r	All mean (SD)	All r	Sm mean (SD)	Sm r	Lg mean (SD)	Lg r	Description
Geomorphic											
ORREG2 (dimensionless)	10,001 (0)	–	363 (0)	–	7,020 (4,490)	0.31***[a]	7,590 (4,250)	0.62***	6,430 (4,740)	0.04	Oregon Region Number
ELEV (m[b])	693 (326)	0.19	1,480 (214)	0.02	935 (469)	0.26***	925 (491)	0.44***	946 (454)	0.07	Mean basin elevation
DISTANCE (km)	83.01 (50.27)	0.36***	72.20 (55.63)	0.15	104.1 (57.64)	0.24***	81.60 (55.63)	0.41***	116.1 (61.58)	0.02	Great-circle distance between sample sites
MINBELEV (m)	258 (275)	−0.10	1,030 (415)	0.21	498 (483)	0.26***	621 (486)	0.39**	370 (454)	0.11	Minimum basin elevation
BSLOPD (degrees)	16 (6.0)	0.15	6.5 (1.6)	−0.03	13 (7)	0.14	16 (8)	0.38***	11 (5)	0.03	Mean basin slope measured in degrees
LATITUDE (decimal degrees)	44.58 (0.560)	0.41***	44.15 (0.546)	0.12	44.45 (0.586)	0.21**	44.28 (0.516)	0.35***	44.62 (0.614)	0.02	Latitudinal coordinate
ELEVMAX (m)	1,720 (930)	0	2,630 (523)	0.26	2,000 (923)	−0.01	1,500 (704)	0.30*	2,520 (845)	0.10	Maximum basin elevation
OR_HIPERMA (percent)	10.9 (13.3)	0.35**	6.89 (7.04)	−0.02	9.64 (11.8)	0.13	5.44 (10.3)	0.17	14.0 (11.9)	0.07	Percent basin surface area containing high permeability aquifer units as defined in SIR 2008-5126
Climatic											
JANMINTMP (degrees C)	−1.40 (1.26)	0.08	−6.89 (0.758)	0.01	−3.09 (2.80)	0.27**	−2.75 (2.77)	0.55***	−3.45 (2.83)	0.04	Mean minimum January temperature
MINTEMP (degrees C)	3.65 (1.25)	0.09	−1.01 (0.975)	0.06	2.21 (2.47)	0.27***	2.38 (2.56)	0.53***	2.02 (2.39)	0.04	Mean annual minimum air temperature over basin surface area as defined in SIR 2008-5126
JANMAXTMP (degrees C)	6.15 (0.99)	−0.10	2.45 (1.00)	0.00	5.01 (1.99)	0.25**	5.23 (2.25)	0.50***	4.77 (1.68)	0.04	Mean maximum January temperature
JANMINT2K (degrees C)	−0.83 (1.18)	−0.09	−6.46 (0.66)	0.11	−2.57 (2.83)	0.22**	−2.12 (2.70)	0.49***	−3.04 (2.93)	0.02	Mean minimum January temperature from 2K resolution PRISM PRISM 1961–1990 data
MAXTEMP (degrees C)	15.2 (1.1)	−0.08	12.6 (1.8)	0.09	14.4 (1.8)	0.23**	14.5 (2.3)	0.46**	14.3 (1.3)	0.10	Mean annual maximum air temperature over basin area from PRISM 1971–2000 800-m grid
JANAVPRE2K (mm)	264 (41)	0.21	141 (66)	0.13	226 (76)	0.17	250 (57)	0.45***	201 (85)	0.05	Mean January precipitation
PRECIP (mm)	1,860 (339)	0.14	979 (440)	0.16	1,590 (552)	0.13	1800 (449)	0.39***	1,370 (569)	0.03	Mean Annual precipitation
JANMAXT2K (degrees C)	6.34 (1.07)	−0.13	4.08 (1.40)	0.33	5.64 (1.57)	0.24***	5.55 (1.84)	0.33**	5.74 (1.26)	0.12	Mean maximum January temperature from 2K resolution PRISM 1961–1990 data
Land-cover											
SOILPERM (mm per hour)	47.7 (28.0)	−0.05	151 (79.3)	−0.02	79.8 (68.8)	0.22*	77.1 (69.1)	0.38**	82.5 (69.8)	0.07	Average soil permeability
LC11FORSHB (percent)	83 (19)	0.34**	89 (6)	0.01	85 (16)	0.10	90 (14)	0.18	79 (17)	0.02	Percentage of forests and shrub lands, classes 41 to 52, from NLCD 2011

[a] *$p < 0.1$, **$p < 0.05$, ***$p < 0.01$ (Bonferroni-adjusted for multiple comparisons).

[b] *StreamStats quantities obtained in English units were converted to metric.*

Note that only basin characteristics that were significantly correlated with microbial community similarity (Bonferroni-adjusted $p < 0.1$) in at least one group of sub-catchments are presented here (see ***Supplementary Table 2*** *for results of all characteristics).*

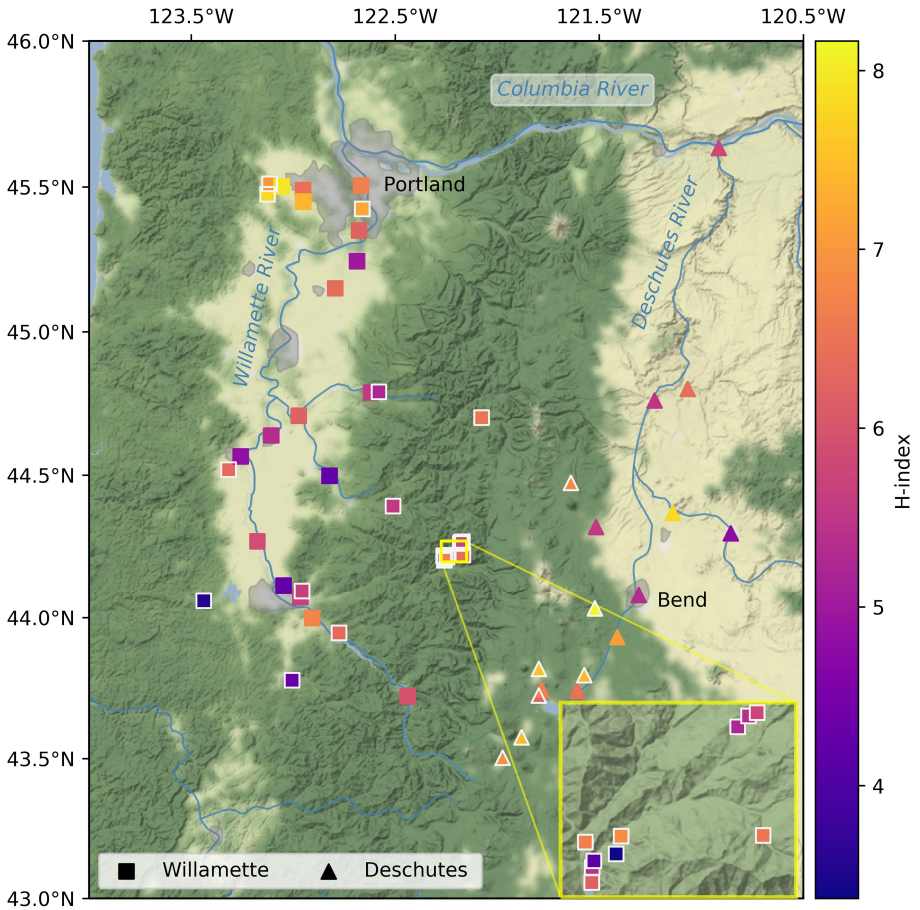

FIGURE 1 | Alpha diversity (Shannon's index [*H*]) of streamwater microbiomes in the Willamette (squares) and Deschutes (triangles) watersheds in Oregon, USA. Outlined symbols indicate small sub-catchments (i.e., those with less than median drainage area). Inset shows vicinity of H.J. Andrews Experimental Forest.

PRJNA642636 at the National Center for Biotechnology Information (NCBI).

Microbial Metrics of Biodiversity

Biodiversity is a fundamental metric used to characterize a microbial community. Alpha diversity describes diversity within a site, whereas beta diversity describes diversity across sites (Whittaker, 1972). Alpha diversity is often described with Shannon's index (*H*), which is the Shannon entropy (Shannon and Weaver, 1949) of measured ASVs within a site. Shannon's index accounts for both the number of ASVs (richness) and the relative abundance of each ASV (evenness). Shannon's index was calculated using the sci-kit bio package (v 0.5.1, http://scikit-bio.org/) developed for the Python programming language. In this implementation, Shannon's index is calculated as

$$H = -\sum_{i=1}^{s} (p_i) \log_2(p_i),$$

where s is the number of ASVs detected and p_i is the proportion of s represented by ASV i. Note that changing the base of the logarithm changes the units of H; when base 2 is used, as here, the resulting quantity is described in units of bits. Larger values of H indicate greater diversity within a site. Diversity data were visually approximately normally distributed, and variance was similar between groups, so two-sample t-tests were used to check for differences in means between groups. Statistical tests were conducted using SciPy in Python 3.7.4 (Virtanen et al., 2020).

Microbial dissimilarity between sites was determined by the Bray-Curtis metric (Bray and Curtis, 1957). Bray-Curtis dissimilarity, $d_{BC}(u, v)$ [unitless], calculates dissimilarity in the number (n) of ASVs between sites u and v as

$$d_{BC}(u, v) = \frac{\sum_i |n_{u,i} - n_{v,i}|}{\sum_i |n_{u,i} + n_{v,i}|}$$

for all ASV i (Bray and Curtis, 1957). Bray-Curtis dissimilarity is more robust than other distance measures like Euclidean distance, for example, where differences in abundance can overwhelm differences in ASVs between sites, leading to counterintuitive results, particularly with large, sparse matrices (Ricotta and Podani, 2017). The denominator of the Bray-Curtis dissimilarity index effectively weights the difference in abundance between sites by the overall abundance of each ASVs, such that rare ASVs contribute less to differences between sites.

Bray-Curtis dissimilarity ranges [0, 1], with a value of one indicating two sites have no ASVs in common and a value of zero indicating identical ASVs composition. The package sci-kit bio was again used to assemble a distance matrix of Bray-Curtis dissimilarity between all possible pairs of sites. Site-pairs were ranked by Bray-Curtis dissimilarity and the top 1% and top 5% most and least dissimilar site-pairs were analyzed to explore whether patterns emerged.

Additionally, we were interested in how relationships between microbial communities and macroscale characteristics might differ between the Willamette and Deschutes watersheds and between small and large sub-catchments. Therefore, distance matrices of Bray-Curtis dissimilarity between all pair of sites in: the Willamette Basin ($n = 38$ sites; 703 unique pairs), the Deschutes Basin ($n = 17$ sites; 136 unique pairs), small sub-catchments ($n = 28$ sites; 378 unique pairs), and large sub-catchments ($n = 27$ sites; 351 unique pairs) were assembled. Note for all 55 sites there were 1,485 unique pairs. Small sub-catchments were simply the smaller half of sample sites (drainage area $\leq$520 km^2) and large sub-catchments were the larger half. Dissimilarity values were skewed low, so to check for differences between groups, a Mann-Whitney U-test, which requires no distribution assumptions, was used. Mann-Whitney U-test assumes independent samples and tests the null hypothesis that the two distributions are equal.

Macroscale Characteristics and Microbial Community Composition

To investigate the relationship between microbial community and macroscale characteristics, differences in microbial community composition were examined in relation to differences in catchment characteristics between sites. Using the basin characteristics from StreamStats, a distance matrix of pairwise differences between sites for each characteristic was assembled. Distances between points (u, v) for StreamStats characteristic c were calculated as absolute value arithmetic differences,

$$d_{SS,c}(u, v) = |c_u - c_v|$$

with the exception of the physical distance between points. The physical distance was the great-circle distance (km), which is the distance between the two points on the surface of a sphere containing the diameter of Earth. As with beta diversity, distances matrices were assembled for all characteristics for all pairs of sites in: the Willamette Basin, the Deschutes Basin, small sub-catchments, large sub-catchments, and all sub-catchments. We used Mantel tests to evaluate the correlation between dissimilarly matrices of community composition and each of the macroscale properties (Mantel, 1967). Mantel correlations assume linear correlations between dissimilarity matrices and have been previously used to evaluate correspondence between microbial communities and other environmental factors (Fagervold et al., 2014; Repert et al., 2014; Read et al., 2015). When applied to raw data tables this approach may introduce bias due to spatial autocorrelation, though extensive testing has found this method is appropriate for evaluation of dissimilarly matrices constructed from autocorrelated data (Legendre et al., 2015). The Mantel statistic is the standardized Pearson correlation between the distance matrices and ranges [−1, 1], with values close to 1 (−1) indicating strong positive (negative) correlation and a value of zero indicating no correlation between the distance matrices. To assess the relationship between microbial community composition and macroscale environment, we examined Mantel statistics between microbial distances $d_{BC}(u, v)$ and individual characteristic distances $d_{SS,c}(u, v)$, as well as mean Mantel statistics for the four groups of related properties: geomorphic, climate, land-cover, and development characteristics. We again used the package sci-kit bio for Python and calculated Mantel statistic (r) and Bonferroni-corrected p-value for multiple comparisons over 10,000 permutations.

We might expect to detect stronger correlations between the microbial community and watershed characteristics when the microbial community samples represent a greater range of conditions. For example, consider the case where catchment characteristics are identical so their standard deviation is zero. Because dissimilarity among catchment characteristics would be zero in this case, correlation between microbial community dissimilarity and catchment dissimilarity (Mantel r) would also necessarily be zero. Thus, as variability in sub-catchment characteristics decreases near to geospatial measurement noise associated with the StreamStats outputs we potentially may see lower Mantel statistics. To explore whether the strength of correlations identified by Mantel tests could be related to variability in those catchment characteristics, we analyzed the relationship between Mantel statistics and the standard deviation of each characteristic. We calculated the relative sensitivity ($\varepsilon_{SS,c}$) [unitless] of the Mantel statistic (r) to the standard deviation (σ) of each StreamStats characteristic (c) as:

$$\varepsilon_{SS,c}(m, n) = \frac{r_m - r_n}{\sigma_m - \sigma_n} \times \frac{\sigma_m}{r_m}$$

The relative sensitivity value quantifies the extent to which a change in variability in a StreamStats characteristics translates to a respective change in the correlation between microbial community composition and that watershed characteristic, where higher absolute values of ε indicate greater sensitivity and a stronger relationship between microbial community similarity and watershed characteristic variability. Values of ε that significantly differ from zero may suggest variability as a potential driver of the strength of correlations and offer insight into the conditions in which microbiomes may be useful monitoring tools. Sensitivity was calculated for each StreamStats variable for both Willamette vs. Deschutes watersheds and small vs. large sub-catchments, and then median sensitivity for each group of characteristics for both sets of sub-catchments was estimated. Sensitivity data contained several outliers and could not be assumed normal. Therefore, the non-parametric one-sample Wilcoxon signed-rank test was used to test the null hypothesis that the median sensitivity value for each group was equal to zero.

Finally, to assess whether and how different ways of grouping sequence data or applying different diversity metrics to characterize the microbial communities impacts the results of

the analysis, the data were reanalyzed several ways. First, rather than using ASVs (100% similar), stream microbial communities were instead characterized by grouping raw sequences into 95%, 97%, or 99% similar operational taxonomic units (OTUs). Sequence data were then rarefied to standardize sampling effort while retaining the greatest number of samples (95% similarity: 1,025 sequences per sample; 97% similarity: 1,023 sequences; 99% similarity: 1,014 sequences). Communities were also alternatively characterized using one of five major groups of ASVs: Actinobacteria (rarefied to 100 sequences per sample), Bacteroidetes (500 sequences), Cyanobacteria (50 sequences), Gammaproteobacteria (500 sequences), or Verrucomicrobia (100 sequences). Two alternative measures of alpha diversity, Chao-1 index of taxonomic diversity and abundance-based coverage estimators (ACE) index, were calculated (also using sci-kit bio). Finally, Weighted UniFrac distances (Lozupone and Knight, 2005) were calculated with QIIME2 as an alternate measure of beta diversity. Unlike the taxon-based Bray-Curtis dissimilarity, divergence-based UniFrac distances (Lozupone and Knight, 2008) consider the similarity of different taxa by incorporating information from a phylogenetic tree relating the genetic sequences from each sample.

All code developed for this analysis is available at www.zenodo.org (URycki and Good, 2020b).

RESULTS

Spatial Patterns in Microbial Community Similarity

We evaluated how 16S rRNA sequence data for 55 DNA samples varied across the Willamette and Deschutes watersheds. Among those samples, 3,530 unique ASVs were detected, including typical freshwater members of the classes Bacteroidetes, Actinobacteria, Verrucomicrobia, and Gammaproteobacteria (which includes Betaproteobacteria; **Figure 2**). Some samples also featured high abundances of Cyanobacteria (up to 28% of community).

Alpha diversity was similar in the Willamette and Deschutes watersheds (Wil: mean $H = 5.81$, SD $= 1.08$; Des: mean $H = 6.58$, SD $= 0.93$; two-sample $t = 2.50$, $p = 0.016$; **Figure 1**) and was not related to the sample volume filtered ($R^2 = 0.04$, $p = 0.76$, **Supplementary Figure 2**). Tributaries exhibited both the highest and lowest biodiversity values in both watersheds. Alpha diversity generally increased from south to north in the Willamette Basin (latitude $R^2 = 0.55$, $p < 0.001$), but this pattern was not observed in the Deschutes Basin (latitude $R^2 = -0.41$, $p > 0.1$; **Figure 3**). Across both watersheds, small and large sub-catchments exhibited similar levels of biodiversity (small sub-catchments: mean $H = 6.09$, SD $= 1.22$, large sub-catchments: mean $H = 6.00$, SD $= 0.95$; two-sample $t = 0.30$, $p = 0.762$), and alpha diversity was not related to sub-catchment drainage area (Willamette: $R^2 = 0.04$, $p = 0.80$; Deschutes: $R^2 = -0.38$, $p = 0.13$; **Supplementary Figure 3**).

The greatest beta diversity in microbial stream communities was observed between watersheds. Bray-Curtis dissimilarity (BC) was higher on average for site-pairs spanning watersheds (mean BC $= 0.912$) than for pairs within watersheds (mean BC $= 0.832$, Mann-Whitney $U = 164584.5$, $p < 0.001$), and the vast majority of the top 5% BC scores were for inter-watershed sample pairs (**Figure 4**). In fact, the most dissimilar pairs (top 1% BC scores) were between points extending from the headwaters of the Deschutes River to the mouth of the Willamette River. A few of the top 5% most dissimilar pairs were points in the same watershed that were geographically distant. Visual inspection reveals no clear patterns between small and large watersheds among the top 5% least similar pairs of samples, and beta diversity was similar within small and large sub-catchments (small: mean BC $= 0.856$, large: 0.875; Mann-Whitney $U = 65169.5$, $p = 0.340$).

Beta diversity was higher within the Willamette Basin (mean BC $= 0.897$) than within the Deschutes Basin (mean BC $= 0.820$; Mann-Whitney $U = 31305.5$, $p < 0.001$). The lowest beta diversity in microbial stream communities (5% lowest BC scores) was observed between samples within in the upper Willamette Basin (**Figure 4**). Points in the HJ Andrews Forest exhibited some of the lowest dissimilarity to other points within the HJ Andrews Forest and to several other points within the Willamette Basin. Also, a few of the lowest dissimilarity scores were between inter-watershed sample pairs, including pairs spanning headwaters of one watershed to the mouth of the other watershed. Almost all of the most similar inter-watershed pairs are samples from large sub-catchments (i.e., points along the mainstem of the rivers).

Relation of Macroscale Catchment Properties to Microbial Community Similarity

Among StreamStats characteristics determined to be statistically significant in at least one group of sub-catchments (**Table 1**), geomorphic-related characteristics were on average the most strongly correlated with microbial community composition in the Willamette Basin (mean $r = 0.19$; **Figure 5**). Land-cover (mean $r = 0.15$) characteristics were more strongly correlated with microbial community composition than climatic (mean $r = 0.01$) characteristics. Among the top five strongest correlates in the Willamette Basin were latitude ($r = 0.41$), percentage of area containing high permeability aquifer units ($r = 0.35$), and percentage of forest and shrublands ($r = 0.34$; **Table 1**). In the Deschutes Basin, climatic (mean $r = 0.11$) characteristics were more strongly correlated with microbial community composition than were geomorphic (mean $r = 0.10$) characteristics. Land-cover characteristics were very weakly anticorrelated (mean $r = -0.01$; **Figure 5**). Among the top five strongest correlates with the microbial community in the Deschutes Basin were mean maximum January temperature ($r = 0.33$), percentage of low-intensity development ($r = 0.30$), topographic index ($r = 0.33$), and topographic relief ($r = 0.29$), although none of these were statistically significant (all $p > 0.1$; **Table 1**, **Supplementary Table 2**). No development-related characteristics were found to be correlated with microbial community similarity in the Willamette or Deschutes watersheds.

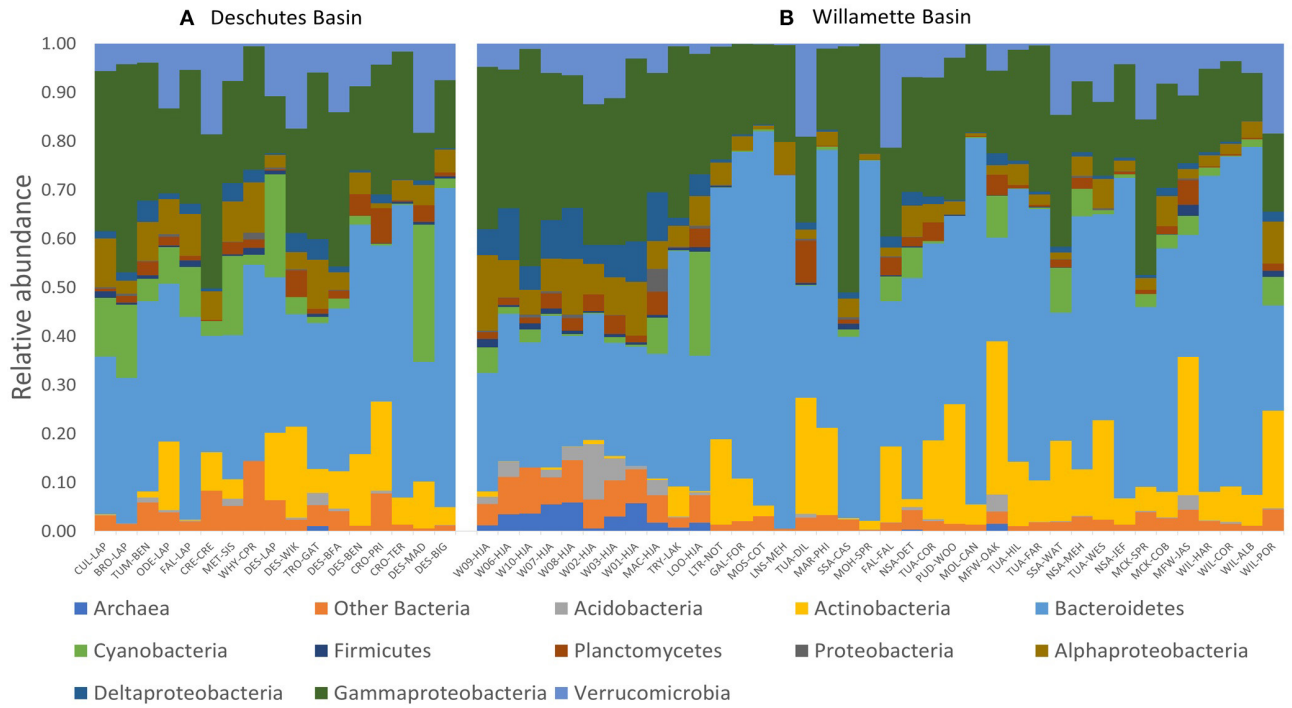

FIGURE 2 | Phylogenetic biodiversity (relative abundance of unique amplified sequences variants [ASVs]) of tributary and main-stem streamwater microbial DNA samples throughout the **(A)** Deschutes and **(B)** Willamette watersheds in Oregon, USA. Samples for each watershed are presented in order of increasing sub-catchment drainage area (**Supplementary Table 1**).

Small sub-catchments exhibited the strongest correlations between macroscale catchment characteristics and microbial community composition. Among StreamStats characteristics determined to be statistically significant in at least one group of sub-catchments (**Table 1**), microbial community composition in small sub-catchments correlated most strongly with climatic characteristics (mean $r = 0.46$), followed by geomorphic (mean $r = 0.38$), and land-cover (mean $r = 0.28$; **Figure 5**) characteristics. The most strongly correlated characteristics were watershed identifier (Willamette or Deschutes; $r = 0.62$), January minimum temperature ($r = 0.55$), and annual minimum temperature ($r = 0.53$; **Table 1**). Microbial community composition in large sub-catchments exhibited much weaker correlations. Mean maximum January temperature ($r = 0.12$), minimum basin elevation ($r = 0.10$), and mean annual maximum temperature ($r = 0.10$) were among the top five strongest correlates with microbial community similarity, although none of these were statistically significant (all $p > 0.1$). No development-related characteristics were found to be statistically correlated with microbial community similarity in small or large watersheds.

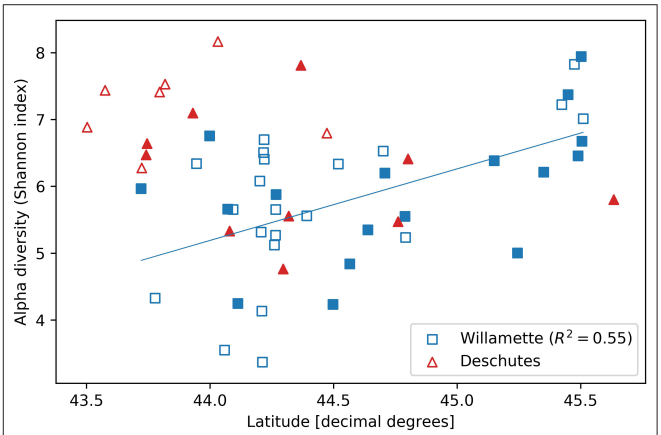

FIGURE 3 | Alpha diversity (Shannon index) vs. latitudinal coordinate of streamwater microbial DNA samples collected from small (unfilled symbols) and large (filled symbols) sub-catchments throughout the Willamette (squares) and Deschutes (triangles) watersheds in Oregon, USA.

For the macroscale characteristics we analyzed, the strength of the correlation with the microbial community was not sensitive to the variability of those characteristics across catchments. Across all sub-catchment characteristics, an increase in the standard deviation of a characteristic did not translate to a statistically significant increase in Mantel statistic for either the Willamette versus Deschutes watersheds (median $\varepsilon = 0.14$; Wilcoxon signed-rank $W = 76.0$, $p = 0.981$) or for small versus large sub-catchments (median $\varepsilon = -3.40$; Wilcoxon signed-rank $W = 58.0$, $p = 0.381$). Similarly, median sensitivity was not statistically different from zero for any of the characteristic groups for either the Willamette vs. Deschutes

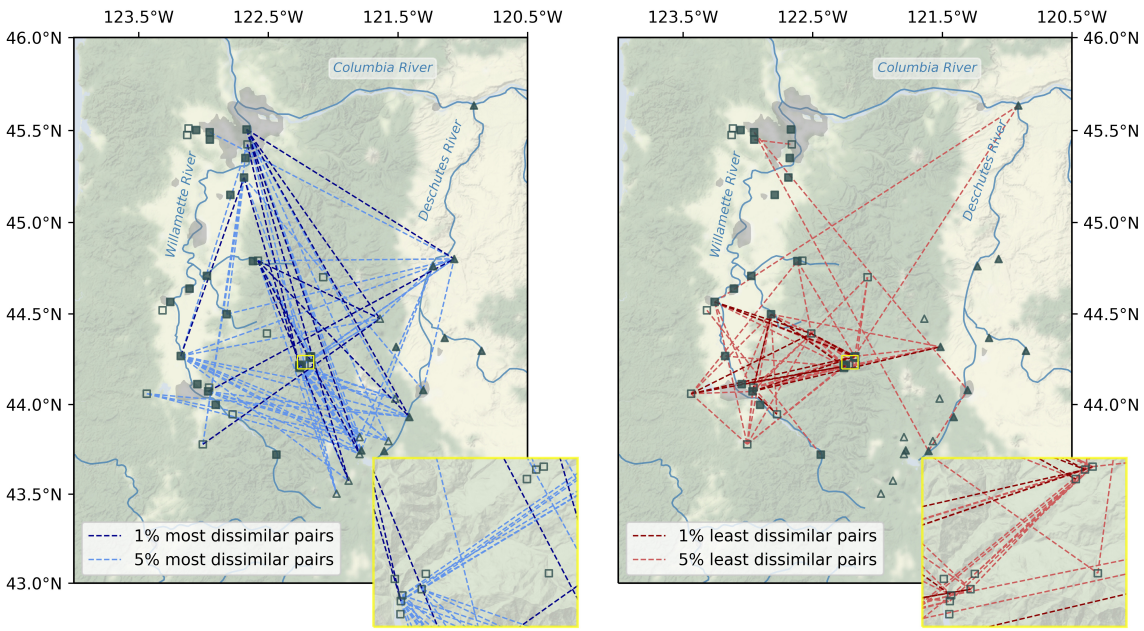

FIGURE 4 | Map of the 1% (dark lines) and 5% (light lines) most (**left**) and least (**right**) dissimilar microbial communities throughout the Willamette and Deschutes watersheds in Oregon, USA. Large (filled symbols) and small (unfilled symbols) sub-catchments are those with more than or less than median drainage area, respectively. Inset shows vicinity of HJ Andrews Experimental Forest.

watersheds or for small vs. large sub-catchments (all Wilcoxon signed-rank $p > 0.1$).

Patterns were consistent when sequence data were grouped into OTUs or when different diversity metrics were applied. The strongest relationships between microbial communities and watershed characteristics were observed in small watersheds at all OTU sequence similarity levels (95%, 97%, 99%, or 100%) and for three major taxonomic groups: Bacteroidetes, Gammaproteobacteria, and Verrucomicrobia (**Supplementary Figure 4**). The microbial groups Actinobacteria and Cyanobacteria exhibited no significant correlations with watershed characteristics. The strongest relationships were observed between microbial communities and geomorphic and climatic related characteristics, although some microbial groups were also related to land cover characteristics (**Supplementary Figure 4**). The Chao-1 and ACE alpha diversity metrics were strongly correlated with Shannon index (Chao-1: Spearman $r = 0.91$, $p << 0.001$; ACE: Spearman $r = 0.90$, $p << 0.001$). Characterizing community similarity using Weighted UniFrac instead of Bray-Curtis dissimilarity also resulted in strong correlations with watershed characteristics in small watersheds. Also, some microbial groups exhibited comparably strong relationships to watershed characteristics in the Willamette and Deschutes watersheds (**Supplementary Figure 5**).

DISCUSSION

We explored the potential influence of the upstream macroscale environment in shaping streamwater microbiomes. Previous studies found that streamwater microbial community composition is more strongly correlated with catchment-scale hydrologic parameters such as stream distance and catchment area than with water sample physio-chemical water properties (Read et al., 2015; Savio et al., 2015). Our study builds on this previous work by expanding the suite of macroscale variables analyzed for relationships with the microbial community assemblage to more than 40 basin characteristics reflecting the geomorphology, climate, land cover, and level of human development in stream catchments.

Our results suggest that, in headwater catchments, microbial community assemblages are shaped by catchment-scale geomorphology and climate, but these influences weaken downstream. The streamwater microbial metacommunity is "seeded" from a diverse amalgamation of microbes dispersed into headwater streams from surrounding soil and groundwater (Crump et al., 2007, 2012), which develops and continually combines with local inputs as the community moves downstream with the flow of water (Ruiz-González et al., 2015). In headwater streams in particular, where the contributing area is large relative to the stream volume (Read et al., 2015; Savio et al., 2015), it follows that this immigrant microbial community would reflect the dispersal area and upslope environment and thus exhibit a stronger correlation with macroscale catchment characteristics. Downstream, however, biotic and abiotic factors increasingly drive ecological succession (i.e., species-sorting; Leibold et al., 2004), and the microbial assemblage shifts to a core riverine community, dampening signals from the upstream catchment (Savio et al., 2015).

The shift from diverse communities of upslope emigrants that are tightly coupled to the catchment to a core riverine community shaped by the local environment may explain the decreasing

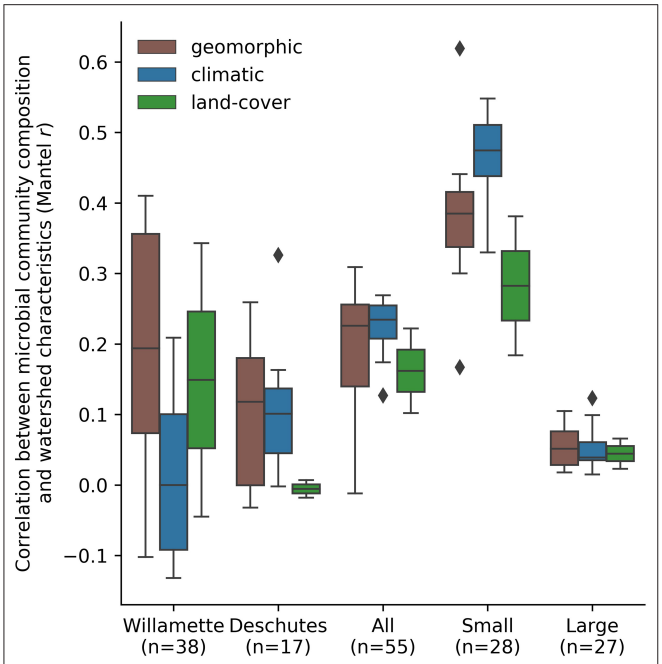

FIGURE 5 | Mean correlation between microbial community composition (Mantel test statistic [*r*]) and land-cover, geomorphic, and climatic related StreamStats basin characteristics by watershed and in small and large sub-catchments across the Willamette and Deschutes watersheds, Oregon, USA.

strength of the relationship between microbial community composition and macroscale watershed characteristics. This is supported by the low overall sensitivity of the correlations to variability in sub-catchment characteristics moving from upstream to downstream, in that moving to more (or less) variable sub-catchment characteristics did not result in higher (or lower) correlations uniformly. Since sensitivity values were distributed between both positive and negative values and not statistically different than zero, we conclude that changes in the homogeneity of the landscape across which samples are collected, as measured by the standard deviation of landscape characteristics, is not uniformly the driving processes determining differences in microbial composition.

Watershed location in either the Willamette or Deschutes basins was the strongest correlate with the microbial community across all basins and within small basins, indicating that there are additional factors shaping distinctive microbial communities in each basin. In the temperate, more developed Willamette Basin, latitude and the percentage of forest and shrub land and were most important characteristics. Due to the north-south orientation of these basins, latitude is likely a proxy for multiple other interacting factors (e.g., elevation and up-stream drainage area), and the Willamette Basin in particular has a strong human-driven gradient due to Portland at the outlet. On the other hand, in the Deschutes Basin, geomorphic characteristics such as topographic index and relief were more important. It is possible that the differences in important influences on streamwater microbial communities between basins is related to basin hydrology and the nature of the inputs to the stream. In the wetter, more crop-dominated landscape of the Willamette Basin, more constant, stable inputs of water—and thus microbes—may contribute to the development of a certain, less diverse community than in the arid, less populated Deschutes Basin, where flashier water inputs result in more variable contributing areas and a different, more diverse streamwater microbial community (Nippgen et al., 2015).

We note that, as with many scientific analyses, our results are a product of the decisions made throughout the analysis. Decisions about DNA extraction methods and sequencing depth may have impacted our results. Some catchment characteristics obtained from StreamStats that were considered redundant were eliminated from analysis (see **Supplementary Table 1**), but correlation among variables was not explored. Eliminating correlated variables may have yielded different results, as could have applying different significance criteria. On the other hand, results were robust to the similarity of ASV groups. When ASVs were grouped into operational taxonomic units (OTUs) based on 95%, 97%, or 99% DNA sequence similarity, the relative strength and importance of characteristic categories and of spatial scale were generally stable (**Supplementary Figure 4**). Although some major microbial groups (e.g., classes Bacteroidetes, Gammaproteobacteria, Verrucomicrobia) exhibited stronger relationships with watershed characteristics than other groups, we are not aware of any method that would allow for reliable targeted sampling or analysis effort in such a way as to appreciably conserve resources. Our results build upon those of Good et al. (2018), in which streamwater microbiomes were used in a machine learning algorithm to predict hydrologic regime of a set of large rivers in adjacent and detached watersheds in the Arctic. Here, we found that the summer microbial community within small headwater streams reflects both the structural configuration of the landscape as well as upstream processes. Coupled with the results of Good et al. (2018), our results offer an encouraging indication that streamwater microbial DNA may thus carry information about upstream macroscale conditions as well as hydrology and may therefore hold potential as a useful tool in watershed monitoring. More research is needed to determine whether these relationships hold in other seasons and how to optimally extract this information from microbiomes.

DATA AVAILABILITY STATEMENT

The datasets generated for this study can be found in the Sequence Read Archive at the National Center for Biotechnology Information (NCBI; https://www.ncbi.nlm.nih.gov/sra/PRJNA642636).

AUTHOR CONTRIBUTIONS

SG conceived the study, produced the original code, and reviewed the manuscript. DU collected the data, contributed to the data analysis, and prepared the manuscript and figures. JC contributed to sample and data analysis. BC contributed sample analysis and reviewed the manuscript. GJ contributed to data collection and reviewed the manuscript. SG and BC secured funding for this

research. All authors contributed to the article and approved the submitted version.

FUNDING

This work was supported by the National Science Foundation grant EAR 1836768. DU would like to acknowledge STEM Scholarship support from NSF grant #1153490.

ACKNOWLEDGMENTS

We conducted part of this research at HJ Andrews Experimental Forest, which was funded by the US Forest Service, Pacific Northwest Research Station. We gratefully acknowledge the efforts of the many graduate and undergraduate students who generously contributed many long hours of lab and field work. We additionally thank Associate Editor TS and two reviewers for their helpful, constructive reviews, which improved this manuscript.

SUPPLEMENTARY MATERIAL

The Supplementary Material for this article can be found online at: https://www.frontiersin.org/articles/10.3389/frwa.2020.574728/full#supplementary-material

REFERENCES

Amaral-Zettler, L. A., McCliment, E. A., Ducklow, H. W., and Huse, S. M. (2009). A method for studying protistan diversity using massively parallel sequencing of V9 hypervariable regions of small-subunit ribosomal RNA genes. *PLoS ONE* 4:e6372. doi: 10.1371/annotation/50c43133-0df5-4b8b-8975-8cc37d4f2f26

Bolyen, E., Rideout, J. R., Dillon, M. R., Bokulich, N. A., Abnet, C. C., Al-Ghalith, G. A., et al. (2019). Reproducible, interactive, scalable and extensible microbiome data science using QIIME 2. *Nat. Biotechnol.* 37, 852–857. doi: 10.1038/s41587-019-0209-9

Bray, J. R., and Curtis, J. T. (1957). An ordination of the upland forest communities of southern wisconsin. *Ecol. Monogr.* 27, 325–349. doi: 10.2307/1942268

Callahan, B. J., McMurdie, P. J., Rosen, M. J., Han, A. W., Johnson, A. J. A., and Holmes, S. P. (2016). DADA2: high-resolution sample inference from illumina amplicon data. *Nat. Methods* 13, 581–583. doi: 10.1038/nmeth.3869

Caporaso, J. G., Lauber, C. L., Walters, W. A., Berg-Lyons, D., Huntley, J., Fierer, N., et al. (2012). Ultra-high-throughput microbial community analysis on the illumina HiSeq and MiSeq platforms. *ISME J.* 6, 1621–1624. doi: 10.1038/ismej.2012.8

Caporaso, J. G., Lauber, C. L., Walters, W. A., Berg-Lyons, D., Lozupone, C. A., Turnbaugh, P. J., et al. (2011). Global patterns of 16S rRNA diversity at a depth of millions of sequences per sample. *Proc. Natl. Acad. Sci. U.S.A.* 108, 4516–4522. doi: 10.1073/pnas.1000080107

Carter, R. W. (1961). Magnitude and frequency of floods in suburban areas. *US Geol. Survey Profess. Pap* 424, 9–11.

Crump, B. C., Adams, H. E., Hobbie, J. E., and Kling, G. W. (2007). Biogeography of bacterioplankton in lakes and streams of an arctic tundra catchment. *Ecology* 88, 1365–1378. doi: 10.1890/06-0387

Crump, B. C., Amaral-Zettler, L. A., and Kling, G. W. (2012). Microbial diversity in arctic freshwaters is structured by inoculation of microbes from soils. *ISME J.* 6, 1629–1639. doi: 10.1038/ismej.2012.9

Crump, B. C., Kling, G. W., Bahr, M., and Hobbie, J. E. (2003). Bacterioplankton community shifts in an arctic lake correlate with seasonal changes in organic matter source. *Appl. Environ. Microbiol.* 69, 2253–2268. doi: 10.1128/AEM.69.4.2253-2268.2003

Delpla, I., Jung, A. V., Baures, E., Clement, M., and Thomas, O. (2009). Impacts of climate change on surface water quality in relation to drinking water production. *Environ. Int.* 35, 1225–1233. doi: 10.1016/j.envint.2009.07.001

Doherty, M., Yager, P. L., Moran, M. A., Coles, V. J., Fortunato, C. S., Krusche, A. V., et al. (2017). Bacterial biogeography across the amazon river-ocean continuum. *Front. Microbiol.* 8:882. doi: 10.3389/fmicb.2017.00882

Droppo, I. G., Liss, S. N., Williams, D., Nelson, T., Jaskot, C., and Trapp, B. (2009). Dynamic existence of waterborne pathogens within river sediment compartments. Implications for water quality regulatory affairs. *Environ. Sci. Technol.* 43, 1737–1743. doi: 10.1021/es802321w

Emilson, C. E., Thompson, D. G., Venier, L. A., Porter, T. M., Swystun, T., Chartrand, D., et al. (2017). DNA metabarcoding and morphological macroinvertebrate metrics reveal the same changes in boreal watersheds across an environmental gradient. *Sci. Rep.* 7:12777. doi: 10.1038/s41598-017-13157-x

Fagervold, S. K., Bourgeois, S., Pruski, A. M., Charles, F., Kerhervé, P., Vétion, G., et al. (2014). River organic matter shapes microbial communities in the sediment of the rhône prodelta. *ISME J.* 8, 2327–2338. doi: 10.1038/ismej.2014.86

Feddema, J. J., Oleson, K. W., Bonan, G. B., Mearns, L. O., Buja, L. E., Meehl, G. A., et al. (2005). The importance of land-cover change in simulating future climates. *Science* 310, 1674–8. doi: 10.1126/science.1118160

Foley, J. A., DeFries, R., Asner, G. P., Barford, C., Bonan, G., Carpenter, S. R., et al. (2005). Global consequences of land use. *Science* 309, 570–574. doi: 10.1126/science.1111772

Fortunato, C. S., Eiler, A., Herfort, L., Needoba, J. A., Peterson, T. D., and Crump, B. C. (2013). Determining indicator taxa across spatial and seasonal gradients in the Columbia river coastal margin. *ISME J.* 7, 1899–1911. doi: 10.1038/ismej.2013.79

Good, S. P., URycki, D. R., and Crump, B. C. (2018). Predicting hydrologic function with aquatic gene fragments. *Water Resour. Res.* 54, 2424–2435. doi: 10.1002/2017WR021974

Goodrich, J. K., Di Rienzi, S. C., Poole, A. C., Koren, O., Walters, W. A., Caporaso, J. G., et al. (2014). Conducting a microbiome study. *Cell* 158, 250–262. doi: 10.1016/j.cell.2014.06.037

Gregory, J. H., Dukes, M. D., Jones, P. H., and Miller, G. L. (2006). Effect of urban soil compaction on infiltration rate. *J. Soil Water Conserv.* 61, 117–124.

Hermans, S. M., Buckley, H. L., Case, B. S., and Lear, G. (2019). Connecting through space and time: catchment-scale distributions of bacteria in soil, stream water and sediment. *Environ. Microbiol.* 22, 1000–1010. doi: 10.1111/1462-2920.14792

IPCC (2019). *Climate Change and Land: An IPCC Special Report on Climate Change, Desertification, Land Degradation, Sustainable Land Management, Food Security, and Greenhouse Gas Fluxes in Terrestrial Ecosystems*, eds P. R. Shukla, J. Skea, E. Calvo Buendia, V. Masson-Delmotte, H.-O. Pörtner, D. C. Roberts.

Jerde, C. L., Olds, B. P., Shogren, A. J., Andruszkiewicz, E. A., Mahon, A. R., Bolster, D., et al. (2016). Influence of stream bottom substrate on retention and transport of vertebrate environmental DNA. *Environ. Sci. Technol.* 50, 8770–8779. doi: 10.1021/acs.est.6b01761

Jiménez Cisneros, B. E., Oki, T., Arnell, N. W., Benito, J. G., Cogley, P., Döll, T., et al. (2014). "Freshwater resources" in *Climate Change 2014: Impacts, Adaptation, and Vulnerability. Part A: Global and Sectoral Aspects. Contribution of Working Group II to the Fifth Assessment Report of the Intergovernmental Panel on Climate Change*, eds C. B. Field, V. R. Barros, D. J. Dokken, K. J. Mach, M. D. Mastrandrea, T. E. Bilir, M. Chatterjee, K. L. Ebi, Y. O. Estrada, R. C. Genova, B. Girma, E. S. Kissel, A. N. Levy, S. MacCracken, P. R. Mastrandrea, and L. L. White (Cambridge, UK; New York, NY: Cambridge University Press), 229–269.

Kolbert, C. P., and Persing, D. H. (1999). Ribosomal DNA sequencing as a tool for identification of bacterial pathogens. *Curr. Opin. Microbiol.* 2, 299–305.

Kozich, J. J., Westcott, S. L., Baxter, N. T., Highlander, S. K., and Schloss, P. D. (2013). Development of a dual-index sequencing strategy and curation pipeline for analyzing amplicon sequence data on the miseq illumina sequencing

platform. *Appl. Environ. Microbiol.* 79, 5112–5120. doi: 10.1128/AEM.01043-13

Legendre, P., Fortin, M., and Borcard, D. (2015). Should the mantel test be used in spatial analysis? *Methods Ecol. Evol.* 6, 1239–1247. doi: 10.1111/2041-210X.12425

Leibold, M. A., Holyoak, M., Mouquet, N., Amarasekare, P., Chase, J. M., Hoopes, M. F., et al. (2004). The metacommunity concept: a framework for multi-scale community ecology. *Ecol. Lett.* 7, 601–613. doi: 10.1111/j.1461-0248.2004.00608.x

Li, P., Yang, S. F., Lv, B. B., Zhao, K., Lin, M. F., Zhou, S., et al. (2015). Comparison of extraction methods of total microbial DNA from freshwater. *Genet. Mol. Res.* 14, 730–738. doi: 10.4238/2015.January.30.16

Lozupone, C., and Knight, R. (2005). UniFrac: a new phylogenetic method for comparing microbial communities. *Appl. Environ. Microbiol.* 71, 8228–8235. doi: 10.1128/AEM.71.12.8228-8235.2005

Lozupone, C. A., and Knight, R. (2008). Species divergence and the measurement of microbial diversity. *FEMS Microbiol. Rev.* 32, 557–578. doi: 10.1111/j.1574-6976.2008.00111.x

Mächler, E., Salyani, A., Walser, J. C., Larsen, A., Schaefli, B., Altermatt, F., et al. (2019). Water tracing with environmental DNA in a high-Alpine catchment. *Hydrol. Earth Syst. Sci. Discuss.* 1–30. doi: 10.5194/hess-2019-551

Mantel, N. (1967). The detection of disease clustering and a generalized regression approach. *Cancer Res.* 27, 209–220.

Moscrip, A. L., and Montgomery, D. R. (1997). Urbanization, flood frequency, and salmon abundance in puget lowland streams. *J. Am. Water Resour. Assoc.* 33, 1289–1297. doi: 10.1111/j.1752-1688.1997.tb03553.x

Newby, D. T., Pepper, I. L., and Maier, R. M. (2009). "Microbial transport," in *Environmental Microbiology*, eds Maier, R. M., Pepper, I. L., and Gerba, C. P. (Amsterdam: Elsevier Inc.), 365–383.

Nippgen, F., Mcglynn, B. L., and Emanuel, R. E. (2015). The spatial and temporal evolution of contributing areas. *Water Resour. Res.* 51, 4550–4573. doi: 10.1002/2014WR016719

Quast, C., Pruesse, E., Yilmaz, P., Gerken, J., Schweer, T., Yarza, P., et al. (2013). The SILVA ribosomal RNA gene database project: improved data processing and web-based tools. *Nucleic Acids Res.* 41:D590. doi: 10.1093/nar/gks1219

Read, D. S., Gweon, H. S., Bowes, M. J., Newbold, L. K., Field, D., Bailey, M. J., et al. (2015). Catchment-scale biogeography of riverine bacterioplankton. *ISME J.* 9, 516–26. doi: 10.1038/ismej.2014.166

Repert, D. A., Underwood, J. C., Smith, R. L., and Song, B. (2014). Nitrogen cycling processes and microbial community composition in bed sediments in the yukon river at pilot station. *J. Geophys. Res. Biogeosci.* 119, 2328–2344. doi: 10.1002/2014JG002707

Ricotta, C., and Podani, J. (2017). On some properties of the bray-curtis dissimilarity and their ecological meaning. *Ecol. Complex.* 31, 201–205. doi: 10.1016/j.ecocom.2017.07.003

Ries, K. G. III, Guthrie, J. D., Rea, A. H., Steeves, P. A., Stewart, D. W. (2008). *StreamStats: A Water Resources Web Application.* Fact Sheet *2008-3067*. U.S. Geological Survey.

Ruiz-González, C., Niño-García, J. P., and del Giorgio, P. A. (2015). Terrestrial origin of bacterial communities in complex boreal freshwater networks. *Ecol. Lett.* 18, 1198–1206. doi: 10.1111/ele.12499

Sales, N. G., McKenzie, M. B., Drake, J., Harper, L. R., Browett, S. S., Coscia, I., et al. (2020). Fishing for mammals: landscape-level monitoring of terrestrial and semi-aquatic communities using eDNA from riverine systems. *J. Appl. Ecol.* 57, 707–716. doi: 10.1111/1365-2664.13592

Savio, D., Sinclair, L., Ijaz, U. Z., Parajka, J., Reischer, G. H., Stadler, P., et al. (2015). Bacterial diversity along a 2600?km river continuum. *Environ. Microbiol.* 17, 4994–5007. doi: 10.1111/1462-2920.12886

Seibert, J., and McDonnell, J. J. (2015). Gauging the ungauged basin: relative value of soft and hard data. *J. Hydrol. Eng.* 20:A4014004. doi: 10.1061/(ASCE)HE.1943-5584.0000861

Shannon, C. E., and Weaver, W. (1949). *The Mathematical Theory of Communication.* Urbana, IL: University of Illinois Press.

Shogren, A. J., Tank, J. L., Andruszkiewicz, E., Olds, B., Mahon, A. R., Jerde, C. L., et al. (2017). Controls on eDNA movement in streams: transport, retention, and resuspension. *Sci. Rep.* 7:5065. doi: 10.1038/s41598-017-05223-1

Sorensen, J. P. R., Maurice, L., Edwards, F. K., Lapworth, D. J., Read, D. S., Allen, D., et al. (2013). Using boreholes as windows into groundwater ecosystems. *PLoS ONE* 8:e70264. doi: 10.1371/journal.pone.0070264

Sugiyama, A., Masuda, S., Nagaosa, K., Tsujimura, M., and Kato, K. (2018). Tracking the direct impact of rainfall on groundwater at Mt. Fuji by multiple analyses including microbial DNA. *Biogeosciences* 15, 721–732. doi: 10.5194/bg-15-721-2018

U.S. Geological Survey (2016a). *National Water Information System Data Available on the World Wide Web (USGS Water Data for the Nation).*

U.S. Geological Survey (2016b). *The StreamStats Program.* Available online at: http://streamstats.usgs.gov (accessed December 4, 2019).

URycki, D. R., and Good, S. P. (2020a). *StreamStats Data Query (Version 1.0.0).* Zenodo. doi: 10.5281/zenodo.3902476

URycki, D. R., and Good, S. P. (2020b). *River Microbiome and Watershed Characteristics Analysis.* Zenodo. doi: 10.5281/zenodo.3902478

Virtanen, P., Gommers, R., Oliphant, T. E., Haberland, M., Reddy, T., Cournapeau, D., et al. (2020). SciPy 1.0: fundamental algorithms for scientific computing in Python. *Nat. Methods* 17, 261–272. doi: 10.1038/s41592-019-0686-2

Wheater, H., and Evans, E. (2009). Land use, water management and future flood risk. *Land Policy* 26, S251–S264. doi: 10.1016/j.landusepol.2009.08.019

Whittaker, R. H. (1972). Evolution and measurement of species diversity. *Taxon* 21, 213–251. doi: 10.2307/1218190

Zhou, J., Bruns, M. A., and Tiedje, J. M. (1996). DNA recovery from soils of diverse composition. *Appl. Environ. Microbiol.* 62, 316–22.

Conflict of Interest: The authors declare that the research was conducted in the absence of any commercial or financial relationships that could be construed as a potential conflict of interest.

frontiers in Water

ORIGINAL RESEARCH
published: 23 November 2020
doi: 10.3389/frwa.2020.551627

Spatial Mapping of Riverbed Grain-Size Distribution Using Machine Learning

Huiying Ren[1], Zhangshuan Hou[1], Zhuoran Duan[1], Xuehang Song[1], William A. Perkins[1], Marshall C. Richmond[1], Evan V. Arntzen[1,2] and Timothy D. Scheibe[3]*

[1] Energy and Environment Directorate, Pacific Northwest National Laboratory, Richland, WA, United States, [2] Environmental Protection and Regulatory Programs, Pacific Northwest National Laboratory, Richland, WA, United States, [3] Environmental Molecular Sciences Laboratory, Pacific Northwest National Laboratory, Richland, WA, United States

Recent alluvial sediments in riverbeds play a significant role in controlling hydrologic exchange flows (HEFs) in river systems. The alluvial layer is usually associated with strong heterogeneity in physical properties (e.g., permeability and hydraulic conductivity), which affects local HEFs and therefore biogeochemical processes. The spatial distribution of these physical properties needs to be determined to inform the numerical models used to reveal the realistic hydro-biogeochemical behaviors. Such information can be obtained based on the intrinsic link between sediment grain-size distribution and hydraulic properties where sediment texture information is available. However, grain-size measurements are usually spatially sparse and do not have adequate coverage and resolution, particularly for a relatively large domain such as the Hanford Reach of the Columbia River. In this paper, we adopted machine learning (ML) approaches for categorizing and mapping the spatial distributions of riverbed substrate grain size and filling in missing areas of substrate data using the ML models along the reach. Such ML models for substrate size mapping were trained at 13,372 locations using measured substrate sizes along with observed and simulated attributes, including bathymetric attributes (e.g., elevation, slope, and aspect ratio) from LIDAR and bathymetric surveys, and hydrodynamic properties (e.g., water depth, velocity, shear stress, and their statistical moments). An ensemble bagging-based ML technique, Random Forest, was adopted to identify the most influential factors as predictors to develop the predictive models with over-fitting issues addressed. The models were evaluated with respect to each individual substrate size class and the lumped group, and then used to generate the final substrate size maps covering all the grid cells in the numerical modeling domain.

Keywords: machine learning, random forest, spatial heterogeneity, grain-size distribution, riverbed permeability, hydrologic exchange flows (HEFs)

OPEN ACCESS

Edited by:
Alexis Navarre-Sitchler, Colorado School of Mines, United States

Reviewed by:
Alberto Bellin, University of Trento, Italy
Oliver Schilling, Université de Neuchâtel, Switzerland

****Correspondence:***
Huiying Ren
huiying.ren@pnnl.gov

Specialty section:
This article was submitted to Water and Critical Zone, a section of the journal Frontiers in Water

Received: *14 April 2020*
Accepted: *07 October 2020*
Published: *23 November 2020*

Citation:
Ren H, Hou Z, Duan Z, Song X, Perkins WA, Richmond MC, Arntzen EV and Scheibe TD (2020) Spatial Mapping of Riverbed Grain-Size Distribution Using Machine Learning. Front. Water 2:551627. doi: 10.3389/frwa.2020.551627

INTRODUCTION

The hyporheic zone (HZ) has been recognized as providing a connection between surface water and groundwater, and is critical for the exchange of water, nutrients, contaminants, microorganisms, and other materials (Cardenas et al., 2004). As one of the key elements of river corridors, the HZ provides and controls the hyporheic fluxes and solutes and their distributions (Boulton et al., 1998; Kasahara and Wondzell, 2003). The importance of HZ interactions, such as hydrologic

exchange flows (HEFs), can be addressed from both hydrological and ecological perspectives by hydrologists, geomorphologists, geochemists, and ecologists (Malcolm et al., 2003; Lu et al., 2012; Harvey and Gooseff, 2015). A variety of factors influence the HEFs, including hydraulic properties, available storage volume, topographic features, flow duration, river and depth, and so on. All of these factors controlling hyporheic exchange and solute reactions are not constant and may vary significantly over a range of temporal scales (Brunke and Gonser, 1997; Hayashi and Rosenberry, 2002; Sophocleous, 2002). Evaluating impacts of spatially heterogeneous structures is also an important research topic (Schilling et al., 2017).

Efforts have been made to develop flow and transport models in the HZ to better understand this complex hydrological system. Because the relationships and interactions among hydraulic, sedimentological, and biological processes are non-linear and dynamic, assigning realistic and accurate hydrogeological properties to the modeling domain is critical to achieving reliable HEF modeling; this, however, is challenging due to lack of direct field measurements. In addition, previous studies showed that the spatial heterogeneity of riverbed properties has a significant impact on HEFs (Irvine et al., 2012; Boano et al., 2014; McCallum et al., 2014; Tang et al., 2015); for example, heterogeneous hydraulic properties in riverbed sediment tend to increase hyporheic flow (Salehin et al., 2004; Sawyer and Cardenas, 2009). Capturing such spatial heterogeneity is another challenge due to the scarcity of spatial data.

Many studies have tried to determine the hydraulic properties, such as permeability or hydraulic conductivity, using information from permeameter tests, grain-size analyses, slug and bail tests, and pumping tests, each of which have their own limitations (Cheng et al., 2011), particularly for a large study domain. The data assimilation approach with ensemble Kalman filter (EnKF) can be used to approximate different levels of heterogeneity of hydraulic properties (Tang et al., 2017, 2018). However, there would be high computational demands for this large study area. There have been studies linking riverbed grain size statistics (e.g., D50) to hydraulic conductivity with empirical formulas (e.g., Shepherd, 1989; Lu et al., 2012). In a recently published paper (Hou et al., 2019), the effective hydraulic conductivity field for a 7-km reach of the Columbia River was estimated based on the integrated relationships amongst shear stress facies, substrate sizes, and point hydraulic conductivity measurements. For large-scale study sites, grain-size analysis is one of the least expensive and most straightforward practical approaches, and it is not dependent on the geometry (Chen, 2000; Landon et al., 2001; Kasenow, 2002; Odong, 2007). Automated grain-size analysis approaches have been developed rapidly by taking the advantage of the growth of image-based analysis. These information provide the basis to generate realistic sedimentary structures usually by integrating geostatistical analysis such as the Multiple Point Statistics (MPS) approach (Brunner et al., 2017). In addition, previous work has been done to derive the streambed hydraulic conductivity from various statistical grain-size parameters. For example, (Shepherd, 1989) introduced the well-known formula for channel sediments after analyzing published results on hydraulic conductivity and grain-size distribution, $k = cd^n$, where d (mm) is the particle diameter at 50% of the cumulative sample weight of smaller size or median particle diameters (i.e., dominant substrate size), and c is a dimensionless constant; the exponent n of the grain diameter may range from 1.11 to 2.05 depending on textural maturity and induration (Hou et al., 2017). The grain-size-based analysis, with adequate spatial coverage and resolution, could provide accurate estimates about hydraulic properties required to model and reveal river-groundwater interactions.

Our study area is the Hanford Reach located in the Columbia River Basin. The Columbia River is the fourth largest river by total discharge in the United States and is known to have a wide range of types and magnitudes of HEFs. Extensive experimental and numerical studies related to heterogeneous subsurface properties have been conducted to improve the understanding of the river's hydrological complexity and its impacts on ecosystems. The U.S. Fish and Wildlife Service (USFWS) sampled 13,372 locations for riverbed-dominant substrate size measurements for fish species and critical habitat study. The substrate size samples were scattered throughout ∼70% of the entire reach and serve as a great bridge to enabling a complete mapping of conductivity or permeability over the entire Hanford Reach. A number of field experiments were also conducted to measure hydraulic conductivity or permeability along the reach (Arntzen et al., 2006; Fritz and Arntzen, 2007; Fritz et al., 2016). The substrate size and hydraulic conductivity data sets enable us to derive realistic and representative coefficients for relationships linking grain size and conductivity. Despite the spatial coverage of the study domain, however, the spatial resolution of these data is too coarse to be used to infer spatial continuity or heterogeneity. Fortunately, bathymetry and hydrodynamics simulations, also available along the reach, have a much finer spatial resolution than those derived from the previous studies. Therefore, the remaining challenge is to build linkage relationships among the collocated bathymetric/hydrodynamic attributes; such relationships can then be used for substrate size and permeability mapping. In this study, we propose machine learning (ML) approaches to identify the most influential factors related to the spatial distributions of dominant riverbed substrate sizes and to develop ML-based predictive models for substrate size and permeability mapping. An ensemble tree-based classification method, Random Forest (RF), is adopted for the high-dimensional data set with mixed continuous and categorical variables.

MATERIALS AND METHODS

Study Site

The study site is the Hanford Reach, which is a section of the Columbia River located in southeastern Washington State, USA, as shown in the upper right panel of **Figure 1**. The reach extends ∼85 km from the tailrace of Priest Rapids Dam to the north end of the city of Richland. The lower end of the reach approximately corresponds to the maximum upstream extent of influence of the downstream reservoir impounded by McNary Dam. The Hanford Reach has been extensively studied because of (1) its proximity to the U.S. Department of Energy Hanford Site, a site of former nuclear materials production that contains

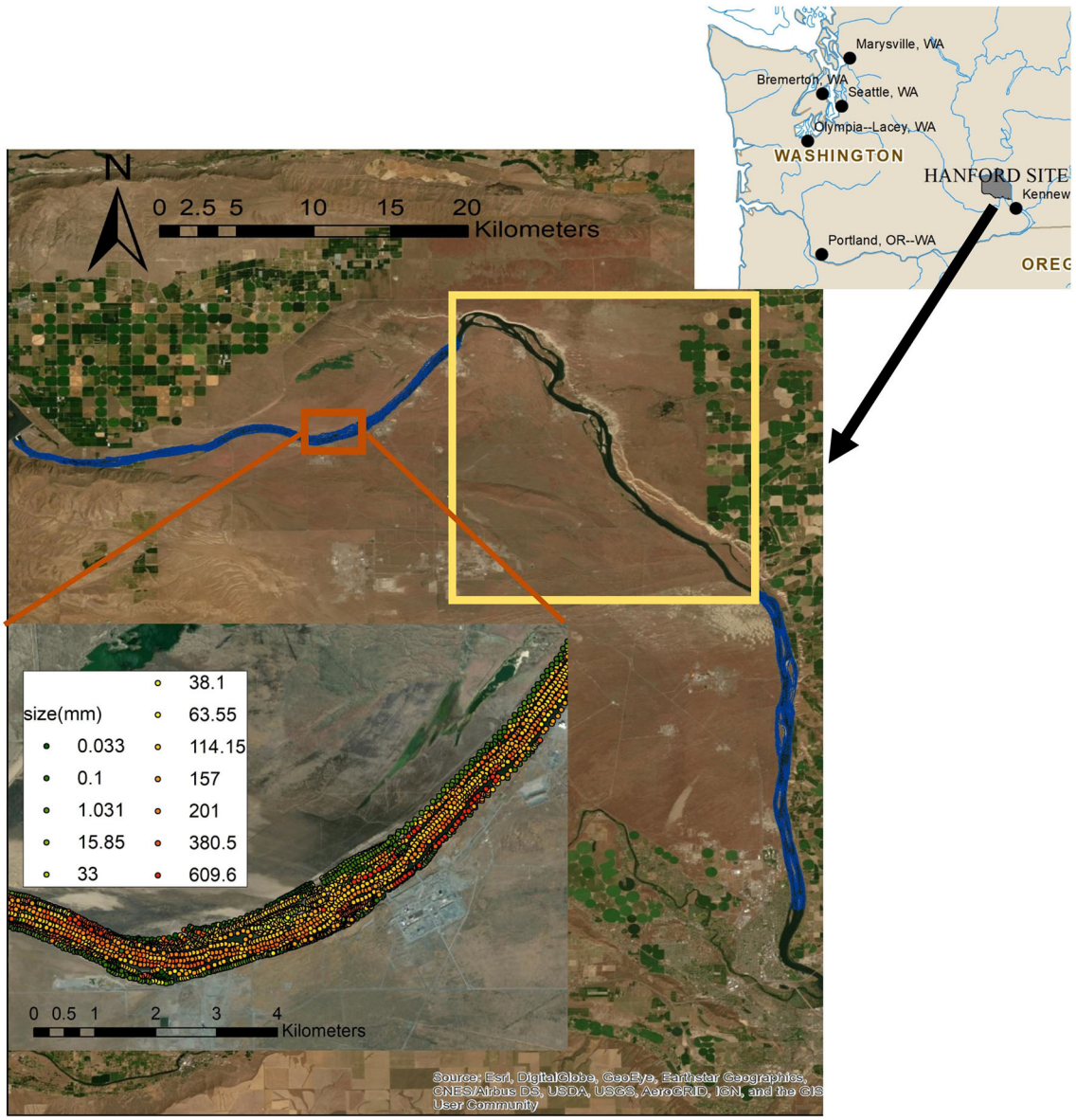

FIGURE 1 | The location of substrate size samples along the Hanford Reach of the Columbia River. The blue dots are the sampling locations and the yellow box is the region without samples. The enlarged subplot shows the substrate size distribution.

extensive legacy contaminants in groundwater and soil; (2) its importance as a salmon spawning area; and (3) the high value of hydropower production in the region. The Hanford Reach has had a protected status since the year 2000 as the Hanford Reach National Monument, which is administered by the USFWS.

Dominant Substrate Size

USFWS conducted survey operations along the reach to characterize grain size distributions in terms of dominant substrate sizes (Anglin et al., 2006; Hou et al., 2019) to study fish habitats. To determine the dominant substrate size, each one square meter area was evaluated by assigning a representative grainsize range equal to the median grain size D50. For water depths >0.5 m, the riverbed was photographed to capture the substrate grain size, and for water depths >0.5 m, the grain size was determined by wading the stream. Over 59 river kilometers, 13,372 locations were sampled and one-third of the sampling locations were in water deep enough to require underwater video sampling (Anglin et al., 2006). Twelve grain size classes were identified—from 0.033 to 609.6 mm—as listed in **Table 1**, and were further lumped to four groups by adopting the particle size classification according to the U.S. Geological Survey's recommendation (Berenbrock and Tranmer, 2008); i.e., silt (0.033 mm), sand (0.062–2.0 mm), gravel (2.0–64 mm), and cobble (>64 mm). The silt group contains only class 1 (i.e., coarse silt); the sand category contains classes 2 and 3; gravel contains

TABLE 1 | Substrate size classification.

Reach-dominant substrate size class	Reach-dominant substrate Size (mm)	Particle classification	Particle diameter (mm)	Lumped particle classification	Particle diameter of the lumped class (mm)
1	0.033	Coarse silt	0.031–0.0625	Silt	0.0078–0.0625
2	0.1	Very fine sand	0.0625–0.125	Sand	0.0625–2
3	1.031	Very coarse sand	1–2	Sand	0.0625–2
4	15.85	Medium gravel	8–16	Gravel	2–64
5	33	Very coarse gravel	32–64	Gravel	2–64
6	38.1	Very coarse gravel	32–64	Gravel	2–64
7	63.55	Very coarse gravel	32–64	Gravel	2–64
8	114.15	Fine cobble	64–128	Cobble	>64
9	157	Coarse cobble	128–256	Cobble	>64
10	201	Coarse cobble	128–256	Cobble	>64
11	380.5	Very coarse cobble	>256	Cobble	>64
12	609.6	Very coarse cobble	>256	Cobble	>64

classes 4–7; and cobble contains the rest of the classes 8–12. The spatial resolution of the samples varies from 50 to 70 m and the sampling locations cover ∼70% of the entire Hanford Reach, as shown in the blue regions in **Figure 1**. The regions without samples are marked in the yellow boxed section.

Bathymetric Attributes

Riverbed digital elevation data have been obtained from prior combined LiDAR and bathymetric surveys on a grid resolution of 1 m (Coleman et al., 2010). The bathymetric derivatives were extracted from the digital elevation survey data. For each grid cell, the slope and aspect were calculated using the "Slope" and "Aspect" tool of the Environmental Systems Research Institute ArcGIS platform. Slope describes the steepness of a grid cell in a raster surface. It is calculated as the inverse tangent of the rise divided by the run, with the higher value representing steeper terrain. Aspect represents the compass direction of a slope and is measured clockwise from 0 to 360 degrees. It is the downslope direction of the maximum rate of change in value from each cell to its neighbors. Aspect variables of non-sloping flat surfaces are flagged with a value of −1. River bathymetry and bathymetric variability are likely to be related to riverbed dominant substrate size distributions, and therefore these bathymetric attributes were included as potential predictors in the ML model development.

Hydrodynamic Attributes

Hanford Reach hydrodynamics were simulated using the Modular Aquatic Simulation System 2D (MASS2) model (Perkins and Richmond, 2007a,b; Niehus et al., 2014). MASS2 is a two-dimensional, depth-averaged hydrodynamic model that uses an orthogonal curvilinear mesh. As part of the previous work, MASS2 was applied from Priest Rapids Dam to near the mouth of the Yakima River, ∼97 km, using a computational mesh with ∼710,000 cells and a nominal resolution of ∼10 m. The bathymetry in the Hanford Reach was assumed to be very stable over the more than 100-year MASS2 simulation period based on the underlying geology (Fecht et al., 2004; Fecht and Marceau, 2006; Hou et al., 2019). MASS2 was calibrated using water surface elevations measured at selected locations along the Hanford Reach, with mean absolute errors ranging from 1 to 12 cm. The calibrated models were then used to simulate the Hanford Reach conditions for a long historical period for which discharge records are available. Model calibration and long-term simulation details are documented by Niehus et al. (2014). Hourly hydrodynamic results from 1917 to 2012 under various flow conditions in the Hanford Reach were available for each grid. The simulation outputs, including the wet percentage, water depth, velocity magnitude, bottom shear stress and shear velocity, and their statistical moments (i.e., mean, variance, skewness, and kurtosis), were used as the predictors of dominant substrate size distribution. Together with the bathymetric predictors and substrate size responses, all the hydrodynamic variables were mapped onto the MASS2 grids.

Random Forest Classification

Given the high dimensionality of the predictors and non-linear relationships between the substrate size and these predictors, we adopted a reliable ensemble tree-based approach called Random Forest (RF) in our problem. RF is an ensemble ML algorithm that uses a collection of decision trees as base classifiers (Breiman, 2001) $\{h(\mathbf{x}, \Theta_k), k = 1, 2, 3 \ldots\ldots\}$, where the Θ_k are independent identically distributed random vectors and $\mathbf{x}$ is the input vector that each tree casts a unit vote for the most popular class. To grow a RF, user-defined parameters are required, including the number of the trees (k) and the number of predictive variables used to split the nodes (m). Each tree is grown using the training data set, which is created using a bootstrap aggregating (bagging) technique to create the resampling randomly and uniformly from the original data with replacement, and is comprised of a series of decision nodes or branching points (Pal, 2005; Rodriguez-Galiano et al., 2012). Past studies have revealed that bagging methods, such

as RF, are not sensitive to noises or outliers (Briem et al., 2002; Chan and Paelinckx, 2008). Because the random feature selection of RF offers correlation reduction between the features which makes RF not vulnerable to the inherent noise existing in the training data. Because there is no deletion of the data sampled from the inputs for creating the next subset, the bagging helps to achieve the stability of classifiers with high accuracy (Breiman, 2001; Gislason et al., 2006). The distribution of the input samples does not change because the bagging uses random resampling instead of reweighting. Each new training set is drawn, with replacement, from the original training set. Then a tree is grown on the new training set using random feature selection. The trees grown are not pruned. Thus, all training classifiers have equal weights during split (Breiman, 2001). The response **y** is predicted by taking the majority vote in the case of classification trees. When each subset is selected by bagging to grow each individual tree, the inputs that are not included in the training and calibration data set in the current growing tree are counted in an out-of-bag (OOB) data set. OOB is the mean prediction error on each training sample $\mathbf{x_i}$, using only the trees that did not have $\mathbf{x_i}$ in their bootstrap sample. The proportion of misclassifications over all OOB data sets is called the OOB error, which is an unbiased estimation of the generalization error without separating the testing data (Breiman, 2001; Peters et al., 2007). To make the generalization error converge, the number of trees (k) needs to be large enough. For a large number of trees, convergence follows from the Strong Law of Large Numbers and the tree structure. The RF can address the overfitting issue by checking and assuring such error convergency. The strength of each individual tree and the correlation between any two trees are used to evaluate the generalization error by the best split of input features or predictive variables. The Gini index, a measure of the impurity of a given input feature with respect to the rest of the classes, is a popular quantity for the best split selection. One of the advantages of RF is that it allows individual decision trees to grow to the maximum depth using a given combination of features, because (Mingers, 1989; Pal, 2005). Meanwhile, the relative importance of features is provided during the classification process.

RF is well-suited for high-dimensional data sets and/or highly correlated input features and has been successfully applied to the soil microbial community, remote sensing classification, water resources, and so on (Heung et al., 2014; Naghibi et al., 2017; Tesoriero et al., 2017). Open-source statistical software R (R Core Team, 2013) was used in this study, where the R implementation of the RF package (Liaw and Wiener, 2002) was used for RF model development, validation, and prediction.

In our study, the variable vector **y** to be classified represents the riverbed substrate classes at various spatial locations along the Hanford Reach. The categorical variables of interest to be predicted **y** can be grouped into 12 classes or 4 lumped groups. The input vector **x** contains bathymetric and hydrodynamic attributes at the collocated positions with categorical variable vector **y**, ensemble decision trees are then constructed using the training dataset; The input variables are selected randomly to get the best split-point to split the node into child notes to grow each decision tree.

RESULTS

ML Data Preparation and RF Model Development

There are 13,372 data samples of dominant substrate sizes collected in the study domain, grouped into 12 classes and 4 categories. These are the "labels" information for ML training. At these sampling locations, information about the predictors is extracted from the high-resolution data sets of bathymetry and hydrodynamics. The bathymetric attributes include local bathymetry, slope, and aspect. The hydrodynamic attributes from multi-year MASS2 simulation include the wet percentage, water depth, velocity magnitude, river bottom shear stress, and shear velocity, together with their first four statistical central moments (e.g., mean, variance, skewness, and kurtosis). All the bathymetric and hydrodynamic attributes are treated as input features for the ML RF model development and the output response variable is the categorical substrate grain size. The ML model builds the relationship between substrate size and the features using the available grain-size measurements. Although there are 13,372 data points, we consider it as a spatially "sparse" dataset as they are dispersed along a 70-km long reach and the adjacent points are usually dozens of meters away from each other. In order to fill the spatial gaps while mapping the substrate size, the developed ML model of grain size can be applied to the numerical grid, with 5–10 m spatial resolution, to enable grain size mapping with adequate spatial coverage and resolution. Note that the spatial coordinates information, e.g., the Easting and Northing cartesian coordinates, contains spatial adjacency information, and can potentially help improve the ML prediction accuracy; but this information should be excluded when considering the generality and transferability of the developed models.

The ML (RF) models were developed through comprehensive model optimization and cross-validation. Different model configurations have been evaluated and compared to achieve the highest performance metrics (e.g., accuracy) and minimum overfitting. For example, the effect of the number of trees (k) and the number of predictive variables of the split nodes (m) were evaluated by six RF models, each of them constructed from up to 10,000 trees for each different value of m. The original database was randomly separated with 85% of the data points used for training and the remaining 15% held back for the testing data set. **Figure 2** shows the OOB error with respect to the number of trees using the training data set with different predictive variables and the minimum size of terminal nodes set to 10. Here the minimum size of the terminal node implicitly sets the depth of trees in the model. The OOB error decreases significantly as the number of trees grows to 200 for all cases. When the number of predictive variables m is three, the OOB error is higher than the rest of the cases regardless of the number of trees. The error

variability becomes very small when there are more than 1,000 trees. In the finalized optimal RF model configurations, m is set to be 15 with the lowest OOB errors and the tree number is set to be 1,000.

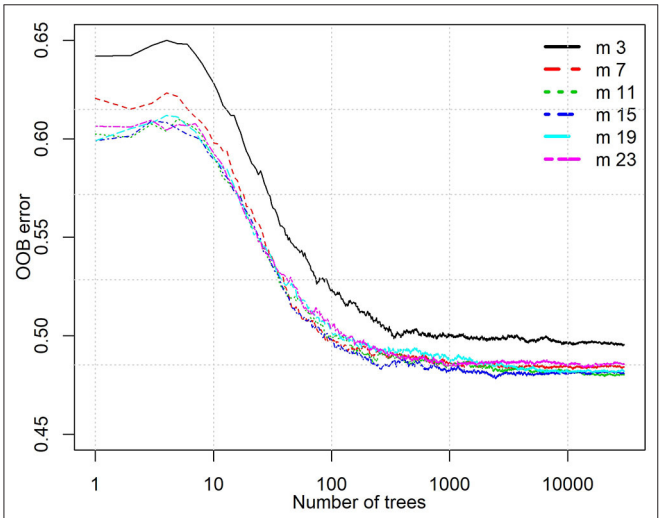

FIGURE 2 | The OOB error with respect to number of trees for different predivtive variables for split node (m).

RF Parameter Ranking and Model Performance

Figure 3 shows the ranked variable importance based on the RF classification. The left panel is the Mean Decrease in Accuracy (MDA), which measures the loss of accuracy by taking variables out one by one. A high value of MDA means that the variable improves the model accuracy. The mean bathymetry is clearly the most important variable, followed by the bathymetric attributes, slope and aspect, water depth's third moment. The right panel in **Figure 3** is the mean decrease in Gini impurity (MDG), which provides both variable contributions to the accuracy and the degree of misclassification. Important predictors correspond to high MDGs. Gini impurity achieves zero if all the responses in the training data in a group fall into a single category (i.e., no classification). The top variable according to MDG is the mean bathymetry, followed by four comparative factors: the slope of bathymetry, the third moment of water depth, aspect and water depth. Based on both the MDA and MDG variable importance, we can conclude that the flow conditions (water depth and its third moment) and the bathymetric attributes are the most influential factors. In addition, the velocity and the kurtosis of bottom shear stress are relatively important. The wet percentage is secondary but not negligible in terms of MDG.

The testing data set was used to evaluate the RF model accuracy in predicting the 12 classes and 4 categories of substrate sizes. The histogram of model predictions is illustrated for each

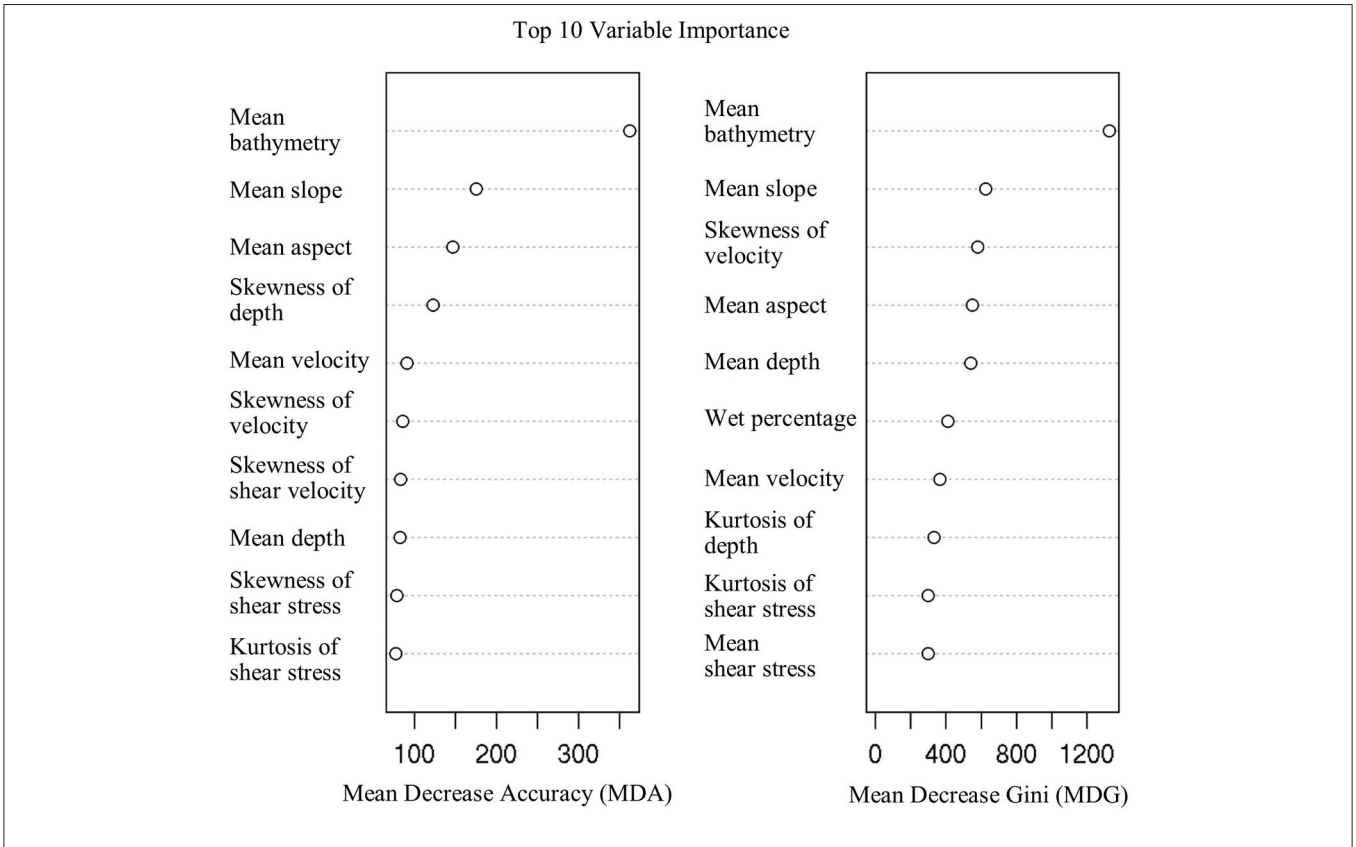

FIGURE 3 | Dot chart of the top 10 features importance as measured by the RF model trained in optimized configuration.

individual class in **Figure 4**. The red bar represents the correct classifications/predictions for each class (classes 1–12) and the blue bars are the additional correct classifications/predictions of each category (silt, sand, gravel, and cobble). In general, the majority of RF predictions of the individual classes are correct; i.e., the red bar has the most counts and the correct classification cases dominate. The second highest bars generally also fall in the same lumped categories, e.g., the blue bars have the second largest values in each category except for classes 2 and 3. This means even if the RF model does not predict correctly the exact class (1–12), it most likely can still predict the correct silt/sand/gravel/cobble category.

Quantitatively, the classification accuracy for individual class ranges from 36 to 81% with a mean accuracy of 53%. Class 8 (substrate size class of 114.15 mm, fine cobble), containing the largest number of testing sample size, had the lowest accuracy. Although 170 testing samples were predicted correctly to fall under class 8, the RF model predicted about 70 samples fall under class 10 (coarse cobble). The model exhibits the best performance for class 12 with the largest substrate size class

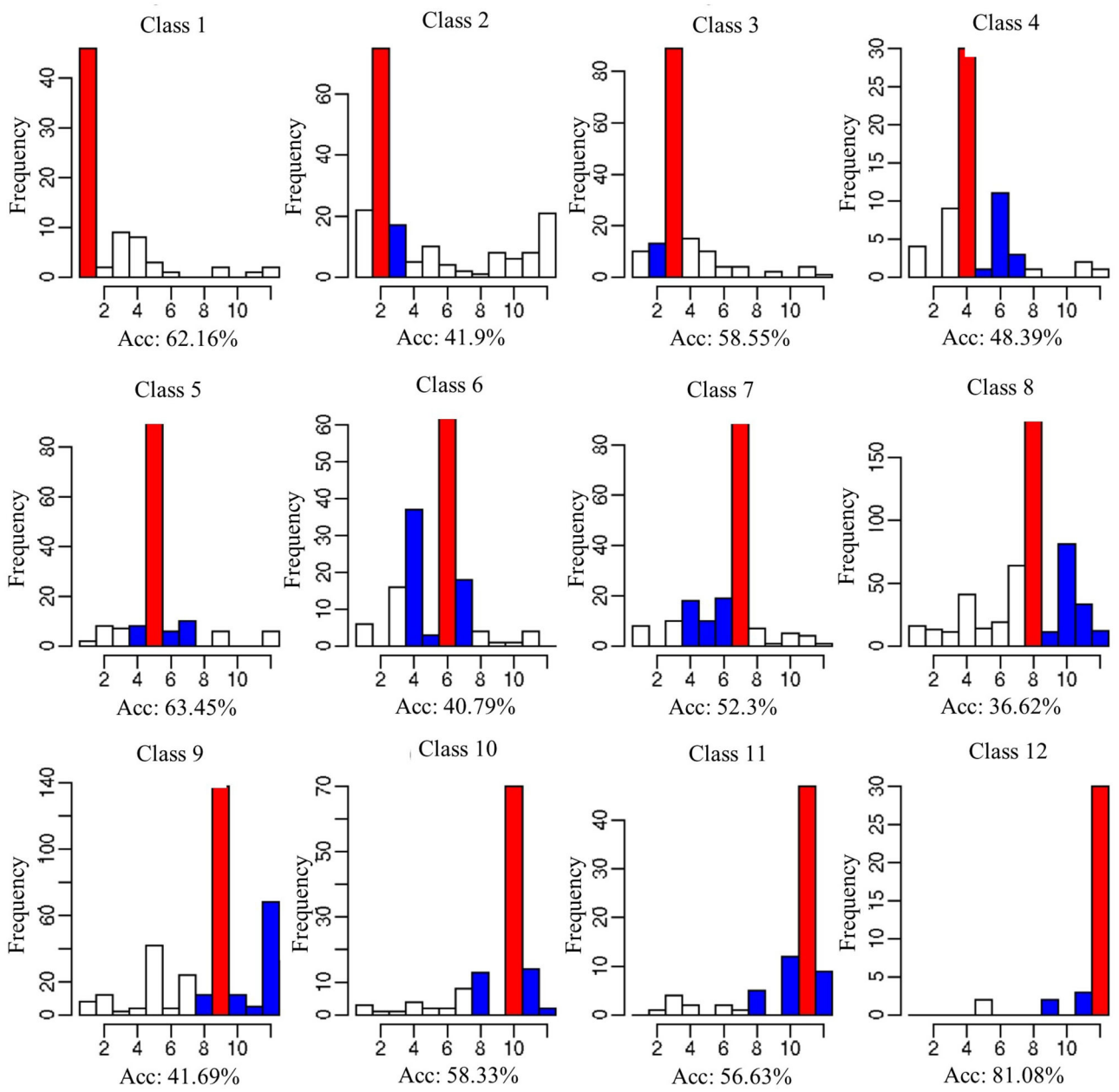

FIGURE 4 | RF prediction for each substrate class. The red bar represents each targeted class. The blue bins represent the classes lumped by silt (class 1), sand (classes 2 and 3), gravel (classes 4 ∼ 7), and cobble (classes 8 ∼ 12). The accuracy of each individual class prediction is listed for each subplot.

of 609.6 mm and is labeled as very coarse cobble. Meanwhile, for class 6 (very coarse gravel with a 63.44 mm substrate size class), ∼40 samples were predicted to fall under class 4 (medium gravel). Similar observations were seen for class 7 as well. The medium gravel class 4 had 30 samples that were classified correctly while ∼15 samples were misclassified into class 6. The model performance is summarized for the four lumped categories in **Figure 5**. The overall prediction accuracies for the silt, sand, gravel, and cobble categories are 62, 59, 79, and 71%, respectively. The model performance is satisfactory, although the uncertainty of substrate size distribution is large in the raw data and can be attributed non-linearly to many factors that have strong cross-dependence.

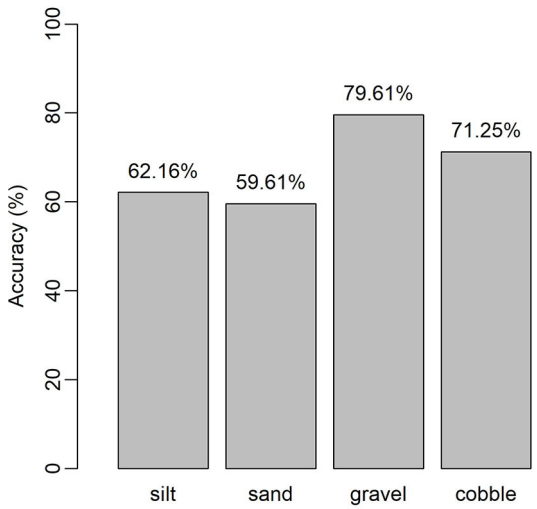

FIGURE 5 | RF prediction accuracy for the four lumped groups: silt, sand, gravel, and cobble.

Spatial Mapping of Substrate Grain Size

Based on the field observations and simulations, we have developed an RF model representing the non-linear relationships between the substrate size and bathymetric and hydrodynamic attributes. The validated and tested RF model can be adopted and applied to all the numerical grids of 5–10 m resolution across the entire Hanford Reach. As a verification, **Figure 6** shows a subsection of four river kilometers that have multiple hydromorphic features (e.g., island, attached bar, and meander), illustrating the comparison between the ground-truthing at a coarse spatial resolution and the model prediction on the finer grids. In **Figure 6**, the distributions of dominant substrate size are shown in 12 color-coded classes, where a larger substrate size corresponds to a larger class number. From the field observations shown in the left panel of **Figure 6**, class 1 (silt) grids are mainly located near the left banks of the shorelines between the meander and the island and near the right banks after the attached bar, corresponding to more of a depositional environment. For comparison, the model predictions on the grids in the right-hand panel of **Figure 6** exhibit very similar patterns. Near a river segment below the island, where no USFWS measurements were available, the RF model predicts the substrate size to have a high probability of being silt. This is realistic by checking the patterns of the actual sampled locations relative to the bars and islands and our boat-based field survey. The sampling locations of class 2 grain sizes (fine sand) are along both sides of the river shoreline, especially on the right bank near the meander and on the left bank of the river below the gravel bar. Class 3 (coarse sand) tends to follow the same distribution of class 2, although it is farther away from the right riverbank near the meander. A few samples of class 4 were located near the tail of the island and no samples of class 5 were taken in this section of the river. Classes 6 and 7 have very few samples, and they are mainly located next to the island. The places with smaller substrate sizes concentrate more on the left shoreline than on the right shoreline. The most frequent

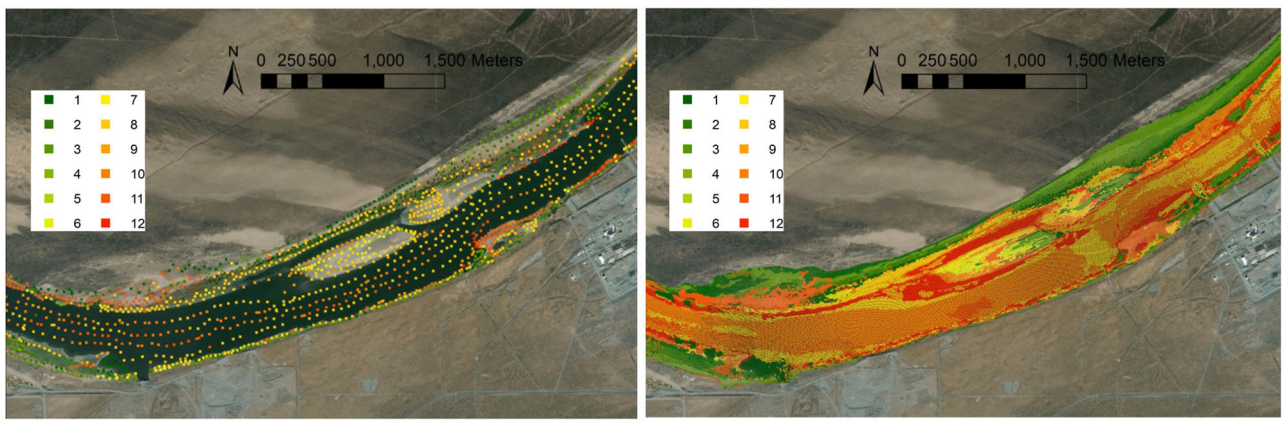

FIGURE 6 | The dominant substrate size distribution of 12 classes with smaller class number representing the smaller dominant substrate size. The left panel is the ground-truthing and the right panel is the model prediction for each simulation grid.

samples in this subsection are class 8 (fine cobble), scattered in the river channel, around the island, near the front of the attached bar, and along both sides of the river channel. The sampling locations for coarse cobble including classes 9 and 10 are mainly located near the head of the island and the middle of the river channel. Most of the very coarse cobble locations are along the left shoreline near the meander and along the right-side bars behind the island. Compared to the ground-truthing data, the RF model predictions produce realistic spatial patterns and reflect reasonable spatial heterogeneity. Additional validation of RF predictions of substrate size categories (silt, sand, gravel, cobble) is shown in **Figure 7**. Generally, the gravel group has a smaller proportion in the predictions than in the field observations in this region. The gravel sampled at the front of the island and left side of the meander area are all classified correctly. In the river channel, mostly cobble is predicted, which is consistent with the field observations. Meanwhile, the spatial variability and heterogeneity can be seen. Such information about heterogeneity in the permeability field enables the development of more realistic and accurate numerical models, rather than assuming uniform or block-wise uniform permeability values.

DISCUSSION

In order to avoid over-fitting in the developed ML models, the ensemble bagging-based RF model was adopted to build the relationships between dominant substrate size and influential factors including bathymetric and hydrodynamic elements. Although RF models have been proven to be effective in terms of prediction accuracy and handling of overfitting issues, it is helpful to compare its performance with other ML approaches, particularly other widely accepted ensemble ML models, such as the boosting-based Extreme Gradient Boosting Model (GBM) (Chen et al., 2015). GBM is also tree-based, but the difference between RF and GBM is that the latter builds one tree at a time, and each tree learns and improves upon the previous one and combines results throughout the tree-building process. The disadvantage of GBM is that it is computationally expensive and sensitive to noises in the data set. Parameter tuning is performed for GBM with respect to the number of trees, the maximum tree depth, and the subsample ratio of columns when constructing each tree. The model accuracy obtained from the cross validation is shown in **Figure 8**. Each subplot in **Figure 8** represents the different subsample ratio of columns when each tree was constructed. The x axis of each subplot is maximum tree depth which controls the depth of each individual tree. The different number of trees are color coded under each subplot showing different boosting iterations. The highest GBM model accuracy is about 55.6% with the optimized parameters, where the maximum tree depth is 10, the total number of trees is about 200, and the subsample ratio of columns is 0.9. The model accuracy for the four lumped substrate size categories using GBM and RF is compared in **Table 2**, which shows that the GBM and RF model prediction accuracies are generally comparable. RF is better at predicting finer materials such as silt, while GBM has stronger skill for predicting coarse cobble. For both methods, the lowest accuracy occurs when the dominant substrate size is <0.0625 mm (i.e., silt), while the highest accuracy ($>80\%$) occurs when the substrate size is in the cobble group, which means the larger dominant substrate size group is relatively easier to predict using the available predictors, likely because the corresponding grains are well-sorted and subject to small variability.

Table 2 shows satisfactory testing accuracy for the testing grids/domain and proven transferability of the developed models. Although in the prediction model we did not include the spatial coordinate information, we did investigate the impact of adding spatial coordinates such as the Northing and Easting coordinate information in the predictor list and repeated the model training and testing. With the RF model, about a 3% improvement in the prediction accuracy was achieved by adding the spatial adjacency information for the finer silt, gravel, and cobble categories. The adjacency information provides more help for the sand category with a 7% increase in the prediction accuracy.

Therefore, spatial substrate grain-size distributions can be reasonably predicted using ML models on high-resolution

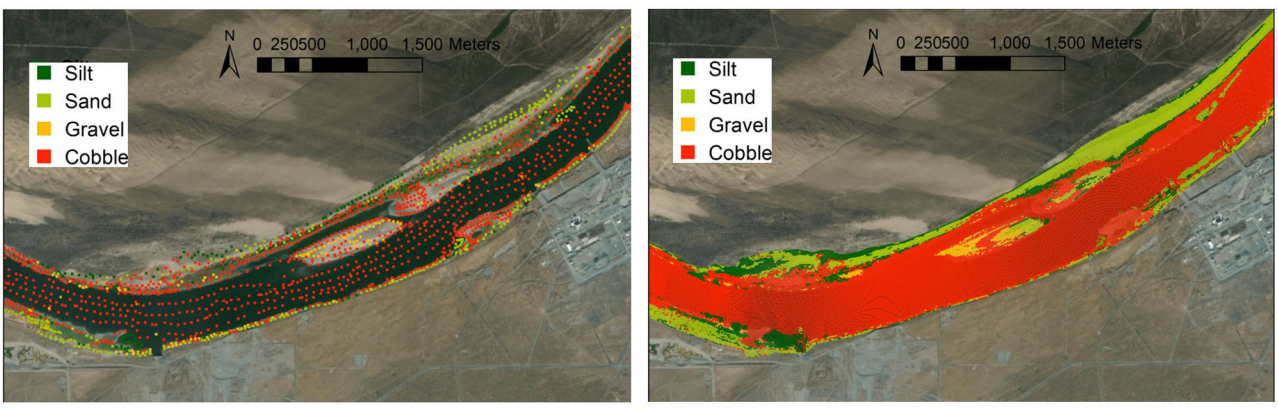

FIGURE 7 | The dominant substrate size distribution of the four lumped classes. The left panel is the ground-truthing and the right panel is the model prediction for each simulation grid.

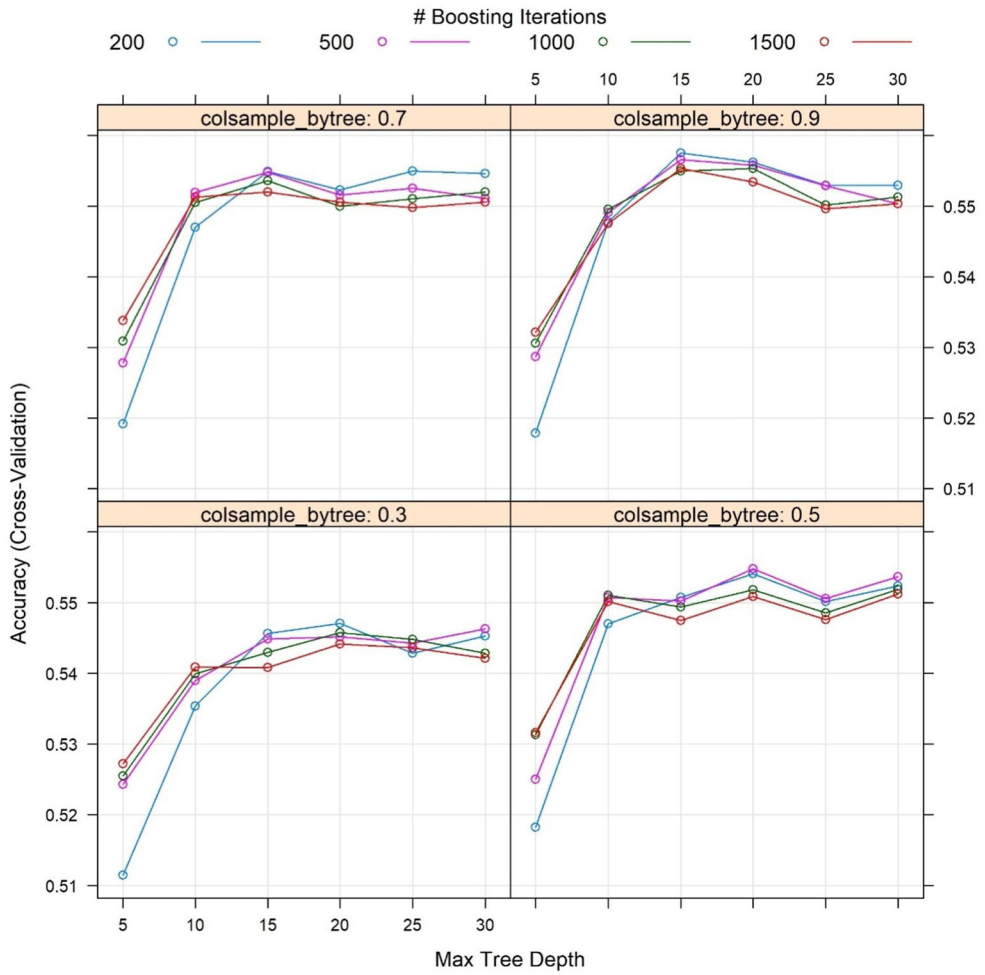

FIGURE 8 | The cross-validation accuracy of the Extreme Gradient Boosting Model (GBM) achieved by tuning the maximum tree depth (x axis), number of trees (different colored lines), and subsample ratio of columns (noted as subtitle "colsample_by tree" for each subplot) when constructing each tree.

TABLE 2 | Predictive accuracy of lumped four groups with different model setups.

Lumped group	Reach-dominant substrate Size (mm)	Predictive accuracy		
		RF	GBM	RF (w/adjacent info)
Silt	0.0078–0.0625	62.2%	37.8%	66.2%
Sand	0.0625–2	58.6%	63.7%	65.6%
Gravel	2–64	78.6%	61.5%	81.1%
Cobble	>64	71.3%	87.0%	74.0%

numerical simulation grids. The spatial map of grain size can then be used to estimate hydraulic properties at the same resolution. The limitations of the approach, on the other hand, include the fact that the field observations of substrate size used in the model development mainly deliver valuable information of 2D spatial patterns near the top of the riverbed (Brunner et al., 2017). Without integration of vertical structural information, the approach seems to have overestimated hydraulic conductivity using grain-size distribution; meanwhile, the approach did not fully consider the degree of anisotropy and preferential flow pathways (Gianni et al., 2019). Given the transient nature of the system, the reliability of the estimation for hydraulic properties may also be affected by the system flow scenarios (Gianni et al., 2016). Nevertheless, our estimates of hydraulic properties

can provide reliable inputs with reduced uncertainty toward improved numerical models in both accuracy and precision. This top of the permeability field is one of the most influential factors that control the magnitude (Lackey et al., 2015; Bao et al., 2018), spatial extent (Schilling et al., 2017), and associated biogeochemical hot spots (Song et al., 2018; Dai et al., 2019) of HEFs.

CONCLUSION

In this work, we developed an ML approach to predict dominant substrate size distribution, which enables to map the permeability field in the Hanford Reach of the Columbia River, providing more accurate and reliable inputs of the heterogeneous property field to the numerical models to obtain more realistic HEFs in river corridor systems. The developed ML models can link dominant substrate size to the available bathymetric and hydrodynamic attributes with high resolution. The traditional geostatistical approach is not applicable to the study site because of the large spatial gaps in the un-sampled locations. Therefore, our ML-based algorithms fill the gaps in mapping spatial grain-size distribution using the abundant indirect information available to us.

Given the satisfactory prediction accuracy of the testing data set, the generated substrate size can reliably provide the needed heterogeneous property input information based on well-reported and calibrated relationships between hydraulic properties and substrate grain-size distributions, which allows the numerical models to evaluate the effects of spatial heterogeneity on model outputs (e.g., HEFs, residence times), and enables a better understanding of the complex hydrological river corridor system.

DATA AVAILABILITY STATEMENT

The datasets presented in this study can be found in online repositories. The names of the repository/repositories and accession number(s) can be found below: SBR SFA PNNL data repository https://sbrsfa.velo.pnnl.gov/datasets/?UUID$=$a165e7a4-427d-4997-845f-032d61975d85.

AUTHOR'S NOTE

Pacific Northwest National Laboratory is operated by Battelle Memorial Institute for the U.S. Department of Energy under Contract No. DE-AC05-76RL01830. Hydrodynamic modeling of the Hanford Reach was performed for Public Utility District No. 2 of Grant County, Ephrata, WA, USA, under contract number 430-2464.

AUTHOR CONTRIBUTIONS

HR and ZH contributed to the design and implementation. ZD processed the bathymetric attributes and generated some plots. WP and MR simulated hydrodynamics. XS and TS discussed the results and commented on the manuscript. All authors contributed to writing the manuscript.

FUNDING

This research was supported by the U.S. Department of Energy, Office of Biological and Environmental Research (BER), as part of BER's Subsurface Biogeochemical Research Program (SBR). This contribution originates from the SBR Scientific Focus Area at the Pacific Northwest National Laboratory (PNNL).

REFERENCES

Anglin, D. R., Haeseker, S. L., Skalicky, J. J., Schaller, H., Tiffan, K. F., Hatten, J. R., et al. (2006). *Effects of Hydropower Operations on Spawning Habitat, Rearing Habitat, and Standing/Entrapment Mortality of Fall Chinook Salmon in the Hanford Reach of the Columbia River*. US Fish and Wildlife Service.

Arntzen, E. V., Geist, D. R., and Dresel, P. E. (2006). Effects of fluctuating river flow on groundwater/surface water mixing in the hyporheic zone of a regulated, large cobble bed river. *River Res. Appl.* 22, 937–946. doi: 10.1002/rra.947

Bao, J., Zhou, T., Huang, M., Hou, Z., Perkins, W., Harding, S., et al. (2018). Modulating factors of hydrologic exchanges in a large-scale river reach: Insights from three-dimensional computational fluid dynamics simulations. *Hydrol. Process.* 32, 3446–3463. doi: 10.1002/hyp.13266

Berenbrock, C., and Tranmer, A. W. (2008). *Simulation of Flow, Sediment Transport, and Sediment Mobility of The Lower Coeur d'Alene River, Idaho*. Reston, VA: US Geological Survey.

Boano, F., Harvey, J. W., Marion, A., Packman, A. I., Revelli, R., Ridolfi, L., et al. (2014). Hyporheic flow and transport processes: mechanisms, models, and biogeochemical implications. *Rev. Geophys.* 52, 603–679. doi: 10.1002/2012RG000417

Boulton, A. J., Findlay, S., Marmonier, P., Stanley, E. H., and Valett, H. M. (1998). The functional significance of the hyporheic zone in streams and rivers. *Annu. Rev. Ecol. Syst.* 29, 59–81. doi: 10.1146/annurev.ecolsys.29.1.59

Breiman, L. (2001). Random forests. *Mach. Learn.* 45, 5–32. doi: 10.1023/A:1010933404324

Briem, G. J., Benediktsson, J. A., and Sveinsson, J. R. (2002). Multiple classifiers applied to multisource remote sensing data. *IEEE Trans. Geosci. Remote Sens.* 40, 2291–2299. doi: 10.1109/TGRS.2002.802476

Brunke, M., and Gonser, T. (1997). The ecological significance of exchange processes between rivers and groundwater. *Freshw. Biol.* 37, 1–33. doi: 10.1046/j.1365-2427.1997.00143.x

Brunner, P., Therrien, R., Renard, P., Simmons, C. T., and Franssen, H. J. H. (2017). Advances in understanding river-groundwater interactions. *Rev. Geophys.* 55, 818–854. doi: 10.1002/2017RG000556

Cardenas, M. B., Wilson, J., and Zlotnik, V. A. (2004). Impact of heterogeneity, bed forms, and stream curvature on subchannel hyporheic exchange. *Water Resour. Res.* 40:W08307. doi: 10.1029/2004WR003008

Chan, J. C.-W., and Paelinckx, D. (2008). Evaluation of Random Forest and Adaboost tree-based ensemble classification and spectral band selection for ecotope mapping using airborne hyperspectral imagery. *Remote Sens. Environ.* 112, 2999–3011. doi: 10.1016/j.rse.2008.02.011

Chen, T., He, T., Benesty, M., Khotilovich, V., and Tang, Y. (2015). *Xgboost: Extreme Gradient Boosting. R package version* 0.4-2, 1–4.

Chen, X. (2000). Measurement of streambed hydraulic conductivity and its anisotropy. *Environ. Geol.* 39, 1317–1324. doi: 10.1007/s002540000172

Cheng, C., Song, J., Chen, X., and Wang, D. (2011). Statistical distribution of streambed vertical hydraulic conductivity along the Platte River, Nebraska. *Water Res. Manag.* 25, 265–285. doi: 10.1007/s11269-010-9698-5

Coleman, A. M., Ward, D. L., Larson, K. B., and Lettrick, J. W. (2010). "Development of a high-resolution bathymetry dataset for the Columbia River through the Hanford Reach," in *Pacific Northwest National Lab*, (Richland, WA: Pacific Northwest National Laboratory).

Dai, H., Chen, X., Ye, M., Song, X., Hammond, G., Hu, B., et al. (2019). Using Bayesian networks for sensitivity analysis of complex biogeochemical models. *Water Resour. Res.* 55, 3541–3555. doi: 10.1029/2018WR023589

Fecht, K., Marceau, T., Bjornstad, B., Horton, D., Last, G., Peterson, R., et al. (2004). *Late Pleistocene and Holocene-Age Columbia River Sediments and Bedforms: Hanford Reach Area, Washington, Part 1: Richland*. Washington, DC: Bechtel Hanford. Inc.

Fecht, K., and Marceau, T. (2006). *Late Pleistocene and Holocene-Age Columbia River Sediments and Bedforms: Hanford Reach Area, Washington-Part 2*. Washington Closure Hanford.

Fritz, B. G., and Arntzen, E. V. (2007). Effect of rapidly changing river stage on uranium flux through the hyporheic zone. *Groundwater* 45, 753–760. doi: 10.1111/j.1745-6584.2007.00365.x

Fritz, B. G., Mackley, R. D., and Arntzen, E. V. (2016). Conducting slug tests in mini-piezometers. *Groundwater* 54, 291–295. doi: 10.1111/gwat.12335

Gianni, G., Doherty, J., and Brunner, P. (2019). Conceptualization and calibration of anisotropic alluvial systems: pitfalls and biases. *Groundwater* 57, 409–419. doi: 10.1111/gwat.12802

Gianni, G., Richon, J., Perrochet, P., Vogel, A., and Brunner, P. (2016). Rapid identification of transience in streambed conductance by inversion of floodwave responses. *Water Resour. Res.* 52, 2647–2658. doi: 10.1002/2015WR017154

Gislason, P. O., Benediktsson, J. A., and Sveinsson, J. R. (2006). Random forests for land cover classification. *Pattern Recognit. Lett.* 27, 294–300. doi: 10.1016/j.patrec.2005.08.011

Harvey, J., and Gooseff, M. (2015). River corridor science: hydrologic exchange and ecological consequences from bedforms to basins. *Water Resour. Res.* 51, 6893–6922. doi: 10.1002/2015WR017617

Hayashi, M., and Rosenberry, D. O. (2002). Effects of ground water exchange on the hydrology and ecology of surface water. *Groundwater* 40, 309–316. doi: 10.1111/j.1745-6584.2002.tb02659.x

Heung, B., Bulmer, C. E., and Schmidt, M. G. (2014). Predictive soil parent material mapping at a regional-scale: a random forest approach. *Geoderma* 214, 141–154. doi: 10.1016/j.geoderma.2013.09.016

Hou, Z., Nelson, W. C., Stegen, J. C., Murray, C. J., Arntzen, E., Crump, A. R., et al. (2017). Geochemical and microbial community attributes in relation to hyporheic zone geological facies. *Sci. Rep.* 7:12006. doi: 10.1038/s41598-017-12275-w

Hou, Z., Scheibe, T. D., Murray, C. J., Perkins, W. A., Arntzen, E. V., Ren, H., et al. (2019). Identification and mapping of riverbed sediment facies in the Columbia River through integration of field observations and numerical simulations. *Hydrol. Process.* 33, 1245–1259. doi: 10.1002/hyp.13396

Irvine, D. J., Brunner, P., Franssen, H.-J. H., and Simmons, C. T. (2012). Heterogeneous or homogeneous? Implications of simplifying heterogeneous streambeds in models of losing streams. *J. Hydrol.* 424, 16–23. doi: 10.1016/j.jhydrol.2011.11.051

Kasahara, T., and Wondzell, S. M. (2003). Geomorphic controls on hyporheic exchange flow in mountain streams. *Water Res. Res.* 39, SBH 3-1–SBH 3-14. doi: 10.1029/2002WR001386

Kasenow, M. (2002). *Determination of Hydraulic Conductivity From Grain Size Analysis*. Water Resources Publication.

Lackey, G., Neupauer, R. M., and Pitlick, J. (2015). Effects of streambed conductance on stream depletion. *Water* 7, 271–287. doi: 10.3390/w7010271

Landon, M. K., Rus, D. L., and Harvey, F. E. (2001). Comparison of instream methods for measuring hydraulic conductivity in sandy streambeds. *Groundwater* 39, 870–885. doi: 10.1111/j.1745-6584.2001.tb02475.x

Liaw, A., and Wiener, M. (2002). Classification and regression by randomforest. *R News* 2, 18–22.

Lu, C., Chen, X., Cheng, C., Ou, G., and Shu, L. (2012). Horizontal hydraulic conductivity of shallow streambed sediments and comparison with the grain-size analysis results. *Hydrol. Process.* 26, 454–466. doi: 10.1002/hyp.8143

Malcolm, I., Soulsby, C., Youngson, A., and Petry, J. (2003). Heterogeneity in ground water–surface water interactions in the hyporheic zone of a salmonid spawning stream. *Hydrol. Process.* 17, 601–617. doi: 10.1002/hyp.1156

McCallum, A. M., Andersen, M. S., Rau, G. C., Larsen, J. R., and Acworth, R. I. (2014). River-aquifer interactions in a semiarid environment investigated using point and reach measurements. *Water Resour. Res.* 50, 2815–2829. doi: 10.1002/2012WR012922

Mingers, J. (1989). An empirical comparison of selection measures for decision-tree induction. *Mach. Learn.* 3, 319–342. doi: 10.1007/BF00116837

Naghibi, S. A., Ahmadi, K., and Daneshi, A. (2017). Application of support vector machine, random forest, and genetic algorithm optimized random forest models in groundwater potential mapping. *Water Res. Manag.* 31, 2761–2775. doi: 10.1007/s11269-017-1660-3

Niehus, S., Perkins, W., and Richmond, M. (2014). *Simulation of Columbia River Hydrodynamics and Water Temperature From 1917 Through 2011 in the Hanford Reach. Final Report PNWD-3278, Battelle-Pacific Northwest Division*. Richland, WA.

Odong, J. (2007). Evaluation of empirical formulae for determination of hydraulic conductivity based on grain-size analysis. *J. Am. Sci.* 3, 54–60.

Pal, M. (2005). Random forest classifier for remote sensing classification. *Int. J. Remote Sens.* 26, 217–222. doi: 10.1080/01431160412331269698

Perkins, W. A., and Richmond, M. C. (2007a). *MASS2, Modular Aquatic Simulation System in Two Dimensions, Theory and Numerical Methods*. Richland, WA: Pacific Northwest National Lab(PNNL).

Perkins, W. A., and Richmond, M. C. (2007b). *MASS2, Modular Aquatic Simulation System in Two Dimensions, User Guide and Reference*. Richland, WA: Pacific Northwest National Lab(PNNL).

Peters, J., De Baets, B., Verhoest, N. E., Samson, R., Degroeve, S., De Becker, P., et al. (2007). Random forests as a tool for ecohydrological distribution modelling. *Ecol. Modell.* 207, 304–318. doi: 10.1016/j.ecolmodel.2007.05.011

R Core Team (2013). *R: A Language and Environment For Statistical Computing*.

Rodriguez-Galiano, V. F., Ghimire, B., Rogan, J., Chica-Olmo, M., and Rigol-Sanchez, J. P. (2012). An assessment of the effectiveness of a random forest classifier for land-cover classification. *ISPRS J. Photogramm. Remote Sens.* 67, 93–104. doi: 10.1016/j.isprsjprs.2011.11.002

Salehin, M., Packman, A. I., and Paradis, M. (2004). Hyporheic exchange with heterogeneous streambeds: Laboratory experiments and modeling. *Water Resour. Res.* 40:W11504. doi: 10.1029/2003WR002567

Sawyer, A. H., and Cardenas, M. B. (2009). Hyporheic flow and residence time distributions in heterogeneous cross-bedded sediment. *Water Resour. Res.* 45:W08406. doi: 10.1029/2008WR007632

Schilling, O. S., Irvine, D. J., Hendricks Franssen, H. J., and Brunner, P. (2017). Estimating the spatial extent of unsaturated zones in heterogeneous river-aquifer systems. *Water Resour. Res.* 53, 10583–10602. doi: 10.1002/2017WR020409

Shepherd, R. G. (1989). Correlations of permeability and grain size. *Groundwater* 27, 633–638. doi: 10.1111/j.1745-6584.1989.tb00476.x

Song, X., Chen, X., Stegen, J., Hammond, G., Song, H. S., Dai, H., et al. (2018). Drought conditions maximize the impact of high-frequency flow variations on thermal regimes and biogeochemical function in the hyporheic zone. *Water Resour. Res.* 54, 7361–7382. doi: 10.1029/2018WR022586

Sophocleous, M. (2002). Interactions between groundwater and surface water: the state of the science. *Hydrogeol. J.* 10, 52–67. doi: 10.1007/s10040-001-0170-8

Tang, Q., Kurtz, W., Brunner, P., Vereecken, H., and Franssen, H.-J. H. (2015). Characterisation of river–aquifer exchange fluxes: the role of spatial patterns of riverbed hydraulic conductivities. *J. Hydrol.* 531, 111–123. doi: 10.1016/j.jhydrol.2015.08.019

Tang, Q., Kurtz, W., Schilling, O., Brunner, P., Vereecken, H., and Franssen, H.-J. H. (2017). The influence of riverbed heterogeneity patterns on river-aquifer exchange fluxes under different connection regimes. *J. Hydrol.* 554, 383–396. doi: 10.1016/j.jhydrol.2017.09.031

Tang, Q., Schilling, O. S., Kurtz, W., Brunner, P., Vereecken, H., and Hendricks Franssen, H. J. (2018). Simulating flood-induced riverbed transience using unmanned aerial vehicles, physically based hydrological modeling, and the ensemble kalman filter. *Water Resour. Res.* 54, 9342–9363. doi: 10.1029/2018WR023067

Tesoriero, A. J., Gronberg, J. A., Juckem, P. F., Miller, M. P., and Austin, B. P. (2017). Predicting redox-sensitive contaminant

concentrations in groundwater using random forest classification. *Water Resour. Res.* 53, 7316–7331. doi: 10.1002/2016WR020197

Conflict of Interest: The authors declare that the research was conducted in the absence of any commercial or financial relationships that could be construed as a potential conflict of interest.

frontiers in Water

ORIGINAL RESEARCH
published: 26 November 2020
doi: 10.3389/frwa.2020.564211

High-Performance Simulation of Dynamic Hydrologic Exchange and Implications for Surrogate Flow and Reactive Transport Modeling in a Large River Corridor

Yilin Fang, Xuehang Song, Huiying Ren, William A. Perkins, Pin Shuai, Marshall C. Richmond, Zhangshuan Hou, Jie Bao, Xingyuan Chen and Timothy D. Scheibe*

Pacific Northwest National Laboratory, Richland, WA, United States

OPEN ACCESS

Edited by:
Carl I. Steefel, Lawrence Berkeley National Laboratory, United States

Reviewed by:
Joseph Guillaume, Australian National University, Australia
Judson Harvey, United States Geological Survey (USGS), United States

***Correspondence:**
Yilin Fang
yilin.fang@pnnl.gov

Specialty section:
This article was submitted to Water and Critical Zone, a section of the journal Frontiers in Water

Received: *20 May 2020*
Accepted: *05 November 2020*
Published: *26 November 2020*

Citation:
Fang Y, Song X, Ren H, Perkins WA, Shuai P, Richmond MC, Hou Z, Bao J, Chen X and Scheibe TD (2020) High-Performance Simulation of Dynamic Hydrologic Exchange and Implications for Surrogate Flow and Reactive Transport Modeling in a Large River Corridor. Front. Water 2:564211. doi: 10.3389/frwa.2020.564211

Hydrologic exchange flows (HEFs) have environmental significance in riverine ecosystems. Key river channel factors that influence the spatial and temporal variations of HEFs include river stage, riverbed morphology, and riverbed hydraulic conductivity. However, their impacts on HEFs were often evaluated independently or on small scales. In this study, we numerically evaluated the combined interactions of these factors on HEFs using a high-performance simulator, PFLOTRAN, for subsurface flow and transport. The model covers 51 square kilometers of a selected river corridor with large sinuosity along the Hanford Reach of the Columbia River in Washington, US. Three years of spatially distributed hourly river stages were applied to the riverbed. Compared to the simulation when riverbed heterogeneity is not ignored, the simulation using homogeneous riverbed conductivity underestimated HEFs, especially upwelling from lateral features, and overestimated the mean residence times derived from particle tracking. To derive a surrogate model for the river corridor, we amended the widely used transient storage model (TSM) for riverine solute study at reach scale with reactions. By treating the whole river corridor as a batch reactor, the temporal changes in the exchange rate coefficient for the TSM were derived from the dynamic residence time estimated from the hourly PFLOTRAN results. The TSM results were evaluated against the effective concentrations in the hyporheic zone calculated from the PFLOTRAN simulations. Our results show that there is potential to parameterize surrogate models such as TSM amended with biogeochemical reactions while incorporating small-scale process understandings and the signature of time-varying streamflow to advance the mechanistic understanding of river corridor processes at reach to watershed scales. However, the assumption of a well-mixed storage zone for TSM should be revisited when redox-sensitive reactions in the storage zones play important roles in river corridor functioning.

Keywords: river corridor, hydrologic exchange flow, residence time, transient storage model, particle tracking, reach-scale flow and transport

INTRODUCTION

The concept of river corridors that integrate in-stream transport with lateral and vertical exchange across interfaces (Harvey and Gooseff, 2015) has been increasingly recognized due to their valuable ecological functions. The surrounding sediments along the river corridor, or the hyporheic zones (HZ), directly relate with the stream surface water in terms of activity and hydrologic connectivity across microscale, stream-reach scale, and catchment scale (Boulton et al., 1998). Bidirectional mixing, or hydrologic exchange flow, at the interface of stream and HZs is important in influencing stream water quality, water temperature, fish conservation, microbial communities, dissolved organic matter processing, and groundwater contamination (Boulton et al., 1998; Edwardson et al., 2003; DiStefano et al., 2009; Febria et al., 2010; Wexler et al., 2011; Dickson et al., 2012; Kawanishi et al., 2017; Haddou et al., 2018; Harjung et al., 2018; Lewandowski et al., 2019).

River corridors are heterogeneous in space, non-stationary, and involve multiscale feedbacks (Ward and Packman, 2019). Previous studies suggested that research on river corridor processes has suffered from the lack of the long-term (weeks to years) investigations on the dynamic driving forces (e.g., streamflow, evapotranspiration) of hyporheic processes across different scales (Boano et al., 2007; Helton et al., 2012; Larsen et al., 2014; Anibas et al., 2018; Galloway et al., 2019; Zheng et al., 2019). A recent kilometer scale simulation of a major gravel bed river corridor along the Columbia River by Zachara et al. (2020) suggested that hyporheic zones must be frequently monitored under different flow conditions for water quality concerns because of the complicated multidirectional flow behaviors. Studies accounting for the dynamic hydrologic processes on hyporheic exchange and biogeochemical reactions have started to emerge in recent years (Larsen et al., 2014; Rahimi et al., 2015; Gomez-Velez et al., 2017; Dwivedi et al., 2018; Liu and Chui, 2018; Singh et al., 2019; Zheng et al., 2019; Kruegler et al., 2020). However, these studies mainly focused on the spatial and temporal patterns of HEFs and biogeochemistry for synthetic individual bedform or two-dimensional cross-sections of single geomorphic features along the river corridor. Scaling these observed complex patterns from small scale localized sampling to reach scale and basin scale investigation is challenging as they are influenced by geomorphic and hydrologic dynamics (Helton et al., 2012), channel morphology, bed roughness, and permeability (Triska et al., 1989; Hassan et al., 2015), hydrologic connectivity (Datry et al., 2008), and vegetation feedbacks (Magliozzi et al., 2019).

On the other hand, reach scale river corridor exchanges are often quantified using the transient storage models (TSM) (e.g., Bencala, 1983; Harvey et al., 1996; Runkel et al., 1998; Briggs et al., 2009). Despite its simplicity, TSM has been extensively used to study riverine solute transport since its first introduction fifty years ago. TSM is a simple expansion of the one-dimensional in-stream transport equation to include bilateral exchange processes between the main-channel and the well-mixed transient storage zones (Bencala, 1983). This model assumes that the amounts of water transferred between the stream and subsurface are insignificant at the reach scale and the water transfer only influences solute transport (Bencala et al., 2011). The exchange process is often represented by a single-rate mass transfer. In the past, the hyporheic exchange rates were obtained from the calibration of field tracer experiments as they are impractical to measure directly over large areas (Boano et al., 2014). Reach scale tracer investigations can also be effective in providing bulk reactivity for a particular biogeochemical constituent of interest (Harvey and Fuller, 1998; Jonsson et al., 2004; Harvey et al., 2013; Lemke et al., 2013), but they rely on data fitting from the observations and mechanistic process understanding cannot be gained (Boano et al., 2014). There were a few examples of TSM applications to reactive tracers (Bencala, 1983; Harvey and Fuller, 1998; Gooseff et al., 2005; Knapp and Cirpka, 2017; Kelleher et al., 2019), but they only focused on a single reactive component.

A recent review article by Ward and Packman (2019) calls for a framework and theoretical models of river corridor exchange to accurately predict the hydrologic exchange in the river corridor at the scales of stream reaches and entire networks. Lewandowski et al. (2019) also highlighted the research focus on HEF processes that link hydrological, biogeochemical and ecological processes. In this research, we investigate how mechanistic understanding from high resolution three-dimensional (3D) simulations of flow and reactive transport induced by multiple years of transient stream discharge in a large gravel bed river corridor can be used to inform the development of reach scale reduced order models, such as the transient storage models. We use synthetic data generated by high-resolution 3D physically-based simulations to derive and test a surrogate TSM model and identify future development needs. Given the physical basis of the high-resolution model it is reasonable to assume that it is a plausible representation of a realistic system, although we recognize that it is not a precise representation of any particular real system. While TSM models can be parameterized and tested using field tracer tests, the size and flow rate of the Columbia River renders such tests impractical in this case. Therefore, testing the performance of a simpler empirical model (the TSM) against the high-resolution model outputs is one reasonable way to assess potential strengths and weaknesses of the TSM for this large system. The results of the 3D simulations were used to parameterize the exchange coefficients of the TSM and were compared with the TSM simulation results, for both conservative and reactive transport, to identify TSM model weaknesses and future model development needs. We hypothesize that transient streamflow and riverbed heterogeneity have significant effects on the zonation of HZs, residence time of HEFs within HZs, and biogeochemical reaction rate constants at the reach scale.

METHODS

Study Area

The study river corridor is located at the 100-H area along the Hanford Reach (an eight-order stream) of the Columbia River in the southeastern Washington State (**Figure 1A**). The Hanford Reach provides a refuge for native fish, riverine wildlife and plants (Rickard and Gray, 1995). The bottom substrate of the river consists mainly of cobbles and boulders, and the flow rate

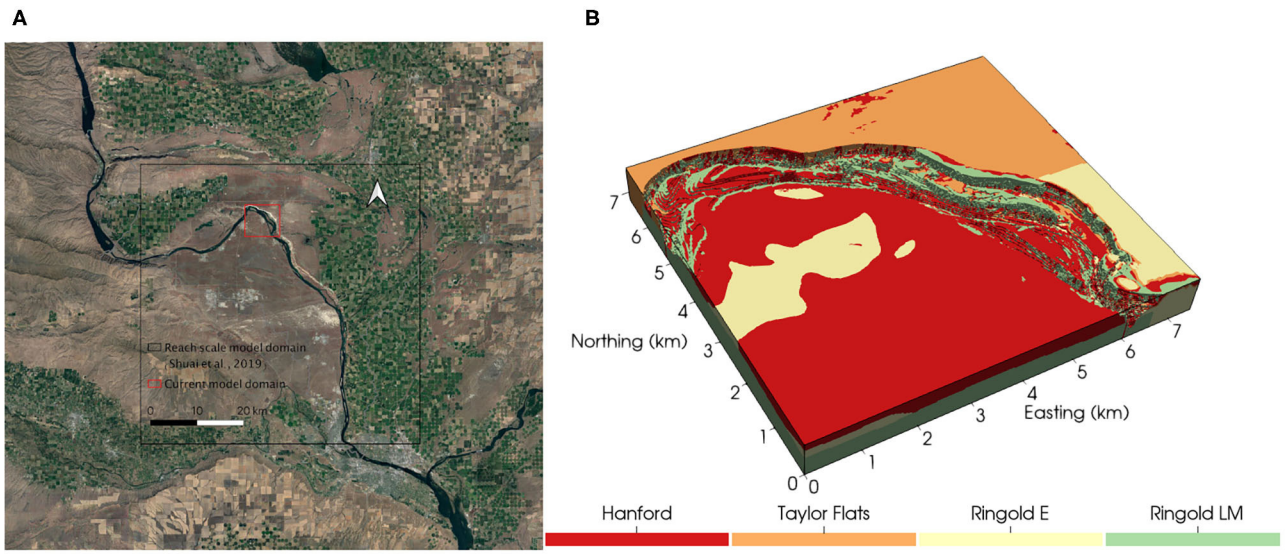

FIGURE 1 | (A) The Hanford reach and the study domain (bounded in red). The reach scale model in Shuai et al. (2019) is bounded in black. **(B)** Geologic units at the study domain.

in the Hanford Reach is regulated by upstream dams in response to hydroelectric power demand (Dauble et al., 1989), ranging between 1,900 and 5,600 m^3/s depending on season (Zachara et al., 2020). The water level fluctuates up to 2 m daily due to discharge variation from the Priest Rapids Dam (Arntzen et al., 2006).

At our selected location, the river meanders north and then southeast (**Figure 1**). The unconfined aquifer of the river corridor consists primarily of the Hanford Formation composed of Pleistocene-age flood deposits and the underlying late-Miocene to late-Pliocene Ringold Formation formed from river and lake sediments (Thorne et al., 2006; Shuai et al., 2019). The Ringold Formation in the 100-H area is broadly divided into Ringold E unit, Ringold Taylor Flats unit, and Ringold Lower Mud unit. The geologic unit of the simulated domain is shown in **Figure 1B** and their hydrologic properties are summarized in **Table 1**. The study domain occupies an area of 50.864 km^2. The domain is discretized into 748 × 680 × 30 (15,096,000) elements of 10 m resolution in the horizontal direction and 1 m in the vertical direction. The bottom elevation is 90 m above sea level. The riverbed is delineated using a combination of LiDAR and other measured bathymetric elevation (Coleman et al., 2010).

Subsurface Flow and Reactive Transport Simulation

To investigate the hydrologic exchange fluxes at the riverbed driven by multi-year stream discharge, we used the state-of-the-art massively parallel subsurface flow and reactive transport code, PFLOTRAN. PFLOTRAN is an open source code, which solves a system of non-linear partial differential equations to describe multiphase, multicomponent and multiscale reactive flow and transport in porous materials (Hammond et al., 2014). For this study, the Richards Equation was solved for the variably saturated flow with the van Genuchten (Van Genuchten, 1980) and Burdine (Burdine, 1953) constitutive relations for saturation and relative permeability, respectively. The simulation period is from 2013 to 2015, which covers two normal flow years and a low flow year in 2015.

TABLE 1 | Hydrogeologic properties of geologic units.

Soil type	Horizontal permeability (m^2)	Vertical permeability (m^2)	Porosity
Hanford	7.38×10^{-9}	7.38×10^{-10}	0.2
Taylor flats	1.05×10^{-12}	1.05×10^{-13}	0.43
Ringold E	4.21×10^{-11}	4.21×10^{-12}	0.25
Ringold lower mud	1.05×10^{-12}	1.05×10^{-13}	0.43

Initial and Boundary Conditions for Flow

The initial pressure of the modeled domain was interpolated from the 2012 results of a coarser reach scale simulation in Shuai et al. (2019). The bottom boundary of the domain was prescribed as no flow condition as it was constrained by the low permeable Ringold units. The top boundary was also set as no-flow as the surface recharge is negligible in the semiarid climate zone (Rockhold et al., 1995). The inland boundaries of the domain were prescribed as hydrostatic conditions, using transient pressures interpolated from the reach scale simulation in Shuai et al. (2019). To represent a low permeable thin alluvium layer at the sediment-water interface, a heterogeneous-conductance type boundary condition was imposed on each grid cell of the riverbed. The conductance type condition is similar to a seepage face, which dampens the effect of river stage fluctuations (Hammond and Lichtner, 2010). The flow rate for

TABLE 2 | Reactive transport conditions.

Condition type	CH_2O (mol/L)	NO_3^- (mol/L)	O_2 (mol/L)	$C_5H_7O_2N$ (mol/L)
Initial condition	4.16×10^{-5}	3.96×10^{-4}	2.66×10^{-4}	1.0×10^{-5}
Lateral boundary condition	4.16×10^{-5}	3.96×10^{-4}	2.66×10^{-4}	1.0×10^{-5}
River boundary condition	2.58×10^{-4}	8.87×10^{-6}	3.59×10^{-4}	1.0×10^{-5}

this type of boundary is proportional to the head difference, with conductance as the constant of proportionality. Hourly river stages simulated using the Modular Aquatic Simulation System in two dimensions (MASS2) simulator (Perkins and Richmond, 2004), as described by Niehus et al. (2014), were assigned to each river boundary cell.

Reactive Transport

To evaluate the effect of dynamic HEFs on reaction rates at the reach scale, we added a conservative tracer and the following two-step denitrification reactions and an oxidative respiration reaction based on previous studies by Song et al. (2018) at a nearby area in the reactive transport simulation:

$$CH_2O + 1.3\,NO_3^- + 0.07\,NH_4^+ = 1.3\,NO_2^- + 0.65\,CO_2 + 0.07\,C_5H_7O_2N \quad (1)$$

$$CH_2O + 1.32\,NO_2^- + 0.002\,NH_4^+ = 0.66\,N_2 + 0.99\,CO_2 + 0.002\,C_5H_7O_2N \quad (2)$$

$$CH_2O + 0.2167\,O_2 + 0.1567\,NH_4^+ = 0.2167\,CO_2 + 0.1567\,C_5H_7O_2N \quad (3)$$

Cell decay or lysis of biomass (Newcomer et al., 2018) and turnover back to CH_2O was also considered in the model. Reaction rate formulations follow a modified dual-Monod type. The maximum uptake rate of O_2, NO_3^-, and NO_2^- are 84.78, 28.26, and 23.28 d^{-1}, respectively. The initial and boundary conditions are shown in **Table 2**. NH_4^+ was assumed to be unlimited. A conservative tracer with a concentration of 10^{-3} mol/L was assigned at the river boundary to indicate the concentration of river water. The four lateral boundaries were treated as tracer free.

Case Scenarios

We ran simulations for five case scenarios:

- Case 1. Flow and solute transport for year 2013–2015 with homogenous riverbed conductance of 10^{-12} m;
- Case 2. Flow and solute transport for year 2013–2015 with heterogeneous riverbed conductance;
- Case 3. Flow and solute transport for year 2014 using the end of the simulation in year 2013 of Case 1 as the initial condition for flow, and setting initial conservative tracer to 0.0 mol/L;
- Case 4. Flow and solute transport for year 2014 using the end of the simulation in year 2013 of Case 2 as the initial condition for flow, and setting initial conservative tracer to 0.0 mol/L;

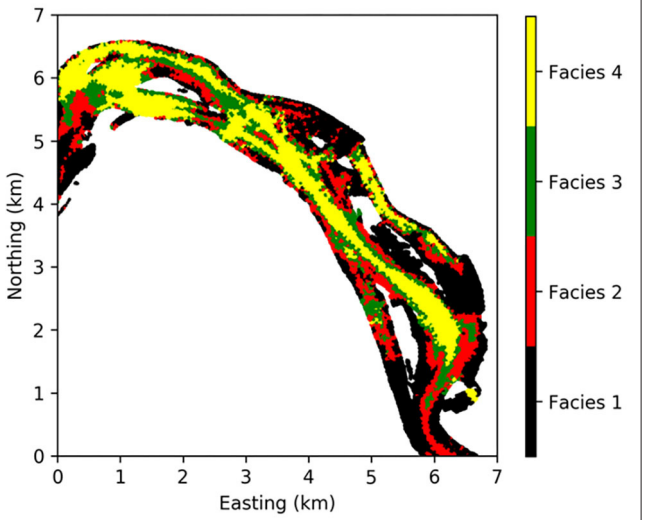

FIGURE 2 | Map of riverbed facies.

- Case 5. Flow and reactive transport for year 2014 using the end of the simulation in year 2013 of Case 1 as the initial condition for flow, and setting initial and boundary conditions of chemical components to those in **Table 2**.

Cases 1 and 2 were used to examine the effect of dynamic discharge and riverbed heterogeneity on HEFs. It is challenging to quantify the spatial distribution of conductance over the reach scale. A recent effort by Hou et al. (2019) provided a map of the riverbed sediments along the Hanford Reach based on the integration of diverse observations with numerical simulations of river hydrodynamics using facies classifications. This map enabled us to assign unique conductance for each of the four facies identified in the study area (**Figure 2**) to evaluate how significant the HEFs can be affected by riverbed heterogeneity. The conductance is 1.07×10^{-13}, 9.11×10^{-13}, 3.97×10^{-12}, and 8.01×10^{-12} m, for facies 1, 2, 3, and 4, respectively. Facies 1 to 4 correspond to increasing mean shear stresses from river hydrodynamics simulation (Hou et al., 2019). The homogeneous conductance is the geometric mean of these heterogeneous values.

Cases 1 and 2 were used to define the hyporheic zones in the river corridor. Results from Cases 3, 4, and 5 were used for reduced order model development for reach-scale simulation. We generated synthetic reach-scale datasets of concentrations in the hyporheic zones for tracer and reactive components from cases 3 to 5 treating the whole simulation domain as a single river corridor of a reach. All simulations were run on the EMSL (the William R. Wiley Environmental Molecular Sciences Laboratory) cascade high performance computing cluster using 1,596 process cores. Hourly outputs of around 9.6 terabytes for each year were recorded for analysis and post-processing.

Reduced-Order Model

The transient storage model (TSM) (Bencala, 1983), a simplified reduced order model, has been extensively used to quantify hyporheic exchange flows based on tracer injection experiments (Bencala et al., 2011). The partial differential formulation of the model is shown in the following equations (Harvey et al., 1996; Boano et al., 2014; Larsen et al., 2014):

$$\frac{\partial C}{\partial t} + \frac{\partial}{\partial x}\left(\frac{Q}{A}C - D\frac{\partial C}{\partial x}\right) = \propto (C_s - C) \quad (4)$$

$$\frac{\partial C_s}{\partial t} = \alpha\frac{A}{A_s}(C - C_s) = \frac{1}{\tau_s}(C - C_s) \quad (5)$$

where C [M L^{-3}] and C_s [M L^{-3}] are the solute concentrations in the main channel and in the hyporheic (storage) zone, respectively, Q [L^3 T^{-1}] is the volumetric streamflow rate, A [L^2] and A_s [L^2] are the cross-sectional areas of the main channel and the hyporheic zone, respectively, D [L^2 T^{-1}] is the longitudinal dispersion coefficient in the river, and α [T^{-1}] is the storage zone exchange coefficient, τ_s [T] is the residence time of the storage zone, (α A/A_s) is the inverse of the residence time in the storage zone (Harvey et al., 1996; Larsen et al., 2014).

The storage zone size and the residence time are the two key parameters required to run the TSM model. In order to use the conservative tracer simulation to provide meaningful parameter estimates for the reduced order model, massively parallel forward particle tracking algorithm was used to find the residence time distribution and flow paths of the hydrologic exchange flows. Particles were released from 100,000 randomly sampled locations on the river boundary at 1,000 time points randomly selected between October 2013 and September 2014.

We assumed a single transient storage zone or hyporheic zone (HZ) for the whole river corridor. After 1-year spinup, the volume of the storage zone was defined as the region with 95% of the stream water, or tracer concentration of 0.0095 mol/L, following the geochemical definition in the literature (Triska et al., 1989; Singh et al., 2019) using the results of Cases 1 and 2 in 2014. The total mass of solutes of Case 3 and Case 4 within the whole transient storage zone volume defined in Case 1 and Case 2 were calculated, respectively. The total mass in each case was then used to calculate the hourly whole reach HZ concentration (mass divided by HZ volume) response. The same procedure was performed for the reactive components, i.e., CH_2O, NO_3^-, and O_2 in Case 5.

We amended the TSM model with reactions and the following equation was used to calculate the hyporheic zone reactive component concentrations at the reach scale by treating it as a batch reactor. Concentrations of reactive species are fixed in the river (i.e., Equation 4 is not solved) as shown in **Table 2**.

$$\frac{dC_s}{dt} = \frac{1}{\tau_s}(C - C_s) + \sum\nolimits_{i=1}^{3} \mu_i R_i \quad (6)$$

where R_i is the reaction rate of reactions shown in Equations (1–3), and μ_i is the stoichiometric coefficient of a species in reaction i, which is negative for reactants and positive for products. For example, the above equation for $C_5H_7O_2N$ and NO_2^- can be written as Equation (7) and Equation (8), respectively.

$$\frac{dC_s}{dt} = \frac{1}{\tau_s}(C - C_s) + 0.07\,R_1 + 0.002\,R_2 + 0.1567\,R_3 \quad (7)$$

$$\frac{dC_s}{dt} = \frac{1}{\tau_s}(C - C_s) + 1.3\,R_1 - 1.32\,R_2 \quad (8)$$

Species concentrations predicted by the reaction amended TSM represented by Equation (6) for CH_2O, NO_3^-, and O_2, will be compared with the average concentrations within the HZ calculated from the PFLOTRAN simulation. Equation 6 is solved using the PFLOTRAN batch reaction module.

Global sensitivity test using the Fourier Amplitude Sensitivity Test (FAST) method will be performed for the TSM as we expect there will be disagreement between the two models for reactive species.

RESULTS AND DISCUSSION

Hydrologic Exchange Flow

We summed up the lateral and vertical hydrologic exchange flow rates for Case 1 and Case 2 after 1-year spinup. The maximum lateral flow is about a tenth of the vertical flow (**Figures 3A,B**). From the hourly PFLOTRAN output during the 2-year simulation, we found that the river gains water from the lateral flow 83.8% of the time for Case 1 and 85.5% of the time for Case 2. The river gains water from the vertical flow 54.7% of the time for Case 1 and 49.8% of the time for Case 2. While the percentages of times for upwelling (denoted as positive value) and downwelling do not make a big difference for the two cases, lateral flows contributed more to the river water for Case 2 with a mean of 0.46 m^3/s due to the heterogenous conductance compared to Case 1 with a mean of 0.21 m^3/s (**Figure 3A**). On the other hand, vertical flow for Case 1 contributed more to the river, with a mean flow rate to the river of 0.47 m^3/s compared to 0.1 m^3/s for Case 2. Vertical downwelling flow rates were stronger than upwelling for both Case 1 and Case 2 (**Figure 3B**). There was a seasonal decrease of lateral flow to the river (**Figure 3C**). Vertical upwelling was strong in the fall, and downwelling is dominant in the wet season (**Figure 3D**). Compared to the Columbia River discharge (1,900–5,600 m^3/s), the hydrologic exchange flow has little effect on river hydrodynamics and transport.

Volume of the Hyporheic Zone

The volume of the hyporheic zone (HZ) for Case 1 and Case 2 was calculated by summing up the pore volumes of those grid cells with tracer concentration equals to or $>$ 0.0095 mol/L (i.e., $\geq$ 95% river water). Hourly HZ volumes varied between 5.7 $\times$ 10^6 and 1.23 $\times$ 10^7 m^3 for Case 1, and between 6.11 $\times$ 10^6 and 1.27 $\times$ 10^7 m^3 for Case 2. The distributions of the HZ volume displayed pronounced multimodal character as shown in the bean plot created using the R package "beanplot" (**Figure 4A**). The difference of mean HZ volume between the two cases was small. The seasonal expansion and contraction of HZ follow the dynamics of stream discharge (**Figure 4B**). HZ volume for

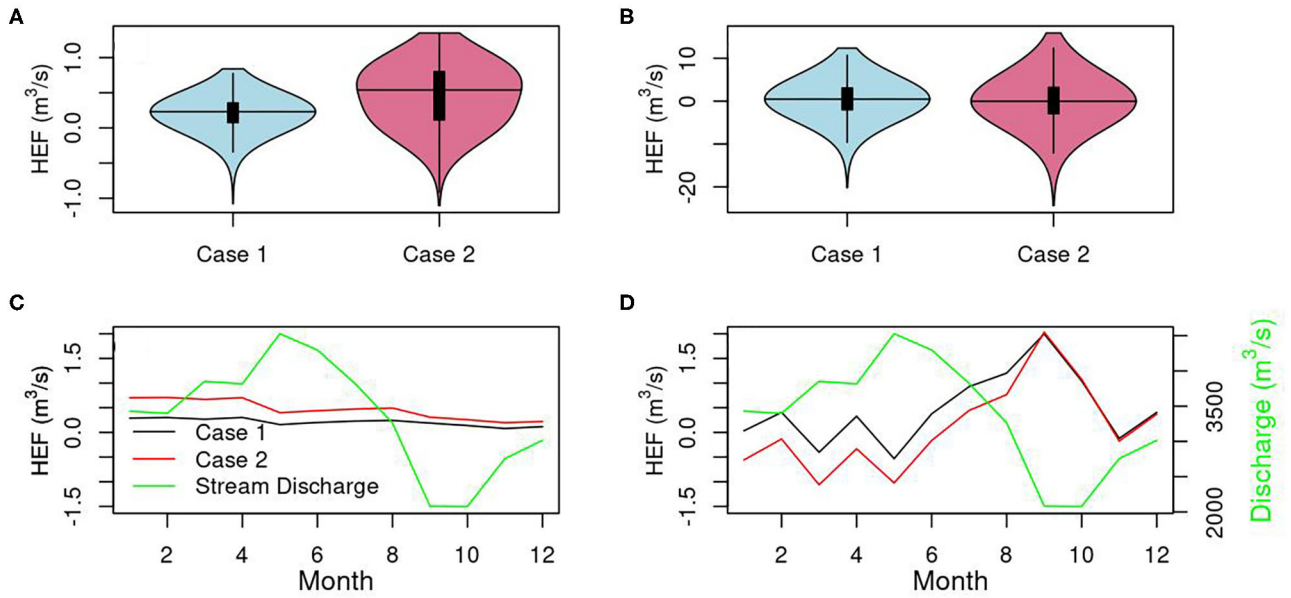

FIGURE 3 | Violin plots of temporal hydrologic exchange flow rate from PFLOTRAN in the lateral **(A)** and vertical **(B)** direction and seasonal hydrologic exchange flow rate and stream discharge in the lateral **(C)** and vertical **(D)** direction. The river gains water for the positive flow.

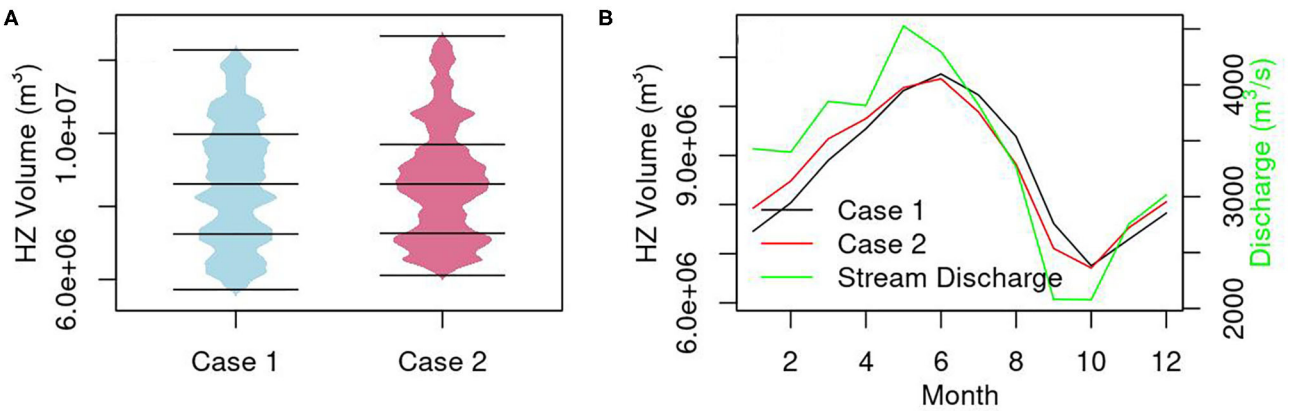

FIGURE 4 | Temporal distribution of HZ volume estimated from the PFLOTRAN simulations **(A)** and seasonal change of HZ volume and stream discharge **(B)**. The solid lines in **(A)** show the quantiles of the HZ volume.

Case 2 was larger than Case 1 when streamflow increased, and smaller when streamflow decreased due to the high riverbed conductance of Facies 4. There was a temporal lag of the peak HZ volume compared to the stream discharge due to the variation in residence time of the hydrologic exchange fluxes.

Reach-Scale Residence Time

A mean residence time of all released particles at a selected time was calculated by weighting the residence time of each particle with its releasing flux. A total of 1,000 reach-scale mean residence times were calculated with the 100 million particles. Compared to Case 1, the longest residence time in Case 2 was shorter than the long-term average of Case 1 (**Figure 5**). Heterogeneous conductance decreased the long-term mean residence time by half, with a mean of 1,639.35 h for Case 1, and 782.89 h for Case 2. Case 1 residence time had a larger variability than Case 2, ranging from 259 to 2,570 h, compared to 291 to 1,520 h for Case 2. In general, the residence time is positively related to stream discharge (**Figure 5B**).

REACTION AMENDED TRANSIENT STORAGE MODEL

Model Validation With Conservative Tracer

Summing up the volume of the grid cells identified as hyporheic zone in year 2014 for Case 1 and Case 2 at every time step, we obtained a reach-scale hyporheic zone volume for

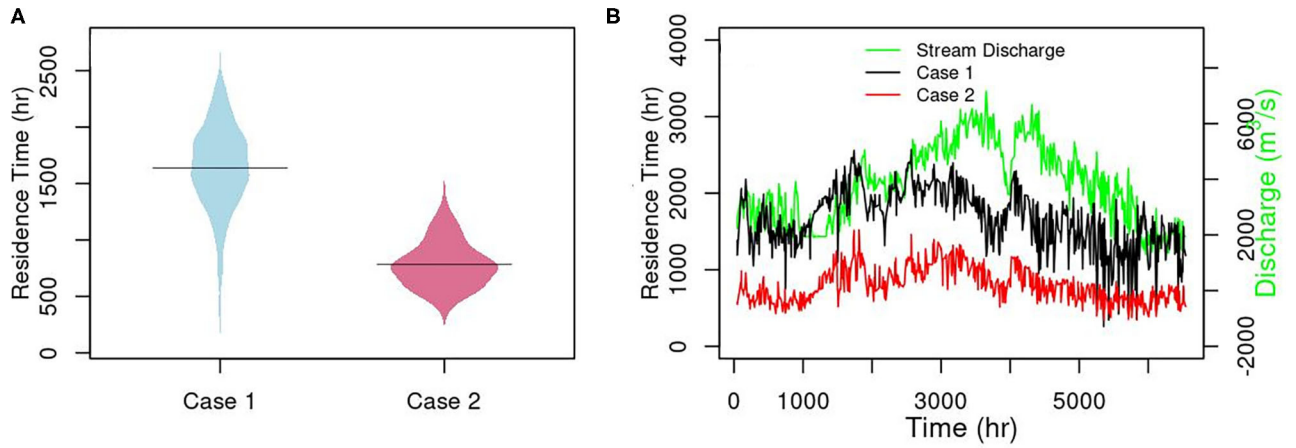

FIGURE 5 | Temporal distribution **(A)**, time series **(B)** of residence time estimated using particle tracking for Case 1 and Case 2.

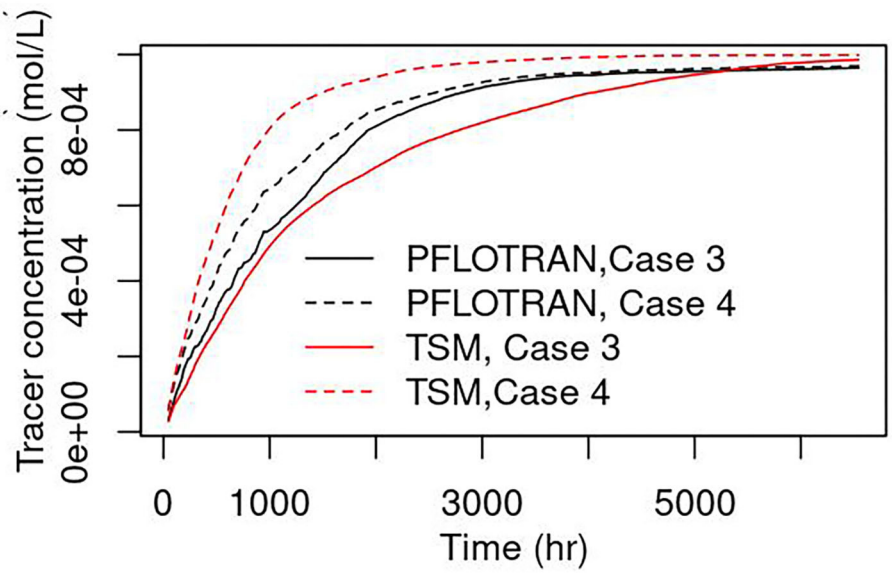

FIGURE 6 | Temporal tracer concentration curves simulated using PFLOTRAN and TSM.

each Case. The mass of conservative tracer simulated in year 2014 from Case 3 and Case 4 in those hyporheic zone grid cells identified in Case 1 were then summed up. Dividing the total mass of conservative tracer by the reach-scale hyporheic zone volume, we obtained a synthetic hourly response of the conservative tracer concentration in the hyporheic zone driven by the dynamic stream discharge. The exchange rate coefficient in Equation (6) is now time-varying. At every time step, the residence time was interpolated from those estimated using particles released during 2014 for both Cases 1 and 2. Our simulation showed that the transient storage model (TSM) without reactions could explain the synthetic tracer data with an R-squared of 0.97 for Case 1 and 0.95 for Case 2 (**Figure 6**). However, TSM underpredicted the concentration for Case 1, and overpredicted for Case 2 compared to the synthetic PFLOTRAN results.

Model Validation With Reactive Components

As shown in **Figure 5**, the minimum reach-scale residence time was $>$ 200 h. Because the time scales of the reactions shown in section Reactive transport were $<$ 1 h, the reaction Damköhler number, Da was $>>$ 1. This means hyporheic exchange flow paths spent too much time in storage, and they were transport limited (Harvey et al., 2019). Case 5 was run for year 2014 using the end of 2013 simulation of Case 1 as the initial condition for flow and chemical initial and boundary conditions as shown in **Table 2**. We summed up the mass of CH_2O, NO_3, and O_2 for

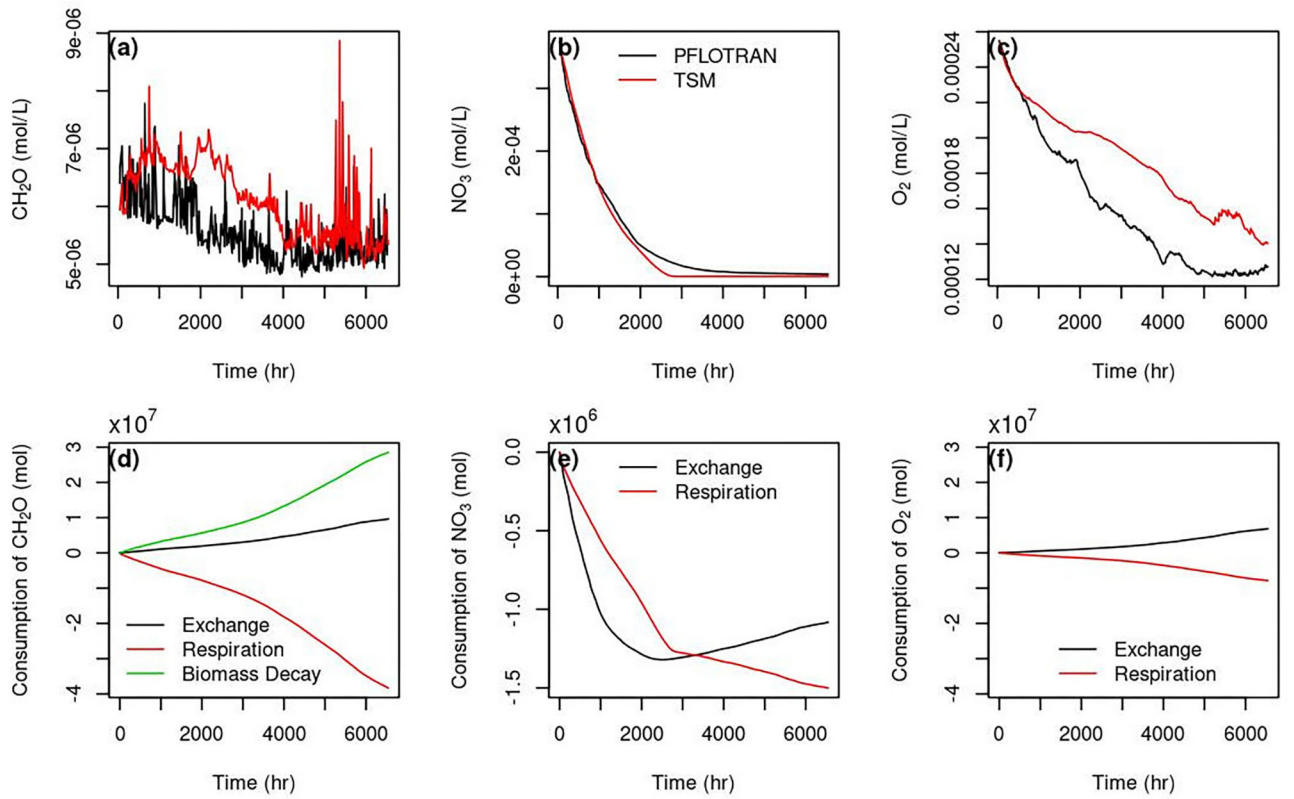

FIGURE 7 | Temporal concentration curves of CH_2O **(a)**, NO_3 **(b)**, and O_2 **(c)** simulated using PFLOTRAN and TSM, and the total consumption (negative) of CH_2O **(d)**, NO_3 **(e)**, and O_2 **(f)** by different processes simulated using TSM.

the hyporheic grid cells identified in Case 1 for 2014, and then normalized to the hyporheic volume calculated for Case 1 at each time step of year 2014 to create a temporal synthetic reach-scale chemical concentration data set. Running the reaction amended TSM using the same exchange rate coefficients as for the tracer validation in Case 3 and the same reaction kinetics in Case 5, the concentration profiles for CH_2O, NO_3, and O_2 are shown in **Figure 7**.

R-squared for CH_2O, NO_3, and O_2 are 0.19, 0.99, and 0.13, respectively. The TSM model has a very good performance for NO_3 except for at low concentrations after 2,000 h (**Figure 7b**), but biased high for CH_2O (**Figure 7a**) and O_2 (**Figure 7c**) compared to the synthetic data. However, the high variability of CH_2O exhibited in the synthetic data was simulated using TSM. The high variability was mainly caused by the balance between the production by biomass decay and exchange, and the consumption by the respiration reactions (**Figure 7d**). The concentration change with time for NO_3 and O_2 are relatively smooth. The hyporheic exchange contributed to the HZ concentrations of CH_2O (**Figure 7d**), and O_2 (**Figure 7f**) during the simulation, but was a sink for HZ NO_3 till 2,000 h (**Figure 7e**). NO_3 consumption was dominated by hyporheic exchange up to 2,000 h. The TSM model performance for NO_3 at low concentrations started to deteriorate when production due to exchange balances the reaction consumption.

Global Sensitivity Analysis

Apart from the residence times, there are 8 reaction kinetic parameters involved in the TSM with reactions. To evaluate whether there exists a single set of rate parameters that can explain the results obtained from the PFLOTRAN simulations using the TSM, we ran simulations using a range of rate parameters previously reported in the literature. Parameter importance was evaluated to identify which rate parameters we should pay our attention to for TSM parameterization. Rate parameters were sampled from 6.24 to 240 (1/d) for the maximum microbial reaction rate of nitrate (k_{NO3}), 0.001–0.05 (mmol/L) for the Monod half-saturation constant of nitrate ($K_{a,NO3}$), 0.0833–0.2583 (mmol/L) for the half-saturation constant of CH_2O ($K_{d,CH2O}$), 4.8–139.2 (1/d) for the maximum microbial reaction rate of aerobic respiration (k_{O2}), 0.001–0.0969 (mmol/L) for the half-saturation constant of O_2 ($K_{a,O2}$) based on parameter bounds in Zarnetske et al. (2011) surveyed from the literature. The lower bound for the maximum microbial reaction rate of nitrite was set to one-tenth of that in Killingstad et al. (2002), and the rest of rate constant bounds for nitrite were the same as nitrate reduction reaction. We also assumed 0.242–3.1536 (1/d) for the biomass decay rate. One thousand six hundred samples were generated using the Fourier Amplitude Sensitivity Test (FAST) method implemented in the Python sensitivity analysis library (SALib) (Herman and Usher, 2017).

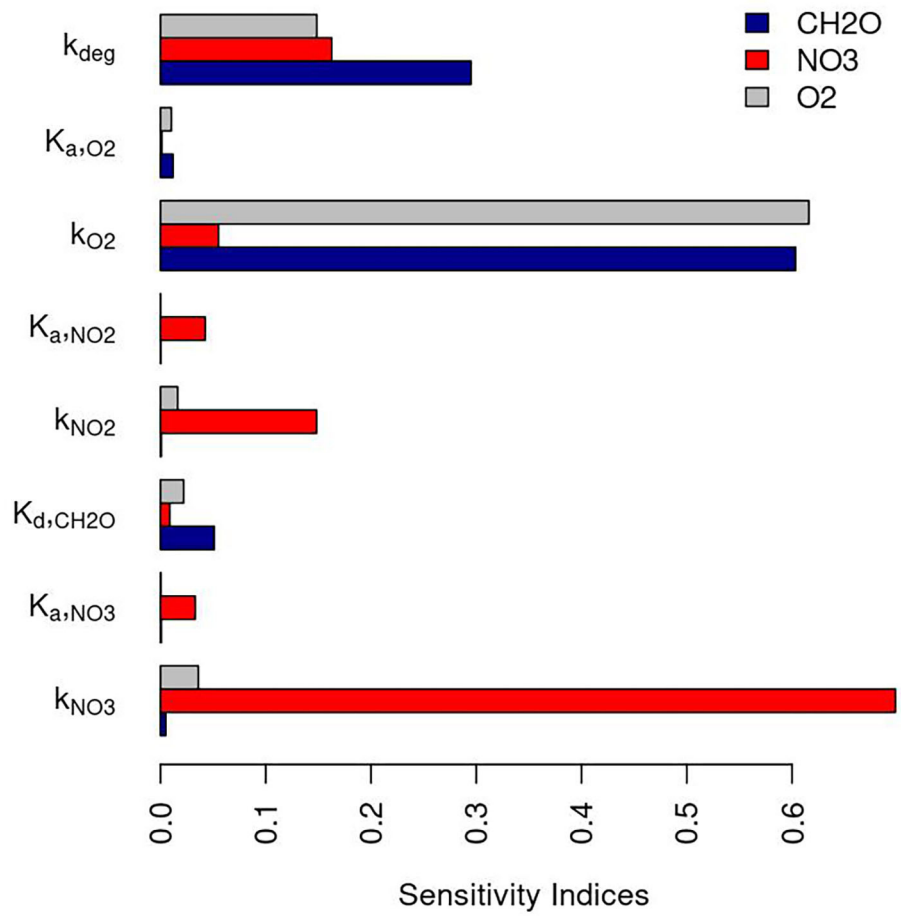

FIGURE 8 | Sensitivity indices of model parameters for TSM simulations.

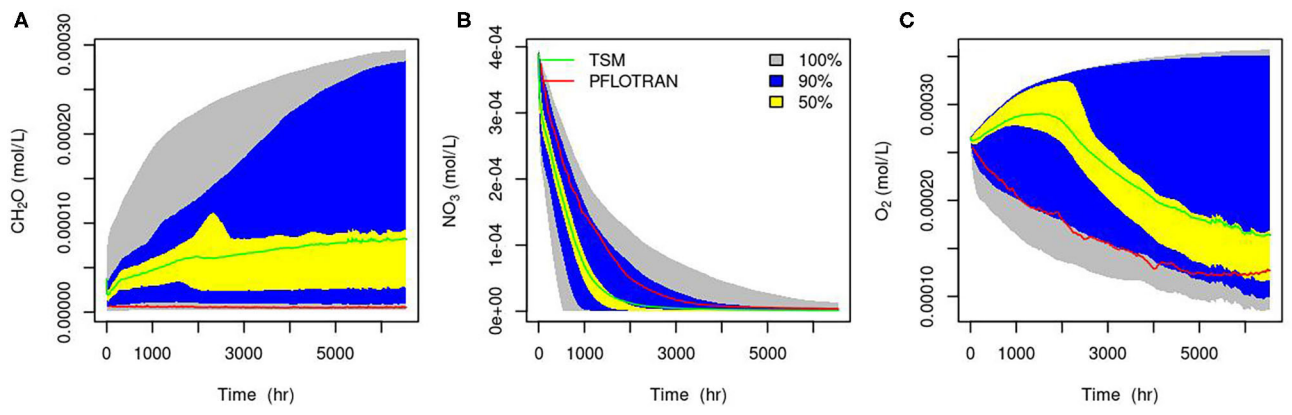

FIGURE 9 | 50, 90, 100% percentiles of 1,600 TSM simulations for the concentrations of CH_2O **(A)**, NO_3^- **(B)**, and O_2 **(C)**, red line is from PFLOTRAN, and green line is the mean of the TSM models at each hour.

Parameter sensitivity were analyzed based on the average of the temporal concentrations of CH_2O, NO_3, and O_2 and the sensitivity indices are shown in **Figure 8**. Reaction rate constants k_{NO3} and k_{O2} are the most important for concentrations of NO_3 and O_2, respectively. The biomass decay rate constant is important for all three reactive components. The maximum rate constant for O_2 reduction (k_{O2}) are of equal importance for O_2 and CH_2O.

The TSM results from the bulk of the simulations did not fit the PLOTRAN results well (**Figure 9**). To check if there is a common set of effective rate parameters for all three reactants, we narrowed down to 5% of the model runs that can explain the observed synthetic concentrations for each reactive component. Plotting the parameters, we were not able to find a common set of important parameters for all of them (**Figure 10**). The parameters also varied with time. For instance, to explain the CH_2O concentration, k_{NO3} is > 100 (1/d) during the earlier time and smaller than 50 (1/d) between 1,000 and 2,000 h (**Figure 10A**). We only showed the parameter space for k_{NO3} as an example. It is challenging to find a constant value for the other parameters too.

DISCUSSION

Do Spatial and Temporal Heterogeneity Matter for Reach-Scale Modeling?

There have been an increasing number of numerical studies emphasizing the impact of spatially and temporally variable conditions on the hyporheic exchange within river corridors. However, none were carried out at the reach-scale accounting for both the long-term dynamics in driving force and the small-scale hydromorphic heterogeneity. This study investigated the response of river corridor hydrologic exchange as a result of time varying streamflow and riverbed heterogeneity for a reach in an eighth-order stream. Riverbed conductance heterogeneity increased the mean lateral hydrologic exchange flow into the river by a factor of 2.2 and decreased the vertical exchange flow into the river by a factor of 4.7. On the other hand, dynamic streamflow changed the dominant downwelling in the wet season to upwelling dominant in the dry season for the vertical flow (**Figure 3D**). As the upwelling becomes stronger in the dry season (**Figure 3D**), the hyporheic volume is significantly reduced (**Figure 4B**), which echoes the findings in Boano et al. (2008) that the upwelling of subsurface water can significantly reduce the volume of hyporheic sediments that receive water from the stream. HEF variability caused by streamflow is larger than that by riverbed conductance for this case study.

Hyporheic volume defined using the geochemical definition showed that the largest expansion at the peak streamflow can be twice as big as that during the low streamflow. The discrepancy in hyporheic volume due to riverbed conductance heterogeneity is not significant compared to that caused by streamflow variability. It is consistent with the conclusion in Sawyer and Cardenas, 2009 that permeability heterogeneity in riverbed sediment is more important in changing the residence times than the volume of the hyporheic zone. Shorter mean residence time can be caused by

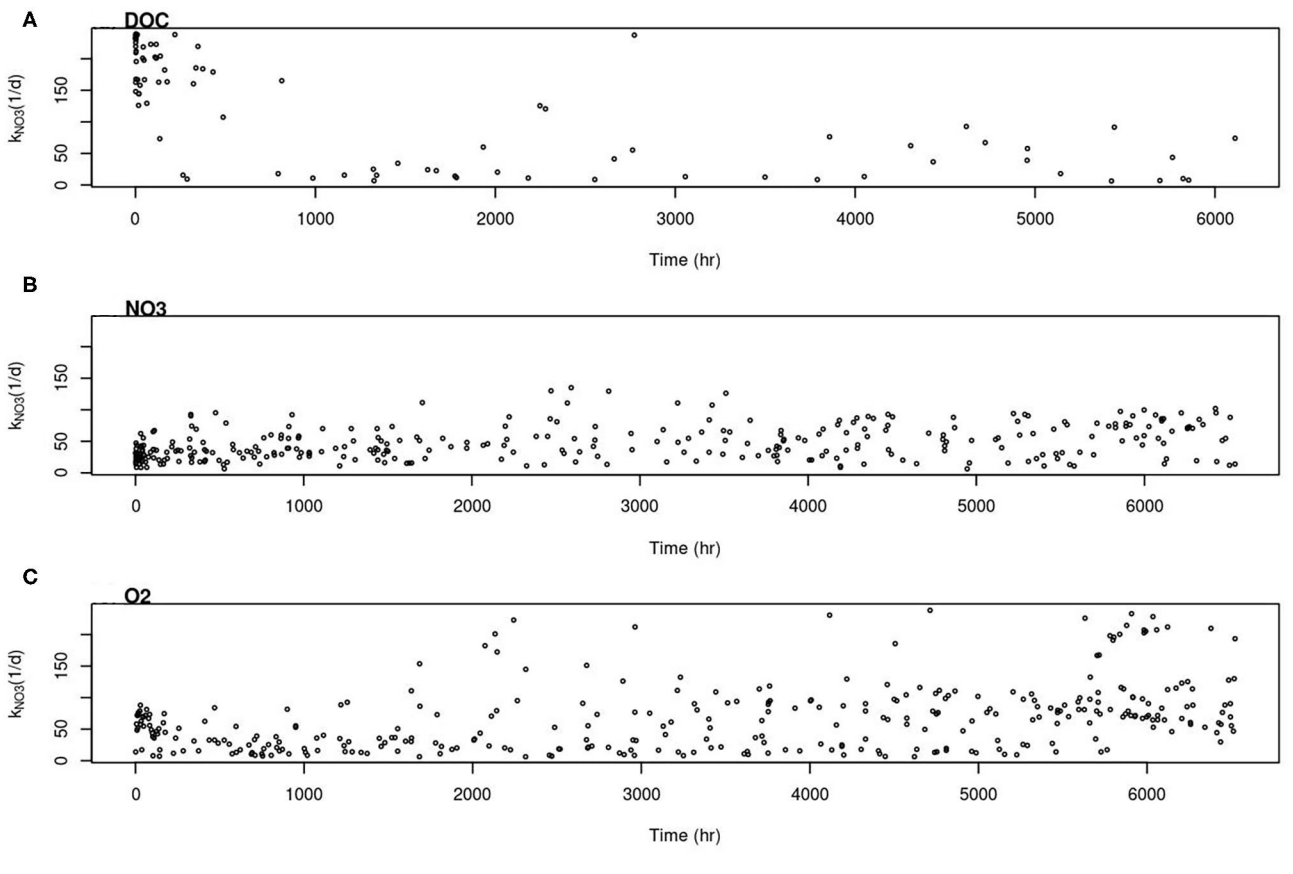

FIGURE 10 | Parameter range of rate constant for nitrate reduction reaction in TSM that can best fit **(A)** CH_2O, **(B)** NO_3^{-1}, and **(C)** O_2.

riverbed heterogeneity compared to the homogenous simulation, which has also been previously reported (Salehin et al., 2004; Tonina et al., 2016).

The riverbed conductance heterogeneity and streamflow variability both have impacts on the reach scale residence times. The difference caused by conductance heterogeneity can be comparable to the difference caused by streamflow variability.

Can a Transient Storage Model Be Developed for Reach-Scale Modeling?

Though not perfect, we showed that it is possible to derive the TSM based on the residence time and synthetic dataset simulated using high resolution flow and reactive transport. We developed a simplified transient storage model (TSM) integrating the streamflow dynamics and riverbed heterogeneity that have been reflected in the residence time to simulate reach-scale processes. The TSM model was agreeable simulating the synthetic reach-scale tracer data. But the discrepancy due to heterogeneity was exaggerated due to the inaccuracy predicting the synthetic observation. The mismatch between the synthetic observations and TSM may be due to the definition of hyporheic zone or some HEF pathways that contributed significantly to the tracer concentrations were not accounted for when deriving the mean residence times. The high bias in O_2 and CH_2O coincided with the low bias of tracer, which may be caused by the cumulative effect of reaction and transport that cannot be simply represented by using the same reaction parameters apart from the aforementioned possible causes.

When including reactions in the TSM, there is a surprisingly good agreement between the TSM and the synthetic observation of nitrate. TSM results shows that the nitrate loss due to the biological reactions varied from 34 to 66% of the total loss combined with hyporheic exchange. For this simulation, nitrate from the hyporheic zone was mainly a source to the river water until HZ nitrate concentration is lower than river concentration. The high bias of CH_2O and O_2 concentrations suggest that the agreement between the TSM and the observations for nitrate might give us a bulk nitrate uptake rate, but it is not enough to explain the other two reactive components. Because the tracer concentration was being underpredicted by the TSM as shown in **Figure 6**, the high bias of CH_2O and O_2 could not be caused by the hyporheic exchange, but effective reaction rates. The results also indicate that the well-mixed assumption in the HZs for TSM should be revisited, especially for redox-sensitive reactions. Adding one-dimensional flow and reactive transport in the HZ might improve the model simulation.

What Did We Learn From the Reduced Order Model?

One of the questions asked in a recent commentary by Knapp and Kelleher (2020) was whether the processes estimated from conceptual parameters are interpretable for TSM. We showed that the TSM model parameters can be interpretable. Our TSM parameters carry the signatures of dynamics streamflow and subsurface heterogeneity. The simplified TSM can assist in uncertainty analysis efficiently to understand the controlling parameters for reach-scale system behavior. Sensitivity analysis on reaction rate parameters showed that they can be time dependent, which is caused by inaccurate conceptualization, such as well-mixed storage zones. The maximum change in cumulative consumption of nitrate is only 2.5% if a constant mean residence time was used for TSM because of the long mean residence time. This suggested that the dynamic exchange rate coefficient was not necessary for this study case. However, the difference between the simulations using a constant vs. time varying residence times became larger if we decreased the residence times by a factor of 10, reaching 7.8%.

High resolution models can give more mechanistic details of a study system, but it is not realistic for every river corridor as it is quite expensive, especially for uncertainty analysis. Combined with TSM models amended with biogeochemical reactions and machine learning (future work) from the high resolution model simulation results, it is possible to better constrain the TSM models and improve the mechanistic understanding of the river corridors and better inform field investigations so that the vulnerability of watersheds to water quality changes due to a variety of stressors can be identified and protected (Ranalli and Macalady, 2010).

CONCLUSIONS

Using high performance flow and reactive transport simulations and a massively parallel particle tracking method, we calculated the dynamic hydrologic exchange fluxes and residence time distributions driven by long-term time-varying stream discharges within a large river corridor, located along an eighth-order stream. While it is possible to interpret the synthetic tracer data at the reach-scale using a transient storage model integrating the signatures of dynamics stream discharge and subsurface heterogeneity, there are still challenges representing multiple reactive components using simplified TSM that's amended with reactions. A bulk reaction rate for a single reactive component may be far from reflecting the true mechanisms in the system of interest. A transferrable, novel multiscale modeling framework integrating multiscale characteristics from high resolution simulations and modified TSMs, e.g., accounting for multirate mass transfer, dynamic reaction kinetics, or depth-resolved flow and transport, is in need in order to improve mechanistic predictions of water quality in streams and map the watersheds of vulnerability for restoration.

DATA AVAILABILITY STATEMENT

The raw data supporting the conclusions of this article will be made available by the authors, without undue reservation.

AUTHOR CONTRIBUTIONS

YF did model simulations and wrote the paper. XS did particle tracking. HR, WP, PS, and MR developed the dataset for model boundary conditions. All co-authors contributed to the writing and model discussion of the paper.

FUNDING

This research described in this publication was supported by the U.S. Department of Energy (DOE), Office of Biological and Environmental Research, Subsurface Biogeochemical Research (SBR) Program through the SBR Scientific Focus Area project at Pacific Northwest National Laboratory. Simulations were performed at EMSL (grid.436923.9), a DOE Office of Science User Facility sponsored by the Office of Biological and Environmental Research. Pacific Northwest National Laboratory is operated for DOE by Battelle.

REFERENCES

Anibas, C., Tolche, A. D., Ghysels, G., Nossent, J., Schneidewind, U., Huysmans, M., et al. (2018). Delineation of spatial-temporal patterns of groundwater/surface-water interaction along a river reach (Aa River, Belgium) with transient thermal modeling. *Hydrogeol. J.* 26, 819–835. doi: 10.1007/s10040-017-1695-9

Arntzen, E. V., Geist, D. R., and Dresel, P. E. (2006). Effects of fluctuating river flow on groundwater/surface water mixing in the hyporheic zone of a regulated, large cobble bed river. *River Res. Appl.* 22, 937–946. doi: 10.1002/rra.947

Bencala, K. E. (1983). Simulation of solute transport in a mountain pool-and-riffle stream with a kinetic mass-transfer model for sorption. *Water Resour. Res.* 19, 732–738. doi: 10.1029/WR019i003p00732

Bencala, K. E., Gooseff, M. N., and Kimball, B. A. (2011). Rethinking hyporheic flow and transient storage to advance understanding of stream-catchment connections. *Water Resour. Res.* 47, 1–9. doi: 10.1029/2010WR010066

Boano, F., Harvey, J. W., Marion, A., Packman, A. I., Revelli, R., Ridolfi, L., et al. (2014). Hyporheic flow and transport processes: mechanisms, models, and biogeochemical implications. *Rev. Geophys.* 52, 603–679. doi: 10.1002/2012RG000417

Boano, F., Revelli, R., and Ridolfi, L. (2007). Bedform-induced hyporheic exchange with unsteady flows. *Adv. Water Resour.* 30, 148–156. doi: 10.1016/j.advwatres.2006.03.004

Boano, F., Revelli, R., and Ridolfi, L. (2008). Reduction of the hyporheic zone volume due to the stream-aquifer interaction. *Geophys. Res. Lett.* 35, 1–5. doi: 10.1029/2008GL033554

Boulton, A. J., Findlay, S., Marmonier, P., Stanley, E. H., and Valett, H. M. (1998). The functional significance of the hyporheic zone in streams and rivers. *Annu. Rev. Ecol. Syst.* 29, 59–81. doi: 10.1146/annurev.ecolsys.29.1.59

Briggs, M. A., Gooseff, M. N., Arp, C. D., and Baker, M. A. (2009). A method for estimating surface transient storage parameters for streams with concurrent hyporheic storage. *Water Resour. Res.* 45, 1–13. doi: 10.1029/2008WR006959

Burdine, N. T. (1953). Relative permeability calculations from pore size distribution data. *T Am. I Min. Met. Eng.* 198, 71–78. doi: 10.2118/225-G

Coleman, A. M., Ward, D. L., Larson, K. B., and Lettrick, J. W. (2010). *Development of a High-Resolution Bathymetry Dataset for the Columbia River through the Hanford Reach. PNNL-19878*. (Richland, WA: Pacific Northwest National Laboratory). doi: 10.2172/1000818

Datry, T., Scarsbrook, M., Larned, S., and Fenwick, G. (2008). Lateral and longitudinal patterns within the stygoscape of an alluvial river corridor. *Fund. Appl. Limnol.* 171, 335–347. doi: 10.1127/1863-9135/2008/0171-0335

Dauble, D. D., Page, T. L., and Hanf, R. W. (1989). Spatial-distribution of juvenile salmonids in the hanford reach, Columbia River. *Fish B Noaa* 87, 775–790.

Dickson, N. E., Carrivick, J. L., and Brown, L. E. (2012). Flow regulation alters alpine river thermal regimes. *J. Hydrol.* 464, 505–516. doi: 10.1016/j.jhydrol.2012.07.044

DiStefano, R. J., Magoulick, D. D., Imhoff, E. M., and Larson, E. R. (2009). Imperiled crayfishes use hyporheic zone during seasonal drying of an intermittent stream. *J. N. Am. Benthol. Soc.* 28, 142–152. doi: 10.1899/08-072.1

Dwivedi, D., Steefel, C. I., Arora, B., Newcomer, M., Moulton, J. D., Dafflon, B., et al. (2018). Geochemical exports to river from the intrameander hyporheic zone under transient hydrologic conditions: east river mountainous Watershed, Colorado. *Water Resour. Res.* 54, 8456–8477. doi: 10.1029/2018WR023377

Edwardson, K. J., Bowden, W. B., Dahm, C., and Morrice, J. (2003). The hydraulic characteristics and geochemistry of hyporheic and parafluvial zones in Arctic tundra streams, North Slope, Alaska. *Adv. Water Resour.* 26, 907–923. doi: 10.1016/S0309-1708(03)00078-2

Febria, C. M., Fulthorpe, R. R., and Williams, D. D. (2010). Characterizing seasonal changes in physicochemistry and bacterial community composition in hyporheic sediments. *Hydrobiologia* 647, 113–126. doi: 10.1007/s10750-009-9882-x

Galloway, J., Fox, A., Lewandowski, J., and Arnon, S. (2019). The effect of unsteady streamflow and stream-groundwater interactions on oxygen consumption in a sandy streambed. *Sci. Rep.* 9:19735. doi: 10.1038/s41598-019-56289-y

Gomez-Velez, J. D., Wilson, J. L., Cardenas, M. B., and Harvey, J. W. (2017). Flow and Residence times of dynamic river bank storage and sinuosity-driven hyporheic exchange. *Water Resour. Res.* 53, 8572–8595. doi: 10.1002/2017WR021362

Gooseff, M. N., Bencala, K. E., Scott, D. T., Runkel, R. L., and McKnight, D. M. (2005). Sensitivity analysis of conservative and reactive stream transient storage models applied to field data from multiple-reach experiments. *Adv. Water Resour.* 28, 479–492. doi: 10.1016/j.advwatres.2004.11.012

Haddou, K., Bendaoud, A., Belaidi, N., and Taleb, A. (2018). A large-scale study of hyporheic nitrate dynamics in a semi-arid catchment, the Tafna River, in Northwest Algeria. *Environ. Earth Sci.* 77:520. doi: 10.1007/s12665-018-7673-2

Hammond, G. E., and Lichtner, P. C. (2010). Field-scale model for the natural attenuation of uranium at the Hanford 300 area using high-performance computing. *Water Resour. Res.* 46:W09527. doi: 10.1029/2009WR008819

Hammond, G. E., Lichtner, P. C., and Mills, R. T. (2014). Evaluating the performance of parallel subsurface simulators: an illustrative example with PFLOTRAN. *Water Resour. Res.* 50, 208–228. doi: 10.1002/2012WR013483

Harjung, A., Sabater, F., and Butturini, A. (2018). Hydrological connectivity drives dissolved organic matter processing in an intermittent stream. *Limnologica* 68, 71–81. doi: 10.1016/j.limno.2017.02.007

Harvey, J., Gomez-Velez, J., Schmadel, N., Scott, D., Boyer, E., Alexander, R., et al. (2019). How hydrologic connectivity regulates water quality in river corridors. *J. Am. Water Resour. Assoc.* 55, 369–381. doi: 10.1111/1752-1688.12691

Harvey, J., and Gooseff, M. (2015). River corridor science: hydrologic exchange and ecological consequences from bedforms to basins. *Water Resour. Res.* 51, 6893–6922. doi: 10.1002/2015WR017617

Harvey, J. W., Bohlke, J. K., Voytek, M. A., Scott, D., and Tobias, C. R. (2013). Hyporheic zone denitrification: controls on effective reaction depth and contribution to whole-stream mass balance. *Water Resour. Res.* 49, 6298–6316. doi: 10.1002/wrcr.20492

Harvey, J. W., and Fuller, C. C. (1998). Effect of enhanced manganese oxidation in the hyporheic zone on basin-scale geochemical mass balance. *Water Resour. Res.* 34, 623–636. doi: 10.1029/97WR03606

Harvey, J. W., Wagner, B. J., and Bencala, K. E. (1996). Evaluating the reliability of the stream tracer approach to characterize stream-subsurface water exchange. *Water Resour. Res.* 32, 2441–2451. doi: 10.1029/96WR01268

Hassan, M. A., Tonina, D., Beckie, R. D., and Kinnear, M. (2015). The effects of discharge and slope on hyporheic flow in step-pool morphologies. *Hydrol. Process.* 29, 419–433. doi: 10.1002/hyp.10155

Helton, A. M., Poole, G. C., Payn, R. A., Izurieta, C., and Stanford, J. A. (2012). Scaling flow path processes to fluvial landscapes: an integrated field and model assessment of temperature and dissolved oxygen dynamics in a river-floodplain-aquifer system. *J. Geophys. Res. Biogeo.* 117:G00N14. doi: 10.1029/2012JG002025

Herman, J., and Usher, W. (2017). An open-source Python library for sensitivity analysis. *J. Open Sourc. Softw.* 2:97. doi: 10.21105/joss.00097

Hou, Z. S., Scheibe, T. D., Murray, C. J., Perkins, W. A., Arntzen, E. V., Ren, H. Y., et al. (2019). Identification and mapping of riverbed sediment facies in the Columbia River through integration of field observations and numerical simulations. *Hydrol. Process* 33, 1245–1259. doi: 10.1002/hyp.13396

Jonsson, K., Johansson, H., and Worman, A. (2004). Sorption behavior and long-term retention of reactive solutes in the hyporheic zone of streams. *J. Environ. Eng. Asce.* 130, 573–584. doi: 10.1061/(ASCE)0733-9372(2004)130:5(573)

Kawanishi, R., Dohi, R., Fujii, A., Inoue, M., and Miyake, Y. (2017). Vertical migration in streams: seasonal use of the hyporheic zone by the spinous loach *Cobitis Shikokuensis*. *Ichthyol. Res.* 64, 433–443. doi: 10.1007/s10228-017-0576-5

Kelleher, C., Ward, A., Knapp, J. L. A., Blaen, P. J., Kurz, M. J., Drummond, J. D., et al. (2019). Exploring tracer information and model framework trade-offs to improve estimation of stream transient strorage processes. *Water Resour. Res.* 55, 3481–3501. doi: 10.1029/2018WR023585

Killingstad, M. W., Widdowson, M. A., and Smith, R. L. (2002). Modeling enhanced *in situ* denitrification in groundwater. *J. Environ. Eng. Asce.* 128, 491–504. doi: 10.1061/(ASCE)0733-9372(2002)128:6(491)

Knapp, J. L. A., and Cirpka, O. A. (2017). Determination of hyporheic travel time distributions and other parameters from concurrent conservative and reactive tracer tests by local-in-global optimization. *Water Resour. Res.* 53, 4984–5001. doi: 10.1002/2017WR020734

Knapp, J. L. A., and Kelleher, C. (2020). A perspective on the future of transient storage modeling: let's stop chasing our tail. *Water Resour. Res.* 56:e2019WR026257. doi: 10.1029/2019WR026257

Kruegler, J., Gomez-Velez, J., Lautz, L. K., and Endreny, T. A. (2020). Dynamic evapotranspiration alters hyporheic flow and residence times in the intrameander zone. *Water* 12:424. doi: 10.3390/w12020424

Larsen, L. G., Harvey, J. W., and Maglio, M. M. (2014). Dynamic hyporheic exchange at intermediate timescales: testing the relative importance of evapotranspiration and flood pulses. *Water Resour. Res.* 50, 318–335. doi: 10.1002/2013WR014195

Lemke, D., Liao, Z. J., Wohling, T., Osenbruck, K., and Cirpka, O. A. (2013). Concurrent conservative and reactive tracer tests in a stream undergoing hyporheic exchange. *Water Resour. Res.* 49, 3024–3037. doi: 10.1002/wrcr.20277

Lewandowski, J., Arnon, S., Banks, E., Batelaan, O., Betterle, A., Broecker, T., et al. (2019). Is the hyporheic zone relevant beyond the scientific community? *Water* 11:2230. doi: 10.3390/w11112230

Liu, S. N., and Chui, T. F. M. (2018). Impacts of different rainfall patterns on hyporheic zone under transient conditions. *J. Hydrol.* 561, 598–608. doi: 10.1016/j.jhydrol.2018.04.019

Magliozzi, C., Coro, G., Grabowski, R. C., Packman, A. I., and Krause, S. (2019). A multiscale statistical method to identify potential areas of hyporheic exchange for river restoration planning. *Environ. Modell. Softw.* 111, 311–323. doi: 10.1016/j.envsoft.2018.09.006

Newcomer, M. E., Hubbard, S. S., Fleckenstein, J. H., Maier, U., Schmidt, C., Thullner, M., et al. (2018). Influence of hydrological perturbations and riverbed sediment characteristics on hyporheic zone respiration of CO2 and N-2. *J. Geophys. Res. Biogeo.* 123, 902–922. doi: 10.1002/2017JG004090

Niehus, S. E., Perkins, W. A., and Richmond, M. C. (2014). *Simulation of Columbia River Hydrodynamics and Water Temperature from 1917 through 2011 in the Hanford Reach*. Final Report PNWD-3278. (Richland, WA: Battelle-Pacific Northwest Division).

Perkins, W. A., and Richmond, M. C. (2004). *MASS2 Modular Aquatic Simulation System in Two Dimensions User Guide and Reference* (Richland, WA: Pacific Northwest National Laboratory), PNNL-14820-1.

Rahimi, M., Essaid, H. I., and Wilson, J. T. (2015). The role of dynamic surface water-groundwater exchange on streambed denitrification in a first-order, low-relief agricultural watershed. *Water Resour Res* 51, 9514–9538. doi: 10.1002/2014WR016739

Ranalli, A. J., and Macalady, D. L. (2010). The importance of the riparian zone and in-stream processes in nitrate attenuation in undisturbed and agricultural watersheds - a review of the scientific literature. *J. Hydrol.* 389, 406–415. doi: 10.1016/j.jhydrol.2010.05.045

Rickard, W. H., and Gray, R. H. (1995). The hanford reach of the columbia river - a refuge for fish and riverine wildlife and plants in Eastern Washington. *Nat. Area J.* 15, 68–74.

Rockhold, M. L., Fayer, M. J., Kincaid, C. T., and Gee, G. W. (1995). *Estimation of Natural Groundwater Recharge for the Performance Assessment of a Low-Level Waste Disposal Facility at the Hanford Site* (Richland, WA: Pacific Northwest National Laboratory).

Runkel, R. L., McKnight, D. M., and Andrews, E. D. (1998). Analysis of transient storage subject to unsteady flow: diel flow variation in an Antarctic stream. *J. N. Am. Benthol. Soc.* 17, 143–154. doi: 10.2307/1467958

Salehin, M., Packman, A. I., and Paradis, M. (2004). Hyporheic exchange with heterogeneous streambeds: laboratory experiments and modeling. *Water Resour. Res.* 40:W11504. doi: 10.1029/2003WR002567

Sawyer, A. H., and Cardenas, M. B. (2009). Hyporheic flow and residence time distributions in heterogeneous cross-bedded sediment. *Water Resour. Res.* 45:W08406. doi: 10.1029/2008WR007632

Shuai, P., Chen, X. Y., Song, X. H., Hammond, G. E., Zachara, J., Royer, P., et al. (2019). Dam Operations and subsurface hydrogeology control dynamics of hydrologic exchange flows in a regulated river Reach. *Water Resour. Res.* 55, 2593–2612. doi: 10.1029/2018WR024193

Singh, T., Wu, L. W., Gomez-Velez, J. D., Lewandowski, J., Hannah, D. M., and Krause, S. (2019). Dynamic hyporheic zones: exploring the role of peak flow events on bedform-induced hyporheic exchange. *Water Resour. Res.* 55, 218–235. doi: 10.1029/2018WR022993

Song, X. H., Chen, X. Y., Stegen, J., Hammond, G., Song, H. S., Dai, H., et al. (2018). Drought conditions maximize the impact of high-frequency flow variations on thermal regimes and biogeochemical function in the hyporheic zone. *Water Resour. Res.* 54, 7361–7382. doi: 10.1029/2018WR022586

Thorne, P., Bergeron, M., Williams, M., and Freedman, V. (2006). *Groundwater Data Package for Hanford Assessments*. Richland, WA: Pacific Northwest National Laboratory. doi: 10.2172/882976

Tonina, D., de Barros, F. P. J., Marzadri, A., and Bellin, A. (2016). Does streambed heterogeneity matter for hyporheic residence time distribution in sand-bedded streams? *Adv. Water Resour.* 96, 120–126. doi: 10.1016/j.advwatres.2016.07.009

Triska, F. J., Kennedy, V. C., Avanzino, R. J., Zellweger, G. W., and Bencala, K. E. (1989). Retention and transport of nutrients in a 3rd-order stream - channel processes. *Ecology* 70, 1877–1892. doi: 10.2307/1938119

Van Genuchten, M. T. (1980). A closed-form equation for predicting the hydraulic conductivity of unsaturated soils. *Soil Sci. Soc. Am. J.* 44, 892–898. doi: 10.2136/sssaj1980.03615995004400050002x

Ward, A. S., and Packman, A. I. (2019). Advancing our predictive understanding of river corridor exchange. *Wires Water* 6:e1327. doi: 10.1002/wat2.1327

Wexler, S. K., Hiscock, K. M., and Dennis, P. F. (2011). Catchment-scale quantification of hyporheic denitrification using an isotopic and solute flux approach. *Environ. Sci. Technol.* 45, 3967–3973. doi: 10.1021/es104322q

Zachara, J., Chen, X., Song, X., Shuai, P., Murray, C., and Tom Resch, C. (2020). Kilometer-scale hydrologic exchange flows in a gravel bed river corridor and their implications to solute migration. *Water Resour. Res.* 56:e2019WR025258. doi: 10.1029/2019WR025258

Zarnetske, J. P., Haggerty, R., Wondzell, S. M., and Baker, M. A. (2011). Dynamics of nitrate production and removal as a function of residence time in the hyporheic zone. *J. Geophys. Res. Biogeo.* 116:G01025. doi: 10.1029/2010JG001356

Zheng, L. Z., Cardenas, M. B., Wang, L. C., and Mohrig, D. (2019). Ripple effects: bed form morphodynamics cascading into hyporheic zone biogeochemistry. *Water Resour. Res.* 55, 7320–7342. doi: 10.1029/2018WR023517

Conflict of Interest: The authors declare that the research was conducted in the absence of any commercial or financial relationships that could be construed as a potential conflict of interest.

frontiers in Water

ORIGINAL RESEARCH
published: 27 November 2020
doi: 10.3389/frwa.2020.572950

Estimating Surface Water Presence and Infiltration in Ephemeral to Intermittent Streams in the Southwestern US

Erika L. Gallo[1,2], *Thomas Meixner*[1], *Kathleen A. Lohse*[2*] *and Hillary Nicholas*[1]

[1] *Department of Hydrology and Atmospheric Sciences, University of Arizona, Tucson, AZ, United States,* [2] *Department of Biological Sciences, Idaho State University, Pocatello, ID, United States*

OPEN ACCESS

Edited by:
Tim Scheibe,
Pacific Northwest National Laboratory (DOE), United States

Reviewed by:
Stefan Julich,
Technische Universität Dresden, Germany
Mikolaj Piniewski,
Warsaw University of Life Sciences, Poland

***Correspondence:**
Kathleen A. Lohse
klohse@isu.edu

Specialty section:
This article was submitted to Water and Critical Zone, a section of the journal Frontiers in Water

Received: *15 June 2020*
Accepted: *12 October 2020*
Published: *27 November 2020*

Citation:
Gallo EL, Meixner T, Lohse KA and Nicholas H (2020) Estimating Surface Water Presence and Infiltration in Ephemeral to Intermittent Streams in the Southwestern US. Front. Water 2:572950. doi: 10.3389/frwa.2020.572950

Streamflow in arid and semi-arid regions is predominantly temporary, an integral part of mountain block hydrology and of significant importance for groundwater recharge and biogeochemical processes. However, temporary streamflow regimes, especially ephemeral flow, remain poorly quantified. We use electrical resistance sensors and USGS stream gauge data in 15 southern Arizona streams spanning a climate gradient (mean annual precipitation from 160 to 750 mm) to quantify temporary streamflow as streamflow presence and water presence, which includes streamflow, ponding and soil moisture. We use stream channel sediment data to estimate saturated hydraulic conductivity and potential annual infiltration. Annual streamflow ranged 0.6–82.4% or 2–301 days; while water presence ranged from 2.6 to 82.4% or 10 to over 301 days, or 4–33 times longer than streamflow. We identified 5 statistically distinct flow regimes based on the annual percent streamflow and water presence: (1) dry-ephemeral, (2) wet-ephemeral, (3) dry-intermittent, (4) wet-intermittent, and (5) seasonally-intermittent. In contrast to our expectations, stream channel density was a better predictor of annual streamflow and water presence than annual rainfall alone. Whereas, the dry-ephemeral and wet-ephemeral flow regimes varied with seasonal precipitation, the dry-intermittent, wet intermittent and seasonally-intermittent flow regimes did not. These results coupled with the potential infiltration estimates indicate that streamflow at the driest sites occurs in response to rainfall and overland flow while groundwater discharge and vadose zone contributions enhance streamflow at the wetter sites. We suggest that on a short temporal scale, and with respect to water presence, wetter sites might be buffered better against shifts in the timing and distribution of precipitation in response to climate change. Flow regime classifications that include both stream flow and water presence, rather than on stream flow alone, may be important for predicting thresholds in ecological functions and refugia in these dryland systems.

Keywords: ephemeral streamflow, flow regime, arid, semi-arid, stream hydrology, surface water

INTRODUCTION

Streamflow is predominantly temporary in water limited regions (Newman et al., 2006; Larned et al., 2010; Datry et al., 2014) such as the Western United States (US), where ∼89% of streams flow intermittently (US Geological Survey, 2008). These brief streamflow episodes have a profound effect on ecohydrological processes (Stromberg et al., 2008; Blasch et al., 2010; Jaeger and Olden, 2012) and groundwater recharge (Constantz, 1982; Goodrich et al., 2004; Coes and Pool, 2005; Blasch et al., 2006; Baillie et al., 2007; Callegary et al., 2007; Cataldo et al., 2010; Tillman et al., 2011). Despite the importance of temporary surface waters to biological processes and water resources, the frequency and temporal distribution of streamflow in water limited regions remains poorly quantified.

Streamflow in the arid and semi-arid Southwest US occurs in response to spatially heterogeneous convective summer precipitation (The North American Monsoon), protracted and widespread winter precipitation, snowmelt and groundwater discharge (Goodrich et al., 2004, 2018; Baillie et al., 2007). Stream channels in this region are areas of focused infiltration and subsequent recharge (Coes and Pool, 2005) resulting in significant streamflow losses (Goodrich et al., 2004). Meanwhile, evapotranspiration losses can alter water redistribution and subsequent streamflow dynamics (Leenhouts et al., 2006; Scott et al., 2008). As a result of the coupling among precipitation patterns, channel infiltration losses and high evapotranspiration fluxes, streamflow, and stream channel wetting can be temporally variable and have a high degree of intermittency in these water-limited regions.

Research shows that streamflow patterns arise from differences in partitioning of precipitation within catchment drainage networks (Leenhouts et al., 2006; Biederman et al., 2014), particularly in water limited systems (Kampf et al., 2016). Hydrologic conceptual models developed in the arid and semi-arid Southwest indicate that streamflow may transition from perennial in mountain headwater streams to intermittent in the mountain fronts and alluvial basins as stream channel infiltration losses and the distance downstream increase (Tillman et al., 2011). These hydrologic discontinuities result in more pronounced streamflow intermittency at lower elevations, a pattern observed by Jaeger and Olden (2012). In addition, geochemical studies show differential partitioning of winter and summer precipitation to infiltration and subsequent recharge (Eastoe et al., 2004; Baillie et al., 2007). For example, Wahi et al. (2008) noted that in the Huachuca Mountains of southern Arizona, high elevations springs are comprised of a greater fraction of winter precipitation than lower elevation shallow riparian waters, which are comprised of a greater fraction of summer rainfall. Despite the geochemical evidence, there is a paucity of knowledge about streamflow patterns across a range of arid and semi-arid streams.

Mountain-system recharge, or recharge that occurs due to percolation along rock fractures and faults (mountain block) and infiltration in the mountain front, is considered to be the main groundwater recharge mechanism in semi-arid systems (Wahi et al., 2008). In these systems, water losses to infiltration along intermittent stream reaches, exclusive of mountain-connected streams may account for 12–19% of recharge in some basins (Coes and Pool, 2005). At a localized scale, intermittent stream recharge can contribute as much 85% to shallow riparian groundwater during the summer rainfall season (Baillie et al., 2007). However, stream channel recharge estimates in intermittent systems can be poorly constrained due to the scarcity of streamflow and stream water presence measurements. Methodologies used to assess intermittent stream infiltration and recharge in arid and semi-arid systems include geochemical studies, water balance approaches, *in-situ* infiltrometers, and thermal monitoring and modeling approaches (Besbes et al., 1978; Sorman and Abdulrazzak, 1993; Constantz et al., 2003; Dowman et al., 2003; Goodrich et al., 2004; Coes and Pool, 2005; Blasch et al., 2006; Baillie et al., 2007; Callegary et al., 2007). However, the temporal dynamics of intermittent streamflow, a major control on potential infiltration, remain to be explicitly quantified.

The objective of this study is to quantify annual streamflow presence and identify temporal streamflow patterns in streams of the arid and semi-arid Southwest. An accompanying paper examines the consequences of these temporary streamflow patterns for organic and nutrient dynamics (Lohse et al., 2020a). Here we ask the following questions: (1) How frequent is streamflow in arid and semi-arid streams and how does it vary with climate and landscape characteristics?, (2) What are the temporal patterns of streamflow across sites?, and (3) What are the rates and potential annual infiltration in arid and semi-arid stream channels? To address these questions, we quantified streamflow and stream channel water presence in 15 stream reaches in southern Arizona spanning an aridity gradient; developed a classification system for streams in arid and semi-arid regions based on the degree of surface water intermittency and generated infiltration estimates for the study sites. We expected streamflow to vary along a climate gradient and increase with elevation and mean annual precipitation, and for streamflow permanence to vary with the timing of precipitation.

MATERIALS AND METHODS

Study Area

We selected 13 temporarily wet stream channels, or washes, in southern Arizona located across three climatic zones (**Figure 1**, **Table 1**) as indicated by their aridity index (Thornthwaite, 1948; UNEP, 1992) and that spanned a range of geomorphic conditions. Precipitation across the region is bimodal. Summertime convective rainfall (the North American Monsoon) is intense, of short duration, spatially heterogeneous and lasts from mid-late June to mid-late September. A second precipitation period is observed primarily between December and March with rainfall of lower intensity and longer duration arising from widespread storm systems.

The monitoring washes were located in largely undisturbed military facilities, long term ecological research areas and a nature preserve (**Table 1**). We used the National Hydrography Dataset

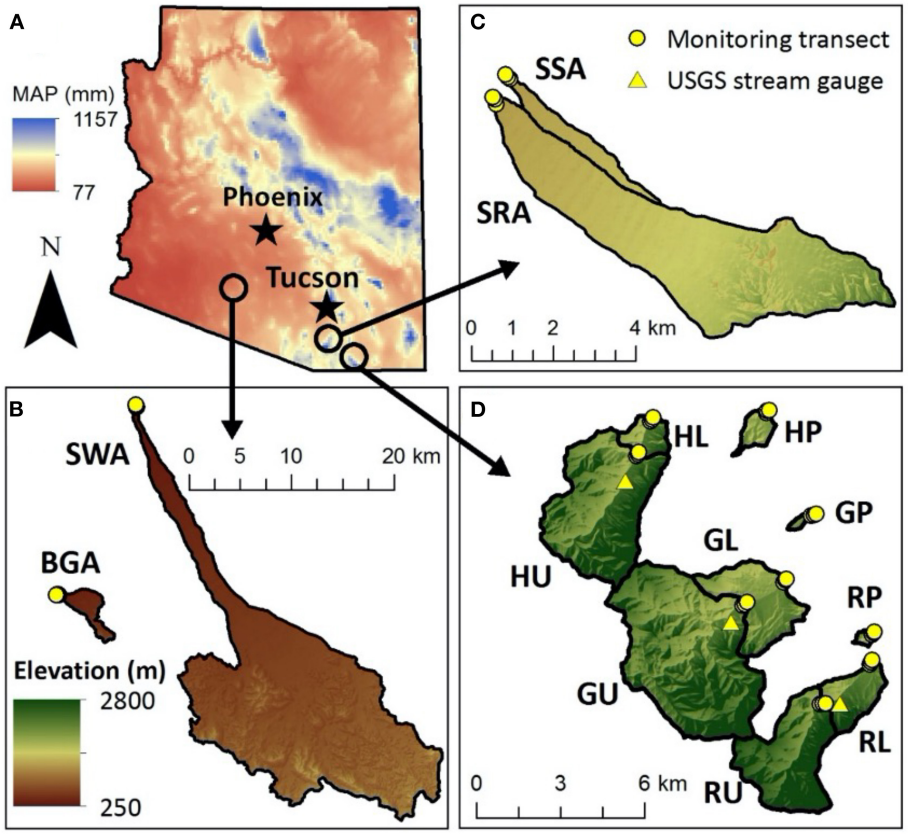

FIGURE 1 | (A) Study sites in southern Arizona across an aridity range. Sites are located at **(B)** the Barry Goldwater Range (SWA, BGA); **(C)** the Santa Rita experimental range (SRA, SSA); and **(D)** in the Huachuca Mountains at Huachuca Canyon (HU, HL, HP) and Garden Canyon (GU, GL, GP), located within the Ft. Huachuca Army base and Ramsey Canyon (RU, RL and RP).

(NHD) (version 2) (US Geological Survey, 2008) and associated watershed boundary dataset in ArcMap 10.2 (ESRI, Redlands, CA) to delineate catchments, and a 3 m USGS digital elevation model (DEM) to delineate and characterize the catchment upstream of each monitoring wash reach. The most arid study washes (AI = 0.14), Black Gap (BGA) and Sauceda Wash (SWA), are located within the Barry M. Goldwater Air Force Base near Gila Bend, Arizona in the Lower Gila River Basin on semi-consolidated alluvial basin fans at 324 and 258 m in elevation, respectively. Both study washes have catchments primarily composed of dacite and sand (**Table 1**). The catchment upstream of the BGA reach is 10.2 km^2 and ranges in elevation from 324 to 676; while the catchment upstream of the SWA reach is the largest of our study sites, 326.4 km^2, and ranges in elevation from 258 to 1,114 m (**Table 1**). The 30-year mean annual precipitation (MAP) at these sites ranges between 160 mm at the lower elevations and 250 mm at the higher elevations (PRISM Climate Group, 2013); while mean annual temperature (MAT) is 23°C and can range between 5° and 43°C (US Climate Data; http://www.ncdc.noaa.gov/). Two semi-arid (AI = 0.25) study washes are located on the Santa Rita Experimental Range near Sahuarita, Arizona in the Santa Cruz River Basin (SSA and SRA). These are center-of-basin braided unconsolidated sandy channels 947 and 952 m in elevation. The catchment upstream of SSA is 1.7 km^2 and ranges in elevation from 947 to 1,105 m, while the catchment upstream of SRA is 18.0 km^2 and ranges in elevation from 952 to 1,748 m. The MAP ranges between 350 mm at the lower elevations and 570 mm at the higher elevations (PRISM Climate Group, 2013); while MAT is 22°C and can range between 6° and 38°C (US Climate Data).

Nine study sites are located on the Huachuca Mountains near Sierra Vista, Arizona and form part of the San Pedro River Basin (AI $\leq$ 0.65). The study sites are located along 3 distinct elevations in 3 canyons: Huachuca Canyon and Garden Canyon which are located within the Fort Huachuca Army Post; and Ramsey Canyon, within the Nature Conservancy's Ramsey Canyon Preserve. These sites have MAP ranging from 430 mm at the lower elevations to 750 mm at the higher elevations, while temperatures range from 1° to 34°C, with MAT of 17°C. The lowest elevation monitoring reaches (HP, GP, and RP) are piedmont semi-consolidated alluvial channels at 1,453–1,533 m in elevation and have MAP ranging from 430 mm to 580 mm.

TABLE 1 | Catchment characteristics including elevation, mean annual precipitation (MAP), and temperature (MAT) from PRISM Climate Group (2013), area, stream density, latitude and longitude in decimal degrees, and parent material.

	Site name (ID)	Elevation (min, max)[a]	MAP (mm)	MAT (°C)	Area (km^2)	Stream density (km/km^2)	Latitude, longitude (dec. deg. N, W)	Parent material
Alluvial	**Barry M. Goldwater Air Force Range**							
	Black Gap (BGA)	(324, 676)	97	22.3	10.21	5.72	(32.711123, −112.831066)	Alluvial
	Sauceda (SWA)	(258, 1,114)	97	21.6	326.38	2.38	(32.878405, −112.752874)	Alluvial
	Santa Rita Experimental Range							
	Small Santa Rita (SSA)	(947, 1,105)	227	19.0	1.69	5.06	(31.885414, −110.88042)	Alluvial
	Large Santa Rita (SRA)	(952, 1,748)	227	18.1	17.99	6.28	(31.880545, −110.883672)	Alluvial Transitional granite
Piedmont	**Huachuca Mountains**							
	Piedmont Huachuca (HP)	(1,453, 1,564)	293	16.7	1.27	4.00	(31.540278, −110.334113)	Alluvial Transitional granite
	Piedmont Garden (GP)	(1,494, 1,556)	335	16.6	0.48	5.12	(31.506705, −110.316744)	Alluvial Transitional granite
	Piedmont Ramsey (RP)	(1,533, 1,762)	397	16.3	0.28	4.99	(31.468538, −110.294548)	Granite
Lower canyon	Lower Huachuca (HL)	(1,592, 2,533)	308	13.6	17.06	1.30	(31.537735, −110.377248)	Mixed igneous and sedimentary
	Lower Garden (GL)	(1,539, 2,630)	409	13.6	29.50	1.22	(31.485624, −110.327657)	Mixed igneous and sedimentary
	Lower Ramsey (RL)	(1,573, 2,798)	443	12.8	13.21	1.24	(31.459062, −110.295734)	Mixed igneous and sedimentary
Upper canyon	Upper Huachuca (HU)	(1,646, 2,533)	276	13.2	15.22	1.37	(31.526465, −110.382684)	Mixed igneous and sedimentary
	Upper Garden (GU)	(1,582, 2,630)	416	13.1	23.09	1.12	(31.478043, −110.342776)	Mixed igneous and sedimentary
	Upper Ramsey (RU)	(1,726, 2,798)	456	11.9	9.81	1.28	(31.445808, −110.313850)	Mixed igneous and sedimentary
	HU @ USGS 09471310 (HU_USGS)	(1,708, 2,533)	276	13.2	10.56	1.09	(31.518056, −110.387222)	Mixed igneous and sedimentary

[a] *The monitoring reach elevation is the minimum catchment elevation.*

The HP, GP and RP catchments are the smallest (1.3, 0.5, and 0.3 km^2, respectively), and have stream channel densities similar to those of the alluvial sites that range between 2.4 and 6.3 km km^{-2}. Three lower canyon monitoring reaches (HL, GL, and RL) range between 1,539 and 1,592 m in elevation and are incised streams with non-cohesive alluvial banks that have MAP_ ranging between 520 and 650 mm.

Finally, three upper canyon monitoring reaches (HU, GU, and RU) are located at 1,582–1,726 m in elevation and are on cohesive bedrock with moderate alluvium present. These sites have MAP ranging from 590 to 750 mm. Both, the lower and upper canyon sites have the lowest stream channel densities of all the study sites and have the highest catchments elevations, from 2,533 to 2,798 m. To further complement our data set, we coupled our monitoring data to USGS data (http://waterdata.usgs.gov) from 3 from discharge (Q) gauges, #09471310, #09470800, and #09470750 located in the Upper Huachuca Canyon (HU_USGS) Upper Garden Canyon (GU_USGS) and Upper Ramsey Canyon (RU_USGS), respectively. In all cases, except Upper Ramsey Site that was coincident with our study reach, the other gauges are located in close proximity of the upper canyon reaches (HU and GU), within 2 km (Huachuca) and 5 km (Garden), and their catchments are similar in elevation, size, and stream channel density (**Table 1**, **Figure 1**).

Precipitation Data

We obtained monthly precipitation from the nearest tipping bucket gauge available to each monitoring reach. For sites BGA and SWA in the Barry M. Goldwater Air force range, we used precipitation data from the Maricopa Alert System Gauge #71000 at Sauceda Wash (http://alert.fcd.maricopa.gov/alert/Google/v3/gmap.html#), located at the outlet of the SWA. For sites SSA and SRA in the Santa Rita experimental Range, we used a dense network of precipitation data from long term research station monitoring tipping bucket rain gauges (24 total within and near the catchment) (http://ag.arizona.edu/SRER/data.html) and for

the sites in the Huachuca Mountains, we used seven gauges located in or near Fort Huachuca. Fort Huachuca data were processed and provided by Lainie Levick and Russ Scott from the USDA-ARS-SWRC in Tucson, AZ (Levick et al., 2015). We estimated the total volume of precipitation to each catchment over a annual time by multiplying the precipitation depth over the annual period of time by the catchment area.

Streamflow and Surface Water Presence

At each of the study washes, we selected a monitoring stream reach of 200 m in length. At each reach, we established three cross-sectional transects 100 m apart and characterized the channel geometry, including channel slope using GPS and differential surveying. We installed electrical resistance sensors (TidbiT v2 UTBI-001 data logger, Onset Corporation, Bourne, MA) at the thalweg of each cross-sectional transect to identify surface water presence frequency and duration, with the exception of the high elevation Ramsey Canyon site (RU), which is classified as a sensitive area. The electrical resistance sensors were temperature sensors modified as outlined in Blasch et al. (2002), with 2 electrical leads exposed; and we followed the method outlined by Jaeger and Olden (2012) to identify the onset and cessation of runoff. In brief, the onset of runoff is marked by the sudden and rapid increase in the relative electrical conductivity (EC) signal to a less negative or a positive number, while the termination of streamflow is also marked by a similarly sudden shift in the EC signal back to a more negative signal (**Figure 2**). In this study, EC = −94 indicates dry conditions. The sensors logged an EC signal every 10 min. We quantified the percent of streamflow at each monitoring transect ($streamflow_{transect}$) as follows:

$$streamflow_{transect} = \sum_{0}^{t} \frac{n_{streamflow}}{n_{total}} \times 100 \quad (1)$$

where $n_{streamflow}$ is the number of "streamflow" signals, or instances of sudden and clear shift in EC to a more positive number indicative of streamflow as illustrated in **Figure 2** over a period of time t, and n_{total} is the total number of EC observations made during that same time period. The site % streamflow was estimated by averaging the % $streamflow_{transect}$ for each stream reach.

We were able to quantify the duration of surface water presence as moist soil or ponded water because the EC signal for runoff is distinct from that of a moist soil and soil-drying conditions (Blasch et al., 2002; Jaeger and Olden, 2012). In contrast to the streamflow presence signal, the surface water presence signal has a distinct inflection point that marks a shift from a steep EC signal recession to a less steep EC signal recession (**Figure 2**). We quantified the % surface water presence at each transect (% $water\ presence_{transect}$) as:

$$water\ presence_{transect} = \sum_{0}^{t} \frac{n_{water\_presence}}{n_{total}} \times 100 \quad (2)$$

where $n_{water\_presence}$ is the number of "surface water presence" signals, or instances of sudden and clear shift in EC from streamflow to a water ponding or soil drying signal as illustrated in **Figure 2** over a period of time *t*. Because it is difficult to distinguish EC signals indicative of water ponding from soil moisture presence, here we define all EC signals indicative of water presence, including streamflow, as "water presence." We were interested in identifying maximum length of time that water might be present in the stream either as ponded water, shallow soil water or streamflow available for biological activity, therefore we used the maximum % $water\ presence_{transect}$ observed at each monitoring reach as the reach % water presence. We treated data from USGS gauges in a similar manner where if the instantaneous discharge (Q, liters *per second*) > threshold, then signal = "streamflow." Because stream gauge data can be noisy at low Q, we used stage-discharge curves generated using the published USGS data (http://waterdata.usgs.gov) to determine "noise" threshold where Q < 0.3 liters *per second* = "no flow" where 0.3 liters *per second* is ∼ 10 times below typical velocity rating limit of 2.8 liters *per second* (Turnipseed and Sauer, 2010). Here we assumed that surface water presence was at minimum the same as streamflow presence for all USGS gauges. Finally, we estimated the ratio of percent annual water presence to percent annual streamflow presence (AWP:ASFP).

Channel Sediment Physical Characteristics

We collected channel sediment samples from 0 to 10 cm depth to determine bulk density and substrate texture at each of the three cross-sectional transects. We used the pipette method for particle size analyses to determine % sand, % silt, % clay (Day, 1965) and soil texture of the channel sediments. We estimated bulk density in g cc^{-1} using a modified cavity method (Grossman and Reinsch, 2002) in which the soil mass of a 8 cm diameter circle was excavated to 10 cm with a trowel. We determined the

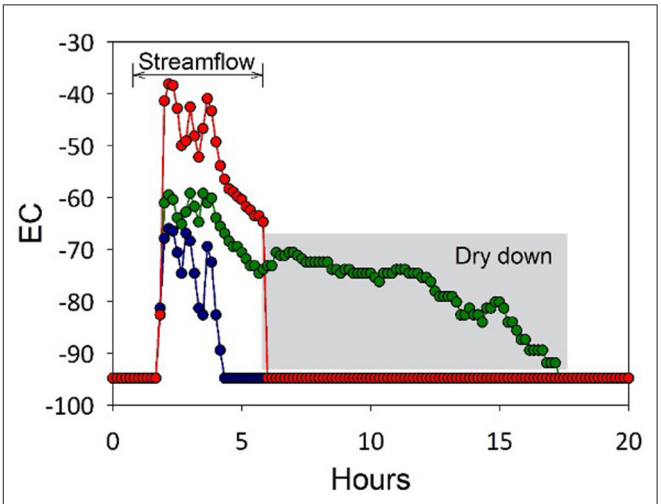

FIGURE 2 | Typical electrical conductivity (EC) profile for a runoff event at a monitoring reach. Each data set (red, green, and blue) represents a different sensor at a single reach. The onset of runoff is marked by a rapid increase in EC (red and blue). The end of streamflow can be identified by either EC returning to −94, the baseline reading, or by an inflection in the rate of change in EC to a less steep slope, indicative of soil drying conditions (green).

volume by lining the void with a plastic bag and filling it with water. Soils collected from this void were then sieved (2 mm), dried for soil moisture, and weighed for mass to determine the fraction of fine earth <2 mm. Particle density was assumed to be 2.65 g/cm^3. Soils for bulk density were not treated to remove organic carbon or carbonates. Data for channels are also reported in Lohse et al. (2020b) but also include other landscape positions; see design in Lohse et al. (2020a), and data are available in Lohse et al. (2020c).

Saturated Hydraulic Conductivity and Infiltration

We used bulk density and soil texture to estimate the saturated hydraulic conductivity (K_{sat}) of the bed sediment at each monitoring transect using Rosetta pedotransfer functions (Schaap and Leij, 2000). We estimated the infiltration depth, I, over time t as follows:

$$I = K_{sat} * (1\text{-}rvf) * t_{sf} \quad (3)$$

Where($1\text{-}rvf$) is the volume of the soil sample, including the rock and void volume normalized to 1, minus the rock volume fraction; and t_{sf} is the duration of streamflow estimated using the EC sensors over a period of time t. We estimated the total catchment potential infiltration ($I_{max-catchment}$) by multiplying the infiltration depth by the total catchment stream channel length and the channel width. We repeated this process for every monitoring transect so that for each catchment we had 3 distinct estimates of $I_{max-catchment}$. Our infiltration estimates assume that every streamflow event the entire stream channel contributed to infiltration and that the stream geometry remained constant during the study period. We estimated the fraction of the catchment that is comprised of stream channels ($fCA_{streams}$) by dividing the product of the total catchment stream channel length and channel width by the catchment area. We repeated this process for every monitoring transect so that for each catchment we had 3 distinct estimates of $fCA_{streams}$. Finally, we estimated the ratio of $I_{max-catchment}$ to total precipitation over the observation period to evaluate the total channel infiltration in channels relative to total precipitation received. We acknowledge these are first-order estimates of infiltration as presence of cobbles and boulders (> 2 mm fraction) was variable and sometimes high at sites and likely led to uncertainties in infiltration estimates; more sophisticated modeling methods are available but these approaches were beyond the scope of this study.

Comparison of Observed Streamflow and Water Presence to Modeled Streamflow Permanence

To evaluate and possibly scale up our observed results to the landscape level for the Huachuca Mountains study area, we compared our observations on streamflow duration (as measured using ER sensors) to modeled data from Levick et al. (2015) and Levick et al. (2018). In brief, Levick et al. (2018) simulated stream flow permanence using the AGWA/SWAT (Automated Geospatial Watershed Assessment Tool/Soil and Water Assessment Tool) for mapped streams in Fort Huachuca as a whole. Validation sites used by Levick et al. (2018) were data from Gallo et al. (2020), also reported in final report by Stromberg et al. (2015), and these cluster validity data indicated that only five flow types existed on Fort Huachuca. However, Levick et al. (2018) further bifurcated the classification tree into eight flow types based on additional remote sensing observations such as vegetation and channel morphology. As described more below, we did not capture the hyper-arid stream types (8 type) and their 3 and 4 types were lumped into the wet-intermittent classes given the rarity of class 3 (2% total stream reaches) (7 classes displayed). We used linear regression to determine the similarity of our two approaches for estimating stream flow permanence.

Statistical Analyses

Statistical analyses were performed using JMP 10 (Cary, NC; SAS Institute Inc.). We used non-standardized Wards Clustering Analyses (Tan et al., 2006; Sall et al., 2012) on percent annual streamflow and percent annual water presence to identify statistically distinct ($p < 0.05$) groups of sites with similar streamflow and water presence responses or regimes. Clusters with a Euclidian vector length > 0.93 were retained for further analyses. Using Wilcoxon non-parametric comparison of means and linear regression models (Zar, 1999), we identified differences in surface water presence and infiltration rates and volumes of each stream channel class, and patterns in how percent streamflow and water presence vary with precipitation over the monitoring period and between seasons. For the purposes of our statistical analyses, and in response to our data structure we define seasons as follows: Spring from April 1 to June 30; Summer from July 1 to September 30; Fall from October 1 to December 31; and Winter from January 1 to March 31; Summer from July 1 to September 30 captures the Arizona monsoon that officially ends Sept 30th and Winter convective storms occur from January 1 through March 31.

RESULTS AND DISCUSSION

Annual Precipitation, Streamflow and, Water Presence Patterns

The mean annual precipitation (mean PPT) observed over our 28-month study period ranged from 97 to 456 mm across sites, with the driest sites being the alluvial sites, where the observed mean annual precipitation was < 250 mm and significantly ($p < 0.5$) lower than at all other sites. Across all sites, at a regional scale, precipitation varied significantly and positively with elevation ($r^2 = 0.74$); however, we did not observe a significant correlation between precipitation and elevation at the Huachuca Mountain sites (piedmont, upper, and lower canyon). At the Huachuca Canyon sites, HP, HL, and HU, we observed lower than expected precipitation given their elevation and mean annual temperature (**Table 2**). Comparison of our monitoring record with MAP (PRISM Climate Group, 2013) (**Table 1**) indicates that these sites consistently receive less rainfall than the adjacent southeastern canyon and piedmont sites. Literature reviews show that in the mountainous Western US, spatial heterogeneity and

TABLE 2 | Annual precipitation (PPT), percent annual streamflow presence (ASFP), percent annual water presence (AWP), and stream substrate characteristics including bulk density (BD) and coarse fraction by volume (%) at each monitoring reach.

	Site	Annual PPT (m)	ASFP (%)	AWP (%)	Sand, silt, clay (%)	BD (g cc^{-1})	Coarse Fraction (% by volume)	Catchment channel length (km)	Wetted channel cross section (m)	K_{sat} (cm day^{-1})	Potential Annual Infiltration (m)	I:PPT 0.5; 1.0
Alluvial												
	BGA	0.18	0.6	2.6	94, 4,2	2.4 (0.5)	56 (13)	26.16	7.37 (1.08)	354 (334)	1 (<1)	0.3 (0.3); 0.6 (0.6)
	SWA	0.18	1.1	17.9	97, 2,1	2.1 (0.7)	79 (8)	776.50	8.95 (1.6)	709 (316)	12 (4)	1.1 (0.5); 2.3 (1)
	SSA	0.23	1.1	36.3	97, 1, 2	2.1 (0.3)	11 (4)	8.54	1.36 (0.2)	303 (198)	11 (7)	0.2 (0.1); 0.3 (0.2)
	SRA	0.23	2.0	17.7	96, 2, 2	1.7 (0.1)	34 (4)	90.77	5.78 (4.7)	601 (113)	29 (4)	1.5 (0.3); 2.9 (0.7)
Piedmont												
	HP	0.36	1.9	17.9	86, 7, 7	1.4 (0.3)	51.9 (13.4)	1.51	1.96 (0.2)	492 (585)	5 (5)	0.1 (0.1); 0.1 (0.1)
	GP	0.36	2.0	15.0	91, 7, 2	1.7 (0.3)	32.4 (6.4)	0.30	2.28 (1.1)	407 (509)	5 (2)	0.1 (0.1); 0.2 (0.2)
	RP	0.36	1.3	32.3	96, 2, 1	1.4 (0.2)	36.3 (8.5)	0.13	1.63 (0.6)	961 (115)	29 (6)	0.3 (0.2); 0.6 (0.3)
Lower Canyon	HL	0.36	33.6	47.4	95, 3, 2	1.3 (0.1)	57.5 (13.4)	1.41	7.05 (1.7)	870 (124)	514 (46)	8.7 (0.2); 17.3 (0.3)
	GL	0.36	23.2	37.1	94, 5, 1	1.5 (0.1)	43.7 (14.8)	9.93	8.61 (4.2)	648 (98)	313 (109)	2.6 (0.6); 5.2 (1.2)
	RL	0.36	3.4	35.4	84, 14, 2	1.4 (0.4)	52.4 (15.5)	2.92	3.24 (0.1)	333 (310)	23 (26)	0.1 (0.1); 0.2 (0.3)
	HU	0.36	16.0	27.7	93, 5, 2	1.4 (0.3)	56.8 (10.9)	18.60	6.41 (1.7)	622 (204)	164 (97)	2.5 (1.1); 4.9 (2.2)
	GU	0.36	50.6	57.2	90, 7, 3	1.5 (0.6)	35.8 (2.3)	25.91	8.12 (2.4)	491 (216)	578 (233)	4.4 (0.8); 8.8 (1.6)
	HU_USGS	0.36	30.2	30.2	90, 7, 3	1.5 (0.6)	56.8 (10.9)	11.50	6.41 (1.7)	622 (204)	311 (183)	6.7 (3); 13.4 (6.1)
	GU_USGS	0.36	82.4	82.4	94, 4, 2	1.9 (<0.1)	35.8 (2.3)	26.60	8.12 (2.4)	491 (216)	941 (379)	7.4 (1.4); 14.8 (2.8)
	RU/RU_USGS	0.36	79.0	79.0	93, 5, 2	1.4 (0.3)	0 (0)	11.05	3.92 (0.6)	235 (17)	679 (48)	3.6 (1.1); 7.2 (2.3)

*The saturated hydraulic conductivity (K_{sat}) was estimated using Rosetta pedotransfer functions (Schaap and Leij, 2000). The potential annual infiltration depth (m) assumes that the entire streambed contributes to infiltration. We report two annual infiltration (I) to annual precipitation (PPT) ratios (I:PPT) based on the volume of precipitation (m^3) by multiplying area of catchment (**Table 1**) by annual observed precipitation (annual PPT) and the volume infiltrated by catchment stream channels (m^3) based on multiplying the wetted channel area (m^2) [as the product of wetted channel cross section and catchment channel length (km)], and infiltration depth (m), the first assuming that only half (0.5) of the streambed contributes to infiltration, the second assumes that the entire streambed contributes to infiltration. The standard deviations are reported as (SD).*

topography can largely control localized patterns precipitation while summertime monsoonal rainfall decreases in a northward direction at the regional scale (Mock, 1996; Adams and Comrie, 1997). Therefore, it is likely that the physical location of Huachuca Canyon coupled with storm rainout result in significantly lower observed mean PPT than at the Garden and Ramsey Canyon sites. Even when accounting for precipitation differences at the Huachuca site, no significant differences in precipitation between the piedmont, lower canyon and upper canyon sites were observed, where rainfall ranged from 276 to 457 mm.

Observed streamflow and stream water presence were highly variable across sites but predictable based on climatic factors and stream channel density (**Figure 3**). Streamflow was observed on average 21.7% of the time or 79 days in 1 year, but ranged from 0.6 to 82.4% corresponding to 2 and 301 days per year. Similarly, surface water presence was observed 35.8% of the time, or 131 days of the year, but ranged from 2.6% to >82.4% or 10 to over 301 days (**Table 2**). Both streamflow and surface water presence increased significantly ($p < 0.05$) and exponentially with MAP (**Figures 3A,B**), and decreased significantly and exponentially with MAT ($r^2 = 0.38$ and 0.53, respectively) and stream channel density (**Figures 3C,D**). These results are consistent with conceptual frameworks of arid and semi-arid streamflow that point to a coupling of decreased precipitation, increased evaporation and evapotranspiration fluxes and increased stream channel infiltration losses as mechanisms that result in intermittent streamflow (Goodrich et al., 1997; Izbicki et al., 2000).

Stream Flow and Water Presence Regimes

Five distinct flow and water presence regimes were identified with the clustering analyses: (1) dry-ephemeral, (2) wet-ephemeral, (3) dry intermittent, (4) wet intermittent, and (5) seasonally-intermittent (**Figure 4**). All alluvial and piedmont sites (**Figure 1**, **Table 1**) were classified as dry or wet ephemeral, and one lower canyon was classified as wet ephemeral. The remaining lower canyon, mid and upper canyon sites were classified as dry-, wet-, and seasonally-intermittent sites. These flow regimes align with previous work in the region that used a geomorphic classification scheme to classify ephemeral channels in alluvial and piedmont areas (Sutfin et al., 2014). The wet-ephemeral name was selected based on field surveys indicating the presence of phreatic vegetation at the sites clustering in this group (Stromberg et al., 2017). Annual streamflow in the dry-ephemeral

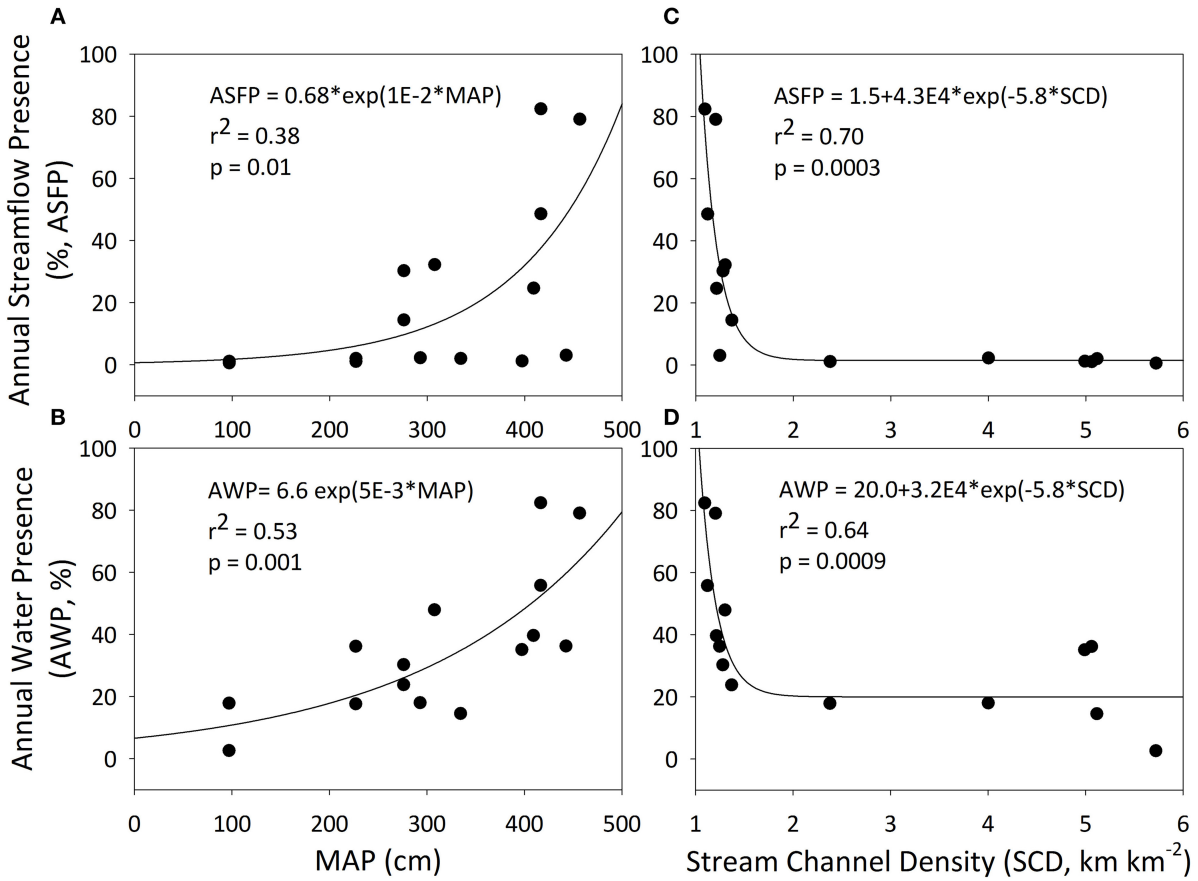

FIGURE 3 | Regressions of percent annual streamflow presence and percent annual water presence vs. mean annual precipitation (MAP, **A,B**) for the observation period and stream channel density **(C,D)**. All regressions were signficicant ($p < 0.05$).

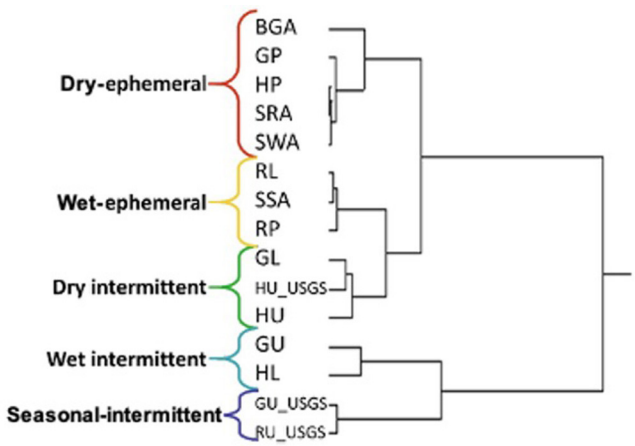

FIGURE 4 | Clustering analysis dendrogram based on percent annual streamflow presence (ASFP) and percent annual water presence (AWP). We identified 5 statistically distinct streamflow categories.

and wet-ephemeral clusters ranged from 0.6 to 2.0% and 1.1 to 3.4%, respectively, and was significantly lower ($p < 0.05$) than the intermittent and seasonally-intermittent groups (**Table 3**, **Figure 5A**), where annual streamflow ranged from 16 to 82.4%. Annual water presence at the dry-ephemeral cluster ranged from 2.6 to 17.9% and was significantly lower than in all other clusters; whereas it was highest at the wet-intermittent and seasonally-intermittent clusters, where it ranged from 47.4 to > 82.4% (**Table 3**, **Figure 5B**).

Across sites, annual streamflow intermittency and water presence regimes varied in response to landscape characteristics and the magnitude of annual rainfall. The streamflow regime classification, the MAP and stream channel regressions (**Figure 3**) and the spatial MAP patterns observed suggest that landscape variables have a larger effect on streamflow and water presence regimes than annual precipitation magnitude. If the annual precipitation magnitude was the main driving mechanism controlling streamflow regimes, then all of the monitoring sites would classify according to a climate gradient,

TABLE 3 | Mean (SD) values of annual % streamflow and % water presence and monthly % streamflow and % water presence for each season.

	Annual	Fall	Winter	Spring	Summer
Streamflow					
Dry ephemeral	1.5 (0.6)	2.0 (1.8)^{a}	0.6 (0.6)^{b}	0.4 (0.5)^{b}	3.1 (2.3)^{a}
Wet ephemeral	1.9 (1.3)	2.3 (2.4)^{a,b}	1.2 (1.4)^{b,c}	0.5 (0.5)^{c}	3.8 (2.1)^{a}
Dry intermittent	23.1 (7.1)	28.2 (20)^{a}	24.5 (19.7)^{a}	0.6 (0.6)^{b}	39.3 (24.9)^{a}
Wet intermittent	42.1 (12.1)	43.5 (21.9)^{b}	73.6 (18.6)^{a}	7.9 (10.6)^{c}	43.4 (33)^{b}
Seasonally-intermittent	80.7 (2.3)	100 (0)^{a}	100 (0)^{a}	48.8 (44.7)^{b}	74 (31.7)^{a,b}
Water presence					
Dry ephemeral	14.2 (6.6)	21.1 (19.4)^{a}	3.7 (3.5)^{b}	1.7 (2.7)^{b}	30.4 (20.4)^{a}
Wet ephemeral	34.7 (2.0)	38.6 (24.5)^{b}	24.3 (25.1)^{b}	3.2 (3.0)^{c}	72.8 (14.9)^{a}
Dry intermittent	31.7 (4.9)	41.2 (26)^{a}	35.3 (25.9)^{a}	0.7 (0.7)^{b}	49.6 (31.2)^{a}
Wet intermittent	52.3 (6.9)	51.4 (26.4)^{b}	84.2 (16.6)^{a}	12.5 (14.8)^{c}	61 (31.1)^{a,b}
Seasonally-intermittent	80.7 (2.3)	100 (0)^{a}	100 (0)^{a}	48.8 (44.7)^{b}	74 (31.7)^{a,b}

Means sharing a superscripted letter across seasons are not significantly different.

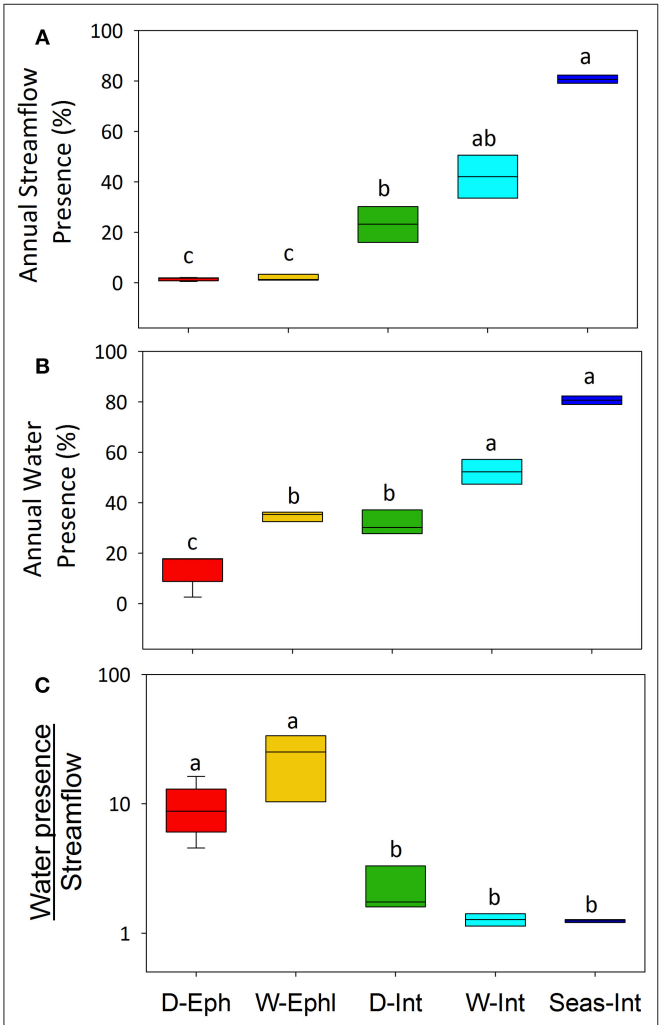

FIGURE 5 | Box plots of **(A)** Percent annual streamflow; **(B)** Percent annual water presence and **(C)** ratio of water presence to streamflow across clusters. Box plots sharing a lowercase letter are not significantly different ($p > 0.05$).

a pattern not supported by our data. For example, piedmont sites HP and GP received more rainfall during the monitoring period than the alluvial SWA and SRA, however, all classified in the "dry-ephemeral" cluster (**Figure 4**) due to similar annual streamflow and water presence (**Table 2**). Percent annual streamflow and water presence varied positively and significantly with precipitation at the dry-ephemeral, wet-ephemeral, and dry-intermittent reaches (**Table 4**). Annual precipitation explained the greatest fraction of the percent annual streamflow and water presence variance at the dry-ephemeral and ephemeral sites (up to 47%); 6 and 11%, respectively at the dry-intermittent sites and no correlations were observed at the wet-intermittent and seasonally-intermittent sites. These data indicate that there is a strong link between flow regime and annual precipitation magnitude, but only at the drier sites, which were the most responsive to rainfall magnitude. The absence of a correlation with annual precipitation at the wet-intermittent and seasonally-intermittent sites, which have a large fraction of annual streamflow and water presence, indicates that flow regimes are likely subsidized by subsurface water resources that discharge to the channel (Izbicki, 2007; Levick et al., 2008; Wahi et al., 2008).

The annual water presence to streamflow presence ratio (AWP:ASFP), a measure of water availability as ponding or soil moisture, varied between 1.0 and 33.6 (**Table 2**), and was on average 8.5. The AWP:ASFP ratio at the dry-ephemeral and wet-ephemeral clusters ranged from 4.6 to 33.6 and was significantly higher than ratios at all other clusters where they ranged from 1.1 to 3.3 (**Table 2**, **Figure 5C**). The large ratios observed at the dry-ephemeral (mean = 9.3, SD = 4.3) and wet-ephemeral (mean = 23.0, SD = 11.8) sites indicate that water as soil moisture and/or ponds is present over 4 times longer than streamflow which has significant implications for biological processes at these dry sites (Lohse et al., 2020a). Indeed, Lohse et al. (2020a) showed that cumulative streamflow presence could explain slightly more variation in rates of litter decomposition in the washes than cumulative streamflow, especially on the dry end of the spectrum.

TABLE 4 | Coefficient of determination (r^2) values for significant ($p < 0.05$) regressions of percent streamflow and water presence vs. precipitation.

	Annual	Fall	Winter	Spring	Summer
Streamflow					
Dry ephemeral	0.31	–	–	–	0.50
Wet ephemeral	0.47	0.40	–	–	0.31
Dry intermittent	0.06	–	–	–	–
Wet intermittent	–	–	–	–	–
Seasonally-intermittent	–	–	–	0.40 (–)	0.45 (–)
Water presence					
Dry ephemeral	0.47	0.38	–	–	0.42
Wet ephemeral	0.33	–	–	0.60	–
Dry intermittent	0.11	–	–	–	–
Wet intermittent	–	–	–	–	–
Seasonally-intermittent	–	–	–	0.40 (–)	0.45 (–)

A "–" indicates a non-significant regression; a (–) indicates a negative correlation.

In arid and semi-arid systems, biological and biogeochemical processes are primarily water limited (Austin et al., 2004; Gallo et al., 2014). Water availability as soil moisture and ponds can therefore offset water demands during non-streamflow periods and extend the period of time during which biologically mediated processes can occur (McCluney and Sabo, 2009; Allen et al., 2014). Indeed, a number of studies show that biogeochemical processes such as respiration and organic matter mineralization can continue under low matric potentials (Carbone et al., 2008; Lohse et al., 2020a). Therefore, we expect biological activity to continue for an extended period of time following streamflow at the drier flow regimes, particularly the wet-ephemeral sites where vegetation can enhance water presence via hydraulic redistribution of water to shallow stream sediments (Naumburg et al., 2005).

Temporal Dynamics

Despite differences in precipitation across years and a large degree of variability in the magnitude of mean monthly streamflow and water presence throughout the monitoring period, generalized patterns of streamflow and water presence/absence were consistent between study years (**Figure 6**). Streamflow and water presence varied differently with the temporal distribution of precipitation within each flow regime group (**Figure 7**). While a clear bimodal distribution of rainfall was observed, this was not the case for streamflow and water presence across flow regimes (**Figures 7A–C**, **Table 3**). The spring months were the driest, with mean precipitation depths of up to 5 mm, accounting for the lowest gains in cumulative annual precipitation (**Figure 7D**). Similar to streamflow patterns described by Ajami et al. (2011) in Santa Catalina Mountains in semi-arid southern Arizona, this period also had the statistically lowest streamflow and water presence across sites and flow regimes (**Table 3**), and therefore had no significant increase in cumulative streamflow and water presence (**Figures 7E,F**).

We expected streamflow and water presence to be of longer duration during the summer (July, August and September) and fall (October, November and December), when precipitation was statistically highest, averaging 220 and 64 mm, respectively, and accounting for 68 and 21% of annual rainfall. Surprisingly, streamflow and water presence were statistically highest during these periods only at the dry-ephemeral and wet-ephemeral sites (**Table 3**). Percent monthly streamflow at the dry-ephemeral sites varied positively and significantly with precipitation during the summer only; and during the summer and fall at the wet-ephemeral sites (**Table 4**). Similarly, percent monthly water presence varied positively and significantly with precipitation at the dry-ephemeral sites during the fall and summer, and only during the spring at the wet-ephemeral sites (**Table 4**). While not explicitly addressed in this study, coupling among the characteristics of seasonal precipitation, streamflow generation mechanisms and channel infiltration losses likely results in these temporal flow regime patterns (Blasch et al., 2002, 2004). For example. summertime precipitation is of high intensity and short duration, resulting in infiltration excess overland flow and rapid streamflow generation following episodic rainfall (Goodrich et al., 1997; Levick et al., 2008), which might explain the positive responses to rainfall during the summer. In contrast, winter rainfall in the region is of low intensity and long duration allowing for significant infiltration and transmission losses, and streamflow occurs in response to saturation excess overall flow and local subsurface flows after rainfall (Levick et al., 2008; Ajami et al., 2011). Finally, a variable not addressed here that warrants further study is that of antecedent moisture conditions, which is not only of great importance for biological processes (Austin et al., 2004; Belnap et al., 2005) but can significantly alter streamflow responses in water limited regions (Blasch et al., 2004; Vivoni et al., 2009; Hawkins and Ellis, 2010).

The seasonal flow regime patterns observed at the canyon sites in the dry-intermittent, wet-intermittent and seasonally-intermittent flow regimes point toward geologic and subsurface connectivity controls on stream flow. Despite the larger magnitude of summer time rainfall, streamflow and water presence at the dry-intermittent sites did not significantly vary between the summer, fall and winter; while at the wet-intermittent sites the highest streamflow and water presence occurred during the winter (**Table 3**). We did not observe any seasonal responses to precipitation in the dry and wet-intermittent flow regimes. In contrast, streamflow and water presence at the seasonally-intermittent sites were greatest during the fall and winter and varied significantly and inversely with precipitation during the summer and spring (**Table 4**). Within the context of generalized mountain block hydrology conceptual models and geochemical evidence of studies in the region (Eastoe et al., 2004; Wilson and Guan, 2004; Wahi et al., 2008; Ajami et al., 2011), it is likely that the streamflow and water presence observed at these canyon sites is sourced from discharge and subsurface flow of water stored within the fractured bedrock matrix. Finally, the flow regimes patterns at these canyon sites appear to be buffered in the short term from varying climate, suggesting that biological riparian and stream channel processes relying on soil moisture might be more resilient to climate change and potential shifts in the regional timing of precipitation.

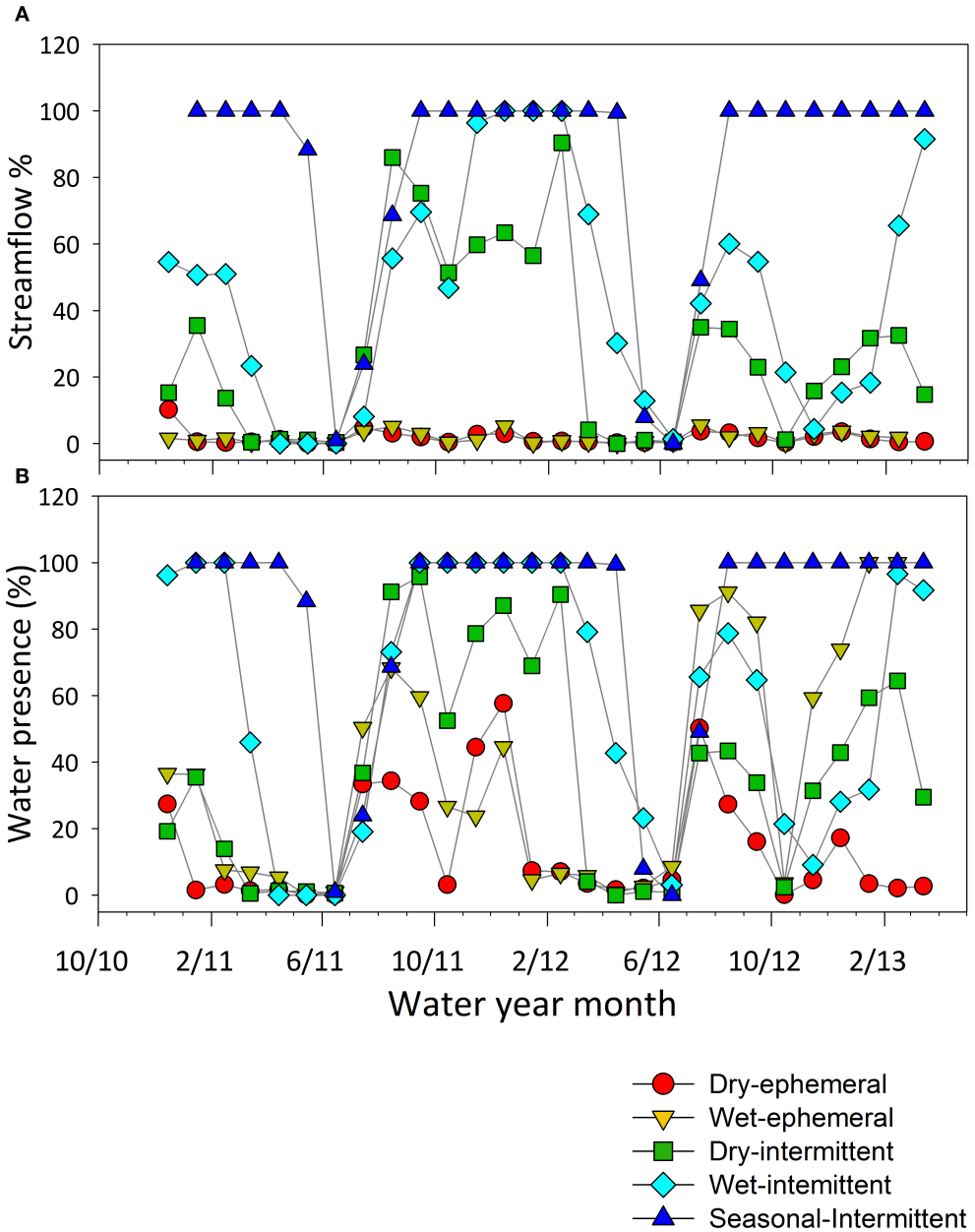

FIGURE 6 | (A) Mean monthly percent streamflow and **(B)** mean monthly percent water presence across streamflow classes over the monitoring period. Calendar year 2011 had greater % streamflow and water presence than calendar year 2012, during which the fall drying period was more drastic.

Saturated Hydraulic Conductivity and Potential Infiltration

The K_{sat} estimates were high and wide ranging, from a reach average of 235–961 cm day^{-1}; while potential infiltration depths varied between < 1 and 941 m per year (**Table 2**). Our potential infiltration estimates also assumed that infiltration occurs every time streamflow occurs. Therefore, it is not surprising that annual potential infiltration depths were significantly higher at the wet-intermittent and seasonally-intermittent sites, which have the greatest streamflow, than at the dry-ephemeral and wet-ephemeral sites (**Table 2**, **Figure 8A**), which have the lowest streamflow. Surprisingly, the fraction of the catchment that can contribute to channel infiltration is statistically greatest at the dry-ephemeral sites, where it varied from 0.8 to 4.2% (**Figure 8B**). The potential annual infiltration to annual PPT ratio (I:PPT), assuming that only 50% of the stream substrate contributes to infiltration, ranged from 0.1 to 8.7; whereas the ratio varied from 0.2 to 14.8 assuming that the entire

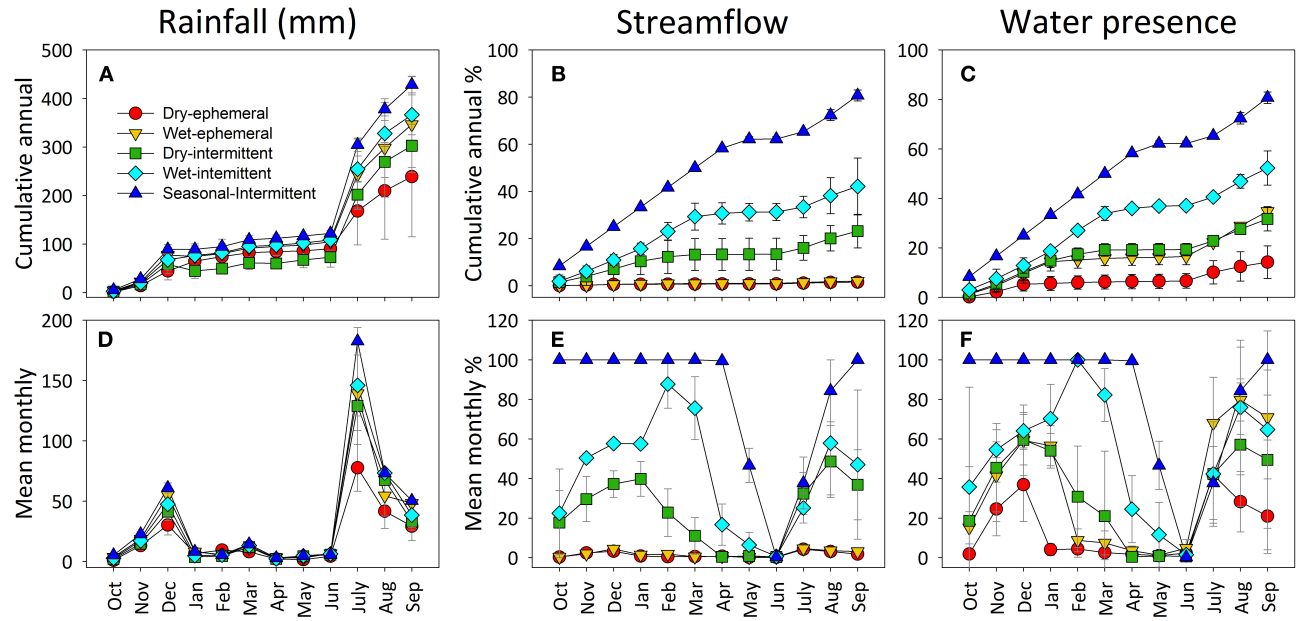

FIGURE 7 | Cumulative **(A)** monthly rainfall (mm), **(B)** cumulative monthly percent streamflow presence, **(C)** cumulative monthly percent water presence, and **(D)** mean monthly rainfall (mm), **(E)** mean monthly percent streamflow presence and **(F)** mean monthly percent water presence for each stream flow cluster class. Bars are standard deviation.

stream channel contributes to infiltration (**Table 2**, **Figure 8C**). The potential annual infiltration to precipitation ratio was significantly lower at the dry-ephemeral and ephemeral sites (0.1–2.9), and was highest at the wet-intermittent and seasonally-intermittent sites (3.6–17.3, **Figure 8C**). Our infiltration depth estimates assume only a vertical flux, no lower boundary condition and that whole channel contributes to infiltration; however, in reality it is difficult to know exactly the fraction of the channel substrate that contributes to infiltration. However, low potential infiltration to precipitation ratios, particularly if we assume that only 30–50% of channel contributes to infiltration so that I:P < 1.5, indicate that streamflow is primarily generated by rainfall at the driest sites. High ratios at the canyon sites provide further evidence of subsurface connectivity resulting in groundwater discharge and vadose zone water contribution consistent with mountain system recharge and streamflow generation mechanisms described in generalized conceptual models (Wilson and Guan, 2004; Wahi et al., 2008; Ajami et al., 2011).

Comparison of Observed Streamflow and Water Presence to Modeled Streamflow Permanence

Results of linear regression showed a high correspondence between our field-based approach for determining stream flow permanence and the modeling approach taken by Levick et al. (2018) for the Huachuca Mountains ($r^2 = 0.76$–0.86, **Figure 9**). We acknowledge that the duration of the monitoring period was limited to 28 months, and further study is merited to evaluate these patterns. However, the agreement of two independently derived stream classifications, our study based on field stream flow presence data that represented two fairly typical seasonal rainy seasons across a diverse gradient of sites and Levick et al. (2018), who modeled stream flow based on 2005–2012 precipitation inputs, channel characteristics, and vegetation lend support that our classification is reasonable.

Given the high correspondence between the two methods, we generated a landscape-scale map of the modeled stream flow using seven categories based on the number of days per year the stream is flowing. We then overlaid our study sites (Stromberg sites) on this map (**Figure 10**). This map indicates that our field sampling in the Huachuca Mountains captured most, but not all, of the hydrological stream types present at Fort Huachuca. Notably, our sampling did not capture the many hyper-ephemeral sites distal from the mountains. In addition, the dry-ephemeral channels on piedmont surfaces were too small to be captured by Levick et al. (2018) and thus could be overlooked by hydrological models. Collectively these findings indicate generalizable patterns in stream flow permanence that may be applied to other regions. Future research will need to fill in hyper-ephemeral sites as these were not captured in our observation efforts.

CONCLUSIONS

We quantified streamflow and stream water presence in streams exhibiting temporary flow across a wide climate gradient

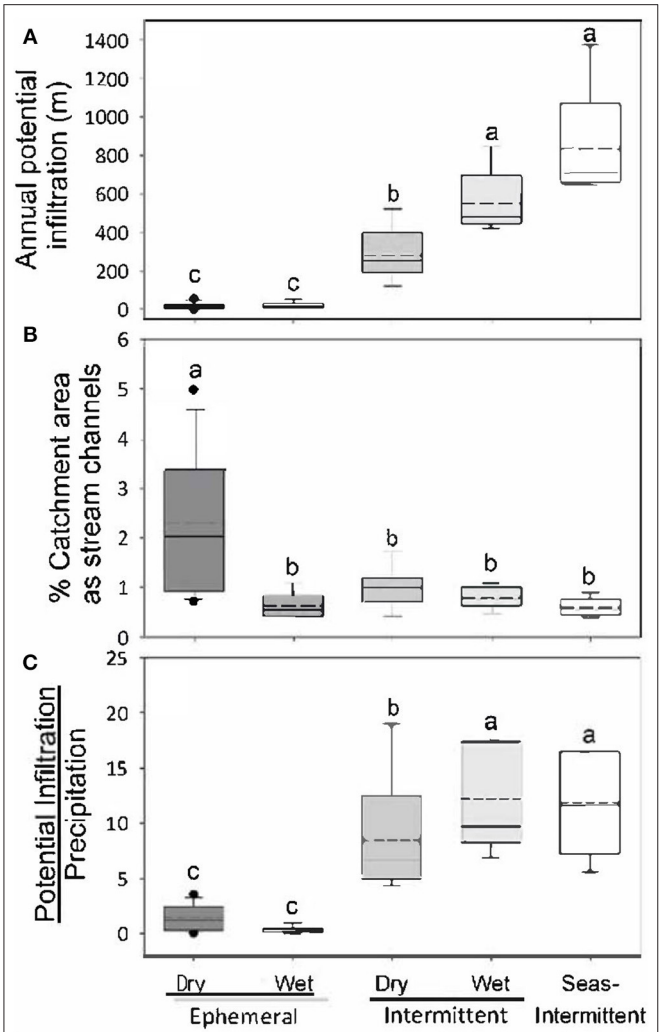

FIGURE 8 | Box plots of **(A)** Annual infiltration depth for each flow cluster; **(B)** percent of catchment that is comprised of stream channels and **(C)** ratio of total annual potential infiltration to precipitation assuming that the entire stream channel bed contributes to infiltration. Box plots dashed lines denote means, solid lines denote medians. Boxplots with distinct lowercase letters have significantly ($p < 0.05$) different means.

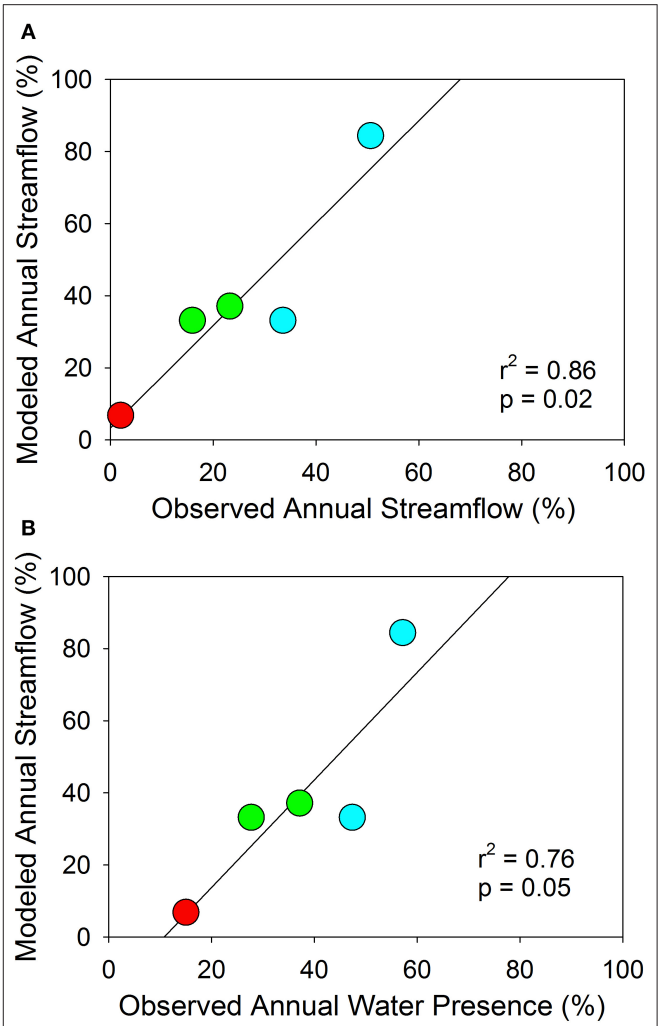

FIGURE 9 | (A) Observed annual streamflow (this study) vs. modeled annual streamflow from Levick et al. (2018) and **(B)** Observed annual water presence (this study) vs. modeled annual streamflow from Levick et al. (2018).

and showed a coupling of landscape characteristics and the magnitude and timing of rainfall in controlling flow regimes. We found that at a regional scale, stream channel density is a better predictor of streamflow and water presence than rainfall alone. Based on the percent of time streamflow and water presence occurred at our sites we identified 5 statistically distinct flow regimes: (1) dry-ephemeral, (2) wet-ephemeral, (3) dry-intermittent, (4) wet-intermittent, and (5) seasonally-intermittent. We showed that water availability as soil moisture and/or surface ponds can be 4–33 times greater than the duration of streamflow at the driest sites, which has important implications for biogeochemical processes. With regards to responses to rainfall, we showed that each of the flow regime groups has a distinct response to the magnitude and temporal distribution of rainfall. All but one group, the seasonally-intermittent group, exhibit a bimodal streamflow and water presence distribution, similar to that of the regional rainfall. The most responsive sites to rainfall were the dry-ephemeral and wet-ephemeral sites, where rainfall could account for up to 50% of streamflow and 60% of water presence; while flow regimes in the intermittent sites did not vary with seasonal rainfall. The infiltration estimates, specifically, the ratio of infiltration to rainfall, indicate that streamflow at the driest sites likely occurs in response to rainfall and overland flow; whereas groundwater discharge and upwelling may also contribute to streamflow at the wetter. This study highlights the high degree of variability in streamflow regimes at the regional scale and across a climate gradient. Our data suggests that wetter sites might be overall better buffered against shifts in the timing and distribution of precipitation in response to climate change. However, we also suggest that additional studies identify the land cover characteristics that have the greatest impact in flow regimes, particularly in the drier sites, where streamflow is highly sensitive to rainfall.

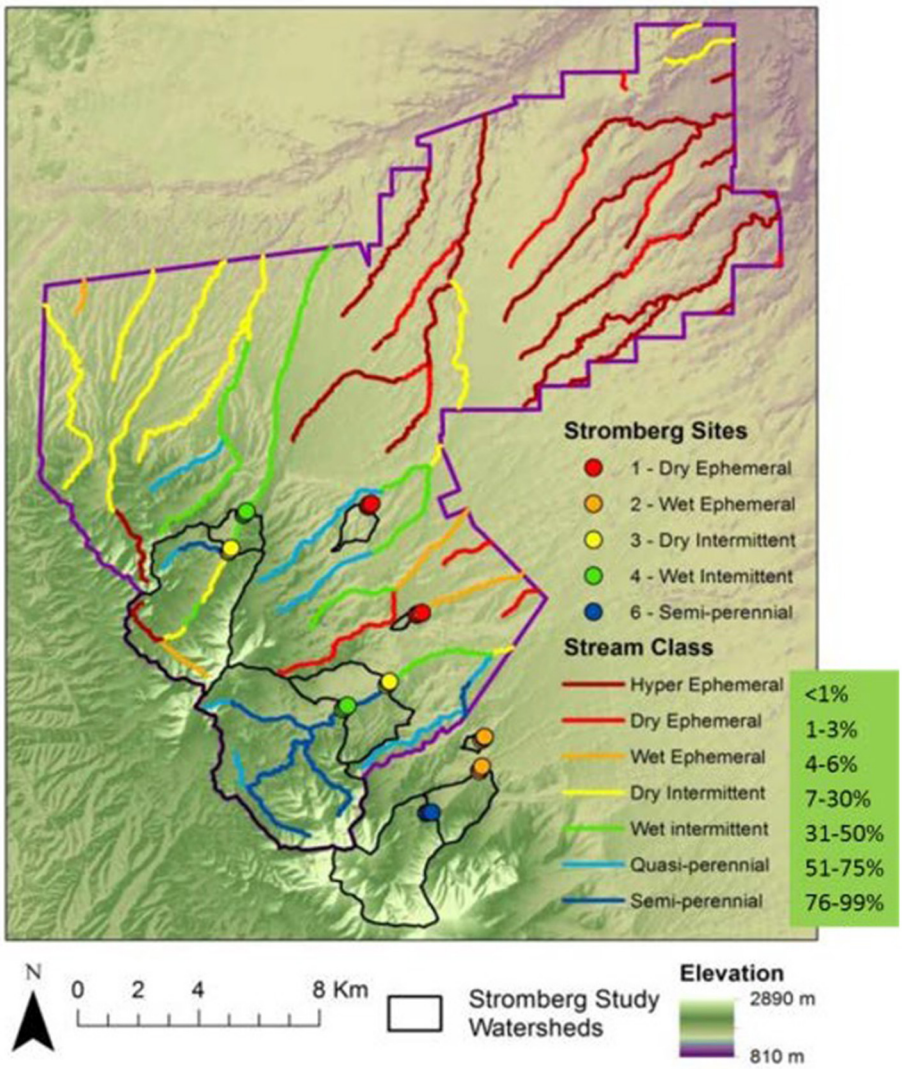

FIGURE 10 | Mapping of observed stream classifications (this study -labeled Stromberg Sites) compared to Levick et al. (2018). We note that hyper ephemeral streams were not captured by our classification scheme and Levick et al. (2018) 3 and 4 types were lumped into the wet-intermittent classes given the rarity of class 3 (2% total stream reaches) such that only 7 classes are displayed.

DATA AVAILABILITY STATEMENT

The datasets generated for this study can be found in online repositories. The names of the repository/repositories and accession number(s) can be found at: BSU ScholarWorks (doi: 10.18122/boisestate/reynoldscreek/17 and doi: 10.18122/reynoldscreek/19/boisestate).

AUTHOR CONTRIBUTIONS

TM, HN, and EG conceived and designed the hydrologic study. HN, EG, and TM performed the data collection. EG and HN analyzed the data. EG and TM contributed new methods to the paper, and EG drafted the manuscript. EG, TM, and KL reviewed and revised the manuscript, and KL prepared and revised the manuscript for publication. All authors contributed to the article and approved the submitted version.

FUNDING

This study was funded by the Department of Defense Strategic Environmental Research and Development Program (SERDP) project number RC-1726. Partial support to EG for analysis and writing was supported by NSF EPSCOR IIA-1301792 and to KL by NSF EAR 1331872.

ACKNOWLEDGMENTS

We acknowledge the contributions of Julie Stromberg at Arizona State University who conceived the overall SERDP project, assisted with design of the study, and compiled the final report to SERDP (Stromberg et al., 2015). Model output was contributed from SERDP project number RC-1727 (Levick et al., 2015). We thank Jason Silvertooth, Allison Peterson, Curtis Miles, Shane Clark, and Chris Ferlin for assistance in the field and laboratory, and Barry M. Goldwater Air Force Base, Fort Huachuca Army Post, and Nature Conservancy Ramsey Canyon Preserve for access to sites.

REFERENCES

Adams, D. K., and Comrie, A. C. (1997). The North American monsoon. *Bull. Am. Meteorol. Soc.* 78, 2197–2214. doi: 10.1175/1520-0477(1997)078<2197:TNAM>.0.CO;2

Ajami, H., Meixner, T., Maddock, T., Hogan, J. F., and Guertin, D. P. (2011). Impact of land-surface elevation and riparian evapotranspiration seasonality on groundwater budget in MODFLOW models. *Hydrogeol. J.* 19, 1181–1188. doi: 10.1007/s10040-011-0743-0

Allen, D. C., McCluney, K. E., Elser, S. R., and Sabo, J. L. (2014). Water as a trophic currency in dryland food webs. *Front. Ecol. Environ.* 12, 156–160. doi: 10.1890/130160

Austin, A. T., Yahdjian, L., Stark, J. M., Belnap, J., Porporato, A., Norton, U., et al. (2004). Water pulses and biogeochemical cycles in arid and semiarid ecosystems. *Oecologia* 141, 221–235. doi: 10.1007/s00442-004-1519-1

Baillie, M. N., Hogan, J. F., Ekwurzel, B., Wahi, A. K., and Eastoe, C. J. (2007). Quantifying water sources to a semiarid riparian ecosystem, San Pedro River, Arizona. *J. Geophys. Res. Biogeosci.* 112:G03S02. doi: 10.1029/2006JG000263

Belnap, J., Welter, J. R., Grimm, N. B., Barger, N., and Ludwig, J. A. (2005). Linkages between microbial and hydrologic processes in arid and semiarid watersheds. *Ecology* 86, 298–307. doi: 10.1890/03-0567

Besbes, M., Delhomme, J. P., and De Marsily, G. (1978). Estimating recharge from ephemeral streams in arid regions: a case study at Kairouan, Tunisia. *Water Resour. Res.* 14, 281–290. doi: 10.1029/WR014i002p00281

Biederman, J. A., Harpold, A. A., Gochis, D. J., Ewers, B. E., Reed, D. E., Papuga, S. A., et al. (2014). Increased evaporation following widespread tree mortality limits streamflow response. *Water Resour. Res.* 50, 5395–5409. doi: 10.1002/2013WR014994

Blasch, K., Ferré, T., and Vrugt, J. (2010). Environmental controls on drainage behavior of an ephemeral stream. *Stochastic Environ. Res. Assess.* 24, 1077–1087. doi: 10.1007/s00477-010-0398-8

Blasch, K. W., Ferré, T. P. A., Christensen, A. H., and Hoffmann, J. P. (2002). New Field method to determine streamflow timing using electrical resistance sensors. *Vadose Zone J.* 1, 289–299. doi: 10.2136/vzj2002.2890

Blasch, K. W., Ferré, T. P. A., and Hoffmann, J. P. (2004). A statistical technique for interpreting streamflow timing using streambed sediment thermographs. *Vadose Zone J.* 3, 936–946. doi: 10.2136/vzj2004.0936

Blasch, K. W., Ferre, T. P. A., Hoffmann, J. P., and Fleming, J. B. (2006). Relative contributions of transient and steady state infiltration during ephemeral streamflow. *Water Resour. Res.* 42:W08405. doi: 10.1029/2005WR004049

Callegary, J. B., Leenhouts, J. M., Paretti, N. V., and Jones, C. A. (2007). Rapid estimation of recharge potential in ephemeral stream channels using electromagnetic methods, and measurements of channel and vegetation characteristics *J. Hydrol.* 344, 17–31. doi: 10.1016/j.jhydrol.2007.06.028

Carbone, M. S., Winston, G. C., and Trumbore, S. E. (2008). Soil respiration in perennial grass and shrub ecosystems: linking environmental controls with plant and microbial sources on seasonal and diel timescales. *J. Geophys. Res. Biogeosci.* 113:G02022. doi: 10.1029/2007JG000611

Cataldo, J., Behr, C., Montalto, F., and Pierce, R. (2010). Prediction of transmission losses in ephemeral streams, western U.S.A. *Open Hydrol. J.* 4, 19–34. doi: 10.2174/1874378101004010019

Coes, A. L., and Pool, D. R. (2005). *Ephemeral-Stream Channel and Basinfloor Infiltration and Recharge in the Sierra Vista Subwatershed of the Upper San Pedro Basin, Southeastern Arizona.* US Geological Survey Open-File Report 2005–1023. doi: 10.3133/ofr20051023

Constantz, J. (1982). Temperature dependence of unsaturated hydraulic conductivity of two soils. *Soil Sci. Soc. Am. J.* 466–470. doi: 10.2136/sssaj1982.03615995004600030005x

Constantz, J., Tyler, S. W., and Kwicklis, E. (2003). Temperature-profile methods for estimating percolation rates in arid environments. *Vadose Zone J.* 2, 12–24. doi: 10.2136/vzj2003.1200

Datry, T., Larned, S. T., and Tockner, K. (2014). Intermittent rivers: a challenge for freshwater ecology. *Bioscience* 64, 229–235. doi: 10.1093/biosci/bit027

Day, P. R. (1965). "Particle fractionation and particle-size analysis," in *Methods of Soil Analysis,* ed C. A. Black (Madison, Wisconsin: American Society of Agronomy, Inc.), 545–567. doi: 10.2134/agronmonogr9.1.c43

Dowman, V., C. E., Ferré, T. P. A., Hoffmann, J. P., Rucker, D. F., and Callegary, J. B. (2003). Quantifying ephemeral streambed infiltration from downhole temperature measurements collected before and after streamflow. *Vadose Zone J.* 2, 595–601. doi: 10.2136/vzj2003.5950

Eastoe, C., Gu, A., and Long, A. (eds.). (2004). *The Origins, Ages and Flow Paths of Groundwater in Tucson Basin: Results of a Study of Multiple Isotope Systems*. Washington, DC: American Geophysical Union. doi: 10.1029/009WSA12

Gallo, E. L., Lohse, K. A., Brooks, P. D., Ferlin, C. and Meixner, T. (2014). Physical and biological controls on trace gas fluxes in semi-arid urban ephemeral waterways. *Biogeochemistry*. 121:189–207. doi: 10.1007/s10533-013-9927-0

Gallo, E. L., Meixer, T., Lohse, K. A., and Nicholas, H. (2020). *Dataset for Estimating Surface Water Presence and Streamflow of Ephemeral and Intermittent Streams in Southwest US.* (Boise: Boise State University ScholarWorks). doi: 10.18122/reynoldscreek/19/boisestate

Goodrich, D. C., Kepner, W. G., Levick, L. R., and Wigington P. J. Jr. (2018). Southwestern intermittent and ephemeral stream connectivity. *J. Am. Water Resour. Assoc.* 54, 400–422. doi: 10.1111/1752-1688.12636

Goodrich, D. C., Lane, L. J., Shillito, R. M., Miller, S. N., Syed, K. H., and Woolhiser, D. A. (1997). Linearity of basin response as a function of scale in a semiarid watershed. *Water Resour. Res.* 33, 2951–2965. doi: 10.1029/97WR01422

Goodrich, D. C., Williams, D. G., Unkrich, C. L., Hogan, J. F., Scott, R. L., Hultine, K. R., et al. (2004). "Comparison of methods to estimate ephemeral channel recharge, walnut gulch, San Pedro River Basin, Arizona," in *Groundwater Recharge in a Desert Environment: The Southwestern United States*, eds H. J. Phillips and B. Scanlon (New York, NY: Water and Science Application 9, American Geophysical Union), 77–99. doi: 10.1029/009WSA06

Grossman, R. B., and Reinsch (2002). "Bulk density and linear extensibility," in *Methods of Soil Analysis. Part 4. Physical Methods,* eds J. H. Dane and C. Topp (Madison, WI: Soil Science Society of America), 201–225.

Hawkins, T. W., and Ellis, A. W. (2010). The dependence of streamflow on antecedent subsurface moisture in an arid climate. *J. Arid. Environ.* 74, 75–86. doi: 10.1016/j.jaridenv.2009.07.003

Izbicki, J. A. (2007). Physical and temporal isolation of mountain headwater streams in the western mojave desert, southern california1. *J. Am. Water Resources Association* 43, 26–40. doi: 10.1111/j.1752-1688.2007.00004.x

Izbicki, J. A., Radyk, J., and Michel, R. L. (2000). Water movement through a thick unsaturated zone underlying an intermittent stream in the western Mojave Desert, southern California, USA. *J. Hydrol.* 238, 194–217. doi: 10.1016/S0022-1694(00)00331-0

Jaeger, K. L., and Olden, J. D. (2012). Electrical resistance sensor arrays as a means to quantify longitudinal connectivity of rivers. *River Res. Appl.* 28, 1843–1852. doi: 10.1002/rra.1554

Kampf, S. K., Faulconer, J., Shaw, J. R., Sutfin, N. A., and Cooper, D. J. (2016). Rain and channel flow supplements to subsurface water beneath hyper-arid ephemeral stream channels. *J. Hydrol.* 536, 524–533. doi: 10.1016/j.jhydrol.2016.03.016

Larned, S. T., T., D., Arscott, D. B., and Tockner, K. (2010). Emerging concepts in temporary-river ecology. *Freshw. Biol.* 55, 717–738. doi: 10.1111/j.1365-2427.2009.02322.x

Leenhouts, J. M., Stromberg, J. C., and Scott, R. L. (Eds.) (2006). Hydrologic requirements of and consumptive groundwater use by riparian vegetation along the San Pedro River, Arizona. *U.S. Geological Survey Scientific Investigations Report 2005-5163*, 154.

Levick, L., Fonseca, J., Goodrich, D., Hernandez, M., Semmens, D., Stromberg, J., et al. (2008). *The Ecological and Hydrological Significance of Ephemeral and Intermittent Streams in the Arid and Semi-arid American Southwest.* Tucson, AZ: U.S. Environmental Protection Agency and USDA/ARS Southwest Watershed Research Center.

Levick, L., Hammer, S., Lyon, R., Murray, J., Birtwistle, A., Goodrich, D. C., et al. (2015). *An Ecohydrological Approach to Managing Intermittent and Ephemeral Streams on Department of Defense Lands in the Southwestern United States in: SERDP Project RC-1727*. Alexandria, VA: Department of Defense Strategic Environmental Research and Development Programme.

Levick, L., Hammer, S., Lyon, R., Murray, J., Birtwistle, A., Guertin, P., et al. (2018). An ecohydrological stream type classification of intermittent and ephemeral streams in the southwestern United States. *J. Arid Environ.* 155, 16–35. doi: 10.1016/j.jaridenv.2018.01.006

Lohse, K. A., Gallo, E. L., and Meixner, T. (2020a). *Influence of Climate and Duration of Stream Water Presence on Rates of Litter Decomposition and Nutrient Dynamics in Temporary Streams and Surrounding Environments of Southwestern USA*. Frontiers in Waters, 2. doi: 10.3389/frwa.2020.571044

Lohse, K. A., Gallo, E. L., and Meixner, T. (2020b). *Dataset on Soil Physio-Chemical Properties and Seasonal Moisture and Nutrient Dynamics in Temporary Stream Channels and Contributing Uplands in Arizona*, USA. Boise, ID: Boise State University ScholarWorks. doi: 10.18122/boisestate/reynoldscreek/17

Lohse, K. A., Gallo, E. L., and Meixner, T. (2020c). *Dataset on Rates of In-Situ Litter Decomposition Across a Range of Ephemeral to Seasonally- Intermittent Stream Reaches and Landscape Positions in Arizona*, *USA*. Boise, ID: Boise State State ScholarWorks. doi: 10.18122/boisestate/reynoldscreek/18

McCluney, K. E., and Sabo, J. L. (2009). Water availability directly determines per capita consumption at two trophic levels. *Ecology* 90, 1463–1469. doi: 10.1890/08-1626.1

Mock, C. J. (1996). Climatic Controls and Spatial Variations of Precipitation in the Western United States. *J. Clim.* 9, 1111–1125. doi: 10.1175/1520-0442(1996)009<1111:CCASVO>2.0.CO;2

Naumburg, E., Mata-gonzalez, R., Hunter, R. G., McLendon, T., and Martin, D. W. (2005). Phreatophytic vegetation and groundwater fluctuations: a review of current research and application of ecosystem response modeling with an emphasis on great basin vegetation. *Environ. Manage* 35, 726–740. doi: 10.1007/s00267-004-0194-7

Newman, B. D., Wilcox, B. P., Archer, S. R., Breshears, D. D., Dahm, C. N., Duffy, C. J., et al. (2006). Ecohydrology of water-limited environments: a scientific vision. *Water Resour. Res.* 42:W06302. doi: 10.1029/2005WR004141

PRISM Climate Group (2013). *Oregon State University*. Available online at: http://prism.oregonstate.edu (accessed 10, 2013).

Sall, J., Lehman, A., Stephens, M. L., and Creighton, L. (2012). *JMP Start Statistics: A Guide to Statistics and Data Analysis Using JMP*. Cary, NC: SAS Institute.

Schaap, M. G., and Leij, F. J. (2000). Improved prediction of unsaturated hydraulic conductivity with the mualem-van genuchten model. *Soil Sci. Soc. Am. J.* 64, 843–851. doi: 10.2136/sssaj2000.643843x

Scott, R. L., Cable, W. L., and Hultine, K. R. (2008). The ecohydrologic significance of hydraulic redistribution in a semiarid savanna. *Water Resour. Res.* 44:W02440. doi: 10.1029/2007WR006149

Sorman, A. U., and Abdulrazzak, M. J. (1993). Infiltration-recharge through wadi beds in arid regions. *Hydrol. Sci. J.* 38, 173–186. doi: 10.1080/02626669309492661

Stromberg, J., Gallo, E., Lohse, K., Meixner, T., Moody, E., Sabo, J., et al. (2015). *Structure and Function of Ephemeral Streams in the Arid and Semiarid Southwest: Implications for Conservation and Management (Project RC-1726)*. Alexandria, VA: Department of Defense Strategic Environmental Research and Development Program).

Stromberg, J., Setaroa, D., Gallo, E., Lohse, K., and Meixner, T. (2017). Riparian vegetation of ephemeral streams. *J. Arid. Environ.* 138, 27–37. doi: 10.1016/j.jaridenv.2016.12.004

Stromberg, J. C., Hazelton, A. F., and White, M. S. (2008). Plant species richness in ephemeral and perennial reaches of a dryland river. *Biodivers. Conserv.* 18:663. doi: 10.1007/s10531-008-9532-z

Sutfin, N. A., Shaw, J. R., Wohl, E. E., and Cooper, D. J. (2014). A geomorphic classification of ephemeral channels in a mountainous, arid region, southwestern Arizona, USA. *Geomorphology* 221, 164–175. doi: 10.1016/j.geomorph.2014.06.005

Tan, P. N., Steinbach, M., and Kumar, V. (2006). "Cluster analysis: basic concepts and algorithms," in *Introduction to Data Mining,* ed P. N. Tan (New York, NY: Pearson Addison-Wesley), 478–568.

Thornthwaite, C. (1948). An approach toward a rational classification of climate. *Geogr. Rev.* 38, 55–94. doi: 10.2307/210739

Tillman, F. D., Cordova, J. T., Leake, S. A., Thomas, B. E., and Callegary, J. B. (2011). "Water availability and use pilot; methods development for a regional assessment of groundwater availability, southwest alluvial basins, Arizona," in *U.S. Geological Survey Scientific Investigations Report 2011*, Reston, VA. doi: 10.3133/sir20115071

Turnipseed, D. P., and Sauer, V. B. (2010). *Discharge Measurements at Gaging Stations: U.S. Geological Survey Techniques and Methods Book 3*, 87. doi: 10.3133/tm3A8

UNEP (1992). *World Atlas of Desertification.* London: Edward Arnold.

US Geological Survey (2008) *National Hydrography Dataset (ver. 2 USGS National Hydrography Dataset (NHD).* Available online at: https://www.usgs.gov/core-science-systems/ngp/national-hydrography/access-national-hydrography-products (accessed October 23, 2019).

Vivoni, E. R., Tai, K., and Gochis, D. J. (2009). Effects of initial soil moisture on rainfall generation and subsequent hydrologic response during the North American Monsoon. *J. Hydrometeorol.* 10, 644–664. doi: 10.1175/2008JHM1069.1

Wahi, A. K., Hogan, J. F., Ekwurzel, B., Baillie, M. N., and Eastoe, C. J. (2008). Geochemical quantification of semiarid mountain recharge. *Groundwater* 46, 414–425. doi: 10.1111/j.1745-6584.2007.00413.x

Wilson, J. L., and Guan, H. (2004). "Mountain-block hydrology and mountain-front recharge," in *Groundwater Recharge in a Desert Environment: The Southwestern United States*, eds F. M. Phillips, J. Hogan and B. Scanlon (Washington, DC: AGU), 113–137. doi: 10.1029/009WSA08

Zar, J. (1999). *Biostatistical Analysis.* Upper Saddle River, NJ: Prentice Hall.

Conflict of Interest: The authors declare that the research was conducted in the absence of any commercial or financial relationships that could be construed as a potential conflict of interest.

frontiers in Water

BRIEF RESEARCH REPORT
published: 17 December 2020
doi: 10.3389/frwa.2020.560707

Dispersible Colloid Facilitated Release of Organic Carbon From Two Contrasting Riparian Sediments

Kenton A. Rod[1†], Kaizad F. Patel[1], Swatantar Kumar[1], Elizabeth Cantando[2], Weinan Leng[2], Ravi K. Kukkadapu[3], Odeta Qafoku[3], Mark Bowden[3], Daniel I. Kaplan[4] and Kenneth M. Kemner[5]*

[1] Pacific Northwest National Laboratory, Richland, WA, United States, [2] Virginia Tech National Center for Earth and Environmental Nanotechnology (NanoEarth), Blacksburg, VA, United States, [3] Environmental and Molecular Sciences Laboratory, PNNL, RIchland, WA, United States, [4] Savannah River National Laboratory, Aiken, SC, United States, [5] Bioscience Division, Argonne National Laboratory, Lemont, IL, United States

OPEN ACCESS

Edited by:
Carl I. Steefel, Lawrence Berkeley National Laboratory, United States

Reviewed by:
Wenming Dong, Lawrence Berkeley National Laboratory, United States
Mohammad Zafar Afsar, University of Delaware, United States

***Correspondence:**
Kenton A. Rod
kenton.rod@gmail.com

†Present address:
Kenton A. Rod, Washington State Department of Ecology, Richland, WA, United States

Specialty section:
This article was submitted to Water and Critical Zone, a section of the journal Frontiers in Water

Received: 10 May 2020
Accepted: 30 November 2020
Published: 17 December 2020

Citation:
Rod KA, Patel KF, Kumar S, Cantando E, Leng W, Kukkadapu RK, Qafoku O, Bowden M, Kaplan DI and Kemner KM (2020) Dispersible Colloid Facilitated Release of Organic Carbon From Two Contrasting Riparian Sediments. Front. Water 2:560707. doi: 10.3389/frwa.2020.560707

In aqueous systems, including groundwater, nano-colloids (1–100 nm diameter) and small colloids (<450 nm diameter) provide a vast store of surfaces to which organic carbon (OC) can sorb, precluding its normal bioavailability. Because nanomaterials are ubiquitous and abundant throughout Earth systems, it is reasonable that they would play a significant role in biogeochemical cycles. As such, mineral nano-colloids (MNC) and small colloids, formed through mineral weathering and precipitation processes, are both an unaccounted-for reservoir and unquantified vector for transport of OC and nutrients and contaminants within watersheds. Water extractions and leaching experiments were conducted under (1) aerobic (ambient) and (2) anaerobic (environmental chamber) conditions for each of two contrasting riparian sediments from (1) Columbia River, Washington and (2) Tims Branch, South Carolina. Water dispersible colloid-adsorbed OC was as high as 48% of OC for Tims Branch anaerobic batch water extraction and as low as 0% for Columbia River aerobic batch water extractions. Anaerobic leaching from column experiments yielded higher colloid and OC release rates. Transmission electron microscopy with electron dispersive spectroscopy mapping revealed organic carbon associated with aggregations of nano-particulate silicate minerals and Mossbauer identified nano-particulate goethite. This exploratory study demonstrates that mineral facilitated release of OC in riparian sediments is both significant and variable between locations.

Keywords: organic-carbon, riparian sediment, nano-colloids, dispersible colloids, Columbia River, Tims Branch

INTRODUCTION

There has already been a recent revolution in understanding how organic carbon (OC) persists in soils. Previous operational definitions and incomplete understanding perpetuated concepts such as "recalcitrant carbon" as an explanation of soil OC persistence. It is now widely accepted that a significant fraction of OC is actually physically and chemically "protected" and is therefore not bioavailable. Bioavailability is restricted by either physical occlusion or by chemical adsorption to mineral surfaces (Schmidt et al., 2011). We are on the frontier of a similar revolution in aqueous systems where the operational definition

of dissolved OC (DOC; solutes passed through a 0.45 μm filter) is incomplete and perhaps incorrect (Yan et al., 2018; Afsar et al., 2020). In aqueous systems, including groundwater, nano-colloids provide a vast store of surfaces to which OC can sorb, precluding its normal bioavailability. Because nanomaterials are ubiquitous and abundant throughout Earth systems (Hochella et al., 2019), it is reasonable that they would play a significant role in biogeochemical cycles. As such, mineral nano-colloids (MNC), formed through mineral weathering and precipitation processes, are both an unaccounted for reservoir and unquantified flux of OC and nutrients within watersheds. They may also serve as a bridge between organic and inorganic nutrient and contaminant cycles. In groundwater systems OC can adsorb to MNC surfaces (MNC-OC) providing protections from mineralization.

MNCs, defined as between 1 and 100 nm in at least one dimension, are ubiquitous in the environment and have been found in iron-oxide surface coatings on soil minerals, as well as moving freely in soil and sediment waters (Hochella et al., 2008, 2012; Henderson et al., 2012). Common natural MNCs have been identified as iron-oxides and many other mineral and amorphous families, especially silicates. They have the same chemistry but often subtly different atomic structure than their larger mineral counterparts. Mineral nano-colloids have highly reactive surfaces that sorb OC to protect it from oxidation and facilitate ion exchange. The colloid morphology and specific sorbed species influence the surface structure and charge of the mineral and, as a result, influence the strength with which OC will bind to the MNC and the transport of MNC-OC through ecosystems. MNCs can be readily transportable between aquatic and terrestrial systems and through soils and sediments.

Mineral nano-colloids may originate from iron oxide nano-crystalline and amorphous iron oxide layers on sediment, which are also known OC adsorption sites (Kleber et al., 2007); iron oxides can release nano-minerals during changes in redox conditions (Henderson et al., 2012). Changing hydrodynamic conditions, particularly fluctuations between extreme wet and dry conditions, accelerate mineral weathering and mineral nano-colloid release. These hydrodynamic fluctuations also solubilize iron surface coatings. However, the interaction between the iron oxides, nano-colloids, and OC has not been fully examined. It has already been demonstrated in soils that chemical adsorption of OC to minerals such as iron oxides provides protection against microbial degradation (Kleber et al., 2007; Schmidt et al., 2011). The surfaces of natural MNCs and colloids can also provide protection in the same manner. This study addresses a gap in watershed science and pore water process understanding by elucidating the dynamic and interconnected role of mineral nano-colloids on OC cycling using highly resolved laboratory experiments.

The objective of this exploratory research was to improve our understanding of the role of water dispersible mineral nanoparticles (MNC) and mineral colloids in biogeochemical cycling and OC transport through watersheds by quantifying release of MNC-OC from riparian sediments from contrasting watersheds. We tested the hypothesis that short-term hydrologic perturbations will release mineral nano-colloids and associated organic carbon to pore water from iron oxide coated sediments. We conducted batch water extractions and column leaching experiments, under aerobic and anaerobic conditions, to study the release of natural MNCs from sediments, and to quantify the amount of OC associated with colloid fractions and to quantify OC release rates.

METHODS

Materials

Riparian capillary fringe sediments were sampled from the Columbia River watershed, near Richland Washington, and Savannah River watershed, near Aiken South Carolina. These rivers represent contrasting systems where Savannah River soils, regionally characterized by Ultisols, are more weathered compared with the Columbia River soil, regionally characterized by Aridisols. The Savannah River watershed was sampled on the banks of Tims Branch tributary, 33°20′15″ N 81°43′6″ W, in a sandy Cg horizon at a depth below 20 cm. The Cg horizon had distinct redoximorphic features along root channels and was inundated with water during the time of sampling. The bank along the Columbia River was sampled, 46°22′23″ N 119°16′19″ W, in a C horizon below 20 cm. This sandy C horizon was partially inundated at sampling but had no signs of gleying nor redoximorphic features. However, due to large intermittent releases of water from an upstream hydro dam, this sediment is inundated daily.

Sediment samples were spread out to dry to near field capacity water content so they could be worked with as sediment rather than slurries. Sediments were homogenized before subsampling and characterized for carbon content. Total carbon (TC) was determined by combustion using a VarioMAX Cube (Elementar Analysensysteme GmbH). Total organic carbon (TOC) was determined indirectly by first ashing the samples in a muffle furnace (450°C for 12 h) to remove OC and then quantifying total inorganic carbon (TIC) on the VarioMAX Cube (detection limit of 0.1 mg C; measured ∼4.3 g sample). TOC was calculated as the difference between TC and TIC. Total OC for Columbia River sediments was measured at 3.04 g kg^{-1}, with TIC at 0.09 g kg^{-1} and for Tims Branch it was 2.11 g kg^{-1}, with TIC of 0.06 g kg^{-1}.

Synthetic water was fabricated for water extractions and column leaching reactions following established groundwater formulations for Tims Branch and the Hanford site 300 area at the Columbia River. These waters represent contrasting conditions—Tims Branch ground water is relatively dilute with a pH of 5.0 (Strom and Kaback, 1992) compared to Columbia River groundwater, which is saturated relative to calcite and has a pH of 8.05 (Um et al., 2010). Groundwater formulations were used with corresponding sediment (**Supplementary Table 1**).

Batch Water Extraction

Surface-adsorbed MNC-OC was extracted from the sediment samples to investigate dispersible colloid and OC composition. The extractions were conducted using 250 g sediment in 2 L synthetic groundwater, with gentle agitation at 10 rpm for 7 days (Guigue et al., 2014). Half of the samples were extracted under aerobic (ambient) conditions with container lids (4 L Nalgene) not sealed tight such that gas exchange was possible. The other

half were treated the same but under anaerobic [$N_{2(g)}$] conditions after 48 h equilibration in an anaerobic chamber (Coy Laboratory Products, Grass Lake, MI) with a CAM-12 monitor.

At the end of the extraction, the samples were fractionated for size by centrifugation (Yan et al., 2017) and characterized for colloid concentration and OC concentration. Fractionating in this manner provides detail as to what size fraction has the greatest influence over fate and transport of OC. Centrifugation of water samples was conducted sequentially for the fractions based on silicate densities for the Stokes law calculations (Yan et al., 2017). The fractions included: <1,000 nm (160 RCF for 10 min); <450 nm (555 RCF for 15 min); and <100 nm (2100 RCF for 80 min). This represents the fractions of colloids, common colloid filtration size, and nano-colloid sizes, respectively. A Beckman L8-70M Ultracentrifuge (110,000 RCF for 3 h) was used to separate all iron oxides and silicates over 6 nm from solution (Henneberry et al., 2012). For the purposes of this study we did not differentiate OC associated with MNC and "dissolved" OC in solution for the <6 nm fraction. For this research we did not differentiate dissolved OC from colloidal OC independent of minerals that stays in suspension after the centrifugation steps.

Aliquots of fractionated samples were acidified with 1% nitric acid before analysis for colloid concentration and OC concentration, for the purpose of ensuring inorganic carbon from the high carbonate Hanford water was released and to preserve the samples for future analyses. Colloid concentration was determined by absorption spectra of water samples with a UV-Vis spectrophotometer (Synergy™ Neo2 Multi-Mode Microplate Reader, BioTek®) with 96 well glass bottom plate (Krystal™). A calibration curve was generated using a suspension of illite at measured concentrations of 3.48, 34.8, 174, and 348 mg L^{-1} (r^2 0.99), and the absorbance was measured at 350 nm wavelength (Cherrey et al., 2003). Absorbance measurement of the sample and calibration solutions then allowed for estimation of concentration of particles in water samples by applying Beer's law, which assumes spectral adsorption changes proportionally with concentration. Dissolved organic carbon concentration was determined by combustion catalytic oxidation on a Shimadzu TOC-L Analyzer.

Aliquots of <1,000 nm fraction were characterized for mineral properties as explained in the next two "Characterization" subsections below.

Aerobic Respiration of Batch Water Extraction

For aerobic respiration rate quantification, batch water extractions from each condition (aerobic and anaerobic) were collected and centrifuged for <1,000 nm colloid fraction. These water samples were immediately transferred and opened in a biosafety cabinet, vortexed, and subsequently allowed to equilibrate with atmospheric air for 2 h at 21°C using a gentle stirrer. Then 43 mL from each water extract was sterilized by autoclaving at 121°C for 20 min, which served as heat-killed controls. Once the autoclaved sediment-suspensions were cooled to room temperature, 40 mL of each heat-killed control water and two sets of 40 mL samples (for each extraction condition) were added to 41.5 mL borosilicate glass bioreactors having pre-attached planar oxygen-sensitive spots (5 mm sensor spots; PreSens GmbH, Regensburg, Germany). To prevent any air contamination in the bioreactors, the caps were sealed with a thin layer of parafilm. Dissolved oxygen concentration (mg L^{-1}) was monitored in these airtight sensor spot bioreactors for 6 days using an oxygen optical meter assembly (Fibox 3; fiber optic oxygen transmitter, a polymer optical fiber) and recorded using PST3v602 software (PreSens Precision Sensing GmbH, Regensburg, Germany). Briefly, capped bioreactors were vortexed for 20 s and three readings of dissolved oxygen (mg L^{-1}) were recorded at the interval of 5 sec. After recording the dissolved oxygen, the bioreactors were immediately transferred to a shaker (300 rpm; platform shaker; Innova® 2100; New Brunswick Scientific) in the environmental chamber with controlled temp (21°C) in dark. Respiration rates were calculated as the slope of the linear regression between dissolved oxygen concentration and incubation time for each bioreactor. The linear regression generates a negative slope which is a function of the oxygen uptake rate and therefore aerobic respiration rates (mg O_2 L^{-1} h^{-1}). A two-point manual calibration was performed prior to the sample analysis per PreSens guidelines using oxygen-free and oxygen-saturated water to ensure the quality control check.

Characterization of Batch Water Extracts: TEM-EDS (Colloids), Zeta Potential

Transmission electron microscopy with electron dispersive spectroscopy (TEM-EDS) was used for visual and elemental identification of MNCs (Wheatland et al., 2017). The particles from water samples were collected onto a 300 mesh copper TEM grid with lacey carbon support film using Beckman ultracentrifuge (274,400 RCF, 24 h). A JEOL 2100 TEM/Scanning-TEM operating at 200 kV, coupled with EDS and selected-area electron diffraction (SAED), were applied to characterize the morphology, composition, and crystal structures of the particles.

Since surface electric potential is significant for the adsorption and desorption of MNC to sediment, we measured the colloid suspensions zeta potentials (Appel et al., 2003). Samples were sonicated for 10 min to disperse them, then analyzed for zeta potential using a Malvern Zetasizer Nano ZS.

Colloid Characterization From Tims Branch Sediment: Mössbauer, μ-XRD, and SEM-EDX

For the Tims Branch sediment aerobic extraction with groundwater, the colloid concentration was high enough to do additional mineral characterization using μ-XRD, SEM-EDX, and Mössbauer spectroscopy. These analyses were performed on the <1,000 nm fraction, collected by spinning samples in an ultra-centrifuge to remove colloids from suspension. The solution was then decanted and the remaining water was allowed to evaporate in a fume hood.

Powder diffraction was performed using a Panalytical X'Pert Bragg-Brentano diffractometer, μ-XRD, with Cu-Kα radiation (λ = 1.5418 Å), a graphite post-diffraction monochromator, and variable divergence and anti-scatter slits (illuminated length = 10 mm). Minerals were identified using JADE software (Materials Data Incorporated, CA) by comparison with reference patterns in the database maintained by the International Center for Diffraction Data (PA).

Mössbauer measurements were carried out on the colloid sample using a SEE Co Mössbauer setup (Edina, MN), a Ritverc ^{57}Co/Rh gamma energy source (75-mCi, initial strength; St. Petersburg, Russia), a scintillation NaI(T1) SGS-2 detector (Ritverc), a closed-cycle cryostat SHI-850 (Janis Research Co., Inc., Wilmington, MA), and a Sumitomo CKW-21 He compressor unit (Allentown, PA). The transmitted counts were stored in a multichannel scalar (MCS) as a function of the energy (transducer velocity) using a 1024-channel analyzer. Calibration spectra were obtained with a 7-μm-thick Fe foil placed in the same position as the samples to minimize any geometry errors. The raw data were folded to 512 channels to provide a flat background and a zero-velocity position corresponding to the center shift (CS) of a metal Fe foil at room temperature (RT). The Mössbauer spectroscopy data were modeled with Recoil software (University of Ottawa, Canada) using a Voigt-based structural fitting routine (Rancourt and Ping, 1991). The sample preparation (type of the sample holder, etc.) was similar to the procedure reported in Peretyazhko et al. (2012), except the samples were dispersed in powdered sugar instead of petroleum jelly.

Scanning Electron Microscopy (SEM) analyses were conducted with a FEI Helios NanoLab 600i field emission electron microscope. A small amount of dried colloid powder was mounted on a SEM aluminum stub and were coated with a 10 nm carbon layer by thermal evaporation using a 108C Auto Carbon Coater (Ted Pella, Inc.). Particle morphology was examined using a secondary electron Everhart-Thornley detector

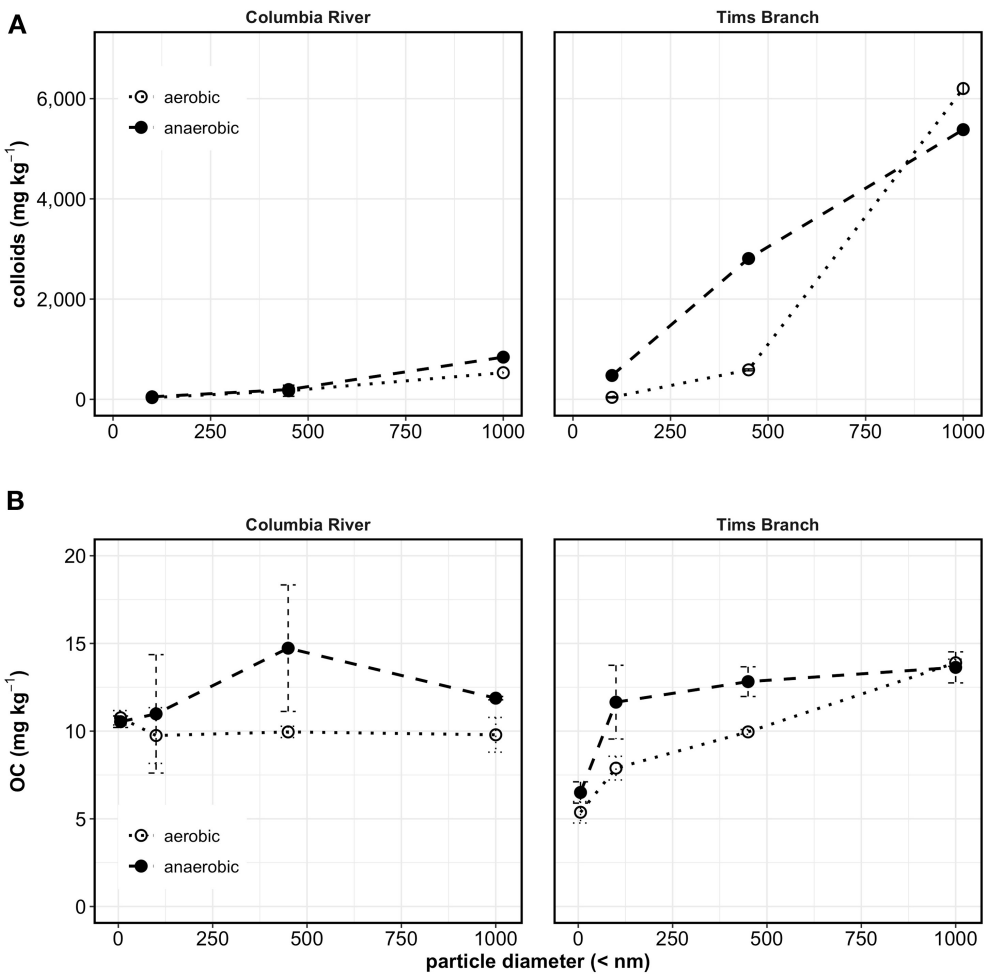

FIGURE 1 | Water dispersible colloid mass released per mass of sediment **(A)**, and OC mass per mass sediment **(B)** fractionated by centrifugation to select colloid diameters <1,000, <450, <100, (and <6 nm for OC) from batch water extractions of Columbia River sediments, and Tims Branch sediments. Error bars represent one standard deviation from measurement replicates; lines between points are to help with visualization and do not represent a regression model.

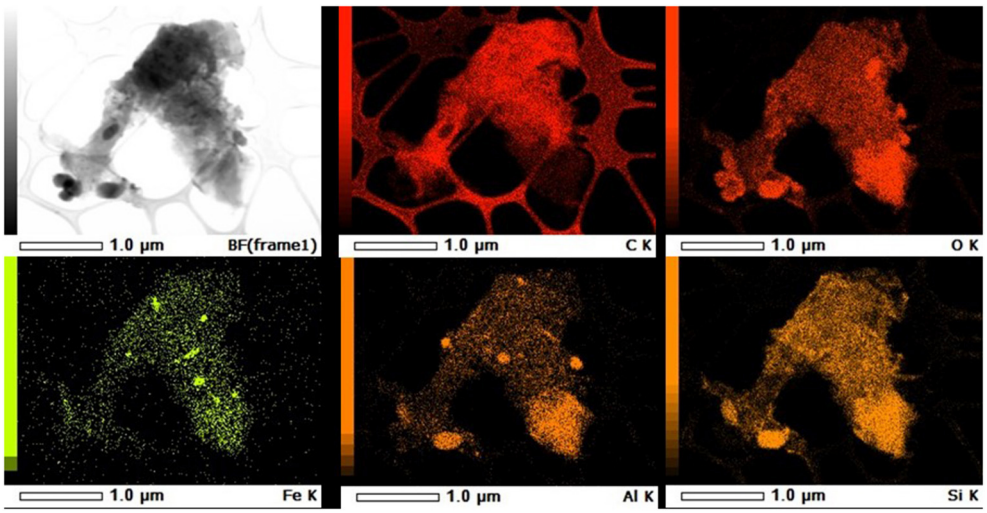

FIGURE 2 | Representative TEM-EDS map of water extracted colloids from Tims Branch Sediment Anaerobic sample. First image is TEM. The remaining images are EDS elemental maps of the same image showing relative intensity of each element. Scale and element are listed in footer for each image.

(ETD) in a field free mode at an acceleration voltage of 3–5 kV and a current of 0.086–0.17 nA at 4 mm working distance. Higher magnification images were collected using through-lens-detector (TLD) with same voltage/current as described above. Energy dispersive x-ray (EDX) spectra were collected with X-Max 80 mm^2 Silicon Drift Detector (SDD) from Oxford Instruments. The EDX analyses were performed at 10–20 kV voltage and 2–3 nA current. Oxford INCA software was used to perform point spectrum analyses and create compositional maps.

Column Leaching

Leaching tests were conducted to measure relative release rates of OC and colloids from the sediments. Columns were packed with sediment into 75 mL internal volume glass columns with 2.54 cm inner diameter. Two columns were packed for each sediment type, to a resultant porosity of 0.48 for the Columbia River columns and 0.44 for the Tims Branch columns. One from each column pair was run under anaerobic conditions, the other aerobic, as described in "Batch water extraction" section. Syringe pumps (IMI-Kloehn) were used to deliver synthetic groundwater at a rate of three pore volumes per day. Effluent was collected twice a day and centrifuged for fraction <450 nm silicate as detailed above. The effluent was analyzed for colloid concentration by UV-Vis and the OC content measured by a Shimadzu TOC-L Analyzer.

RESULTS AND DISCUSSION

Fractionation of Released Colloids From Batch Extractions

Release of colloids from Columbia River sediments (**Figure 1A**) was 58% greater for anaerobic than aerobic extracts for the <1,000 nm fraction and 45% greater for the <100 nm fraction. The higher release during the induced anoxia was expected as it has been well-documented in the literature and is attributed to the reductive dissolution of cementing ferric iron oxides to more soluble ferrous iron, resulting in the release of aggregated colloids (Henderson et al., 2012; Liang et al., 2019). Tims Branch sediments released an order of magnitude more colloids due to anoxia for the <100 nm fraction but the <1,000 nm fraction had 15% more released from aerobic extraction compared to anaerobic (**Figure 1A**). The lower value for the anaerobic extraction may be attributed to aggregation and settling before analysis or subsample variability. Aggregation was noticed at multiple points of analysis, and occurred despite additional preparation (acidification, sonication) before analysis. The release of colloids from Tims Branch sediments was three to ten times greater than from Columbia River sediments in all instances except for <100 nm aerobic extraction which was 14% higher for Tims Branch. Higher colloid concentrations are most likely due to a combination of the very low ionic strength of the SRS artificial groundwater, 0.2 mM (compared to 6.4 mM Hanford artificial groundwater), and the high concentrations of highly dispersible OC-coated Fe-oxyhydroxides and fine kaolinite particles common in these weathered soils (Kaplan et al., 1993, 1997).

Colloid Mineralogy

Colloids collected from each of the extractions were imaged using TEM-EDX (**Figure 2** and **Supplementary Figures 1–4**). All of the images displayed aggregations of minerals that had primarily round scale-like morphology with the occasional elongated mineral (**Supplementary Figures 2**, **4**). The minerals had high relative element concentrations of Si, Al, and O, suggesting that these are primarily silicate minerals (**Figure 2** and **Supplementary Figures 1–4**). Tims Branch soils have documented kaolinite as a significant colloid (Kaplan et al., 1993, 1997) and clays from the Hanford 300 area have been reported as dominantly muscovite, smectite, and clinochlore (Um et al., 2010). The EDX showed even distribution of Fe

across most of the minerals for the Columbia River colloids (**Supplementary Figures 1**, **2**), whereas the Tims Branch colloids had small concentrated points scattered over the mineral surfaces (**Figure 2** and **Supplementary Figures 3**, **4**). It is possible that these points with high Fe concentration are nano colloids aggregated with the larger minerals. The presence of C on the Tims Branch colloids (**Figure 2** and **Supplementary Figures 3**, **4**) was much more evident compared to the Columbia River colloids (**Supplementary Figures 1**, **2**). Organic coatings on colloids from soils of the same region as Tims Branch have previously been noted (Kaplan et al., 1997).

The μ-XRD pattern of colloids from Tims Branch aerobic water extraction (**Supplementary Figure 5**) was crystalline with sharp peaks for kaolinite. There were also peaks for quartz and gibbsite, minor illite or montmorillonite, and trace hematite. The presence of these minerals is consistent with previous work on soils from this watershed (Kaplan et al., 1993, 1997). The morphology of the minerals from SEM analysis showed that most of the material was rounded flakes and the EDX data shows high relative concentrations of Si, Al, and O as would be expected in a silicate clay mineral like kaolinite (**Supplementary Figure 6**). High relative Fe concentrations point to Fe- "coatings" adsorbed on the larger minerals.

The Mössbauer spectra from Tims Branch aerobic water extraction (**Supplementary Figure 7**) confirms the presence of hematite, with <3% Fe being hematite. Approximately 80% of the sample's Fe was nanoparticulate goethite (<10 nm) with a somewhat complex particle-size distribution, but appeared to be a mixture of three different pools of varying particle size/carbon coating content (Bhattacharyya et al., 2018; Arredondo et al., 2019). More importantly, the sample was free of poorly crystalline/amorphous Fe-oxide minerals, such as ferrihydrite. The remaining Fe in the colloids sample (∼20%) was likely associated with silicate minerals—primarily (14.9%) as Fe(III), but there was some (4.8%) Fe(II).

The silicates, kaolinite, and quartz identified from Tims Branch should have lower adsorptive capacity compared to the previously identified muscovite, smectite, and clinochlore at Columbia River (Um et al., 2010). This suggests a significant role that the Fe-particles and Fe-coatings on silicates have on the adsorption of the OC.

Fractionation of Released Mineral Colloid-Associated OC From Batch Extractions

Similar to colloids, there was more release of OC from the anaerobic extraction (**Figure 1B**), suggesting that it was released during induced anoxia by similar desorption mechanisms (Adhikari et al., 2017; Han et al., 2019). Using the <6 nm fraction as an estimated cut off for dissolved OC (DOC), the OC associated with Columbia River mineral colloids was 29% of the maximum measured OC (26% in 100–450 nm fraction, 3% in 6–100 nm fraction of the maximum measured OC for that extraction) for the anaerobic extraction. For the Columbia River aerobic extracts, the <6 nm fraction had 10.8 mg kg^{-1} DOC, compared to the mineral colloid fraction <100 nm of 9.7 mg kg^{-1}, suggesting that there was no mineral colloid-associated OC in these extracts (**Figure 1B**). As with the colloids, some aggregation and settling may have impacted the measurement of OC as can be seen for the <1,000 nm fraction from the Columbia River sediments (**Figure 1B**). Alternately this lower value for <1,000 nm was data noise as evidenced by the wide measurement replicate error bars for the <450 nm sample (**Figure 1B**). For Tims Branch, 48% of anaerobic extracted OC was associated with mineral colloids with 38% in the 6–100 nm fraction and 8% in the 100–450 nm fraction (**Figure 1B**). The mineral colloid associated OC released during aerobic water extraction was 40% of total released, with 18% in the 6–100 nm fraction and 15% in the 100–450 nm fraction, and 7% in the 450–1,000 nm fraction.

Reducing conditions have been known to desorb OC from Fe colloids (Adhikari et al., 2017; Han et al., 2019), and the different responses for the two sediments may be explained by the natural redox conditions at these sites. The subsurface along the Hanford reach of the Columbia River is largely aerobic, so contribution of mineral colloids and MNCs to OC cycling may be minimal based on the results from this experiment. However, Tims Branch sediments had redoximorphic features from repeated oxic and anoxic periods, which could result in fluctuating release concentrations of MNC-OC and OC associated with small colloids.

Microbial degradation reducing the measured OC was a concern for impacting the measurement of OC concentrations

TABLE 1 | Batch water properties (microbial respiration, zeta potential) and column effluent data (OC and colloid release rates, pore velocity) for Columbia River sediment and Tims Branch sediment reacted with groundwater under aerobic and anaerobic conditions.

			Batch		Column		
Sample	**Condition**	**Microbial respiration rate ($mg\ L^{-1}hr^{-1}$)**	**pH**	**Zeta potential (mV)**	**OC release rate ($mg\ kg^{-1}\ d^{-1}$; r^2)***	**Colloid release rate ($mg\ kg^{-1}\ d^{-1}$; r^2)***	**Calculated pore velocity ($m\ d^{-1}$)****
Columbia River	Aerobic	0.011	7.38	−8.77	0.92; 0.99	2.8; 0.98	0.876
	Anaerobic	0.009	6.95	−12.8	1.36; 0.75	8.8; 0.98	0.894
Tims Branch	Aerobic	0.011	6.02	−8.43	0.36; 0.90	13.4; 0.87	0.973
	Anaerobic	0.010	3.84	−18.9	0.76; 0.90	28.7; 0.98	0.955

OC and colloid rates normalized to mass per sediment mass. OC rate did not use data from first 2 days due early non-linear release. TOC for Columbia River sediment was 3.04 g kg^{-1} and for Tims Branch sediment was 2.11 g kg^{-1} (mass OC per mass sediment); **porosity for columns: Columbia River sediment columns were 0.48 and for Tims branch sediment columns were 0.44. Column data plots for colloid and OC release are provided in* ***Supplementary Figure 8**.*

and calculated OC release rates. However, respiration was very low in all water samples (**Table 1**) and there was no effective difference between the conditions in this experiment.

Leaching Rates of Colloids and OC From Columns

The initial release of colloids for Columbia River sediment columns within the first day was lower than colloids from Tims Branch sediment columns, but the OC had a proportionally larger release from Columbia River columns (**Supplementary Figure 8**). This initial release difference is likely due to desorption of the OC occurring more rapidly than detachment of colloids.

Following the initial release there was a sustained release, from day 1 to 5, of colloids and OC from the columns that showed a higher release rate for anaerobic conditions compared to aerobic reaction conditions (**Table 1**). The increase in release rates with anaerobic extraction was expected and coincided with more negative zeta potential for the anaerobic reacted water extractions (**Table 1**). Li et al. (2013) found that colloids amended with organics decreased the zeta potential and the colloid-OC material transported more readily through sediment. In our study, the Tims Branch colloids had a higher release rate compared to the Columbia River colloids (**Table 1**), which could be due to a combination of factors. This higher release could be due to a more dilute groundwater, greater repulsive forces due to lower zeta potential for the organic coated colloids (**Table 1** and **Figure 2**), or there was an abundance of colloids which would be present in a region with highly weathered soils. The matrix in both of these sediments is sand with large pore spaces that would allow easy transport of the colloids with minimal surface interaction or straining. Ultimately this demonstrates that, even when there is OC adsorbed to—colloids, release of the bulk OC differs from that of the bulk colloids regardless of whether the release is aerobic or anaerobic.

ENVIRONMENTAL IMPLICATIONS

Colloids can play a significant role in the fate and transport of natural OC through watersheds, particularly in redox dynamic environments where reductive dissolution of Fe minerals can facilitate increased concentrations of colloids within porewaters. This is particularly relevant for Tims Branch sediments that, upon reduction, can release up to 48% of their OC in association with colloids. Most of the OC was attached to MNCs, which with their size of $<$100 nm can be transported readily through sediment, making nano-colloid-facilitated transport a significant agent of C biogeochemical cycling. However, this may not be the case in all riparian sediments such as found from Columbia River sediments under aerobic conditions where there is no measurable adsorption of OC to colloids of any size. The importance of colloidal and MNC facilitated transport of OC in watersheds appears to be location specific. Since MNCs have high surface charge, they can potentially limit bioavailability of OC while adsorbed to them and while being transported through a watershed. This control on the bioavailability of OC while adsorbed to MNCs must be accounted for in modeling OC transport as the transport of colloids is different than dissolved OC.

DATA AVAILABILITY STATEMENT

The raw data supporting the conclusions of this article will be made available by the authors, without undue reservation, to any qualified researcher.

AUTHOR CONTRIBUTIONS

KR: conceptualized, field data collection, experimentation, data analysis, and writing. KP: data generation, data analysis, and writing. SK: respiration experiments and writing. EC: nano-colloid characterization, TEM, and writing. WL: nano-colloid characterization, zeta potential, and writing. RK: mossbauer, analysis, and writing. OQ: SEM, analysis, and writing. MB: uXRD, analysis, and writing. DK: field data collection, senior review, and writing. KK: senior review and writing. All authors contributed to the article and approved the submitted version.

FUNDING

This work was supported by Pacific Northwest National Laboratory SEED-LDRD [DE-AC05-76RLO 1830, AC02-06CH11357, AC09-08SR22470, and NSF(ECCS 1542100)].

ACKNOWLEDGMENTS

This research described in this paper was conducted under the Laboratory Directed Research and Development Program at Pacific Northwest National Laboratory (PNNL). A portion of this research was performed in the W. R. Wiley Environmental Molecular Sciences Laboratory (EMSL), a national scientific user facility sponsored by the Office of Biological and Environmental Research (BER) and located at PNNL. PNNL is a multiprogram national laboratory operated by Battelle for the U.S. Department of Energy (DOE) under contract DE-AC05-76RLO 1830. Support for DK and KK was provided by the Argonne Wetland Hydrobiogeochemistry Science Focus Area funded by the Subsurface Biogeochemical Research Program of the Office of Biological and Environmental Research, Office of Science, U.S. Department of Energy (DOE), under contracts DE-AC02-06CH11357 (Argonne National Laboratory) and AC09-08SR22470 (Savannah River Nuclear Solutions). This work was supported by the Virginia Tech National Center for Earth and Environmental Nanotechnology Infrastructure (NanoEarth), a member of the National Nanotechnology Coordinated Infrastructure (NNCI), supported by NSF (ECCS 1542100 and ECCS 2025151).

SUPPLEMENTARY MATERIAL

The Supplementary Material for this article can be found online at: https://www.frontiersin.org/articles/10.3389/frwa.2020.560707/full#supplementary-material

REFERENCES

Adhikari, D., Zhao, Q., Das, K., Mejia, J., Huang, R., Wang, X., et al. (2017). Dynamics of ferrihydrite-bound organic carbon during microbial Fe reduction. *Geochim. Cosmochim. Acta* 212, 221–233. doi: 10.1016/j.gca.2017.06.017

Afsar, M. Z., Goodwin, C., Beebe, T. P., Jaisi, D. P., and Jin, Y. (2020). Quantification and molecular characterization of organo-mineral associations as influenced by redox oscillations. *Sci. Total Environ.* 704:135454. doi: 10.1016/j.scitotenv.2019.135454

Appel, C., Ma, L. Q., Rhue, R. D., and Kennelley, E. (2003). Point of zero charge determination in soils and minerals via traditional methods and detection of electroacoustic mobility. *Geoderma* 113, 77–93. doi: 10.1016/S0016-7061(02)00316-6

Arredondo, M. G., Lawrence, C. R., Schulz, M. S., Tfaily, M. M., Kukkadapu, R., Jones, M. E., et al. (2019). Root-driven weathering impacts on mineral-organic associations in deep soils over pedogenic time scales. *Geochim. Cosmochim. Acta* 263, 68–84. doi: 10.1016/j.gca.2019.07.030

Bhattacharyya, A., Campbell, A. N., Tfaily, M. M., Lin, Y., Kukkadapu, R. K., Silver, W. L., et al. (2018). Redox fluctuations control the coupled cycling of iron and carbon in tropical forest soils. *Environ. Sci. Technol.* 52, 14129–14139. doi: 10.1021/acs.est.8b03408

Cherrey, K. D., Flury, M., and Harsh, J. B. (2003). Nitrate and colloid transport through coarse Hanford sediments under steady state, variably saturated flow. *Water Resour. Res.* 39:1165. doi: 10.1029/2002WR001944

Guigue, J., Mathieu, O., Lévêque, J., Mounier, S., Laffont, R., Maron, P. A., et al. (2014). A comparison of extraction procedures for water-extractable organic matter in soils. *Eur. J. Soil Sci.* 65, 520–530. doi: 10.1111/ejss.12156

Han, L., Sun, K., Keiluweit, M., Yang, Y., Yang, Y., Jin, J., et al. (2019). Mobilization of ferrihydrite-associated organic carbon during Fe reduction: adsorption versus coprecipitation. *Chem. Geol.* 503, 61–68. doi: 10.1016/j.chemgeo.2018.10.028

Henderson, R., Kabengi, N., Mantripragada, N., Cabrera, M., Hassan, S., and Thompson, A. (2012). Anoxia-induced release of colloid- and nanoparticle-bound phosphorus in grassland soils. *Environ. Sci. Technol.* 46, 11727–11734. doi: 10.1021/es302395r

Henneberry, Y. K., Kraus, T. E. C., Nico, P. S., and Horwath, W. R. (2012). Structural stability of coprecipitated natural organic matter and ferric iron under reducing conditions. *Org. Geochem.* 48, 81–89. doi: 10.1016/j.orggeochem.2012.04.005

Hochella, M. F., Aruguete, D., Kim, B., and Madden, A. S. (2012). "Naturally occuing inorganic nanoparticles: general assessment and a global budget for one of earths's last unexpored major geochemical components," in *Nature's Nanostructures*, eds A. S. Barnard and H. Guo (Victoria: Pan Stanford Publishing Pte. Ltd.), 1–42.

Hochella, M. F., Lower, S. K., Maurice, P. A., Penn, R. L., Sahai, N., Sparks, D. L., et al. (2008). Nanominerals, mineral nanoparticles, and Earth systems. *Science* 319, 1631–1635. doi: 10.1126/science.1141134

Hochella, M. F., Mogk, D. W., Ranville, J., Allen, I. C., Luther, G. W., Marr, L. C., et al. (2019). Natural, incidental, and engineered nanomaterials and their impacts on the Earth system. *Science* 363:eaau8299. doi: 10.1126/science.aau8299

Kaplan, D. I., Bertsch, P. M., and Adriano, D. C. (1997). Mineralogical and physicochemical differences between mobile and nonmobile colloidal phases in reconstructed pedons. *Soil Sci. Soc. Am. J.* 61, 641–649. doi: 10.2136/sssaj1997.03615995006100020038x

Kaplan, D. I., Bertsch, P. M., Adriano, D. C., and Miller, W. P. (1993). Soil-borne mobile colloids as influenced by water flow and organic carbon. *Environ. Sci. Technol.* 27:6. doi: 10.1021/es00043a021

Kleber, M., Sollins, P., and Sutton, R. (2007). A conceptual model of organo-mineral interactions in soils: self-assembly of organic molecular fragments into zonal structures on mineral surfaces. *Biogeochemistry* 85, 9–24. doi: 10.1007/s10533-007-9103-5

Li, D., Chang, H. S., Seaman, J. C., and Kaplan, D. I. (2013). Effects of matrix heterogeneity and aqueous humic acid on transport and deposition of mineral colloids in sandy sediments. *J. Environ. Chem. Eng.* 1, 875–883. doi: 10.1016/j.jece.2013.07.032

Liang, X. L., Radosevich, M., Loffler, F., Schaeffer, S. M., and Zhuang, J. (2019). Impact of microbial iron oxide reduction on the transport of diffusible tracers and non-diffusible nanoparticles in soils. *Chemosphere* 220, 391–402. doi: 10.1016/j.chemosphere.2018.12.165

Peretyazhko, T. S., Zachara, J. M., Kukkadapu, R. K., Heald, S. M., Kutnyakov, I. V., Resch, C. T., et al. (2012). Pertechnetate (TcO4-) reduction by reactive ferrous iron forms in naturally anoxic, redox transition zone sediments from the Hanford Site, USA. *Geochim. Cosmochim. Acta*. 92, 48–66. doi: 10.1016/j.gca.2012.05.041

Rancourt, D. G., and Ping, J. Y. (1991). Voigt-based methods for arbitrary-shape static hyperfine parameter distributions in mossbauer-spectroscopy. *Nuclear Instrum. Methods Phys. Res. Sect. B Beam Interact. Mater. Atoms* 58, 85–97. doi: 10.1016/0168-583X(91)95681-3

Schmidt, M. W. I., Torn, M. S., Abiven, S., Dittmar, T., Guggenberger, G., Janssens, I. A., et al. (2011). Persistence of soil organic matter as an ecosystem property. *Nature* 478, 49–56. doi: 10.1038/nature10386

Strom, R., and Kaback, D. (1992). *SRP Baseline Hydrogeologic Investigation: Aquifer Characterization Groundwater Geochemistry of the Savannah River Site and Vicinity, WSRC-RP-92-450*. Aiken, SC: Westinghouse Savannah River Company. doi: 10.2172/10103229

Um, W., Zachara, J. M., Liu, C. X., Moore, D. A., and Rod, K. A. (2010). Resupply mechanism to a contaminated aquifer: a laboratory study of U(VI) desorption from capillary fringe sediments. *Geochim. Cosmochim. Acta* 74, 5155–5170. doi: 10.1016/j.gca.2010.02.001

Wheatland, J. A. T., Bushby, A. J., and Spencer, K. L. (2017). Quantifying the Structure and composition of flocculated suspended particulate matter using focused ion beam nanotomography. *Environ. Sci. Technol.* 51, 8917–8925. doi: 10.1021/acs.est.7b00770

Yan, J., Manelski, R., Vasilas, B., and Jin, Y. (2018). Mobile colloidal organic carbon: an underestimated carbon pool in global carbon cycles? *Front. Environ. Sci.* 6:148. doi: 10.3389/fenvs.2018.00148

Yan, J., Meng, X., and Jin, Y. (2017). Size-dependent turbidimetric quantification of suspended soil colloids. *Vadose Zone J.* 16, 1–8. doi: 10.2136/vzj2016.10.0098

Conflict of Interest: The authors declare that the research was conducted in the absence of any commercial or financial relationships that could be construed as a potential conflict of interest.

frontiers in Water

ORIGINAL RESEARCH
published: 23 December 2020
doi: 10.3389/frwa.2020.563841

Influence of Drying and Wildfire on Longitudinal Chemistry Patterns and Processes of Intermittent Streams

Ruth B. MacNeille[1], Kathleen A. Lohse[1], Sarah E. Godsey[2], Julia N. Perdrial[3] and Colden V. Baxter[1]*

[1] Department of Biological Sciences, Idaho State University, Pocatello, ID, United States, [2] Department of Geosciences, Idaho State University, Pocatello, ID, United States, [3] Department of Geology, University of Vermont, Burlington, VT, United States

Stream drying and wildfire are projected to increase with climate change in the western United States, and both are likely to impact stream chemistry patterns and processes. To investigate drying and wildfire effects on stream chemistry (carbon, nutrients, anions, cations, and isotopes), we examined seasonal drying in two intermittent streams in southwestern Idaho, one stream that was unburned and one that burned 8 months prior to our study period. During the seasonal recession following snowmelt, we hypothesized that spatiotemporal patterns of stream chemistry would change due to increased evaporation, groundwater dominance, and autochthonous carbon production. With increased nutrients and reduced canopy cover, we expected greater shifts in the burned stream. To capture spatial chemistry patterns, we sampled surface water for a suite of analytes along the length of each stream with a high spatial scope (50-m sampling along ~2,500 m). To capture temporal variation, we sampled each stream in April (higher flow), May, and June (lower flow) in 2016. Seasonal patterns and processes influencing stream chemistry were generally similar in both streams, but some were amplified in the burned stream. Mean dissolved inorganic carbon (DIC) concentrations increased with drying by 22% in the unburned and by 300% in the burned stream. In contrast, mean total nitrogen (TN) concentrations decreased in both streams, with a 16% TN decrease in the unburned stream and a 500% TN decrease (mostly nitrate) in the burned stream. Contrary to expectations, dissolved organic carbon (DOC) concentrations varied more in space than in time. In addition, we found the streams did not become more evaporative relative to the Local Meteoric Water Line (LMWL) and we found weak evidence for evapoconcentration with drying. However, consistent with our expectations, strontium-DIC ratios indicated stream water shifted toward groundwater-dominance, especially in the burned stream. Fluorescence and absorbance measurements showed considerable spatial variation in DOC sourcing each month in both streams, and mean values suggested a temporal shift from allochthonous toward autochthonous carbon sources in the burned stream. Our findings suggest that the effects of fire may magnify some chemistry patterns but not the biophysical controls that we tested with stream drying.

Keywords: intermittent streams, fire, carbon, nitrogen, spatiotemporal patterns, allochthonous and autochthonous, evaporation, groundwater

OPEN ACCESS

Edited by:
Alexis Navarre-Sitchler, Colorado School of Mines, United States

Reviewed by:
Adam L. Atchley, Los Alamos National Laboratory, United States
Ashley Johnson Rust, Colorado School of Mines, United States
Adam Wymore, University of New Hampshire, United States

****Correspondence:***
Ruth B. MacNeille
macnruth@isu.edu

Specialty section:
This article was submitted to Water and Critical Zone, a section of the journal Frontiers in Water

Received: *19 May 2020*
Accepted: *08 October 2020*
Published: *23 December 2020*

Citation:
MacNeille RB, Lohse KA, Godsey SE, Perdrial JN and Baxter CV (2020) Influence of Drying and Wildfire on Longitudinal Chemistry Patterns and Processes of Intermittent Streams. Front. Water 2:563841. doi: 10.3389/frwa.2020.563841

INTRODUCTION

Intermittent streams, those streams experiencing periods of disconnected surface water flow (Larned et al., 2010), currently constitute ∼30% of the total river length and discharge of the world river network and about half of the United States (US) network (Datry et al., 2014). Despite the ubiquity of stream drying, perennial streams have historically dominated our understanding of stream chemistry patterns. Indeed, study and understanding of intermittent streams have lagged behind perennial ones (Costigan et al., 2016; Allen et al., 2020; Busch et al., 2020). For example, traditional stream chemistry studies have often focused on temporally intensive measurements at the outlet of a catchment and assumed that downstream patterns are representative of the upstream segment (e.g., Fisher and Likens, 1973; Schiff and Aravena, 1990; Boyer et al., 1997). However, this assumption may not be valid and the approach is unlikely to capture the spatiotemporal variability of intermittent streams (Godsey and Kirchner, 2014; Costigan et al., 2016). To address this assumption, the scope of intermittent stream studies, which is determined by the extent (area or time-period over which measurements are conducted) and the grain (frequency of measurement through space or time) need to be adjusted (Schneider, 2001; Fausch et al., 2002). Indeed, high spatial-scope studies adopting a spatially continuous sampling approach (fine-grain) carried out over larger stream segment lengths (greater extent) have revealed previously undetected spatial patterns along the length of perennial streams and stream networks (Fausch et al., 2002; Likens and Buso, 2006; McGuire et al., 2014). Stream intermittence is characterized by contractions and disconnections that occur with drying at the scale of meters with consequences for stream structure at segment to network scales (Stanley et al., 1997; Dent and Grimm, 1999; Zimmer et al., 2013; Hale and Godsey, 2019; Jensen et al., 2019). Thus, temporally repeated high-spatial scope investigations seem necessary to understand patterns and mechanisms associated with stream intermittence.

Stream intermittency is projected to increase in extent, frequency, and duration as climate changes (Datry et al., 2014), with potentially important consequences for stream chemistry. In the western US, 80% of streams experience drying (US Geological Survey USGS, 2006)[1], and by 2050, intermittent streams and ephemeral streams (those that only experience event-based flow) are projected to increase by 5–7% (Döll and Schmied, 2012). In basins with moderate relief and elevation, such as the Snake, Great Salt Lake, and Oregon Closed Basins, snowmelt-fed streams are particularly susceptible to future stream drying as these areas may experience 100% loss of snow by 2050 (Klos et al., 2014). In most of the western US, projections include earlier snowmelt (Stewart et al., 2004; Abatzoglou et al., 2014). Although watershed geomorphology and vegetation determine hydrologic responses to precipitation shifts (Tague and Grant, 2009; Godsey et al., 2014), potential climate change impacts to streams include early-season drying (Datry et al., 2014; Jaeger et al., 2014; Tennant et al., 2015), lower base flows, and increased groundwater sourcing (Tague and Grant, 2009; Godsey et al., 2014). Stream surface water chemistry patterns will likely reflect and respond to these anticipated changes, but the patterns and processes dominating these responses are complex because of potential feedbacks.

Coincident with changing snowmelt and low-flow patterns, wildfire is also increasing in its frequency and spatial extent in the western US (Abatzoglou and Williams, 2016; Parks et al., 2016), which alters land cover and influences stream chemistry (Hauer and Spencer, 1998; Mast et al., 2016). In particular, fire combusts vegetation and biotic soil components and releases mineral forms of nutrients and ions into soils (Murphy et al., 2006; Rau et al., 2007) that can be transported into streams (Spencer et al., 2003; Mast et al., 2016). Fire impacts to the water budget of a catchment can be substantial, especially in forested systems (Kinoshita and Hogue, 2015; Wine and Cadol, 2016; Atchley et al., 2018). Reduced terrestrial vegetation can lower evapotranspiration (ET) rates (Poon and Kinoshita, 2018), which can increase stream flow (Kinoshita and Hogue, 2015; Costigan et al., 2016; Wine and Cadol, 2016; Atchley et al., 2018), increase sediment yields (Subiza and Brand, 2018; Vega et al., 2020), and decrease terrestrial carbon inputs (Bixby et al., 2015; Cooper et al., 2015). Moreover, fire opens up the stream canopy increasing radiation, temperature, and wind (Naiman and Sedell, 1980; Poole and Berman, 2001; Bixby et al., 2015), which can increase evaporation (Poole and Berman, 2001; Maheu et al., 2014) and in-stream primary production (Davis et al., 2013; Rugenski and Minshall, 2014; Cooper et al., 2015). To date, most studies have focused on forested watersheds with less attention paid to seasonally snow-dominated mountain areas where sagebrush steppe vegetation often predominates. In these ecosystems, fire regimes are shifting with the spread of invasive *Bromus tectorum* (cheatgrass; Bradley, 2009; Bradley et al., 2016) and increasing fire frequency and fuel availability (Link et al., 2006; Abatzoglou and Kolden, 2011). The few studies conducted in these ecosystems have rapid recovery of ET losses due to increased grass and herbaceous cover with only marginal and short-term effects on streamflow (Flerchinger et al., 2016; Fellows et al., 2018). Because stream drying and fire are accelerating, there is a critical need to understand how both phenomena will affect spatiotemporal patterns of stream surface water chemistry in these contexts.

Natural drivers of stream drying and stream chemistry patterns include increases in surface water evaporation (Brooks and Lemon, 2007; Gallo et al., 2012) or ET losses (Poon and Kinoshita, 2018; Warix, 2020) and/or changes in subsurface connectivity (Brooks et al., 2015; Costigan et al., 2016); fire may have consequences for these processes as well (Kinoshita and Hogue, 2015; Wine and Cadol, 2016; Atchley et al., 2018; Poon and Kinoshita, 2018). For example, increased in-stream evaporation may cause evapoconcentration, or an increased concentration of solutes as the amount of water decreases as found in hot desert streams at low flows (Brooks and Lemon, 2007; Gallo et al., 2012). Under low-flow conditions, evapoconcentration may occur in patches of open canopy stream that experience particularly high radiation, and contribute to overall patchiness in stream solute patterns. Fire may promote

[1] http://nhd.usgs.gov/index.html

such processes by opening stream canopies (Cooper et al., 2015), which can increase evaporative processes in streams by increasing radiation and wind (Maheu et al., 2014) or increase streamflow by reducing evapotranspiration (Kinoshita and Hogue, 2015; Costigan et al., 2016; Wine and Cadol, 2016; Atchley et al., 2018; Poon and Kinoshita, 2018). Alternatively, patchiness may arise from subsurface processes like changing patterns of hillslope connectivity and water residence times that influence groundwater inputs of water and solutes (Zimmer and McGlynn, 2017; Dohman, 2019; van Meerveld et al., 2019). Dynamic dissolved organic carbon (DOC) patterns in streams have been linked to springtime upland snowmelt and lateral flushing in alpine catchments of the Rocky Mountains (Boyer et al., 1997). However, the flushing process in the headwaters at Reynolds Creek Critical Zone Observatory (RC CZO) located in southwest Idaho was found to be slightly more complex (Radke et al., 2019) than Boyer et al.'s (1997) lateral flushing paradigm. At RC CZO, geophysical and hydrochemical evidence pointed to vertical and then lateral springtime flushing. The prior year's soil-water and DOC flushed vertically to the saprolite during snowmelt and then laterally along this interface to the stream. DOC in the stream was primarily allochthonous, presumably sourced from DOC that had accumulated in the soil matrix during the dry summer rather than from in-stream processes (Radke et al., 2019).

As streams dry, connectivity to hillslope carbon sources may shift and in-stream primary production may also be patchy. The resulting stream chemistry reflects the relative magnitudes of these processes and whether these changes occur synchronously or not. Both autochthonous (in-stream) and allochthonous (terrestrially produced) sources of carbon may shift as hydrologic and biologic inputs change seasonally, with stream size, or following fire (Minshall et al., 1989; Cooper et al., 2015). For example, high DOC concentrations can result from autochthonous carbon production during low flows in desert streams in Arizona (Jones et al., 1996; Brooks and Lemon, 2007). Similarly, in warm, humid systems in Tennessee, low flows and open canopy in autumn are associated with high DOC concentrations driven by increased autochthonous processing (Mulholland and Hill, 1997). Immediately following fire, stream algal blooms can result from elevated nutrient levels and open canopy that increase sunlight while also reducing the amount of available allochthonous carbon (Cooper et al., 2015). The chemical signatures of the organic carbon in the dissolved organic matter (DOM) can characterize organic carbon as autochthonous or allochthonous in origin. Fluorescence Index (FI) is a metric of spectral properties of fulvic acids component of DOM and absorbance coefficient ($a_{254}[m^{-1}]$) is a metric of carbon aromaticity; both tools help to evaluate autochthonous or allochthonous sourcing (McKnight et al., 2001; Brooks and Lemon, 2007; Inamdar et al., 2012). The connectivity of streams to the terrestrial surroundings may impact the variability of DOM sourcing. We expect that smaller headwater catchments may be more hydrologically connected to proximal terrestrial carbon (Hornberger et al., 1994; Brooks et al., 1999) and thus, more impacted by terrestrial processes (Creed et al., 2015). However, hillslope connections may also vary more in low-flow conditions and across the seasonal streamflow recession following snowmelt.

In this exploratory study, we measured spatial patterns of biogeochemistry in two mountainous, intermittent headwater streams as they dried. We sampled along the length of each stream, hereafter referred to as the longitudinal sampling or patterns. Sampling occurred following snowmelt through mid-summer in both streams: one unburned stream and one recently burned stream. We used a spatially continuous sampling approach over 2.5 km repeated over 3 months during the growing season to assess changes in solute sourcing patterns and processes. We asked three questions: (1) How does surface stream chemistry vary longitudinally and temporally in intermittent streams as they begin to dry? (2) What are potential driving processes that can explain these patterns? and (3) How do these patterns and processes change following fire? We hypothesized stream chemistry would vary spatially downstream as a function of different physical and biological processes, that spatial patterns would shift temporally as a function of seasonal drying, and that these shifts would be more pronounced following fire. Specifically, we hypothesized that carbon concentrations would increase owing to in-stream evapoconcentration, groundwater connectivity, and in-stream primary production (**Table 1**). On the other hand, we hypothesized that nutrient concentrations would decrease owing to increased uptake with drying, with higher nitrogen losses following fire in the burned stream owing to an open canopy and high nitrogen availability (**Table 1**). To test our hypotheses, we performed an initial cluster analysis to evaluate similarity and dissimilarity amongst chemical properties including solute concentrations, water isotopes, and spectral indices. We then evaluated spatial and temporal patterns and tested hypotheses about associated processes using a combination of these properties that emerged as relevant to our questions.

METHODS

Experimental Design

Study Site

Our study took place at the Reynolds Creek Experimental Watershed (RCEW) and RC CZO, a 239 km^2 watershed located southwest of Boise, ID, USA. The USDA Agricultural Research Service (ARS) established RCEW in 1960 as an experimental watershed representative of the Intermountain West region in the United States (Marks et al., 2011), and the ARS has monitored long-term precipitation and stream discharge trends (Seyfried et al., 2000, 2018). The RCEW extends over a steep climatic gradient with mean annual precipitation varying from 250 to 1,100 mm/yr and mean annual temperatures from 5.5 to 11°C. This climatic variability is driven by the nearly 1,000 m elevation range. At lower elevations, rain is the dominant form of precipitation in the RCEW whereas snow is dominant at the highest elevations (Nayak et al., 2010; Kormos et al., 2014). Peak stream discharges across the watershed are driven by snowmelt patterns (Pierson et al., 2001). Vegetation includes Wyoming sagebrush steppe in the lower elevations, transitioning to mountain big sagebrush (*Artemisia tridentata*), antelope bitterbrush (*Purshia tridentata*), rabbitbrush (*Chrysothamnus viscidiflorus*), western juniper (*Juniperus occidentalis*), aspen (*Populus tremulodes*) and coniferous forest [mostly Douglas fir

TABLE 1 | Outlines the study framework and aims (left two columns under "Study aims" in bold outline), expectations, and rationale for stated expectations.

Study aims			**Expectations as streams dry (April to June) for unburned and burned streams**	**Rationale**
Patterns observed	Spatial		Analytes will group into those that behave more conservatively and those that behave more reactively. Distinct longitudinal patterns will be observed, and these will differ between groups of analytes. *Approach:* solute concentrations, isotope, and spectral indices collected at high-spatial scope (50-m intervals over 2,500 m). Initial cluster analysis.	Source/sink dynamics will become more pronounced due to less surface water connectivity and increased local in-stream production and/or unique chemical signature of deeper groundwater sources with distinct flow path chemistry; this will be greater following fire when nutrients are high and uptake/biological production can be highly heterogeneous in the stream.
	Temporal		Changes in the longitudinal spatial patterns and increases in conservative concentrations; decreases in bio-reactive solutes with greater shifts in burned stream. *Approach:* repeated solute concentration measurements across 3 months (April, May, and June) as stream shifts from snowmelt to low flow. Initial cluster analysis.	Higher conservative solutes concentrations during lower water flow due to decreased snowmelt and increased groundwater sourcing. Lower observed bio-reactive solute concentrations due to in-stream biotic uptake.
Processes and mechanisms tested	Physical hydrological	Evaporation, evapoconcentration, dilution	Temporal shifts with heavier stable water isotopes later in the season and increased evidence of in-stream evapoconcentration, greater shifts in burned stream. *Analyses:* stable water isotopes slopes, source/sink chloride dynamics.	As ambient air temperature increases, evaporative processes will increase including evapoconcentration, especially in burned stream where an open canopy offers no sun or wind protection.
		Groundwater influence	Increases in cation concentrations, shifts toward groundwater sourcing in water isotope intercept. *Analyses:* stable water isotopes and conservative solutes end members.	As snow melt diminishes, water will shift from shallow subsurface water to deeper groundwater.
	Biological	Autochthonous or allochthonous carbon sourcing	Shifts toward autochthonous sourcing, greater shifts in burned stream. *Analyses:* FI and abs coefficient a_{245}[m^{-1}].	As growing season progresses and water velocity flows, nutrients will be more labile and in-stream production will contribute.

The approach and method employed to observe patterns and test processes are described under each expectation.

(*Pseudotsuga menziesii*)], at higher elevations (Seyfried et al., 2018). The site is underlain by Cretaceous granites and volcanic rocks such as the Miocene Salmon Creek Volcanics (McIntyre, 1972).

To evaluate spatial and temporal variation in stream chemistry, we studied two headwater streams within the RCEW known to be intermittent, Johnston Draw (basin area 1.83 km^2) and Murphy Creek (basin area 1.32 km^2; Seyfried et al., 2000; Pierson et al., 2001; Patton et al., 2018). Johnston Draw was ideal for this study owing to the availability of streamflow data measured at a dropbox v-notch 90° weir (Seyfried et al., 2000; Godsey et al., 2018). We opportunistically studied Murphy Creek to evaluate possible extremes in spatial and temporal variation in stream chemistry following wildfire. Specifically, the Soda Fire burned 68 km^2 of RCEW in August 2015, including Murphy Creek (Vega et al., 2020). Briefly, the fire was classified as moderate severity in the study area and consumed nearly all above-ground live vegetation resulting in more than 60% bare ground (bare soil, ash, and rock), with high sediment delivery to the stream (Vega et al., 2020). In October 2015, a dropbox v-notch 90° weir with pressure transducer for discharge measurements was re-activated in Murphy Creek. Hereafter we refer to Johnston Draw as "unburned JD" and Murphy Creek as "burned MC."

Unburned JD and burned MC are comparable in basin area, discharge, elevation, mean annual precipitation (MAP), and

aspect (Seyfried et al., 2000; **Table 2**). Annual water yields for 2016 were lower than the long-term average for both watersheds (Glossner, 2019). Though some studies find increased water yield after fire due to loss of vegetation (Atchley et al., 2018), in burned MC, the 2016 water year represented the third lowest streamflow year out of 12 years (1968–1977 and 2016–2017) of RC CZO data (Vega et al., 2020). The major differences between the two catchments are recent fire history and lithology (**Table 2**). The lithology of unburned JD is predominantly granodiorite with minor lithologic discontinuities including a combination of quartz latite and rhyolite flows underlying the high plateau at the top of the catchment, and a small olivine-rich basalt flow that extends into the outflow (McIntyre, 1972). Basalt and Salmon Creek Volcanics, underlies the burned MC. Unburned JD is described in more detail by Godsey et al. (2018) and Patton et al. (2018, 2019) and burned MC is described in more detail in Seyfried et al. (2000), Pierson et al. (2001), and Vega et al. (2020).

TABLE 2 | Characteristics of the unburned JD and burned MC sub-catchments.

	Unburned JD	Burned MC
Drainage area (km^2)	1.8	1.32
Streamflow direction	East with upper ~500 flowing south	East
Mean annual discharge (Q, m^3/s)	0.007	0.007
Weir type	Dropbox v-notch 90°	Dropbox v-notch 90°
Elevation (m)	1,490–1,850	1,383–1,822
MAP (mm/year)	550	500–600
Lithology	Granodiorite	Salmon Creek Volcanics and basalt
2015 Fire	No	Yes
Primary vegetation	Mountain big sagebrush, juniper, alder, aspen, bunch grasses	(pre fire) Mountain big sagebrush, antelope bitterbrush, rabbitbrush, bunch grasses

Sampling Design

To investigate spatiotemporal chemistry patterns in unburned JD and burned MC, we used a high-spatial scope approach: temporally repeated high-spatial density measurements at the km extent. In April, May, and June 2016, we sampled each stream at 50 m intervals (the grain of our study) over ~2,500 m distance (the extent of our study; **Figure 1**). Each 50 m site is referred to as a reach site (blue dots in **Figure 1**) and the reach sites span over ~2,500 m distance, the extent, which we refer to as the stream segment (**Figure 1**). In each stream segment, sampling started at the weir and continued to the uppermost observed surface flows (**Figure 1**) to include the entire sub-catchment. We refer to the suite of 50 m reach sites collectively as the stream longitudinal profile, and the spatial patterns identified using these sites as

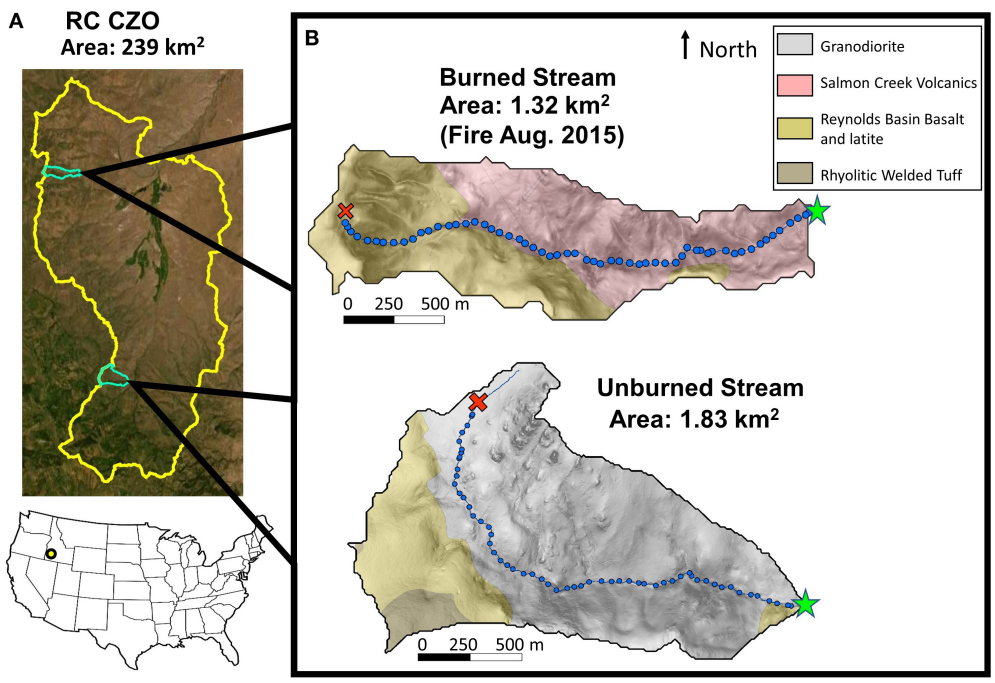

FIGURE 1 | (A) Reynolds Creek Critical Zone Observatory (RC CZO) in southwestern, Idaho, USA (yellow dot). Outlined in turquoise are two headwater sub-catchments, unburned JD and burned MC, which are nested within the RC CZO, the perimeter of which is outlined in yellow. **(B)** Shows the study scope with the unburned JD (lower) and burned MC (upper) longitudinal sampling grain of 50 m interval, or stream reach sites (blue circles), spanning ~2,500 m extent. Longitudinal sampling sites start at a weir (green star) and extend to the uppermost reach with observed surface flow in each stream (red "x"), as identified in the field in April 2016. Colors indicate lithology based on McIntyre (1972).

longitudinal patterns. Water samples were collected in pools at the stream thalweg following Dent and Grimm (1999).

Biogeochemical Characterization of Intermittent Streams

Physical and Chemical Field Properties

We characterized each stream reach site by measuring a suite of *in situ* properties including temperature (°C), pH, dissolved oxygen (DO mg/L), and estimated canopy cover. Water temperature (°C) and pH were measured at each stream reach site using an Oakton pH 110 Series probe (Vernon Hills, IL) calibrated with 4, 7, and 10 pH standard solutions; DO was similarly measured at each reach site with a YSI dissolved oxygen probe (Burlington, VT). Canopy cover was visually estimated in July at half of the stream sites using upward-oriented fisheye lens photos at pool height. Maximum canopy coverage was estimated at alternating sites from photos taken during full leaf-out. Canopy coverage was categorized based on the proportion of the photo covered by foliage (0–25, 25–50, 50–75, and 75–100%). Discharge (m^3/s) was calculated from continuous stage measurements using a stage-discharge rating curve only at the outlet weir of each stream segment (**Figure 1B**). We acknowledge that direct measures of discharge and associated water balance at stream reach site would have augmented our understanding of stream dynamics and local water balance, but this was beyond this study. Accurately measuring discharge throughout a stream network at low flows is methodologically challenging and time-consuming. Instead, we focus here on concentration patterns and use indirect and environmental tracer approaches described below to understand inputs to and outputs from each reach site.

Surface Water Collection

To establish biogeochemical patterns in each stream, we collected surface water samples in the field and then filtered and analyzed them in the lab for the concentrations of a suite of chemical constituents. In the field, samples were collected in 250 mL amber high-density polyethylene bottles (HDPE) bottles, which had been rinsed three times and pre-leached in 18.2 MOhm distilled (DI) water. Bottles were then rinsed three times in the field with the stream sample and then filled to eliminate headspace. Samples were transported by backpack out of the steep terrain (∼35–60 total per stream per sample period), and the water samples were kept refrigerated (4°C) until filtered and analyzed. For carbon and total nitrogen (TN) analysis, water samples were filtered within 72 h (typically within 24 h) in the lab using vacuum filtration through pre-combusted 0.7 μm Whatman glass fiber filters (GFF) into DI- and sample-rinsed 60 ml amber HDPE bottles. Amber HDPE bottles were used instead of glass owing to transport hazards (Sanderman et al., 2009). The remaining sample was syringe-filtered through a 0.45 μm Puradisc nylon filter into four 60 ml clear HDPE bottles for analysis of nutrients, anions, cations, isotopes, and fluorescence index. Samples were collected moving from downstream to upstream to minimize disturbance.

Laboratory Analysis

Stream chemistry was analyzed for a suite of chemical constituents, including dissolved inorganic carbon (DIC), DOC, TN, nutrients including ammonium-N, nitrate (NO_3^--N), orthophosphate (PO_4^{3-}-P), anions including chloride (Cl^-) and sulfate (SO_4^{2-}), and cation concentrations including base cations and rare earth elements such as strontium (Sr). In addition, we analyzed stream water for stable water isotopes ($\delta^{18}O$ and δ^2H), fluorescence index (FI), and absorbance coefficient (a_{254} [m^{-1}]. FI and a_{254} methods are discussed in the DOC sourcing section. DIC, DOC and TN concentrations were measured on a Shimadzu TOC-V CSH (Columbia, MA, USA) equipped with an ASI-V autosampler and TNM-1 chemiluminescence detector for TN. Errors <2–3% were accepted for concentrations >1 mg C/L. High DIC concentrations (∼10–30 mg DIC/L as C) resulted in difficulty using the non-purgeable organic carbon method (NPOC). Thus, we calculated DOC as the difference between TC and DIC and propagated the errors associated with this calculation (∼0.3–0.9 mg/L). Cross validation of our DOC values with the Perdrial Environmental Biogeochemistry Lab at the University of Vermont (Burlington, VT) showed reasonable agreement ($n = 140$, $r = 0.65$). Owing to the higher error associated with DOC by difference, we approached DOC concentrations with some caution but retained them because DOC and spectral characteristics showed similarly variable patterns, and DOC provided an interesting contrast to other nutrients and DIC. Nutrients were measured on a Westco Discrete Analyzer (Unity Scientific, Brookfield, CT, USA), an automated chemical spectrophotometer. We accepted a <10% error for NO_3^- -N and PO_4^{3-} -P concentrations <1 mg/L and a 20% error for NH_4^+ -N <0.10 mg/L. For most of the analyses, we utilize TN because both NO_3^- and NH_4^+ were below detection limit, with the exception of early season samples and those from burned MC. Anions Cl^- and SO_4^{2-} were analyzed on a Dionex ion chromatograph (ICS-5000, Sunnyvale, CA, USA) with AS18 column 4 X 250 mm, and we accepted <10% error for sample <1 mg/L and 2–3% for samples > 1 mg/L. Cations were measured by the Center for Archaeology, Materials and Applied Spectroscopy (CAMAS) lab (Idaho State University, Pocatello, ID) on a Thermo X-II 283 series Inductively Coupled Plasma Mass Spectrometer (ICP-MS) equipped with a Cetac 240-position 284 liquid autosampler (ThermoFisher Scientific). Dilutions were 1:10 sample to de-ionized water. Some cations were below the detection limit of 10 ppb. We reliably measured Sr, Ba, Na, Mg, Al, Si, K, Ca, Sc, Ti, Fe, and Zn for all 3 months. Lastly, stable water isotope samples were analyzed at ISU/CAMAS Stable Isotope Laboratory on a Thermo Scientific, High Temperature Conversion Elemental Analyzer (TC-EA) interfaced to a Delta V Advantage mass spectrometer. Precision for both $\delta^{18}O$ and δ^2H was better than ± 0.2‰ and ± 2.00‰ respectively.

Lastly, autochthonous and allochthonous DOC sourcing was investigated by analyzing the spectral characteristics of DOM in the lab, specifically Fluorescence Index (FI) and absorbance. Completed by the Perdrial Environmental Biogeochemistry Lab at the University of Vermont (Burlington, VT), these characteristics were measured using the Aqualog Fluorescence

and Absorbance Spectrometer (Horiba, Irvine, CA, USA). The excitation (EX) wavelength range spanned from 250 to 600 nm (increment 3 nm) and emission (EM) ranged from 212 to 619 nm (increment 3.34 nm). All excitation emission matrices (EEMs) were blank-subtracted (nanopure water, resistivity 18 MΩ cm^{-1}), corrected for inner filter effects, and Raman-normalized (Ohno, 2002; Miller et al., 2010). All samples were diluted to absorbance values below 0.3 and we computed relevant indices, including the FI (calculated as the intensity at Emission 470 nm divided by the intensity at Emission 520 nm for Excitation at 370 nm (Cory and McKnight, 2005). Absorbance (a) at 254 nm can also be used as a direct measure of aromaticity of DOM. We report the absorption coefficient (a_{254} [m^{-1}]) which is calculated independently of DOC concentrations and using Equation 1 (Green and Blough, 1994; Inamdar et al., 2012) below:

$$a_{254}[\mathrm{m}^{-1}] = (\text{UV absorbance at 254 nm}) \times 2.303 \times 100. \quad (1)$$

Even though specific UV absorbance ($SUVA_{254}$) is the most commonly used indicator for DOM aromaticity (Weishaar et al., 2003), we refrained from its use due to the high error in DOC measurements and report a_{254} [m^{-1}] instead.

Spatiotemporal Pattern Analyses

Initial Clustering of Water Properties and Biogeochemistry

To assess possible common synchronous or asynchronous drivers of biogeochemistry, we initially identified chemical variables within each stream that were strongly and weakly related over time using cluster analysis. We explored highly correlated groupings among chemical variables described above using cluster variable analysis for each month in order to understand a given variable's relationship with other variables over time. The loaded variables were the chemical properties and analyte concentrations measured in the field and lab including temperature, pH, DO, carbon (DIC and DOC), anions (Cl^-), nutrients (TN and PO_4^{3-}), all cations measurable across the 3 months (Sr, Ba, Na, Mg, Al, Si, K, Ca, Sc, Ti, Fe, and Zn), and stable water isotopes ($\delta^{18}O$ and δ^2H). The cluster variable analyses were conducted in JMP (version 14.2) which first grouped variables into cluster components determined by first and second principal components and then ranked variables within cluster components based on the strength determined by a cluster algorithm (SAS Institute Inc., 2017). This algorithm iteratively clusters variables based on a combination of strength of the principal component and relative eigenvalue strength. The order in which the analytes and chemical properties are reported within each cluster is based on the highest Pearson correlation coefficient (r) within the cluster. The results of these analyses informed our choice of analytes used for longitudinal pattern reporting and testing our specific process hypotheses. We chose analytes that juxtapose each other by selecting both highly ranked variables within clusters of strongly temporally correlated variables as well as analytes that were not strongly clustered. We did this in order to represent a spectrum of more conservative solutes such as Cl^- to more biological reactive ones such as TN in each stream. The above criteria supported reporting longitudinal patterns for DIC, Cl^-, Sr, DOC, TN, and PO_4^{3-}. However, we assessed temporal patterns from April to June in all chemical properties and solutes as well.

Longitudinal Spatial Patterns and Temporal Tendencies

To explore the biogeochemical patterns both along the length of the stream and monthly changes as the stream dried, we plotted the longitudinal patterns of all solutes for each month, but focused on those identified above in the cluster analysis: DIC, Cl^-, Sr, DOC, TN, and PO_4^{3-}. These analytes also represent more conservative analytes and more reactive analytes as defined by Baker and Webster (2017). Stream data collected longitudinally from non-perennial streams presented challenges. First, samples collected 50 m apart in a stream are not statistically independent, second as streams dried April to June, it was impossible to sample in some locations and stream sample sizes changed, and third underlying longitudinal patterns complicated typical methods of quantifying spatial heterogeneity (details in statistical challenges of stream drying discussion section). Overall temporal comparisons of chemical properties, solutes, and cations from high to low flow were analyzed using mean differences and propagated errors from April to June within each stream. We determined differences to be substantial when they were larger than errors. As detailed above (**Table 1**), we expected to observe longitudinal and temporal similarities in both streams from April to June and predicted higher concentrations of carbon with evapoconcentration, lower concentrations of nutrients as in-stream primary production seasonally increased, and increasing cation concentrations as both streams became increasingly groundwater-dominated. However, we expected differences between the two streams like higher TN due to fire and higher cation loss due to volcanic lithology in burned MC.

Explaining Patterns: Testing Hypothesized Processes

Evaporative Processes

The potential evaporative signature of stream water was assessed by plotting stable water isotopes $\delta^{18}O$ and δ^2H against the Global Meteoric Water Line (GMWL) as well as the Local Meteoric Water Line (LWML; $\delta^2H = 7.1(\delta^{18}O)$-6.3), with data derived by Tappa et al. (2016). We compared monthly $\delta^{18}O$ and δ^2H data within each stream to the LMWL and calculated the monthly best-fit slopes based on simple linear regression and the LMWL-intercepts. To test for statistical differences between months and streams, we ran *t*-tests on the slopes of the regressed isotopic relationships. We hypothesized that the streams would undergo evaporation with drying in this semi-arid system (Fritz and Clark, 1997), and thus, that streams' isotopic data would fall below the LMWL (Gat, 1996). In addition, we predicted both streams would exhibit an increasingly evaporative signature as the streams dried, with a stronger shift in burned MC.

We evaluated the role of in-stream evapoconcentration in explaining chemistry patterns associated with stream drying by comparing the behavior of $\delta^{18}O$ to Cl^- between upstream and downstream sites. We calculated predicted downstream

values of Cl^- concentration ($[Cl_D^-]$) based on ratios of $\delta^{18}O$ from upstream (subscript "U" in Equation 2) and downstream (subscript "D") samples and the observed upstream Cl^- ($[Cl_U^-]$) values (Mulholland and Hill, 1997; Gallo et al., 2012):

$$[Cl_D^-] = \frac{[Cl_U^-][\delta 18O_D]}{[\delta\ 18O_U]} \quad (2)$$

Because both $\delta^{18}O$ and Cl^- are expected to be conservative tracers (Baker and Webster, 2017), Equation 2 should lead to accurate predictions of Cl^- and each downstream site unless evapoconcentration or flushing were dominant processes. Therefore, we compared the predicted $[Cl_D^-]$ and observed Cl^- concentrations for each downstream site. If evapoconcentration were driving patterns in the water samples, we would expect to observe differences in the predicted vs. observed Cl^- concentrations. To explain any differences, we would need to parse out the role of flushing vs. evapoconcentration (Gallo et al., 2012).

Groundwater Influence

We used water isotopes and the Sr/DIC ratio to evaluate the potential influence of groundwater as streams dried. First, we calculated unburned JD's and burned MC's isotopic intercepts with the LMWL (Tappa et al., 2016) using each monthly regression (Fritz and Clark, 1997) and evaluated temporal shifts. We then compared the stream's LMWL-intercepts to the mean rain, snow, and groundwater samples collected by Radke et al. (2019) in a nearby but higher elevation watershed within RC CZO (Reynolds Mountain East ∼2,100 m elevation). In this way, isotopic means of rain (δ^2H −66.5 ± 12.7 and $\delta^{18}O$ −8.4 ± 2.4, mean ± SE), snow (δ^2H −129 ± 10.2 and $\delta^{18}O$ −16.8 ± 1.3, mean ± SE) and groundwater samples (δ^2H −121 ± 1.04 and $\delta^{18}O$ −16.4 ± 0.18, mean ± SE) were assumed to be reasonable endmembers for our sites as well. As the streams dried, we expected the stream-LMWL intercepts to shift toward the groundwater signature later in the season if groundwater made up a larger component of the streams' surface water.

We also plotted Sr against DIC for each month because a previous study showed Sr to be a good indicator of groundwater at the RC CZO (Radke et al., 2019). We calculated RC CZO groundwater and precipitation (rain and snow) averages from samples collected by Radke et al. (2019) in late summer (August 2017), and used these values as endmembers in our analysis. Sr averaged 142.74 ± 8.77 ppb (mean ± SE) and DIC averaged 21.20 ± 0.55 mg C/L (mean ± SE). Rain and snow water samples had average values of 1.37 ± 1.63 ppb (mean ± SE) and 1.54 ± 1.80 mg C/L (mean ± SE) for Sr and DIC, respectively (Radke et al., 2019). We compared the upstream/downstream Sr-DIC relationship by comparing the uppermost 1,000 m sites with those in the lowest 1,000 m. We expected to observe a shift toward the groundwater ratio reflected in the late summer Sr/DIC ratios in unburned JD and burned MC that would be consistent with the shift in isotopic signatures.

Autochthonous or Allochthonous DOC Sourcing

Allochthonous carbon can be spectrally distinguished from autochthonous due to the structural carbon components in terrestrial vegetation, like lignin, which are also more aromatic. FI and a_{254} [m^{-1}] measure these spectral components and help classify carbon sources as allochthonous or autochthonous (McKnight et al., 2001; Inamdar et al., 2012). We compared FI to published ranges of these values associated with more autochthonous or allochthonous sources (Inamdar et al., 2012). Based on these values, we interpreted FI values between 1.2 and 1.5 as reflecting an allochthonous signature whereas FI above 1.7 reflects an autochthonous/microbial signature (McKnight et al., 2001). Furthermore, we report the variability using coefficient of variation (CV) because FI had no underlying longitudinal patterns in either stream (see discussion section, "Statistical Challenges of Stream Drying Data"). However, in our calculations, we controlled for sample size in each stream by including only those sites that had water flowing all 3 months so as not to bias any one month.

Aromatic and humic DOM is a product of terrestrial vegetation so that a higher aromatic a_{254} signature reflects a more allochthonous DOM with structural carbon. Thus, the relationship between FI and a_{254} is inverted, such that lower a_{254} result from less aromatic DOM, more autochthonous/microbial derived carbon and higher a_{254} result from more aromatic, more allochthonous derived carbon (Inamdar et al., 2012). Due to increased in-stream primary production as both streams dried, we expected to observe FI to increase reflecting shifts from more allochthonous to autochthonous carbon, and a_{254} to decrease reflecting diminished aromatic properties with a more pronounced shift in burned MC.

RESULTS

Biogeochemical Characterization of Intermittent Streams

Stream Hydrologic Conditions

Seasonal drying in both intermittent headwater streams was similar, with weir discharges (Q) decreasing in April, May, and June 2016 (**Figure 2A**). Drying occurred in both streams between April and June. For unburned JD, all of the April sampling sites (n = 57) had surface flow, 89% persisted in May (n = 51), and only 65% sustained surface flows in June (n = 37). Drying occurred in reaches interspersed throughout the unburned JD stream. Similarly, all of the reach sites in burned MC were flowing in April (n = 59), but only 73% in May (n = 43), and 64% sustained flow in June (n = 38). Unlike in unburned JD, drying in burned MC occurred from the top of the stream to the bottom as though the entire stream contracted longitudinally (though subsequent work showed this pattern did not persist later in the summer; Warix, 2020). Thus, by June, 35% of unburned JD's and 36% of burned MC's reach sites had dried, with the highest proportion of sites drying from May to June in unburned JD stream and from April to May in burned MC stream. Over the sample period, unburned JD stream discharge exhibited a slightly greater relative change (April Q ∼ 0.022 m^3/s to June Q < 0.005

m^3/s) than burned MC (April Q ∼0.017 m^3/s to June Q ∼0.005 m^3/s; **Figure 2A**). Burned MC also exhibited flashier stream flow as spikes in discharge, presumably responding to event-based precipitation or snowmelt inputs (**Figure 2A**) that did not occur as strongly in unburned JD.

Physical and Chemical Field Properties

The streams were similar in physical and chemical properties measured in the field but as expected, canopy cover differed between the unburned stream and burned stream. Stream temperature showed strong longitudinal and increasing temporal shifts in both streams, whereas pH and DO were more variable longitudinally and temporally (**Figures 2B–G** and **Supplementary Table 1**). The two streams differed in canopy cover in that 44% of unburned JD had >25% canopy cover during full leaf-out whereas 100% of sites sampled in burned MC had <25% canopy cover, and most sites fell very close to 0% canopy cover even in July 2016 (**Figures 2B,C**). Although some burned MC sites had >0% canopy cover in July, the post-fire vegetation differed from the vegetation in the unburned JD. The riparian vegetation of burned MC in July was dominated by fast-growing, non-woody shrubs and small, young willows because all vegetation, namely sagebrush and bunch grasses were charred to the ground (Vega et al., 2020). This contrasted with the overhanging riparian alder, willow, and juniper in unburned JD.

Biogeochemical Pattern Analysis

Initial Clustering of Water Properties and Biogeochemistry

Correlations between stream analytes varied between streams and these relationships changed as each stream dried. We identified groups of solutes that behaved similarly or dissimilarly for each stream at different moments in the season. For example, in unburned JD, we observed positive correlations between Sr, Mg, Ca, K, Na, Ba, Fe, DOC, temperature (Temp), DIC, $\delta^{18}O$, TN, Cl^-, Sc, and Si in April. Ti, Al, DO, pH, PO_4^{3-}, and Zn were negatively correlated with these analytes and chemical properties, but positively correlated with each other (**Figure 3A**). By June, Mg, Fe, Cl^-, K, Temp, TN, $\delta^{18}O$, Sc, and Si were positively correlated with each other, but shifted to being negatively correlated with other analytes or chemical properties. From April to June, shifts from negatively to positively correlated analytes were observed between Ti, DO, pH, and PO_4^{3-} and other analytes or properties in unburned JD (**Figure 3E**). We observed similar (though not identical) patterns within burned MC (**Figures 3B,D,F**). Strongly correlated (either positively or negatively) analytes were placed into clusters for each month and stream (**Supplementary Table 2**). Based on these results, we selected representative analytes to illustrate different clusters and behaviors for the longitudinal analysis, including DIC, DOC, TN, PO_4^{3-}, Sr and Cl^-.

Longitudinal Spatial Patterns

Common longitudinal patterns were evident in both unburned JD and burned MC streams (**Figure 4**) for many of the more conservative analytes (e.g., DIC, Sr, and Cl^-) than the biologically reactive ones (e.g., DOC, TN, and PO_4^{3-}). As expected, mean concentrations generally increased for DIC, Sr, and Cl^- downstream (**Figures 4A–F**). The exception to this pattern were consistently high concentrations at the top of unburned JD (relative to downstream concentrations) at reach sites that were south-facing and meadow-like. Concentrations of more reactive analytes, DOC, TN, and PO_4^{3-}, tended to decrease downstream in unburned JD whereas DOC and PO_4^{3-} were relatively invariant longitudinally in the burned MC stream. TN was exceptional in that it varied in the uppermost portions of both streams with patterns that changed each month of the sampling campaign.

Temporal Shifts

As expected, mean differences in concentrations between April and June showed that TN concentrations substantially decreased over the growing season in each stream, and by an order of magnitude in burned MC (**Figure 5B**). Mean TN concentration decreased by >80% from April to June (**Figure 5B**) in burned MC stream (1.14 ± 0.03 to 0.19 ± 0.02 mg N/L, mean ± SE); TN was composed mostly of NO_3^-; even in April, NH_4^+ was largely below our instrument detection limit. We observed a similar but less pronounced decrease in TN in unburned JD (**Figure 5A**), where a 39% decrease occurred over the same months (0.36 ± 0.04 to 0.22 ± 0.03 mg N/L, mean ± SE). Unlike TN, PO_4^{3-} decreased only slightly in the burned MC stream over the growing season and did not exhibit a measurable change in unburned JD (**Figures 5A,B** and **Supplementary Table 3**). In contrast to our expectations, DOC exhibited no clear temporal shift from April to June in unburned JD and slightly decreased in burned MC (**Figure 5**).

In both streams, we observed similar temporal patterns in the average differences from April to June for base cations and other solutes (**Figures 5C,D**). Like DIC and Cl^-, most cations increased from April to June in both streams as indicated by negative difference values between April and June mean concentrations (**Figures 5C,D**). However, in unburned JD, some cation concentrations decreased as indicated by positive difference values as was the case for Si, Fe, and Ba. As expected, burned MC exhibited three to ten times larger cation differences than unburned JD for several cations including Na, Mg, Si, K, and Ca (**Figures 5C,D** and **Supplementary Table 4**).

Explaining Patterns: Testing Hypothesized Processes

Evaporative Processes

Isotopic signatures for both streams showed that evaporation was occurring, which we expected. However, counter to our predictions, we did not find evidence of temporal shifts toward increasing evaporation with stream drying in either stream. The regression slopes of the $\delta^{18}O$-δ^2H relationships for all months for both unburned JD and burned MC fell below the GMWL and LMWL (Tappa et al., 2016), indicating an evaporative signature in these two streams compared to local precipitation (**Figures 6A,B**). In the unburned JD, we observed a lower-sloped evaporative trend with drying as April's slope (± SE) was 2.7 ± 0.16, May's was 3.6 ± 0.27, and June's slope 4.7 ± 0.30 (**Table 3**). All months within unburned JD were statistically different so that April differed from May ($t = -5.2$, $p = < 0.0001$, df = 103), May differed from June ($t = -4.4$, $p = 3.7E\text{-}05$, df = 81), and

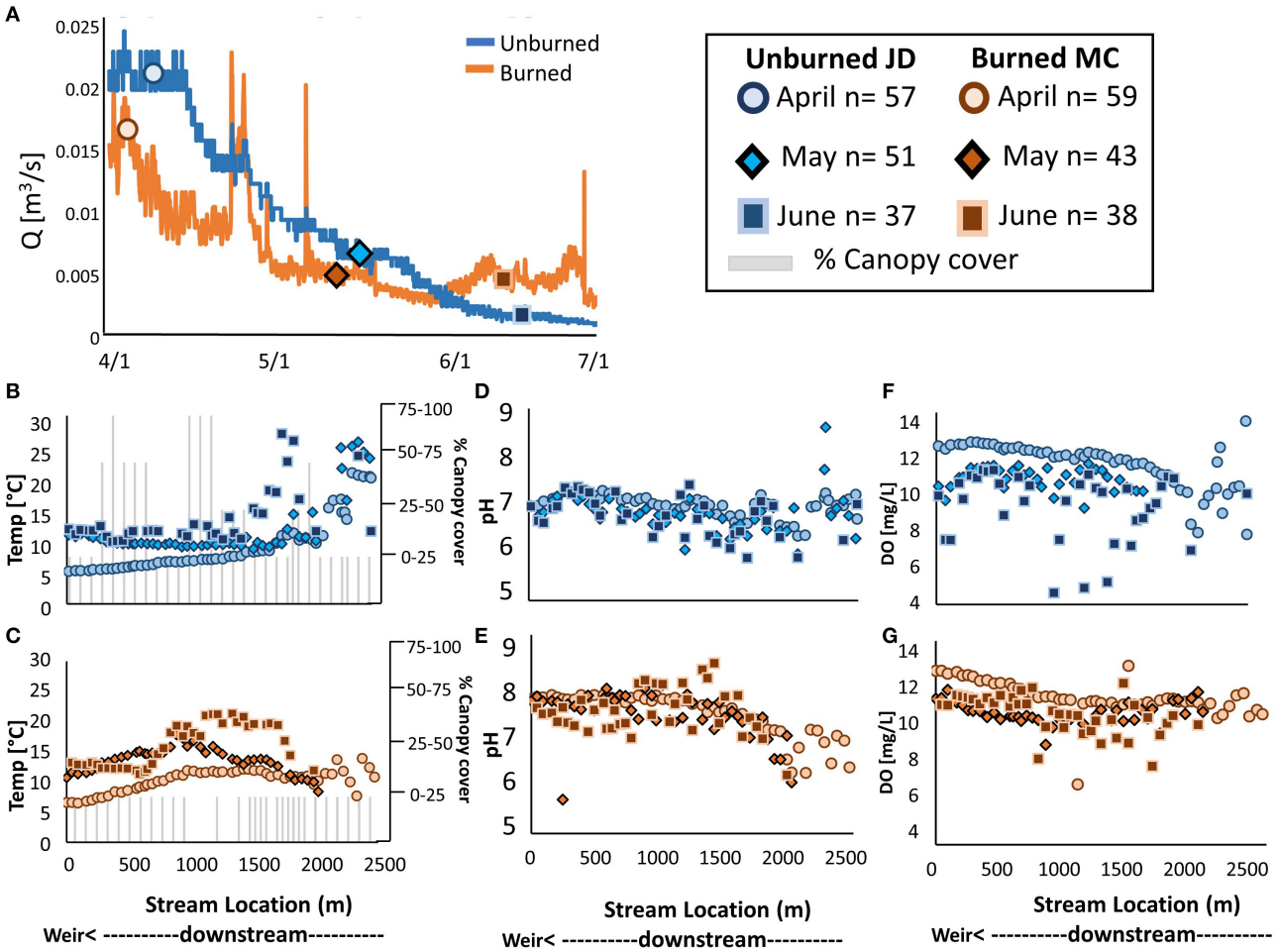

FIGURE 2 | 2016 discharge **(A)** of the unburned JD (blue) and burned MC (orange) measured at the weir (most downstream sample point); symbols reflect the discharge on the sample dates. Longitudinal patterns of **(B,C)** temperature (°C) and estimated canopy cover (% cover in gray bars) **(D,E)**, pH (-log [H+]), and **(F,G)** dissolved oxygen (DO mg/L).

April from June ($t = -14.14$, $p = < 0.0001$, df = 84). In the burned MC stream, April's slope (± SE) was 4.3 ± 0.30, May's was 3.0 ± 0.26, and June's was 4.5 ± 0.23 (**Table 3**). In contrast to unburned JD, burned MC slopes for April and June did not statistically differ from each other ($t = -0.51$, $p = 0.61$, df = 91), although both differed from May ($t = -2.6$, $p = 0.01$, df = 95 and $t = -5.1$, $p = < 0.0001$, df = 76, respectively), which had the most evaporative signature over the study period. Between the two streams, slopes were only significantly different from each other in April ($t = -10.24$, $p = < 0.0001$, df = 108) and not in May ($t = 1.0$, $p = 0.32$, df = 89) or June ($t = 0.6$, $p = 0.56$, df = 70). We generally did not observe longitudinal patterns of evaporation (**Figures 6A,B**), with the exception of the uppermost portion of unburned JD. There, the aspect and vegetative cover of the stream was distinct from downstream reaches: these south-facing meadow sites had a strong evaporative signature in April (**Figure 6A**) and had dried by May.

In-stream Evapoconcetration or Dilution Influences on Solute Concentrations

To investigate potential effects of evaporation or dilution on the concentration of solutes as streams dried, we evaluated source-sink dynamics of chloride compared to $\delta^{18}O$. In both streams, most measured Cl^- fell within the error of the predicted Cl^- based on $\delta^{18}O$, indicating the two analytes behaved conservatively, with no major new gains or losses of water. Given this finding, we did not further investigate spatial or temporal deviations due to either evapoconcentration or dilution (**Figures 6C,D**). Although we hypothesized that in-stream evapoconcentration would be a driver of increased analyte concentrations, we found few sites in either stream that showed concentrations outside of the $\delta^{18}O$-based prediction intervals. Additionally, counter to our predictions, we observed no differences between streams despite their difference in canopy cover.

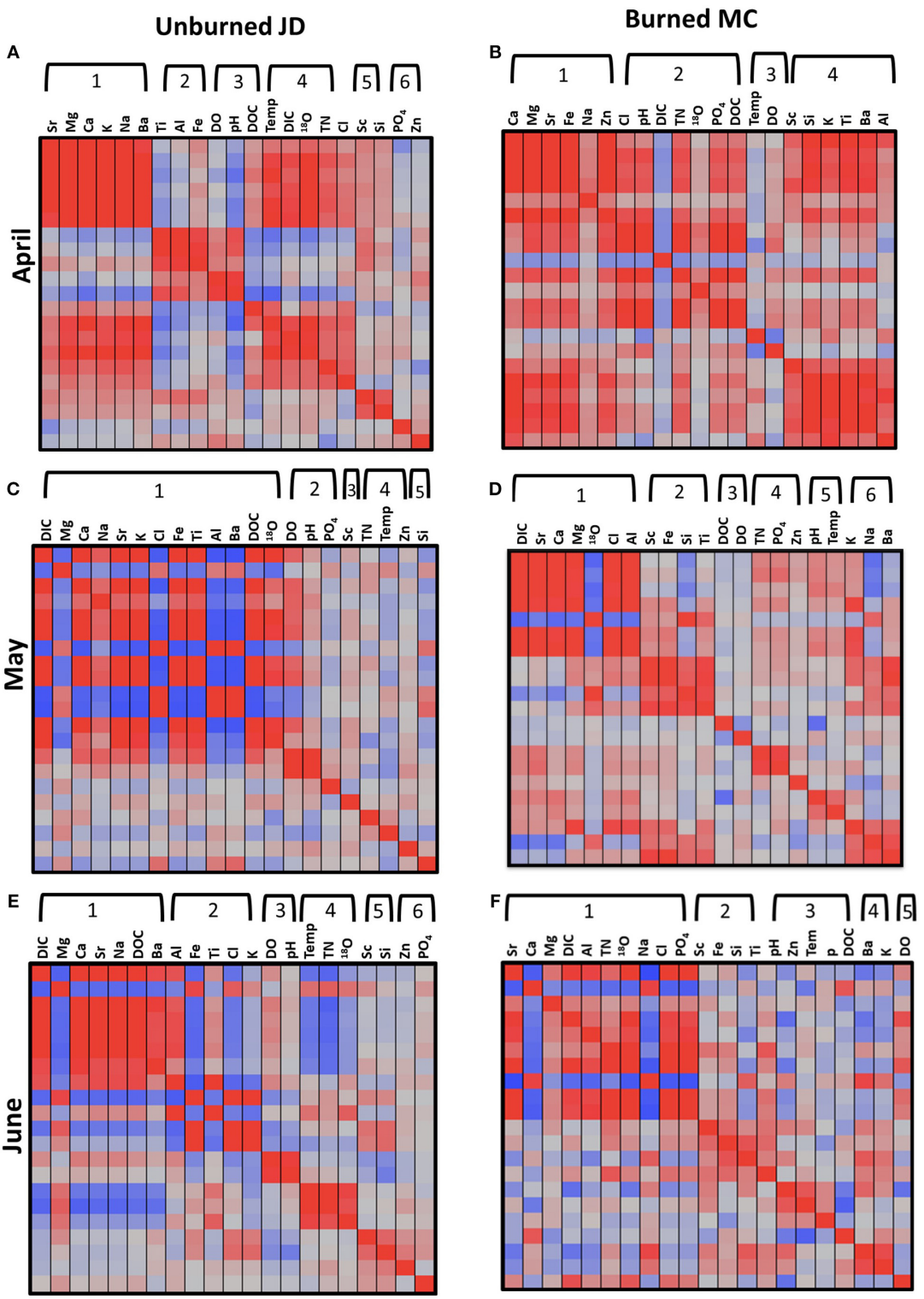

FIGURE 3 | Cluster analysis shows correlations between analytes by rows for April **(A,B)**, May **(C,D)**, and June **(E,F)** for unburned JD (left column) and burned MC (right column). Analytes include: temperature, or Temp (°C), DO (mg/L), pH, DIC (mg C/L), Cl^- (mg Cl/L), DOC (mg C/L), TN (mg N/L), PO_4^{3-} (mg P/L), $\delta^{18}O$, and cations (ppb): Sr, Ba, Na, Mg, Al, Si, K, Ca, Sc, Ti, Fe, and Zn. Analytes are labeled across the top of each x-axis and are listed in the same order along the y-axis in each panel. Analyte order is based on cluster analysis groupings where analytes within each cluster are more strongly correlated (higher Pearson correlation coefficient or *r*-value) to each other than to other groups of analytes. The *r*-values are colored by saturation where the higher the *r*-value, the more saturated the color, and gray represents a low *r*-value and low correlation. Red indicates positive correlations and blue negative correlations.

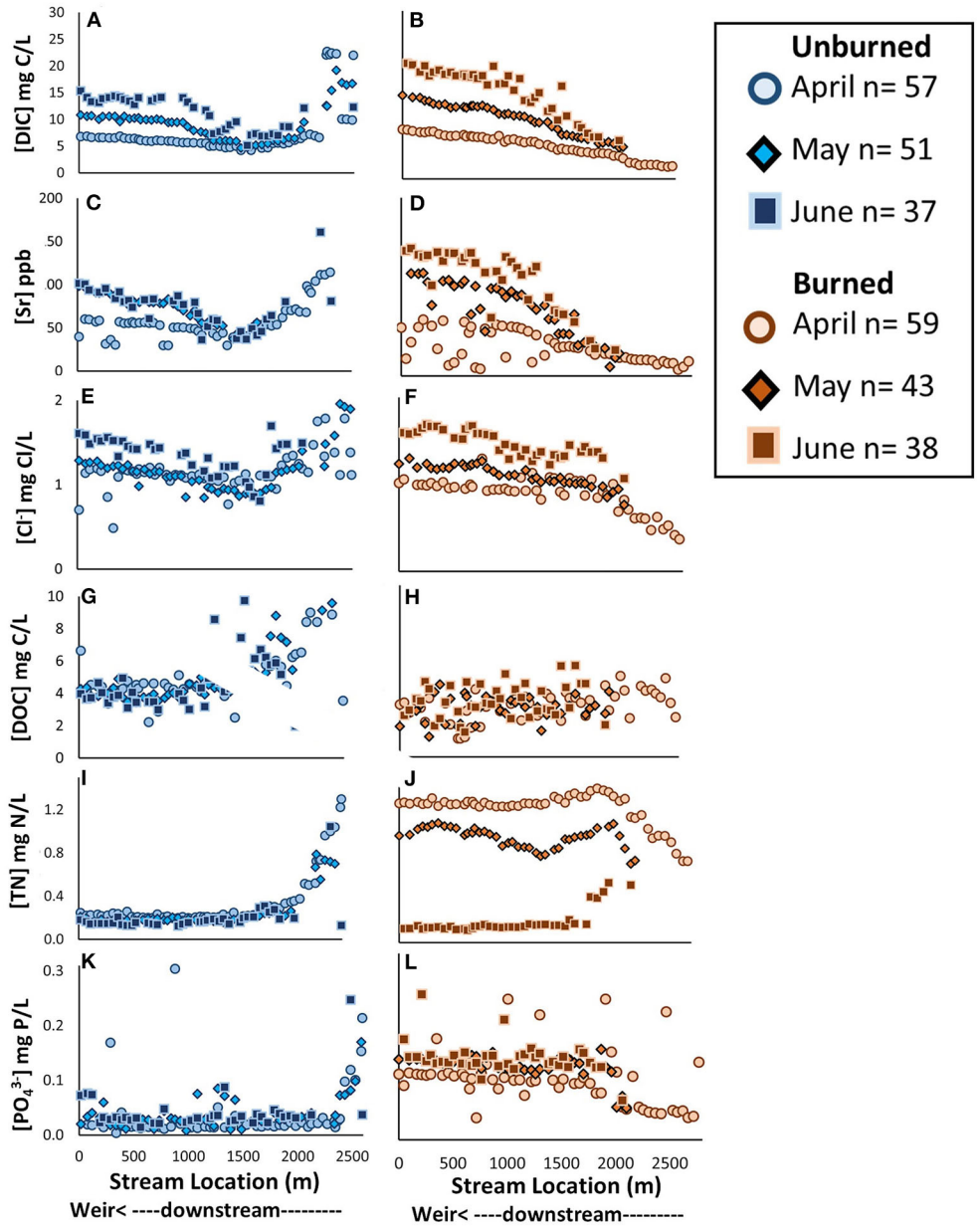

FIGURE 4 | Longitudinal patterns of **(A,B)** dissolved inorganic carbon (DIC mg C/L) **(C,D)**, strontium (Sr ppb) **(E,F)**, chloride (Cl^- mg Cl/L) **(G,H)**, dissolved organic carbon (DOC mg C/L) **(I,J)**, total nitrogen (TN mg N/L) **(K,L)**, phosphate (PO_4^{3-} mg P/L) for unburned JD (blue, left column) and burned MC (orange, right column) streams. Values from April are represented by circles, May sites are diamonds, and June sites are squares along the length of the stream where 0 m is the weir and ~2,500 m is the upper stream reach.

Groundwater Influence

The isotopic signature of both streams showed surface water sources to be mixed contributions of snowmelt and rain: each stream's isotope values fell between the snow and rain mean values reported by Radke et al. (2019; **Figures 6A,B**). Based on intercepts, water in both streams had dominant contributions from snow/groundwater; snow sources for unburned JD reflected a larger rain contribution as indicated by isotopic-intercepts with the LMWL (~−111 δ^2H per mil) whereas the LMWL-intercept for burned MC stream (~−120 δ^2H per mil) reflected a larger snow and/or groundwater contribution (**Figures 6A,B**). Because the groundwater and snow isotopic signatures were similar, we could not distinguish between the two sources with isotopic tracers. Counter to our expectations, no clear temporal shifts in water sources emerged in the isotope data in either stream (**Table 3**).

However, temporal shifts in groundwater-precipitation mixing were apparent by pairing the isotopic patterns with

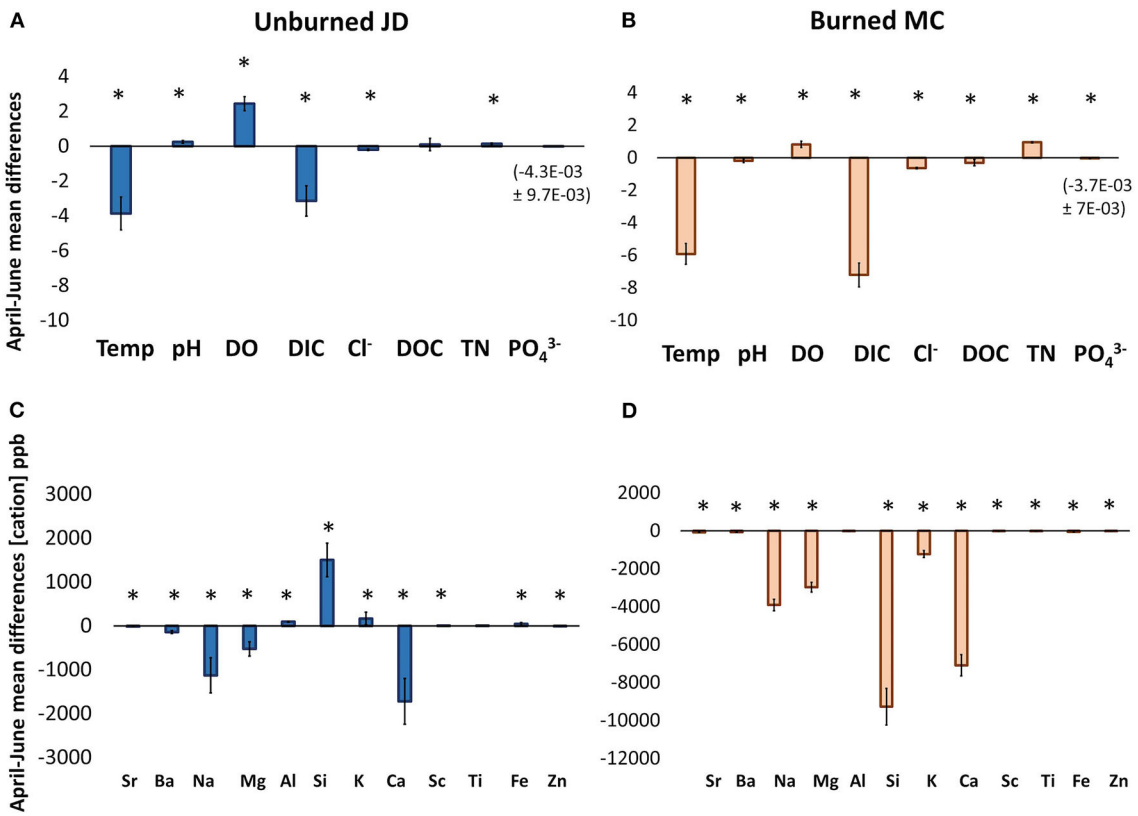

FIGURE 5 | Mean solute differences from April to June are shown for **(A)** unburned JD and **(B)** burned MC for temperature, or Temp, (°C), pH (-log [H+]), DO (mg/L), DIC (mg C/L), DOC (mg C/L), TN (mg N/L), PO_4^{3-}(mg P/L), Cl^-(mg Cl/L), DOC (mg C/L), TN (mg N/L), PO_4^{3-}(mg P/L). Mean cation differences (ppb) from April to June are shown for unburned JD **(C)** and burned MC **(D)**. Error bars show propagated error and asterisks indicate where differences are greater than the propagated error. Positive differences indicate decreasing in concentration from April to June and negative differences indicate increasing concentration from April to June (arrows for reference). Note pH measures are representative of log scale, so small changes are not equivalent to raw concentrations of other solutes. Additionally, please note the difference in axes scales between panel **(C,D)**.

observed shifts in DIC and other analyte concentrations. For example, we observed that DIC and Sr were strongly correlated (**Figure 3**). When compared to the average precipitation (rain and snow) and late summer groundwater Sr/DIC endmembers, stream water was sourced from precipitation in April and shifted toward groundwater sourcing in June in each stream (**Figures 6E,F**). In contrast to isotopes of water, rain and snow precipitation had similar DIC and Sr signatures and these signatures were substantially different from groundwater DIC and Sr signatures (Radke et al., 2019). We likely did not capture an additional endmember in unburned JD in the upper portion of the catchment (**Figure 6E**) whereas most of the variation in the burned MC was captured by two endmembers, potentially with exception of a few downstream sites (**Figure 6F**). The uppermost reach sites (>2,000 m) of each stream (flowing in April and May) had different signatures; the signatures from the upstream reaches in unburned JD fell close to groundwater and burned MC upstream reach sites fell close to a precipitation signature (**Figures 6E,F** and **Supplementary Figure 1**).

Organic Carbon Sourcing: Autochthonous and Allochthonous Processes

DOM sources and spectral characteristics varied along the profile of each stream during each month; FI varied by similar amounts in both streams whereas a_{254} [m^{-1}] varied more in unburned JD (**Figure 7**). Many FI values fell between the 1.5 allochthonous derived threshold and the 1.7 autochthonous/microbially derived threshold (**Figures 7A,B**), indicating mixed carbon sources in both streams. Unburned JD had a slight but surprising longitudinal FI pattern in April (mean 1.59 ± 0.01 SE) when we observed a more autochthonous/microbial FI signature downstream, while the upper reach of the stream had a more allochthonous signature (**Figure 7A**, circles). May generally had an allochthonous signature (mean 1.49 ± 0.003 SE) as did June (mean 1.50 ± 0.007 SE), and this similarity between seasons was counter to our predictions. Interestingly, while May and June mean FI values were similar, June exhibited greater variation (CV 2.8) than May (CV 1.2), with points spanning the thresholds between autochthonous and allochthonous sources in both months (**Supplementary Table 5**).

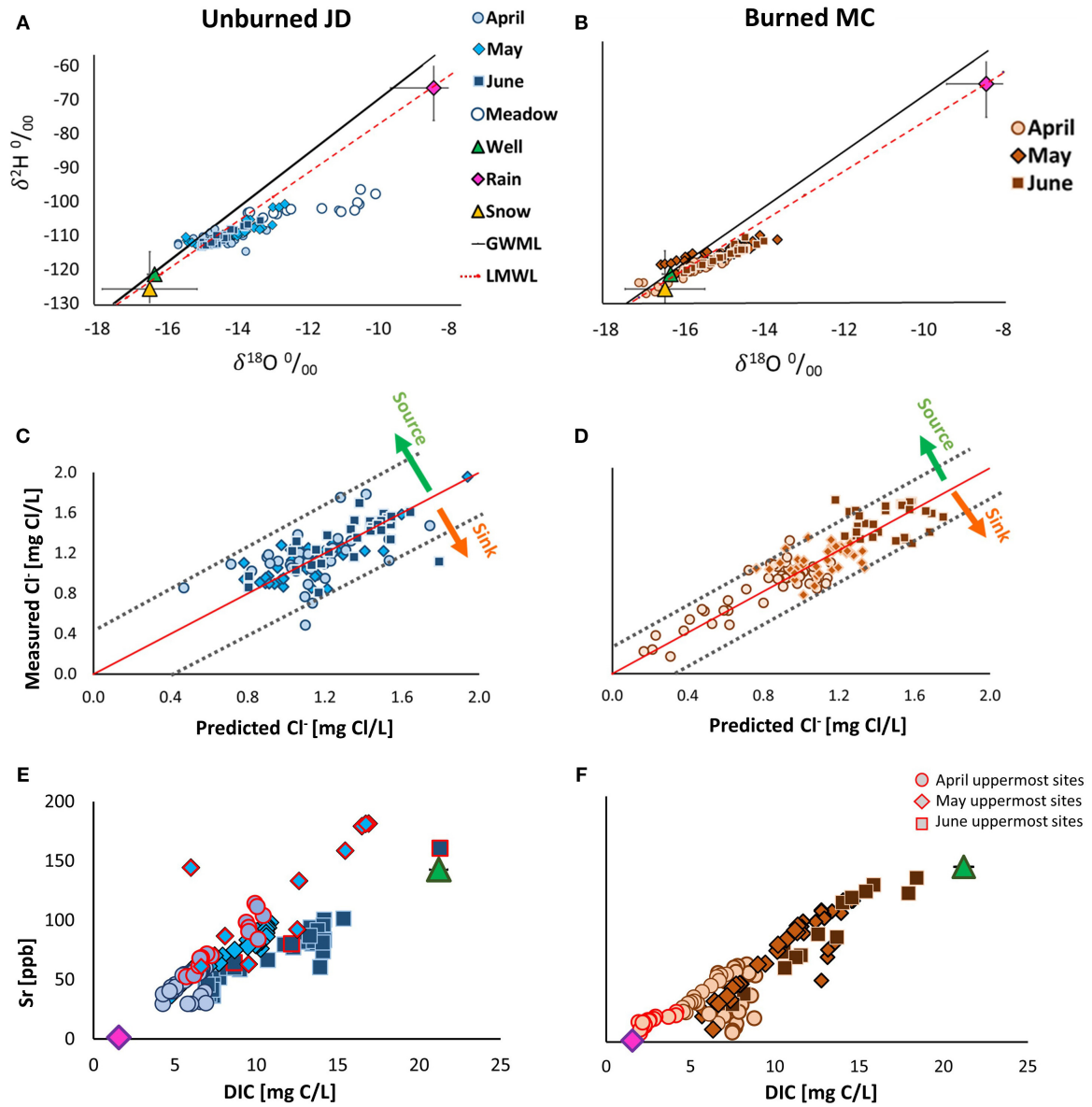

FIGURE 6 | Stable water isotopes ($\delta^{18}O$ and $\delta^{2}H$) for sites in both unburned JD **(A)** and burned MC **(B)** in April (light circles), May (mid-tone diamonds), and June (dark squares). The global meteoric water line (GMWL) is shown in solid black and the local meteoric water line (LMWL) is the dashed red line ($\delta^{2}H = 7.1(\delta^{18}O)$-6.3; Tappa et al., 2016). Mean rain (pink diamond), mean snow (yellow triangle), and mean well values (green triangle) samples were collected by Radke et al. (2019) at a higher elevation site in Reynolds Creek watershed. Measured vs. predicted Cl^{-} concentrations calculated using $\delta^{18}O$ upstream and downstream site ratios for the unburned JD **(C)** and the burned MC **(D)**. Red solid line represents identical measured and predicted concentrations and the dashed gray lines enclose the prediction interval. Cl^{-} values above the red line indicate Cl^{-} concentrations greater than expected (potential source) and Cl^{-} concentration below the red line indicate Cl^{-}-values that are less than expected (potential sink). Sr and DIC relationships for the unburned JD **(E)** and the burned MC **(F)**. Mean precipitation (both snow and rain) and mean groundwater endmembers from Radke et al. (2019) are represented by pink diamonds and green triangles, respectively. Gray bars on endmembers show the SE. Uppermost reach sites (>2,000 m) of each stream are outlined in red for each month water was present.

In burned MC (**Figure 7B**), we observed a mixed autochthonous and allochthonous FI signature in April (mean 1.55 ± 0.005 SE), and a similar but more varied FI signature in May (mean 1.50 ± 0.009 SE). June's FI varied along the stream profile with an overall downstream increase toward autochthonous/microbial signature (mean 1.62 ± 0.02 SE). This tendency matched our expectations of increasing in-stream productivity, which we expected would be more pronounced in the burned stream. In addition, burned MC's higher mid-summer FI variation was reflected in the relatively high June FI CV (7.5) compared to that of April (1.0) and May (3.5; **Supplementary Table 5**). Despite the overall autochthonous tendency in June, there were also sites for which the FI value fell below or close to the allochthonous threshold

(1.5, **Figure 7B**, squares). We did not expect to observe this high variation.

We expected that as streams dried, DOC aromaticity (high in terrestrially derived carbon) would be decreasing due to increased in-stream productivity, especially in burned MC, and thus, we expected decreases in a_{254} values. Overall, unburned JD had higher a_{254} values that were more longitudinally and seasonally variable than burned MC (**Figures 7C,D** and **Supplementary Table 5**). We expected higher overall aromaticity in unburned JD. Though we expected to see higher FI values coupled with low a_{254} values, we did not observe these relationships consistently. In April, unburned JD had higher a_{254} values (mean 44.5 ± 1.4 SE) coupled with higher FI values (**Figure 7E**). The unburned JD maintained higher a_{254} values in May (mean 48.1 ± 3.0 SE) and dropped in June (mean 38.5 ± 2.9 SE); this decrease in aromaticity suggests less terrestrial carbon and followed our expectations. Compared to unburned JD, burned MC a_{254} values shifted less from April (mean 26.2 ± 0.48 SE) to May (mean 27.2 ± 0.54 SE) and June (mean 29.1 ± 0.53 SE, **Figure 7D**). The differences in a_{254} temporal patterns between the streams were illustrated by the relationship of FI and a_{254} (**Figures 7E,F**) where the spread of FI values was greater in the burned MC, but the spread of a_{254} was greater in the unburned JD. We hypothesized that increased in-stream productivity would result in shifts of increased FI and decreased a_{254} values. However, the spatial patterns we observed in both streams were more longitudinally varied and had less clear seasonal shifts than expected.

TABLE 3 | The slope ± standard error and the LWML-intercept extracted from the data presented in **Figures 6A,B**.

Isotope analyses		Slope	± SE	LMWL intercept (per-mil)
Unburned JD	April	2.7	0.16	−111.47
	May	3.6	0.27	−111.09
	June	4.7	0.30	−114.04
Burned MC	April	4.3	0.30	−122.36
	May	3.0	0.26	−117.04
	June	4.5	0.23	−121.73

DISCUSSION

Stream intermittency and fire regimes are changing in the Intermountain West and cold montane shrubland ecosystems that characterize the northern Rocky Mountains and Great Basin are especially vulnerable to these changes. We hypothesized stream chemistry patterns would change seasonally and longitudinally in response to both drying and fire, and that process shifts would explain these biogeochemical patterns. Specifically, we hypothesized that with drying, in-stream evaporative processes, increased groundwater influence, and shifts in DOC sourcing from allochthonous to autochthonous would contribute to differences in these longitudinal stream chemistry patterns. In a recently burned watershed, we expected the impacts of these processes would be amplified.

Stream Drying: Non-linear Spatiotemporal Biogeochemical Patterns

Both streams exhibited non-linear longitudinal patterns in chemistry that changed with stream drying. Spatially variable and distinct patterns among analytes were revealed by this study's high-scope sampling approach and breadth of measured chemical constituents. For instance, we identified potential springs/deeper groundwater inputs where temperature or solute concentrations remained stable despite seasonal shifts at other locations longitudinally along the streams (e.g., around ∼1,500 m in unburned JD and ∼ 2,000 m in burned MC). In contrast to our expectations, we found similar longitudinal patterns and processes driving these patterns in both streams. This provides some evidence for emerging regional behavior in the subsurface processes (i.e., groundwater contributions) driving stream chemistry. Our findings collectively point to the power of high-scope sampling to capture both the temporal and spatial variability in intermittent stream processes, and they contribute empirical data on how spatiotemporal patterns and processes may change with stream drying in headwater streams like these.

Streams Similarities: DIC Dominance With Drying

Given the differences in fire history and lithology, the similarity of chemistry patterns and shifting processes between these two streams was surprising. In both unburned JD and burned MC, DIC and many cations exhibited clear longitudinal patterns that increased in mean concentration with stream drying. Though we did not directly analyze concentration-discharge relationships longitudinally at each 50 m reach site, chloride source/sink dynamics did not suggest strong spatial inputs or outputs in any month. Monthly increases in DIC and other conservative solute concentrations were consistent with dilution behavior of concentration-discharge observed over the water year at the weir of each stream (Glossner, 2019). While conservative solutes in larger streams often display chemostatic behavior (Godsey et al., 2009), our data is consistent with chemodynamic concentration-discharge relationships documented in smaller catchments (Hunsaker and Johnon, 2017) and intermittent streams (Bernal et al., 2019). Instead of evapoconcentration or dilution, our findings point to deeper groundwater sources driving increased concentrations as the streams dried. Our findings are consistent work by Wlostowski et al. (2020), whose findings describe loamy and sand-rich soils and relatively shallow bedrock in unburned JD resulting in more baseflow-dominated streamflow with less subsurface water storage compared to CZOs with clay-rich soils. Distinct from other baseflow dominated streams, groundwater contributed to low flow in our streams, not high flow as observed in the Jemez River Basin Critical Zone observatory in New Mexico (McIntosh et al., 2017). Our results build off of those reported by Radke et al. (2019) at a higher elevation RC CZO catchment during snowmelt, where deeper flow paths rather than shallow subsurface flow

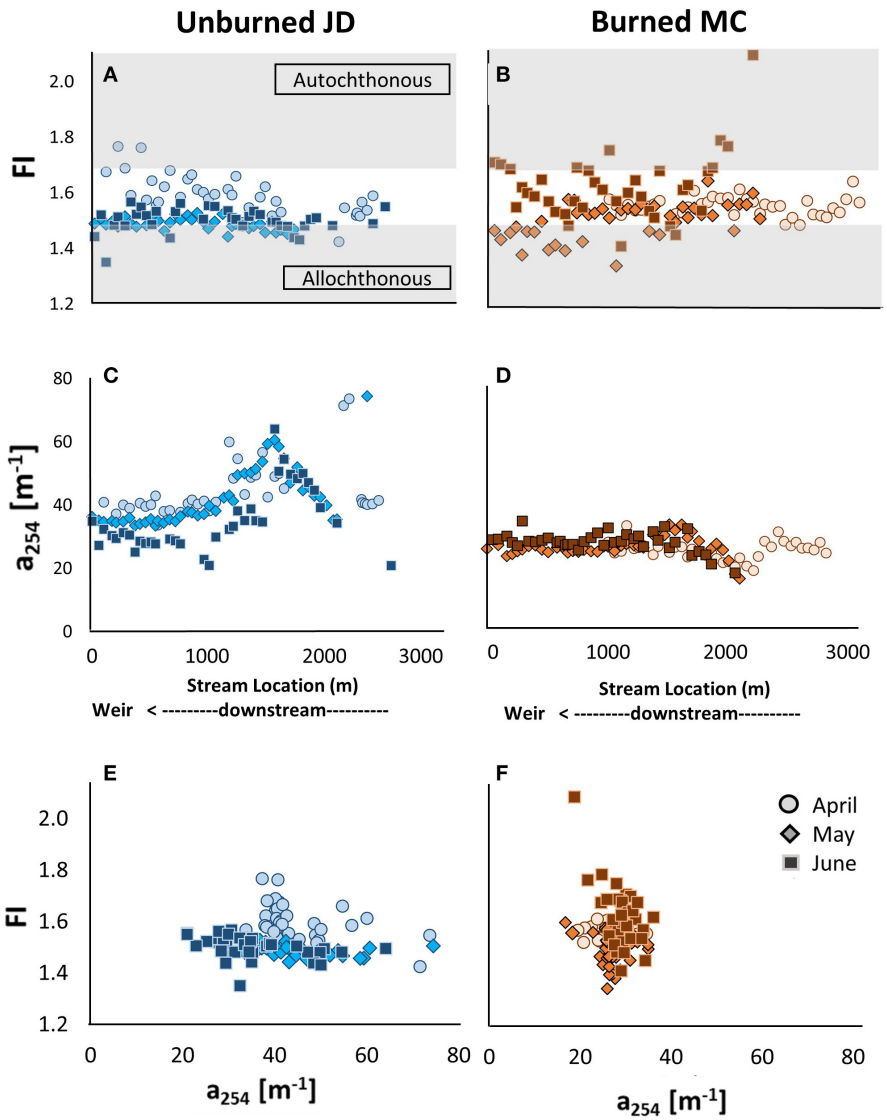

FIGURE 7 | (A,B) Fluorescence index (FI) **(C,D)**, absorbance coefficient (a_{254} [m^{-1}]), and **(E,F)** the relationship of FI to a_{254} for stream profile of unburned JD (blue, left) and burned MC (orange, right); shape, shade, and color of months are described in **Figure 2**. Gray shaded boxes **(A,B)** indicate the 1.5-1.2 allochthonous-derived threshold and the 1.7–2.0 autochthonous/microbial-derived threshold.

paths contributed to stream DOC as observed by Boyer et al. (1997). Deeper flow paths also contribute to increasing ion concentration patterns at low flow in Dry Creek Experimental Watershed near Boise, ID (McNamara et al., 2005). Our findings, along with these earlier works suggest a regional occurrence of limited near-surface storage capacity due to loamy soils and the importance of deeper groundwater for stream water.

In contrast to DIC, more biologically reactive solutes TN, DOC, and PO_4^{3-} either decreased or were relatively invariant with stream drying. Mean TN concentrations decreased throughout the growing season, and DOC showed relatively high variability and no clear longitudinal pattern or large seasonal shift in either stream. With respect to TN, we expected temporal decreases because nitrogen is biologically reactive and often subject to uptake, especially during low flows and low concentrations (Moatar et al., 2017). On the other hand, many studies of stream carbon dynamics have found clear seasonal patterns in DOC (Hornberger et al., 1994; Boyer et al., 1997; Mulholland and Hill, 1997; McGuire et al., 2014; Hale and Godsey, 2019). However, we did not observe a strong DOC pattern with drying in either stream. Rather, we found strong temporal shifts in DIC, and DIC concentrations that were 2–3 fold higher than DOC in unburned JD and burned MC. Thus, DIC, rather than DOC, appeared to dominate stream carbon dynamics at our sites.

Non-linear spatial patterns in longitudinal stream chemistry spatial patterns have been observed in other studies that employed high spatial-scope measurements, but few have examined these longitudinal patterns in the context of stream drying or across such a broad suite of biologically reactive and conservative analytes. In one such example, within snowmelt-driven, deciduous forested streams at Hubbard Brook, NH, Likens and Buso (2006) sampled at 100 m intervals over a network and observed non-linear spatial patterns in a wide suite of constituents including DOC, DIC, K, Na, SO_4^{2-}, NO_3^-, Sc, dissolved Si, and Ca (also see McGuire et al., 2014; Zimmer and Lautz, 2014). Similarly, Dent and Grimm (1999) found that NO_3^- -N and soluble reactive phosphorus (SRP or PO_4^{3-}) varied longitudinally in the hot desert at Sycamore Creek, AZ. Moreover, based on 25 m intervals over 10 km of stream, they observed that NO_3^- -N decreased and SRP increased with succession following monsoonal flooding. These findings agree with our observations of decreasing TN concentrations and relatively invariant (unburned JD) or slightly decreasing PO_4^{3-} (burned MC) with drying.

Stream Differences: Lithology and Fire Impacts

We found differences between the two streams we studied in cation concentrations, the proportion of open canopy, and magnitude of seasonal decrease in TN, organic carbon and water sourcing. Lithological differences likely account for higher cation concentrations in volcanic burned MC compared to granitic unburned JD stream (Meybeck, 1987; Ibarra et al., 2016). It is also likely that fire impacts increased cation concentrations through ash and sediment inputs and/or mineralization of these inputs, especially during snow melt. At the watershed scale, sediment losses were high during winter and snowmelt in the year following fire, a low flow year, and sustained in 2017 (>450 compared to 20 g m^{-2} yr^{-1} mean sediment yield in Johnston). Sediment losses were low during the drying summer months (<5% of annual sediment yield) indicating low contributions of particulates during this study period (Glossner, 2019); mineralization of these ash-derived products warrants further study.

Elevated nitrogen levels in April and May in burned MC decreased by >80% in June. These TN results supported our hypothesis that nitrogen levels would be elevated immediately following wildfire but that decreases in TN would be observed as burned MC dried due to potentially increased nutrient uptake. Other studies such as Murphy et al. (2006) and Rau et al. (2007) have documented that there is often a lag in nitrate uptake following fire due to the time required to re-establish uptake by denitrifying bacteria populations and vegetation. In some cases, high nitrogen levels have been documented in streams for years following fire (Hauer and Spencer, 1998; Mast et al., 2016), potentially related to low DOC from terrestrial carbon losses (Rodríguez-Cardona et al., 2020). However, TN levels in burned MC decreased relatively quickly to concentrations similar to those of unburned JD by June. Finally, DOM sourcing followed different temporal tendencies in the two streams: burned MC shifted as expected from more allochthonous to autochthonous whereas unburned JD showed more mixed contributions. These findings will be discussed further below in the "Statistical Challenges of Stream Drying Data".

Fire can have a large effect on water budget and cause increases in stream flow as catchment ET diminishes following vegetation losses (Kinoshita and Hogue, 2015; Atchley et al., 2018), but we did not find strong evidence of this influencing stream chemistry drying patterns. This in part may be because burned MC experienced a relatively low water year in 2016 (Glossner, 2019; Vega et al., 2020) and rapid growth of grasses and herbaceous was observed. Rapid fire recovery (within a year) has been observed previously at RC CZO with regards to gross ecosystem production (Fellows et al., 2018) and ET (Flerchinger et al., 2016), with statistically marginal short-term increases to stream flow (Flerchinger et al., 2016). Moreover, ET rates have been shown to be relatively low in sagebrush in RC CZO (Sharma et al., 2020). Isotopic LMWL-intercepts indicated differing water sources between the streams and suggested unburned JD was more rainfed than burned MC, which was fed more by groundwater/snow. Given the vegetation differences, it is possible unburned JD had more shallow subsurface storage of rainwater than burned MC. However, as vegetation regrew in burned MC, there was no clear LMWL-intercept shift from April to June suggesting changes in soil water storage capacity. Alternatively, water source differences may have reflected pre-fire differences and further study would be required to parse this out. As mentioned, we observed stream chemistry responses to fire in some instances like elevated TN, but we did not detect increased stream flow. These observations are consistent with the weak evidence of monthly changes in evapoconcentration or dilution processes and burned MC's lack of shifts in water isotopic water sources or evaporative slopes. In addition to the similarity of stream patterns indicating the importance of deeper subsurface processes on stream chemistry, the similarity may indicate muted effects of fire on stream chemistry in the burned watershed.

Processes Explaining Spatiotemporal Patterns

Our findings highlight the utility of stream chemistry to elucidate both hydrological processes (evaopconcentration or dilution and water sourcing) and the in-stream biological processes (potential autochthonous carbon-sourcing) that contribute to spatiotemporal patterns as streams dry seasonally and following wildfire. A strength of our data was that we were able to evaluate surface-groundwater interactions, which has been identified as a key research priority to understanding intermittent stream controls (Costigan et al., 2016). Our inferences are only made possible by the high spatial scope sampling approach we employed.

Evaluating Hydrological Processes: Shift Toward Groundwater With Drying

By quantifying evaporation and groundwater influence, we could distinguish between chemistry drying patterns driven by surface processes and chemistry drying patterns driven by subsurface hydrologic processes in these streams. Isotopic slopes showed both streams were evaporative; however, we observed no temporal shifts toward increased in-stream evaporation with

drying. Contrary to our expectations and despite differences in canopy cover, both streams showed similar evaporative trends in water isotopes with no statistical difference in slope between the two streams in May or June. Furthermore, we found only weak evidence of in-stream evapoconcentration or dilution on the spatial stream chemistry patterns in either stream during any month. In contrast, Sr-DIC ratios provided strong evidence that stream surface water shifted toward a deeper groundwater signature with drying. These low-flow groundwater contributions differ from the lateral input dominance of snowmelt described by Boyer et al. (1997). The Sr-DIC relationships varied longitudinally and were better captured by precipitation and groundwater endmembers in burned MC than unburned JD. In April, the Sr-DIC signature of the uppermost portion of unburned JD led us to reason that either that these sites are spring-fed or that our sampling missed the shift from precipitation to groundwater sourcing. In general, increased contact time between water and soil/bedrock may explain elevated cation and DIC concentrations in groundwater (Fritz and Clark, 1997; Richter and Billings, 2015; Olshansky et al., 2019), each of which increased with drying in both streams. Although isotope intercepts did not show strong shifts in water sourcing between months as Sr-DIC ratios did, the isotopic signatures of snow and groundwater were indistinguishable. This suggests two potential scenarios. First, as snowmelt recharges deeper groundwater, snowmelt increases its solute concentrations. Alternatively, shallow subsurface evaporation could cause evapoconcentration (Radke et al., 2019). Quantifying subsurface processes such as those that would affect the residence times of water (Brooks et al., 2015), carbon in groundwater, or potential evapoconcentration in soils (Radke et al., 2019) may be important for understanding stream dynamics at RC CZO and warrants further regional study.

Evaluating Biological Processes: Carbon Sourcing Is Longitudinally Variable

Rather than exhibiting distinct seasonal shifts over time, biologically active solutes, such as organic carbon, showed a mixed signature of allochthonous/autochthonous sourcing and composition in both streams each month. We found DOC sourcing (FI) and aromatic properties a_{254} varied in both streams, but burned MC was less aromatic overall (lower a_{254}). Longitudinally, unburned JD had mixed sourcing (FI values) and a wide spanning aromatic signature (a_{254}) even in June, though there was a tendency toward being less aromatic. Although unburned JD FI observations were similar to summer 2017 samples from higher elevation streams at RC CZO (Radke et al., 2019), they were counter to our expectations. Canopy cover in the unburned JD was heterogeneous: leaf out may have decreased sunlight availability to the stream, limiting productivity and contributing more allochthonous material throughout the summer. Burned MC more closely matched our expectations of increased in-stream productivity with a more autochthonous FI in June and an overall less aromatic signature, but FI was nevertheless unexpectedly variable. More in-stream productivity may have been supported by high (∼20-fold more) nitrogen availability in the early season and an open canopy from April to June, combined with the generally reduced vegetation as allochthonous carbon sources post fire. While there were temporal differences between the streams, the high variability that characterized DOM sourcing and spectral characteristics reflected a mixed organic carbon signature in both streams. This may be typical of small-area catchments that are often hydraulically connected to surrounding terrestrial uplands (Creed et al., 2015). Nevertheless, burned MC showed clearer, and potentially less complex patterns of increasing groundwater influence and autochthonous DOC. Though it is unclear how characteristic these patterns may have been before the fire in burned MC, it is possible the fire's reduction of canopy cover and increase of TN may have contributed to more pronounced temporal shifts toward autochthonous DOC.

Study Approach: Pros and Cons

Power of High Spatial-Scope Sampling and Integrated Methodology

Collectively, our findings have contributed to recognizing and understanding stream chemistry patterns that cannot be addressed with traditional sampling approaches that rely on a small number of spatially discrete locations, such as stream outlets (e.g., Fisher and Likens, 1973; Boyer et al., 1997; Mulholland and Hill, 1997; Hood et al., 2006; Jaffe et al., 2008 etc.). For instance, Jaffe et al. (2008) found FI to vary from 1.15 to 1.75 at the landscape to biome scale. We found comparable variation both longitudinally down the 2.5 km stream segments at a 50 m grain and temporally across months we studied. This finding suggests that traditional coarse-grain spatial sampling of DOM sources (1) may not capture heterogeneity of the streams above or below a sampling point and (2) may lead to inappropriate inferences about a given stream network. It is unclear if network convergence would occur downstream in DOM sourcing, as has been observed in DOC concentrations (Asano et al., 2009; Hale and Godsey, 2019), and if so, at what scales (Creed et al., 2015). Our findings provide evidence to support the Creed et al. (2015) hypothesis that DOM sourcing dynamics within a single catchment may be more complex than thought and may have consequences for the chemical composition and quality of organic matter being transported downstream.

Stream chemistry studies have traditionally either focused on hydrological processes (Brooks et al., 2015) or on in-stream biological processes (e.g., Minshall et al., 1989; Dent and Grimm, 1999), and study scope determines at what scale(s) patterns can be detected or processes can be assessed (Schneider, 2001; Fausch et al., 2002). In this observational study, our aim was to explore both hydrological and biological processes that may drive stream chemistry patterns using integrated methodology at a high spatial scope as streams dry. Taking this spatial approach required that we balance trade-offs between distance covered (extent) and sampling interval (spatial grain); we did not study a large stream network, but focused on the headwater stream segment, where we expected to see the most pronounced drying and biogeochemical patterns and variation. Although we also used repeated monthly sampling to investigate temporal patterns, we focused our efforts at the beginning of the drying season with moderate temporal

resolution (monthly) over a limited temporal extent (3 months at the beginning of one drying season).

Due to their small size, headwater streams are highly variable with regards to stream chemistry (Zimmer et al., 2013; Creed et al., 2015; Hunsaker and Johnon, 2017), and thus they are likely to be more susceptible to seasonal and spatial regime shifts such as increased stream intermittency and fire, both promoted by climate change. The particulars of these shifts in headwaters are important to understand in various biomes for study design as well as water quality monitoring (Abbott et al., 2018). Future work might include spatially distributed streamflow measurements to accompany stream chemistry observations because it is possible that the local water balance differs seasonally and longitudinally, affecting in-stream evapoconcentration/dilution dynamics (e.g., Glossner, 2019; Warix, 2020). Lastly, we balanced sampling intensity and number of streams studied. Although our inferences are limited by the fact that we studied only two streams, the similarities between the two suggest some of the patterns we observed may be expected throughout the RC CZO and region. Our analysis of a wide range of chemical constituents at 50 m reach intervals complimented the work of Hale and Godsey (2019) who measured DOC at 200 m intervals at the network scale in southeastern Idaho, USA, showing that additional analytes can improve process interpretation. We suggest that exploratory studies, such as this one, are important to tease apart which processes are effectively uniform throughout a stream reach, and which are likely to be spatially heterogeneous and seasonally dynamic.

Statistical Challenges of Stream Drying Data

Additional challenges existed applying typical statistical approaches used to describe perennial stream chemistry patterns to spatiotemporal drying patterns. It was particularly challenging to describe temporal patterns, compare the longitudinal spatial variation between months as streams dried, and to quantify the spatial patterns of a given month. Much of this difficulty stemmed from the loss of data points as streams dried, impacting the extent and resolution and effectively reducing the sample size each month and leaving few perfect statistical approaches. Some authors have reported maximums and minimums to capture seasonal differences within a network (Likens and Buso, 2006; Brooks and Lemon, 2007; Zimmer et al., 2013), but this limits comparisons between variables, particularly of different magnitudes or different units of measure. Coefficient of variation (CV; calculated by the standard deviation, SD, divided by the mean) is a unitless tool for quantifying variation and is therefore appealing to compare different variables. As streams dry, CV has been used to quantify temporal patterns (Likens and Buso, 2006), spatial patterns at varying scales (Dent et al., 2001), and spatiotemporal stream chemistry patterns (Hale and Godsey, 2019) to compare across varying monthly means and sample sizes. However, CV is sensitive to changes in the mean, as Dent and Grimm (1999) point out, as well as the sample size which makes CV potentially problematic for drying streams. For example, in our data if April and June solute concentrations have the same SD (representing spatial variation) but June has a higher mean, June will have a lower CV. This could reflect the loss of sampling locations rather than changes in spatial variability of the sites that remained wet in June. Dent and Grimm (1999) acknowledged the limitation and emphasized CV only in specific instances.

We also faced difficulties in quantifying spatial patterns in our streams due to underlying, non-linear longitudinal patterns, which changed with stream drying. Brooks and Lemon (2007) addressed this issue by reporting means and SD for an upper, middle, and lower region of the San Pedro River, AZ. To control for differences in the mean, sample size and underlying longitudinal patterns, we calculated CV in instances for which underlying longitudinal patterns did not change with drying, which occurred only for FI. More sophisticated approaches have included constructing semivariograms to quantify spatial patterns (McGuire et al., 2014) and spatiotemporal patterns (Dent and Grimm, 1999). The data from our study required an in-depth approach to detecting and quantifying spatiotemporal patterns which was beyond the scope of this paper, and we more thoroughly addressed quantifying patterns in a separate, forthcoming publication (MacNeille, 2020). Continued development of robust statistical methods and conceptual models that incorporate drying (changes in sample size) is merited. This is a vital step to developing more appropriate approaches and tools to understand patterns and mechanisms of steam drying (Jensen et al., 2019).

CONCLUSIONS

Understanding intermittent stream ecosystem structure and processes requires a shift in stream conceptual models to include stream drying (Allen et al., 2020) and testing controls on drying like surface water-groundwater interactions (Costigan et al., 2016). Exploring patterns using a high-spatial scope approach, biogeochemical data enabled us to test several hypotheses about processes associated with stream drying and following fire. We found headwater streams had distinct chemical patterns that shifted longitudinally with seasonal drying and showed similar patterns despite fire history differences. In this study, an unburned and a burned stream exhibited similar temporal patterns with stream drying and similar shifts in processes. We argue that detecting shifts in the processes that influenced these patterns required measurements at a fine grain over an intermediate extent. DIC dominated carbon dynamics in both streams, with increasing concentrations with drying. We observed similar drying shifts in increasing Sr and Cl^-, relatively invariant DOC, decreasing TN, and relatively invariant PO_4^{3-}. Cations generally increased from April to June with more substantial losses in burned MC potentially due to volcanic bedrock. The most striking difference in temporal patterns between the unburned JD and burned MC was the dramatic loss of TN from April to June in the burned MC. As the streams dried, surface water chemistry patterns could be influenced by surface evaporative processes, dilution, and/or from subsurface

processes with shallow and deep groundwater influence. During stream drying, the snow-fed, semi-arid mountainous catchments we studied were both characterized as evaporative streams, but with weak evidence for in-stream evapoconcentration or dilution as either stream dried. There were not substantial in-stream evaporative differences despite canopy cover differences between unburned JD and burned MC. Instead, stronger evidence for deeper groundwater processes influencing stream chemistry patterns with longitudinal distinctions were observed in these streams, with more clear chemistry shifts with drying in burned MC. The similarities between streams may suggest that subsurface structure mutes the effects of fire and lithology differences at RC CZO. Organic carbon sourcing was mixed and highly longitudinally varied in both streams, but with an overall shift toward autochthonous in burned MC. These findings contribute to understanding streams in the sagebrush steppe by exploring spatiotemporal stream chemistry patterns and processes shifts as stream drying and following wildfire. Such empirical data are critical to the development of more sophisticated stream models, which are especially needed as climate changes across the western U.S.

DATA AVAILABILITY STATEMENT

The datasets presented in this study can be found in online repositories. The names of the repository/repositories and accession number(s) can be found at: http://dx.doi.org/10.18122/td/1332/boisestate/reynoldscreek/16, Boise State ScholarWorks.

AUTHOR CONTRIBUTIONS

RM: contributed to project conception, experimental design, primary researcher conducting sampling, lab analysis, statistical analysis, manuscript writing and editing, and major concepts/framing. KL: contributed to project conception and experimental design, primary supervisor of sampling, lab analysis, statistical analysis, manuscript editing, major concepts/framing, Reynolds Creek Critical Zone Observatory PI, and funding. SG: data and statistical analysis consultant, manuscript editing, and contributed to major concepts/framing. JP: supervisor for laboratory analysis of organic carbon and fluorescence data, data analysis consultant, manuscript editing, and major concepts/framing. CB: project conception, experimental design, data analysis consultant, manuscript editing, and major concepts/framing. All authors contributed to the article and approved the submitted version.

FUNDING

This research was supported by NSF RC CZO Cooperative Agreement #EAR 1331872, USDA-ARS, and the Idaho State University Doctorate of Arts fellowship in biology.

ACKNOWLEDGMENTS

Special thanks to the Northwest Watershed Management Center personnel for logistical and infrastructure support in addition to Lohse Lab and Idaho State University. Additional acknowledgments include Dr. DeWayne Derryberry, Dr. Bruce Finney, Susan Parsons, Emma McCorkle, Kayla Glossner, and Anna Radke. Special dedication to the memory of Dr. Wayne "Doc" Minshall.

SUPPLEMENTARY MATERIAL

The Supplementary Material for this article can be found online at: https://www.frontiersin.org/articles/10.3389/frwa.2020.563841/full#supplementary-material

REFERENCES

Abatzoglou, J. T., and Kolden, C. A. (2011). Climate change in Western US deserts: potential for increased wildfire and invasive annual grasses. *Rangel. Ecol. Manag.* 64, 471–478. doi: 10.2111/REM-D-09-00151.1

Abatzoglou, J. T., Rupp, D. E., and Mote, P. W. (2014). Seasonal climate variability and change in the pacific northwest of the United States. *J. Clim.* 27, 2125–2142. doi: 10.1175/JCLI-D-13-00218.1

Abatzoglou, J. T., and Williams, A. P. (2016). Impact of anthropogenic climate change on wildfire across western US forests. *Proc. Natl. Acad. Sci. U.S.A.* 113, 11770–11775. doi: 10.1073/pnas.1607171113

Abbott, B. W., Gruau, G., Zarntske, J. P., Moatar, F., Barbe, L., Thomas, Z., et al. (2018). Unexpected spatial stability of water chemistry in headwater stream networks. *Ecol. Lett.* 21, 296–308. doi: 10.1111/ele.12897

Allen, D., Datry, T., Boersma, K., Bogan, M., Boulton, A. J., Bruno, D., et al. (2020). River ecosystem conceptual models and non-perennial rivers: a critical review 1. *Wiley Interdiscip. Rev. Water* 7:e1473. doi: 10.1002/wat2.1473

Asano, Y., Uchida, T., Mimasu, Y., and Ohte, N. (2009). Spatial patterns of stream solute concentrations in a steep mountainous catchment with a homogeneous landscape. *Water Resour. Res.* 45. doi: 10.1029/2008WR007466

Atchley, A. L., Kinoshita, A. M., Lopez, S. R., Trader, L., and Middleton, R. (2018). Simulating surface and subsurface water balance changes due to burn severity. *Vadose Zone J.* 17, 1–13. doi: 10.2136/vzj2018.05.0099

Baker, M., and Webster, J. R. (2017). Conservative and reactive solute dynamics. *Methods Stream Ecol.* 2, 129–146. doi: 10.1016/B978-0-12-813047-6.00008-5

Bernal, S., Lupon, A., Wollheim, W. M., Sabater, F., Poblador, S., and Marti, E. (2019). Supply, demand, and in-stream retention of dissolved organic carbon and nitrate during storms in mediterranean forested headwater streams. *Front. Environ. Sci.* 7:60. doi: 10.3389/fenvs.2019.00060

Bixby, R. J., Cooper, S. D., Gresswell, R. E., Brown, L. E., Dahm, C. N., and Dwire, K. A. (2015). Fire effects on aquatic ecosystems: an assessment of the current state of the science. *Fire Ecol.* 34, 1340–1350. doi: 10.1086/684073

Boyer, E. W., Hornberger, G. M., Bencala, K., and McKight, D. M. (1997). Response characteristics of DOC flushing in an alpine catchment. *Hydrol. Process.* 11, 1635–1647. doi: 10.1002/(SICI)1099-1085(19971015)11:12<;1635::AID-HYP494>;3.0.CO;2-H

Bradley, B. (2009). Regional analysis of the impacts of climate change on cheatgrass invasion shows potential risk and opportunity. *Glob. Change Biol.* 15, 196–208. doi: 10.1111/j.1365-2486.2008.01709.x

Bradley, B. A., Curtis, C. A., and Chambers, J. C. (2016). "Bromus response to climate and projected changes with climate change," in *Exotic Brome-Grasses in Arid and Semiarid Ecosystems of the Western US*, eds E. D. McArthur, E. M. Romney, S. D. Smith, and P. T. Tueller (Switzerland: Springer International Publishing), 257–274. doi: 10.1007/978-3-319-24930-8_9

Brooks, P. D., Chorover, J., Fan, Y., Godsey, S. E., Maxwell, R. M., McNamara, J. P., et al. (2015). Hydrological partitioning in the critical zone: recent advances and opportunities for developing transferable understanding of water cycle dynamics. *Water Resour. Res.* 51, 6973–6987. doi: 10.1002/2015WR017039

Brooks, P. D., and Lemon, M. M. (2007). Spatial variability in dissolved organic matter and inorganic nitrogen concentrations in a semi-arid stream, San Pedro River, Arizona. *J. Geophys. Res. Biosci.* 112:262. doi: 10.1029/2006JG000262

Brooks, P. D., McKight, D. M., and Bencala, K. E. (1999). The relationship between soil heterotrophic activity, soil dissolved organic carbon (DOC) leachate, and catchment-scale DOC export in headwater catchments. *Water Resour. Res.* 35, 1895–1902. doi: 10.1029/1998WR900125

Busch, M. H., Costigan, K. H., Fritz, K. M., Datry, T., Krabbenhoft, C. A., Hammond, J. C., et al. (2020). What is a name? Patterns, trends, and suggestions for defining non-perennial rivers and streams. *Water* 12:1980. doi: 10.3390/w12071980

Cooper, S. D., Page, H. M., Wiseman, S. M., Klose, K., Bennett, D., Even, T., et al. (2015). Physicochemical and biological responses of stream to wildfire severity in riparian zones. *Freshw. Biol.* 60, 2600–2619. doi: 10.1111/fwb.12523

Cory, R. M., and McKnight, D. M. (2005). Fluorescence spectroscopy reveals ubiquitous presence of oxidized and reduced quinones in dissolved organic matter. *Environ. Sci. Technol.* 39, 8142–8149. doi: 10.1021/es0506962

Costigan, K. H., Jaeger, K. L., Goss, C. W., Fritz, K. M., and Goebel, P. C. (2016). Understanding controls on flow permanence in intermittent rivers to aid ecological research: integrating meteorology, geology, and land cover. *Ecohydrology* 9, 1141–1153. doi: 10.1002/eco.1712

Creed, I. F., McKnight, D. M., Pellerin, B. A., Green, M. B., Bergamaschi, B. A., Aiken, G. R., et al. (2015). The river as a chemostat: fresh perspectives on dissolved organic matter flowing down the river continuum. *Can. J. Fish. Aquat. Sci.* 78, 1272–1285. doi: 10.1139/cjfas-2014-0400

Datry, T., Larned, S. T., and Tockner, K. (2014). Intermittent rivers: a challenge for freshwater ecology. *BioScience* 64, 229–235. doi: 10.1093/biosci/bit027

Davis, J. M., Baxter, C. V., Rosi-Marshall, E. J., Pierce, J. L., and Crosby, B. T. (2013). Anticipating stream ecosystem responses to climate change: toward predictions that incorporate effects via land-water linkages. *Ecosystems* 16, 909–922. doi: 10.1007/s10021-013-9653-4

Dent, C. L., Grimm, N. B., and Fisher, S. G. (2001). Multiscale effects of surface-subsurface exchange on stream water nutrient concentrations. *North Am. Benthol. Soc.* 20, 162–181. doi: 10.2307/1468313

Dent, L. C., and Grimm, N. B. (1999). Spatial heterogeneity of stream water nutrient concentrations over successional time. *Ecology* 80, 2283–2298. doi: 10.1890/0012-9658(1999)0802283:SHOSWN2.0.CO;2

Dohman, J. (2019). *Three-Dimensional Subsurface Controls on Stream Intermittency in a Semi-Arid Landscape: A Case Study in Gibson Jack Creek, Pocatello, ID*. (Master's thesis). Pocatello, ID: Idaho State University.

Döll, P., and Schmied, H. M. (2012). How is the impact of climate change on river flow regimes related to the impact on mean annual runoff? A global-scale analysis. *Environ. Res. Lett.* 7, 1–11. doi: 10.1088/1748-9326/7/1/014037

Fausch, K. D., Torgersen, C. E., Baxter, C. V., and Li, H. W. (2002). Landscapes to riverscapes: bridging the gap between research and conservation of stream fishes. *BioScience* 52, 83–489. doi: 10.1641/0006-3568(2002)0520483:LTRBTG2.0.CO;2

Fellows, A., Flerchinger, G., Lohse, K., and Seyfried, M. (2018). Rapid recovery of gross production and respiration in a mesic mountain big sagebrush ecosystem following prescribed fire. *Ecosystems* 21, 1283–1294. doi: 10.1007/s10021-017-0218-9

Fisher, S. G., and Likens, G. E. (1973). Energy flow in bear brook, new hampshire: an integrative approach to stream ecosystem metabolism. *Ecol. Monogr.* 43, 421–439. doi: 10.2307/1942301

Flerchinger, G. N., Seyfried, M. S., and Hardegree, S. P. (2016). Hydrologic response and recovery to prescribed fire and vegetation removal in a small rangeland catchment. *Ecohydrology* 9, 1604–1619. doi: 10.1002/eco.1751

Fritz, P., and Clark, I. D. (Eds.). (1997). "Tracing the hydrological cycle," in *Environmental Isotopes in Hydrogeology* (New York: CRC Press LLC), 36–61.

Gallo, E. L., Lohse, K. A., Brooks, P. D., McIntosh, J. C., Meixner, T., and McLain, J. E. T. (2012). Quantifying the effects of stream channels on storm water quality in a semi-arid urban environment. *J. Hydrol.* 98, 470–471. doi: 10.1016/j.jhydrol.2012.08.047

Gat, J. R. (1996). Oxygen and hydrogen isotopes in the hydrologic cycle. *Annu. Rev. Earth Planet. Sci.* 24, 225–262. doi: 10.1146/annurev.earth.24.1.225

Glossner, K. (2019). *Transport and Fluxes of Suspended Sediment and Carbon Across Multiple Spatio-Temporal Scales in a Semi-Arid Region*. (Master's thesis). Pocatello, ID: Idaho State University.

Godsey, S. E., and Kirchner, J. W. (2014). Dynamic, discontinuous stream networks: hydrologically driven variations in active drainage density, flowing channels and stream order. *Hydrol. Process.* 28, 5791–5803. doi: 10.1002/hyp.10310

Godsey, S. E., Kirchner, J. W., and Clow, D. W. (2009). Concentration-discharge relationships reflect chemostastic characteristics of US catchments. *Hydrol. Process.* 23, 1844–1864. doi: 10.1002/hyp.7315

Godsey, S. E., Kirchner, J. W., and Tague, C. L. (2014). Effects of changes in winter snowpacks on summer low flows: case studies in the Sierra Nevada, California, USA. *Hydrol. Process.* 28, 5048–5056. doi: 10.1002/hyp.9943

Godsey, S. E., Marks, D., Kormos, P. R., Seyfried, M. S., Enslin, C. L., Winstral, A. H., et al. (2018). Eleven years of mountain weather, snow, soil moisture, and streamflow data from the rain-snow transition zone-the Johnston draw catchment, reynolds creek experimental watershed and critical zone observatory, USA. *Earth Syst. Sci. Data* 10, 1207–1216. doi: 10.5194/essd-10-1207-2018

Green, S., and Blough, N. (1994). Optical absorption and fluorescence properties of chromophoric dissolved organic matter in natural waters. *Limnol. Oceanogr. Methods* 39, 1903–1916. doi: 10.4319/lo.1994.39.8.1903

Hale, R. L., and Godsey, S. E. (2019). Dynamic stream network intermittence explains emergent dissolved organic carbon chemostasis in headwaters. *Hydrol. Process.* 33, 1926–1936. doi: 10.1002/hyp.13455

Hauer, F. R., and Spencer, C. N. (1998). Phosphorous and nitrogen dynamics in streams associated with wildfire: a study of immediate and longterm effects. *Int. J. Wildland Fire* 8, 183–198. doi: 10.1071/WF9980183

Hood, E., Gooseff, M. N., and Johnson, S. L. (2006). Changes in the character of stream water dissolved organic carbon during flushing in three small watersheds, Oregon. *J. Geophys. Res.* 111:82. doi: 10.1029/2005JG000082

Hornberger, G. M., Bencala, K. E., and McKight, D. M. (1994). Hydrological controls on dissolved organic carbon during snowmelt in the Snake River near Montezuma, Colorado. *Biogeochemistry* 25, 147–165. doi: 10.1007/BF00024390

Hunsaker, C. T., and Johnon, D. W. (2017). Concentration-discharge relationships in headwater streams of the Sierra Nevada, California. *Water Resour. Res.* 53, 7869–7884. doi: 10.1002/2016WR019693

Ibarra, D. E., Caves, J. K., Moon, S., Thomas, D. L., Hartman, J., Chamberlain, C. P., et al. (2016). Differential weathering of basaltic and granitic catchments from concentration-discharge relationships. *Geochim. Cosmochim. Acta* 190, 265–293. doi: 10.1016/j.gca.2016.07.006

Inamdar, S., Finger, N., Singh, S., Mitchell, M., Levia, D., Bais, H., et al. (2012). Dissolved organic matter (DOM) concentration and quality in a forested mid-Atlantic watershed, USA. *Biogeochemistry* 108, 55–76. doi: 10.1007/s10533-011-9572-4

Jaeger, K. L., Olden, J. D., and Pelland, N. A. (2014). Climate change poised to threaten hydrologic connectivity and endemic fishes in dryland streams. *Proc. Natl. Acad. Sci. U.S.A.* 111, 13894–13899. doi: 10.1073/pnas.1320890111

Jaffe, R., McKnight, D., Maie, N., Cory, R., McDowell, W. H., and Campbell, J. L. (2008). Spatial and temporal variations in DOM composition in ecosystems: the importance of long-term monitoring of optical properties. *J. Geophys. Res.* 113, 1–15. doi: 10.1029/2008JG000683

Jensen, C. K., McGuire, K. J., McLaughlin, D. L., and Durelle, T. S. (2019). Quantifying spatiotemporal variation in headwater stream length using flow intermittency sensors. *Environ. Monit. Assess.* 191:226. doi: 10.1007/s10661-019-7373-8

Jones, J. B., Fisher, S. G., and Grimm, N. B. (1996). A long-term perspective of dissolved organic carbon transport in Sycamore Creek, Arizona, USA. *Hydrobiologia* 317, 183–188. doi: 10.1007/BF00036468

Kinoshita, A. M., and Hogue, T. S. (2015). Increased dry season water yield in burned watersheds in Southern California. *Environ. Res. Lett.* 10:14003. doi: 10.1088/1748-9326/10/1/014003

Klos, P. Z., Link, T. E., and Abatzoglou, J. T. (2014). Extent of the rain-snow transition zone in the western U.S. under historic and projected climate. *Geol. Res. Lett.* 41, 4560–4568. doi: 10.1002/2014GL060500

Kormos, P. R., Marks, D., McNamara, J. P., Marshall, H. P., Winstral, A., and Flores, A. N. (2014). Snow distribution, melt and surface water input to the soil in the mountain rain-snow transition zone. *J. Hydrol.* 519, 190–204. doi: 10.1016/j.jhydrol.2014.06.051

Larned, S. T., Datry, T., Arscott, D. B., and Tockner, K. (2010). Emerging concepts in temporary-river ecology. *Freshw. Biol.* 55, 717–738. doi: 10.1111/j.1365-2427.2009.02322.x

Likens, G. E., and Buso, D. C. (2006). Variation in streamwater chemistry throughout the hubbard brook valley. *Biogeochemistry* 78, 1–30. doi: 10.1007/s10533-005-2024-2

Link, S. O., Keeler, C. W., Hill, R. W., and Hagen, E. (2006). Bromus tectorum cover mapping and fire risk. *Int. J. Wildland Fire* 15, 113–119. doi: 10.1071/WF05001

MacNeille, R. B. (2020). *Quantifying patterns and processes of intermittent stream biogeochemistry and of introductory STEM classroom behavior* (Doctorate of Arts dissertation). Idaho State University, Pocatello, ID, United States.

Maheu, A., Caissie, D., St-Hilaire, A., and El-Jabi, N. (2014). River evaporation and corresponding heat fluxes in forested catchments. *Hydrol. Process.* 28, 5725–5738. doi: 10.1002/hyp.10071

Marks, D., Cooley, K. R., Robertson, D. C., and Winstral, A. (2011). Long-term snow database, reynolds creek experimental Watershed, Idaho, United States. *Water Resour. Res.* 37, 2835–2838. doi: 10.1029/2001WR000416

Mast, M. A., Murphy, S. F., Clow, D. W., Penn, C. A., and Sexstone, G. A. (2016). Water-quality response to a high-elevation wildfire in the colorado front range. *Hydrol. Process.* 30, 1811–1823. doi: 10.1002/hyp.10755

McGuire, K. J., Torgersen, C. E., Likens, G. E., Buso, D. C., Lowe, W. H., and Bailey, S. W. (2014). Network analysis reveals multiscale controls on streamwater chemistry. *Proc. Natl. Acad. Sci. U.S.A.* 111, 7030–7035. doi: 10.1073/pnas.1404820111

McIntosh, J. C., Schaumberg, C., Perdrial, J., Harpold, A., Vazquez-Ortega, A., Meixner, T., et al. (2017). Geochemical evolution of the critical zone across variable time scales inform concentration-discharge relationships: jemez river basin critical zone observatory. *Water Resour. Res.* 53, 4169–4196. doi: 10.1002/2016WR019712

McIntyre, D. H. (1972). *Cenozoic Geology of the Reynolds Creek Experimental Watershed.* Idaho: Bur Mines.

McKnight, D. M., Boyer, E. W., Westerhoff, P. K., Doran, P. T., Kulbe, T., and Andersen, D. T. (2001). Spectrofluorometric characterization of dissolved organic matter for indication of precursor material and aromaticity. *Limnol. Oceanogr. Methods* 46, 38–48. doi: 10.4319/lo.2001.46.1.0038

McNamara, J. P., Chandler, D., Seyfried, M., and Achet, S. (2005). Soil moisture states, lateral flow, and streamflow generation in a semi-arid, snowmelt-driven catchment. *Hydrol. Process.* 19, 4023–2038. doi: 10.1002/hyp.5869

Meybeck, M. (1987). Global chemical weathering of surficial rocks estimates from river dissolved loads. *Am. J. Sci.* 287, 401–428. doi: 10.2475/ajs.287.5.401

Miller, M. P., Simone, B. E., McKnight, D. M., Cory, R. M., Williams, M. W., and Boyer, E. W. (2010). New light on a dark subject: comment. *Aquat. Sci.* 72, 269–275. doi: 10.1007/s00027-010-0130-2

Minshall, G. W., Brock, J. T., and Varley, J. D. (1989). Wildfires and yellowstone's stream ecosystem. *BioScience* 39, 707–715. doi: 10.2307/1311002

Moatar, F., Abbott, B. W., Minaudo, C., Curie, F., and Pinay, G. (2017). Elemental properties, hydrology, and biology interact to shape concentration-discharge curves for carbon, nutrients, sediment, and major ions. *Water Resour. Res.* 53, 1270–1287. doi: 10.1002/2016WR019635

Mulholland, P. J., and Hill, W. R. (1997). Seasonal patterns in streamwater nutrient and dissolved organic carbon concentrations: separating catchment flow path and in-stream effects. *Water Resour. Res.* 33, 1297–1306. doi: 10.1029/97WR00490

Murphy, J. D., Miller, W. W., Walker, R. F., Carroll, E. F., and Blank, R. R. (2006). Wildfire effects on soil nutrients and leaching in a tahoe basin watershed. *J. Environ. Qual.* 35, 479–489. doi: 10.2134/jeq2005.0144

Naiman, R. J., and Sedell, J. R. (1980). Relationships between metabolic parameters and stream order in oregon. *Can. J. Fish. Aquat. Sci.* 37, 834–847. doi: 10.1139/f80-112

Nayak, A., Marks, D. G., and Seyfried, M. (2010). Long-term snow, climate, and streamflow trends at the reynolds creek experimental watershed, Owyhee Mountains, Idaho, United States. *Water Resour. Res.* 46, 1–15. doi: 10.1029/2008WR007525

Ohno, T. (2002). Fluorescence inner-filtering correction for determining the humification index of dissolved organic matter. *Environ. Sci. Technol.* 36, 742–746. doi: 10.1021/es0155276

Olshansky, Y., Knowles, J. F., Barron-Gafford, G., Rasmussen, C., Abramson, N., and Chorover, J. (2019). Soil fluid biogeochemical response to climatic events. *J. Geophys. Res. Biogeosci.* 124, 2866–2882. doi: 10.1029/2019JG005216

Parks, S. A., Miller, C., Abatzoglou, J. T., Holsinger, L. M., Parisien, M.-A., and Dombrowski, S. Z. (2016). How will climate change affect wildland fire severity in the western US? *Environ. Res. Lett.* 11, 1–10. doi: 10.1088/1748-9326/11/3/035002

Patton, N. R., Lohse, K. A., Godsey, S. E., Crosby, B. T., and Seyfried, M. S. (2018). Predicting soil thickness on soil mantled hillslopes. *Nat. Commun.* 9:3329. doi: 10.1038/s41467-018-05743-y

Patton, N. R., Lohse, K. A., Seyfried, M. S., Godsey, S. E., and Parsons, S. B. (2019). Topographical controls of soil organic carbon on soil-mantled landscapes. *Sci. Rep.* 9:6390. doi: 10.1038/s41598-019-42556-5

Pierson, F. B., Slaughter, C. W., and Cram, Z. K. (2001). Long-term stream discharge and suspended-sediment database, reynolds creek experimental Watershed, Idaho, United States. *Water Resour. Res.* 37, 2857–2861. doi: 10.1029/2001WR000420

Poole, G. C., and Berman, C. H. (2001). An ecological perspective on in-stream temperature: natural heat dynamics and mechanisms of human-caused thermal degradation. *Environ. Manage.* 27, 787–802. doi: 10.1007/s002670010188

Poon, P. K., and Kinoshita, A. M. (2018). Spatial and temporal evapotranspiration trends after wildfire in semi-arid landscapes. *J. Hydrol.* 559, 71–83. doi: 10.1016/j.jhydrol.2018.02.023

Radke, A. G., Godsey, S. E., Lohse, K. A., McCorkle, E., Perdrial, J., Seyfried, M. S., et al. (2019). Spatiotemporal heterogeneity of water flowpaths controls dissolved organic carbon sourcing in a snow-dominated, headwater catchment. *Front. Ecol. Evol.* 7:46. doi: 10.3389/fevo.2019.00046

Rau, B. M., Blank, R. R., Chambers, J. C., and Johnson, D. W. (2007). Prescribed fire in a great basin sagebrush ecosystem: dynamics of soil extractable nitrogen and phosphorus. *J. Arid Environ.* 71, 362–375. doi: 10.1016/j.jaridenv.2007.05.006

Richter, D. B., and Billings, S. A. (2015). "One physical system": tansley's ecosystem as earth's critical zone. *New Phytol.* 206, 900–912. doi: 10.1111/nph.13338

Rodríguez-Cardona, B. M., Coble, A. A., Wymore, A. S., Kolosov, R., Podgorski, D. C., Zito, P., et al. (2020). Wildfires lead to decreased carbon and increased nitrogen concentrations in upland artic streams. *Sci. Rep.* 10:8722. doi: 10.1038/s41598-020-65520-0

Rugenski, A. T., and Minshall, G. W. (2014). Climate-moderated responses to wildfire by macroinvertebrates and basal food resources in montane wilderness streams. *Ecosphere* 5, 1–24. doi: 10.1890/ES13-00236.1

Sanderman, J., Lohse, K. A., Baldock, J., and Amundson, R. (2009). Linking soils and streams: sources and chemistry of dissolved organic carbon in a Mediterranean catchment. *Water Resour. Res.* 45, 1–13. doi: 10.1029/2008WR006977

Schiff, S. L., and Aravena, R. (1990). Dissolved organic carbon cycling in forested watersheds: a carbon isotope approach. *Water Resour. Res.* 26, 2949–2957. doi: 10.1029/WR026i012p02949

Schneider, D. C. (2001). The rise of the concept of scale in ecology: the concept of scale is evolving from verbal expression to quantitative expression. *BioScience* 51, 545–553. doi: 10.1641/0006-3568(2001)0510545:TROTCO2.0.CO;2

Seyfried, M., Harris, R. C., Marks, D., and Jacob, B. (2000). A geographic database for watershed research, reynolds creek experimental watershed, Idaho, USA. *ARS Tech. Bull.* 3, 1–26.

Seyfried, M. S., Lohse, K. A., Marks, D., Flerchinger, G. N., and Pierson, F. (2018). Reynolds creek experimental watershed and critical zone observatory. *Vadose Zone J.* 17:180129. doi: 10.2136/vzj2018.07.0129

Sharma, H., Reinhardt, K., Lohse, K. A., and Aho, K. (2020). Summer-time carbon and water fluxes in sagebrush ecosystems spanning rain-to snow-dominated precipitation regimes. *Rangel. Ecol. Manag.* 73, 266–275. doi: 10.1016/j.rama.2019.11.002

Spencer, C. N., Gabel, K. O., and Hauer, F. R. (2003). Wildfire effects on stream food webs and nutrient dynamics in Glacier National Park, USA. *For. Ecol. Manag.* 178, 141–153. doi: 10.1016/S0378-1127(03)00058-6

Stanley, E. H., Fisher, S. G., and Grimm, N. B. (1997). Ecosystem expansion and contraction in streams. *BioScience* 47, 427–435. doi: 10.2307/1313058

Stewart, I. T., Cayan, D. R., and Dettinger, M. D. (2004). Changes in snowmelt runoff timing in Western North America under a "business as usual" climate chang scenario. *Clim. Change* 62, 217–232. doi: 10.1023/B:CLIM.0000013702.22656.e8

Subiza, E. A. W., and Brand, C. (2018). Short-term effects of wildfire on patagonian headwater streams. *Int. J. Wildland Fire* 27, 457–470. doi: 10.1071/WF17164

Tague, C., and Grant, G. E. (2009). Groundwater dynamics mediate low-flow response to global warming in snow-dominated alpine regions. *Water Resour. Res.* 45, 1–12. doi: 10.1029/2008WR007179

Tappa, D. J., Kohn, M. J., McNamara, J. P., Benner, S. G., and Flores, A. N. (2016). Isotopic composition of precipitation in a topographically steep, seasonally snow-dominated watershed and implications of variations from the global meteoric water line. *Hydrol. Process.* 30, 4582–4592. doi: 10.1002/hyp.10940

Tennant, C. J., Crosby, B. T., and Godsey, S. E. (2015). Elevation-dependent response of streamflow to climate warming. *Hydrol. Process.* 29, 991–1001. doi: 10.1002/hyp.10203

US Geological Survey USGS (2006). *National Hydrography Dataset Web Site.* Available online at: http://nhd.usgs.gov/index.html (accessed September, 2017).

van Meerveld, H. J. I., Kirchner, J. W., Vis, M. J. P., Assendelft, R. S., and Seibert, J. (2019). Expansion and contraction of the flowing stream network alter hillslope flowpath lengths and the shape of the travel time distribution. *Hydrol. Earth Syst. Sci.* 23, 4825–4834. doi: 10.5194/hess-23-4825-2019

Vega, S. P., Williams, C. J., Brooks, E. S., Pierson, F. B., Strand, E. K., Robichaud, P. R., et al. (2020). Interaction of wind and cold-season hydrologic processes on erosion from complex topography following wildfire in sagebrush steppe. *Earth Syst. Process. Landf.* 45, 841–861. doi: 10.1002/esp.4778

Warix, S. (2020). *Stream Drying Controls in Semi-Arid Headwater Streams: Baseflow, Topographic Metrics, and Diel Cycles*. (Master's thesis). Pocatello (ID): Idaho State University.

Weishaar, J. L., Aiken, G. R., Bergamaschi, B. A., Fram, M. S., Fujii, R., and Mopper, K. (2003). Evaluation of specific ultraviolet absorbance as an indicator of the chemical composition and reactivity of dissolved organic carbon. *Environ. Sci. Technol.* 37, 4702–4708. doi: 10.1021/es030360x

Wine, M. L., and Cadol, D. (2016). Hydrological effects of large southwestern USA wildfires significantly increase regional water supply: fact or fiction? *Environ. Res. Lett.* 11:085006. doi: 10.1088/1748-9326/11/8/085006

Wlostowski, A., Molotch, N., Anderson, S. P., Brantley, S. L., Chorover, J., Dralle, D., et al. (2020). Signatures of hydrologic function across the critical zone observatory network. *Water Resour. Res.* doi: 10.1029/2019WR026635

Zimmer, M. A., Bailey, S. W., McGuire, K. J., and Bullen, T. D. (2013). Fine scale variations of surface water chemistry in an ephemeral to perennial drainage network. *Hydrol. Process.* 27, 3438–3451. doi: 10.1002/hyp.9449

Zimmer, M. A., and Lautz, L. K. (2014). Temporal and spatial response of hyporheic zone geochemistry to a storm event. *Hydrol. Process.* 28, 2324–2337. doi: 10.1002/hyp.9778

Zimmer, M. A., and McGlynn, B. L. (2017). Bidirectional stream-groundwater flow in response to ephemeral and intermittent streamflow and groundwater seasonality. *Hydrol. Process.* 31, 1–10. doi: 10.1002/hyp.11301

Conflict of Interest: The authors declare that the research was conducted in the absence of any commercial or financial relationships that could be construed as a potential conflict of interest.

frontiers in Water

ORIGINAL RESEARCH
published: 07 January 2021
doi: 10.3389/frwa.2020.580727

The River Corridor's Evolving Connectivity of Lotic and Lentic Waters

Judson W. Harvey and Noah M. Schmadel*

U.S. Geological Survey, Earth System Processes Division, Reston, VA, United States

River corridors supply a substantial proportion of the fresh water for societal and ecological needs. Individual functions of flowing (lotic) streams and rivers and ponded (lentic) waterbodies such as lakes and reservoirs are well-studied, but their collective functions are not as well understood. Here we bring together nationally consistent river corridor datasets to characterize the contributions of lotic and lentic features and to estimate changes over the past centuries. High-resolution datasets describing waterbodies across 10 million kilometers of the conterminous U.S. (CONUS) river network were classified by waterbody type and origin (historic vs. human-made or intensively managed), surface areal coverage, and degree of connectivity as estimated by a change in water residence timescale in river corridors. Four centuries of human disturbance drove large swings in river corridor makeup, with a transition toward more lotic systems caused by beaver extirpation and abandonment of waterwheel mill ponds by end of the nineteenth century. The twentieth century saw a vast expansion (49%) in river corridor areal coverage resulting from construction and management of small ponds and reservoirs for drinking water, hydropower, irrigation and livestock watering, and stormwater control. Water residence timescale in river corridors doubled or quadrupled over large areas, and more in specific locations, during the twentieth century as a result of the increased coverage of reservoirs and managed small ponds. Although reservoirs and lakes now dominate river corridor surface areas, we found that the growing number of small ponds impacts a greater proportion of network length through their influence on headwater streams where most water and chemical runoff enters the river corridor. We close with an agenda for integrated modeling of the physical, biogeochemical, and ecological drivers of river corridor functions, trajectories of change, and management opportunities.

Keywords: lakes, small ponds, lentic, reservoirs, hydraulic load, residence time, hydrologic connectivity, river corridor

OPEN ACCESS

Edited by:
Sarah E. Godsey,
Idaho State University, United States

Reviewed by:
Eve-Lyn S. Hinckley,
University of Colorado Boulder, United States
Adam Wymore,
University of New Hampshire, United States

****Correspondence:***
Judson W. Harvey
jwharvey@usgs.gov

Specialty section:
This article was submitted to Water and Critical Zone, a section of the journal Frontiers in Water

Received: *06 July 2020*
Accepted: *04 December 2020*
Published: *07 January 2021*

Citation:
Harvey JW and Schmadel NM (2021) The River Corridor's Evolving Connectivity of Lotic and Lentic Waters. Front. Water 2:580727. doi: 10.3389/frwa.2020.580727

INTRODUCTION

River corridors comprise a small portion of the landscape, on the order of a percent, yet they have outsized importance in supporting freshwater needs of humans and ecosystems (Sparks, 1995; Downing, 2010; Padowski and Jawitz, 2012; Woodward et al., 2012). They store and convey substantial quantities of clean water that support healthy and biodiverse aquatic ecosystems as well as serving societies' water needs for potable and industrial uses, irrigation and livestock,

energy production, and more. The resilience of river corridors to changing flow, increasing chemical runoff, higher temperatures, and accelerating water extraction lies in part in their overall functions. River corridors exchange water back and forth between the main channel and the shallower and more slowly moving ponded areas and subsurface zones in the bed, banks, riparian areas, and floodplains (Harvey et al., 2019). The storage zones within river corridors are important in water retention and slow release that moderates effects of floods and drought (National Research Council, 2002). The prolonged interactions with shallow areas and sediments also tend to benefit ecological health and water quality, for example, promoting filtering of fine particulates and transformation of solutes and contaminants in hyporheic zones (Boano et al., 2014). Water purification may therefore be enhanced in river corridors; however, too much storage time may facilitate undesirable algal blooms and hypoxia (Beaulieu et al., 2013). Healthy river corridors have achieved a balance in water residence time, nutrient delivery, and water column depth, light, temperature, and benthic exchange that promote appropriate levels of metabolic activity that process carbon and cycle nutrients (Harvey and Gooseff, 2015; Bernhardt et al., 2018) in amounts that support productive food webs, a diverse fauna, and related ecological services for society.

Comparatively little attention has been paid to the role of lentic features in river corridors, for example, the small ponds, reservoirs, and lakes. Streams and rivers dominate the downstream conveyance of water and materials in river networks, but it is the lentic waterbodies in the river network that dominate water storage. The character of river corridors shift toward wider, deeper, and more slowly moving lentic waters where stream and river valleys abruptly widen and/or lessen in their slope (Wohl, 2020). Geologic features such as glacial moraines, debris flows, or downed logs, or biologically enhanced features such as beaver dams, are some of the constraints on lentic water occurrence in river corridors (Livers and Wohl, 2016). Constructed features such as earthen embankments, culverts, bridge under crossings, low-water fords, and dams of all sizes are increasingly important features associated with human disturbance of river corridors (Nilsson et al., 2005; Doyle et al., 2008; Bellmore et al., 2017). The role of lentic waterbodies in river corridors is hypothesized to vary on a continuum of hydrogeomorphic, climatic, ecological, and anthropogenic gradients according to Ward and Stanford (1995) serial discontinuity concept and related works by Swanson et al. (1998), Soranno et al. (1999), Dunne et al. (1998), Bencala (1993), Stanford and Ward (1993), and Wetzel (1990). However, testing of those ideas has been largely limited to site-specific studies.

Lentic waterbodies in river corridors cause seasonal shifts in the patterns and drivers of primary productivity and the processing rates and storage dynamics of nutrients and sediments (Baker et al., 2016; Schmadel et al., 2019). Their strong biogeochemical influences arise from their larger surface area, greater input of solar energy, longer water residence time, and weak vertical mixing that promotes stratification, with bed sediments that may be light limited or devoid of oxygen compared to streams and rivers. For example, natural lakes below mountain headwaters slow the velocity through river corridors and attenuate the downstream propagation of solutes and particulates during spring snowmelt (Arp et al., 2006). Greater summer autotrophic production in the lakes can promote pulses of dissolved organic matter downstream through the river corridor. Thus, lentic waters strongly influence organic carbon dynamics in river corridors (Goodman et al., 2011). Lentic waters can alter downstream constituent loads by retaining fine sediments (Vörösmarty et al., 2003), organic carbon (Mendonça et al., 2017; Anderson et al., 2020), and nutrients (Harrison et al., 2009; Maavara et al., 2015), while also episodically releasing those constituents to downstream river reaches after long periods of storage (Taguchi et al., 2020).

Human alterations of the river corridor over the past century added substantial areas of reservoirs and small ponds to serve needs for a ready water supply, hydropower production, farm use, as well as stormwater control to reduce nutrient runoff and sedimentation of waterways, and to lower flood risk (Doyle, 2012; Wohl, 2013; Bellmore et al., 2017; Foley et al., 2017; Leyk et al., 2020). The sharp increase in fertilizer and chemical use after World War II substantially increased chemical concentrations in U.S. rivers (Raymond et al., 2008). At the same time the incentives increased for farming intensity and urban expansion, including into less suitable and lower-relief riparian areas and floodplains. These changes were accompanied by widespread tiling of agricultural soils, ditching of roadsides, and paving over and piping of urban streams (National Research Council, 2002). The higher runoff peak flows that resulted mobilized pulses of sediment, nutrients, road salts, and trace metals and exacerbated bank and bed erosion and downstream transport of sediment and constituents through river corridors (Raymond et al., 2008). As the negative consequences became apparent in the later part of the twentieth century there was increasing construction of stormwater retention ponds intended to physically store and enhance the biogeochemical reactions that retain and transform the growing loads of constituents (Liu et al., 2014; Moore et al., 2017; Snodgrass et al., 2017; Schmadel et al., 2019). Construction of tens of thousands of small stormwater retention and recreational ponds in river corridors in the latter twentieth century added to the thousands of water supply and flood control reservoirs and farm irrigation and livestock ponds that had already been constructed earlier in the century.

A key question guiding our study was "how has loss of terrestrial water storage and replacement by construction of lentic waterbodies during the twentieth century affected river corridor functions?" We sought to address that question through analysis of nationally consistent data, for which impressive progress has been made in river ecology and limnology datasets. For example, the National Hydrography Dataset (NHDPlus Version 2.1 medium resolution dataset; U.S. Geological Survey, 2016) has geospatial, land cover, and hydrology data for catchments, rivers, and lentic waterbodies. More specifically for limnology, there is the comprehensive LAGOS dataset (Soranno et al., 2015) for 17 U.S. states with geospatial data on lakes larger than 0.04 km^2 (50,000 lakes) including climate, atmospheric deposition, land cover, hydrology, geology, topography, and water quality data. To our knowledge, however, there has yet to be a continental-scale analysis of temporal changes in the character

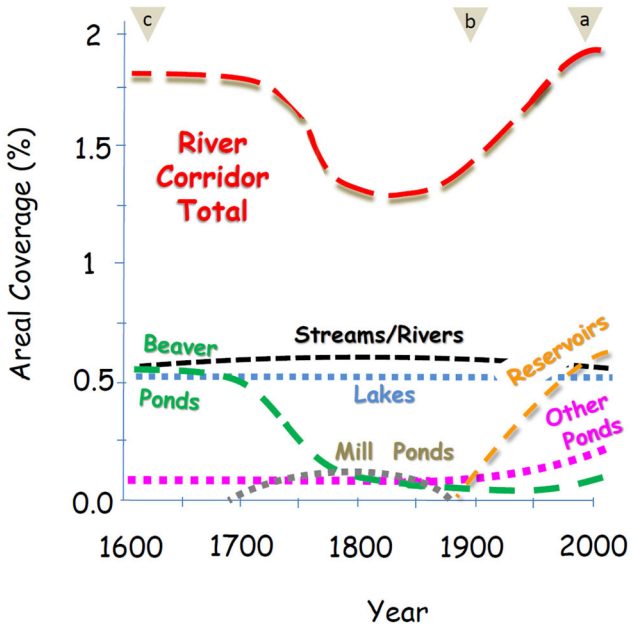

FIGURE 1 | Four hundred years of river corridor change summarized as trends in surface areal coverage of lotic and lentic waterbodies. Key estimation periods are indicated by tan triangles showing present-day time period (circa 2000) analysis of high-resolution National Hydrography Dataset (NHD) and National Inventory of Dams (NID) data sources for streams and rivers, lakes, reservoirs, and small ponds (a), early twentieth century time period (circa 1900) estimates based on subtracting reservoirs and managed small ponds from present-day values (b), and pre-Colonial time period (circa 1600) estimates based on published estimates of the CONUS beaver population and pond area prior to the near extermination of beavers during the 1700s and 1800s (c) (see **Supplementary Material**). Trends between those periods are inferred based on less certain information from published accounts cited in Changing Balance of Lotic and Lentic Contributions section of the Discussion.

of lotic and lentic features of river corridors using high-resolution data that encompass lentic features as small as 0.0001 km^2.

We analyzed trends in the size and network position of nearly two million lentic waterbodies along 10 million kilometers of river corridor across the conterminous U.S. (CONUS) using high-resolution data that include lentic waterbodies as small as 0.0001 km^2. Our analysis assessed lotic and lentic contributions to river corridor surface area, hydraulic loading, and water residence timescale. Those metrics are fully defined in section River Corridor Metrics, and we quantified them at scales ranging from individual waterbodies to major river basins to the CONUS. We also assessed changes over time in river corridors based on a classification of lentic waterbodies either as existing historically or having been built or heavily managed during the past century, along with less certain estimations of changes in beaver pond area and mill ponds associated with waterwheel powered granaries (**Figure 1**).

Our analysis of the changing physical template of river corridors helps explain how lotic and lentic elements of river corridors function together. Our discussion concentrates on hydrologic functions such as water storage. Ultimately the need is for integrated modeling of flow and storage, water use, biogeochemical processing, water purification, and ecological health of river corridors. Isolating where and why management has been effective in protecting water resources of some areas, but not in others, is the ultimate goal. Such integrated analyses will form the basis for improved management strategies that meet societal needs to protect ecological functions and values of river corridors.

METHODS

River Corridor Data Sources and Analysis

We used publicly available high-resolution datasets for the CONUS to account for the effects of over 90,000 lakes, 34,000 reservoirs, 10 million kilometers of streams and rivers, and 1.7 million small ponds (Schmadel and Harvey, 2020). Lotic and lentic sizes, network positions, and distributions across the nation were quantified to reveal regional patterns in the contribution of lentic waterbody types to river corridor areal coverage, hydraulic load, and water residence timescale. Our estimation of river corridor metrics is the first we know of to incorporate the recently available high-resolution datasets on small pond and small streams with datasets on larger streams, rivers, lakes, and reservoirs in a CONUS-extent analysis (Downing, 2010; Berg et al., 2016).

For reasons of data quality and consistency we restricted our analysis to the time-averaged surface-water expressions of river corridors (e.g., perennial or intermittent stream and river channels and the intersecting ponds, reservoirs, and lakes). Therefore, this analysis disregards other important river corridor features such as riparian wetlands, floodplains, and subsurface hyporheic zones (Harvey and Gooseff, 2015). Although there has been progress in national-scale estimation of those other river corridor features (Dahl, 2011; Gomez-Velez et al., 2015; Scott et al., 2019), we judged that either key elements were lacking for a consistent CONUS-scale analysis or a change-over-time analysis. Also disregarded for this analysis are the upland ponds and wetlands that are geographically isolated from the river corridor (i.e., having no mapped surface water connection) although those watershed features are known to have important subsurface or ephemeral surface (i.e., episodic fill-and-spill) connections that drain to the river corridor (e.g., Cohen et al., 2015; Marton et al., 2015; Schmadel et al., 2019). For the future we envision analyses of terrestrial-aquatic linkages that will bring together all perennial and intermittent surface water features in the uplands and in the river corridor.

River Corridor Network Analysis and Waterbody Classification

We started by merging the medium-resolution NHD (NHDPlus Version 2.1; U.S. Geological Survey, 2016) with the newly available high-resolution NHD (U.S. Geological Survey, 2020) that includes many more small ponds and small streams. At the time of our study the high-resolution NHD was offered without all of the attributes of the medium-resolution NHD and thus we followed Schmadel et al.'s (2019) approach of extending the medium-resolution NHD to include the high-resolution information (see details in **Supplementary Material**).

This "merged" approach permits use of the extensive existing NHDPlus attributes [e.g., land cover, etc., see Wieczorek et al. (2018)] and avoids what will be a major effort to develop high-resolution attributes and model inputs throughout the NHD. Eventually those technical challenges will be overcome, but until then, the merging of medium and high-resolution datasets can provide a robust, accurate, and useful approach for hydrologic analysis and water quality modeling.

Medium-resolution NHD provides surface areas for lentic waterbodies that are generally larger than 1 ha (0.01 km^2), except for a limited number of small ponds (10% of medium-resolution lentic waterbodies) that have surface areas as small as 0.1 ha (0.001 km^2). Paired with that information in NHD are mean annual volumetric discharge estimates, drainage areas for NHD medium-resolution catchments, and additional attributes across most of the CONUS (see **Supplementary Material**). Small ponds are commonly classified as having 1 ha (0.01 km^2) or smaller surface areas (Downing et al., 2006; Holgerson and Raymond, 2016), which encompass over 90% of the newly mapped lentic waters available in high-resolution NHD down to a size approaching a typical beaver pond, 0.02 ha (0.0002 km^2) (Karran et al., 2017). Combining information from high-resolution NHD increased the number of lentic waterbodies considered by a factor of 14 beyond those available in medium-resolution NHD. A small percentage of the medium-resolution waterbodies are duplicated in the high-resolution dataset and thus we eliminated duplicates, likely subject to small errors, from our final dataset before analysis. High-resolution NHD also includes additional coverage of finer resolution small streams beyond the main streams and rivers cataloged in medium-resolution NHD.

We separated lentic waters into four distinct classes: (i) lakes, (ii) reservoirs, (iii) historic small ponds that are naturally functioning and without intensive management during the past century, and (iv) managed small ponds that were constructed for water supply, farm use, or another purpose and that are managed accordingly (**Figure 2**). Lakes and historic small ponds are therefore interpreted as being long-lasting features that were present more than a century ago and are only marginally managed if at all for human use. Managed waterbodies such as reservoirs and managed small ponds are interpreted as having been created by excavation of impoundments or construction of dams or by other extensive alterations or management of what may have historically been a natural waterbody or that may be altogether a newly created ponded water feature.

Lakes were identified in this analysis as any medium-resolution lentic waterbody in NHD that was not a reservoir. The 34,000 reservoirs were identified as those waterbodies defined by the National Inventory of Dams (NID; U.S. Army Corps of Engineers, 2020) that were previously included on the medium-resolution NHD (Wieczorek et al., 2018). We identified small managed ponds as the additional 13,000 small impoundments in NID that were below a size of 0.01 km^2; those small ponds also were included on the medium-resolution NHD network by Wieczorek et al. (2018) and they also appear in high-resolution NHD, and so we were careful to eliminate duplicates. However, the vast majority of the 1.7 million small ponds in the high-resolution dataset are not cataloged as dammed impoundments in NHD nor are they duplicated in medium-resolution NHD. We classified those waterbodies as either managed small ponds or historic small ponds depending on local indicators of human disturbance (e.g., land cover classification) as explained in the next paragraph.

Small ponds without cataloged dams were classified as managed if located in a NHD catchment where the land cover indicated intensive human management, e.g., where crops, pasture, urban, and grassland had a sum >60% as specified by the 2011 National Land Cover Dataset (NLCD; Homer et al., 2015) which has been linked to medium-resolution NHD (Wieczorek et al., 2018). A justification for the 60% land use threshold is based on a previous analysis in the northeastern U. S. indicating that catchments with 60% or more agriculture or urban cover contain substantially higher densities of small ponds, compared with similar physiographic areas that were not intensively managed (Schmadel et al., 2019). Grasslands are widely used for grazing with many constructed small ponds or ponds that are modified to support livestock (Homer et al., 2015). Therefore, small ponds in catchments covered by 60% or more grassland were classified as managed. Scrub/shrub lands are also used for grazing, but grazing pressure is usually far less than in grasslands. We therefore made a conservative decision not to classify small ponds in scrub/shrublands as managed. All high-resolution small ponds not classified as managed using the above described land cover criteria or without cataloged dams or impoundments were classified as historic small ponds.

We performed many spot checks to ensure accuracy of classification of NHD streams, rivers, and lentic waterbodies and to minimize overlap errors in the combined medium-and-high-resolution dataset. We did not compare to independent data other than NID as that would be an enormous effort for 1.7 million small ponds but conclude through hundreds of spot checks that potential overlap errors occur in a very small proportion (on the order of a few percent or less) of reaches. We do not consider seasonal persistence of waterbodies although it is possible that some waterbodies mapped in NHD only are present for part of the year.

River Corridor Metrics

We quantify the influence of each class of lentic and lotic waters within the river corridor by estimating local and cumulative metrics of areal coverage (or percent cover), hydraulic load, water residence timescale (inverse hydraulic load), and also estimated changes due to management of lentic waters over the past century.

Areal coverage, D [%], is estimated as the percent cover of the upstream accumulated drainage area by the river corridor or by a specified class of lotic or lentic component of the river corridor:

$$D_{m,i} = \frac{\sum_j^{N_i} A_{S,m,j}}{A_{D,i}} x\ 100\% \quad (1)$$

where i is the reach index; m is a specific waterbody type, e.g., lake, reservoir, historic or managed small pond, stream, or combination thereof; N is the total number of m upstream of

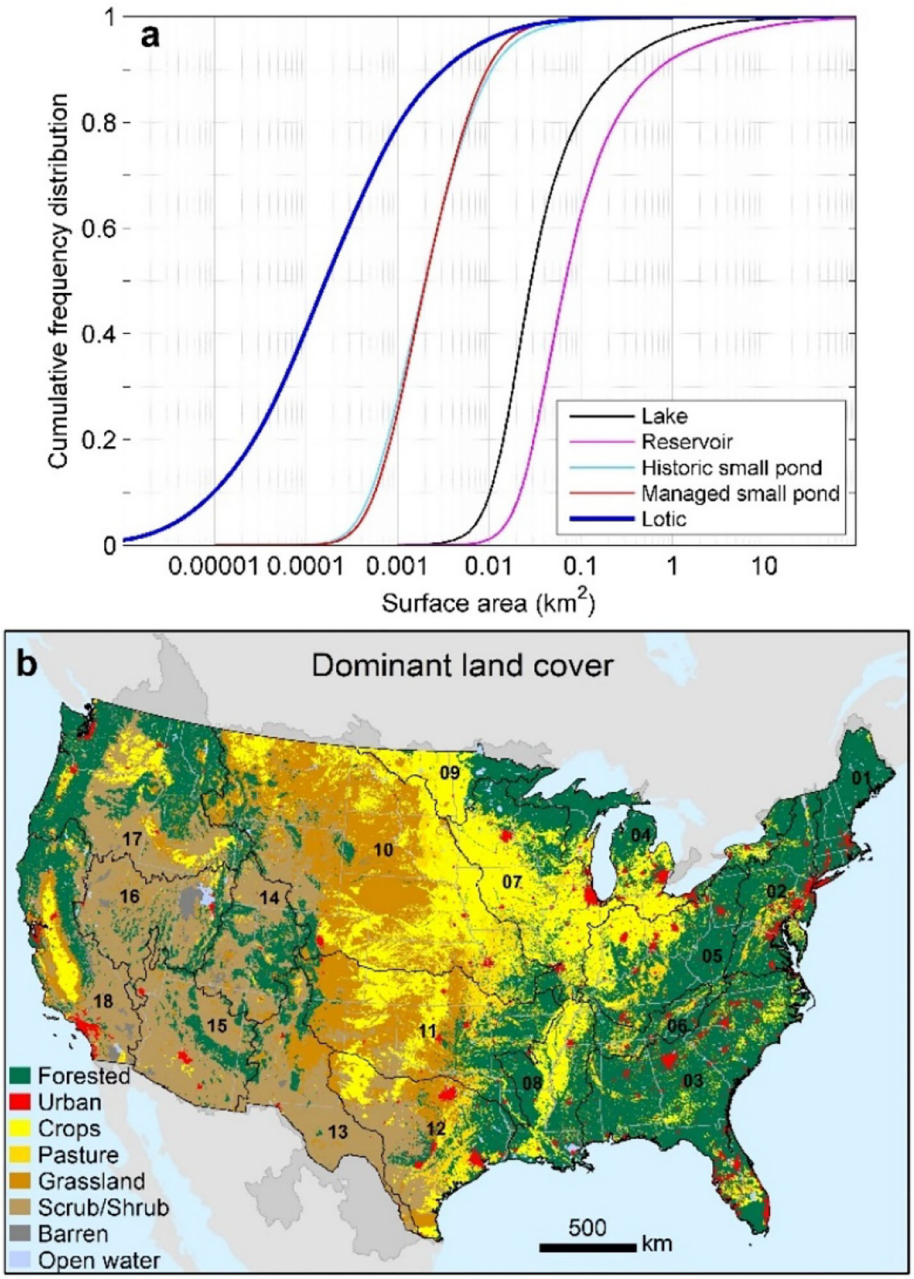

FIGURE 2 | Size distribution of river corridor features for over 90,000 lakes, 34,000 reservoirs, 1.7 million small ponds with over 800,000 managed, and 10 million kilometers of streams and rivers in the CONUS **(a)** and major land use and land cover in the CONUS and within HUC-2 river basins designated by black numbers and associated basin boundaries **(b)**.

reach i; $j = 1, \ldots, N$; A_S [area, L^2] is the wetted surface area of specific waterbody m; and A_D [area, L^2] is the drainage area at reach i. This metric provides a general assessment of how river corridor areal coverage varies across the CONUS as well as densities of the component waterbodies.

A standard metric for estimating water flux in lotic and lentic waterbodies is the hydraulic load. Hydraulic load, or H_L [L T^{-1}], is the volumetric flux of water per unit surface area of a given waterbody. The inverse of hydraulic load is the residence timescale, or R [T L^{-1}], which is the time required to flush a unit volume of water (Brett et al., 2012):

$$R_{m,i} = \frac{A_{S,m,i}}{Q_{m,i}} \quad (2)$$

where Q [L^3 T^{-1}] is the volumetric discharge which for our purposes is the annual average discharge exiting the waterbody as provided by NHD. Both medium- and high-resolution NHD products provide volumetric discharges that were estimated using an enhanced unit runoff method involving estimation of unit runoff for each catchment and then accumulation downstream and comparison with measured average flows at gages. Differences at each gage were applied to adjust the upstream unit runoff and provide long-term (1971–2000) estimates of streamflow for all reaches (Moore et al., 2019). The wetted surface areas of streams and rivers were approximated from an estimate of the velocity and width using the equations of Jobson (1996) and Leopold and Maddock (1953). More precise slopes of river reaches used in the velocity estimates were obtained from enhanced NHD attributes (Brakebill et al., 2018).

To understand effects of waterbody types, sizes, and their distributions through river basins, we quantified a cumulative residence timescale, R_w [T L^{-1}], that was weighted by the surface areas of the contributing lentic and lotic waterbodies:

$$R_{w,m,i} = \sum_{j}^{N_i} w_{m,j} \left(\frac{A_{S,m,j}}{Q_{m,j}} \right) \quad (3)$$

$$w_{m,j} = \left(\frac{A_{S,m,j}}{\sum_j^{N_i} \sum_m A_{S,m,j}} \right) \quad (4)$$

where the summation in Equation (3) estimates the weighted residence timescale, R_w, for all m upstream waterbodies of a given type, e.g., lakes, reservoirs, or for all the river corridor as a whole, as weighted by their surface areas as shown in Equation (4). As for any weighting factor the sum of the surface-area weights equals one, i.e., $\sum_j^{N_i} \sum_m w_{m,j} = 1$. Newly accounted for high-resolution small ponds and streams were aggregated per medium-resolution NHD catchment following Equation (3) prior to accumulating downstream, which provides an accurate approach to quantify and accumulate high-resolution information while retaining a linkage to the medium-resolution framework.

The cumulative water residence timescale is useful for estimating how the distribution of various waterbody types in the river basin, or how a change in waterbodies over time, affects the average water residence timescale. When computed for all upstream lotic and lentic waterbodies, equation [3] computes the cumulative river corridor water residence timescale. The cumulative hydraulic load is estimated as the inverse of the cumulative water residence timescale.

Present-Day and Historic Analysis

We quantified changes over time in river corridor surface water areal densities, water residence timescales, and hydraulic loads by comparing present-day conditions to estimated conditions approximately a century ago. The present-day river corridor is defined as containing the existing database of lakes, reservoirs, historic small ponds, managed small ponds, and streams and rivers. For our purposes the early twentieth century river corridor is defined as containing existing lakes, historic small ponds, and present-day streams and rivers. Also included are the estimated stream and river reaches that were displaced by construction of reservoirs or managed small ponds. The surface areas of displaced stream and river reaches were approximated using the flowline length provided by NHD that intersects the corresponding lentic waterbody, an estimate of stream velocity from Jobson (1996) and a width estimate from Leopold and Maddock (1953) and the present-day discharge estimate. Both present-day and early twentieth century river corridor estimates assume the same average annual discharge, which is uncertain but is a practical assumption for these purposes. Also, the early twentieth century river corridor estimates assume that the construction of reservoirs and small ponds always replaced a stream or river, which may overestimate the increase in river corridor surface areas in cases where lakes or historic small ponds were expanded by dam construction to create an even larger reservoir (Hayes et al., 2017). To our knowledge there are no comprehensive pre-1900 data to estimate the areas of historic lakes and ponds that were expanded by reservoir construction and thus we assume that only streams and rivers were replaced.

The change in areal coverage from early twentieth century to present, ΔD, and change in residence timescale, ΔR_w, were estimated as:

$$\Delta D_i = \frac{D_{pres,i} - D_{his,i}}{D_{his,i}} \, x \, 100\% \quad (5)$$

$$\Delta R_{w,i} = \frac{R_{wpres,i} - R_{whis,i}}{R_{whis,i}} \, x \, 100\% \quad (6)$$

where D_{pres} and D_{his} [%] are the areal coverages of present-day and historic early twentieth century river corridors (i.e., both lentic and lotic waters), respectively; and R_{wpres} and R_{whis} [T L^{-1}] are the surface-area-weighted residence timescales of present-day and historic river corridors, respectively.

RESULTS

River Corridor Areal Coverage

The total areal coverage of river corridors is 1.8% across the CONUS of which more than two-thirds (∼69%) are lentic waterbodies including lakes, reservoirs, and small ponds (**Table 1**). River corridor areal coverage varies from east to west with higher coverage in the more humid areas (2.2%) generally to the east of the 100th meridian and lower (1.2%) in the drier western basins (**Figure 3**). The river corridor areal coverage is highest (∼4%) in historically glaciated basins such as New England, Lower Mississippi, and Souris-Red-Rainy basins and lowest in the arid western interior in the Rio Grande and Upper and Lower Colorado basins (<1%) (**Figure 3**, **Table 1**).

Streams and rivers account for 31% of the river corridor surface area in the CONUS (areal coverage of 0.6%) with nearly twice the areal coverage in the east (0.7%) compared to the west (0.3%) (**Supplementary Table 1**). In contrast, lentic waterbodies account for 69% of the river corridor surface area (areal coverage of 1.3%) with generally higher coverages of lakes and reservoirs in the humid eastern basins (0.5 AND 0.7% for lakes and reservoirs, respectively) compared to the more arid western basins (0.4% for both lakes and reservoirs) (**Supplementary Table 1**). Small

ponds are distributed more unevenly across the CONUS, with areal coverages in the east (0.2%) that are approximately three times greater than in the west (0.06%) (**Supplementary Table 1**). Managed small ponds are even more unevenly distributed, with areal coverages that are approximately eight times more common in the east compared to the west (0.08 vs. 0.01%, respectively) (**Supplementary Table 1**).

Lake areal coverage is greatest in historically glaciated New England, Great Lakes, and the Souris-Red-Rainy basins (∼2%), and also in humid eastern areas of the Upper and Lower Mississippi and Tennessee basins where lake coverage generally exceeds 1%, and in isolated areas of the west such as the Great Basin (**Supplementary Table 1**). Reservoir areal coverage is highest (>1.7%) in coastal New England, eastern Pennsylvania, eastern Texas, Oklahoma, and Kansas, and in the South Atlantic and Tennessee basins (**Figure 3**, **Supplementary Table 1**). Small pond areal coverages are everywhere less than lakes and reservoirs but may be similar to reservoirs or higher in certain areas of New England, Great Lakes, South Atlantic, and Lower Mississippi basins, as well as in other areas of the Upper Midwest and eastern Texas (**Figure 3**, **Supplementary Table 1**).

River Corridor Hydraulic Loads and Water Residence Timescales

The median hydraulic load for streams and rivers is 1 m d^{-1} and varies between 0.1 and 100 m d^{-1} across the CONUS (**Figure 4b**). The median hydraulic load for small ponds (0.08 m d^{-1}) is an order of magnitude lower than in streams and rivers, and it varies between 0.001 and 60 m d^{-1}. Lakes and reservoirs have the lowest median hydraulic load (0.03 m d^{-1}) that is approximately a third of small ponds (**Supplementary Table 2**) with a range between 0.001 and 10 m d^{-1} across the CONUS (**Figure 4b**).

The median water residence timescale is on the order of 1 d m^{-1} for streams and rivers, 13 d m^{-1} for small ponds, and 30 d m^{-1} for lakes and reservoirs across the CONUS (**Figure 4a**, **Table 2**). Water residence timescale varies between 0.01 and 10 d m^{-1} for streams and rivers, 0.01 to 1,000 d m^{-1} for small ponds, and 0.1 to 1,000 d m^{-1} for lakes and reservoirs (**Figure 4a**). However, lakes and reservoirs in the west generally have shorter residence timescales, indicating faster turnover in lentic waterbodies in the west compared to the east. Lakes and reservoirs together have a median residence timescale of 21 d m^{-1} in the west compared with 33 d m^{-1} in the east (**Table 2**). However, the median residence timescale for managed small ponds in the west is double that of the east (23 vs. 12 d m^{-1}, respectively) due to lower average runoff in the west. Our estimates of water residence timescale for individual lakes and reservoirs are similar to field-based estimates, ranging from 0.1 to 1,000 d m^{-1} (Brett et al., 2012). Small ponds have shorter water residence timescales compared with lakes and reservoirs, which agrees with the field-based estimates of Fairchild and Velinsky (2006) who observed a maximum residence timescale of 800 d m^{-1} for small ponds during the low-flow season.

When compared between major river basins, lotic and lentic residence timescales are highly variable (**Supplementary Figure 1**). Western streams and rivers have a longer median residence timescale compared to the east (1.1 vs. 0.9 d m^{-1}, respectively). The median stream and river residence timescales range from a low of 0.4 d m^{-1} in New England to highs ranging from 3.5 to 4.3 d m^{-1} in the arid Rio Grande, Great Basin, and Lower Colorado, which reflects the lower average runoff in those more arid basins. Median lake and reservoir timescales range from a low of 9 d m^{-1} in the Great Lakes to highs of 82 and 83 d m^{-1} in the Missouri and Rio Grande basins, respectively; median small pond timescales range from a low of 2 d m^{-1} in New England to a high of 58 d m^{-1} in the Rio Grande basin (**Table 2**).

Not surprisingly, cumulative hydraulic load across much of the CONUS river corridor is dominated by streams and rivers (**Figure 4c**), where hydraulic loads on the order of 1 m d^{-1} indicate rapid hydraulic turnover and downstream flow through lotic elements of the river corridor. However, there are also vast areas where the cumulative hydraulic load is orders of magnitude lower, 0.006 m d^{-1} or less (most evident in the Great Plains, Upper Mississippi, and South Atlantic basins), indicating areas where lentic waterbodies have a much stronger influence on flow.

Lentic waterbodies impart their strongest influence on cumulative water residence timescales in areas where the lentic contribution to river corridor areal coverage is highest (**Table 1**, **Figure 5d** compared to **Figures 5a–c**). High lentic influence is apparent in the southern Great Plains and Upper Mississippi basins and South Atlantic basin where cumulative residence

TABLE 1 | Surface water areal coverage of river corridor and lentic waterbody percentage summarized as total values for CONUS, eastern and western regions, and major HUC-2 river basins (delineations shown in **Figure 2**).

River basin	HUC-2 basin	River corridor areal coverage (%)	Lentic percent of river corridor (%)
New England	01	4.1	81
Mid Atlantic	02	2.2	60
South Atlantic	03	2.6	68
Great Lakes	04	2.9	70
Ohio	05	1.9	38
Tennessee	06	3.3	75
Upper Mississippi	07	2.3	68
Lower Mississippi	08	4.3	56
Souris-Red-Rainy	09	4.0	93
Missouri	10	1.2	72
Arkansas-White-Red	11	1.5	68
Texas-Gulf	12	1.8	77
Rio Grande	13	0.3	62
Upper Colorado	14	0.8	68
Lower Colorado	15	0.5	71
Great Basin	16	2.5	95
Pacific Northwest	17	1.5	52
California	18	1.7	80
CONUS		1.8	69
East of 100th Meridian		2.2	68
West of 100th Meridian		1.2	71

Eastern and western regions are defined by basin position relative to the 100th Meridian.

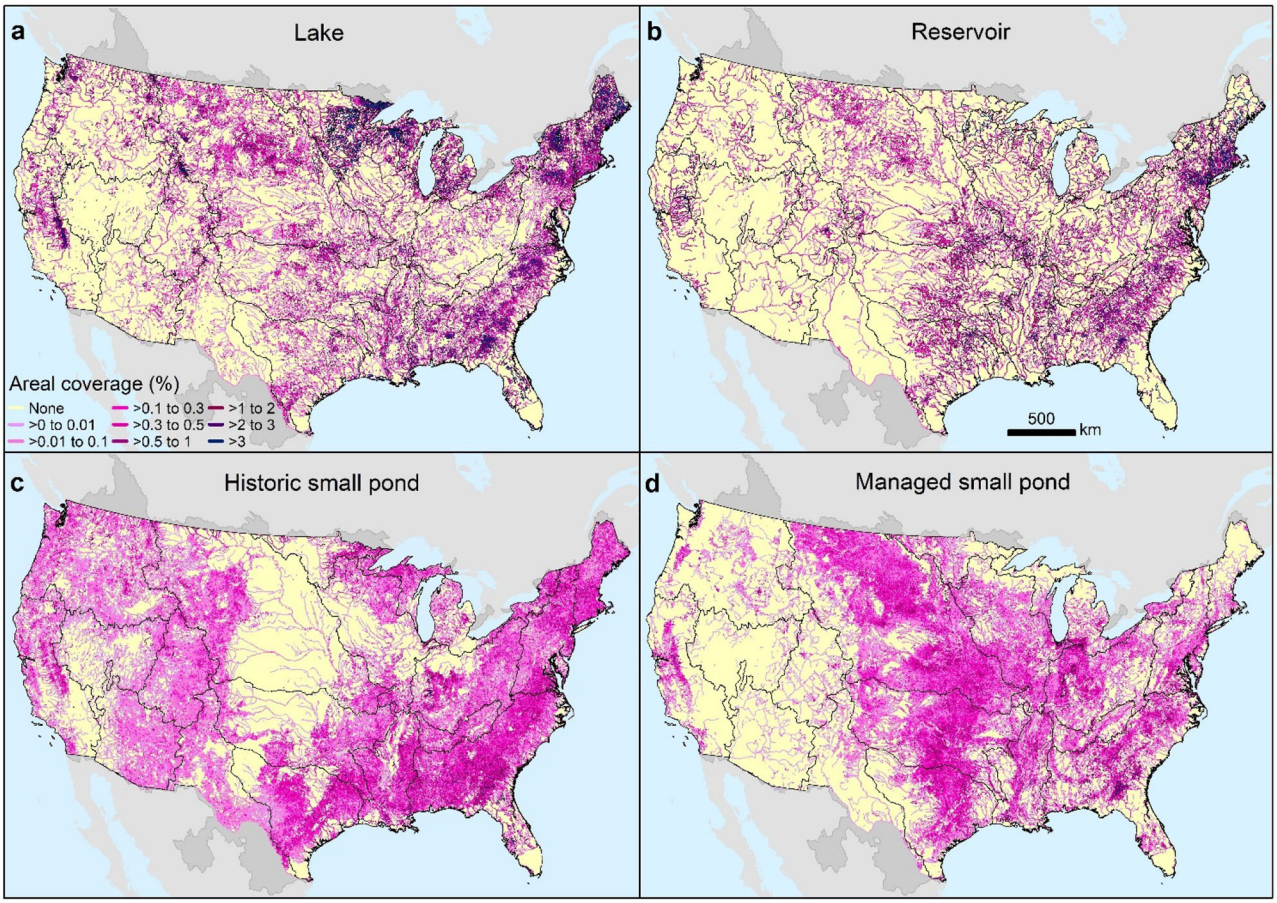

FIGURE 3 | Mapped distribution of surface water areal coverage for lakes **(a)**, reservoirs **(b)**, historic small ponds **(c)**, and managed small ponds **(d)**. The lentic percentage of total river corridor area varies little across the CONUS with reservoirs accounting for most of the lentic surface area (48%) followed by lakes (40%) and small ponds (12% total small ponds with 8% historic small ponds and 4% managed small ponds (**Table 1**). Black boundaries designate the eighteen 2-digit hydrologic unit code (HUC-2) major river basins of the CONUS.

timescales are as high as 365 d m^{-1}, which is two orders-of-magnitude slower than lotic dominated areas with values on the order of 1 d m^{-1} (**Figure 5d**). Small ponds and reservoirs dominate water residence timescales in the Great Plains basins (Texas-Gulf, Arkansas-White-Red, and Missouri basins) and in the Upper Colorado and Rio Grande basins while lakes dominate in the Upper Mississippi and New England basins. In contrast, all types of lentic waterbodies are important in lengthening water residence timescales in the South Atlantic basin.

Dramatic Reshaping of River Corridors During the Twentieth Century

The areal densities of lentic and lotic waters in river corridors changed substantially during the past century as a result of human disturbance. River corridors were altered much earlier, of course, and we summarize some of the important changes associated with European exploration, fur trading, and early settlement (pre 1600) and Colonial-era expansion (circa 1700) in **Figure 1** and in Discussion section Changing Balance of Lotic and Lentic Contributions. Our detailed quantitative analysis focuses on the twentieth century because the changes brought about by dam building and impoundments on CONUS river corridors (mostly after 1900) are well-constrained by our dataset. Expansion of waterbodies behind those dams caused an estimated 49% increase in river corridor surface area over the past century (**Table 3**). The largest total increases were in the western U.S. and Great Plains basins, led by a 119% increase in the river corridor surface area of the Lower Colorado basin, a 111% increase in the Arkansas-White-Red basin, and 99 and 96% increases in the Missouri and Texas-Gulf basins. Other areas experienced comparatively smaller increases in river corridor surface area over the past century, including the Great Basin (16%), Rio Grande and Lower Mississippi basins (35 and 13%), and Great Lakes basin (31%).

Reservoirs were the greatest contributor to the expansion in river corridor surface area over the past century, contributing on average 91% of the change across the CONUS basins. For example, almost 100% of the increase in the river corridor surface area of the Upper Colorado basin was accounted for by reservoirs. In contrast, small ponds contributed much less

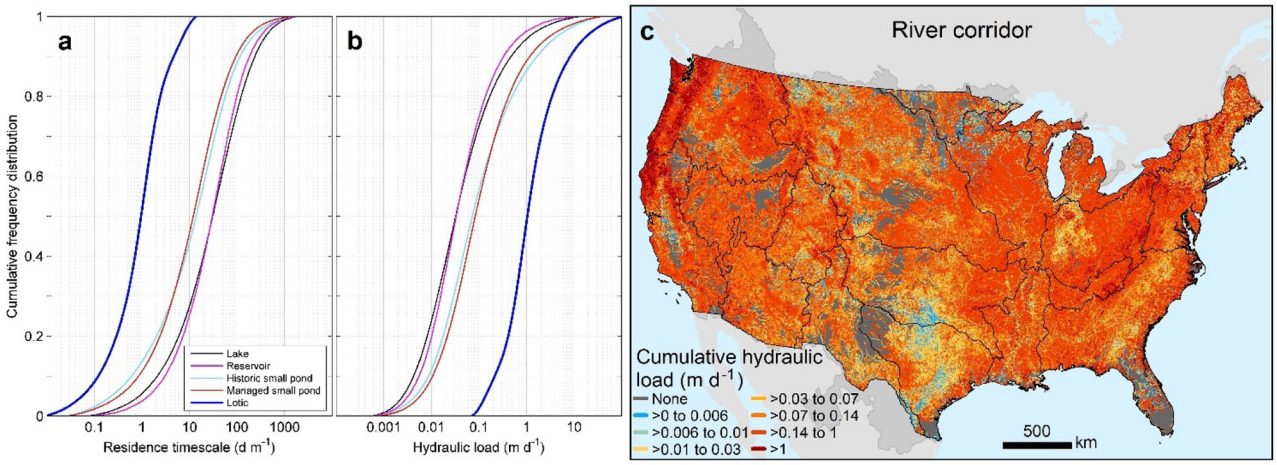

FIGURE 4 | Frequency distributions of residence timescale **(a)** and hydraulic load **(b)** of individual waterbodies and cumulative hydraulic load across the CONUS **(c)**. The cumulative hydraulic load is the inverse of the cumulative area-weighted residence timescale across the CONUS shown in **Figure 5d**. Black boundaries designate HUC-2 river basins.

TABLE 2 | Summary table of the median water residence timescale for individual lotic and lentic features of the CONUS, eastern and western regions, and major river basins.

		Water residence timescale, median (d m^{-1})				
River basin	**HUC-2 basin**	**Lake**	**Reservoir**	**Historic small pond**	**Managed small pond**	**Stream and river**
New England	01	14	11	2	3	0.4
Mid Atlantic	02	16	12	6	7	0.6
South Atlantic	03	33	21	18	18	0.7
Great Lakes	04	18	9	2	18	0.7
Ohio	05	14	18	14	22	0.7
Tennessee	06	15	12	10	10	0.8
Upper Mississippi	07	37	32	12	15	1.0
Lower Mississippi	08	22	24	27	25	0.8
Souris-Red-Rainy	09	30	36	20	3	0.9
Missouri	10	82	82	8	7	1.4
Arkansas-White-Red	11	49	42	18	16	1.4
Texas-Gulf	12	47	62	23	26	1.5
Rio Grande	13	48	83	58	28	4.3
Upper Colorado	14	29	25	7	21	1.7
Lower Colorado	15	48	22	19	12	3.9
Great Basin	16	23	20	5	42	3.5
Pacific Northwest	17	12	17	6	13	0.7
California	18	19	24	8	31	1.0
CONUS		31	30	14	12	1.0
East of 100th Meridian		33	31	14	12	0.9
West of 100th Meridian		21	24	11	23	1.1

to expanded surface areas, ranging from 0.1 to 0.5% (Great Basin and New England basins) to 15 and 17% (Arkansas-White-Red and Missouri basins) (**Table 3**). In the Great Plains basins reservoirs dominated change but accounted for a somewhat smaller percentage of the increase (82 to 87%) with managed small ponds accounting for the rest, e.g., managed small ponds contributed 15 and 17% to increases in river corridor surface area in the Arkansas-White-Red and Missouri basins, respectively.

Increases in river corridor surface areas caused by construction of reservoirs and small ponds were partially offset by the loss of the stream and rivers that were present before construction and that were replaced by the lentic waterbodies.

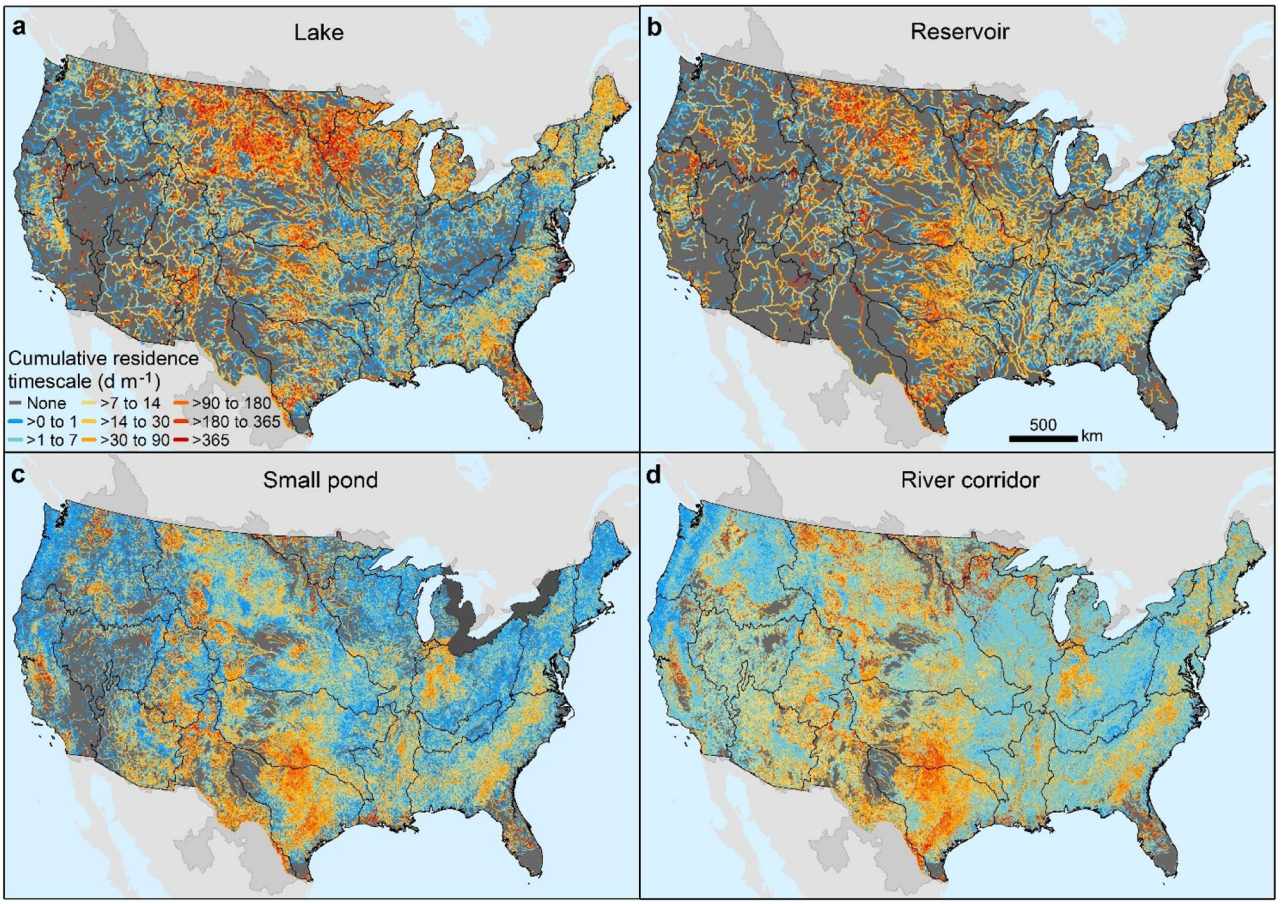

FIGURE 5 | Cumulative area-weighted water residence timescale for lakes **(a)**, reservoirs **(b)**, small ponds **(c)**, and the river corridor **(d)**. Black boundaries designate HUC-2 river basins.

We estimate that ∼8% of the total stream and river surface area in 1900 was eliminated by construction of small ponds and reservoirs during the twentieth century (**Table 3**). The estimated loss of stream and river surface area assumes that constructed waterbodies only replaced rivers and streams, rather than expanding on historic lakes and ponds, however, no comprehensive datasets are available to identify or estimate those replaced lentic waterbodies.

Together, reservoirs and small managed ponds substantially increased the cumulative water residence timescale of CONUS river corridors (**Figure 6**). Increases in cumulative residence timescale of a factor of five or more occurred throughout the Great Plains, Midwest, New England, Mid-Atlantic, and South Atlantic basins and in isolated areas in the west. Reservoirs dominated those increases in southern New England and in certain areas of the South Atlantic and Great Plains basins (**Figures 6a,b**). Small ponds dominated water residence timescale increases in the western Great Plain grasslands, and in the Midwest, and Mid-Atlantic, Pacific Northwest, and California agricultural areas, and in urbanizing basins across the CONUS (**Figures 6a,c**).

DISCUSSION

River corridor studies typically overlook the lentic waterbodies that fragment river networks (Baker et al., 2016; Gardner et al., 2019). In fact watershed hydrologists often ignore the lake, reservoir, and small pond effects; transit times are assumed to be short through a stream and river network only (Kirchner et al., 2001; Lindgren and Destouni, 2004; Lindgren et al., 2004; Knapp et al., 2019). As a result, hydrologic models now being built for larger drainage basins often assume that stream water exits the catchment in 10 days or less (Maxwell et al., 2016). Actual transit times through watersheds are likely much slower because of storage in lentic waterbodies (Schmadel et al., 2018) but also because of storage caused by river exchange with hyporheic zones (Gomez-Velez et al., 2015) and floodplains (Scott et al., 2019).

Our study found that the river corridor's surface area in the CONUS grew by 49% during the twentieth century as a result of the construction of reservoirs and managed small ponds. At present the total of lakes, reservoirs, and historic and managed small ponds comprise two thirds of the river corridor's surface area. The past century saw a transition toward more lentic waterbodies in CONUS river corridors. We estimated a 45%

TABLE 3 | Approximate change since early twentieth century in river corridor surface water areal coverage for the CONUS, eastern and western regions, and major river basins.

River basin	HUC-2 basin #	Percent change in areal coverage (%)			
		Total change in river corridor (%)	Change due to reservoirs (%)	Change due to managed small ponds (%)	Change in streams (%)
New England	01	71.8	71.3	0.5	−8.6
Mid Atlantic	02	27.5	25.3	2.2	−3.6
South Atlantic	03	57.4	53.4	4.1	−11.0
Great Lakes	04	31.3	29.7	1.6	−5.4
Ohio	05	34.8	28.4	6.4	−7.5
Tennessee	06	60.2	58.8	1.4	−36.4
Upper Mississippi	07	40.7	37.4	3.3	−3.3
Lower Mississippi	08	12.7	10.5	2.2	−1.6
Souris-Red-Rainy	09	30.9	29.3	1.6	−4.0
Missouri	10	98.9	82.4	16.6	−14.2
Arkansas-White-Red	11	111.3	96.6	14.7	−12.7
Texas-Gulf	12	95.7	86.6	9.1	−8.5
Rio Grande	13	34.5	32.6	1.9	−3.9
Upper Colorado	14	81.9	81.1	0.8	−12.0
Lower Colorado	15	119.2	118.7	0.5	−15.2
Great Basin	16	15.6	15.5	0.1	−3.7
Pacific Northwest	17	32.1	31.4	0.7	−6.4
California	18	83.8	80.7	3.1	−6.7
CONUS		49.0	44.8	4.2	−8.5
East of 100th Meridian		51.4	46.1	5.3	−8.8
West of 100th Meridian		41.3	40.4	1.0	−7.2

and 4% increase in areal coverage of river corridors brought about by a century of construction of reservoirs and small ponds, respectively. The changes in water residence times caused by the addition of reservoirs and small ponds was even more substantial, doubling or quadrupling the water residence timescale over large areas of the CONUS with local increases in water residence time scale of more than an order of magnitude (**Figure 6**).

Overall, present-day lentic waterbodies on the river corridor lengthen the water transit times through watersheds by months or even years rather compared with the 10 days or less often assumed by many CONUS hydrologic models. In addition to lengthening transit times, the lentic waters moderate downstream flow variability in river corridors by lowering the flow peaks exacerbated by impervious surfaces and piped and tiled drainage (Graf, 2006; Poff et al., 2006, 2007; Eng et al., 2013). Lentic waters in river corridors often elevate and shorten the frequency of low flows, although low-flow responses are variable and can depend on hydroclimatic condition and management style of dams (Eng et al., 2013).

Changing Balance of Lotic and Lentic Contributions

How the lentic functions of river corridors evolved with human activities is the key question addressed by our paper. A rapid and large scale transition in river corridors began about four centuries ago in the eastern U.S. with fur trapping that eradicated beaver colonies and their ponds (Naiman et al., 1988). Using beaver population and beaver pond area numbers from the published literature (Naiman et al., 1988; Whitfield et al., 2015; Goldfarb, 2018) we estimate a total areal coverage of the pre-Colonial river corridor similar to the present day (1.72 vs. 1.85% for present day) but with very different makeup. Approximately a third of the pre-Colonial river corridor surface area was comprised of beaver ponds (see **Supplementary Material**) compared to the present-day river corridor where reservoirs now comprise 33% of the total river corridor surface area and beaver ponds are a minor contributor. Human activities caused the river corridor to shrink dramatically (26%) in surface area between 1700 and 1900 because of beaver extirpation, followed by dam building that stabilized the surface area and then caused a dramatic increase in river corridor surface area after 1900 (**Figure 1**). Below we evaluate those changes in more detail.

The era of European exploration and early settlement of North America gave way toward larger scale Colonial era settlements that expanded along river corridors (Fang and Jawitz, 2019). Many thousands of low-head dams were constructed every 5 km or so on streams of the eastern U.S. to power grain mills that operated for decades (Copenheaver et al., 2007). Most of the mill dams were abandoned by the latter nineteenth century, but the sediments captured by the mill ponds that had been mobilized by deforestation on the surrounding uplands remained. After dam breakup the legacy sediments were downcut by the streams, transforming river corridors that previously had exhibited a hybrid lotic-lentic character (e.g., wide, anabranching,

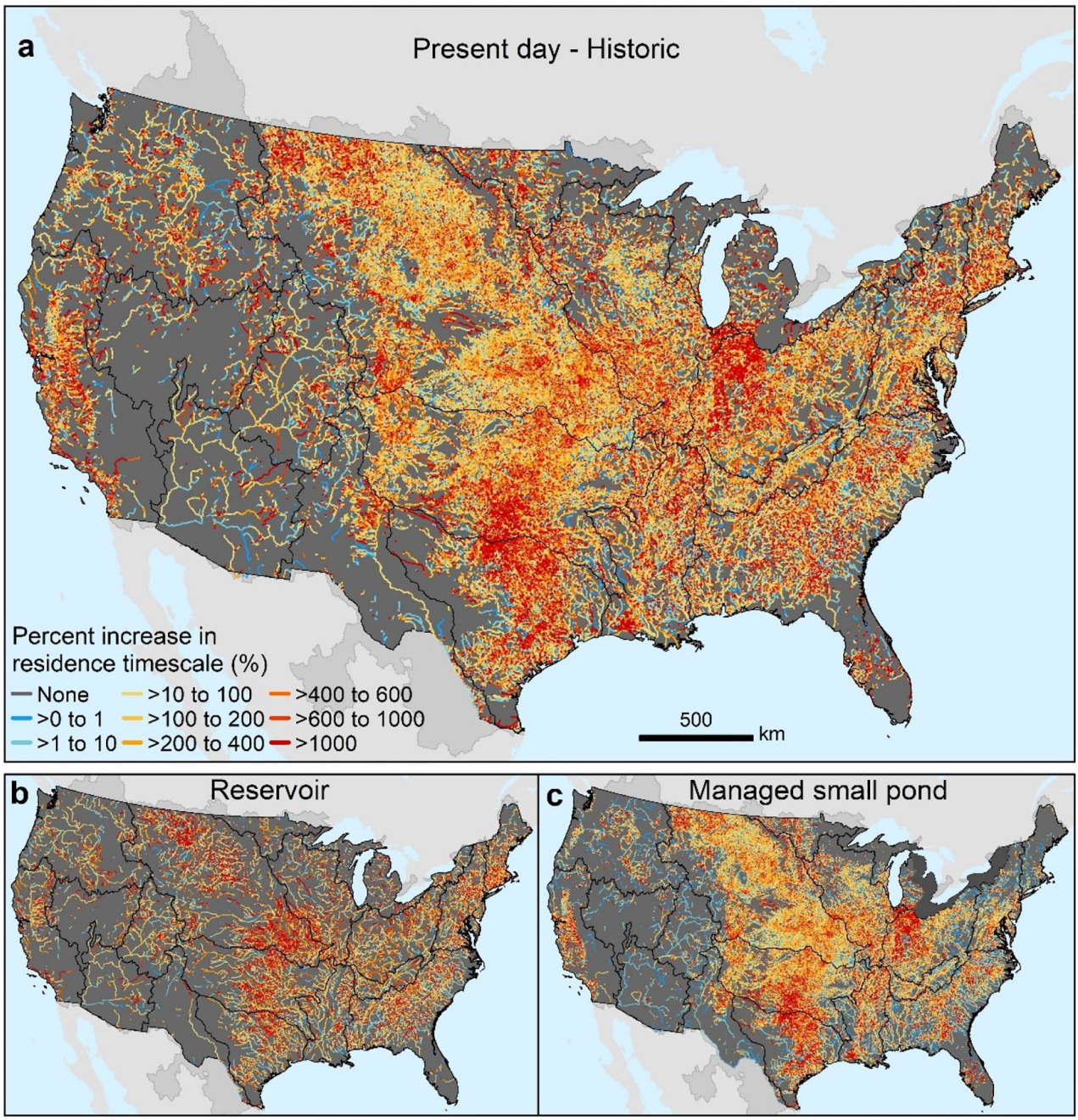

FIGURE 6 | Estimated change, in percent, in river corridor water residence timescale during the twentieth century **(a)** and estimated twentieth century change in reservoir and managed small pond water residence timescale associated with construction of reservoirs and management of small ponds **(b,c)**. Black boundaries designate HUC-2 river basins.

slow-flowing streams and beaver ponds) into less sinuous and faster-flowing streams flowing through single thread channels between tall cutbanks (Marris, 2008; Merritts et al., 2013).

The nineteenth and early twentieth centuries saw increased ditching and drag lining to drain ponds and wetlands and to increase drainage and flood conveyance away from the expanding agricultural lands and settled areas. Likewise, a century of logging in many forested watersheds changed the river corridors from spatially heterogeneous, multichannel systems closely connected to their floodplains into single-thread channels (Wohl, 2020) that adjusted to higher peak runoff by eroding bed and banks and incising until becoming disconnected from floodplains.

Increasingly their morphologies became pipe-like, which further exacerbated flooding and translated erosion to downstream areas (Merritts et al., 2013).

On the rivers there was extensive dam construction in the early to mid-twentieth century to expand water supply, control floods, improve navigation, and increase recreation for growing population centers (Lehner et al., 2011; U.S. Army Corps of Engineers, 2020). The era of big dams and resulting flow discontinuities wreaked havoc on biological communities, threatening native river organism dispersal and biodiversity worldwide (Collier et al., 1996; Magilligan and Nislow, 2005; Graf, 2006; Poff et al., 2007, 2015). Later the negative consequences and diminished values of river corridors drove more environmentally conscious engineering in the lentic components of river corridors, e.g., tens of thousands of lentic stormwater retention features were constructed on small streams to moderate and reduce peak flows, sustain low flows, and retain sediment and contaminants in order to lengthen storage times and improve downstream water quality (Villarreal et al., 2004; Liu et al., 2014). Most recently a new era of dam removal has begun (Bellmore et al., 2017; Ho et al., 2017).

To summarize, by the early twentieth century human activities had decreased the surface areas of the CONUS river corridor to a low point. The pre-Colonial river corridor surface area had been on the order of 26% larger because of widespread beaver activity, and dam building after 1900 expanded the river corridor surface area by ∼49%. The pre-Colonial and present-day river corridor may have been similar in size compared with the early twentieth century, however, it differed substantially in that beaver ponds comprised on the order of a third (31%) of the pre-Colonial river corridor surface area, whereas reservoirs are the dominant waterbody type contributing to present-day river corridors (33%).

Lotic and Lentic Drivers of Water Quality in River Corridors

The ubiquitous imprint of lakes, reservoirs, and small ponds often has been ignored in watershed biogeochemical modeling [but see Harrison et al. (2009) and Seitzinger et al. (2005)]. Recent modeling studies suggest a critical role for ponded waters in structuring nutrient cycles and aquatic health through river networks (Schmadel et al., 2019; Anderson et al., 2020). Lentic waters affect primary productivity, storage and release of nutrients, and also tendencies for out-of-balance ecological behaviors such as hypoxia and harmful algal blooms (HABs). Our analysis suggests a particularly important role for managed small ponds in modifying aquatic biogeochemistry. This is because of the sheer abundance of small ponds and because of their location in headwaters that are the locus of water and chemical inflows to river corridors through runoff and groundwater inflow (Alexander et al., 2007). Small ponds are therefore the early receptors and processors of watershed outputs of constituents and may dominate nutrient reactivity and sediment dynamics in some regions (Schmadel et al., 2019). Even though reservoirs dominated the growth in river corridor surface area in the twentieth century, those reservoirs are few in number (∼34,000) compared to small ponds (1.7 million) that impact approximately (82,000 km that are replaced by reservoirs compared to 81,000 km that are replaced by managed small ponds). Reservoir effects are concentrated farther downstream on relatively few larger streams and mid-size rivers compared with small ponds where effects are distributed widely across headwaters where the principal inputs of water and chemicals enter the river corridor (**Figure 4**).

Continental-scale analyses of lotic vs. lentic contributions to water quality and ecological health of river corridors are in a nascent stage (Baker et al., 2016; Bernhardt et al., 2018). Previous authors have discussed how to potentially integrate all the important water-quality and biological processes that influence function in several key metrics. Hydrologic connectivity is an example (Alexander et al., 2015; Harvey and Gooseff, 2015; Covino, 2017; Ward and Packman, 2019) but rarely has it been actually quantified for river corridors. Harvey et al. (2019) quantified turbulent exchange, hyporheic, and floodplain contributions to hydrologic connectivity, however lentic waters were not included. Lake and reservoir influences on water quality of river corridors were modeled using connectivity metrics such as lentic waterbody aerial coverage (Schmadel et al., 2018, 2019), lentic waterbody perimeter (Winslow et al., 2014), individual waterbody shape (Cohen et al., 2015), and lentic waterbody centeredness on the network (Schmadel et al., 2018). Schmadel et al. (2018) used the lentic connectivity metrics to model outcomes for nitrogen transport and reaction through the northeastern U.S. Those authors evaluated the significance of the lentic connectivity metrics on nitrogen budgets and also compared outcomes of their northeastern river corridor model with the same corridor modeled with replacement of lentic water bodies by appropriately sized streams or rivers. The areal coverage of lentic waterbodies, their size and shape characteristics (perimeter), and centeredness on the river network were all indicated as being important in affecting biogeochemical and energy exchanges with the terrestrial landscape and with the lotic river network. Our paper lays the groundwork for quantifying effects of hydrologic alteration of lentic waterbodies everywhere in the CONUS, using a high-resolution network that is ready for integrated modeling of flow, water quality, and aquatic health. The challenge grows with new understanding that the constructed lentic waterbodies are more vulnerable to harmful and undesirable outcomes (e.g., hypoxia and cyanobacteria blooms) than their lotic countertypes, which has long-term implications for river corridor health (Bernhardt, 2013; Finlay et al., 2013).

Summary and Needs for the Future

Our research builds on the pioneering work of Downing et al. (2006); Downing et al., 2010 who set a framework for large-scale quantification of river corridor attributes and functions. We used emerging data sources to improve the resolution of surface water areas and integrated those with an analysis of water residence timescales, both individually and cumulatively for lotic and lentic components of U.S. river corridors. Our change-over-time analysis observed the effects of humans driving large swings in physical character of river

corridors. Several 100 years ago a rebound toward lotic features in small streams during the twentieth century caused by enhanced runoff peaks from tiled farm fields, roadside ditches, and urban impervious areas. The mid twentieth century saw the peak of the era of big dam building on mid-size and larger rivers that expanded water supply and hydropower production and construction of small ponds that expanded livestock grazing into the drier western grasslands. During the latter twentieth century, environmentally conscious engineering and regulatory measures instigated massive investments in building small ponds for stormwater retention in urban and agricultural areas.

Our analysis demonstrated a net result of human disturbances in river corridors during the twentieth century – a 49% total increase in areal coverage of CONUS river corridors and a doubling to quadrupling in water residence timescales, or more, brought about by construction of reservoirs and managed small ponds. Lakes and reservoirs now dominate the river corridor surface area. However, small ponds occupy a greater number of stream kilometers compared with reservoirs (175,000 km in total for small ponds compared to 82,000 km for reservoirs). The surface area of small ponds is currently growing at a faster rate compared with reservoirs, and their collective influence on water residence time dominates the lentic waterbody influence in the headwaters where most water and chemical inputs occur.

Our estimates of hydraulic load (and its inverse, water residence timescale) for the CONUS are a first step toward improved assessment of physical controls on biogeochemistry and water quality of the river corridor. High-resolution small pond surface areas, alone, can vastly improve greenhouse gas evasion estimates (Holgerson and Raymond, 2016). Improved accuracy of flow and depth estimation through the much longer high-resolution river corridor will permit, for the first time, the accurate quantification of water residence time (and not just *timescale*) as well as travel times – estimation of contaminant fate and transport from river spills and non-point sources can be vastly improved with more accurate travel times. Also, better estimated river, lake, reservoir and small pond depths will themselves aid in quantifying the water volume to sediment area ratio in millions of waterbodies – a key metric needed to upgrade the physical basis for biogeochemical reaction modeling and its cumulative downstream effects on water quality. There is also need for expanding the analysis of hydrologic exchange fluxes (HEFs) beyond rivers and their sediment beds and banks (e.g., Gomez-Velez et al., 2015) to include lakes, reservoirs, and small ponds, as well as into riparian wetlands and floodplains. Accurate quantification of both "connectivity" and "reactivity" in the most highly biogeochemically active sub-environments of rivers corridors will determine where and when (and what the management opportunities are) for specific reactions such as denitrification (e.g., Bernhardt et al., 2018; Harvey et al., 2019) across the lotic and lentic features of river corridors. Furthermore, most CONUS-scale models of water quality are static models for average annual flow conditions, which will not be sufficient in the future as there is substantial need for representing flow dynamics (Walker et al., 2020), including reservoir operations and seasonally changing runoff and human water use.

There is increasing opportunity to integrate ecological and water-quality processes in models for large basins. Light and temperature are fundamental physical controls on biogeochemistry and ecological health that are still not yet well-predicted at large scales. In addition to comprehensive modeling of water temperature and its controls, modeling of light availability to river corridors is needed including effects of shading by topography and riparian trees and light attenuation within the water column. Also needed is modeling of vertical mixing in lotic and lentic waterbodies, including stratification and gas exchange (reaeration) and modeling of dissolved oxygen dynamics to help increase understanding of river corridor energetics and health through estimation of aquatic ecosystem respiration and gross primary production. Metrics of aquatic ecosystem health, e.g., contaminant bioaccumulation and toxicology metrics and indices of tolerance to water-quality disturbances for aquatic insects and fish communities, also need better integration with water quality modeling. Many existing data sets have yet to be assimilated and harmonized to make them nationally consistent. New data collection priorities need assessment to fill gaps for trends analysis that will increase the power of integrated, large-basin modeling of water availability and ecosystem health.

Our results set the stage for addressing emerging challenges with models and analysis tools that represent the full continuum of river corridor features and functions across the 10 million kilometers of CONUS river corridors, including water storage and purification functions, habitat, and resilience to out-of-balance ecosystem behaviors such as hypoxia and harmful aquatic blooms. The focus for the future will be improved forecasting capabilities that anticipate the likely challenges and prioritize strategies for preservation or restoration of river corridor functions.

DATA AVAILABILITY STATEMENT

Publicly available datasets were analyzed in this study. This data can be found here: The medium and high-resolution datasets used to produce analyses and results for this study are publicly available and can be found in the National Hydrography Dataset repository [https://nhd.usgs.gov] with additional attributes defined by Wieczorek et al. (2018) found in https://doi.org/10.5066/F7765D7V. Expressions and equation in the Methods can be used to reproduce results. In addition, the compiled information used for our study are available in the ScienceBase repository at https://doi.org/10.5066/P9TCH5J7.

AUTHOR CONTRIBUTIONS

JH conceived the study and wrote the manuscript first draft. JH and NS contributed equally to the study design, data assimilation, data analysis, interpretation, and revision of the manuscript. Both authors contributed to the article and approved the submitted version.

FUNDING

JH was supported by the U.S. Geological Survey (USGS) Water Availability and Use Science Program (WAUSP). NS was supported by a USGS Water Mission Area Mendenhall Post-doctoral Fellowship.

ACKNOWLEDGMENTS

The authors gratefully acknowledge their colleagues from the Watershed Storage Controls and River Corridor Synthesis working groups at the John Wesley Powell Center for Analysis and Synthesis for the early discussions that sparked this research. Also acknowledged are colleagues from the USGS Water Quality Gap Analysis project and the USGS Integrated Watershed Prediction program who have been generous with their interest and feedback. Any use of trade, firm, or product names is for descriptive purposes only and does not imply endorsement by the U.S. Government.

SUPPLEMENTARY MATERIAL

The Supplementary Material for this article can be found online at: https://www.frontiersin.org/articles/10.3389/frwa.2020.580727/full#supplementary-material

REFERENCES

Alexander, L. C., Autrey, B., DeMeester, J., Fritz, K. M., Golden, H. E., Goodrich, D. C., et al. (2015). *Connectivity of Streams and Wetlands to Downstream Waters: A Review and Synthesis of the Scientific Evidence*. Washington, DC: Office of Research and Development U.S. Environmental Protection Agency EPA/600/R.

Alexander, R. B., Boyer, E. W., Smith, R. A., Schwarz, G. E., and Moore, R. B. (2007). The Role of Headwater Streams in Downstream Water Quality. *J. Am. Water Resour. Assoc.* 43, 41–59. doi: 10.1111/j.1752-1688.2007.00005.x

Anderson, N. J., Heathcote, A. J., and Engstrom, D. R. (2020). Anthropogenic alteration of nutrient supply increases the global freshwater carbon sink. *Sci. Adv.* 6:eaaw2145. doi: 10.1126/sciadv.aaw2145

Arp, C. D., Gooseff, M. N., Baker, M. A., and Wurtsbaugh, W. (2006). Surface-water hydrodynamics and regimes of a small mountain stream–lake ecosystem. *J. Hydrol.* 329, 500–513. doi: 10.1016/j.jhydrol.2006.03.006

Baker, M. A., Arp, C. D., Goodman, K. J., Marcarelli, A. M., and Wurtsbaugh, W. A. (2016). "Stream-lake interaction: understanding coupled hydro-ecological systems," in *Stream Ecosystems in a Changing Environment*, eds J. B. Jones, and E. H. Stanley (Amsterdam: Academic Press), 321–348. doi: 10.1016/B978-0-12-405890-3.00007-5

Beaulieu, M., Pick, F., and Gregory-Eaves, I. (2013). Nutrients and water temperature are significant predictors of cyanobacterial biomass in a 1147 lakes data set. *Limnol. Oceanogr.* 58, 1736–1746. doi: 10.4319/lo.2013.58.5.1736

Bellmore, J. R., Duda, J. J., Craig, L. S., Greene, S. L., Torgersen, C. E., Collins, M. J., et al. (2017). Status and trends of dam removal research in the United States. *WIREs Water* 4:e1164. doi: 10.1002/wat2.1164

Bencala, K. E. (1993). A perspective on stream-catchment connections. *J. North Am. Benthol. Soc.* 12, 44–47. doi: 10.2307/1467684

Berg, M. D., Popescu, S. C., Wilcox, B. P., Angerer, J. P., Rhodes, E. C., McAlister, J., et al. (2016). Small farm ponds: overlooked features with important impacts on watershed sediment transport. *J. Am. Water Resour. Assoc.* 52, 67–76. doi: 10.1111/1752-1688.12369

Bernhardt, E. S. (2013). Cleaner Lakes Are Dirtier Lakes. *Science* 342, 205–206. doi: 10.1126/science.1245279

Bernhardt, E. S., Heffernan, J. B., Grimm, N. B., Stanley, E. H., Harvey, J. W., Arroita, M., et al. (2018). The metabolic regimes of flowing waters. *Limnol. Oceanogr.* 63, S99–S118. doi: 10.1002/lno.10726

Boano, F., Harvey, J. W., Marion, A., Packman, A. I., Revelli, R., Ridolfi, L., et al. (2014). Hyporheic flow and transport processes: mechanisms, models, and biogeochemical implications. *Rev. Geophys.* 52, 603–679. doi: 10.1002/2012RG000417

Brakebill, J. W., Schwarz, G. E., and Wieczorek, M. E. (2018). *An Enhanced Hydrologic Network in Support of SPARROW Modeling*. U.S. Department of Interior, U.S. Geological Survey Scientific Investigations Report, 5127.

Brett, M. T., Arhonditsis, G. B., Chandra, S., and Kainz, M. J. (2012). Mass flux calculations show strong allochthonous support of freshwater zooplankton production is unlikely. *PLoS ONE* 7:e39508. doi: 10.1371/journal.pone.0039508

Cohen, M. J., Creed, I. F., Alexander, L. C., Basu, N., Calhoun, A. J. K., Craft, C., et al. (2015). Do geographically isolated wetlands influence landscape functions? *Proc. Natl. Acad. Sci. U.S.A.* 113, 1978–1986. doi: 10.1073/pnas.1512650113

Collier, M., Webb, R. H., and Schmidt, J. C. (1996). *Dams and Rivers: A Primer on the Downstream Effects of Dams*. U.S. Geological Survey. doi: 10.3133/cir1126

Copenheaver, C. A., Prisley, S. P., Pittman, J. R., Yonce, M. E., Issem, C. M. S., and Jensen, K. A. (2007). The geography of grist, flour, and saw mills. *Southeast. Geogr.* 47, 138–154. doi: 10.1353/sgo.2007.0004

Covino, T. (2017). Hydrologic connectivity as a framework for understanding biogeochemical flux through watersheds and along fluvial networks. *Geomorphology* 277, 133–144. doi: 10.1016/j.geomorph.2016.09.030

Dahl, T. E. (2011). *Status and Trends of Wetlands in the Conterminous United States 2004 to 2009*. Washington, DC: U.S. Department of Interior, Fish and Wildlife Service.

Downing, J., Prairie, T., Cole, J., Duarte, M., JL, T., Striegl, G., et al. (2006). The global abundance and size distribution of lakes, ponds, and impoundments. *Limnol. Oceanogr.* 51, 2388–2397. doi: 10.4319/lo.2006.51.5.2388

Downing, J. A. (2010). Emerging global role of small lakes and ponds: little things mean a lot. *Limnetica* 29, 9–24. doi: 10.23818/limn.29.02

Doyle, M. W. (2012). America's rivers and the American experiment. *J. Am. Water Resour. Assoc.* 48, 820–837. doi: 10.1111/j.1752-1688.2012.00652.x

Doyle, M. W., Stanley, E. H., Havlick, D. G., Kaiser, M. J., Steinbach, G., Graf, W. L., et al. (2008). Aging infrastructure and ecosystem restoration. *Science* 319, 286–287. doi: 10.1126/science.1149852

Dunne, T., Mertes, L. A. K., Meade, R. H., Richey, J. E., and Forsberg, B. R. (1998). Exchanges of sediment between the flood plain and channel of the Amazon river in Brazil. *GSA Bull.* 110, 450–467. doi: 10.1130/0016-7606(1998)110andlt;0450:EOSBTFandgt;2.3.CO;2

Eng, K., Wolock, D. M., and Carlisle, D. M. (2013). River flow changes related to land and water management practices across the conterminous United States. *Sci. Total Environ.* 463–464, 414–422. doi: 10.1016/j.scitotenv.2013.06.001

Fairchild, G. W., and Velinsky, D. J. (2006). Effects of small ponds on stream water chemistry. *Lake Reserv. Manag.* 22, 321–330. doi: 10.1080/07438140609354366

Fang, Y., and Jawitz, J. W. (2019). The evolution of human population distance to water in the USA from 1790 to 2010. *Nat. Commun.* 10:430. doi: 10.1038/s41467-019-08366-z

Finlay, J. C., Small, G. E., and Sterner, R. W. (2013). Human influences on nitrogen removal in lakes. *Science* 342, 247–250. doi: 10.1126/science.1242575

Foley, M., Bellmore, J., O'Connor, J., Duda, J., East, A., Grant, G., et al. (2017). Dam removal: listening in. *Water Resour. Res.* 53, 5229–5246. doi: 10.1002/2017WR020457

Gardner, J. R., Pavelsky, T. M., and Doyle, M. W. (2019). The abundance, size, and spacing of lakes and reservoirs connected to river networks. *Geophys. Res. Lett.* 46, 2592–2601. doi: 10.1029/2018GL080841

Goldfarb, B. (2018). Beavers, rebooted. *Science* 360, 1058–1061. doi: 10.1126/science.360.6393.1058

Gomez-Velez, J. D., Harvey, J. W., Cardenas, M. B., and Kiel, B. (2015). Denitrification in the mississippi river network controlled by flow through river bedforms. *Nat. Geosci.* 8, 941–945. doi: 10.1038/ngeo2567

Goodman, K. J., Baker, M. A., and Wurtsbaugh, W. A. (2011). Lakes as buffers of stream dissolved organic matter (DOM) variability: temporal patterns of DOM characteristics in mountain stream-lake systems. *J. Geophys. Res. Biogeosci.* 116:G00N02. doi: 10.1029/2011JG001709

Graf, W. L. (2006). Downstream hydrologic and geomorphic effects of large dams on American rivers. *Geomorphology* 79, 336–360. doi: 10.1016/j.geomorph.2006.06.022

Harrison, J. A., Maranger, R. J., Alexander, R. B., Giblin, A. E., Jacinthe, P.-A., Mayorga, E., et al. (2009). The regional and global significance of nitrogen removal in lakes and reservoirs. *Biogeochemistry* 93, 143–157. doi: 10.1007/s10533-008-9272-x

Harvey, J., Gomez-Velez, J., Schmadel, N., Scott, D., Boyer, E., Alexander, R., et al. (2019). How hydrologic connectivity regulates water quality in river corridors. *J. Am. Water Resour. Assoc.* 55, 369–381. doi: 10.1111/1752-1688.12691

Harvey, J., and Gooseff, M. (2015). River corridor science: hydrologic exchange and ecological consequences from bedforms to basins. *Water Resour. Res.* 51, 6893–6922. doi: 10.1002/2015WR017617

Hayes, N. M., Deemer, B. R., Corman, J. R., Razavi, N. R., and Strock, K. E. (2017). Key differences between lakes and reservoirs modify climate signals: a case for a new conceptual model. *Limnol. Oceanogr. Lett.* 2, 47–62. doi: 10.1002/lol2.10036

Ho, M., Lall, U., Allaire, M., Devineni, N., Kwon, H. H., Pal, I., et al. (2017). The future role of dams in the United States of America. *Water Resour. Res.* 53, 982–998. doi: 10.1002/2016WR019905

Holgerson, M. A., and Raymond, P. A. (2016). Large contribution to inland water CO_2 and CH_4 emissions from very small ponds. *Nat. Geosci.* 9:222. doi: 10.1038/ngeo2654

Homer, C. G., Dewitz, J. A., Yang, L., Jin, S., Danielson, P., Xian, G., et al. (2015). Completion of the 2011 national land cover database for the conterminous United States-representing a decade of land cover change information. *Photogramm. Eng. Remote Sens.* 81, 345–354. doi: 10.14358/PERS.81.5.345

Jobson, H. E. (1996). Prediction of traveltime and longitudinal dispersion in rivers and streams. *U.S. Geol. Surv. Water-Resources Investig. Rep.* 96–4013:69.

Karran, D. J., Westbrook, C. J., Wheaton, J. M., Johnston, C. A., and Bedard-Haughn, A. (2017). Rapid surface-water volume estimations in beaver ponds. *Hydrol. Earth Syst. Sci.* 21, 1039–1050. doi: 10.5194/hess-21-1039-2017

Kirchner, J. W., Feng, X., and Neal, C. (2001). Catchment-scale advection and dispersion as a mechanism for fractal scaling in stream tracer concentrations. *J. Hydrol.* 254, 82–101. doi: 10.1016/S0022-1694(01)00487-5

Knapp, J. L. A., Neal, C., Schlumpf, A., Neal, M., and Kirchner, J. W. (2019). New water fractions and transit time distributions at Plynlimon, Wales, estimated from stable water isotopes in precipitation and streamflow. *Hydrol. Earth Syst. Sci.* 23, 4367–4388. doi: 10.5194/hess-23-4367-2019

Lehner, B., Liermann, C. R., Revenga, C., Vörösmarty, C., Fekete, B., Crouzet, P., et al. (2011). High-resolution mapping of the world's reservoirs and dams for sustainable river-flow management. *Front. Ecol. Environ.* 9, 494–502. doi: 10.1890/100125

Leopold, L. B., and Maddock, T. (1953). The hydraulic geometry of stream channel and some physiographic implications. *Geol. Surv. Prof. Pap.* 252:64. doi: 10.3133/pp252

Leyk, S., Uhl, J. H., Connor, D. S., Braswell, A. E., Mietkiewicz, N., Balch, J. K., et al. (2020). Two centuries of settlement and urban development in the United States. *Sci. Adv.* 6:eaba2937. doi: 10.1126/sciadv.aba2937

Lindgren, G. A., and Destouni, G. (2004). Nitrogen loss rates in streams: scale-dependence and up-scaling methodology. *Geophys. Res. Lett.* 31:LI3501. doi: 10.1029/2004GL019996

Lindgren, G. A., Destouni, G., and Miller, A. V. (2004). Solute transport through the integrated groundwater-stream system of a catchment. *Water Resour. Res.* 40:W03511. doi: 10.1029/2003WR002765

Liu, Y., Yang, W., Yu, Z., Lung, I., Yarotski, J., Elliott, J., et al. (2014). assessing effects of small dams on stream flow and water quality in an agricultural watershed. *J. Hydrol. Eng.* 19:5014015. doi: 10.1061/(ASCE)HE.1943-5584.0001005

Livers, B., and Wohl, E. (2016). Sources and interpretation of channel complexity in forested subalpine streams of the southern rocky mountains. *Water Resour. Res.* 52, 3910–3929. doi: 10.1002/2015WR018306

Maavara, T., Parsons, C. T., Ridenour, C., Stojanovic, S., Dürr, H. H., Powley, H. R., et al. (2015). Global phosphorus retention by river damming. *Proc. Natl. Acad. Sci. U.S.A.* 112, 15603–15608. doi: 10.1073/pnas.1511797112

Magilligan, F. J., and Nislow, K. H. (2005). Changes in hydrologic regime by dams. *Geomorphology* 71, 61–78. doi: 10.1016/j.geomorph.2004.08.017

Marris, E. (2008). What does a natural stream look like? *Nature*. doi: 10.1038/news.2008.448

Marton, J. M., Creed, I. F., Lewis, D. B., Lane, C. R., Basu, N. B., Cohen, M. J., et al. (2015). Geographically isolated wetlands are important biogeochemical reactors on the landscape. *Bioscience* 65, 408–418. doi: 10.1093/biosci/biv009

Maxwell, R. M., Condon, L. E., Kollet, S. J., Maher, K., Haggerty, R., and Forrester, M. M. (2016). The imprint of climate and geology on the residence times of groundwater. *Geophys. Res. Lett.* 43, 701–708. doi: 10.1002/2015GL066916

Mendonça, R., Müller, R. A., Clow, D., Verpoorter, C., Raymond, P., Tranvik, L. J., et al. (2017). Organic carbon burial in global lakes and reservoirs. *Nat. Commun.* 8:1694. doi: 10.1038/s41467-017-01789-6

Merritts, D., Walter, R., Rahnis, M., Cox, S., Hartranft, J., Scheid, C., et al. (2013). The rise and fall of Mid-Atlantic streams: millpond sedimentation, milldam breaching, channel incision, and stream bank erosion. *Rev. Eng. Geol.* 21, 183–203. doi: 10.1130/2013.4121(14)

Moore, R. B., McKay, L. D., Rea, A. H., Bondelid, T. R., Price, C. V., Dewald, T. G., et al. (2019). *User's Guide for the National Hydrography Dataset Plus (NHDPlus) High Resolution*. U.S. Geological Survey Open-File Repert. doi: 10.3133/ofr20191096

Moore, T. L., Rodak, C. M., and Vogel, J. R. (2017). Urban stormwater characterization, control, and treatment. *Water Environ. Res.* 89, 1876–1927. doi: 10.2175/106143017X15023776270692

Naiman, R. J., Johnston, C. A., and Kelley, J. C. (1988). Alteration of North American streams by beaver. *Bioscience* 38, 753–762. doi: 10.2307/1310784

National Research Council (2002). *Riparian Areas: Functions and Strategies for Management*. Washington, DC: The National Academies Press

Nilsson, C., Reidy, C. A., Dynesius, M., and Revenga, C. (2005). Fragmentation and flow regulation of the world's large river systems. *Science* 308, 405–408. doi: 10.1126/science.1107887

Padowski, J. C., and Jawitz, J. W. (2012). Water availability and vulnerability of 225 large cities in the United States. *Water Resour. Res.* 48:W12529. doi: 10.1029/2012WR012335

Poff, N. L., Bledsoe, B. P., and Cuhaciyan, C. O. (2006). Hydrologic variation with land use across the contiguous United States: geomorphic and ecological consequences for stream ecosystems. *Geomorphology* 79, 264–285. doi: 10.1016/j.geomorph.2006.06.032

Poff, N. L., Brown, C. M., Grantham, T. E., Matthews, J. H., Palmer, M. A., Spence, C. M., et al. (2015). Sustainable water management under future uncertainty with eco-engineering decision scaling. *Nat. Clim. Chang.* 6:25. doi: 10.1038/nclimate2765

Poff, N. L., Olden, J. D., Merritt, D. M., and Pepin, D. M. (2007). Homogenization of regional river dynamics by dams and global biodiversity implications. *Proc. Natl. Acad. Sci. U.S.A.* 104, 5732–5737. doi: 10.1073/pnas.0609812104

Raymond, P. A., Oh, N.-H., Turner, R. E., and Broussard, W. (2008). Anthropogenically enhanced fluxes of water and carbon from the Mississippi River. *Nature* 451:449. doi: 10.1038/nature06505

Schmadel, N. M., and Harvey, J. W. (2020). *NHD-RC: Extension of NHDPlus Version 2.1 With High-Resolution River Corridor Attributes*. U.S. Geological Survey data release.

Schmadel, N. M., Harvey, J. W., Alexander, R. B., Schwarz, G. E., Moore, R. B., Eng, K., et al. (2018). Thresholds of lake and reservoir connectivity in river networks control nitrogen removal. *Nat. Commun.* 9:2779. doi: 10.1038/s41467-018-05156-x

Schmadel, N. M., Harvey, J. W., Schwarz, G. E., Alexander, R. B., Gomez-Velez, J. D., Scott, D., et al. (2019). Small ponds in headwater catchments are a dominant influence on regional nutrient and sediment budgets. *Geophys. Res. Lett.* 46, 9669–9677. doi: 10.1029/2019GL083937

Scott, D. T., Gomez-Velez, J. D., Jones, C. N., and Harvey, J. W. (2019). Floodplain inundation spectrum across the United States. *Nat. Commun.* 10:5194. doi: 10.1038/s41467-019-13184-4

Seitzinger, S. P., Harrison, J. A., Dumont, E., Beusen, A. H. W., and Bouwman, A. F. (2005). Sources and delivery of carbon, nitrogen, and phosphorus to the coastal zone: an overview of global nutrient export from watersheds (NEWS) models and their application. *Global Biogeochem. Cycles* 19:GB4S01. doi: 10.1029/2005GB002606

Snodgrass, J. W., Moore, J., Lev, S. M., Casey, R. E., Ownby, D. R., Flora, R. F., et al. (2017). Influence of modern stormwater management practices on

transport of road salt to surface waters. *Environ. Sci. Technol.* 51, 4165–4172. doi: 10.1021/acs.est.6b03107

Soranno, P. A., Bissell, E. G., Cheruvelil, K. S., Christel, S. T., Collins, S. M., Fergus, C. E., et al. (2015). Building a multi-scaled geospatial temporal ecology database from disparate data sources: fostering open science and data reuse. *Gigascience* 4:28. doi: 10.1186/s13742-015-0067-4

Soranno, P. A., Webster, K. E., Riera, J. L., Kratz, T. K., Baron, J. S., Bukaveckas, P. A., et al. (1999). Spatial variation among lakes within landscapes: ecological organization along lake chains. *Ecosystems* 2, 395–410. doi: 10.1007/s100219900089

Sparks, R. E. (1995). Need for ecosystem management of large rivers and their floodplains: these phenomenally productive ecosystems produce fish and wildlife and preserve species. *Bioscience* 45, 168–182. doi: 10.2307/13 12556

Stanford, J. A., and Ward, J. V. (1993). An ecosystem perspective of alluvial rivers: connectivity and the hyporheic corridor. *J. North Am. Benthol. Soc.* 12, 48–60. doi: 10.2307/1467685

Swanson, F. J., Johnson, S. L., Gregory, S. V., and Acker, S. A. (1998). Flood disturbance in a forested mountain landscape: interactions of land use and floods. *Bioscience* 48, 681–689. doi: 10.2307/1313331

Taguchi, V. J., Olsen, T. A., Natarajan, P., Janke, B. D., Gulliver, J. S., Finlay, J. C., et al. (2020). Internal loading in stormwater ponds as a phosphorus source to downstream waters. *Limnol. Oceanogr. Lett.* 5, 322–330. doi: 10.1002/lol2. 10155

U.S. Army Corps of Engineers (2020). *National Inventory of Dams*. Washington, DC: Federal Emergency Management Agency. Available online at: https://nid.sec.usace.army.mil (accessed July 06, 2020).

U.S. Geological Survey (2016). *National Hydrography Dataset*. Available online at: https://nhd.usgs.gov/ (accessed May 6, 2018).

U.S. Geological Survey (2020). *NHDPlus High Resolution*. Available online at: https://nhd.usgs.gov/ (accessed April 20, 2020).

Villarreal, E. L., Semadeni-Davies, A., and Bengtsson, L. (2004). Inner city stormwater control using a combination of best management practices. *Ecol. Eng.* 22, 279–298. doi: 10.1016/j.ecoleng.2004. 06.007

Vörösmarty, C. J., Meybeck, M., Fekete, B., Sharma, K., Green, P., and Syvitski, J. P. (2003). Anthropogenic sediment retention: major global impact from registered river impoundments. *Glob. Planet. Change* 39, 169–190. doi: 10.1016/S0921-8181(03)00023-7

Walker, J. J., Soulard, C. E., and Petrakis, R. E. (2020). Integrating stream gage data and Landsat imagery to complete time-series of surface water extents in Central Valley, California. *Int. J. Appl. Earth Obs. Geoinf.* 84:101973. doi: 10.1016/j.jag.2019.101973

Ward, A. S., and Packman, A. I. (2019). Advancing our predictive understanding of river corridor exchange. *WIREs Water* 6:e1327. doi: 10.1002/wat2.1327

Ward, J. V., and Stanford, J. A. (1995). The serial discontinuity concept: extending the model to floodplain rivers. *Regul. Rivers Res. Manag.* 10, 159–168. doi: 10.1002/rrr.3450100211

Wetzel, R. G. (1990). Land-water interfaces: metabolic and limnological regulators. *SIL Proc. 1922-2010* 24, 6–24. doi: 10.1080/03680770.1989.11898687

Whitfield, C. J., Baulch, H. M., Chun, K. P., and Westbrook, C. J. (2015). Beaver-mediated methane emission: the effects of population growth in Eurasia and the Americas. *Ambio* 44, 7–15. doi: 10.1007/s13280-014-0575-y

Wieczorek, M. E., Jackson, S. E., and Schwarz, G. (2018). *Select Attributes for NHDPlus Version 2.1 Reach Catchments and Modified Network Routed Upstream Watersheds for the Conterminous United* States. U.S. Geological Survey data release.

Winslow, L. A., Read, J. S., Hanson, P. C., and Stanley, E. H. (2014). Lake shoreline in the contiguous United States: quantity, distribution and sensitivity to observation resolution. *Freshw. Biol.* 59, 213–223. doi: 10.1111/fwb.12258

Wohl, E. (2013). Landscape-scale carbon storage associated with beaver dams. *Geophys. Res. Lett.* 40, 3631–3636. doi: 10.1002/grl.50710

Wohl, E. (2020). Wood process domains and wood loads on floodplains. *Earth Surf. Process. Landforms* 45, 144–156. doi: 10.1002/esp.4771

Woodward, G., Gessner, M. O., Giller, P. S., Gulis, V., Hladyz, S., Lecerf, A., et al. (2012). Continental-scale effects of nutrient pollution on stream ecosystem functioning. *Science* 336, 1438–1440. doi: 10.1126/science.1219534

Conflict of Interest: The authors declare that the research was conducted in the absence of any commercial or financial relationships that could be construed as a potential conflict of interest.

frontiers in Water

ORIGINAL RESEARCH
published: 18 January 2021
doi: 10.3389/frwa.2020.574692

Coupled Biotic-Abiotic Processes Control Biogeochemical Cycling of Dissolved Organic Matter in the Columbia River Hyporheic Zone

*Jane D. Fudyma[1], Rosalie K. Chu[2], Nathalia Graf Grachet[1], James C. Stegen[2] and Malak M. Tfaily[1,2]**

[1] Department of Environmental Science, The University of Arizona, Tucson, AZ, United States, [2] Pacific Northwest National Laboratory, Richland, WA, United States

A critical component of assessing the impacts of climate change on watershed ecosystems involves understanding the role that dissolved organic matter (DOM) plays in driving whole ecosystem metabolism. The hyporheic zone—a biogeochemical control point where ground water and river water mix—is characterized by high DOM turnover and microbial activity and is responsible for a large fraction of lotic respiration. Yet, the dynamic nature of this ecotone provides a challenging but important environment to parse out different DOM influences on watershed function and net carbon and nutrient fluxes. We used high-resolution Fourier-transform ion cyclotron resonance mass spectrometry to provide a detailed molecular characterization of DOM and its transformation pathways in the Columbia river watershed. Samples were collected from ground water (adjacent unconfined aquifer underlying the Hanford 300 Area), Columbia river water, and its hyporheic zone. The hyporheic zone was sampled at five locations to capture spatial heterogeneity within the hyporheic zone. Our results revealed that abiotic transformation pathways (e.g., carboxylation), potentially driven by abiotic factors such as sunlight, in both the ground water and river water are likely influencing DOM availability to the hyporheic zone, which could then be coupled with biotic processes for enhanced microbial activity. The ground water profile revealed high rates of N and S transformations via abiotic reactions. The river profile showed enhanced abiotic photodegradation of lignin-like molecules that subsequently entered the hyporheic zone as low molecular weight, more degraded compounds. While the compounds in river water were in part bio-unavailable, some were further shown to increase rates of microbial respiration. Together, river water and ground water enhance microbial activity within the hyporheic zone, regardless of river stage, as shown by elevated putative amino-acid transformations and the abundance of amino-sugar and protein-like compounds. This enhanced microbial activity is further dependent on the composition of ground water and river water inputs. Our results further suggest that abiotic controls on DOM should be incorporated into predictive modeling for understanding watershed dynamics, especially as climate variability and land use could affect light exposure and changes to ground water essential elements, both shown to impact the Columbia river hyporheic zone.

Keywords: FTICR-MS, hyporheic zone, biogeochemical cycling, dissolved organic matter, river water, ground water

OPEN ACCESS

Edited by:
Sarah E. Godsey, Idaho State University, United States

Reviewed by:
Eve-Lyn S. Hinckley, University of Colorado Boulder, United States
Benjamin W. Abbott, Brigham Young University, United States

***Correspondence:**
Malak M. Tfaily
tfaily@email.arizona.edu

Specialty section:
This article was submitted to Water and Critical Zone, a section of the journal Frontiers in Water

Received: *20 June 2020*
Accepted: *18 December 2020*
Published: *18 January 2021*

Citation:
Fudyma JD, Chu RK, Graf Grachet N, Stegen JC and Tfaily MM (2021) Coupled Biotic-Abiotic Processes Control Biogeochemical Cycling of Dissolved Organic Matter in the Columbia River Hyporheic Zone. Front. Water 2:574692. doi: 10.3389/frwa.2020.574692

INTRODUCTION

Climate changes such as rising temperatures, more frequent extreme storms and changes in season precipitation rates are expected to have a profound impact on biogeochemical cycling within hydrological systems (i.e., rivers, lakes, and streams). Dissolved organic matter (DOM) plays an essential role in watershed ecosystem energy budgets as it can drive whole-ecosystem metabolic processes (Yamashita et al., 2011; Adrian et al., 2016). DOM quality and composition are influenced by new plant and soil inputs into water systems, biotic, and abiotic processing in these systems and overall hydrological transportation controls (Watts et al., 2001), the majority of which may be altered in the future by a changing climate (Ritson et al., 2014). Abiotic (e.g., light, temperature) and biotic (e.g., microbial, enzymatic) factors can transform DOM to either more or less bio-available forms (He et al., 2016; Lønborg et al., 2018; Bowen et al., 2019) with follow-on effects across river corridor food webs (Graham et al., 2019). Further, perturbations to the rates and types of DOM introduced into watersheds from climate variability and land use can impact the extent of abiotic and biotic degradation, subsequently influencing CO_2 emissions to the atmosphere. For instance, prolonged exposure of DOM to sunlight can produce more bioavailable forms of DOM to microorganisms, thus influencing microbial respiration rates (Ward et al., 2017). At the same time, changes in the climate could induce changes in cloud cover and storm intensities. Recently, Young et al. (2019) showed that human-induced temperature changes were accompanied by an increase in cloudiness over northern Scandinavia, which in turn has reduced the impact of warming. Similarly, the increase in the frequency and intensity of extreme weather events induced by climate change can promote erosion and enhance turbidity in watersheds driven by increased distribution of suspended sediment along the river (Chen and Chang, 2019). The increase in cloud cover and turbidity could reduce abiotic degradation of DOM by sunlight. Similarly, land use can affect the rate in which inorganic compounds are introduced into watershed systems that can either hinder microbial interactions with DOM (Newbold et al., 2006) or enhance nutrient turnover (Johnson et al., 2009), resulting in the transport of more labile substrates across watersheds that can heighten microbial activity elsewhere. In terms of the hyporheic zone, the biogeochemically active zone in hydrological systems, the degree of DOM degradability and composition of ground and river water inputs can thus strongly influence microbial hyporheic communities and lotic respiration as a whole. Parsing DOM differences between these regions (ground water, river water, hyporheic zone) is critical to understanding biogeochemical cycling and net fluxes through integrated river systems.

The hyporheic zone is an important ecosystem control point (Bernhardt et al., 2017) where ground water and river water mix (Boulton et al., 1998; White et al., 2015; Wohl, 2015). DOM plays an especially important role in the hyporheic zone, and its origins and bioavailability have been extensively shown to drive microbial activity and organic matter turnover in these control points (i.e., hyporheic zones). (Wagner et al., 2014; Stegen et al., 2016, 2018; Stern et al., 2017). Due to the physical nature of how river and ground water interact, plant and soil organic matter and microorganisms from different ecosystems are introduced into the hyporheic zone at different rates, temperature, and flow gradients are connected, organic matter composition is diversified, and oxygenation is accelerated, which can provide terminal electron acceptors for microbial metabolic processes and stimulate microbial activity (Boano et al., 2014; Merill and Tonjes, 2014). As such, the hyporheic zone can contribute to over 90% of river system respiration (Naegeli and Uehlinger, 1997). Previous studies have provided exhaustive insight on many of the complex interactions between physical, chemical, and biological processes that impact hyporheic zone ecology and hydrology. Flow and transport processes (Sophocleous, 2002; Boano et al., 2014; Fasching et al., 2016), geologic factors (Naiman et al., 2000; Kasahara and Wondzell, 2003; Hester and Doyle, 2008; Banks et al., 2019), water and redox chemistry (Briggs et al., 2015; Kaufman et al., 2017), microbial population dynamics (Clinton et al., 2010; Nogaro et al., 2013; Wagner et al., 2014; Graham et al., 2016), and their overlapping interactions (Stegen et al., 2016, 2018; Hou et al., 2017) can all change the rates of substrate degradation and transformation within the hyporheic zone. Further, altered metabolism of hyporheic zone organisms and their transformed byproducts can consequently affect the productivity of both the river and ground water systems it interacts with, as well as downstream ecological processes (Boulton et al., 2010).

Earth System Models (ESMs) continue to evolve as field-based observations necessitate increasing conceptual complexity (Burd et al., 2016); for example, the acknowledgment that terrestrial-aquatic interfaces are highly active zones of DOM transformation has created a knowledge gap because the dynamic mechanisms by which DOM is transformed in these zones remain under constrained. Reaction transport models (RTMs) are a powerful tool for simulating DOM transformation mechanisms by integrating thermodynamics, kinetics, and multidimensional transport in a process-based framework. Incorporation of omics data including metabolomics into RTMs has been identified as a key new direction in the development of RTM capabilities for understanding critical zone processes (Li et al., 2017) as it can reveal new geochemical signatures that are currently undefined in watersheds. Recently, gene expression data coupled with metabolomics data, helped uncover new reactive components of DOM that represent a previously unidentified and likely sizable portion of marine organic carbon and sulfur cycling (Durham et al., 2015). Based on these and other examples, molecular datasets from across watersheds will likely uncover an intricate web of chemical–biological interactions that can be used to improve predictions of hydro-biogeochemical function in response to disturbance. While microbial and DOM cycling reactions have been to some extent incorporated into RTMs to provide a more realistic framework for simulating DOM turnover, the great complexity of possible organic reactions and microbial redox makes full parameterization difficult (Lawrence et al., 2014). Therefore, characterizing the most critical reactions for DOM turnover and mineralization will be

highly useful to identify reactions for incorporation into RTM modeling frameworks.

Here, we used high resolution Fourier-transform ion cyclotron resonance mass spectrometry (FTICR-MS) to provide an in-depth characterization of DOM chemical composition and molecular signature of the Columbia River hyporheic zone and its ground water and river constituents. Previous research of this region (Stegen et al., 2016, 2018) found that mixing of ground water with river water stimulates respiration at the Columbia river hyporheic zone. The low dissolved organic carbon concentration in ground water protects thermodynamically favorable carbon (C) from decomposition and allows it to accumulate. At the same time, the recalcitrant nature of river water DOM protects it from microbial oxidation, allowing it to accumulate in river water. Mixing of ground water and river water removes these protection mechanisms in both systems and stimulates aerobic respiration [dissolved organic carbon (DOC) to CO_2] at the hyporheic zone. Yet, information about DOM molecular signatures in both river water and ground water systems, their overlap within the hyporheic zone as well as the different chemical transformations by which DOM is being degraded and transformed in these systems is still a significant knowledge gap. Providing insight into these signatures and mechanisms will help clarify how microorganisms influence and are influenced by DOM composition in the hyporheic zone. Here, we build upon this research to further understand (1) DOM molecular signatures (i.e., DOM character) in both river water and ground water systems and their overlap within the hyporheic zone, (2) how do DOM compositional differences in river water and ground water further explain the current established understanding of biogeochemical cycling in the hyporheic zone, and (3) the different chemical transformations (biotic and abiotic) or reactions by which DOM is being degraded and transformed in these systems. This knowledge is crucial for disentangling the organic matter drivers in hydrologic ecosystems and how those relate to broader biogeochemical processes. High-resolution chemical composition data, and the detailed properties of organic matter and degradation pathways outlined in this research, can reveal patterns of conserved reaction-scale processes and provide information that can be used in numerical hydro-biogeochemical and reaction transport models to improve predictions of hydro-biogeochemical function in response to disturbance. Resulting enhancements to predictive capacity will be important for accurately forecasting the ecological consequences of ongoing global environmental change. Once these in-depth interactions are explained, a better understanding of biogeochemical cycling and dynamics in watershed systems can be established.

MATERIALS AND METHODS

Field Sampling

Samples were collected as previously described in Stegen et al. (2016). Briefly, samples were collected from four ground water wells (GW) (adjacent unconfined aquifer underlying the Hanford 300 Area-sediment porosity of ∼0.20 and hydraulic conductivity of ∼7,000–8,000m per day), Columbia river water (RW), and its hyporheic zone (HZ) (sediment porosity of ∼0.18 and hydraulic conductivity of ∼1–4 m per day) (**Figure 1**; **Supplementary Table 1**). The hyporheic zone was sampled at five locations (named p2, p3, p4, p5, and p6, respectively where p stands for "piezometer") at multiple depths ("1" represents shallow depths and "6" represents deeper sampling depths—**Supplementary Table 1**) to capture spatial heterogeneity within the hyporheic zone using a custom-built multi-level sampling device installed with stainless steel piezometers; 1.2 m screen length and 5.25 cm inside diameter (MAAS Midwest, Huntley, IL). The five sampled piezometers were not meant to be replicates but were assumed to capture different physical features of the hyporheic zone to provide access to a broader range of mixing conditions. Ground water contribution to hyporheic zone water increased with piezometer location number as shown by substantial variation in Cl^- concentration within hyporheic zone samples (**Supplementary Table 1**, with p2 having lowest Cl^-/least ground water and p5 having highest Cl^- concentration/highest ground water); Cl^- concentration was used as a conservative tracer.

Ground water was sampled from four wells across the top of the subsurface aquifer and river water was sampled near the piezometers. Samples from all the listed locations (5× hyporheic zone, 4× ground water, and 1× river) were collected at four-time intervals (A-D) in November 2013 across ∼ 1 week, relating to different river level stages as outlined in Stegen et al. (2016). River stage was monitored ∼300 m downstream of the field sampling locations using a pressure transducer coupled to a CR1000 data logger (Campbell Scientific Inc., for both). Within the week of 11/17/2013–11/25/2013, river elevation fluctuated between 104.6 and 105.8 m. The four time points that were chosen for sampling represented short-term fluctuations caused by up-river flow regulation at the Priest Rapids dam. Time intervals A and D were low river stage (river elevation was ∼104.8 m and 104.6 m, respectively) and time intervals B and C were high river stage (river elevation was ∼105.2 m and 105.4 m, respectively). As such the four time intervals described above will be referred to: stage A, stage B, stage C, and stage D. Temporal fluctuations in the river stage can cause variation in the degree of ground water–surface water mixing, which in turn changes the resource environment experienced by hyporheic zone microbial community. Water from the hyporheic zone and the river were sampled using a peristaltic pump and the subsurface aquifer was sampled using submersible pumps; all systems were purged—the equivalent of at least three volumes—before sample collection. At each location, pumped water passed through 0.22 μm polyethersulfone Sterivex filters (Millipore Co., Billerica, MA) for either ∼30 min or until 10 L had passed through a filter, whichever came first; sampled volume ranged from 1.33 to 10 L. Samples for FTICR-MS analysis were filtered and collected into 40 ml borosilicate vials and frozen at – 20°C. Monthly climatological data summaries, as well as other information, are available at the following two links: https://www.hanford.gov/page.cfm/hms and https://www.hanford.gov/files.cfm/Nov20131.pdf. Briefly, for the month of November 2013, the average daily temperature within the Hanford 300 Area ranged between −5° and 12°C, with warmer temperatures the first 20 days of the month (average maximum of 12°C)

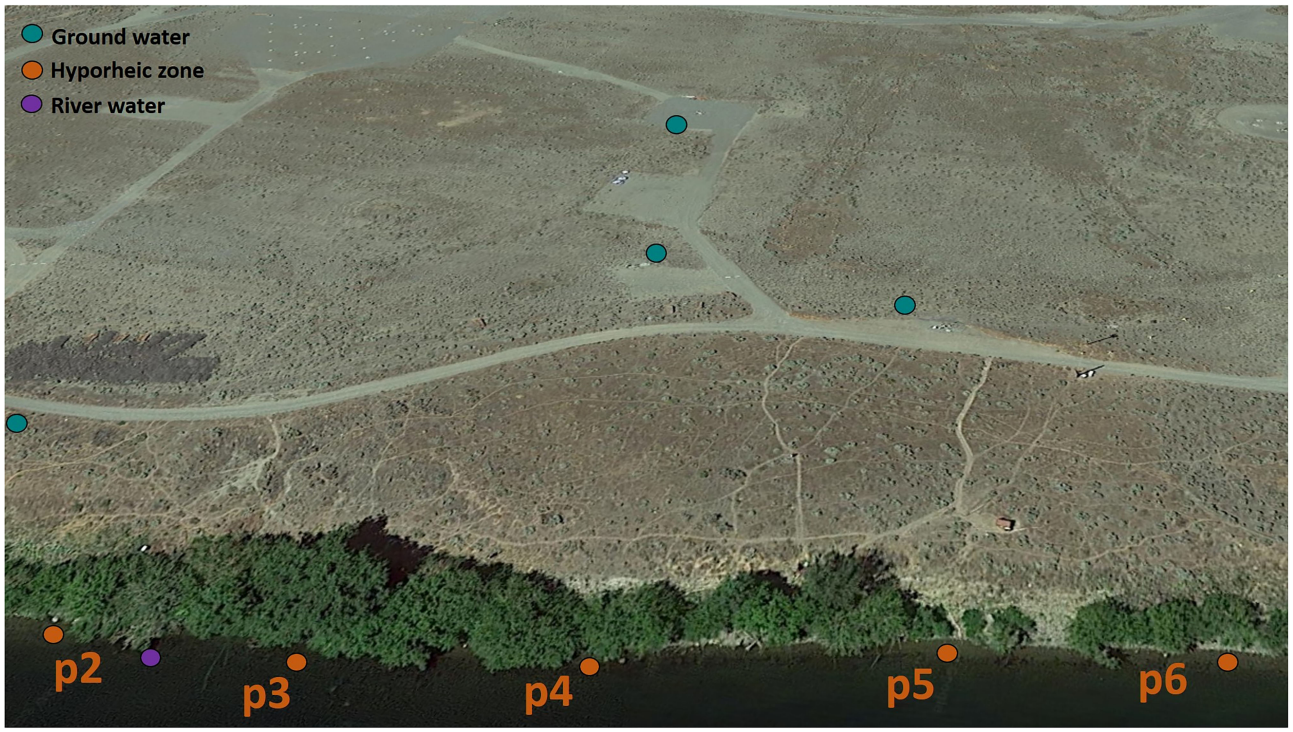

FIGURE 1 | Sampling schematic within the Hanford field sampling site (Google Earth, earth.google.com/web/) of the Ground water, River water, and Hyporheic zone. Piezometer 6 was sampled within the depth intervals of ∼1–11 and ∼41–51 cm whereas piezometers 2–5 were sampled within the depth intervals of ∼10–20 and 110–120 cm.

followed by a significant drop toward the end of the month (average maximum of −5°C). The total water equivalence was around 9 mm with only 4 days of rain. Ten days in the month of November were cloudy with an average sky cover metric, defined as the average sky cover between sunrise and sunset in tenths of sky covered, of 10 (100%) meaning clouds covered the entire sky for that day. During the week when the samples were collected, the sky cover was very low with relatively high observed daily shortwave radiation (solrad) [∼187.2 langleys per day (ly/d)]. For objectives 1 and 2, we combined the data for each system (GW, HZ, and RW) from all staging events and regardless of location. For objective 3, we are distinguishing between the five different locations within the hyporheic zone. More details are included below.

FTICR-MS Data Acquisition

A 12 Tesla Bruker SolariX FTICR spectrometer located at EMSL, a DOE-BER national user facility located in Richland, WA, was used to collect high resolution mass spectra of the DOM water samples by direct injection, as previously described in Tfaily et al. (2018). Approximately, 100 μl of water was mixed with methanol (1:2) before injection onto the mass spectrometer to enhance ionization. Briefly, a standard Bruker ESI source was used to generate negatively charged molecular ions and then samples were introduced directly to the ESI source. The instrument was externally calibrated weekly to a mass accuracy of <0.1 ppm using a tuning solution from Agilent, which contains the following compounds: $C_2F_3O_2$, $C_6HF_9N_3O$, $C_{12}HF_{21}N_3O$, $C_{20}H_{18}F_{27}N_3O_8P_3$, and $C_{26}H_{18}F_{39}N_3O_8P_3$ with a mass-to-charge ratio (m/z) ranging between 112 and 1,333. The instrument settings were optimized by tuning on a Suwannee River Fulvic Acid (SRFA) standard. Blanks (HPLC grade MeOH) were ran at the beginning and the end of the day to monitor potential carry over from one sample to another and the instrument was flushed between samples using a mixture of water and methanol. The ion accumulation time (IAT) varied to account for differences in C concentration between samples. One hundred and forty-four individual scans were averaged for each sample and internally calibrated using OM homologous series separated by 14 Da (-CH_2 groups). The mass measurement accuracy was <1 ppm for singly charged ions across a broad m/z range (i.e., $100 < m/z < 1100$). The mass resolution was 350,000 at 339.112 Da. To further reduce cumulative errors, all sample peak lists for the entire dataset were aligned to each other prior to formula assignment to eliminate possible mass shifts that would impact formula assignment.

Formula and Biogeochemical Class Assignment

Putative chemical formulas were assigned using Formularity software (Tolić et al., 2017). Chemical formulas were assigned based on the following criteria: signal-to-noise (S/N) > 7, and mass measurement error <1 ppm, taking into consideration

the presence of C, H, O, N, S, and P and excluding other elements. Peaks with large mass ratios (m/z values > 500 Da) often have multiple possible candidate formulas. These peaks were assigned formulas through propagation of CH_2, O, and H_2 homologous series. Additionally, to ensure consistent choice of molecular formula when multiple formula candidates are found the following rules were implemented: the formula with the lowest error with the lowest number of heteroatoms was consistently picked and the assignment of one phosphorus atom required the presence of at least four oxygen atoms.

Data was filtered to select for m/z with mass range of 200–900 where most peaks appeared. Compounds were then plotted on van Krevelen diagram based on their molar H:C ratios (y-axis) and molar O:C ratios (x-axis) (Kim et al., 2003). Van Krevelen diagrams provide a means to visualize and compare the average properties of organic compounds and assign compounds to the major biochemical classes (e.g., lipid-, protein-, lignin-, carbohydrate-, and condensed aromatic-like). Biochemical compound classes were reported as relative abundance values based on counts of C, H, and O for the following H:C and O:C ranges: lipids ($0 < O{:}C \leq 0.3$ and $1.5 \leq H{:}C \leq 2.5$), unsaturated hydrocarbons ($0 \leq O{:}C \leq 0.125$ and $0.8 \leq H{:}C < 2.5$), proteins ($0.3 < O{:}C \leq 0.55$ and $1.5 \leq H{:}C \leq 2.3$), amino sugars ($0.55 < O{:}C \leq 0.7$ and $1.5 \leq H{:}C \leq 2.2$), lignin ($0.125 < O{:}C \leq 0.65$ and $0.8 \leq H{:}C < 1.5$), tannins ($0.65 < O{:}C \leq 1.1$ and $0.8 \leq H{:}C < 1.5$), and condensed hydrocarbons (aromatics; $0 \leq 200$ $O{:}C \leq 0.95$ and $0.2 \leq H{:}C < 0.8$) (Tfaily et al., 2017). Further, to disentangle essential elements and their relation to chemical class, each mass was then subsequently filtered with N>0, P>0 or S>0 and then plotted again on van Krevelen diagrams.

Compositional Data Normalization, Multivariate, and Statistical Analysis

Relative abundance of biochemical compound classes was normalized for multivariate statistical analysis by performing centered log ratio (CLR) on each sample. The CLR function of the R package compositions (van den Boogaart and Tolosana-Delgado, 2008) was used for CLR transformation. This approach allows for confident application of statistical analysis on each compositional dataset (e.g., each sample) (Aitchison, 1994; Pawlowsky-Glahn and Buccianti, 2011). Principal component analysis (PCA) was performed on all sample replicate CLR-transformed chemical class abundances. Hierarchal cluster analysis (dendogram-heatmap) of the CLR transformed abundances was used to map sample replication by class abundance as well as visualize class abundance differences as a function of each ecosystem (ground water, hyporheic zone, and river water). To determine the significance of these observed differences between organic compound class assignment abundances by location, relative abundances of ground water, hyporheic zone, and river organic compounds were subjected to Kruskal–Wallis rank sum tests. Following a significance observed by a p-value of <0.05, Dunn *post-hoc* tests were performed between ecosystem and chemical class composition, then coupled with box plots of compound class abundances to visualize the statistical significance between compound class groups within each system. These non-parametric tests were chosen in this study due to the low number of replicates per sample. All normalization and statistical analysis were executed in R (version 3.6.1).

Unique Mass Comparisons and Gibbs Free Energy

After checking the reproducibility of biological replicates using van Krevelen diagrams above, replicate m/z counts of each ecosystem (ground water, river water, and hyporheic zone) were combined regardless of stage or location in order to probe at the characteristics of each system rather than temporal differences. Unique peaks (i.e., peaks present in one ecosystem but not the other) were filtered as pairwise comparisons between the following groups: ground water vs. river water, ground water vs. hyporheic zone, hyporheic zone vs. river water. The unique peaks were plotted on van Krevelen diagrams, as described above, using R (version 3.6.1) to observe biochemical compound class differences. Further, Gibbs free energy (GFE) was calculated, as described previously in Boye et al. (2018), for all unique peaks assigned a molecular formula. Briefly, each assigned molecular formula was used to calculate the nominal oxidation state of C (NOSC) according to the following equation:

$$NOSC = -\left(\frac{4 \times C + H - 3 \times N - 2 \times O + 5 \times P - 2 \times S}{C}\right) + 4 \quad (1)$$

NOSC values were then used to calculate the GFE of each unique compound according to Equation 2. Low GFE values are an indication of compounds more thermodynamically favored to undergo metabolic and chemical reactions (i.e., available for microbial communities), whereas higher values reflect microbially degraded and transformed (i.e., recalcitrant) DOM. GFE of all unique peaks in each pairwise comparisons were then plotted using R (version 4.4.0) and a list is provided in **Supplementary Table 2**.

$$\Delta G\text{-}Cox = 60.3 - 28.5 \times (NOSC) \quad (2)$$

Network Analysis

To identify and contrast putative DOM transformation or decomposition pathways across different ecosystems, the mass differences between FTICR–MS peaks within each sample were compared with precise mass differences for commonly observed biochemical transformations adopted from Breitling et al. (2006). This approach is possible because of the ultra-high mass accuracy of FTICR–MS. For example, a mass of 2.0156 Da, e.g., represents a hydrogentation/dehydrogentation reaction, whereas a mass difference of 71.0371 indicates a reaction in which one alanine (C_3H_5NO) was lost. Within each sample, the number of times each putative transformation was observed was counted based on precise mass differences between FTICR–MS peaks. Values were then normalized based on percentage of transformation counts per sample. Transformation data were combined across ecosystem type and both multivariate

(PCA) and univariate (Kruskal– Wallis, Tukey Post-Hoc) analysis were performed using MetaboAnalyst (version 4.0) to determine driving transformations of each ecosystem. A list of all significant transformations between paired groups are listed in **Supplementary Table 3**.

Transformation analysis data for all samples (stages A–D) were then plotted on a network analysis using MetaNetter (Burgess et al., 2017), a Cytoscape Version 3.8.0 (Shannon et al., 2003) plug-in, as described previously by Longnecker and Kujawinski (2016). Briefly, mass difference between the two *m/z* values resulting from a chemical transformation were demonstrated as an edge in the network, and the initial and final compounds (namely, reactant, and product) as nodes (Breitling et al., 2006; Burgess et al., 2017). For example, the gain or loss of CO_2 (i.e., mass difference $\Delta m/z = 43.9898$) between two compounds would be represented as two "nodes" connected by an edge named "$CO_{2\_}$." For each putative transformation, there may be a series of connected *m/z* values, and one *m/z* value may be connected to other *m/z* values by more than one transformation. For a biochemical reaction to be considered valid by this method, both the reactant and the product should be present. Network analyzer was performed to calculate network heterogeneity of each sample. The network heterogeneity reflects the tendency of a network to contain hub nodes where a hub is a node with a number of transformations that greatly exceeds the average. Thus, higher network heterogeneity signifies a larger and more diverse rate of node connections, signifying a more transformed system (i.e., the same compound could be produced through a multitude of reactions and/or the same compound can be degraded in many different pathways). Statistical analysis (Tukey HSD) was performed on combined network heterogeneity between combined values for each ecosystem.

To further visualize differences in putative DOM transformation pathways between ground water, hyporheic zone, and river water samples, nodes were colored based on their compound class as assigned using van Krevelen diagrams. Edges were colored (1) yellow in the ground water network if they originated from H_2S, PO_4^{3-}, NO_3^-, $S_2O_3^{2-}$, and diphosphate, (2) red in both the river water and hyporheic samples if they originated from putative abiotic transformations upregulated in the river (carboxylation, acetylation, hydroxylation, and glycoxylation), and (3) blue in the hyporheic zone samples if they originated from any of the 20 putative amino acids transformations. While this approach was applied to all samples from different stages, we only chose stage A to visually represent the differences between the HZ, river water and ground water since the differences observed in the chemical transformations between the HZ, river water and ground water in stage A were similar to those observed in stages B–D. We further distinguished between the five different locations within the hyporheic zone to see whether river stage and thus changes in ground water-river water mixing ratios can influence the quality and quantity of chemical transformations observed in the hyporheic zone.

To further confirm that the transformations observed in the hyporheic zone were not merely due to pure mixing of ground water and river water, we calculated the number of transformations that could be expected under pure transport and compared it to the transformation profile that was observed in the hyporheic zone. This approach was tested on samples collected from stage A sampling event. To do so, ground water mass spectral features from stage A were grouped together to generate one ground water peak list for stage A. Similarly, mass spectral features from all the hyporheic zone samples that were collected during stage A sampling event were grouped together to generate one hyporheic zone peak list. We eventually had three peak lists: one from river water (stage A), one for ground water (stage A), and one for the hyporheic zone (stage A). The peak lists from ground water and river water were considered pure end members. We then prepared three new peak lists using three different scenarios (i.e., three ground water-river water mixing ratios) (90%GW:10%RW, 50%GW: 50%RW, and 10%GW:90%RW) by randomly sampling from the pure end members peak list in proportion to the ground water-surface water mixing ratio. We then performed transformation analysis (as described above) on each of these three peak lists. The transformation results from these peak lists were then compared to the transformations observed at the hyporheic zone from stage A sampling event.

Kendrick Mass Defect Analysis

Samples from stage A were further analyzed independently by Kendrick mass defect analysis (Hughey et al., 2001), another useful approach for representing and comparing large molecular data sets. Kendrick mass analysis is based on rescaling each identified formula according to Equation 3. This rescaling is equivalent to assigning each mass of CH_2 as 14.0000 amu instead of the International Union of Pure and Applied Chemistry (IUPAC) mass of 14.01565 amu.

$$Kendrick\ mass = IUPAC\ mass\ x\ (\frac{14.0000}{14.01565}) \tag{3}$$

Members of a homologous series (namely, compounds that contain the same heteroatom and number of rings plus double bonds, but different number of CH_2 groups) have identical Kendrick mass defect (KMD). The KMD is calculated from difference between the Kendrick mass and the IUPAC nominal mass as shown in Equation 4:

$$Kendrick\ mass\ defect\ \ (KMD) = (Kendrick\ nominal\ mass - Kendrick\ \ mass) \tag{4}$$

Nominal Kendrick mass is determined by rounding the Kendrick mass up to the nearest whole number. A Kendrick plot is then plotted using all formulas reduced to their KMD plotted against Nominal Kendrick mass. The KMD value for any molecule increases as the oxygen content and the degree of unsaturation increase. Thus, high KMD values for any given nominal mass indicate extensive oxygenation and/or unsaturation. As a result, elemental compositions differing in the number of oxygen atoms and/or the number of double bonds (i.e., homologous species) are separated vertically due to their different KMD values.

RESULTS

DOM Composition Is Driven by Ecosystem Type, Not River Stage

Principal component analysis (PCA) was performed on the center log ratio-transformed organic compound abundances of four sampling events from different stages in the ground water, hyporheic zone, and river ecosystems. The events were defined by different river stages, outlined Stegen et al. (2016). Three distinct groupings were observed and explained 55.7% of the organic compounds' variance (**Figure 2A**). Ecosystem type drove more of the variance within the data set rather than river stage during sampling event, which was shown by both the PCA clusters grouping by ecosystem not sampling time as well as the hierarchal clustering dendrogram grouping by ecosystem type (**Supplementary Figure 1A**). However, ground water sampled during stage C showed some similarities to the hyporheic zone composition (**Figure 2A**, **Supplementary Figures 1A,B**). This overlap could likely have to do with river stage, as it was the highest during sampling stage C, and could be due to the inland movement of hyporheic zone pore fluids. However, considering more of the variance was driven by ecosystem type, and because one of our goals was to define the overall signatures of the ecosystem rather than river stage fluctuations, we combined events (i.e., stages) for characterization of each ecosystem. However, we do recognize that river level fluctuations play an important role in hyporheic zone dynamics, thus further molecular characterization of river level influences on DOM changes should be explored in future work.

Ground water was characterized by significantly larger abundances of unsaturated hydrocarbon- like compounds (p value = 0.0017, **Supplementary Table 4**), with elevated levels of lipid- and tannin- like compounds (**Figure 2B**). Further, a large diversity of N and S- containing compounds were observed as compared to the river, yet most were concentrated the lipid-like region (**Figure 3**). On the other hand, the river water contained a significantly higher abundance of both lignin- and protein-like compounds (p values = 0.0024 and 0.0107, respectively, **Figure 2B**, **Supplementary Table 4**). The river system had lower diversity of N and S containing compounds compared to the ground water, and compounds containing these elements were primarily localized to condensed hydrocarbons (**Figures 3A,B**). Unsurprisingly, the hyporheic zone reflected an overlap of both of its water inputs, shown by gradients in condensed hydrocarbon-, lignin-, lipid-, protein- and unsaturated hydrocarbon-like compounds (**Figure 2B**). However, the hyporheic zone was characterized by elevated levels of amino sugars and carbohydrates as well (**Figure 2B**) and an abundance of N-containing compounds in the protein- and amino sugar-like region (**Figure 3A**). The diversity of N, S, and P containing compounds in the hyporheic zone were overall greater than both of the ground and river water inputs (**Figure 3**). Both the hyporheic zone and ground water had elevated N and P compounds within the lipid-like region.

Thermodynamic Driving Forces of the Ground Water, Hyporheic Zone, and River Corridor

Organic compounds distribution of each system revealed that the hyporheic zone, as expected, was influenced by organic compounds from both the river water and ground water (**Figure 4A**). However, we wanted to understand the molecular signature of DOM that is driving the underlying thermodynamics that could control microbial respiration in the hyporheic zone. Thus, unique compounds to each system were generated from pairwise comparisons (unique masses in ground water vs. river, hyporheic zone vs. ground water, and hyporheic zone vs. river—**Figure 4B**) and their thermodynamic favorability was calculated by Gibbs free energy (GFE—**Figure 4C**). Briefly, a higher GFE signifies more degraded organic matter that is less favorable for microbial oxidation, where conversely, a lower GFE denotes greater thermodynamic favorability. GFE is also dependent on other variables, such as oxygen, which can catalyze the degradation of DOM even if it is not bioavailable.

Ground water was characterized by an overall greater range of GFE, and a larger abundance of lower GFE compounds (GFE below 50) (**Figure 4C**). While both river water and hyporheic zone had less thermodynamically favorable DOM overall, the hyporheic zone was still comprised of slightly more labile DOM (**Figure 4C**). This could be indicative of microbial transformations of DOM inputs from both the river and ground water systems to different degrees of bioavailable compounds, both more degraded and more utilizable, with varying GFE. This phenomenon is further elucidated by a larger abundance and broader range of unique organic compounds that appear in the hyporheic zone but are not present in either of its inputs (i.e., ground and river water) (**Figure 4B**).

Chemical Transformations Are Driven by Abiotic, Biotic, or Essential Element Dynamics

Putative chemical transformation analysis (biotic and abiotic transformation abundance) can provide better insight on how DOM dynamics are varying and subsequently influencing DOM degradation and bioavailability within the hyporheic zone. Multivariate analysis indicated that transformations were still driven by their ecosystem groupings (25.3% of variance), yet more overlap was observed between the hyporheic zone and river systems (**Figure 5A**, **Supplementary Figure 2**). The hyporheic region was strongly driven by an abundance of putative amino acid transformations (i.e., an increase in the abundance of chemical transformations that involve a loss or a gain of an amino acid), which could suggest that the ability to degrade or synthesize proteins may be a key functional trait for microbial communities in the hyporheic zone (**Figures 5B**, **6A**). While the ground water also showed fluctuating amounts of amino acid transformations, the river was practically void of these reactions (**Figure 6A**). The river water had a significantly higher rate of carboxylation (e.g., gain or loss of carboxylic acid group, mostly abiotic) and acetylation reactions, and was further driven by more putative

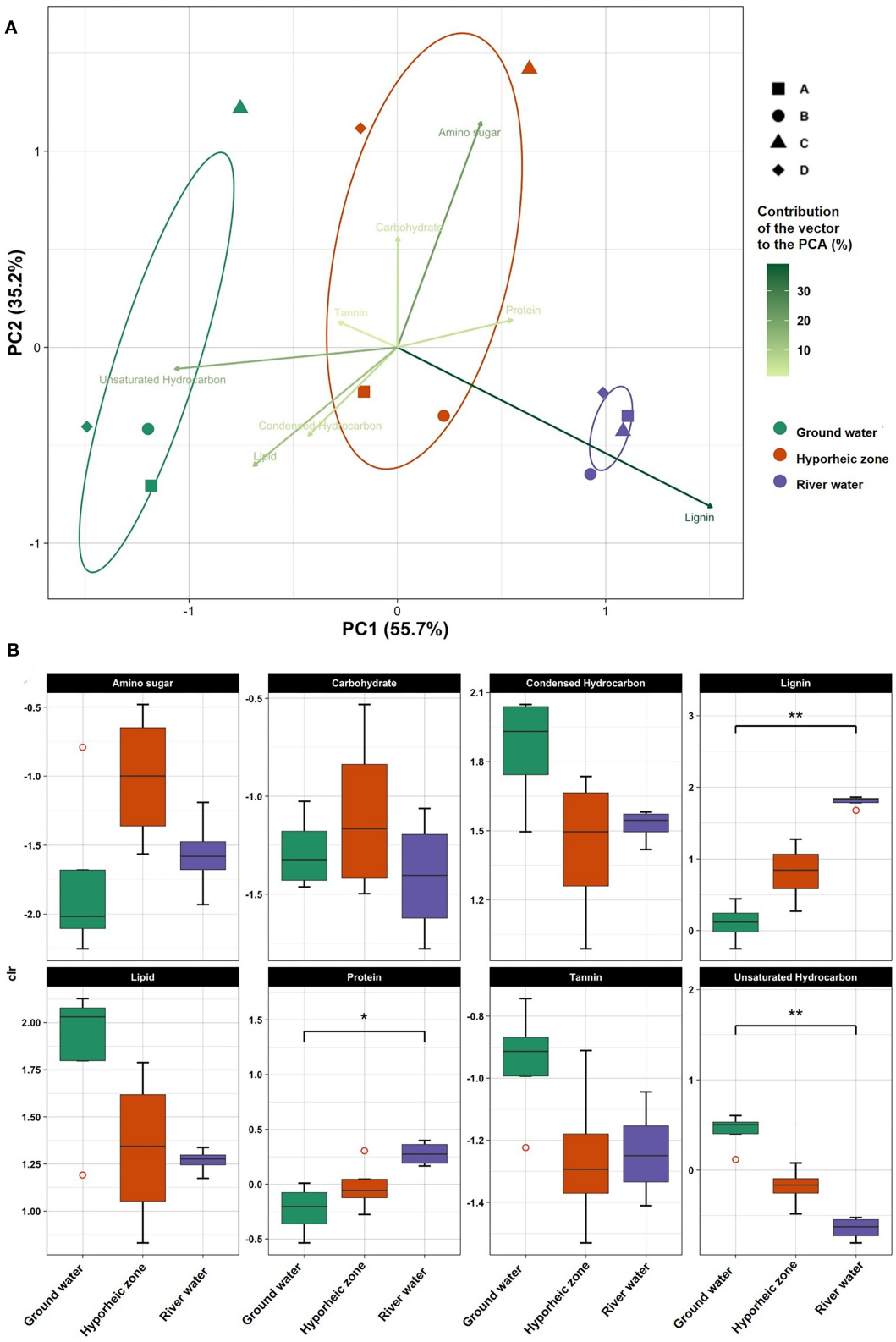

FIGURE 2 | (A) Principle component analysis (PCA) on centered log ratio (CLR) transformed chemical class abundances in each system (ground water, hyporheic, and river water) at four-time intervals (A–D) (i.e., different river level stages) in November 2013; **(B)** Box plots of CLR transformed chemical class abundances in each system (ground water, hyporheic zone, and river water). Dunn *post-hoc* tests were performed between ecosystem and chemical class composition to visualize the statistical significance (represented by an *if $p < 0.05$ and **if $p < 0.001$).

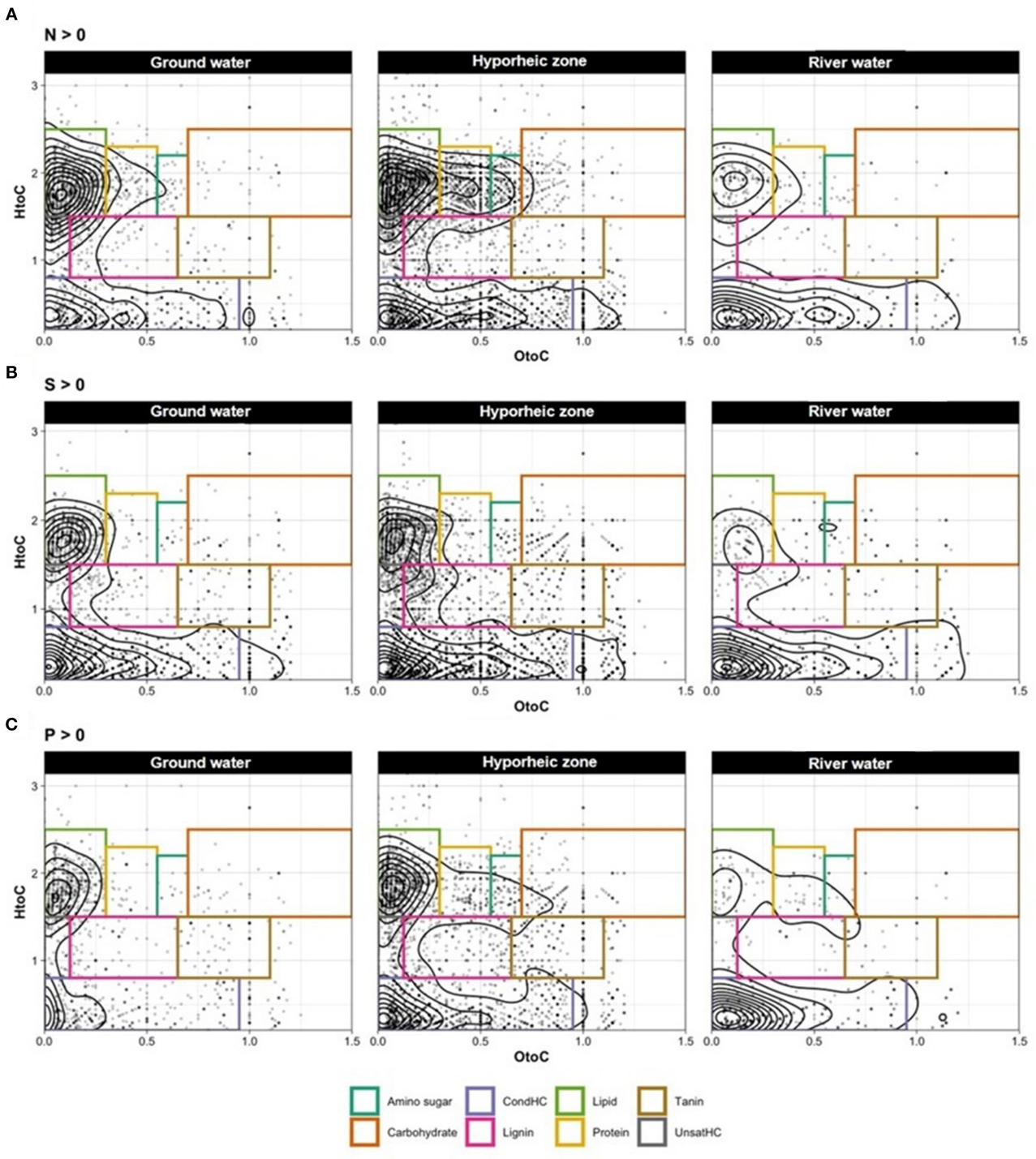

FIGURE 3 | Van Krevelen (VK) diagrams (with contoured lines) for compounds containing only **(A)** nitrogen (N), **(B)** sulfur (S), and **(C)** phosphorus (P) in the samples ground water (left panel), hyporheic zone (middle panel), and river water (right panel).

abiotic and sugar transformations (**Figures 6B,C**). The ground water DOM was characterized by a diverse suite of N, P, and S containing transformations (**Figures 6D–F**), including H_2S, NO_3^-, and PO_4^{3-} (**Figures 6D–F**, respectively). This is concurrent with the larger observed abundance of organic compounds with N, S, and P in ground water compared to river as shown in **Figure 3**.

End-member transformation data (i.e., transformations expected under pure transport) in proportion to the different ground water-surface water mixing ratio at

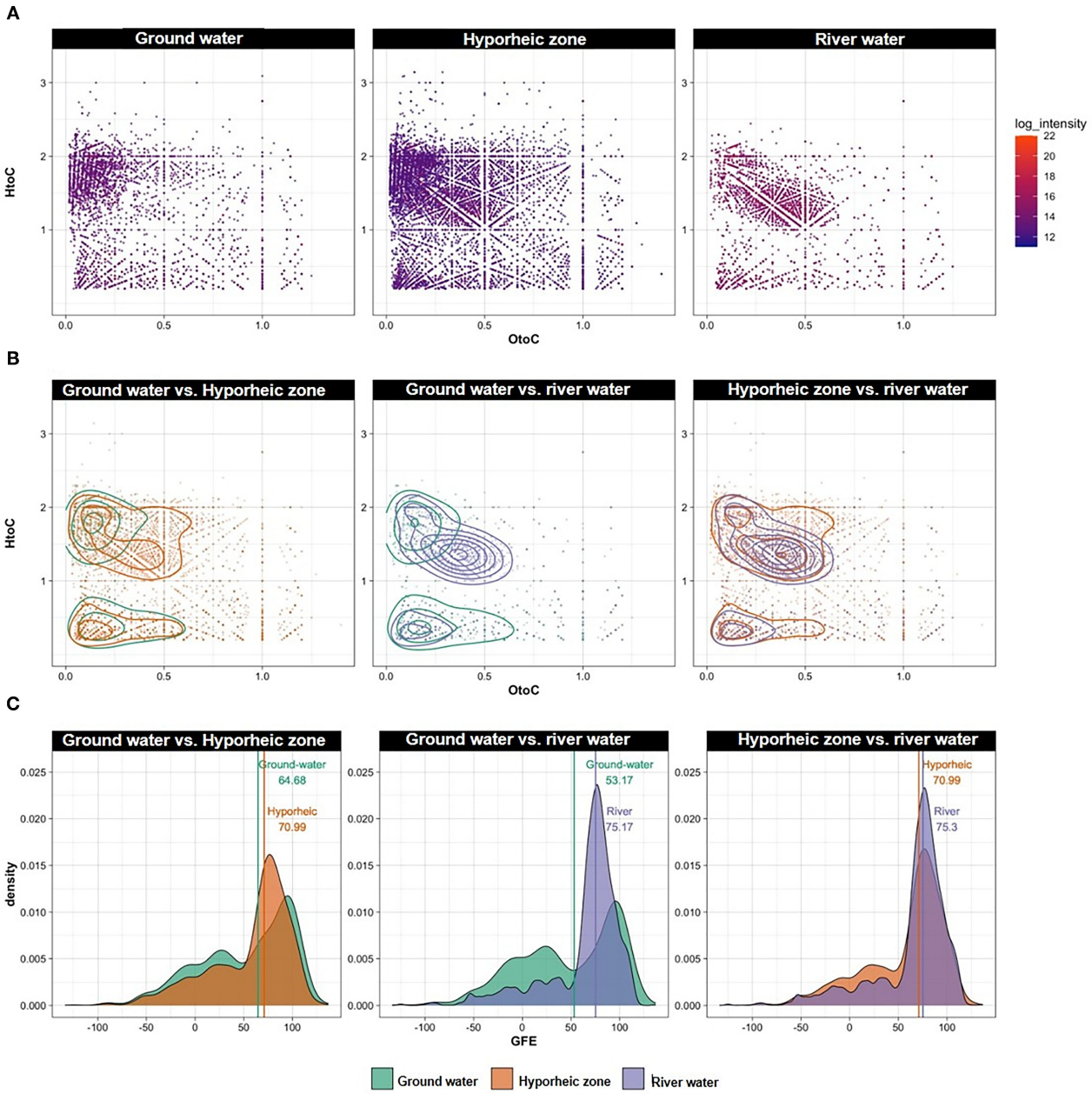

FIGURE 4 | (A) Van Krevelen (VK) diagrams of all peaks observed in each system combined over different river stages, ground water wells and piezometers locations; **(B)** VK diagrams (with contoured lines) and **(C)** Gibbs free energy (GFE) ridge lines of unique peaks (i.e., peaks present in one ecosystem but not the other), filtered as pairwise comparisons between the following groups: ground water vs. river water, ground water vs. hyporheic zone, hyporheic zone vs. river water, regardless of river stage and piezometers location. Lines along with numbers in panel C represent the median of each distribution.

sampling stage A revealed an increase in the number of transformations with the increase in river water contribution (**Supplementary Figures 2A,B**) regardless of transformation type. However, the number of transformations observed in the hyporheic zone at sampling stage A were significantly higher than those predicted under pure transport, regardless of mixing ratio and transformation type (**Supplementary Figures 3A,B**). Furthermore, when the number of transformations observed in the hyporheic zone were plotted as a function of those observed under pure mixing (**Supplementary Figure 4**), steeper slopes were observed under pure mixing conditions which indicate significantly higher transformation in hyporheic zone. The high number of transformations observed in the hyporheic zone was also independent of the total number of peaks observed in these sample, in contrast to those observed under pure transport (**Supplementary Figure 5**).

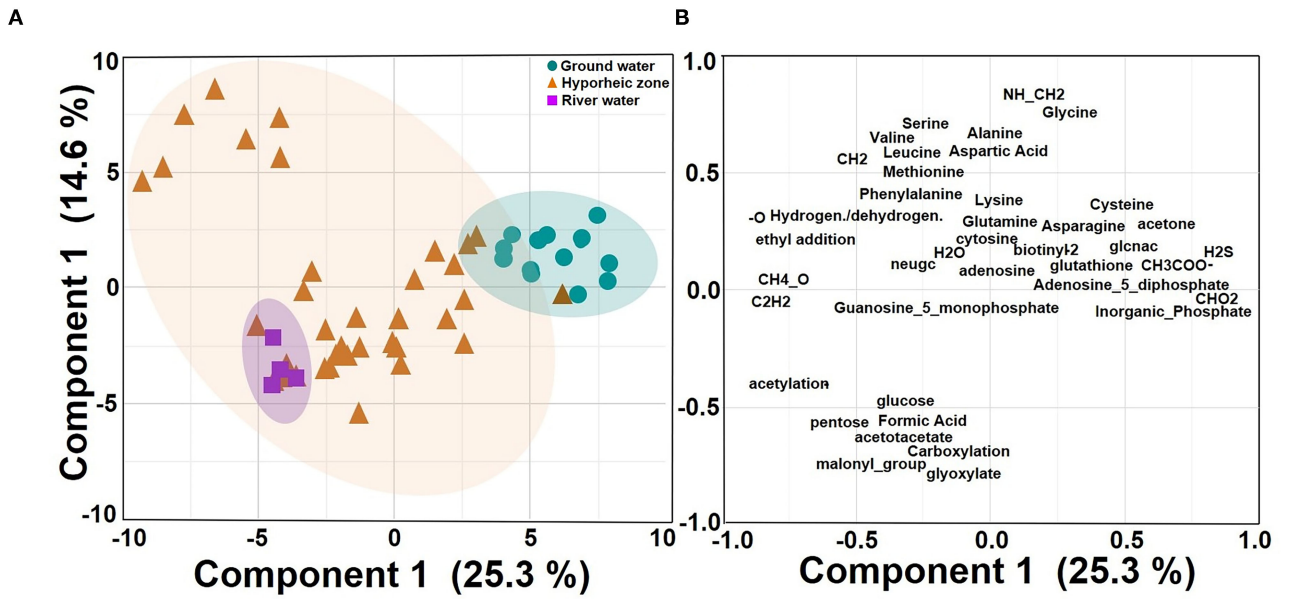

FIGURE 5 | Principle component analysis (PCA) on centered log ratio (CLR) transformed putative chemical transformation abundances in each system (ground water, hyporheic zone, and river water) from the four-time intervals (A–D) (i.e., different river level stages) and piezometer locations in November 2013; **(A)** Score plot **(B)** Loading plot. Shaded circles represent 95% confidence regions.

DOM Transformations in River System Are Driven by Abiotic Factors

Network analysis was utilized to reveal patterns of biochemical transformations by plotting all exact masses within a system connected by their related transformations. This allowed us to visualize how each mass was connected to others, providing a graphical illustration of all putative organic compounds' connections and transformations. Network heterogeneity was then calculated from these networks to gauge the extent to which molecules were transformed. Briefly, a higher network heterogeneity signifies more connections and greater variation of connection types between each mass, indicating more organic compounds transformations, turnover, and degradation to different types of species (i.e., a more transformed system). For visual simplicity, the networks provided here only relate to river stage "A" since similar trends were observed between GW, HZ, and RW from all stages. Network heterogeneity, however, is comprised of values from all river stages and replication to provide a holistic analysis. Across the ground water to river gradient, networks of the hyporheic zone visually looked like those closer to their source (i.e., piezometer 2 contained less ground water contribution as compared to piezometer 5, which contained the most). Interestingly, across a gradient of increasing river water contribution within the hyporheic and ultimately to river water itself, there was an increasing cluster of compounds removed from the main larger cluster (**Figure 7A**). This is herein called the small cluster or network. These two networks (large and small) were connected primarily through three transformation types: palmitoylation, lysine addition, and ethyl addition. To discern the origin of the small network organic compounds, we colored the transformations of the hyporheic zone and river system networks based on transformations that were significantly more common in the river (**Supplementary Table 3**) (colored red—carboxylation, acetylation, hydroxylation, glycoxylation, **Figure 7A**). These side clusters were composed primarily of transformations that were significantly more common in the river (i.e., >50% of the transformations observed in these small networks were attributed to carboxylation, acetylation, hydroxylation, and glycoxylation), of which carboxylation reactions were the dominant transformations. Network heterogeneity increased significantly across the ground water to river water gradient (p values = 0.0058, 0.0010, and 0.0072, **Figures 7B,C**, **Supplementary Table 5**). Additionally, when parsing out river stage variability, the hyporheic zone showed an increase in network heterogeneity in stages C and D compared to stages A and B; hence the contribution of river water to the HZ was higher.

We used Kendrick mass defect (KMD, normalized by -CH_2) to further understand differences between each system's molecular composition (**Figure 8**). Homologous species (i.e., those with the same Kendrick mass) that have larger KMD values signify less degraded, more oxygen incorporated compounds. Compounds with lower KMD values in a homologous species are more degraded, less oxygenated, and H-enriched. Interestingly, the ground water only showed one grouping of masses with higher KMD, and a greater abundance of high molecular weight compounds (average m/z ratio ~375, **Supplementary Figure 6**). Two distinct groupings were revealed in both the hyporheic zone and river water, and when assessed further, the lower mass deficit

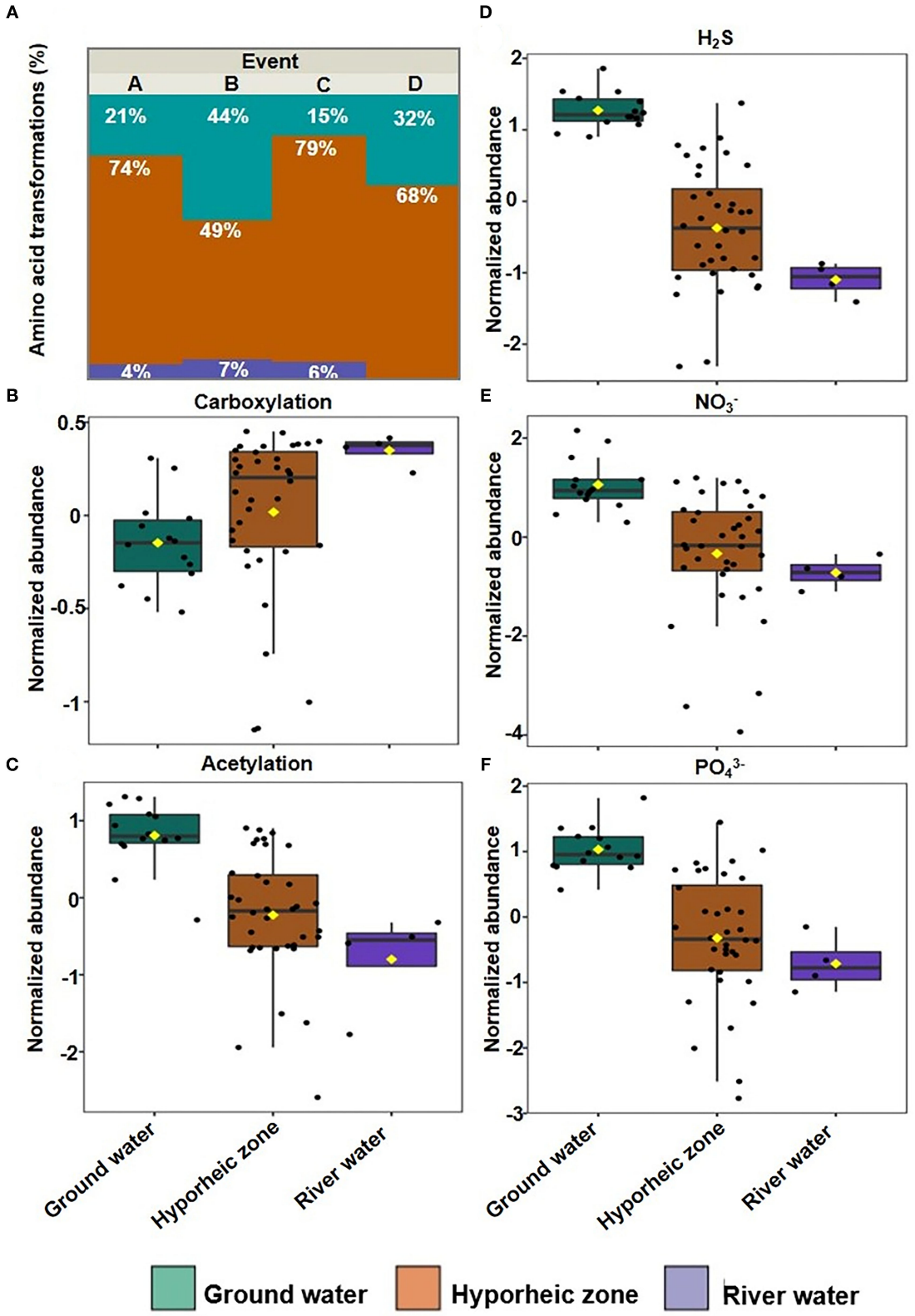

FIGURE 6 | (A) Bar plot of the relative abundance of putative amino acid transformations in each system grouped over four stages (A–D); Box plot of normalized abundance of putative **(B)** carboxylation, **(C)** Acetylation, **(D)** H_2S, **(E)** NO_3^-, and **(F)** PO_4^{3-} transformations in each system grouped over four-time intervals.

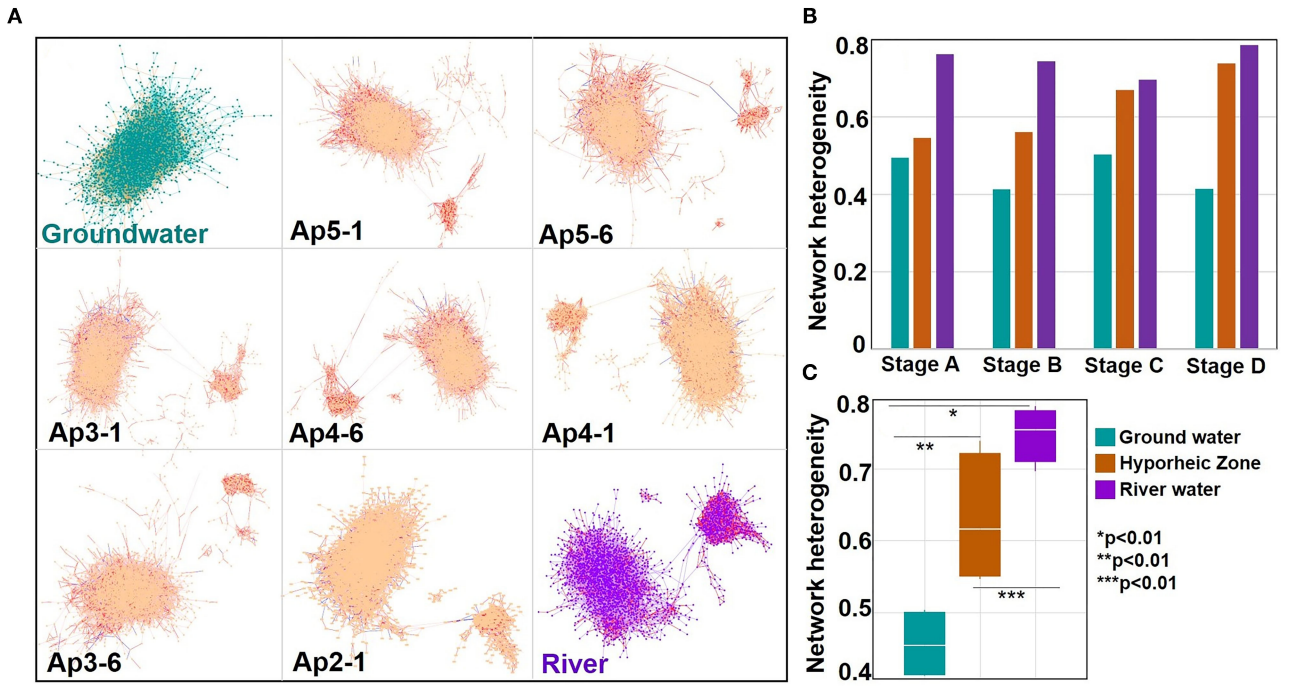

FIGURE 7 | (A) Networks calculated during the network analysis using the full set of chemical transformations (88 transformations) for time interval (river stage) A for each system (ground water, hyporheic zone per piezometer location (where P stands for "piezometer" where as the number next to it refers to the P number. The number after the hyphen refers to the piezometer depth), and river with the system name indicated at the bottom left corner of each panel. Each dot within the figure is an *m/z* value found within a sample. The lines connecting the *m/z* values, defined as edges, are chemical transformations. Yellow edges within the ground water network represent the following ground water upregulated transformations (H_2S, NO_3^-, and PO_4^{3-}, inorganic phosphate, diphosphate, $S_2O_3^{2-}$) intervals. Red edges within the river and hyporheic network represent the following river upregulated transformations (carboxylation, acetylation, malonyl group, glucose transformation, and glycoxylation). Blue edges within the hyporheic network represent the upregulated 20 amino-acids transformations from **Figure 5A**. Samples from the Hyporheic Zone are organized in descending order which relates to declining ground water input. Large to small networks in hyporheic and river samples are connected by three types of putative transformations: palmitoylation, lysine addition, and ethyl addition; Bar and box plots of changes in the network heterogeneity index (calculated from the network) **(B)** as function of four-time intervals for each system and **(C)** grouped over all river stages respectively (with ANOVA and Tuckey test significance represented as*).

compounds were associated with the distinct clusters observed in the network analysis and were of lower molecular weight. This suggests that the subnetwork clusters observed in the hyporheic zone and river network plots are associated with less oxygen-incorporated, more degraded low molecular weight (LMW) compounds. These LMW KMD compounds were also classified as lignin-like molecules in van Krevelen diagram. Overall, the hyporheic zone and river water compounds were composed of slightly less LMW compounds as compared to the ground water (average *m/z* ratio ∼325–375 and ∼325–350, respectively, **Supplementary Figure 6**).

The dynamic nature of ground water and river water mixing within the hyporheic zone is illustrated by the variation in KMD composition between two different hyporheic zone samples (**Figure 7D**–Hyporheic zone AP5-1 vs. AP2-1). The hyporheic zone sample with greater river contribution (AP2-1) showed closer similarity to river water KMD distribution, as opposed to the hyporheic zone sample (AP5-1) with larger ground water contribution (**Figures 1**, **7A**, **8D**).

DISCUSSION

We used high resolution, Fourier transform ion cyclotron resonance mass-spectrometry to provide an in-depth molecular characterization of the Columbia River hyporheic zone DOM, and its constituents (river water and ground water). These in depth profiles (1) provided a deeper understanding of DOM chemical composition of the Columbia River hyporheic zone, and ground and river water (**Figures 2**–**4**), (2) confirmed and extrapolated upon a previous hypothesized mechanism by which microbial activity is enhanced in the hyporheic zone (**Figures 5**–**7**), (3) revealed abiotic drivers in river systems are transforming DOM before it is introduced into the hyporheic zone (**Figures 6**, **8**).

The ground water profile was characterized by a more diverse suite of N and S containing compounds than the river, P compounds localized within the lipid- and condensed hydrocarbon-region of the van Krevelen diagram (**Figure 3**), as well as transformations that cycle these nutrients (NO_3^-, H_2S, and PO_4^{3-}) (**Figures 5**, **6**). Further, more thermodynamically

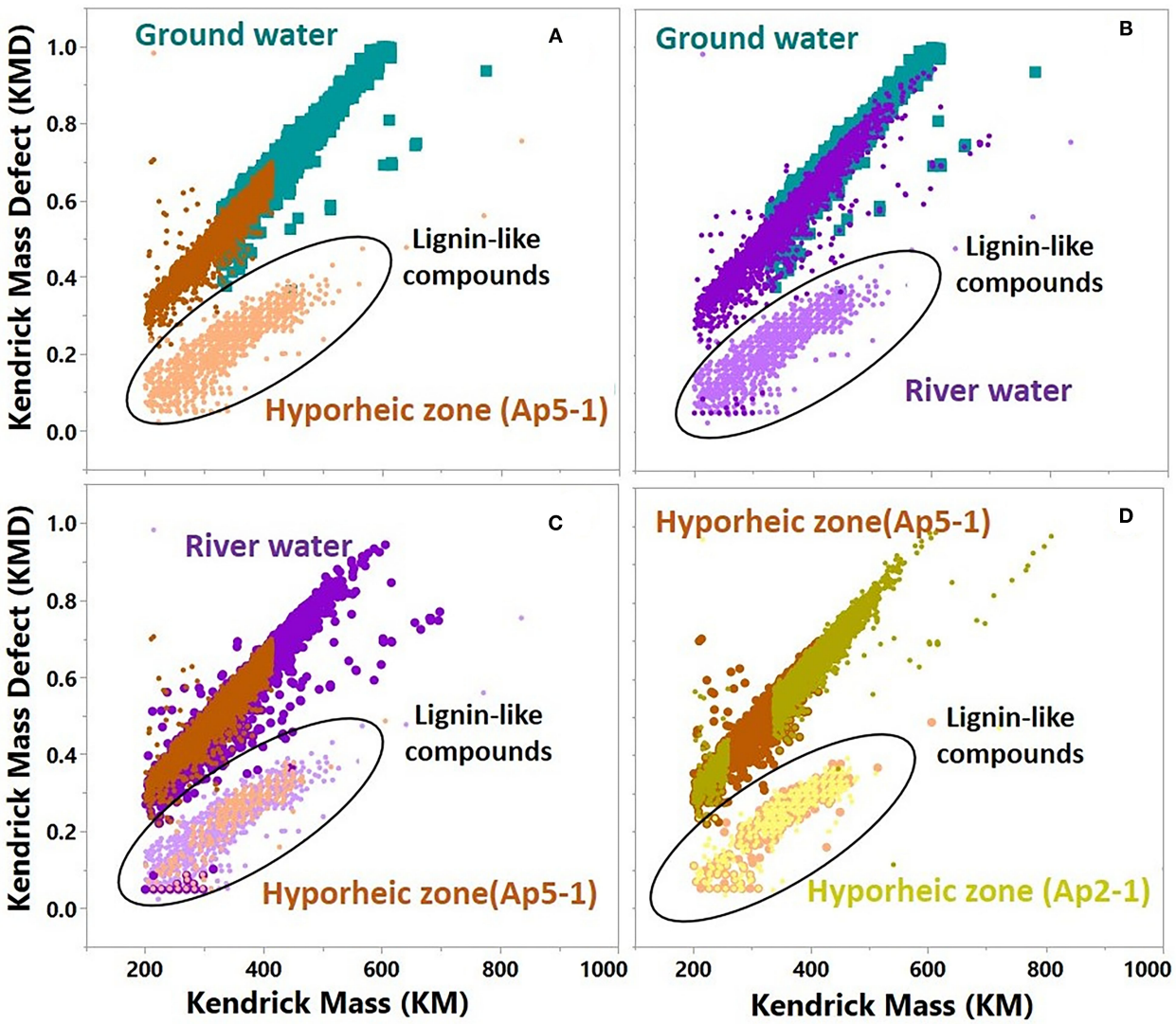

FIGURE 8 | Kendrick plot comparison of molecular formulas that were used in network analysis for representative samples from time interval A. **(A)** Ground water vs. Hyporheic zone (AP5-1); **(B)** Ground water vs. River water; **(C)** River water vs. Hyporheic zone (AP5-1); **(D)** Hyporheic zone (AP5-1) vs. Hyporheic zone (AP2-1), For river water and Hyporheic zone samples, peaks that were part of the small network (represented by the black empty circle) from subpanel A were identified as lignin-like compounds and were colored with a lighter color than peaks that were part of the big network from subpanel A.

favorable DOM and lower network heterogeneity suggest that DOM in the ground water was not as actively transformed as the river water and hyporheic zone, even though microorganisms were present (**Figure 4**). While these data together could suggest anaerobic respiration, a slower and less energetically favorable reaction utilizing NO_3^- and SO_4^{2-} as terminal electron acceptors (Kim et al., 2015; U.S. Geological Survey, 2016), the ground water aquifer is known to be highly oxygenated (Stegen et al., 2018), and thus, persistence of labile DOM would not be limited by anaerobic conditions. While the effective rates of such reactions were shown to be as fast as aerobic mineralization (Kolbe et al., 2019; Bochet et al., 2020), Oldham et al. 2013 showed that the exposure time (i.e., the proportion of residence time with requisite conditions) plays a major role in regulating reactions (Oldham et al., 2013). The low residence time of DOM in ground water, which is dependent on river water fluctuations, could play a role in decreased DOM processing. Stegen et al. (2018) further showed that DOM within the ground water aquifer was at low enough concentrations that this labile C was likely protected more so by the energetics of the system—that is, the odds a microbial cell comes across a DOM molecule is unlikely, and even if it does, it is not worth the microorganism's energy to consume it. Due to the limitation of electron donors in this system, we hypothesize the upregulation of putative -NO_3 and -H_2S transformations (**Figures 5**, **6**) could be due to the abiotic incorporation of these elements into DOM (Sleighter et al., 2014;

Pohlabeln et al., 2017). This hypothesis suggests that N and S "nutrients" could be supplied to the hyporheic zone as abiotically transformed DOM. Chemical reactions involving P such as loss of gain of a phosphate group are attributed to agricultural inputs in the area, likely due to phosphate leaching from surrounding sediments (Reddy and DeLaune, 2008). Predicted increase in the frequency of extreme events, induced by climate change, could alter DOM residence time in ground water and the input of phosphate from surrounding land, leading to changes in ground water DOM composition with direct impact on DOM composition and microbial metabolism in the hyporheic zone.

Considering a larger diversity of N and S containing compounds were observed in the ground water as compared to the river water (**Figure 3**) in this current study, it is likely that a more heterogeneous set of substrates with these incorporated essential elements could be provided to the hyporheic zone. This diversity could in turn be utilized in a larger suite of microbial processes. Our results also further enhance the hypothesis that labile DOM is protected within the ground water ecosystem (**Figure 4C**), since we observed an abundance of labile DOM even in the presence of microorganisms. This implies that labile DOM with abiotically incorporated essential elements could be energetically protected until these compounds enter the hyporheic zone, which would only further influence microbial activity and respiration. Abiotic-driven DOM sources of essential elements to the hyporheic zone is an important topic for further exploration as it is speculated that hyporheic zone microorganisms within the Columbia river are N-limited (Stegen et al., 2018). Future research should be performed to understand how various land inputs, residence time and temperature can affect abiotic transformations of these molecules, explore the different levels of bioavailability of these DOM essential elements to microorganisms, and confirm linkages between essential elements integrated into labile DOM and how these molecules affect hyporheic zone microbial activity.

DOM composition (**Figures 2**–**4**) and transformation data (**Figures 5**–**7**) results revealed that the hyporheic zone is metabolically active with an over-representation of N containing compounds, relative to river water and ground water. These results were consistent with the conceptual model that was developed by Stegen et al. (2016, 2018) that suggests a stimulation of respiration by mixing of ground water with river water. While we show that changes in stage can either increase or decrease hyporheic exchange depending on the substrate materials and driver of the change in flow with direct impact on DOM composition in the hyporheic zone (**Figure 8**) (Wroblicky et al., 1998; Sawyer et al., 2009; Mojarrad et al., 2019), our end-member transformation data results revealed that all chemical transformations were deviated from mixing expectations regardless of mixing ratios and thus river stage. A clear direction for future research is to use our chemical transformation approach to combine mixing models with biogeochemistry to better characterize how the hyporheic response to changes in river stage, driven by climate change (e.g., extreme events, sunlight, temperature, water turbidity, and land inputs) would influence biogeochemistry and microbial activity at the watershed scale.

DOM of river systems is a mixture of autochthonous and allochthonous DOM (Creed et al., 2015; Bertuzzo et al., 2017; Abbott et al., 2018; Shogren et al., 2019) with the latter been widely understood to be composed of plant-inputs, generally in the form of recalcitrant lignin phenols (Raymond and Spencer, 2015). Previous research on DOM processing within the river suggested complicated interactions between autochthonous and allochthonous DOM (Creed et al., 2015; Bertuzzo et al., 2017; Abbott et al., 2018; Shogren et al., 2019). Lignin-like compounds can undergo continuous degradation and mineralization within the river corridor, which can either be completely mineralized or only partially degraded for microbial utilization in the hyporheic zone (Hedges et al., 1997; Koehler et al., 2012; Raymond and Spencer, 2015; Stegen et al., 2016, 2018). At first look, our results revealed that the river profile was composed of less thermodynamically favorable (high GFE) and lignin-like organic matter, which would suggest less bioavailable compounds to microorganisms (**Figure 4**). However, this does not fully illustrate the dynamics of how these lignin-like compounds are being degraded and how degradation influences microbial activity in the hyporheic zone. That is, are larger lignin-like compounds themselves being introduced into the hyporheic zone, which then undergo degradation under heightened biogeochemical activity (e.g., the priming effect)? Or, are lignin-like compounds from the river entering the hyporheic zone as lignin degradation biproducts, changing their bioavailability to microorganisms in the hyporheic zone? And if the latter is true, do river water transformations of lignin molecules enhance or decrease the bioavailability of these biproducts to hyporheic microbial communities?

The answer to "where" lignin degradation reactions occur can be partially unveiled by network analysis. A distinct small network of organic compounds was observed only in the river and hyporheic zone systems and was composed of lignin-like molecules (**Figure 7**). By coloring the transformations in these clusters by significant transformations to each system, the transformations inherent to these small networks were those observed to be significantly more common in the river system. Further, network heterogeneity values were highest in the river (p value $= 0.0072$, **Supplementary Table 5**). This suggests that the total DOM of the river system is more transformed and degraded, which in part is related to this lignin-like compound small network. Taken together, it is likely that a component of DOM lignin degradation is occurring predominantly within the river, and the byproducts of these reactions subsequently enter the hyporheic zone.

Interestingly, around half of the transformations within the small networks were characterized by carboxylation reactions, and further, carboxylation transformations were significantly more common in the river compared to both the hyporheic zone and ground water (**Figures 7**, **8**). Carboxylation has been widely thought to be a byproduct of DOM photo-chemical oxidation (Ward and Cory, 2016), and photodegradation of lignin in river systems has been well established (Opsahl and and, 1998; Spencer et al., 2009; Raymond and Spencer, 2015). Additionally, the sky cover was very low throughout the sampling period in November 2013 with relatively high

observed daily shortwave radiation. Thus, our results may suggest that photo-chemical oxidation is partially oxidizing lignin-like compounds within the river system to lower molecular weight compounds. The Kendrick mass defect analysis of these subset of compounds confirms this observation—the organic compounds were (1) lower in molecular weight compared to other compounds in the system (i.e., more degraded), and (2) lower in Kendrick mass deficit values (i.e., loss of oxygen), likely a product of carboxylic acid group removal via photo-chemical oxidation. This finding has important implications to the extent that the relative change in photo-oxidative control on bioavailability can either amplify or hamper microbial respiration within the hyporheic zone. It has been shown that byproducts of photo-chemical oxidation of DOM in water systems can largely stimulate microbial respiration (Judd et al., 2007; Ward et al., 2017). However, these pathways are complex, since utilization of partially photo-oxidized biproducts depends on microbial community composition as well as the extent of DOM degradation from sun exposure. A recent study by Soares et al. (2019) illustrated that DOM bioavailability in streams actually increased as water residence time and photo exposure increased, suggesting longer exposure of water to sun can enhance the transformation of DOM to usable substrates. While the abundance of LMW compounds in our system from abiotic degradation pathways such as photodegradation, as revealed by transformation analysis revealed, could potentially be used by microorganisms, the relatively large separation of these compounds from others in the hyporheic zone network analysis suggests that lignin photo-oxidized biproducts are not significantly being used by microorganisms. Future research should focus on how changes in environmental conditions such sky cover, temperature and observed daily shortwave radiation could impact abiotic degradation of DOM in river water and how the increase in the intensity of extreme events could impact water turbidity and water residence time.

The two network clusters observed in **Figure 7**, however, were still connected rather than completely separate (**Figure 7**). Across all hyporheic zone networks, three types of putative transformations made up the majority of all connections between large and small networks in the hyporheic zone: palmitoylation, lysine addition, and ethyl addition. Palmitic acid plays an important role in cell membrane organization, signal transduction and energy storage. In palmitoylation reactions, proteins are modified by the addition of palmitoyl chains, which are subsequently used in protein localization for biotic cellular membrane interactions and processes (Linder and Deschenes, 2003). This process typically occurs with cysteine amino acid-containing peptides, although it can also occur with lysine (Smotrys and Linder, 2004). While putative, these transformation data suggest it is possible that photo degraded organic compounds from the river system are then partially utilized for biotic palmitoylation processes in the hyporheic zone, even if only to a minimal extent. Ethyl-addition is also generally indicative of abiotic DOM degradation, which could further suggest coupled abiotic-biotic DOM degradation influences on hyporheic zone DOM turnover.

It is also interesting to note that network heterogeneity (indicative of larger transformations and degradation) was always greater in the river than the hyporheic zone, regardless of river stage (**Figure 7**). These results directly oppose the current dogma of watershed organic matter degradation, where much of DOM turnover is thought to occur due to enhanced microbial activity in the hyporheic zone but agrees with recent work by Lee-Cullin et al. (2018), which suggested that hyporheic exchange homogenizes DOM diversity in surface water. Our results suggest abiotic degradation may be playing a significant role in DOM degradation within watershed systems. Therefore, we believe it is important to consider the abiotic controls on Columbia River DOM and its influence on hyporheic zone respiration. It remains unclear, however, how representative this site is of the whole Columbia River system, and more generally to other river systems in different ecological contexts. This is an open research question that can only be evaluated through future work that involves distributed sampling/experimental campaigns across river corridors.

Currently models such as CLM4.5 classify OM lability broadly using operationally defined categories derived from mineral soils (Campbell and Paustian, 2015) by defining three categories of OM stabilization mechanisms: (1) mineral-associations (chemical protection); (2) physical protection through aggregate compartmentalization; and (3) protection through inherent recalcitrance of OM (biochemical protection), with the remaining OM in the unprotected pool (Six and Paustian, 2014). These categories, however, fail to capture the full complexity of DOM, and are not necessarily representative of the chemical classes observed in watersheds. The high-resolution analytical techniques that were employed in this study can address these critiques and improve the efficiency of models like CLM4.5 by providing a quantitative assessment of OM quality, quantity, complexity, and heterogeneity (GFE and network heterogeneity). Further, the relationship is mathematically simple to describe, applicable to both terrestrial and aquatic systems, and could replace the operationally defined, often ambiguous, compound classes currently being used. DOM complexity and heterogeneity may also affect DOM resident time with implication on GHG emissions, which is thought to enhance the stability and productivity of an ecosystem.

While the importance of rivers in watershed functioning, particularly with regard to DOM chemistry, transport and production of CO_2 is becoming widely recognized, these processes remain underrepresented in current Earth System Models (Regnier et al., 2014) leading to overestimation of the terrestrial C sink (Lauerwald et al., 2017). In response, Bisht et al. (2017) recently described CP v1.0 a coupled Community Land Model (CLM4.5) and reactive transport model (PFLOTRAN) which they implemented at the Hanford Reach Columbia River site and optimized using ground water monitoring wells, river gaging, vegetation surveys, and topographic surveys of the site. Their simulations suggested that riparian zone inundation and enhanced moisture in the vadose zone could increase coupling among terrestrial-aquatic-subsurface processes (Bisht et al., 2017), both of which could influence DOM transformation through expansion of

the anaerobic zone and may alter the relative contribution of abiotic processes to mineralization rates. However, it remains unclear how expansion of the anaerobic zone will alter the relative contribution of abiotic DOM transformations to CO_2 production. Hence, more observation-level data is needed to parameterize both microbial and abiotic DOM transformation rates and interactions with the physiochemical conditions of the system. In PFLOTRAN, microbial redox reactions are modeled via a microbial biomass term. However, reaction rates are not necessarily correlated with biomass or even abundances of the specific microorganism performing the reaction of interest. Proteomic and transcriptomic data provide more direct measures of microbial activity useful for informing rates. While incorporation of all microbial activities for each reaction will likely remain computationally impractical, identifying the critical reactions for the process of interest, and the activities of the microorganisms responsible for those is within the reach of current omics approaches. We believe that our study can narrow this gap by providing information regarding specific DOM transformations leading to mineralization/CO_2 production. Future work should focus on how these reactions interact with environmental parameters such as pH and temperature thereby informing future transcriptomic and proteomics studies that could be used to parameterizing RTMs.

CONCLUSIONS

Here, we show that in-depth molecular characterization of DOM in watershed ecosystems can be used to understand the potential mechanisms by which ground and river water influence microbial turnover of DOM in the Columbia River hyporheic zone. The results of DOM composition and chemical transformation revealed that the hyporheic zone is metabolically active with an over-representation of N containing compounds relative to river and ground water, regardless of river stage. Abiotic degradation, potentially driven by sunlight due to low sky cover and high observed daily shortwave radiation, in both the ground water and river water can influence DOM availability to the hyporheic zone, which could then be coupled with biotic processes for enhanced microbial activity. These results can be used to identify chemical transformations that are most important for CO_2 production in this system, informing further studies to determine equilibrium and rate constants, and other key parameters that will facilitate the inclusion of these critical reactions into RTMs. In ground water systems, future work should be performed to understand the mechanisms behind nutrient (N, P, and S) incorporation into labile DOM in ground water aquifers with special consideration to land use. Changes in land use could affect ground water DOM lability and subsequently impact hyporheic zone respiration. Additionally, research that aims to understand coupled hydrologic, biogeochemical, and microbial function within river corridors experiencing recurring, episodic, or chronic hydrologic perturbations will be highly valuable to ultimately provide the scientific basis for improved management of dynamic river corridors throughout the world. Similarly, as climate effects could contribute to changes in upstream DOM river inputs, such as pronounced abiotic photodegradation of lignin to more bioavailable substrates for hyporheic respiration, incorporating abiotic controls on DOM chemistry into predictive models should be further established. Using molecular characterization to unravel watershed biogeochemical cycling can thus provide important insights into the hydrologic ecosystems and how these influence essential Critical Zone processes.

DATA AVAILABILITY STATEMENT

The datasets presented in this study can be found in online repositories. The names of the repository/repositories and accession number(s) can be found below: https://doi.org/10.17605/OSF.IO/82QYV, NA/.

AUTHOR CONTRIBUTIONS

JS and MT conceptualized the study and secured funding to support the research. MT, JF, RC, JS, and NG participated in the data analysis and writing of the study. NG conducted the statistical analyses. All authors contributed to the article and approved the submitted version.

FUNDING

This research is part of the Scientific Focus Area (SFA) project at PNNL, sponsored by the U.S. Department of Energy, Office of Science, Environmental System Science (ESS) Program. This contribution originates from the ESS Scientific Focus Area (SFA) at the Pacific Northwest National Laboratory (PNNL) and by the startup program at the University of Arizona. PNNL is operated for DOE by Battelle under contract DE-AC06-76RLO 1830. A portion of the research was performed using EMSL, a national scientific user facility sponsored by the U.S. Department of Energy's Office of Biological and Environmental Research and located at Pacific Northwest National Laboratory. We thank the field team members of the PNNL-SFA for sample collection.

ACKNOWLEDGMENTS

The authors acknowledge this would not have been possible without support from their home institutions and the sampling team of the PNNL SFA. Any use of trade, firm, or product names is for descriptive purposes only and does not imply endorsement by the U.S. Government nor the authors' institutions.

SUPPLEMENTARY MATERIAL

The Supplementary Material for this article can be found online at: https://www.frontiersin.org/articles/10.3389/frwa.2020.574692/full#supplementary-material

REFERENCES

Abbott, B. W., Gruau, G., Zarnetske, J. P., Moatar, F., Barbe, L., Thomas, Z., et al. (2018). Unexpected spatial stability of water chemistry in headwater stream networks. *Ecol. Lett.* 21, 296–308. doi: 10.1111/ele.12897

Adrian, R., Hessen, D. O., Blenckner, T., Hillebrand, H., Hilt, S., Jeppesen, E., et al. (2016). "Environmental impacts—lake ecosystems," in *North Sea Region Climate Change Assessment*, eds M. Quante and F. Colijn (Cham: Springer International Publishing), 315–340. doi: 10.1007/978-3-319-39745-0_10

Aitchison, J. (1994). "Principles of compositional data analysis," in *Multivariate Analysis and Its Applications*, eds T. W. Anderson, K. T. Fang, and I. Olkin (Hayward, CA: Institute of Mathematical Statistics), 73–81. *IMS Lecture Notes-Monograph Series* 24. doi: 10.1214/lnms/1215463786

Banks, V., Palumbo-Roe, B., and Russell, C. (2019). "The hyporheic zone," in *Hydrology—The Science of Water*, ed M. S. Javaid. doi: 10.5772/intechopen.85218

Bernhardt, E. S., Blaszczak, J. R., Ficken, C. D., Fork, M. L., Kaiser, K. E., and Seybold, E. C. (2017). Control points in ecosystems: moving beyond the hot spot hot moment concept. *Ecosystems* 20, 665–682. doi: 10.1007/s10021-016-0103-y

Bertuzzo, E., Helton, A. M., Hall, R. O., and Battin, T. J. (2017). Scaling of dissolved organic carbon removal in river networks. *Adv. Water Resour.* 110, 136–146. doi: 10.1016/j.advwatres.2017.10.009

Bisht, G., Huang, M., Zhou, T., Chen, X., Dai, H., Hammond, G. E., et al. (2017). Coupling a three-dimensional subsurface flow and transport model with a land surface model to simulate stream–aquifer–land interactions (CP v1. 0). *Geosci. Model Dev.* 10,4539–4562. doi: 10.5194/gmd-10-4539-2017

Boano, F., Harvey, J. W., Marion, A., Packman, A. I., Revelli, R., Ridolfi, L., et al. (2014). Hyporheic flow and transport processes: mechanisms, models, and biogeochemical implications. *Rev. Geophys.* 52, 603–679. doi: 10.1002/2012RG000417

Bochet, O., Bethencourt, L., Dufresne, A., Farasin, J., Pédrot, M., Labasque, T., et al. (2020). Iron-oxidizer hotspots formed by intermittent oxic–anoxic fluid mixing in fractured rocks. *Nat. Geosci.* 13, 149–155. doi: 10.1038/s41561-019-0509-1

Boulton, A. J., Datry, T., Kasahara, T., Mutz, M., and Stanford, J. A. (2010). Ecology and management of the hyporheic zone: stream-ground water interactions of running waters and their floodplains. *J. North Am. Benthol. Soc.* 29, 26–40. doi: 10.1899/08-017.1

Boulton, A. J., Findlay, S., Marmonier, P., Stanley, E. H., and Maurice Valett, H. (1998). The functional significance of the hyporheic zone in streams and rivers. *Annu. Rev. Ecol. Syst.* 29, 59–81. doi: 10.1146/annurev.ecolsys.29.1.59

Bowen, J. C., Kaplan, L. A., and Cory, R. M. (2019). Photodegradation disproportionately impacts biodegradation of semi-labile DOM in streams. *Limnol. Oceanogr.* 66, 13–26. doi: 10.1002/lno.11244

Boye, K., Herrmann, A. M., Schaefer, M. V., Tfaily, M. M., and Fendorf, S. (2018). Discerning microbially mediated processes during redox transitions in flooded soils using carbon and energy balances. *Front. Environ. Sci.* 6:15. doi: 10.3389/fenvs.2018.00015

Breitling, R., Ritchie, S., Goodenowe, D., Stewart, M. L., and Barrett, M. P. (2006). Ab initio prediction of metabolic networks using Fourier transform mass spectrometry data. *Metabolomics* 2, 155–164. doi: 10.1007/s11306-006-0029-z

Briggs, M. A., Day-Lewis, F. D., Zarnetske, J. P., and Harvey, J. W. (2015). A physical explanation for the development of redox microzones in hyporheic flow. *Geophys. Res. Lett.* 42, 4402–4410. doi: 10.1002/2015GL064200

Brunner, P., Therrien, R., Renard, P., Simmons, C. T., and Franssen, H. J. H. (2017). Advances in understanding river-ground water interactions. *Rev. Geophys.* 55, 818–854. doi: 10.1002/2017RG000556AQ not cited

Burd, A. B., Frey, S., Cabre, A., Ito, T., Levine, N. M., Lønborg, C., et al. (2016). Terrestrial and marine perspectives on modeling organic matter degradation pathways. *Glob. Change Biol.* 22, 121–136. doi: 10.1111/gcb.12987

Burgess, K. E. V., Borutzki, Y., Rankin, N., Daly, R., and Jourdan, F. (2017). MetaNetter 2: a cytoscape plugin for ab initio network analysis and metabolite feature classification. *J. Chromatogr. B Anal. Technol. Biomed. Life Sci.* 1071, 68–74. doi: 10.1016/j.jchromb.2017.08.015

Campbell, E. E., and Paustian, K. (2015). Current developments in soil organic matter modeling and the expansion of model applications: a review. *Environ. Res. Lett.* 10:123004. doi: 10.1088/1748-9326/10/12/123004

Chen, J., and Chang, H. (2019). Dynamics of wet-season turbidity in relation to precipitation, discharge, and land cover in three urbanizing watersheds, Oregon. *River Res. Appl.* 35, 892–904. doi: 10.1002/rra.3487

Clinton, S. M., Edwards, R. T., and Findlay, S. E. G. (2010). Exoenzyme activities as indicators of dissolved organic matter composition in the hyporheic zone of a floodplain river. *Freshw. Biol.* 55, 1603–1615. doi: 10.1111/j.1365-2427.2009.02383.x

Creed, I. F., McKnight, D. M., Pellerin, B. A., Green, M. B., Bergamaschi, B. A., Aiken, G. R., et al. (2015). The river as a chemostat: fresh perspectives on dissolved organic matter flowing down the river continuum. *Can. J. Fish. Aquat.* 72, 1272–1285. doi: 10.1139/cjfas-2014-0400

Durham, B. P., Sharma, S., Luo, H., Smith, C. B., Amin, S. A., Bender, S. J., et al. (2015). Cryptic carbon and sulfur cycling between surface ocean plankton. *Proc. Natl. Acad. Sci. U.S.A.* 112, 453–457. doi: 10.1073/pnas.1413137112

Fasching, C., Ulseth, A. J., Schelker, J., Steniczka, G., and Battin, T. J. (2016). Hydrology controls dissolved organic matter export and composition in an Alpine stream and its hyporheic zone. *Limnol. Oceanogr.* 61, 558–571. doi: 10.1002/lno.10232

Graham, E. B., Crump, A. R., Resch, C. T., Fansler, S., Arntzen, E., Kennedy, D. W., et al. (2016). Coupling spatiotemporal community assembly processes to changes in microbial metabolism. *Front. Microbiol.* 7:1949. doi: 10.3389/fmicb.2016.01949

Graham, E. B., Stegen, J. C., Huang, M., Chen, X., and Scheibe, T. D. (2019). Subsurface biogeochemistry is a missing link between ecology and hydrology in dam-impacted river corridors. *Sci. Total Environ.* 657, 435–445. doi: 10.1016/j.scitotenv.2018.11.414

He, W., Choi, I., Lee, J. J., and Hur, J. (2016). Coupling effects of abiotic and biotic factors on molecular composition of dissolved organic matter in a freshwater wetland. *Sci. Total Environ.* 544, 525–534. doi: 10.1016/j.scitotenv.2015.12.008

Hedges, J. I., Keil, R. G., and Benner, R. (1997). What happens to terrestrial organic matter in the ocean? *Org. Geochem.* 27, 195–212. doi: 10.1016/S0146-6380(97)00066-1

Hester, E. T., and Doyle, M. W. (2008). In-stream geomorphic structures as drivers of hyporheic exchange. *Water Resour. Res.* 44:W03417. doi: 10.1029/2006WR005810

Hou, Z., Nelson, W. C., Stegen, J. C., Murray, C. J., Arntzen, E., Crump, A. R., et al. (2017). Geochemical and microbial community attributes in relation to hyporheic zone geological facies. *Sci. Rep.* 7:12006. doi: 10.1038/s41598-017-12275-w

Hughey, C. A., Hendrickson, C. L., Rodgers, R. P., Marshall, A. G., and Qian, K. (2001). Kendrick mass defect spectrum: a compact visual analysis for ultrahigh-resolution broadband mass spectra. *Anal. Chem.* 73, 4676–4681. doi: 10.1021/ac010560w

Johnson, L. T., Tank, J. L., and Arango, C. P. (2009). The effect of land use on dissolved organic carbon and nitrogen uptake in streams. *Freshw. Biol.* 54, 2355–2350. doi: 10.1111/j.1365-2427.2009.02261.x

Judd, K. E., Crump, B. C., and Kling, G. W. (2007). Bacterial responses in activity and community composition to photo-oxidation of dissolved organic matter from soil and surface waters. *Aquat. Sci.* 69, 96–107. doi: 10.1007/s00027-006-0908-4

Kasahara, T., and Wondzell, S. M. (2003). Geomorphic controls on hyporheic exchange flow in mountain streams. *Water Resour. Res.* 39, SBH 3-1-SBH 3-14. doi: 10.1029/2002WR001386

Kaufman, M. H., Cardenas, M. B., Buttles, J., Kessler, A. J., and Cook, P. L. M. (2017). Hyporheic hot moments: dissolved oxygen dynamics in the hyporheic zone in response to surface flow perturbations. *Water Resour. Res.* 53, 6642–6662. doi: 10.1002/2016WR020296

Kim, H., Kaown, D., Mayer, B., Lee, J. Y., Hyun, Y., and Lee, K. K. (2015). Identifying the sources of nitrate contamination of ground water in an agricultural area (Haean basin, Korea) using isotope and microbial community analyses. *Sci. Total Environ.* 533, 566–575. doi: 10.1016/j.scitotenv.2015.06.080

Kim, S., Kramer, R. W., and Hatcher, P. G. (2003). Graphical method for analysis of ultrahigh-resolution broadband mass spectra of natural organic matter, the Van Krevelen Diagram. *Anal. Chem.* 75, 5336–5344. doi: 10.1021/ac034415p

Koehler, B., Von Wachenfeldt, E., Kothawala, D., and Tranvik, L. J. (2012). Reactivity continuum of dissolved organic carbon decomposition in lake water. *J. Geophys. Res.* 117:G01024. doi: 10.1029/2011JG001793

Kolbe, T., Dreuzy, J.-R., Abbott, B. W., Aquilina, L., Babey, T., Green, C. T., et al. (2019). Stratification of reactivity determines nitrate removal in ground water. *Proc. Natl. Acad. Sci. U. S. A.* 201816892. doi: 10.1073/pnas.1816892116

Lauerwald, R., Regnier, P., Camino-Serrano, M., Guenet, B., Guimberteau, M., and Ducharne, A. et al. (2017). ORCHILEAK (revision 3875): a new model branch to simulate carbon transfers along the terrestrial–aquatic continuum of the Amazon basin. *Geosci. Model Dev.* 10, 3821–3859. doi: 10.5194/gmd-10-3821-2017

Lawrence, C., Harden, J., and Maher, K. (2014). Modeling the influence of organic acids on soil weathering. *Geochim. Cosmochim. Acta* 139, 487–507. doi: 10.1016/j.gca.2014.05.003

Lee-Cullin, J. A., Zarnetske, J. P., Ruhala, S. S., and Plont, S. (2018). Toward measuring biogeochemistry within the stream-ground water interface at the network scale: an initial assessment of two spatial sampling strategies. *Limnol. Oceanogr. Methods* 16, 722–733. doi: 10.1002/lom3.10277

Li, L., Maher, K., Navarre-Sitchler, A., Druhan, J., Meile, C., Lawrence, C., et al. (2017). Expanding the role of reactive transport models in critical zone processes. *Earth-Sci. Rev.* 165, 280–301. doi: 10.1016/j.earscirev.2016.09.001

Linder, M. E., and Deschenes, R. J. (2003). New insights into the mechanisms of protein palmitoylation. *Biochemistry* 42, 4311–4320. doi: 10.1021/bi034159a

Lønborg, C., Álvarez-Salgado, X. A., Letscher, R. T., and Hansell, D. A. (2018). Large stimulation of recalcitrant dissolved organic carbon degradation by increasing ocean temperatures. *Front. Mar. Sci.* 4:436. doi: 10.3389/fmars.2017.00436

Longnecker, K., and Kujawinski, E. B. (2016). Using network analysis to discern compositional patterns in ultrahigh-resolution mass spectrometry data of dissolved organic matter. *Rapid Commun. Mass Spectrom.* 30, 2388–2394. doi: 10.1002/rcm.7719

Merill, L., and Tonjes, D. J. (2014). A review of the hyporheic zone, stream restoration, and means to enhance denitrification. *Crit. Rev. Environ. Sci. Technol.* 44, 2337–2379. doi: 10.1080/10643389.2013.829769

Mojarrad, B. B., Betterle, A., Singh, T., Olid, C., and Wörman, A. (2019). The effect of stream discharge on hyporheic exchange. *Water* 11:1436. doi: 10.3390/w11071436

Naegeli, M. W., and Uehlinger, U. (1997). Contribution of the hyporheic zone to ecosystem metabolism in a prealpine gravel-bed river. *J. North Am. Benthol. Soc.* 16, 794–804. doi: 10.2307/1468172

Naiman, R. J., Bilby, R. E., and Bisson, P. A. (2000). Riparian ecology and management in the pacific coastal rain forest. *Bioscience* 60, 996–1011. doi: 10.1641/0006-3568(2000)050[0996:REAMIT]2.0.CO;2

Newbold, J. D., Bott, T. L., Kaplan, L. A., Dow, C. L., Jackson, J. K., Aufdenkampe, A. K., et al. (2006). Uptake of nutrients and organic C in streams in New York City drinking-water-supply watersheds. *J. North Am. Benthol. Soc.* 25, 998–1017. doi: 10.1899/0887-3593(2006)025[0998:UONAOC]2.0.CO;2

Nogaro, G., Datry, T., Mermillod-Blondin, F., Foulquier, A., and Montuelle, B. (2013). Influence of hyporheic zone characteristics on the structure and activity of microbial assemblages. *Freshw. Biol.* 58, 2567–2583. doi: 10.1111/fwb.12233

NRC (2001). *Basic Research Opportunities in Earth Science*. Washington, DC: National Academy Press.

Oldham, C. E., Farrow, D. E., and Peiffer, S. (2013). A generalized Damköhler number for classifying material processing in hydrological systems. *Hydrol. Earth Syst. Sci.* 17, 1133–1148. doi: 10.5194/hess-17-1133-2013

Opsahl, S., and, Benner, R. (1998). Photochemical reactivity of dissolved lignin in river and ocean waters. *Limnol. Oceanogr.* 43, 1297–1304. doi: 10.4319/lo.1998.43.6.1297

Pawlowsky-Glahn, V., and Buccianti, A. (2011). *Compositional Data Analysis: Theory and Applications*. Hoboken, NJ: Wiley. doi: 10.1002/9781119976462

Pohlabeln, A. M., Gomez-Saez, G. V., Noriega-Ortega, B. E., and, Dittmar, T. (2017). Experimental evidence for abiotic sulfurization of marine dissolved organic matter. *Front. Mar. Sci.* 4:364. doi: 10.3389/fmars.2017.00364

Raymond, P. A., and Spencer, R. G. M. (2015). "Chapter 11 - Riverine DOM," in *Biogeochemistry of Marine Dissolved Organic Matter, 2nd Edn*, eds D. A. Hansell and C. A. Carlson (Boston: Academic Press) 509–533. doi: 10.1016/B978-0-12-405940-5.00011-X

Reddy, K. R., and DeLaune, R. D. (2008). "Organic Phosphorous," in *Biogeochemistry of Wetlands: Science and Applications*. doi: 10.1201/9780203491454

Regnier, P., Lauerwald, R., and Ciais, P. (2014). Carbon leakage through the terrestrial-aquatic interface: Implications for the anthropogenic CO2 budget. *Proc. Earth Planet Sci.* 10, 319–324. doi: 10.1016/j.proeps.2014.08.025

Ritson, J. P., Graham, N. J. D., Templeton, M. R., Clark, J. M., Gough, R., and, Freeman, C. (2014). The impact of climate change on the treatability of dissolved organic matter (DOM) in upland water supplies: a UK perspective. *Sci. Total Environ.* 473–474, 714–730. doi: 10.1016/j.scitotenv.2013.12.095

Sawyer, A. H., Cardenas, M. B., Bomar, A., and Mackey, M. (2009). Impact of dam operations on hyporheic exchange in the riparian zone of a regulated river. *Hydrol. Process.* 23, 2129–2137. doi: 10.1002/hyp.7324

Shannon, P., Markiel, A., Ozier, O., Baliga, N. S., Wang, J. T., Ramage, D., et al. (2003). Cytoscape: a software environment for integrated models of biomolecular interaction networks. *Genome Res.* 13, 2498–2504. doi: 10.1101/gr.1239303

Shogren, A. J., Zarnetske, J. P., Abbott, B. W., Iannucci, F., Frei, R. J., Griffin, N. A., and Bowden, W. B. (2019). Revealing biogeochemical signatures of Arctic landscapes with river chemistry. *Sci. Rep.* 9, 1–11. doi: 10.1038/s41598-019-49296-6

Six, J., and Paustian, K. (2014). Aggregate-associated soil organic matter as an ecosystem property and a measurement tool *Soil Biol. Biochem.* 68, A4–9. doi: 10.1016/j.soilbio.2013.06.014

Sleighter, R. L., Chin, Y.-P., Arnold, W. A., Hatcher, P. G., McCabe, A. J., McAdams, B. C., et al. (2014). Evidence of incorporation of abiotic S and N into Prairie Wetland dissolved organic matter. *Environ. Sci. Lett.* 1, 345–350. doi: 10.1021/ez500229b

Smotrys, J. E., and Linder, M. E. (2004). Palmitoylation of intracellular signaling proteins: regulation and function. *Annu. Rev. Biochem.* 73, 559–587. doi: 10.1146/annurev.biochem.73.011303.073954

Soares, A. R. A., Lapierre, J. F., Selvam, B. P., Lindström, G., and Berggren, M. (2019). Controls on dissolved organic carbon bioreactivity in river systems. *Sci. Rep.* 9:14897. doi: 10.1038/s41598-019-50552-y

Sophocleous, M. (2002). Interactions between ground water and surface water: The state of the science. *Hydrogeol. J.* 10, 52–67. doi: 10.1007/s10040-001-0170-8

Spencer, R. G. M., Stubbins, A., Hernes, P. J., Baker, A., Mopper, K., Aufdenkampe, A. K., et al. (2009). Photochemical degradation of dissolved organic matter and dissolved lignin phenols from the Congo River. *J. Geophys. Res.* 114:G03010. doi: 10.1029/2009JG000968

Stegen, J. C., Fredrickson, J. K., Wilkins, M. J., Konopka, A. E., Nelson, W. C., Arntzen, E. V., et al. (2016). Ground water-surface water mixing shifts ecological assembly processes and stimulates organic carbon turnover. *Nat. Commun.* 7:11237. doi: 10.1038/ncomms11237

Stegen, J. C., Johnson, T., Fredrickson, J. K., Wilkins, M. J., Konopka, A. E., Nelson, W. C., et al. (2018). Influences of organic carbon speciation on hyporheic corridor biogeochemistry and microbial ecology. *Nat. Commun.* 9:585. doi: 10.1038/s41467-018-02922-9

Stern, N., Ginder-Vogel, M., Stegen, J. C., Arntzen, E., Kennedy, D. W., Larget, B. R., et al. (2017). Colonization habitat controls biomass, composition, and metabolic activity of attached microbial communities in the Columbia River hyporheic corridor. *Appl. Environ. Microbiol.* 83, e00260–17. doi: 10.1128/AEM.00260-17

Tfaily, M. M., Chu, R. K., Toyoda, J., Tolić, N., Robinson, E. W., Paša-Tolić, L., et al. (2017). Sequential extraction protocol for organic matter from soils and sediments using high resolution mass spectrometry. *Anal. Chim. Acta.* 972, 54–61. doi: 10.1016/j.aca.2017.03.031

Tfaily, M. M., Hess, N. J., Koyama, A., and Evans, R. D. (2018). Elevated [CO_2] changes soil organic matter composition and substrate diversity in an arid ecosystem. *Geoderma* 330, 1–8. doi: 10.1016/j.geoderma.2018.05.025

Tolić, N., Liu, Y., Liyu, A., Shen, Y., Tfaily, M. M., Kujawinski, E. B., et al. (2017). Formularity: software for automated formula assignment of natural and other organic matter from ultrahigh-resolution mass spectra. *Anal. Chem.* 89, 12659–12665. doi: 10.1021/acs.analchem.7b.03318

U.S. Geological Survey (2016). *Redox Conditions in Contaminated Ground Water*. Available at: https://pubs.water.usgs.gov/sir20065056 (accessed December 5, 2020).

van den Boogaart, K. G., and Tolosana-Delgado, R. (2008). "compositions": a unified R package to analyze compositional data. *Comput. Geosci.* 34, 320–338. doi: 10.1016/j.cageo.2006.11.017

Wagner, K., Bengtsson, M. M., Besemer, K., Sieczko, A., Burns, N. R., Herberg, E. R., et al. (2014). Functional and structural responses of hyporheic biofilms to varying sources of dissolved organic matter. *Appl. Environ. Microbiol.* 80, 6004–6012. doi: 10.1128/AEM.01128-14

Wang, Q., and Zhan, H. (2015). "Characteristic and role of ground water in the critical zone," in *Developments in Earth Surface Processes* (Elsevier), 295–318. doi: 10.1016/B978-0-444-63369-9.00010-0AQ

Ward, C. P., and Cory, R. M. (2016). Complete and partial photo-oxidation of dissolved organic matter draining permafrost soils. *Environ. Sci.* 50, 3545–3553. doi: 10.1021/acs.est.5b05354

Ward, C. P., Nalven, S. G., Crump, B. C., Kling, G. W., and Cory, R. M. (2017). Photochemical alteration of organic carbon draining permafrost soils shifts microbial metabolic pathways and stimulates respiration. *Nat. Commun.* 8:772. doi: 10.1038/s41467-017-00759-2

Watts, P. S., Naden, J., and Machell, J. (2001). Banks Long term variation in water colour from Yorkshire catchments. *Sci. Total Environ*. 278, 57–72. doi: 10.1016/S0048-9697(00)00888-3

White, T., Brantley, S., Banwart, S., Chorover, J., Dietrich, W., Derry, L., et al. (2015). "Chapter 2 - The role of critical zone observatories in critical zone science," in *Developments in Earth Surface Processes*, eds J. R. Giardino and C. Houser (Elsevier) 19, 15–78. doi: 10.1016/B978-0-444-63369-9.00002-10

Wohl, E. (2015). "Chapter 9 - Rivers in the critical zone," in *Developments in Earth Surface Processes*, eds J. R. Giardino and C. Houser (Elsevier), 19, 267–294. doi: 10.1016/B978-0-444-63369-9.00009-4

Wroblicky, G. J., Campana, M. E., Valett, H. M., and Dahm, C. N. (1998). Seasonal variation in surface-subsurface water exchange and lateral hyporheic area of two stream-aquifer systems. *Water Resour. Res.* 34, 317–328. doi: 10.1029/97WR03285

Yamashita, Y., Kloeppel, B. D., Knoepp, J., Zausen, G. L., and Jaffé, R. (2011). Effects of watershed history on dissolved Organic matter characteristics in headwater streams. *Ecosystems* 14, 1110–1122. doi: 10.1007/s10021-011-9469-z

Young, G. H. F., Gagen, M. H., Loader, N. J., McCarroll, D., Grudd, H., Jalkanen, R., et al. (2019). Cloud cover feedback moderates fennoscandian summer temperature changes over the past 1,000 years. *Geophy. Res. Lett.* 46, 2811–2819. doi: 10.1029/2018GL081046

Conflict of Interest: The authors declare that the research was conducted in the absence of any commercial or financial relationships that could be construed as a potential conflict of interest.

frontiers in Water

ORIGINAL RESEARCH
published: 03 February 2021
doi: 10.3389/frwa.2020.595538

On the Representation of Hyporheic Exchange in Models for Reactive Transport in Stream and River Corridors

*Scott L. Painter**

Environmental Sciences Division, Oak Ridge National Laboratory, Oak Ridge, TN, United States

Efforts to include more detailed representations of biogeochemical processes in basin-scale water quality simulation tools face the challenge of how to tractably represent mass exchange between the flowing channels of streams and rivers and biogeochemical hotspots in the hyporheic zones. Multiscale models that use relatively coarse representations of the channel network with subgrid models for mass exchange and reactions in the hyporheic zone have started to emerge to address that challenge. Two such multiscale models are considered here, one based on a stochastic Lagrangian travel time representation of advective pumping and one on multirate diffusive exchange. The two models are formally equivalent to well-established integrodifferential representations for transport of non-reacting tracers in steady stream flow, which have been very successful in reproducing stream tracer tests. Despite that equivalence, the two models are based on very different model structures and produce significantly different results in reactive transport. In a simple denitrification example, denitrification is two to three times greater for the advection-based model because the multirate diffusive model has direct connections between the stream channel and transient storage zones and an assumption of mixing in the transient storage zones that prevent oxygen levels from dropping to the point where denitrification can progress uninhibited. By contrast, the advection-based model produces distinct redox zonation, allowing for denitrification to proceed uninhibited on part of the hyporheic flowpaths. These results demonstrate that conservative tracer tests alone are inadequate for constraining representation of mass transfer in models for reactive transport in streams and rivers.

Keywords: hyporheic zone, reactive transport, multiscale modeling, stochastic hydrological modeling, contaminant transport

OPEN ACCESS

Edited by:
Tim Scheibe,
Pacific Northwest National Laboratory (DOE), United States

Reviewed by:
Reza Soltanian,
University of Cincinnati, United States
Clare Robinson,
Western University, Canada

***Correspondence:**
Scott L. Painter
paintersl@ornl.gov

Specialty section:
This article was submitted to Water and Critical Zone, a section of the journal Frontiers in Water

Received: *17 August 2020*
Accepted: *02 December 2020*
Published: *03 February 2021*

Citation:
Painter SL (2021) On the Representation of Hyporheic Exchange in Models for Reactive Transport in Stream and River Corridors. Front. Water 2:595538. doi: 10.3389/frwa.2020.595538

INTRODUCTION

Efforts to understand and model the fate and transport of solutes through streams and rivers have focused much attention on regions of stagnant or relatively slow-moving water known as transient storage zones. Transient storage zones include in-stream eddies and pools, biofilms, vegetation beds and especially the regions of saturated sediment below and surrounding the flowing channel known as hyporheic zones. Hyporheic zones in particular are widely recognized as biogeochemical hotspots where transformation and retention rates of solutes are elevated relative to the flowing

channel (Boano et al., 2014; Ward, 2016). Hyporheic exchange flow (HEF), the movement of water from the channel into the hyporheic zone and back, allows solutes to access those reactive zones. As a result, hyporheic exchange flow is important in the biogeochemical processing of nutrients (Duff and Triska, 2000; Böhlke et al., 2004; Mulholland et al., 2008), organic carbon (Grimm and Fisher, 1984; Battin et al., 2008), metals (Bourg and Bertin, 1993; Fuller and Harvey, 2000; Palumbo-Roe et al., 2012), and organic contaminants (Kim et al., 1995; Conant et al., 2004; Schaper et al., 2018).

Despite the disproportionate role played by hyporheic exchange flow in regulating downstream water chemistry, the representation of the effects of HEF in watershed- and basin-scale models of biogeochemical processing and water quality remains a challenge. Helton et al. (2011) evaluated common modeling approaches for modeling biogeochemistry in stream networks using scaling of *in situ* denitrification from headwater streams to river networks as a concrete example. They identify the need to include hydrologic exchanges between the stream channel and subsurface waters coupled to more mechanistic representations of coupled biogeochemical cycles and conclude that limitations in our current modeling approaches "restrict our ability to simulate biogeochemical dynamics among diverse river networks."

Models for transport of non-reacting tracers in stream corridors have progressed from the classical transient storage model (TSM) (Bencala and Walters, 1983) which conceptualizes a single well-mixed transient storage zone coupled to the stream channel by first-order mass exchange, to integrodifferential models that accommodate a diversity of hyporheic flowpaths with a distribution of travel times (Haggerty et al., 2002; Wörman et al., 2002; Gooseff et al., 2003; Marion et al., 2008; Liao and Cirpka, 2011; Lemke et al., 2013; Liao et al., 2013). The integrodifferential models have been highly successful at representing results of in-stream tracer tests. In particular, they are able to reproduce late-time tailing of breakthrough curves, which is commonly observed in stream tracer tests, important biogeochemically, and not represented by the TSM. However, the integrodifferential approach uses a convolution of the in-stream solute concentration with the hyporheic travel-time distribution to represent exchange of solutes between the stream and multiple hyporheic zone flowpaths, an approach that does not generalize to nonlinear multicomponent chemistry.

Recognizing the advantages of a travel-time-based model for representing the diversity of hyporheic flowpaths and the limitations of the integrodifferential models for reactive transport, Painter (2018) introduced an alternative formulation that uses the standard one-dimensional advection-dispersion-reaction equation for the channel and couples that equation at each channel location to a one-dimensional advection-reaction subgrid model. Written in Lagrangian form, each subgrid model represent an ensemble of streamlines that are diverted into the hyporheic zone before returning to the channel. That approach, which is referred to here as ADELS (Advection Dispersion Equation with Lagrangian Subgrid), is formally equivalent to the integrodifferential model for non-reacting tracers and steady channel discharge. However, the ADELS approach generalizes to nonlinear reactive chemistry, and thus provides a tractable method for multicomponent reactive transport in fluvial corridors from reach to river basin scales.

Motivated by similar considerations, Fang et al. (2020) coupled a generalization of the TSM to the geochemical reaction model PFLOTRAN (Hammond et al., 2014). Like ADELS, the TSM model and generalizations are readily coupled to full multicomponent reaction models. The TSM has been linked, for example, to the equilibrium geochemistry code MINTEQ (Allison et al., 1991) to form the OTIS/OTEQ model (Runkel et al., 1996). As noted already, the single-zone TSM is not able to represent the long-time behavior of breakthrough curves with slowly decaying tails, which is particularly problematic for understanding nutrient processing in streams, as the longer travel time pathways are responsible for denitrification (e.g., Zarnetske et al., 2012). Fang et al. (2020) addressed that limitation by adopting a multirate generalization of the TSM. Multirate mass transfer models were developed for the study of transport in porous media (Haggerty and Gorelick, 1995; Carrera et al., 1998; Haggerty et al., 2000; Wang et al., 2005; Gouze et al., 2008; Benson and Meerschaert, 2009) including multicomponent reactive transport (Donado et al., 2009). Multirate mass transfer models have been used previously to model non-reacting transport in fluvial corridors (Silva et al., 2009; Anderson and Phanikumar, 2011; Haggerty, 2013). Those Multirate Transient Storage Models (mTSM) use multiple transient storage zones, each with its own coefficient for mass transfer with the stream channel. Importantly, mTSM and integrodifferential models are equivalent for non-reactive tracers in steady flow with a known relationship between the distribution of rate constants and the hyporheic travel time distribution (Haggerty et al., 2000; Wang et al., 2005; Silva et al., 2009).

Since both are equivalent to the integrodifferential model for non-reacting tracers in steady flow, the ADELS and mTSM are thus equivalent in that situation. Unlike the integrodifferential form, both generalize to fully nonlinear chemical reaction models and provide tractable strategies for basin-scale simulation without sacrificing fidelity to contemporary process understanding. However, the two models use fundamentally different conceptualizations of the hyporheic zone and hyporheic exchange flow, as shown schematically in **Figure 1**. In mTSM, the hyporheic zone is represented as multiple well-mixed stagnant zones, each connected by diffusive (first-order reversible) exchange with the channel but not to each other. In contrast, the ADELS model conceptualizes an ensemble of one-dimensional hyporheic pathways that each takes its upstream boundary condition from the channel and provides a mass flux back to the channel at its outlet as in the advective pumping model. Once discretized for computation, computational cells representing the hyporheic zone in mTSM are connected in parallel to the channel while in ADELS they are connected in series. Because of that difference in model structure, it is not clear that the two approaches would produce the same results for reactive transport even though they are equivalent for non-reactive transport.

Here we explore the field-scale reactive transport implications of different conceptualizations of the hyporheic zone that are equivalent for non-reactive transport. Specifically, we compare

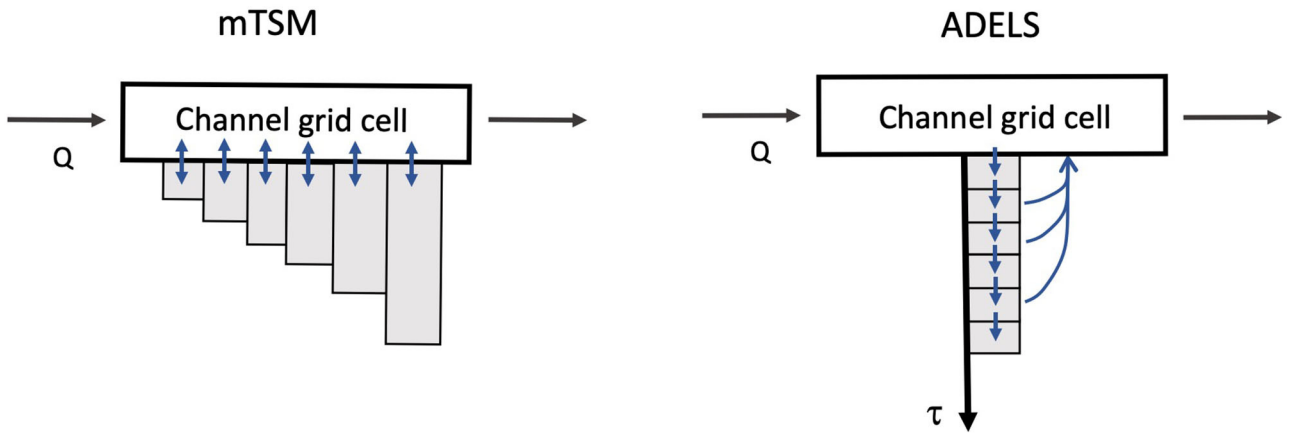

FIGURE 1 | Schematic showing mesh topology for two approaches for representing the effects of hyporheic exchange in models of reactive transport in stream and river corridors. The multirate Transient Storage Model (mTSM) considers multiple transient storage zones of different sizes that are each coupled to the channel by first-order reversible mass exchange. The ADELS model represent an ensemble of streamlines that are diverted into the hyporheic zone before returning to the stream channel using a one-dimensional advection-reaction equation written in Lagrangian form with hyporheic age τ replacing the spatial coordinate. The two conceptualizations are equivalent for non-reacting tracer transport, but not for reactive transport.

the ADELS and mTSM conceptualizations using denitrification as a concrete example. Results are also compared to a simple estimate (Painter, 2018) that accounts for hyporheic exchange but treats denitrification as a first-order kinetic process. The objectives are to identify conditions where the two models produce similar results and where they differ and to explore implications for the development of reactive transport models applicable to stream and river corridors. The focus here is on steady channel flow conditions. However, mTSM and to a limited extend ADELS are generalizable to unsteady flow conditions in contrast to convolution-based models.

The effect of hyporheic-zone model structure on transport of reactive solutes has been explored previously. Kerr et al. (2013) adopted 2-zone variants (Briggs et al., 2009) of the TSM and explored differences between nested (series) and competing (parallel) configurations focusing on transport with first-order degradation. Kelleher et al. (2019) compared reactive tracer transport assuming 1-zone and 2-zone TSMs. Yakirevich et al. (2017) compared reactive tracer transport assuming 2-zone and 3-zone TSMs. Here we go beyond the 2- and 3-zone TSM and focus on methods (ADELS and mTSM) that provide flexible representations of hyporheic residence times resulting from diverse flowpaths and include nonlinear reactive chemistry.

METHODS

Transport of Non-reacting Solutes

ADELS

A recently introduced multiscale approach (Painter, 2018) uses a one-dimensional advection-dispersion-reaction equation for the channel and couples that equation at each channel location to a one-dimensional advection-reaction subgrid model representing an ensemble of streamlines that are diverted into the hyporheic zone before returning to the channel. The ADELS model adopts a Lagrangian travel time framework for the hyporheic subgrid models. Here we refer to hyporheic age τ as the time elapsed by a tracer since it starts moving on a hyporheic streamline and hyporheic lifetime or travel time T as the total time spent on a given hyporheic streamline. Thus, each streamline has a single value of T and τ replaces the spatial coordinate on that streamline with $0 \leq \tau \leq T$. Noting that the streamlines all have the same upstream boundary condition, which is governed by the concentration in the stream channel, the concentration vs. age are the same along the streamlines. Computationally, we thus need consider reactive transport along only one representative streamline. Solute flux from the hyporheic zone to the stream channel can then be computed from results at intermediate locations along that representative streamline, properly weighted by the probability density for hyporheic travel time ϕ (T). The concentration in the channel C_{ch} is then a function of position x along the channel and time t, $C_{ch} = C_{ch}(t,x)$, whereas the concentration C_{hz} in the hyporheic zone is a function of x, t and the hyporheic age, $C_{hz} = C_{hz}(t,x,\tau)$.

The model for non-reacting tracers on a single reach is expressed mathematically as

$$\frac{\partial}{\partial t}(AC_{ch}) + \mathcal{T}C_{ch} = -\alpha A C_{ch} + \alpha A \int_0^\infty C_{hz}(t,x,T)\,\phi(\mathrm{T})dT \quad 0 \leq x \leq L \tag{1}$$

$$\frac{\partial C_{hz}}{\partial t} + \frac{\partial C_{hz}}{\partial \tau} = 0 \qquad 0 \leq \tau \leq \infty \tag{2}$$

$$C_{hz}(t,x,0) = C_{ch}(t,x) \tag{3}$$

plus initial conditions and suitable boundary conditions on the stream channel ($x = 0$ and $x = L$). Here the transport operator $\mathcal{T}C \equiv \frac{\partial}{\partial x}(QC) - \frac{\partial}{\partial x}\left(AD\frac{\partial C}{\partial x}\right)$ is used to simplify the notation. Note that the accumulation term $\frac{\partial}{\partial t}(AC_{ch})$ was

previously (Painter, 2018) included in $\mathcal{T}$. The accumulation term is written separately from the transport operator here to facilitate a more compact representation of reactive transport. Equation 3 and the last term in Equation (1) provide the coupling between the channel and hyporheic zone, with the latter acting as a solute source to the channel and the channel concentration providing the upstream boundary condition on the canonical streamline for the hyporheic zone. The constant α [1/s] is the rate constant for hyporheic exchange. Physically it is the volumetric flowrate for recirculating water in the hyporheic zone per unit channel volume.

An important numerical detail is how to calculate the integral in Equation (1). The integral can be efficiently approximated by considering $C_{hz}(t,x,T)$ as piecewise constant over N subintervals with the subintervals selected to be equally spaced in probability. That is, the i-th subinterval is the quantile interval from T_{i-1} to T_i with $T_i = \Phi^{-1}\left(\frac{i}{N}\right)$. In that interval $C_{hz}(t,x,T)$ is approximated as $C_{hz}(t,x,T_{i-1/2})$. Here Φ(T) is the cumulative lifetime distribution and Φ^{-1} its inverse. Noting that our choice of T_i means $\int_{T_{i-1}}^{T_i} \phi\,(\mathrm{T})\,dT = \frac{1}{N}$ we have.

$$\int_0^\infty C_{hz}\,(t,x,T)\,\phi\,(T)d\mathrm{T} = \frac{1}{N}\sum_{i=1}^{N} C_{hz}\left(t,x,T_{i-1/2}\right) \quad (4)$$

$$T_{i-1/2} = \Phi^{-1}\left(\frac{i-\frac{1}{2}}{N}\right) \quad (5)$$

Numerical tests with conservative tracers on single reaches showed (Painter, 2018) this representation to be highly efficient in that it converges quickly as N increases, thus reducing the size of the number of unknowns in the the subgrid representation.

mTSM

The multirate generalization of the TSM represents a transient storage zone not as one zone but as a collection of sub-zones that are each exchanging mass with the flowing channel with different rate constants. This multirate TSM model is conceptually equivalent to multirate sorption models used to represent subsurface transport. They can represent an arbitrary residence time distribution by proper choice of the distribution of rate constants and are formally equivalent to convolution (Haggerty et al., 2000; Pruess and Wang, 2001; Wang et al., 2005) and thus to our multiscale model for non-reacting tracers and in steady flow. Although equivalent for non-reacting transport, the two conceptualizations differ in how the mass exchange is represented, which has consequences for reactive transport. In the multirate TSM conceptualization, all computational cells in the hyporheic zone exchange mass with the channel. That is, all reaction cells in the hyporheic zone are coupled in parallel to the channel. By contrast, the ADELS conceptualization couples a one-dimensional advection reaction system to each channel grid cell, thus connecting hyporheic grid cells in series, consistent with advective pumping. Here we explore how that difference in mass exchange representations results in different results reactive transport using a model denitrification system.

We adopt a parsimonious version of the multirate TSM. For a single non-reacting species, a continuous version of the multirate model can be written

$$\frac{\partial}{\partial t}\left(AC_{ch}\right) + \mathcal{T}C_{ch} = -\gamma A\int_0^\infty \beta\,(C_{ch} - C_{hz}\,(\beta))f\,(\beta)\,d\beta \quad (6)$$

$$\frac{\partial C_{hz}(\beta)}{\partial t} = \beta\,(C_{ch} - C_{hz}\,(\beta)) \quad \forall\,\beta \quad (7)$$

where γ is the ratio of hyporheic zone volume to channel volume and $f\,(\beta)$ is the probability density for the hyporheic exchange coefficients β. Here the explicit dependence of C_{ch} and C_{hz} on time t and position x are suppressed for clarity.

Following the same type of approximation used for Equation (4), a discrete version of the mTSM can be obtained by approximating $C_{hz}(\beta)$ as piecewise constant over N subintervals with the subintervals selected to be equally spaced in probability. That is, the i-th subinterval is the quantile interval from β_{i-1} to β_i where $\beta_i = F^{-1}\left(\frac{i}{N}\right)$. The interval on the right in Equation (6) then becomes

$$\int_0^\infty \beta\,(C_{ch} - C_{hz}\,(\beta))f\,(\beta)\,d\beta = \frac{1}{N}\sum_{i=1}^{N}\left(C_{ch} - C_{hz,i}\right)\beta_{i-1/2} \quad (8)$$

A discrete mTSM is then given by

$$\frac{\partial}{\partial t}\left(AC_{ch}\right) + \mathcal{T}C_{ch} = -\frac{\gamma A}{N}\sum_{i=1}^{N}\beta_{i-1/2}\left(C_{ch} - C_{hz,i}\right) \quad (9)$$

$$\frac{\partial C_{hz,i}}{\partial t} = \beta_{i-1/2}\left(C_{ch} - C_{hz,i}\right) \quad \forall\, i \quad (10)$$

$$\beta_{i-1/2} = F^{-1}\left(\frac{i-\frac{1}{2}}{N}\right) \quad (11)$$

Equivalence Between the ADELS and mTSM Models

Assuming, for the purposes of this comparison, that solute concentration in the hyporheic zone is initially zero, the continuous version of the multirate model has an equivalent convolution form (e.g., Wang et al., 2005), which can be written

$$\frac{\partial}{\partial t}\left(AC_{ch}\right) + \mathcal{T}C_{ch} = -A\gamma\,\langle\beta\rangle\,C_{ch} + A\gamma\,\langle\beta\rangle\int_0^t \phi\,(t-\tau)C_{ch}\,(\tau)\,d\tau \quad (12)$$

where the hyporheic lifetime density $\phi\,(t)$ is the derivative of the so-called memory function (Carrera et al., 1998; Haggerty et al., 2000) normalized by the mean exchange rate constant $\langle\beta\rangle$. The hyporheic lifetime density is explicitly related to $f\,(\beta)$ (e.g., Wang et al., 2005)

$$\phi\,(t) = \frac{1}{\langle\beta\rangle}\int_0^\infty f\,(\beta)\,\beta^2\exp\left(-\beta t\right)d\beta \quad (13)$$

Equation 10 is equivalent to the ADELS model when the hyporheic exchange rate is $\alpha = \gamma\,\langle\beta\rangle$ and hyporheic lifetime density is given by Equation (13).

The discrete forms of the ADELS and mTSM models can be related by selecting the quantiles T_i of the hyporheic lifetime distribution in ADELS based on the distribution of rate constants in mTSM. The hyporheic lifetime quantile T_i in the ADELS model [see Equation (5)].

$$\int_0^{T_{i-1/2}}\phi\,(T)\,dT = \frac{i-\frac{1}{2}}{N} \quad (14)$$

Integrating both sides of Equation (13) with respect to t from 0 to $T_{i-1/2}$ gives

$$\frac{1}{\langle\beta\rangle}\int_0^\infty \beta f(\beta)\left[1-e^{-\beta\, T_{i-1/2}}\right]d\beta = \frac{i-\frac{1}{2}}{N} \tag{15}$$

Given a probability density for the exchange rate constants in the mTSM $f(\beta)$, Equation (15) can be solved for each $i = 1, N$ to determine the hyporheic lifetime quantiles $T_{i-1/2}$ for use in the ADELS model.

Multicomponent Reactive Transport

Both ADELS and mTSM generalize to general multicomponent reactive transport. To keep things simple, we assume the reaction system is completely kinetically controlled. Although not addressed here, large reaction systems involving a combination of kinetically controlled and equilibrium reactions are easily accommodated by placing the system in canonical form (Lichtner, 1985, 1996) where algebraic mass action equations replace the differential equations for a subset of the species.

ADELS

Although mathematically equivalent to a convolution in the case of steady flow and no reactions, the Lagrangian subgrid formulation generalizes to include nonlinear reactions (Painter, 2018) while the convolution does not. Neglecting non-reactive zones for clarity (although easily included) and adopting the quadrature Equations (4), (5) the reactive transport system can be written

$$\frac{\partial \mathbf{C}_{ch}}{\partial t} + \mathcal{T}\mathbf{B}\circ\mathbf{C}_{ch} = -A\alpha_{hz}\mathbf{B}\circ\mathbf{C}_{ch} + \frac{A\alpha_{hz}}{N}\sum_{i=1}^{N}\mathbf{B}\circ\mathbf{C}_{hz}\left(t,x,T_{i-\frac{1}{2}}\right) + A\mathbf{P}_{ch}(\mathbf{C}_{ch}) + A\mathbf{S}_{ch} \tag{16}$$

$$\frac{\partial \mathbf{C}_{hz}}{\partial t} + \mathbf{B}\circ\frac{\partial \mathbf{C}_{hz}}{\partial \tau} = \mathbf{P}_{hz}(\mathbf{C}_{hz}) \tag{17}$$

$$\mathbf{C}_{hz}(t,x,0) = \mathbf{C}_{ch}(t,x) \tag{18}$$

Here bold quantities represent column vectors, $\mathbf{C}_{ch}(t,x)$ and $\mathbf{C}_{hz}(t,x,\tau)$ contain the species concentrations in the channel and hyporheic zones, respectively, $\mathbf{S}_{ch}$ is the direct solute source to the channel, $\mathbf{B}$ is a column vector with elements equal to 1 for mobile species and 0 for immobile species, and the operator $\circ$ denotes element-wise multiplication. The element-wise multiplications by $\mathbf{B}$ ensure that immobile species are not transported and not transferred between the hyporheic zone and channel. The vector-valued vector functions $\mathbf{P}_{ch}(\mathbf{C}_{ch})$ and $\mathbf{P}_{hz}(\mathbf{C}_{hz})$ describe the transformation (production/consumption) rates caused by reactions as functions of local concentrations. Note that each species depends on all the other species through the reaction terms.

mTSM

The mTSM model generalizes to multicomponent reactive transport in a similar way:

$$\frac{\partial \mathbf{C}_{ch}}{\partial t} + \mathcal{T}\mathbf{B}\circ\mathbf{C}_{ch} = -\frac{\gamma A}{N}\sum_{i=1}^{N}\beta_{i-1/2}\left(\mathbf{C}_{ch} - \mathbf{C}_{hz,i}\right)\circ\mathbf{B} + A\,\mathbf{P}_{ch}(\mathbf{C}_{ch}) + A\mathbf{S}_{ch} \tag{19}$$

$$\frac{\partial \mathbf{C}_{hz,i}}{\partial t} = \beta_{i-1/2}\left(\mathbf{C}_{ch} - \mathbf{C}_{hz,i}\right)\circ\mathbf{B} + \mathbf{P}_{hz}\left(\mathbf{C}_{hz,i}\right) \quad \forall\, i \tag{20}$$

Here the element-wise multiplication with $\mathbf{B}$ again prevents immobile species from being transported and transferred between the storage zones and the channel.

Model Reaction System

A simple denitrification example is used here to compare how different representations of hyporheic exchange impact reactive transport simulations. The denitrification example tracks a single representative dissolved organic carbon (DOC) species with chemical composition CH_2O, dissolved oxygen, and nitrate with aerobic respiration and denitrification reactions

$$CH_2O + O_2\,(\mathrm{aq}) \rightarrow CO_2\,(\mathrm{aq}) + H_2O \tag{21}$$

$$CH_2O + \frac{4}{5}NO_3^- + \frac{4}{5}H^+ \rightarrow \frac{4}{10}N_2\,(\mathrm{aq}) + CO_2\,(\mathrm{aq}) + \frac{7}{5}H_2O \tag{22}$$

in the subgrid system, but not in the channels. Dissolved oxygen is held constant in the channel to represent re-aeration. Nitrate and DOC are introduced at the upstream boundary of the channel reach and tracked throughout. Carbon released from buried particulate organic carbon is neglected here. This example uses an implicit representation of microbially mediated denitrification. That is, the dynamics of microbial biomass is not explicitly simulated. Instead, the net effects of those reactions are described by dual-Monod kinetics with oxygen inhibiting denitrification. Explicit representations of microbial dynamics are available (e.g., Sanz-Prat et al., 2015) and have been used in the ADELS framework by Painter (2018). Implicit variants with more complete description of the reaction system are also available (e.g., Fang et al., 2020). For the purposes of our comparison, we adopt a simple but still nonlinear version. Production rates are represented as

$$r_{DOC} = -r_{O2} - \frac{5}{4}r_{NO3} \tag{23}$$

$$r_{O2} = -k_{aer}\mathrm{M}\left(C_{O2}, K_{aer}^{O2}\right)\mathrm{M}\left(C_{doc}, K_{aer}^{doc}\right) \tag{24}$$

$$r_{NO3} = -k_{den}\mathrm{M}\left(C_{NO3}, K_{den}^{NO3}\right)\mathrm{M}\left(C_{doc}, K_{den}^{doc}\right) M\left(K_{den}^{O2inh}, C_{O2}\right) \tag{25}$$

Here $\mathrm{M}(A,B) \equiv \frac{A}{A+B}$ represents Monod kinetics or an inhibition function, depending on the order of concentration and model parameter in the argument list. That is, if C is a concentration and

TABLE 1 | Reference case reaction parameters.

Symbol	Description	Value	Units
k_{aer}	Maximum respiration rate for aerobes	0.1	μM s^{-1}
k_{den}	Maximum denitrification rate	0.016	μM s^{-1}
K_{aer}^{doc}	Monod half-saturation for DOC in aerobic degradation	45	μM
K_{aer}^{O2}	Monod half-saturation for oxygen in aerobic degradation	6	μM
K_{den}^{doc}	Monod half-saturation for DOC in denitrification	45	μM
K_{den}^{NO3}	Monod half-saturation for nitrate in denitrification	50	μM
K_{den}^{O2inh}	Oxygen inhibition constant for denitrifiers	0.3	μM
C_{DOC}^{in}	Upstream boundary condition on DOC	500	μM
C_{O2}^{in}	In-stream value of oxygen (fixed)	250	μM
C_{NO3}^{in}	Upstream boundary condition on nitrate	130	μM

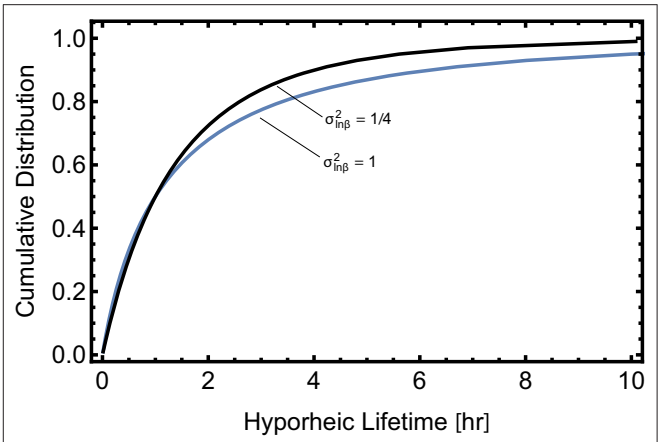

FIGURE 2 | Cumulative distribution of hyporheic lifetime for two choices of the distribution of β, the hyporheic exchange rate coefficient, as calculated from Equation (15). The blue curve is for the reference case, a log-normal distribution of β with with log-variance of 1. The black curve uses a narrower distribution with log-variance 0.25. In both cases, the median travel time was constrained to be 1 h.

K is a constant, then $M(C, K)$ represents Monod kinetics with Monod half-saturation K. Switching the order of the arguments, $M(K, C)$, defines an inhibition function with the constant K taking the role of inhibition constant. Symbol definitions and reaction parameter values for the reference case are defined in **Table 1**. The rate constants k_{aer} and k_{den} were selected to make the half-lives for oxygen consumption and denitrification to be 1 and 5 h, respectively (Gomez-Velez et al., 2015). The Monod parameters are from Gu et al. (2007).

Numerical Experiments

Several numerical experiments with different physical hydrology parameters and different assumptions about the geochemical inputs exemplify sensitivity of reactive transport to how hyporheic exchange is represented. In these examples, the two-point flux finite-volume method was used for spatial discretization of the discrete-rate form of the mTSM and ADELS. The resulting system of nonlinear ordinary differential equations where then solved using the NDSolve routine in Mathematica™. In all examples, the channel was discretized into 50 computational cells. No significant differences were found in mesh convergence tests with 25 cells (not shown).

Channel parameters for the reference case are $Q = 1$ m^3/s, $A = 1.1$ m^2, $D = 2$ m^2/s, and channel width of 2.78 m. The channel area A and width w were chosen to be consistent with well-known hydraulic geometry rating curves (Leopold and Maddock, 1953) and the assumed discharge Q. Empirical relationships shown graphically in **Figure 1** of Gomez-Velez and Harvey (2014) were then used to select values for the hyporheic exchange coefficient α and median hyporheic lifetime that are consistent with the discharge and channel width. The reference case values $\alpha = 2.5 \times 10^{-4} s^{-1}$ and median lifetime of 1 h correspond to a median grain size of ∼1.5 mm and geomorphic features dominated by dune-shaped bedforms. Note that **Figure 1** of Gomez-Velez and Harvey, 2014, uses hyporheic flux q_{hz} instead of our hyporheic exchange coefficient; the two are related as $\alpha = q_{hz}/d$ where d is water depth in the channel.

To complete the physical hydrology model, a distribution of the exchange rate constant β is needed for the mTSM model and a corresponding set of hyporheic lifetime quantiles T_i is needed for the ADELS model. A distribution shape was first assumed for the mTSM model. Then Equation (15) was used to calculate the corresponding hyporheic lifetime quantiles T_is for use in the ADELS model. A log normal distribution with log-variance of 1.0 was used for the reference case. The arithmetic mean was selected as 0.38 hr^{-1} to make the median hyporheic lifetime 1 h. Finally, the hyporheic volume fraction γ for use in the mTSM model was then selected as $\gamma = \alpha / \langle \beta \rangle$ to make the two models equivalent (see Section "Equivalence Between the ADELS and mTSM Models").

A variant case with $Q = 10$ m^3/s and $A = 1.1$ m^2 is also considered. For this case, the hyporheic exchange coefficient is $\alpha = 1.0 \times 10^{-3} s^{-1}$ and the median hyporheic lifetime is 0.5 h, correspond to a median grain size of ∼3 mm and geomorphic features dominated by submerged alternate bars (Gomez-Velez and Harvey, 2014).

Figure 2 shows the resulting cumulative distribution of hyporheic lifetimes, as calculated from Equation (15) for the reference case with log-variance $\sigma^2_{ln\beta} = 1$ and a variant case with log-variance $\sigma^2_{ln\beta} = 0.25$. The geometric mean exchange rate was selected to keep the median hyporheic lifetime T_{50} to same at 1 h. The variant case with $\sigma^2_{ln\beta} = 0.25$ lacks the slowly decaying tail of the reference case.

Several variant cases illustrate sensitivities, including different mean and log-variance for the exchange rate coefficient distribution, different median travel times, different DOC concentration, and different Monod parameters. In each case,

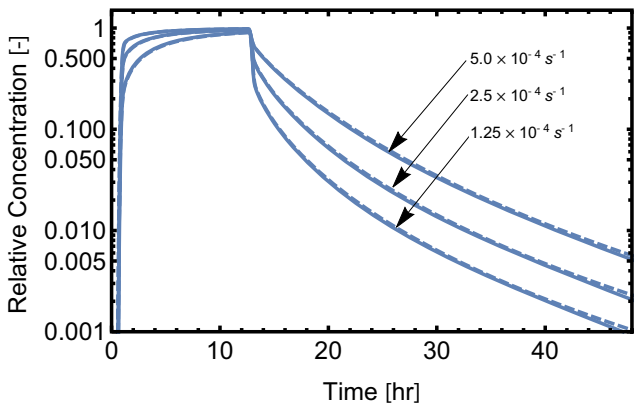

FIGURE 3 | Channel concentration at 3 km relative to the inlet concentration for a conservative tracer test for three values of α, the hyporheic exchange rate constant. The solid curves are for the ADELS model and the dashed curves are for the mTSM.

denitrification result for the ADELS and mTSM models are compared to a first-order kinetic estimate (Painter, 2018) that neglects carbon limitations and assumes the entire hyporheic zone is active in denitrification

$$\frac{C_{out}}{C_{in}} = \frac{1 - \eta x\left(1 - e^{-Da}\right)}{1 + \eta x\left(1 - e^{-Da}\right)} \tag{26}$$

where $\eta = \frac{\alpha wd}{2Q}$ is one-half the ratio of hyporheic exchange flux to channel discharge, $Da = \lambda T_{50}$ is the Damköhler number for the hyporheic flowpath, T_{50} is the median hyporheic lifetime, and $\lambda = \frac{k_{den}}{C^{in}_{NO3}}$ is the first-order decay constant for nitrate removal.

RESULTS

Conservative Tracer Transport

Figure 3 shows concentration in the stream channel as calculated by the mTSM and ADELS models assuming a hypothetical tracer test in a single reach of length 3,000 m. In these examples, a conservative tracer is injected into a steady stream discharge for a period of 12 h. Solid curves are the concentration in the channel at 3,000 m assuming the ADELS model and the dashed curve are from the equivalent mTSM model. The three cases shown are for different values of the exchange coefficient α. The tailing in all three cases is caused by solutes returning to the channel from the hyporheic zone after the solute injection is finished, the result of exchange with the hyporheic zone. Larger α results in more pronounced tailing. As expected, results from the two models overlay each other and are indistinguishable on this scale. The cases in **Figure 3** and all cases shown here used $N = 50$. When smaller $N = 25$ is used, corresponding to fewer transient storage zones in the mTSM model and coarser discretization of the hyporheic lifetime, relatively small differences between the two models are apparent in the extreme tail of the breakthrough curve (result not shown). Although the mTSM and ADELS models are equivalent in their continuous versions, their discrete versions are not guaranteed to be equivalent unless N is large.

Reference Case Reactive Transport

Although the mTSM and ADELS model can be made equivalent for conservative tracers by appropriate choice of the mass exchange coefficients in the mTSM model, the two models have different connectivity to the stream channel, which has the potential to affect biogeochemical processes. Here we use denitrification as an example to explore the biogeochemical consequences of that difference in coupling between transient storage zones and the flowing channel.

The fraction of the initial nitrate removed is shown vs. distance in **Figure 4** for the mTSM (dashed) and ADELS models (solid). **Figure 4A** is for the reference case and **Figure 4B** is or the case $Q = 10$ m^3/s. In these examples, the hyporheic zone and channel were initially free of solutes. At t = 0, the upstream boundary conditions shown in **Table 1** were imposed and the system was then allowed to come to steady state. The mTSM model predicts nitrate removal that is approximately one-third that of the ADELS model at 3 km despite the fact that conservative transport is identical. Moreover, the difference is increasing downstream and would be larger when modeling larger sections of streams and rivers.

The reason for the lower denitrification rates in the mTSM model can be seen by examining DOC, oxygen and nitrate concentrations in the hyporheic zone, as shown in **Figure 5**. Concentrations are shown vs. hyporheic age for the ADELS model. The mTSM does not have a direct equivalent to hyporheic age. For comparison purposes the half-life for storage zone i, that is $\ln 2/\beta_i$, is used for the characteristic time. The channel location in this case is 1.5 km from the inlet. The LS model shows the classic pattern of redox zonation with oxygen dropping to negligible levels after about 1 h of hyporheic age. Oxygen is resupplied to the transient storage subzones in the mTSM through direct diffusive exchange with the channel. As a result, oxygen is never completely consumed in the mTSM and oxygen concentrations remain above value of the inhibition constant K^{O2inh}_{den}, which partially suppresses denitrification. As a result, denitrification rates are lower in the mTSM model, as shown in **Figure 4.**

In **Figure 4**, the first-order model predicts larger denitrification rates than ADELS for both the Q = 1 and Q = 10 cases. Those differences are partly due to the fact that the short-lifetime part of the hyporheic lifetime distribution experiences only aerobic conditions and thus does not contribute to denitrification, a process that is accounted for in ADELS but not in the first-order model. The other contributing factor is carbon limitation, which is modest on the upstream side of the reach but becomes more important moving downstream as DOC is consumed, causing the nitrate removal to depend nonlinearly on distance downstream in **Figure 4** for ADELS.

Sensitivity to Model Parameters and Environmental Conditions

Shown in **Table 2** are percent of nitrate removed at 1 and 3 km for different assumed values for α, the β distribution, and selected chemical parameters. In all cases examined, ADELS predicts significantly greater removal of nitrate, further emphasizing the sensitivity of reactive transport to model structure. Relative differences between the two models is not particularly sensitive

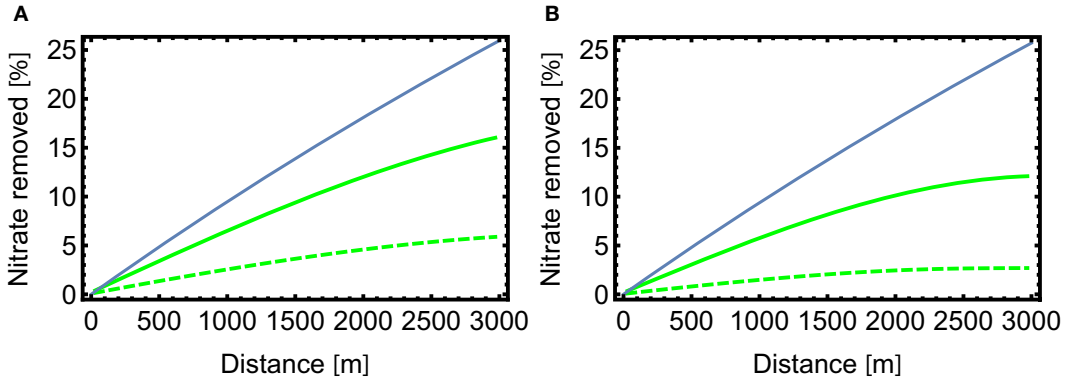

FIGURE 4 | Percentage of incoming nitrate removed vs. travel distance for the ADELS model (solid curve) and the mTSM model (dashed curve) for reference case assumptions **(A)** and a variant case with channel discharge of 10 m^3/s **(B)**. The blue line is a first-order estimate that neglects reactant depletion and oxygen inhibition.

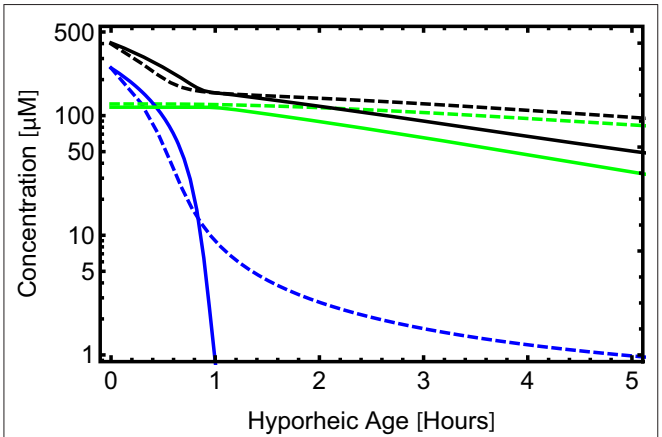

FIGURE 5 | Hyporheic zone concentration for the ADELS model (solid curves) and the mTSM (dashed curves). The blue curve represents oxygen concentration, the green curve nitrate, and the black curve DOC. The *x*-axis is hyporheic age in the ADELS model and a characteristic time related to the exchange coefficient in the mTSM. Note that oxygen concentrations in the mTSM model do not drop below the inhibition constant for denitrification, thus partially inhibiting denitrification in the mTSM model.

to the physical or biogeochemical assumptions, with mTSM predicting nitrate removal that is 32–55% that of ADELS. The linear first-order model predicts significantly greater denitrification compared to ADELS, highlighting the role of the non-idealities noted above (i.e., carbon limitations and inhibition of denitrification by oxygen) that are not accounted for in the first-order estimate.

Nitrate removal in the ADELS model is sensitive to the nitrate/DOC ratio if that ratio is below a threshold value. Increasing the incoming DOC concentration by 50% compared to the reference case results in a modest increase in denitrification (**Table 2**). However, decreasing the incoming DOC concentration by 20% results in a significant decrease in denitrification. That asymmetric sensitivity indicates the reference case condition is at the threshold for carbon limitation.

TABLE 2 | Percent of nitrate removed at 1,000 and 3,000 meters for the ADELS and mTSM models.

	1,000 m			3,000 m		
	Equation (26)	ADELS	mTSM	Equation (26)	ADELS	mTSM
Reference case	9.5	6.1	2.4	26	16	5.9
$T_{50} = 2\,h$	15	9.8	5.5	39	23	12
$\sigma_\beta^2 = 0.25$	9.5	5.0	2.0	26	13	5.0
$\alpha = 5 \times 10^{-4}\ s^{-1}$	18	11	4.3	45	18	6.3
$\alpha = 1.25 \times 10^{-4}\ s^{-1}$	4.8	3.1	1.2	14	9.2	3.5
$C_{DOC}^{in} = 750\ \mu M$	9.5	6.6	2.9	26	19	8.6
$C_{DOC}^{in} = 400\ \mu M$	9.5	4.7	1.7	26	8.4	2.7
$k_{den} = 0.04 \mu M s^{-1}$	15	8.0	3.7	39	20	8.8

Figure 6 shows nitrate removal as a function of distance along the reach for the ADELS and mTSM models when the incoming DOC concentration is increased by 50% over the reference case. In this case, the nitrate removal in the ADELS model is close to linear with distance and tracks closer to the first-order estimate. As in the reference case, the ADELS model is predicting significantly greater removal of nitrate.

Figure 7 shows calculated concentrations vs. distance for the same high DOC case. With sufficient DOC, the ADELS model shows redox zonation with oxygen dropping to negligible levels after about 1 h of hyporheic age and nitrate dropping to negligible levels after approximately 10 h. By contrast the mTSM model does not produce complete redox zonation.

DISCUSSION AND CONCLUSIONS

In the situation of conservative tracers and steady stream discharge, the two models compared here, mTSM and ADELS, are equivalent to well-known integrodifferential representations of tracer transport, which have been very successful in

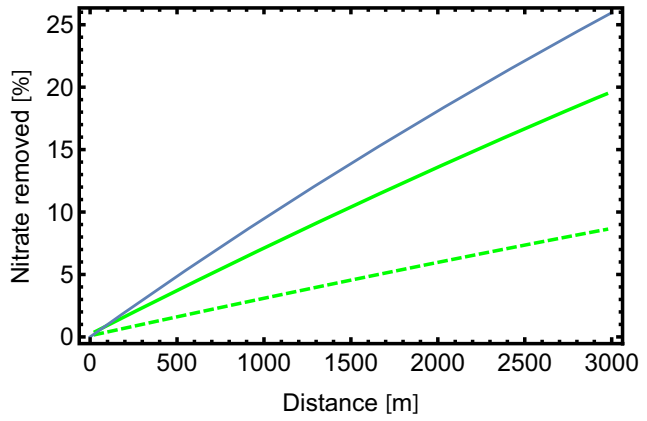

FIGURE 6 | Percentage of incoming nitrate removed vs. travel distance for the ADELS model (solid curve) and the mTSM model (dashed curve) for a variant case with higher incoming DOC.

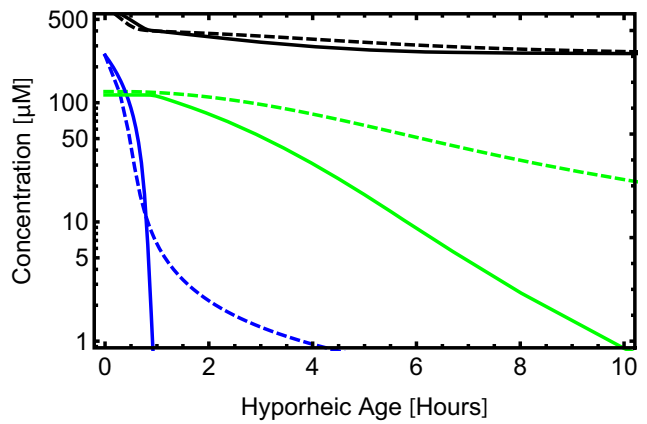

FIGURE 7 | Hyporheic zone concentration for the ADELS model (solid curves) and the mTSM (dashed curves). The blue curve represents oxygen concentration, the green curve nitrate, and the black curve DOC. The *x*-axis is hyporheic age in the ADELS model and a characteristic time related to the exchange coefficient in the mTSM.

reproducing results of conservative tracer tests. Unlike the integrodifferential formulations, mTSM and ADELS generalize to multicomponent reactive transport. It was shown here that although the two model structures produce equivalent results for conservative tracers, they predict very different results for reactive transport.

Significantly, distinct redox zonation did not fully develop in any of the mTSM cases considered here despite the fact that a significant fraction of the hyporheic lifetimes were long enough to consume oxygen. That significant oxygen remains is a result of the mTSM model structure, which assumes that each transient storage zone is well mixed and imposes direct connections between the channel and each transient storage subzone, effectively mixing waters of different hyporheic ages and preventing oxygen from being fully consumed. By contrast, the ADELS model produces the expected redox zonation in the hyporheic zone submodel with complete consumption of oxygen and, when sufficient DOC is available, complete consumption of nitrate. As a result of its inability to represent distinct redox zonation with full consumption of oxygen, the mTSM model does not fully activate denitrification and results in significantly smaller reach-scale denitrification as compared to ADELS.

The ADELS and the mTSM model both produced smaller nitrate removal as compared to the linear first-order model. Deviations from the linear first-order model have two causes in these examples. First, the linear first-order model does not account for the portion of the hyporheic lifetime distribution that lies in the aerobic range and thus does not contribute to denitrification. Second, carbon limitations become important in these examples as we move downstream, which are accounted for in both multiscale models, but not in the first-order estimate. Of course, that carbon limitation may not be relevant in systems where DOC is produced by dissolution of buried particulate organic carbon, which is important in some systems (e.g., Gu et al., 2007; Zarnetske et al., 2011). Overall, both ADELS and mTSM are able to represent a richer range of physical phenomena, as compared to a simple first-order denitrification model.

The inability of the mTSM model to represent redox zonation has implications for the ability of that model to represent the processing of other redox-sensitive contaminants. An important example is the methylation of inorganic mercury to the neurotoxin methylmercury, which requires fully anaerobic conditions. Given environmental conditions favorable for methylation—sufficiently long hyporheic lifetimes and sufficient DOC—the ADELS model will generate fully anaerobic local conditions in the long-lifetime portion of the hyporheic subgrid model.

Efforts to include more detailed representations of biogeochemical processes in basin-scale water quality simulation tools naturally lead to multiscale models that use relatively coarse representations of the channel network with subgrid models for mass exchange with, and reactions in, transient storage zones. A wide variety of model structures could be imagined for such multiscale models, depending on the mesh topology and whether the mass exchange is diffusive or advective. The two model structures explored here may be regarded as end members of such multiscale models. The mTSM is consistent with diffusively controlled exchanges between the channel and multiple well-mixed and mutually independent transient storage subzones. The ADELS model is based on advective exchange between the channel and hyporheic zone and an ensemble of one-dimensional flowpaths through the hyporheic zone.

Given that the two conceptualizations predict different results for reactive transport, an obvious question is how to constrain the model structure. At a conceptual level, ADELS is consistent with advective pumping through channel bedforms, pool-rifle complexes, alternating point bars, and meander bends, well-established processes for many streams. The diffusion-controlled exchange implicit in the mTSM model is consistent with

low-permeability sediments and is thus also relevant for many streams and rivers. The well-mixed approximation for each subzone in mTSM is arguably difficult to reconcile with physical intuition especially for transient storage zones that have long residence times, where we would expect significant gradients to exist in the subzones. Indeed, the neglect of those gradients is the reason the mTSM fails to represent fully developed redox zonation. An extension of multirate models that represents one-dimensional diffusion into transient storage subzones instead of well-mixed subzones would resolve that inconsistency. Another potential model structure would be to combine diffusion- and advection-based conceptualizations.

Questions about model structure in multiscale models for reactive transport in stream corridors must be decided from available data. It might be expected that model structure for mass transfer could be resolved from conservative tracer tests alone leaving only reaction processes and parameters to be inferred by other means. However, these results show the opposite: conservative tracer tests alone are insufficient for distinguishing between different conceptualizations of mass transfer for use in reactive transport models and must be augmented by other types of data. Clearly, reactive or "smart" tracers have an important role to play, as do insights gained from sampling along hyporheic flowpaths and detailed three-dimensional simulations of individual hydrogeomorphological structures. In addition, synoptic sampling of stream chemistry across multiple stream orders combined with uncertainty-aware inverse modeling will likely be necessary to reduce model structural uncertainty to acceptable levels in emerging multiscale models for reactive transport in stream corridors.

DATA AVAILABILITY STATEMENT

The original contributions presented in the study are included in the article/**Supplementary Materials**, further inquiries can be directed to the corresponding author/s.

AUTHOR CONTRIBUTIONS

SP conceived the study, performed all the work, and wrote the paper.

FUNDING

This work was funded by the U.S. Department of Energy, Office of Science, Biological and Environmental Research, Subsurface Biogeochemical Research (SBR) Program, and is a product of the SBR Science Focus Area (SFA) at ORNL and the IDEAS-Watersheds project.

ACKNOWLEDGMENTS

The author is grateful to Saubhagya Rathore for careful review of the manuscript.

SUPPLEMENTARY MATERIAL

The Supplementary Material for this article can be found online at: https://www.frontiersin.org/articles/10.3389/frwa.2020.595538/full#supplementary-material Mathematica™ (Wolfram Research, 2014) scripts used to generate the figures may be found in the supporting information.

REFERENCES

Allison, J. D., Brown, D. S., and Novo-Gradac, K. J. (1991). *MINTEQA2/PRODEFA2, a Geochemical Assessment Model for Environmental Systems: Version 3.0 User's Manual*. Athens, GA: Environmental Research Laboratory, Office of Research and Development.

Anderson, E. J., and Phanikumar, M. S., (2011). Surface storage dynamics in large rivers: comparing three-dimensional particle transport, one-dimensional fractional derivative, and multirate transient storage models. *Water Resour. Res.* 47. doi: 10.1029/2010WR010228

Battin, T. J., Kaplan, L. A., Findlay, S., Hopkinson, C. S., Marti, E., Packman, A. I., et al. (2008). Biophysical controls on organic carbon fluxes in fluvial networks. *Nat. Geosci.* 1, 95–100. doi: 10.1038/ngeo101

Bencala, K. E., and Walters, R. A. (1983). Simulation of solute transport in a mountain pool-and-riffle stream: a transient storage model. *Water Resour. Res.* 19, 718–724. doi: 10.1029/WR019i003p00718

Benson, D. A., and Meerschaert, M. M. (2009). A simple and efficient random walk solution of multi-rate mobile/immobile mass transport equations. *Adv. Water Resour.* 32, 532–539. doi: 10.1016/j.advwatres.2009.01.002

Boano, F., Harvey, J. W., Marion, A., Packman, A. I., Revelli, R., Ridolf, I, L., et al. (2014). Hyporheic flow and transport processes: mechanisms, models, and biogeochemical implications. *Rev. Geophy.* 52, 603–679. doi: 10.1002/2012RG000417

Böhlke, J. K., Harvey, J. W., and Voytek, M. A. (2004). Reach-scale isotope tracer experiment to quantify denitrification and related processes in a nitrate-rich stream, midcontinent United States. *Limnol. Oceanogr.* 49, 821–838. doi: 10.4319/lo.2004.49.3.0821

Bourg, A. C., and Bertin, C. (1993). Biogeochemical processes during the infiltration of river water into an alluvial aquifer. *Environ. Sci. Technol.* 27, 661–666. doi: 10.1021/es00041a009

Briggs, M. A., Gooseff, M. N., Arp, C. D., and Baker, M. A. (2009). A method for estimating surface transient storage parameters for streams with concurrent hyporheic storage. *Water Resour. Res.* 45. doi: 10.1029/2008WR006959

Carrera, J., Sánchez-Vila, X., Benet, I., Medina, A., Galarza, G., and Guimerà, J. (1998). On matrix diffusion: formulations, solution methods and qualitative effects. *Hydrogeol. J.* 6, 178–190. doi: 10.1007/s100400050143

Conant, B. Jr, Cherry, J. A., and Gillham, R. W. (2004). A PCE groundwater plume discharging to a river: influence of the streambed and near-river zone on contaminant distributions. *J. Contamin. Hydrol.* 73, 249–279. doi: 10.1016/j.jconhyd.2004.04.001

Donado, L. D., Sanchez-Vila, X., Dentz, M., Carrera, J., and Bolster, D. (2009). Multicomponent reactive transport in multicontinuum media. *Water Resour. Res.* 45. doi: 10.1029/2008WR006823

Duff, J. H. and Triska, F. J. (2000) "8 - Nitrogen biogeochemistry and surface–subsurface exchange in streams," in *Streams and Ground Waters*, eds Jones, J. B. and Mulholland, P. J. (San Diego, CA: Academic Press). 197–220. doi: 10.1016/B978-012389845-6/50009-0

Fang, Y., Chen, X., Gomez Velez, J., Zhang, X., Duan, Z., Hammond, G. E., et al. (2020). A multirate mass transfer model to represent the interaction of multicomponent biogeochemical processes between surface water and hyporheic zones (SWAT-MRMT-R 1.0). *Geosci. Model Dev.* 13, 3553–3569. doi: 10.5194/gmd-2019-301

Fuller, C. C., and Harvey, J. W. (2000). Reactive uptake of trace metals in the hyporheic zone of a mining-contaminated stream, Pinal Creek, Arizona. *Environ. Sci. Technol.* 34, 1150–1155. doi: 10.1021/es990714d

Gomez-Velez, J. D., and Harvey, J. W., (2014). A hydrogeomorphic river network model predicts where and why hyporheic exchange is important in large basins. *Geophys. Res. Lett.* 41, 6403–6412. doi: 10.1002/2014GL061099

Gomez-Velez, J. D., Harvey, J. W., Cardenas, M. B., and Kiel, B. (2015). Denitrification in the Mississippi River network controlled by flow through river bedforms. *Nat. Geosci.* 8:941. doi: 10.1038/ngeo2567

Gooseff, M. N., Wondzell, S. M., Haggerty, R. and Anderson, J. (2003). Comparing transient storage modeling and residence time distribution (RTD) analysis in geomorphically varied reaches in the Lookout Creek basin, Oregon, USA. *Adv.Water Resour.* 26, 925–937. doi: 10.1016/S0309-1708(03)00105-2

Gouze, P., Melean, Y., Le Borgne, T., Dentz, M., and Carrera, J. (2008). Non-Fickian dispersion in porous media explained by heterogeneous microscale matrix diffusion. *Water Resour. Res.* 44. doi: 10.1029/2007WR006690

Grimm, N. B., and Fisher, S. G. (1984). Exchange between interstitial and surface water: implications for stream metabolism and nutrient cycling. *Hydrobiologia* 111, 219–228. doi: 10.1007/BF00007202

Gu, C., Hornberger, G. M., Mills, A. L., Herman, J. S., and Flewelling, S. A. (2007). Nitrate reduction in streambed sediments: effects of flow and biogeochemical kinetics. *Water Resour. Res.* 43. doi: 10.1029/2007WR006027

Haggerty, R., (2013). Analytical solution and simplified analysis of coupled parent-daughter steady-state transport with multirate mass transfer. *Water Resour. Res.* 49, 635–639. doi: 10.1029/2012WR012821

Haggerty, R., and Gorelick, S. M. (1995). Multiple-rate mass transfer for modeling diffusion and surface reactions in media with pore-scale heterogeneity. *Water Resour. Res.* 31, 2383–2400. doi: 10.1029/95WR10583

Haggerty, R., Mckenna, S. A., and Meigs, L. C. (2000). On the late-time behavior of tracer test breakthrough curves. *Water Resour. Res.* 36, 3467–3479. doi: 10.1029/2000WR900214

Haggerty, R., Wondzell, S. M., and Johnson, M. A. (2002). Power-law residence time distribution in the hyporheic zone of a 2nd-order mountain stream. *Geophys. Res. Lett.* 29, 18-1-18-4. doi: 10.1029/2002GL014743

Hammond, G. E., Lichtner, P. C., and Mills, R. T., (2014). Evaluating the performance of parallel subsurface simulators: an illustrative example with PFLOTRAN. *Water Resour. Res.* 50, 208–228. doi: 10.1002/2012WR013483

Helton, A. M., Poole, G. C., Meyer, J. L., Wollheim, W. M., Peterson, B. J., Mulholland, P. J., et al. (2011). Thinking outside the channel: modeling nitrogen cycling in networked river ecosystems. *Front. Ecol. Environ.* 9, 229–238. doi: 10.1890/080211

Kelleher, C., Ward, A., Knapp, J. L., Blaen, P. J., Kurz, M. J., Drummond, J. D., et al. (2019). Exploring tracer information and model framework trade-offs to improve estimation of stream transient storage processes. *Water Resour. Res.* 55, 3481–3501. doi: 10.1029/2018WR023585

Kerr, P., Gooseff, M., and Bolster, D. (2013). The significance of model structure in one-dimensional stream solute transport models with multiple transient storage zones–competing vs. nested arrangements. *J. Hydrol.* 497, 133–144. doi: 10.1016/j.jhydrol.2013.05.013

Kim, H., Hemond, H. F., Krumholz, L. R., and Cohen, B. A. (1995). *In-situ* biodegradation of toluene in a contaminated stream. Part 1. Field studies. *Environ. Sci. Technol.* 29, 108–116. doi: 10.1021/es00001a014

Lemke, D., Liao, Z., Wöhling, T., Osenbrück, K., and Cirpka, O. A. (2013). Concurrent conservative and reactive tracer tests in a stream undergoing hyporheic exchange. *Water Resour. Res.* 49, 3024–3037. doi: 10.1002/wrcr.20277

Leopold, L. B., and Maddock, T. (1953). *The Hydraulic Geometry of Stream Channels and Some Physiographic Implications*. Professional Paper. Washington, D.C: U.S. Government Printing Office. doi: 10.3133/pp252

Liao, Z., and Cirpka, O. A. (2011). Shape-free inference of hyporheic traveltime distributions from synthetic conservative and "smart" tracer tests in streams. *Water Resour. Res.* 47, doi: 10.1029/2010WR009927

Liao, Z., Lemke, D., osenbrück, K., and Cirpka, O. A. (2013). Modeling and inverting reactive stream tracers undergoing two-site sorption and decay in the hyporheic zone. *Water Resour. Res.,* 49, 3406–3422. doi: 10.1002/wrcr.20276

Lichtner, P. C. (1985). Continuum model for simultaneous chemical reactions and mass transport in hydrothermal systems. *Geochim. Cosmochim. Acta* 49, 779–800. doi: 10.1016/0016-7037(85)90172-3

Lichtner, P. C. (1996). Reactive transport in porous media. *Mineral. Soc. Am. Rev. Mineral.* 34:438.

Marion, A., ZAramella, M., and Bottacin-Busolin, A. (2008). Solute transport in rivers with multiple storage zones: The STIR model. *Water Resour. Res.* 44, doi: 10.1029/2008WR007037

Mulholland, P. J., Helton, A. M., Poole, G. C., Hall, R. O., Hamilton, S. K., Peterson, B. J., et al. (2008). Stream denitrification across biomes and its response to anthropogenic nitrate loading. *Nature* 452:202. doi: 10.1038/nature06686

Painter, S. L. (2018). Multiscale framework for modeling multicomponent reactive transport in stream corridors. *Water Resour. Res.* 54, 7216–7230. doi: 10.1029/2018WR022831

Palumbo-Roe, B., Wragg, J., and Banks, V. J. (2012). Lead mobilisation in the hyporheic zone and river bank sediments of a contaminated stream: contribution to diffuse pollution. *J. Soils Sediment.* 12, 1633–1640. doi: 10.1007/s11368-012-0552-7

Pruess, K., and Wang, J. S. Y., (2001). *Numerical Modeling of Isothermal and Nonisothermal Flow in Unsaturated Fractured Rock: A Review. Flow and Transport Through Unsaturated Fractured Rock*. Washington, DC: American Geophysical Union.

Runkel, R. L., Bencala, K. E., Broshears, R. E., and Chapra, S. C. (1996). Reactive solute transport in streams: 1. Development of an equilibrium-based model. *Water Resour. Res.* 32, 409–418. doi: 10.1029/95WR03106

Sanz-Prat, A., Lu, C., Finkel, M., and Cirpka, O. A. (2015). On the validity of travel-time based nonlinear bioreactive transport models in steady-state flow. *J. Contamin. Hydrol.* 175–176, 26–43. doi: 10.1016/j.jconhyd.2015.02.003

Schaper, J. L., Posselt, M., MCcallum, J. L., Banks, E. W., Hoehne, A., Meinikmann, K., et al. (2018). Hyporheic exchange controls fate of trace organic compounds in an urban stream. *Environ. Sci. Technol.* 52, 12285–12294. doi: 10.1021/acs.est.8b03117

Silva, O., Carrera, J., Dentz, M., Kumar, S., Alcolea, A., and Willmann, M. (2009). A general real-time formulation for multi-rate mass transfer problems. *Hydrol. Earth Syst. Sci.* 13, 1399–1411. doi: 10.5194/hess-13-1399-2009

Wang, P. P., Zheng, C., and Gorelick, S. M., (2005). A general approach to advective–dispersive transport with multirate mass transfer. *Adv. Water Resour.* 28, 33–42. doi: 10.1016/j.advwatres.2004.10.003

Ward, A. S. (2016). The evolution and state of interdisciplinary hyporheic research. *WIREs Water* 3, 83–103. doi: 10.1002/wat2.1120

Wolfram Research, I. (2014). *Mathematica Version 10, 10th Edn*. Champaign, IL: Wolfram Research, Inc.

Wörman, A., Packman, A. I., Johansson, H., and Jonsson, K. (2002). Effect of flow-induced exchange in hyporheic zones on longitudinal transport of solutes in streams and rivers. *Water Resour. Res.* 38, 2-1-2-15. doi: 10.1029/2001WR000769

Yakirevich, A., Shelton, D., Hill, R., Kiefer, L., Stocker, M., Blaustein, R., et al. (2017). Transport of conservative and "smart" tracers in a first-order creek: role of transient storage type. *Water* 9:485. doi: 10.3390/w9070485

Zarnetske, J. P., Haggerty, R., wondzell, S. M., and Baker, M. A. (2011). Labile dissolved organic carbon supply limits hyporheic denitrification. *J. Geophys. Res. Biogeosci.* 116. doi: 10.1029/2011JG001730

Zarnetske, J. P., Haggerty, R., Wondzell, S. M., Bokil, V. A., and González-Pinzón, R. Coupled transport and reaction kinetics control the nitrate source-sink function of hyporheic zones. (2012). *Water Resour. Res.* 48. doi: 10.1029/2012WR011894

Conflict of Interest: The author declares that the research was conducted in the absence of any commercial or financial relationships that could be construed as a potential conflict of interest.

frontiers in Water

ORIGINAL RESEARCH
published: 09 February 2021
doi: 10.3389/frwa.2021.590378

Historical Contingency in Microbial Resilience to Hydrologic Perturbations

Hyun-Seob Song[1,2,3]*, *James C. Stegen*[1], *Emily B. Graham*[1,4] *and Timothy D. Scheibe*[1]

[1] Earth and Biological Sciences Directorate, Pacific Northwest National Laboratory, Richland, WA, United States, [2] Department of Biological Systems Engineering, University of Nebraska-Lincoln, Lincoln, NE, United States, [3] Department of Food Science and Technology, Nebraska Food for Health Center, University of Nebraska-Lincoln, Lincoln, NE, United States, [4] School of Biological Sciences, Washington State University, Pullman, WA, United States

Development of reliable biogeochemical models requires a mechanistic consideration of microbial interactions with hydrology. Microbial response to and its recovery after hydrologic perturbations (i.e., resilience) is a critical component to understand in this regard, but generally difficult to predict because the impacts of future events can be dependent on the history of perturbations (i.e., historical contingency). Fundamental issues underlying this phenomenon include how microbial resilience to hydrologic perturbations is influenced by historical contingency and how their relationships vary depending on the characteristics of microbial functions. To answer these questions, we considered a simple microbial community composed of two species that redundantly consume a common substrate but specialize in producing distinct products and developed a continuous flow reactor model where the two species grow with trade-offs along the flow rate. Simulations of this model revealed that (1) the history of hydrologic perturbations can lead to the shifts in microbial populations, which consequently affect the community's functional dynamics, and (2) while historical contingency in resilience was consistently predicted for all microbial functions, it was more pronounced for specialized functions, compared to the redundant function. As a signature of historical contingency, our model also predicted the emergence of hysteresis in the transitions across conditions, a critical aspect that can affect transient formation of intermediate compounds in biogeochemistry. This work presents microbial growth traits and their functional redundancy or specialization as fundamental factors that control historical contingencies in resilience.

Keywords: microbial communities, hysteresis, trade-offs, trait-based modeling, co-existence, biogeochemistry

OPEN ACCESS

Edited by:
Alexis Navarre-Sitchler, Colorado School of Mines, United States

Reviewed by:
Laurie Boithias, UMR5563 Géosciences Environnement Toulouse (GET), France
Blake Warren Stamps, UES, Inc., United States

***Correspondence:**
Hyun-Seob Song
hsong5@unl.edu

Specialty section:
This article was submitted to Water and Critical Zone, a section of the journal Frontiers in Water

Received: *01 August 2020*
Accepted: *15 January 2021*
Published: *09 February 2021*

Citation:
Song H-S, Stegen JC, Graham EB and Scheibe TD (2021) Historical Contingency in Microbial Resilience to Hydrologic Perturbations. Front. Water 3:590378. doi: 10.3389/frwa.2021.590378

INTRODUCTION

Interactions between hydrologic and microbial processes control the cycling of dissolved organic matter and other chemical substrates (Covino et al., 2018) in biogeochemical hotspots such as river corridors (Singer et al., 2016; Graham et al., 2019). Predictive biogeochemical modeling therefore necessitates development of reliable models of the dynamics of microbial populations and their interactions with hydrology. For this purpose, it is important to understand how hydrologic inputs alter microbial diversity, abundances, interactions, spatial organization, and functions.

While specific microbial phenotypes of interest are assumed to be definable based on known gene functions and environmental conditions (Jansson and Hofmockel, 2018), their dynamics often exhibit non-intuitive, complex dynamics under the influence of the history of perturbations, a phenomenon known as historical contingency (also termed ecological memory or legacy effect) (Fukami, 2015; Ogle et al., 2015; Vass and Langenheder, 2017). Despite its critical impact, we do not know much about how microbial functional responses to hydrologic perturbations are controlled by historical contingencies and how to account for these effects in microbial models (Hawkes and Keitt, 2015).

Historical contingencies of environmental microbial systems have been frequently observed in diverse contexts (Bouskill et al., 2013; Peralta et al., 2013, 2014). For example, microbial enzyme activity and respiration in soil that increased with moisture were shown to be constrained by previous climate such as precipitation history (Averill et al., 2016; Hawkes et al., 2017). As another example, soil systems showed an enhanced protection of plants against a pathogen through the induced presence of disease-suppressive microbes by pre-exposure to the same pathogen in the past, just like an adaptive human immune system (Raaijmakers and Mazzola, 2016). In a recent study, it was shown that different land use significantly affected the transfer of soil organic carbon and bacterial diversity and functions in surface water runoff (Le et al., 2020). Historical contingencies related to hydrologic perturbations were reported by Goldman et al. (2017) where the biogeochemical response (i.e., CO_2 flux) of parafluvial hyporheic zone sediments to re-inundation was contingent on hydrologic history. Goldman et al. (2017) interpreted lower and higher CO_2 fluxes in sediment samples as being caused by relative dominance of fungal and bacterial species, respectively. All examples here indicate the importance of accounting for the role of microbial species controlling historical contingencies for predictive biogeochemical modeling. While a current trend is to increasingly incorporate microbial physiology and processes into biogeochemical models (Wieder et al., 2013; Wang et al., 2017), accounting for historical contingencies still remains a challenge due to the lack of understanding of controlling aspects in microbial systems, severely limiting our ability to reliably predict biogeochemical function (Widder et al., 2016).

As a critical step toward addressing this challenge, we designed an *in silico* study to examine historical effects on microbial responses to hydrological perturbations. Inspired by the field observations of Goldman et al. (2017) that linked biogeochemical historical contingency with the shifts in microbial populations in a community, we formulated a mathematical model of a microbial consortium composed of two competing microbial species growing with different growth traits in a continuous flow reactor. In the model, one species grows more effectively in lower flow rates and the other species in higher flow conditions so that they hold microbial growth traits as observed in Goldman et al. (2017). We used this model to test the hypothesis that trade-offs in individual growth strategies underlie historical contingencies observed at the community level

In this work, we explored how hydrologic history and population dynamics lead to historical contingency of resilience, whereby microbial responses to future perturbations are dependent on past perturbations (Holling, 1996; Allison and Martiny, 2008; Shade et al., 2012; Song et al., 2015; Martiny et al., 2017). Our model revealed that historical contingencies in resilience can be more pronounced for specialized functions associated with individual species, compared to community functions to which member species commonly contribute, indicating the distribution of growth traits among member species plays a controlling role. The model also predicted the sophisticated dynamics of microbial communities including hysteresis (as an outcome of historical contingency), and endogenous dynamics (i.e., the continued changes in microbial populations in the absence of environmental variation). Beyond highlighting the importance of representing the dynamics of individual species for predictive microbial community modeling, this work provides a specific model structure for parameterization in the context of resilience and historical contingency toward predictive ecological and biogeochemical modeling.

METHODS

Design of the Study

Before providing the details on model development and specific metrics used for quantifying the effect of hydrologic perturbations on microbial function in the context of historical contingencies, we here provide a brief overview of the design of our study. Our major goal is to examine how the history of hydrologic perturbations will drive the composition and functions in microbial communities depending on the microbial growth traits and their trade-offs; how this effect will be shown differently for redundant vs. specialized functions among member species. For this purpose, we formulate a mathematical model of a continuous-flow stirred-tank (i.e., well-mixed) reactor where two species competitively grow on the shared nutrient (S) and produce distinct products (P_1 by species 1 and P_2 by species 2). This setting enables assessing the impact of past hydrologic perturbations on microbial functions (i.e., historical contingencies of resilience) based on the following two categories: (1) consumption of S, which represents a function commonly performed among two species and (2) production of P_1 and P_2, which exemplify unshared functions uniquely associated with individual species. To account for growth traits observed in Goldman et al. (2017), we design the kinetics of microbial growth such that species 1 grows faster in lower flow rates, while species 2 grows faster in higher flow rates. This allows us to examine the effect of the trade-off in growth along the flow rate as a key mechanism for the resilience of community functions, particularly those redundantly shared among member species (i.e., the consumption of S). Using the resulting model, we assess resilience based the time-to-recovery after perturbations. For generalizable analysis across scales, we provide the final model equations in dimensionless form. In the following, we begin model description with theories for the co-existence of competing microbial species, which is a pre-requisite in building a microbial community model.

Mechanism for the Coexistence of Competing Species

Implementation of species co-existence in a community model requires a special consideration because simple kinetics will end up with the dominance by a fast grower due to the competitive exclusion principle, a classical ecological theory asserting that only one species can survive the competition (Hardin, 1960). As one of the simplest mechanisms enabling the coexistence of competing organisms in a continuous flow reactor setting considered in this work, we chose density-dependent growth (including flocculation or crowding effect) (De Leenheer et al., 2006; Haegeman and Rapaport, 2008), while several other plausible mechanisms are also available, including: spatial heterogeneity (Stephanopoulos and Fredrickson, 1979), externally imposed temporal fluctuations (Stephanopoulos et al., 1979; Smith, 1981), endogenously induced temporal fluctuations through a specific type of interactions (Hsu et al., 1978; Butler et al., 1983), dormancy (Lennon and Jones, 2011), nutrient storage (Revilla and Weissing, 2008), exchange of metabolic by-products (Hesseler et al., 2006), and time delay in the nutrient uptake and growth (Freedman et al., 1989). Density-dependent growth is a reasonable representation of the growth of microorganisms in natural environments that often form biofilms in sediments and soils where the growth of inside species is limited due to lower availability of nutrients along the depth, indicating that the overall specific growth can be suppressed by crowding as the density increases (Roughgarden, 1971). Even in the case where no biofilm is formed, the density-dependent growth mechanism is still valid in situations where species do not effectively distribute in space because cells surrounded by others will have the same difficulty in accessing nutrients as the local population density increases.

Microbial Growth Kinetics

Based on the density-dependent growth mechanism, we modeled specific growth rates of species i (μ_i), which are split into nutrient- and density-dependent terms, i.e., $\mu_i'(s)$ and $\rho_i(x_1, x_2)$ as follows:

$$\mu_i(s, x_1, x_2) = \mu_i'(s)\rho_i(x_1, x_2), \quad i = 1, 2 \tag{1}$$

where

$$\mu_i'(s) = \frac{k_i s}{K_i + s} \tag{2}$$

and

$$\rho_i(x_1, x_2) = \begin{cases} \exp(-a x_1)\left(1 - \dfrac{x_1 + x_2}{C}\right), & i = 1 \\ 1 - \dfrac{x_1 + x_2}{C}, & i = 2 \end{cases} \tag{3}$$

As shown in Equation (3), we imposed environmental constraints (such as limited space and resources) on both organisms to limit the total population of the community below a given carrying capacity (C). Species 1 was chosen to have faster growth kinetics in this work, i.e., $\mu_1'(s) > \mu_2'(s)$. Therefore, we additionally considered the exponential term in $\rho_1(x_1, x_2)$ so that μ_1 is suppressed as the population density increases because otherwise co-existence becomes impossible due to the dominance of species 1.

Reaction Stoichiometries and Mass Balances

We considered two reactions (R_1 and R_2), respectively driven by species 1 and 2 (X_1 and X_2) such that they compete for the shared substrate (S) to produce distinct products (P_1 and P_2):

$$\begin{aligned} &R_1: Y_{S_1} S \rightarrow X_1 + Y_{P_1} P_1 \\ &R_2: Y_{S_2} S \rightarrow X_2 + Y_{P_2} P_2 \end{aligned} \tag{4}$$

where stoichiometric coefficients Y_{S_i} and $Y_{P_i} (i = 1,2)$ denote how many quantities of S and P_i are consumed or produced whenever a unit mass of biomass is produced through R_i. Specific values of Y_{S_i} and Y_{P_i} depend on the chemical formulae of S, X_i and P_i, as well as their mass units (i.e., mole or gram). For simplicity, we set all stoichiometric coefficients with unity values i.e.,

$$\begin{aligned} &R_1: S \rightarrow X_1 + P_1 \\ &R_2: S \rightarrow X_2 + P_2 \end{aligned} \tag{5}$$

Note that the resulting reaction stoichiometries above equate the production rates of P_1 and P_2 with the growth rates of X_1 and X_2, respectively.

To mimic microbial growth in river corridor sediments, we considered a continuous-flow well-mixed reactor where the substrate is fed through water flow into the sediment as illustrated in **Figure 1A**. A continuous flow reactor configuration has been frequently used in the literature as a model system for addressing ecological questions [e.g., Kraft et al. (2014)] and provides advantages over batch cultures in studying mixed populations (Veldkamp and Jannasch, 1972). Under well-mixed conditions, dynamic mass balances for microbial populations, substrate, and products can be written as follows:

$$\frac{dx_i}{dt} = \mu_i(s, x_1, x_2)x_i - k_d x_i, \quad i = 1, 2 \tag{6}$$

$$\frac{ds}{dt} = -\mu_1(s, x_1, x_2)x_1 - \mu_2(s, x_1, x_2)x_2 + D(s_{in} - s) \tag{7}$$

$$\frac{dp_i}{dt} = \mu_i(s, x_1, x_2)x_i - D p_i, \quad i = 1, 2 \tag{8}$$

where x_i denote the population size of X_i, s and p_i are the concentrations of S and P_i, t is the time, μ_i denotes the specific growth rate (1/time) of X_i (mass/volume), k_d is the specific death rate (1/time) fixed as constant, D is the dilution rate (1/time), and the subscript *in* represents the quantities associated with the inlet feed flow, respectively. As implied by the same notation of k_d for species 1 and 2, we assumed no difference in the specific death rate between the two organisms.

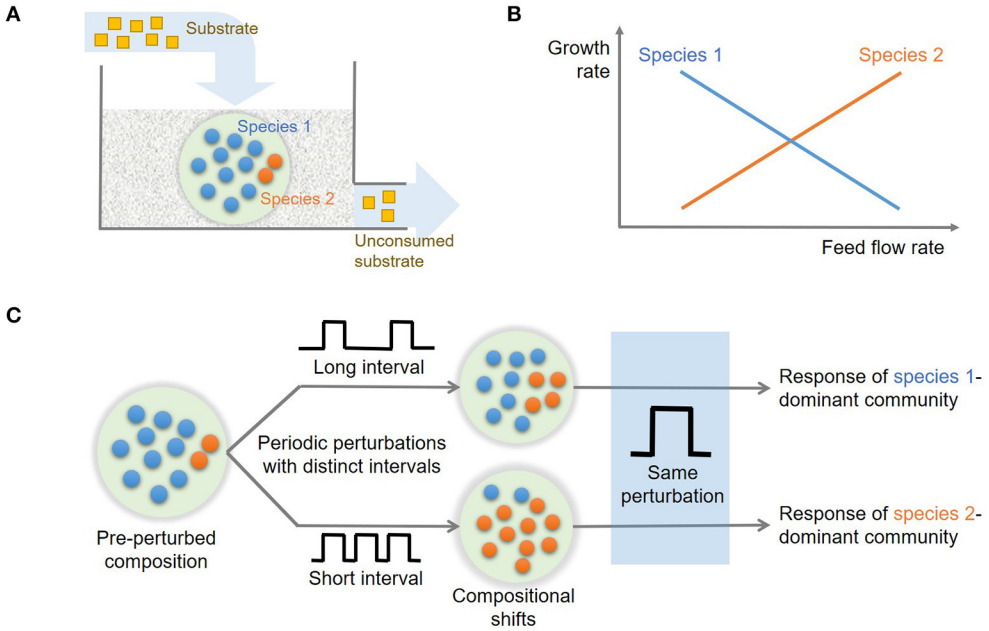

FIGURE 1 | Conceptual model to investigate historical contingencies in microbial response to hydrologic perturbations: **(A)** a continuous flow reactor configuration for competitive growth of two microbial species on a shared substrate in a homogeneous environment, **(B)** trade-offs in microbial growth along the flow rate gradient, and **(C)** expected compositional changes driven by the history of hydrologic perturbations.

Non-dimensionalization

For scale independence, we non-dimensionalized the equations as follows:

$$\frac{dx}{d\tau} = f(x,y,z)\,x - \lambda x$$

$$\frac{dy}{d\tau} = g(x,y,z)\,y - \lambda y \quad (9)$$

$$\frac{dz}{d\tau} = -f(x,y,z)\,x - g(x,y,z)\,y + \delta(1-z) \quad (10)$$

$$\frac{dp}{d\tau} = f(x,y,z)\,x - \delta p \quad (11)$$

$$\frac{dq}{d\tau} = g(x,y,z)\,y - \delta q \quad (12)$$

where

$$f(x,y,z) = \frac{k_x z}{K_x + z} e^{-\alpha x}\left(1 - \frac{x+y}{\kappa}\right)$$
$$g(x,y,z) = \frac{k_y z}{K_y + z}\left(1 - \frac{x+y}{\kappa}\right) \quad (13)$$

Definitions of dimensionless variables and parameters used in the above equations were provided in **Table 1**. The values of kinetic parameters k_x, K_x, k_y, and K_y in Equation (13) were derived from the flocculation model by Haegeman and Rapaport (2008). Nutrient concentration in the feed flow in the last term of Equation (10) was set to 1 due to the normalization with respect to itself.

TABLE 1 | Definitions of dimensionless variables and parameters contained in the model.

Dimensionless variable	Definition	Dimensionless parameter	Definition
Time, τ	$tr_1(s_{in})$	Reaction rate constant for species 1, k_x (= 1.2)	$\frac{k_1}{r_1(s_{in})}$
Population of species 1, x	$\frac{x_1}{s_{in}}$	Reaction rate constant for species 2, k_y (= 1.2)	$\frac{k_2}{r_1(s_{in})}$
Population of species 2, y	$\frac{x_2}{s_{in}}$	Half saturation constant for species 1, K_x (= 0.2)	$\frac{K_1}{s_{in}}$
Nutrient concentration, z	$\frac{s}{s_{in}}$	Half saturation constant for species 2, K_y (= 0.4)	$\frac{K_2}{s_{in}}$
Dilution rate, δ	$\frac{D}{r_1(s_{in})}$	Parameter denoting density dependence, α (= 1.25)	$s_{in}a$
		Carrying capacity, κ (= 1)	$\frac{C}{s_{in}}$
		Cell death rate, λ (= 0.12)	$\frac{k_d}{r_1(s_{in})}$

Metrics for Resilience

We imposed hydrologic perturbation by fluctuating the dilution rate following a rectangle-shaped wave. Based on the concept of engineering resilience (Holling, 1996; Song et al., 2015), we used "time-to-recovery" as a measure of resilience, i.e., how quickly a chosen system variable or function recovers the pre-perturbed state, while other metrics could also be considered (Hillebrand et al., 2018). Key variables and functions of interest in this work

include: microbial and chemical compositions (i.e., x, y, and z) and their associated functions such as consumption rate of z (i.e., $r_z \equiv -fx - gy$) and production rates of p (i.e., $r_p \equiv fx$) and q (i.e., $r_q \equiv gy$). These rates represent redundant (r_z) and unique functions (r_p and r_q) among member species.

In quantifying the resilience of a chosen variable or function among those mentioned above, we ensured the system to be exposed to a cyclic perturbation of dilution rate for a sufficient time period; when the system reached a sustained oscillation, we stopped imposing perturbation and started to measure time-to-recovery. We used two different metrics for the time-to-recovery as defined below:

- **Hitting time** is when the variable or function hits the pre-perturbed level for the first time. We measured this as the first time when the variable hits an upper or lower boundary of the band around the pre-perturbed level. The bandwidth was defined by the 2 and 5% values above and below the pre-perturbed level.
- **Settling time** is the time required for the variable or function to finally reach and remain within a given band of the pre-perturbed level. This quantity needs to be distinguished from hitting time when the system recovery takes place in an oscillatory way so that it may touch the boundaries of the band more than one time. In this case, the first and last times that the nutrient profile crosses the boundaries of the band correspond to hitting and settling times, respectively. If there are no oscillations during the post-perturbation period, hitting and settling times are identical. In measuring the settling time, we considered 2 and 5% bandwidths as defined above.

RESULTS

Using a model of microbial community growing in a homogenous continuous flow reactor (**Figure 1A**), we test the following hypotheses: (**H1**) distinct growth traits and their trade-offs along the flow rate gradient (**Figure 1B**) leads to the shifts in the community composition subject to hydrologic perturbations with different intervals, (**H2**) the resulting microbial communities dominated by species 1 or 2 will show distinct responses to future perturbations (**Figure 1C**), and (**H3**) the extent of historical contingencies in microbial functions depend on their redundancy or specialization, i.e., whether a given functions is performed in common among multiple species or uniquely associated with specific organisms.

Trade-Off in Microbial Growth Traits in Steady State

We examined how state variables including species abundances (x and y) and substrate concentration (z) vary along the dilution rate (δ) (**Figure 2A**), which are dimensionless variables of x_1, x_2, s, and D (Methods). The values of x, y, and z in **Figure 2A** denote their steady-state values that change as a function of δ. For very low dilution rates (i.e., $\delta \leq 0.05$), species 2 (y) could not survive the competition with species 1 (x). In this regime, x linearly increased with δ as the supply of substrate accordingly increased. For higher dilution rates above the threshold, two species coexisted with the opposite dependence of their growth rates on the dilution rate, i.e., x decreased with δ, while y increased, so that their population curves intersect at $\delta \approx 0.1$. This shows that species 1 is more competitive in lower flow rate conditions, while species 2 can grow faster in the higher flow rate regime, confirming that the parameter setting in our model leads to the expected microbial growth traits as indicated in Methods (also see **Figure 1B**)

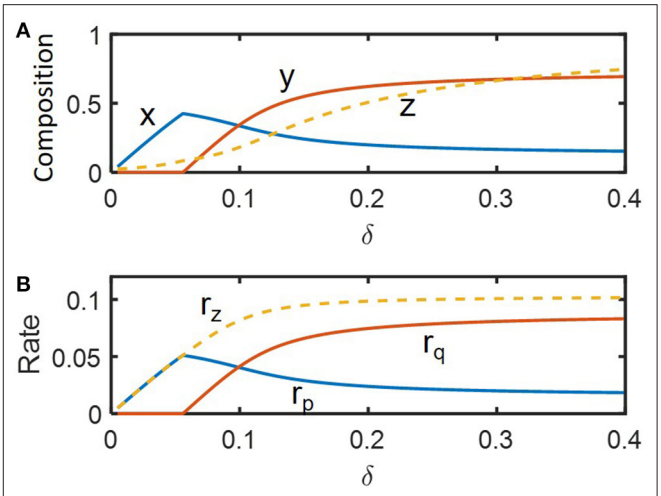

FIGURE 2 | The changes in key variables and functions in steady state as a function of flow rate (δ): **(A)** species abundances (x and y) and substrate concentration (z), and **(B)** consumption rate of the shared substrate (r_z) and production rates of distinct products (r_p and r_q).

Similar trends were observed for community functions such as consumption rate of the shared substrate (r_z) and production rates of distinct products (r_p and r_q) (**Figure 2B**). As the conversion rate of z (r_z) includes the contribution from both species that competitively consume the shared substrate, the function r_z showed milder changes over $\delta \geq 0.05$, compared to specialized functions (r_p and r_q) that are uniquely associated with only one species. As will be discussed more in the follow-up section, the trade-off in growth traits of the two species provides a mechanistic basis for enhanced resilience of the community. We used the steady state profiles in **Figure 2** as a guide map to identify distinct operating zones where the system shows qualitatively different dynamics.

Compositional and Functional Responses to Hydrologic Perturbations

We performed dynamic simulations to examine how microbial communities respond to hydrologic perturbations. Disturbances were imposed by periodically changing the dilution rate (δ) between pre-chosen nominal (i.e., pre-perturbed) ($\delta_{norm} = 0.09$) and inundated conditions (0.19) (following a rectangular shape in time). For illustration, we simulated compositional and functional responses to the two specific cycles of perturbations with the inundation intervals of 3.5 and 9.5 imposed over $0 \leq \tau \leq 200$ (**Figure 3**). Among the three state variables denoting microbial and chemical compositions (x, y, and z), z showed the most significant fluctuation in time because the substrate was being fed into the reactor while microorganisms were not. As species 1 is a faster grower at the nominal flow rate ($\delta = 0.09$) and

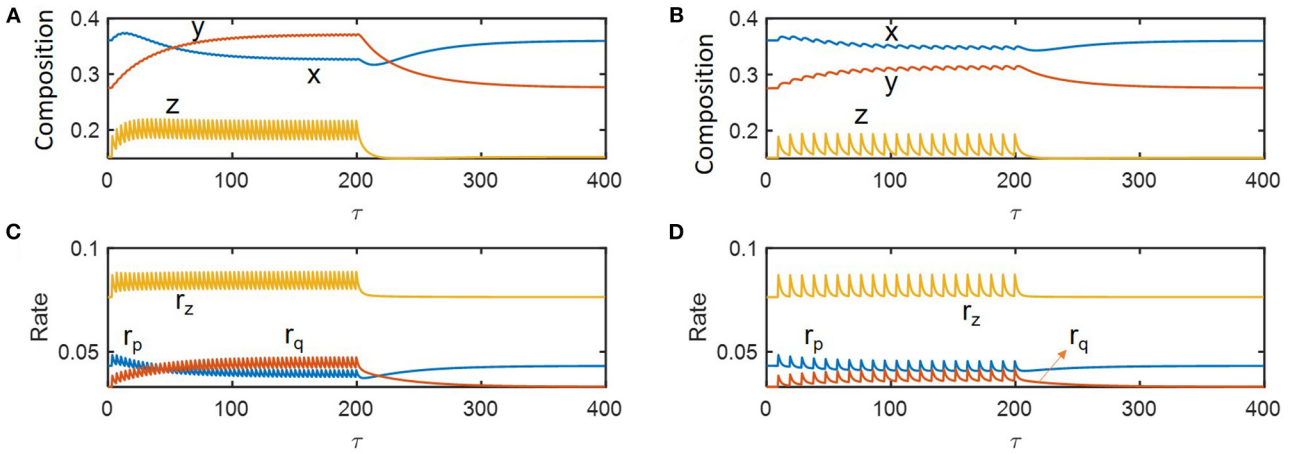

FIGURE 3 | Microbial response to periodic change of the inlet flow (δ) between 0.09 and 0.19: **(A,C)** perturbation interval of 3.5, and **(B,D)** perturbation interval of 9.5. The periodic perturbation was imposed over $0 \leq \tau \leq 200$ and released afterwards.

species 2 grows faster following inundation ($\delta = 0.19$) (**Figure 2**), the abundances of species 1 and 2, respectively decreased and increased under periodic inundation (**Figures 3A,B**). That is, in the case of the shorter inundation interval (i.e., 3.5), species dominance was switched over from x to y (**Figure 3A**), while the original composition was recovered after periodic perturbation was stopped. This result supported our hypothesis on the effect of hydrological perturbations on microbial populations (**H1**). Similar trends were observed for functional responses including production rates of products (r_p and r_q) and consumption rate of the shared substrate (r_z). Temporal fluctuations of r_p and r_q were more significant than those of their populations (x and y) because r_p and r_q are functions of substrate concentration as well as species abundances.

Even in this simple simulation setting, we found several interesting dynamics: (1) species 1 (x) showed inverse responses (i.e., the initial change in its abundance in a direction opposite to the final outcome) when periodic inundation was stopped at $\tau = 200$, while such over- or under-shooting was suppressed for species 2 and substrate concentration; (2) the deviation of r_z during periodic perturbation was the least significant among others (when evaluated based on the minimum values of fluctuation); and (3) the recovery of r_z was the fastest among others. The result (1) indicates that species 1 with relatively fast dynamics and high momentum can show complex dynamics (such as inverse response). The results (2) and (3) partially supported the hypotheses **H2** and **H3** by showing the highest resilience for r_z, which may be ascribable to the functional compensation from member species with growth trade-off. In the next section, these two hypotheses are more rigorously addressed based on the quantification of time-to-recovery in response to perturbations.

Historical Contingencies in Resilience

We performed a more thorough analysis of how resilience is influenced by historical contingencies. Based on the concept of *engineering* resilience, i.e., the rate of return to the pre-perturbed state (Holling, 1996; Allison and Martiny, 2008; Shade et al., 2012; Song et al., 2015; Martiny et al., 2017), we evaluated the system's resilience based on time-to-recovery such as hitting and settling times with 2 and 5% criteria as defined in Methods. For $\delta_{norm} = 0.09$ (as previously considered), we examined how state variables and their recovery times change as a function of inundation interval (**Figures 4A–C**). In support of the hypothesis **H1**, state variables including microbial (x, y) and chemical compositions (z) changed as a function of dilution rate. This change was significant in the regime where inundation intervals were small (i.e., when perturbation frequencies were high) (**Figure 4A**), while the time-to-compositional recovery did not show such a sharp increase over the corresponding regime (**Figure 4B**). For x and z, the hitting time (solid line) was not always the same as the settling time (open circle), meaning that these variables first entered the area within 2 or 5% range of the nominal (i.e., pre-perturbed) values and later escaped them prior to ultimately returning to pre-perturbation conditions (**Figures 4B,C**). The time-to-recovery for z was shorter than those for x and y as indicated by the result in the previous section.

Many of these trends observed from compositional variables (x, y, and z) were reproduced for functional variables (r_p, r_q, and r_z) (**Figures 4D–F**). As a notable difference, however, r_z showed suppressed changes compared to z due to the functional compensation from member species as explained earlier. Consequently, the time-to-functional recovery for r_z not only was significantly lower than those for r_x and r_y, but also showed a milder dependence on inundation interval (**Figures 4E,F**). These results provide a clear support for **H2** and **H3**.

Hysteresis in Transition Across Two Distinct Perturbation Cycles

As shown in **Figures 5A,B**, we simulated sustained oscillations of compositional (x, y, and z) and functional variables (r_p, r_q,

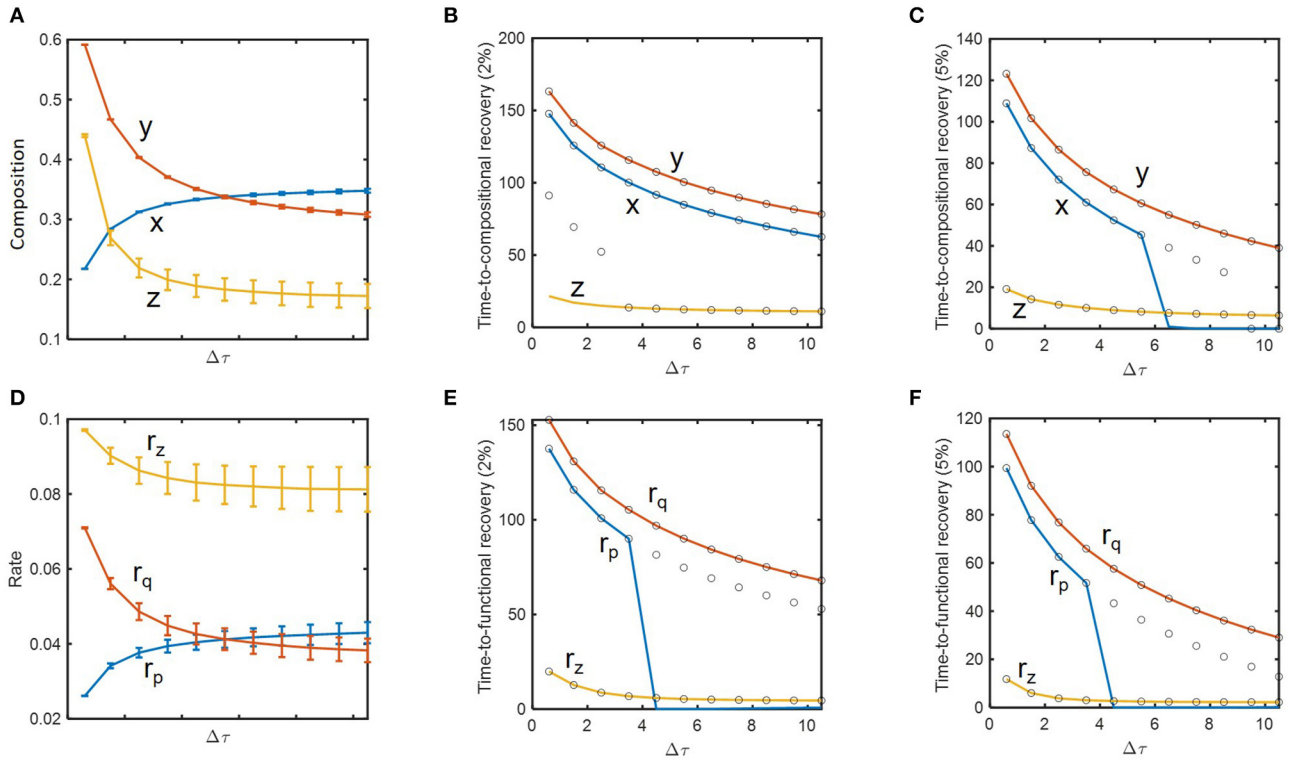

FIGURE 4 | The impact of perturbation interval ($\Delta\tau$) on species abundances, substrate concentration, microbial functions, and their time-to-recoveries: **(A)** microbial (x and y) and chemical compositions (z), **(B)** time-to-compositional recovery calculated by the 2% criterion, **(C)** time-to-compositional recovery calculated by the 5% criterion, **(D)** consumption rate of the shared substrate (r_z) and production rates of distinct products (r_p and r_q), **(E)** time-to-functional recovery calculated by the 2% criterion, **(F)** time-to-functional recovery calculated by the 5% criterion. In **(B,C,E, and F)**, solid lines and open circles denote hitting and settling times, respectively.

and r_z) at two different inundation intervals (5 and 15) to see how the transitions occur between them. Consideration of these two intervals (wider than those considered the previous case) was to ensure the dramatic differences in the fluctuation patterns so that one can see transition trajectories more clearly. We initially imposed the periodic perturbation with the interval of 5 and when sustained oscillation was reached (i.e., at $\tau = 200$), switched to the interval of 15 – this process was repeated afterwards. Phase diagrams in **Figures 5C–E** showed the existence of hysteresis in the transition between the two periodically perturbed conditions with distinct intervals. The transition between the two limit cycles formed by periodic perturbations with intervals of 5 and 15 occurred through different trajectories. The hysteresis was most effectively shown for the phase diagram of the two compositional variables (x and y) (**Figure 5C**).

DISCUSSION

A growing body of data indicate critical effects of historical contingency in biogeochemistry and microbial ecology, but theoretical frameworks that can predict the sophisticated behavior of environmental systems are still lacking. In this study, we formulated a mathematical model of a minimal complexity to reveal how historical contingencies in resilience to hydrologic perturbations are driven by microbial growth traits and their trade-offs. Our model enabled us to reveal important aspects of resilience and its historical contingencies as summarized below.

Historical contingency in the resilience of microbial systems was significantly affected by the degree of functional redundancy or specialization. Redundant functions commonly performed by multiple species (such as the consumption rate of the shared substrate in this work) were more readily recovered from perturbations, while specialized functions associated with individual species (such as the production rates of distinct products by species 1 and 2) showed slower recovery. Consequently, historical contingencies in resilience were more pronounced for specialized functions partitioned only into specific species. The enhanced resilience for redundant functions performed by majority of species is ascribable to their compensating roles in contributing to a total biomass stock that is more robust to disturbances than individual species. Related to this, we also found that the compositional recovery of microbial populations was prolonged even after a certain community function (e.g., the substrate consumption rate) became stable. While this endogenous dynamics was discussed as an intrinsic characteristic of compositionally complex natural communities (Konopka et al., 2015; Song et al., 2015), our model demonstrated that even structurally simple communities can develop those subtle dynamics in the process of stabilizing microbial functions against perturbations. Our work therefore provides a minimal

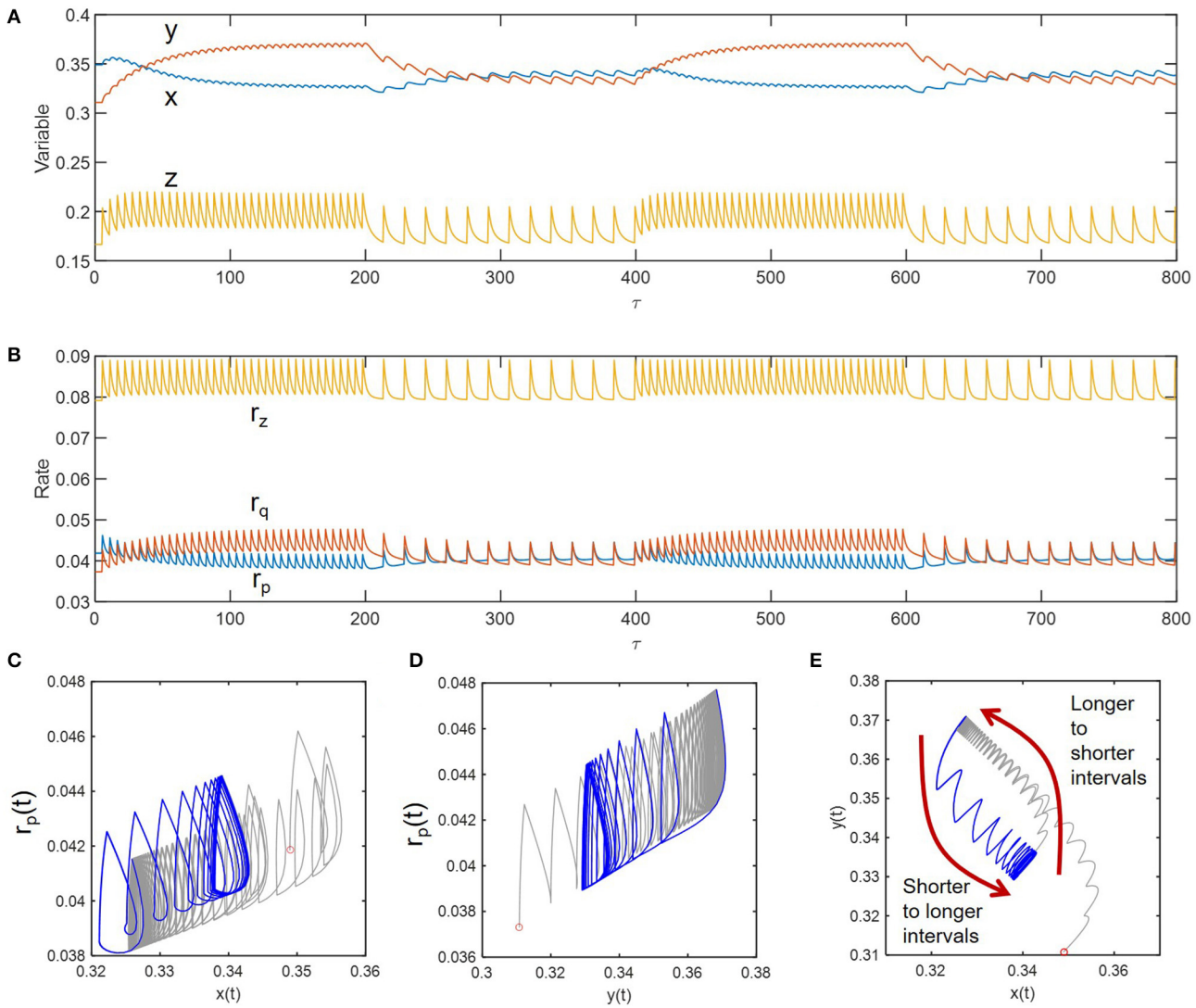

FIGURE 5 | Hysteresis in dynamic transitions between the two distinctively perturbed conditions with the intervals of 5 and 15: **(A)** compositional fluctuations, **(B)** functional fluctuations, and **(C–E)** phase diagrams. Curves in gray and blue, respectively denote the transitions from longer to shorter intervals and from shorter to longer intervals.

structure of model for studying a mechanistic linkage between endogenous dynamics, functional redundancy, resilience, and historical contingency.

As an outcome of historical contingency, we also observed hysteresis, whereby the system takes different routes in transitioning across conditions. Hysteresis of biological systems has been typically reported based on forward and backward trajectories of state variables between multiple steady states (Kim et al., 2012; Gedeon et al., 2018), but the hysteresis in this work is defined in a more dynamic context, i.e., as being characterized by distinct transient paths between two sustained oscillations maintained across different inundation intervals. As a signature of historical contingency, a predictive understanding of hysteresis is critically important because it can lead to the unexpected formation of intermediate chemical compounds during the transitions when microbial communities undergo the dynamic shifts in their composition and functions through different trajectories. The lack of understanding of hysteric behaviors in microbial communities therefore may cause a significant error in model predictions, particularly for those associated with specific organisms, the populations of which undergo a more significant dynamic variation than the total community biomass.

Our work offers a direction toward building more mechanistic biogeochemical models. Stronger historical contingencies of specialized functions as predicted by the model highlights the importance of representing distinct traits of individual species for predictive modeling – because the lumped description based on community-level properties such as the total biomass and/or carbon use efficiency cannot predict complex aspects of biogeochemical function such as resilience and historical

contingency driven by the interplay between distinct microbial species. In this regard, model extension though linking conceptualized microbial functions with specific biogeochemical pathways would be an important next step. Two reaction pathways driven by species 1 and 2 considered in our model can be translated as specific biogeochemical pathways, for example, such as denitrification and anammox, i.e., once NO_3^- is converted to NO_2^- (as the first step of denitrification), the subsequent reaction paths bifurcated afterwards are driven by distinct microbial functional groups. Therefore, this type of model that has both redundant (i.e., conversion of NO_3^- to NO_2^-) and specialized functions (i.e., conversion afterwards through two pathways) would be suitable for investigating function-specific resilience and historical contingencies as demonstrated in our study. For this direction, trait-based modeling approaches that appropriately combine the concepts of functional guilds and functional enzymes should be considered as an appropriate modeling framework (Allison, 2012; Bouskill et al., 2012; Song et al., 2014, 2017). We expect that accounting for individual growth rates, and species-associated specific biogeochemical traits will significantly improve predictive capabilities for multi-scale hydrobiogeochemical models.

DATA AVAILABILITY STATEMENT

The datasets presented in this study can be found in online repositories. The names of the repository/repositories and accession number(s) can be found below: https://github.com/hyunseobsong/history.

AUTHOR CONTRIBUTIONS

H-SS developed the modeling concept and performed simulations. H-SS drafted out the article, which was edited by JS and EG. All authors contributed to the design of the research, read and approved the final manuscript.

FUNDING

This research was supported by the U.S. Department of Energy, Office of Science, Office of Biological and Environmental Research, Environmental System Science (ESS) program through subcontract to the River Corridor Scientific Focus Area project at Pacific Northwest National Laboratory.

REFERENCES

Allison, S. D. (2012). A trait-based approach for modelling microbial litter decomposition. *Ecol. Lett.* 15, 1058–1070. doi: 10.1111/j.1461-0248.2012.01807.x

Allison, S. D., and Martiny, J. B. H. (2008). Resistance, resilience, and redundancy in microbial communities. *Proc. Natl. Acad. Sci. U. S. A.* 105, 11512–11519. doi: 10.1073/pnas.0801925105

Averill, C., Waring, B. G., and Hawkes, C. V. (2016). Historical precipitation predictably alters the shape and magnitude of microbial functional response to soil moisture. *Glob. Chang. Biol.* 22, 1957–1964. doi: 10.1111/gcb.13219

Bouskill, N. J., Lim, H. C., Borglin, S., Salve, R., Wood, T. E., Silver, W. L., et al. (2013). Pre-exposure to drought increases the resistance of tropical forest soil bacterial communities to extended drought. *Isme J.* 7, 384–394. doi: 10.1038/ismej.2012.113

Bouskill, N. J., Tang, J., Riley, W. J., and Brodie, E. L. (2012). Trait-based representation of biological nitr fication: model development testing, and predicted community composition. *Front. Microbiol.* 3:364. doi: 10.3389/fmicb.2012.00364

Butler, G. J., Hsu, S. B., and Waltman, P. (1983). Coexistence of competing predators in a chemostat. *J. Math. Biol.* 17, 133–151. doi: 10.1007/BF00305755

Covino, T., Golden, H. E., Li, H. Y., and Tang, J. Y. (2018). Aquatic carbon-nutrient dynamics as emergent properties of hydrological, biogeochemical, and ecological interactions: scientific advances. *Water Resour. Res.* 54, 7138–7142. doi: 10.1029/2018WR023588

De Leenheer, P., Angeli, D., and Sontag, E. D. (2006). Crowding effects promote coexistence in the chemostat. *J. Math. Anal. Appl.* 319, 48–60. doi: 10.1016/j.jmaa.2006.02.036

Freedman, H. I., So, J. W. H., and Waltman, P. (1989). Coexistence in a model of competition in the chemostat incorporating discrete delays. *SIAM J. Appl. Math.* 49, 859–870. doi: 10.1137/0149050

Fukami, T. (2015). Historical contingency in community assembly: integrating niches, species pools, and priority effects. *Annu. Rev. Ecol. Evol. Syst.* 46, 1–23. doi: 10.1146/annurev-ecolsys-110411-160340

Gedeon, T., Cummins, B., Harker, S., and Mischaikow, K. (2018). Identifying robust hysteresis in networks. *PLoS Comput. Biol.* 14:e1006121. doi: 10.1371/journal.pcbi.1006121

Goldman, A. E., Graham, E. B., Crump, A. R., Kennedy, D. W., Romero, E. B., Anderson, C. G., et al. (2017). Biogeochemical cycling at the aquatic-terrestrial interface is linked to parafluvial hyporheic zone inundation history. *Biogeosciences* 14, 4229–4241. doi: 10.5194/bg-14-4229-2017

Graham, E. B., Stegen, J. C., Huang, M. Y., Chen, X. Y., and Scheibe, T. D. (2019). Subsurface biogeochemistry is a missing link between ecology and hydrology in dam-impacted river corridors. *Sci. Total Environ.* 657, 435–445. doi: 10.1016/j.scitotenv.2018.11.414

Haegeman, B., and Rapaport, A. (2008). How flocculation can explain coexistence in the chemostat. *J. Biol. Dyn.* 2, 1–13. doi: 10.1080/17513750801942537

Hardin, G. (1960). The competitive exclusion principle. *Science* 131, 1292–1297. doi: 10.1126/science.131.3409.1292

Hawkes, C. V., and Keitt, T. H. (2015). Resilience vs. historical contingency in microbial responses to environmental change. *Ecol. Lett.* 18, 612–625. doi: 10.1111/ele.12451

Hawkes, C. V., Waring, B. G., Rocca, J. D., and Kivlin, S. N. (2017). Historical climate controls soil respiration responses to current soil moisture. *Proc. Natl. Acad. Sci. U. S. A.* 114, 6322–6327. doi: 10.1073/pnas.1620811114

Hesseler, J., Schmidt, J. K., Reichl, U., and Flockerzi, D. (2006). Coexistence in the chemostat as a result of metabolic by-products. *J. Math. Biol.* 53, 556–584. doi: 10.1007/s00285-006-0012-3

Hillebrand, H., Langenheder, S., Lebret, K., Lindstrom, E., Ostman, O., and Striebel, M. (2018). Decomposing multiple dimensions of stability in global change experiments. *Ecol. Lett.* 21, 21–30. doi: 10.1111/ele.12867

Holling, C. S. (1996). Engineering resilience vs. ecological resilience. *Eng. Ecol. Const.* 31:32.

Hsu, S. B., Hubbell, S. P., and Waltman, P. (1978). Competing predators. *SIAM J. Appl. Math.* 35, 617–625. doi: 10.1137/0135051

Jansson, J. K., and Hofmockel, K. S. (2018). The soil microbiome - from metagenomics to metaphenomics. *Curr. Opin. Microbiol.* 43, 162–168. doi: 10.1016/j.mib.2018.01.013

Kim, J. I., Song, H. S., Sunkara, S. R., Lali, A., and Ramkrishna, D. (2012). Exacting predictions by cybernetic model confirmed experimentally: steady state multiplicity in the chemostat. *Biotechnol. Prog.* 28, 1160–1166. doi: 10.1002/btpr.1583

Konopka, A., Lindemann, S., and Fredrickson, J. (2015). Dynamics in microbial communities: unraveling mechanisms to identify principles. *Isme J.* 9, 1488–1495. doi: 10.1038/ismej.2014.251

Kraft, B., Tegetmeyer, H. E., Meier, D., Geelhoed, J. S., and Strous, M. (2014). Rapid succession of uncultured marine bacterial and archaeal populations in a denitrifying continuous culture. *Environ. Microbiol.* 16, 3275–3286. doi: 10.1111/1462-2920.12552

Le, H. T., Rochelle-Newall, E., Ribolzi, O., Janeau, J. L., Huon, S., Latsachack, K., et al. (2020). Land use strongly influences soil organic carbon and bacterial community export in runoff in tropical uplands. *Land Degr. Dev.* 31, 118–132. doi: 10.1002/ldr.3433

Lennon, J. T., and Jones, S. E. (2011). Microbial seed banks: the ecological and evolutionary implications of dormancy. *Nat. Rev. Microbiol.* 9, 119–130. doi: 10.1038/nrmicro2504

Martiny, J. B. H., Martiny, A. C., Weihe, C., Lu, Y., Berlemont, R., Brodie, E. L., et al. (2017). Microbial legacies alter decomposition in response to simulated global change. *Isme J.* 11, 490–499. doi: 10.1038/ismej.2016.122

Ogle, K., Barber, J. J., Barron-Gafford, G. A., Bentley, L. P., Young, J. M., Huxman, T. E., et al. (2015). Quantifying ecological memory in plant and ecosystem processes. *Ecol. Lett.* 18, 221–235. doi: 10.1111/ele.12399

Peralta, A. L., Ludmer, S., and Kent, A. D. (2013). Hydrologic history influences microbial community composition and nitrogen cycling under experimental drying/wetting treatments. *Soil Biol. Biochem.* 66, 29–37. doi: 10.1016/j.soilbio.2013.06.019

Peralta, A. L., Ludmer, S., Matthews, J. W., and Kent, A. D. (2014). Bacterial community response to changes in soil redox potential along a moisture gradient in restored wetlands. *Ecol. Eng.* 73, 246–253. doi: 10.1016/j.ecoleng.2014.09.047

Raaijmakers, J. M., and Mazzola, M. (2016). Soil immune responses soil microbiomes may be harnessed for plant health. *Science* 352, 1392–1393. doi: 10.1126/science.aaf3252

Revilla, T., and Weissing, F. J. (2008). Nonequilibrium coexistence in a competition model with nutrient storage. *Ecology* 89, 865–877. doi: 10.1890/07-1103.1

Roughgarden, J. (1971). Density-dependent natural selection. *Ecology* 52, 453–468. doi: 10.2307/1937628

Shade, A., Peter, H., Allison, S. D., Baho, D. L., Berga, M., Burgmann, H., et al. (2012). Fundamentals of microbial community resistance and resilience. *Front. Microbiol.* 3:417. doi: 10.3389/fmicb.2012.00417

Singer, M. B., Harrison, L. R., Donovan, P. M., Blum, J. D., and Marvin-Dipasquale, M. (2016). Hydrologic indicators of hot spots and hot moments of mercury methylation potential along river corridors. *Sci. Total Environ.* 568, 697–711. doi: 10.1016/j.scitotenv.2016.03.005

Smith, H. L. (1981). Competitive coexistence in an oscillating chemostat. *SIAM J. Appl. Math.* 40, 498–522. doi: 10.1137/0140042

Song, H.-S., Cannon, W. R., Beliaev, A. S., and Konopka, A. (2014). Mathematical modeling of microbial community dynamics: a methodological review. *Processes* 2, 711–752. doi: 10.3390/pr2040711

Song, H. S., Renslow, R. S., Fredrickson, J. K., and Lindemann, S. R. (2015). Integrating ecological and engineering concepts of resilience in microbial communities. *Front. Microbiol.* 6:1298. doi: 10.3389/fmicb.2015.01298

Song, H. S., Thomas, D. G., Stegen, J. C., Li, M. J., Liu, C. X., Song, X. H., et al. (2017). Regulation-structured dynamic metabolic model provides a potential mechanism for delayed enzyme response in denitrification process. *Front. Microbiol.* 8:1866. doi: 10.3389/fmicb.2017.01866

Stephanopoulos, G., and Fredrickson, A. G. (1979). Effect of spatial inhomogeneities on the coexistence of competing microbial-populations. *Biotechnol. Bioeng.* 21, 1491–1498. doi: 10.1002/bit.260210817

Stephanopoulos, G., Fredrickson, A. G., and Aris, R. (1979). The growth of competing microbial-populations in a cstr with periodically varying inputs. *Aiche J.* 25, 863–872. doi: 10.1002/aic.690250515

Vass, M., and Langenheder, S. (2017). The legacy of the past: effects of historical processes on microbial metacommunities. *Aquat. Microb. Ecol.* 79, 13–19. doi: 10.3354/ame01816

Veldkamp, H., and Jannasch, H. W. (1972). Mixed culture studies with the chemostat. *J. Appl. Chem. Biotechnol.* 22, 105–123. doi: 10.1002/jctb.5020220113

Wang, K. F., Peng, C. H., Zhu, Q. A., Zhou, X. L., Wang, M., Zhang, K. R., et al. (2017). Modeling global soil carbon and soil microbial carbon by integrating microbial processes into the ecosystem process model TRIPLEX-GHG. *J. Adv. Model. Earth Syst.* 9, 2368–2384. doi: 10.1002/2017MS000920

Widder, S., Allen, R. J., Pfeiffer, T., Curtis, T. P., Wiuf, C., Sloan, W. T., et al. (2016). Challenges in microbial ecology: building predictive understanding of community function and dynamics. *Isme J.* 10, 2557–2568. doi: 10.1038/ismej.2016.45

Wieder, W. R., Bonan, G. B., and Allison, S. D. (2013). Global soil carbon projections are improved by modelling microbial processes. *Nat. Clim. Chang.* 3, 909–912. doi: 10.1038/nclimate1951

Conflict of Interest: The authors declare that the research was conducted in the absence of any commercial or financial relationships that could be construed as a potential conflict of interest.

frontiers in Water

ORIGINAL RESEARCH
published: 23 February 2021
doi: 10.3389/frwa.2021.590314

Modeling the Impact of Riparian Hollows on River Corridor Nitrogen Exports

D. Brian Rogers[1,2], Michelle E. Newcomer[1], Jonathan H. Raberg[3], Dipankar Dwivedi[1], Carl Steefel[1], Nicholas Bouskill[1], Peter Nico[1], Boris Faybishenko[1], Patricia Fox[1], Mark Conrad[1], Markus Bill[1], Eoin Brodie[1], Bhavna Arora[1], Baptiste Dafflon[1], Kenneth H. Williams[1,4] and Susan S. Hubbard[1]*

[1] Earth and Environmental Sciences Area, Lawrence Berkeley National Laboratory, Berkeley, CA, United States, [2] Department of Earth System Science, Stanford University, Stanford, CA, United States, [3] Department of Geological Sciences, University of Colorado Boulder, Boulder, CO, United States, [4] Rocky Mountain Biological Laboratory, Gothic, CO, United States

OPEN ACCESS

Edited by:
Jon Chorover, University of Arizona, United States

Reviewed by:
Kalyana Babu Nakshatrala, University of Houston, United States
Thomas Meixner, University of Arizona, United States
Amalia Handler, United States Environmental Protection Agency (EPA), United States

***Correspondence:**
D. Brian Rogers
rogersdb@stanford.edu

Specialty section:
This article was submitted to Water and Critical Zone, a section of the journal Frontiers in Water

Received: *01 August 2020*
Accepted: *20 January 2021*
Published: *23 February 2021*

Citation:
Rogers DB, Newcomer ME, Raberg JH, Dwivedi D, Steefel C, Bouskill N, Nico P, Faybishenko B, Fox P, Conrad M, Bill M, Brodie E, Arora B, Dafflon B, Williams KH and Hubbard SS (2021) Modeling the Impact of Riparian Hollows on River Corridor Nitrogen Exports. Front. Water 3:590314. doi: 10.3389/frwa.2021.590314

Recent studies in snowmelt-dominated catchments have documented changes in nitrogen (N) retention over time, such as declines in watershed exports of N, though there is a limited understanding of the controlling processes driving these trends. Working in the mountainous headwater East River Colorado watershed, we explored the effects of riparian hollows as N-cycling hotspots and as important small-scale controls on observed watershed trends. Using a modeling-based approach informed by remote sensing and *in situ* observations, we simulated the N-retention capacity of riparian hollows with seasonal and yearly hydrobiogeochemical perturbations imposed as drivers. We then implemented a scaling approach to quantify the relative contribution of riparian hollows to the total river corridor N budget. We found that riparian hollows primarily serve as N sinks, with N-transformation rates significantly limited by periods of enhanced groundwater upwelling and promoted at the onset of rainfall events. Given these observed hydrologic controls, we expect that the nitrate (NO_3^-) sink capacity of riparian hollows will increase in magnitude with future climatic perturbations, specifically the shift to more frequent rainfall events and fewer snowmelt events, as projected for many mountainous headwater catchments. Our current estimates suggest that while riparian hollows provision ~5–20% of NO_3^- to the river network, they functionally act as inhibitors to upland NO_3^- reaching the stream. Our work linking transient hydrological conditions to numerical biogeochemical simulations is an important step in assessing N-retaining features relative to the watershed N budget and better understanding the role of small-scale features within watersheds.

Keywords: riparian, nitrogen, DNRA, reactive transport, snowmelt, microtopography

INTRODUCTION

Watershed nitrogen (N) fluxes driven by in-stream N exports can have formative impacts on downstream terrestrial and aquatic ecosystems (Appling et al., 2014; Lucas et al., 2016; Pinay et al., 2018) and water quality for agricultural and municipal usage (Bernard-Jannin et al., 2017; Castaldelli et al., 2020; Lutz et al., 2020). Several studies have documented changes in watershed N

exports, such as decadal shifts in watersheds functioning as N sources versus N sinks (Yanai et al., 2013), increases in N exports across several decades or centuries (Van Meter et al., 2017), declines in in-stream N exports (Lucas et al., 2016; Newcomer et al., 2019), and interannual variability in peak N exports (Duncan et al., 2015). The controlling multi-scale processes driving these trends, however, are not well-defined, limiting our predictive understanding of the controls on N exports in freshwater watersheds. Quantifying the major controls on total watershed N exports will therefore be important in predicting future changes in N exports and associated implications under rapid climatic shifts.

Previous studies have shown that microtopographic features (e.g., hummocks and hollows) throughout riparian floodplains are important controls on shallow biogeochemical kinetics (Frei et al., 2012; Duncan et al., 2013). These features are potentially important sites for groundwater-surface water interactions (Frei et al., 2012), as groundwater in riparian floodplains can exhibit seasonal hydrologic connectivity to surface water (Zilli and Paggi, 2013; Reid et al., 2016; Carroll et al., 2018), thus creating biogeochemically active flow paths for infiltrating surface water to travel through before reaching streams. In snowmelt-dominated catchments, groundwater can contribute up to 50% of total stream discharge during baseflow conditions and up to nearly 30% under snowmelt conditions (Carroll et al., 2018). Such connectivity allows these riparian features to function as "ecosystem control points" with respect to in-stream N exports (Frei et al., 2012; Duncan et al., 2013), where ecosystem control points are defined as features essential in understanding aggregate ecosystem behavior (Bernhardt et al., 2017). In a study conducted by Duncan et al., riparian hollows were shown to account for >99% of total denitrification, though they represented less than 1% of the total catchment area (Duncan et al., 2013). In another study, Frei et al. described the importance of coupled hummock-hollow features, which facilitate the introduction of surface water into shallow aquifers, where less-reduced surface water initiates greater microbial growth than older, more-reduced groundwater (Frei et al., 2012). These studies have established riparian hollows as potentially significant drivers to changes in watershed N budgets. There is still uncertainty, however, in how N transformations within riparian hollows respond to transient hydrologic conditions, such as those associated with snowmelt timing, rainfall patterns, and groundwater fluctuations. Delineating and quantifying these transient responses could allow for more accurate temporal and spatial scaling of the impact of riparian hollows on catchment-scale N budgets.

It is well-established that snowmelt-dominated catchments are exhibiting earlier peak snowmelt runoff (McCabe and Clark, 2005; Knowles et al., 2006; Adam et al., 2009; Dudley et al., 2017), declines in net and peak snow water equivalent (SWE) (Clark and Pitlick, 2005; Stewart, 2009; Clow, 2010; Fassnacht et al., 2018), and increasingly more precipitation falling as rain than as snow (Knowles et al., 2006; Adam et al., 2009; Pederson et al., 2011; Dudley et al., 2017). Since spring snowmelt pulses have been found to contribute up to 75% of total annual runoff in some watersheds (Fritze et al., 2011), shifts in snowmelt timing and magnitude have important implications for streamflow dynamics and thus in-stream exports of nutrients (Suecker et al., 2000; Pellerin et al., 2012). In a seasonally snow-covered catchment in the northeastern U.S., 37% of the annual nitrate (NO_3^-) yield and 56% of the annual dissolved organic carbon (DOC) yield were accounted for within a 56-day snowmelt (Pellerin et al., 2012). Declines in snowmelt-dominated streamflow driven by decreases in SWE (Barnhart et al., 2016) suggest that the frequency and magnitude of bankfull overflow (riparian zone inundation) events will decrease during this time of especially high in-stream nutrient loading. This trend potentially imposes limits on the duration of high denitrification potential within the shallow subsurface of the riparian zone. In addition to affecting streamflow dynamics, changes in snowmelt magnitude and timing also have sustained implications for soil moisture content (Blankinship et al., 2014; Maurer and Bowling, 2014; Harpold and Molotch, 2015; Yano et al., 2019). As part of a study conducted in a snowmelt-dominated conifer forest, Yano et al. observed that low peak SWE is associated with lower spring soil moisture, which can result in lower soil moisture throughout the dry season and early monsoon season than that observed during years with high peak SWE (Yano et al., 2019). Such impacts on soil moisture in turn affect N-transformation conditions throughout riparian floodplains (Yano et al., 2019).

Biogeochemical mechanisms relevant to N-cycling in riparian hollows include nitrification (NI), a two-step process during which organisms oxidize ammonium (NH_4^+) to nitrite (NO_2^-) and subsequently to NO_3^-, as well as denitrification (DN) and dissimilatory nitrate reduction to ammonium (DNRA), during which microbes reduce NO_3^- primarily to dinitrogen (N_2) and NH_4^+, respectively (Kuypers et al., 2018). DNRA is not commonly included in reactive transport models, since little is known about its environmental importance; however, recent advancements in genome-resolved models have demonstrated that DNRA can be the favored nitrate-reduction pathway in certain systems (Kuypers et al., 2018). Other reduction-oxidation pathways, including those for carbon (C), sulfur (S), and iron (Fe), can interact with these N-cycling pathways by altering the availability of dissolved organic carbon, which often serves as the electron donor and thus provides energy for NO_3^--reducing reactions (i.e., DN and DNRA) (Appelo and Postma, 2005).

In this study we expand upon the current understanding of riparian hollows as ecosystem control points by integrating the effects of transient hydrologic conditions observed within a snowmelt-dominated catchment and quantifying the potential for these zones to transition between a N source and sink depending on surface water sources and groundwater conditions. We conduct a synthetic modeling study representative of these topographic features in the East River watershed located in Colorado, using site-specific data to force the model and examine how the hydro biogeochemical dynamics of riparian hollows respond to hydrological and meteorological perturbations. We first describe site-specific data, followed by the methods used to determine the hydrological and geochemical boundary conditions for the reactive transport simulations. We detail the analysis used to determine periods and sources of surface flux. Finally, we discuss the importance of surface

water origin on the transient N-transformation potential of riparian hollows.

METHODOLOGY

Site Background

The reference site is located in the East River watershed, a mountainous headwater near Crested Butte, CO in the Upper Colorado River Basin (**Figure 1A**). In this study, we synthesized data sets collected within the intra-meander region of a lower montane floodplain, located between 38.9226°N and 38.9242°N and between −106.9508°W and −106.9494°W (**Figure 1**). The surface of the floodplain is comprised of ∼5 m of unconsolidated alluvium, underlain by the Cretaceous Mancos Shale (Hubbard et al., 2018). The alluvium consists of an upper layer of fine-grained overbank deposits ∼1-m thick underlain by 4 m of coarse-grained cobbles (**Figure 2**). Mancos Shale is the primary bedrock in this portion of the watershed and is a key source of metals, metalloids, and pyrite (Hubbard et al., 2018).

The study site and encompassing floodplain are located along a meandering stretch (sinuosity = 1.8) of the East River that extends ∼11 km. The river discharge is driven primarily by snowmelt, which typically occurs between early March and late June. River discharge also increases during the monsoon season, mid-July through late September (Carroll et al., 2018), though these increases are often isolated and do not contribute to river discharge as significantly as snowmelt does (Hubbard et al., 2018). A majority of the annual precipitation (30-year-average = 670 ± 120 mm per/year) falls as snow and occurs between October and May (Carroll et al., 2018). This hydrologic regime is similar to and representative of many other headwater systems throughout the Upper Colorado River Basin (Hubbard et al., 2018).

In situ Geochemical Sampling

A sampling campaign took place from May 2017 through August 2017 to better understand the transient hydrogeochemical characteristics of the intra-meander area (Newcomer M. E. et al., 2020). The sampling efforts encompassed surface water samples in the stream and in ponded water throughout the floodplain, groundwater samples throughout the floodplain at 20-cm depth intervals up to 100 cm deep, and water samples throughout the hyporheic zone. Samples were gathered using a sediment coring device when appropriate and a peristaltic pump equipped with Norprene® tubing. Samples were analyzed in the field for pH, temperature, oxidation-reduction potential (ORP), and electrical conductivity (EC) using a multi-parameter probe. Additional samples were filtered using 0.45 μm polyvinylidene fluoride (PVDF) membranes and were analyzed in the field using a CHEMetrics V-2000 Multi-Analyte Photometer and CHEMetrics Vacu-vials® Instrumental Kits for the following analytes (information in parentheses indicates CHEMetrics Vacu-vials® Instrumental Kit ID #K-xxxx, range, and method): total and ferrous iron [#K-6203, 0–6.00 ppm, phenanthroline method), sulfide (#K-9503, 0–3.00 ppm, methylene blue method), and dissolved oxygen (#K-7513 (high range) and #K-7553 (low range), 0–15.0 ppm (high range), and 0-1.000 ppm (low range), indigo carmine method (high range) and Rhodazine D method (low range)]; all samples were analyzed using both low range and high range methods for dissolved oxygen.

For cation concentrations [calcium (Ca^{2+}), iron (Fe^{2+} + Fe^{3+}), potassium (K^+), sodium (Na^+)], filtered samples were collected in 20 mL plastic scintillation vials and preserved through acidification using 200 μL ULTREX® ultrapure nitric acid. Cation concentrations were measured using inductively coupled plasma mass spectrometry (ICP-MS) (ELAN DRC II, PerkinElmer SCIEX, USA). For anion concentrations [nitrate (NO_3^-), chloride (Cl^-), phosphate (PO_4^{3-}), sulfate (SO_4^{2-})], filtered samples were collected in 20 mL plastic scintillation vials and preserved through freezing. Anion concentrations were measured using ion chromatography (IC) (Dionex ICS-2100, Thermo Scientific, USA). For dissolved organic carbon (DOC) and dissolved inorganic carbon (DIC) concentrations, samples were collected in 40 mL amber glass vials and preserved through chilling. DOC and DIC were measured using a Shimadzu total organic carbon analyzer (TOC-VCPH, Shimadzu Corporation, Japan). Acidified samples were also analyzed for ammonia-N (NH_3-N), which was measured using a Lachat QuikChem® 8500 Series 2 Flow Injection Analysis System (Lachat Instruments, QuikChem® 8500 Series 2, Automated Ion Analyzer, Loveland, Colorado).

Model Development

Model Domain and Spatial Discretization

Two-dimensional models were developed in MIN3P to simulate transient hydrological and geochemical inputs into a generalized riparian hollow located within the intra-meander region of the floodplain. MIN3P is a variably saturated flow and reactive transport code that has been benchmarked against several widely used flow and reactive transport codes for a range of hydrological and geochemical applications (Mayer, 1999; Mayer et al., 1999, 2002; Mayer and MacQuarrie, 2010; Molins et al., 2015; Xie et al., 2015). MIN3P is formulated to protect against negative (non-physical) aqueous concentrations and mineral volume fractions by representing these parameters as logarithmic values (Lipnikov et al., 2010; Nakshatrala et al., 2013). All simulations were run using a parallelized version of MIN3P equipped with unstructured grid support (Su et al., 2019). The model was run over periods for which sufficient field data were available in 2016 (March–May), 2017 (March–October), 2018 (April–June and September–October), and 2019 (May–October). The model domain is a 2 m (width) by 5 m (height) cross-section of the volume shown in **Figure 3A**. The domain includes a generalized hollow that is 0.4 m deep and 1.5 m wide, which is representative of field observations and visual inspection of a 0.5-m digital elevation model (DEM) of the meander region (Falco et al., 2019). The cell sizes (defined by the average edge-length of a cell) were chosen so that higher spatial resolution was obtained near the surface of the model domain, where the most biogeochemical heterogeneity and transiency were expected. This was achieved in Gmsh (http://gmsh.info) using a Delaunay triangulation algorithm, in which the smallest cell

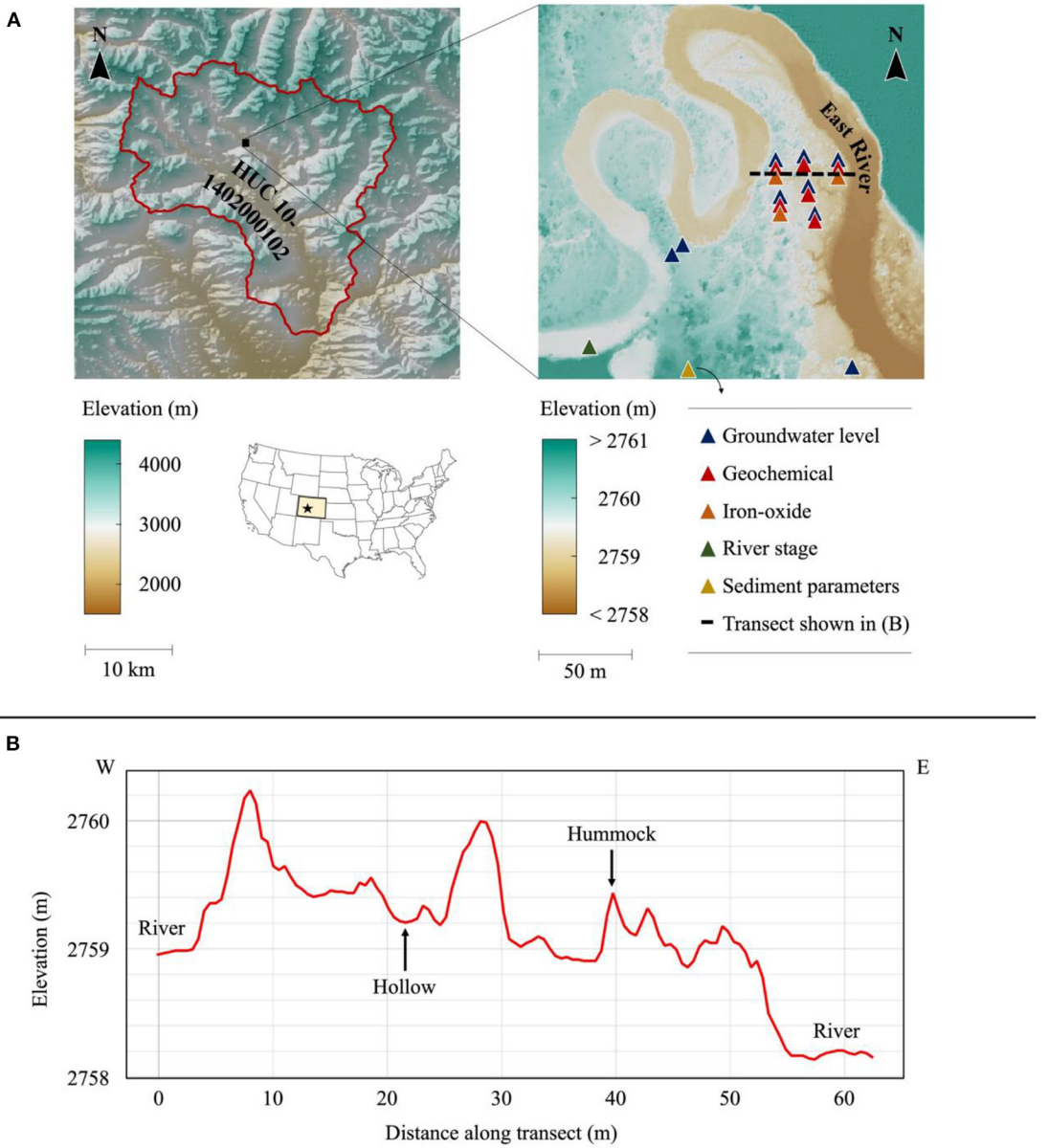

FIGURE 1 | (A) (left) East River watershed (outlined in red) and study site location; (right) data collection locations and types of data measured; overlapping symbols indicate measurements were taken at the same location; sediment parameters were taken at the base of the hillslope at the southern end of the meander (not encompassed in figure); geochemical measurements were also taken at several points throughout the stream and streambed. **(B)** Floodplain elevation profile with example microtopographic features labeled.

size (at the upper boundary) was 0.05 m and the largest cell size (at the lower boundary) was 0.30 m (**Figure 3A**) (Geuzaine and Remacle, 2009). Both hydrological and geochemical boundary conditions were updated at a maximum of 6-h time steps, while the initial time step was 10^{-9} days. The boundary condition types are shown in **Figure 3B**.

Sediment Parameterization

Sediment parameterization of the model domain was based on field measurements taken in the floodplain at the base of the hillslope directly adjacent to the study site. Sand, silt, and clay percentages and bulk density were measured for soil samples taken at 20-cm intervals throughout the top 100 cm of the soil column (Faybishenko, 2020). These measurements were then used to calculate hydraulic conductivity in the z-direction [$K_{sat(z)}$], porosity (n_p), residual water content (θ_r), saturated water content (θ_s), α (van Genuchten water retention parameter corresponding approximately to the inverse of the air-entry value), and n (van Genuchten empirical parameter related to the width of the pore-size distribution)

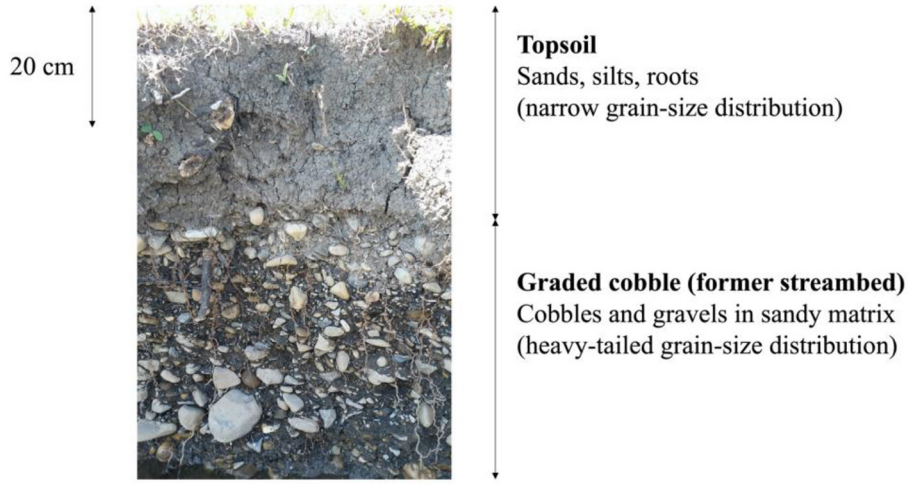

FIGURE 2 | Exposed floodplain cross-section used to inform model parameters.

(Peters et al., 2011; Faybishenko, 2020). An anisotropic ratio of 1/3 was assumed for determining hydraulic conductivity in the x-direction [$K_{sat(x)}$] (Fetter, 2001). Since the samples acquired were only representative of the upper 100 cm and its comparatively high fraction of fine-grained (<2 mm) materials, the physical parameters for the graded cobble were determined using representative values gathered from previous studies (**Table 1**).

Hydrologic Boundary Conditions

In situ hydrologic conditions from 15-min-resolution groundwater elevation data collected across multiple shallow piezometers in the floodplain were used to force the hydraulic head of the left (inflow) boundary of the model (**Figure 3B**; Dafflon et al., 2020). The lateral groundwater flow was assumed to be left to right in the model, where the hydraulic head of the right (outflow) boundary was calculated by subtracting the change in head (horizontal gradient multiplied by a lateral distance of 2 m) from the hydraulic head at the left (inflow) boundary. The horizontal gradient was calculated using a triangulation method on the time-series groundwater level data, allowing the gradient to reflect seasonal hydrologic perturbations. The lower boundary was specified as a no-flow boundary, justified by the relatively low permeability of the Mancos Shale compared to the overlying cobble layer (**Figure 3B**; Hettinger and Kirschbaum, 2002; Ridgley et al., 2013).

A specified flux boundary was applied at the surface of the model to allow the forcing of transient surface infiltration rates. Positive surface flux (representing infiltration and hereon referred to as surface flux) was hypothesized to occur under four different conditions: snowmelt, rainfall, bankfull overflow, and groundwater upwelling (**Figure 4**). It was expected that snowmelt, bankfull overflow, and groundwater upwelling would occur during the snowmelt season (March through June), while surface flux due to rainfall would primarily occur during the dry and monsoon seasons (July through October). Given these approximate seasonal bounds, we temporally bounded our simulations to take place between March and October.

Meteorological Data

All meteorological data used to calculate surface infiltration fluxes from snowmelt and rainfall were obtained at 15-min temporal resolution from a WeatherUnderground station located 1.2 km southwest of our study site (Weather Station ID: KCOMTCRE2; Station Name: Gold Link) (The Weather Company, 2020). All data went through a quality assurance and quality control process and were gap-filled to produce continuous time series (Newcomer and Rogers, 2020). These data were then used to calculate partitioned snowfall/rainfall rates and potential evapotranspiration rates, which were key parameters in determining snowmelt and rainfall surface flux rates, described in detail in the following subsections.

Delineating Periods of Snowmelt

The "EcoHydRology" package in R (v3.6.2) was used to partition total precipitation rates into separate snowfall and rainfall rates and to calculate daily snowmelt rates (R Core Team, 2020). The functions used for these calculations were provided with *in situ* precipitation, temperature, slope, aspect, albedo, wind speed, solar radiation, snow depth, and snow density data. The snowmelt rate was directly interpreted as the surface flux rate to impose in the MIN3P simulations, implying that all of the snowmelt directly above the hollow infiltrated into the soil. This assumption is reasonable for this model, since the domain is a closed depression.

Delineating Periods of Bankfull Overflow

Periods of bankfull overflow onto the floodplain were delineated by comparing river water absolute elevations to the absolute elevations of each groundwater well. At each well, we first identified the nearest location in the river for which we needed an estimate of river water absolute elevation. We calculated river

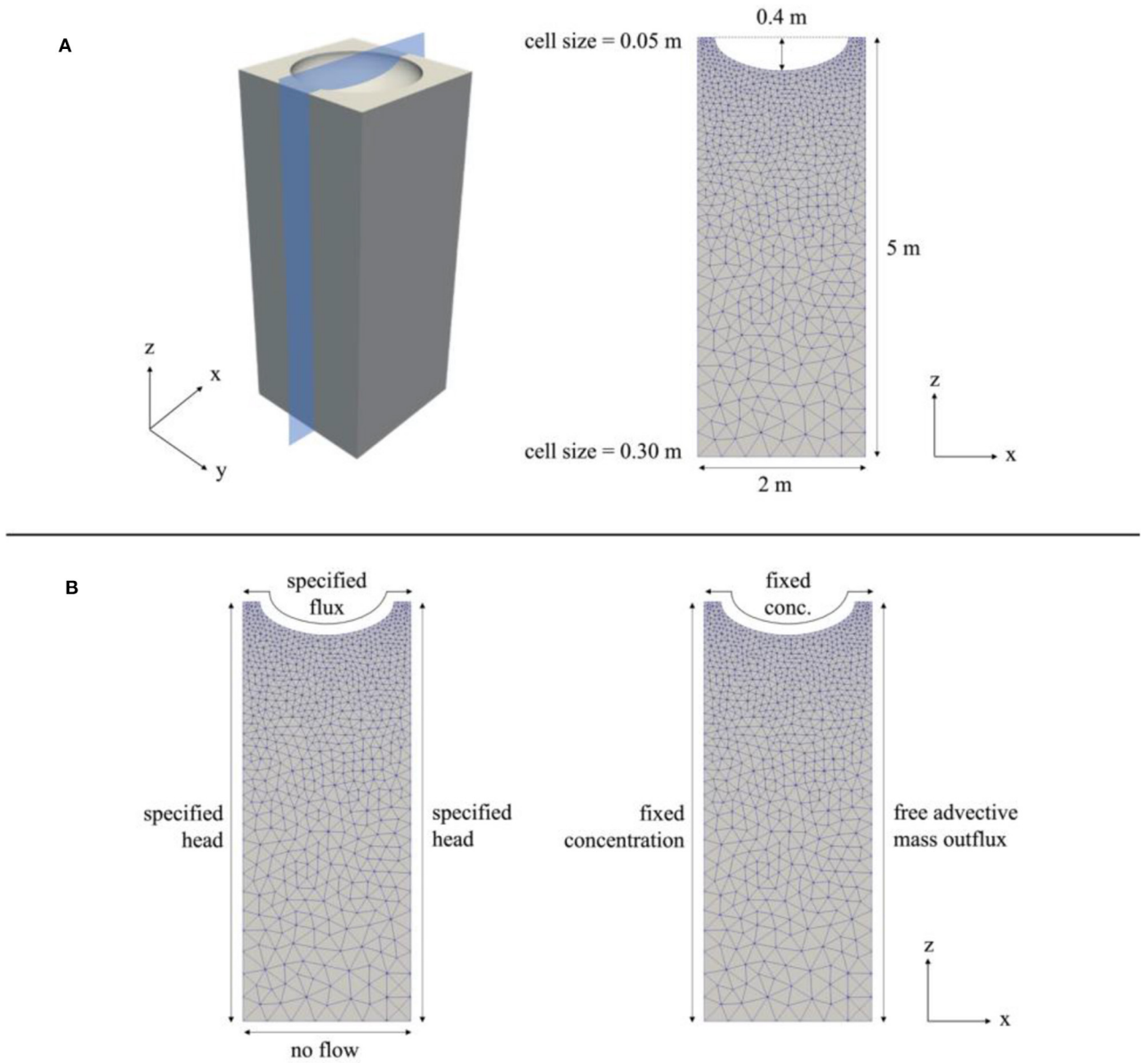

FIGURE 3 | (A) 3D schematic of model domain and 2D cross-section used as model domain in simulations. **(B)** Hydrologic boundary conditions (left) and geochemical boundary conditions (right).

TABLE 1 | Porous media physical parameters.

Material	$K_{sat(z)}$ (m/s)	$K_{sat(x)}$ (m/s)	n_p (–)	θ_r (–)	θ_s (–)	α (m^{-1})	n (–)	$L^{(d)}$ (–)
Topsoil	$4.0{\cdot}10^{-6}$ [(a)]	$1.2{\cdot}10^{-5}$ [(b)]	0.45 [(a)]	0.2 [(c)]	0.45 [(a)]	2.0 [(c)]	1.35 [(c)]	0.5 [(e)]
Graded cobble	$1.6{\cdot}10^{-5}$ [(f)]	$4.8{\cdot}10^{-5}$ [(f)]	0.40 [(f)]	0.11 [(f)]	0.40 [(f)]	2.5 [(f)]	1.15 [(f)]	0.5 [(e)]

[(a)] *Field data (Faybishenko, 2020).*
[(b)] *Anisotropic ratio of 1/3.*
[(c)] *Calculated using pedotransfer function (Faybishenko, 2020).*
[(d)] *Empirical parameter accounting for tortuosity and connectivity.*
[(e)] *Assumed value (Rassam et al., 2018).*
[(f)] *(Wolff, 1982).*

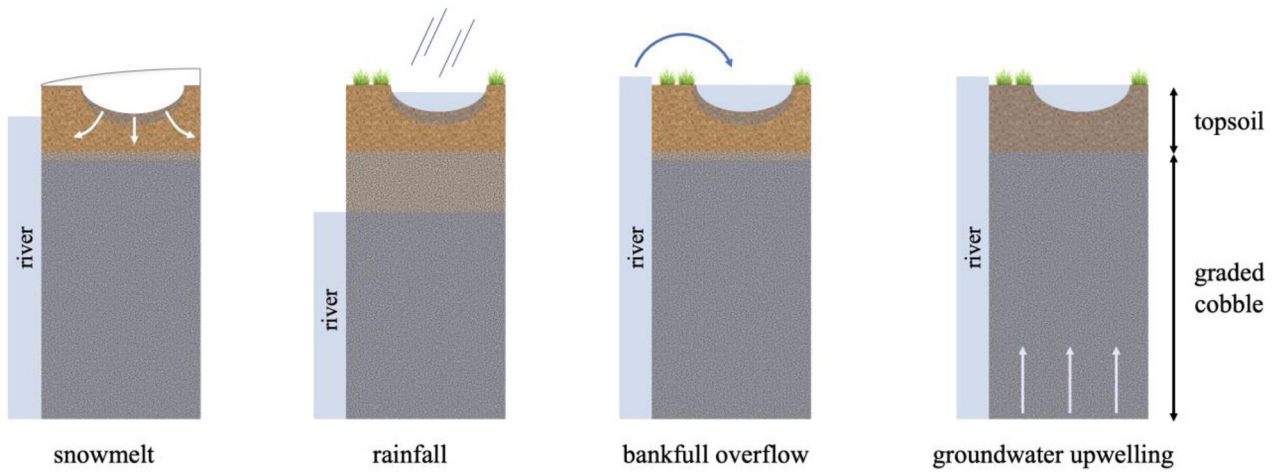

FIGURE 4 | Modes of surface flux modeled in simulations.

water elevations at all points around the meander by subtracting the drop in head between each point and a reference point upstream, where 10-min-resolution river stage data was collected using a pressure transducer (Carroll and Williams, 2019). To calculate the drop in head between each point and the reference point, the distance between each point and the reference point was multiplied by a fixed gradient of −0.0024. This gradient was determined using surface water elevations captured by a 0.5-m DEM of the meander region (Falco et al., 2019). The head drop was subtracted from the river stage data collected at the reference point to obtain an approximate time series of the river stage at each point along the meander. Surface flux due to bankfull overflow was assumed to occur when the nearest river water absolute elevation was greater than the absolute elevation of the ground surface at each groundwater well.

Delineating Periods of Groundwater Upwelling

Periods of groundwater upwelling contributing to surface water ponding were delineated by comparing 15-min-resolution groundwater elevation data to the ground surface elevation of the well. Groundwater upwelling was assumed to occur when the groundwater elevation was greater than the ground surface elevation of the well.

Delineating Periods of Surface Flux Due to Rainfall

In order to obtain infiltration rates from the previously described ponding due to bankfull overflow and ponding due to rain events, we used HYDRUS-1D to calculate ponding heights and subsequent infiltration from both of these events. First, HYDRUS-1D was used to delineate periods of surface flux due to rainfall (Rassam et al., 2018). We used HYDRUS-1D because of the surface ponding capabilities and to calculate infiltration in response to variable atmospheric and ponding conditions. The model domain was designed to replicate the domain used in MIN3P, with a 5-m column comprised of 1 m of topsoil overlying 4 m of graded cobble, using the same physical sediment parameters described in section "Sediment Parameterization". The only difference between the HYDRUS-1D domain and MIN3P domain was the removal of the lateral (x) dimension in the HYDRUS-1D domain. The upper boundary condition was an atmospheric boundary with a surface layer, which allowed accumulation of water at the surface. Rainfall and evapotranspiration were applied at the soil-atmosphere interface using the meteorological data described in section "Meteorological data". The rainfall rates were multiplied by a factor of 2.0 to account for the fact that topographic depressions can function as hydrologic sinks that accumulate runoff from surrounding areas. A multiplication factor of 2.0 was chosen using trial-and-error and visual comparison to measured ponding depths following storms impacting the meander. A maximum time step of 15 min was used to capture shorter-duration rainfall events. The lower boundary condition was a variable head condition, which was forced using the previously described groundwater elevation data.

The data corresponding to ponding by either bankfull overflow or rainfall were then imposed in a HYDRUS-1D simulation as a variable head surface boundary. The model domain, sediment parameters, and lower boundary conditions in these simulations were directly transferred from the previous HYDRUS-1D simulations. The infiltration rates obtained in the outputs of these HYDRUS-1D models were then imposed as specified flux boundaries in the main MIN3P simulations. Infiltration rates during periods of surface flux with *no ponding*, which occurred during snowmelt and certain rainfall events where flux rates were low enough to dampen but not saturate the soil, were also imposed as specified flux boundaries in MIN3P. This analysis workflow (**Figure 5**) was performed for all available data from the snowmelt, dry, and monsoon seasons in 2016–2019.

Geochemical Boundary Conditions

A fixed concentration Dirichlet-type boundary condition was applied at the left side (input) of the model domain, while

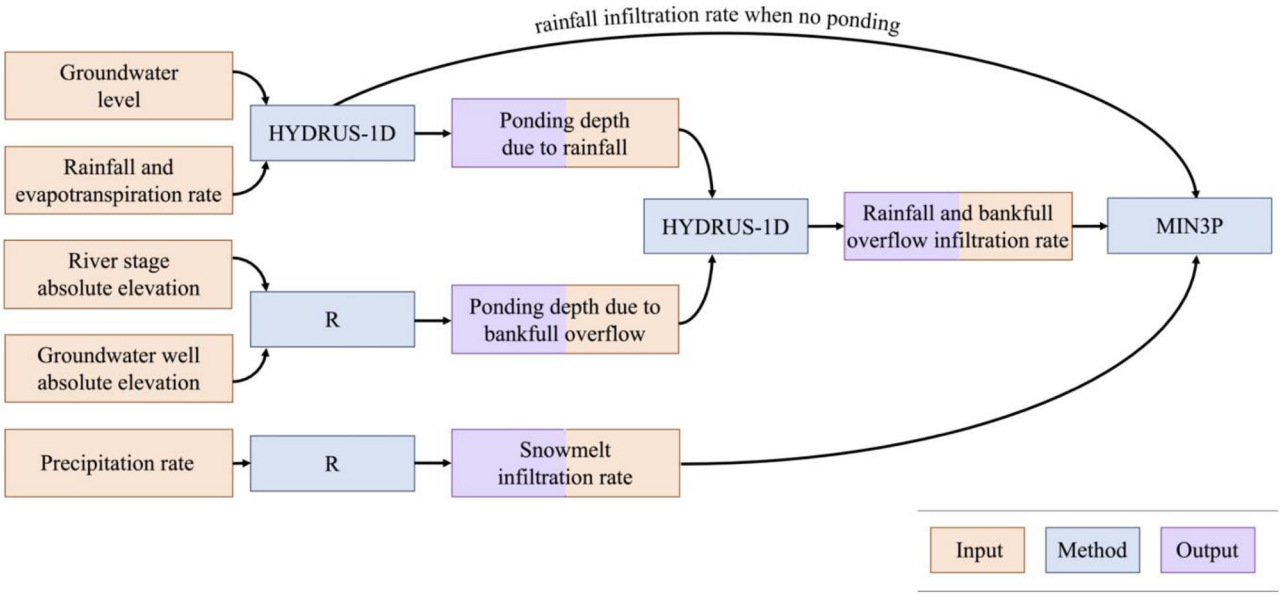

FIGURE 5 | Analysis workflow to obtain specified flux surface boundary for input into MIN3P.

the right side (output) of the domain was specified as a free advective mass outflux boundary (**Figure 3B**). The upper surface (soil-atmosphere interface) of the model was provided with fixed aqueous species concentrations that reflected the source of surface water for each time step. The three possible types of surface water sources were snowmelt, bankfull overflow, and rainfall. For time steps during which there was no surface ponding, the concentrations reflecting the most recent source of surface water were applied. The geochemical makeup of the bankfull overflow was determined using median concentration values of several river chemistry measurements taken along the meander. The geochemical makeup of the snowmelt and rainfall were determined using data provided by the National Atmospheric Deposition Program and documented values from similar field sites. The geochemical makeup of the groundwater was determined using field data and subsequent calibration, which was performed so that aqueous species concentrations were within the same magnitude of those measured in the field (**Supplementary Table 1**).

Reaction Network

The reaction network consisted of 12 primary aqueous species and 34 secondary aqueous species. Three gases, dinitrogen (N_2), carbon dioxide (CO_2), and dioxygen (O_2), were also considered in the reaction network. Ten intra-aqueous kinetic reactions were implemented to model N-cycling and its indirect interactions (mediated via competition for dissolved organic carbon) with iron oxidation-reduction reactions and sulfur oxidation-reduction reactions (**Figure 6**) (Arora et al., 2016; Dwivedi et al., 2018a,b). The reaction kinetics of the biogeochemical network were formulated using Monod-type reaction kinetics. In this formulation, the activation of a reaction pathway is primarily controlled by concentrations of reacting aqueous species and the associated half-saturation constant (K_s) for each reactant; inhibition constants for aqueous components can also be specified to deactivate a reaction pathway when the concentration of a specified aqueous component is greater than the inhibition constant (**Supplementary Table 2**; Su et al., 2019).

Dissimilatory nitrate reduction to ammonium (DNRA) was included in the reaction network due to the high organic carbon to nitrogen ratios (mean ponded surface water C:N = 15.0, mean groundwater C:N = 19.6) and relatively low nitrate concentrations measured at the site, both of which are key controls on the growth of DNRA-performing organisms. DNRA follows two primary pathways, fermentative ($DNRA_{FR}$) and chemolithoautotrophic ($DNRA_{AT}$), the former using organic carbon as the primary electron donor and the latter using sulfide as the primary electron donor (Giblin et al., 2013; Yin et al., 2017). Both DNRA pathways were included in the reaction network. Dissolved organic carbon (DOC) used in heterotrophic reactions was supplied as CH_2O through decomposition of soil organic matter (SOM), which was implemented in the model as a mineral (Dwivedi et al., 2018b; Newcomer et al., 2018). The domain also included pyrite, the initial volume-fraction of which was calculated using sequential iron-oxide extraction techniques on shallow soil samples gathered throughout the floodplain (Fox et al., 2019).

Model Analysis

Model Validation

For hydrologic validation of our model simulations, we compared simulated soil moisture content (θ) at depths of 10 and 60 cm to *in situ* θ measured at the same depths within an intra-meander floodplain located ∼200 m downstream of

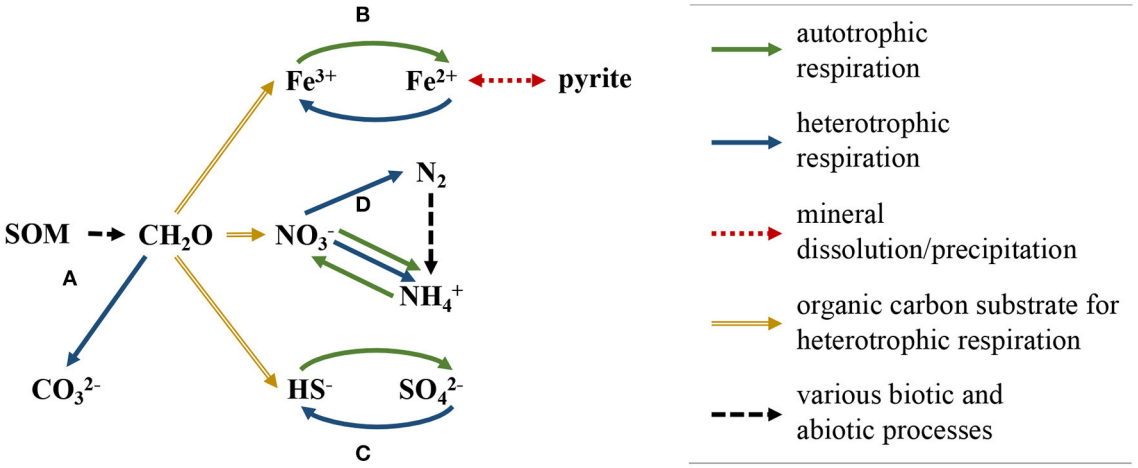

FIGURE 6 | Schematic of biogeochemical reaction network implemented in model simulations. SOM degrades to CH_2O, which then participates in the following reaction pathways; **(A)** organic matter oxidation, **(B)** Fe(III)/Fe(II) reduction-oxidation, which affects the rate of pyrite dissolution/precipitation, **(C)** sulfide/sulfate reduction-oxidation, and **(D)** nitrogen reduction-oxidation, which includes nitrogen fixation, nitrification, dissimilatory nitrate reduction to ammonium, and denitrification.

the primary study site (Wu, 2017). We focused this analysis on the 2017 simulation period, since this was the longest continuous simulation, allowing us to compare both short-term and long-term trends. For biogeochemical validation, we considered transient aqueous concentrations for three species integral to N-cycling, NO_3^-, NH_4^+, and $O_{2(aq)}$. For each species, we compared *in situ* concentrations measured at depths of 20 cm to 100 cm below the ground surface of the intra-meander floodplain from 05/20/2017 to 08/30/2017 (see section "*In Situ* Geochemical Sampling") to simulated aqueous concentrations at a depth of 60 cm below the ground surface (midpoint of *in situ* geochemical measurements) for the same time period. Because all model domains are inherently a generic simplified representation of reality, we treat the model domain as a tool for *enhancing* understanding of processes and controls on nitrogen cycling, and not as a tool to simply recreate measured values. Indeed, even the worst models can perfectly predict measurements with the "right" parameter set, thus we take great care in this study to make sure measured parameters (soil K, etc.) and measured state conditions (soil chemistry, soil hydrology) generally agree with model simulations.

N Transformation Rates

We focus our analysis on the relevant N-cycling pathways, including denitrification (DN), both DNRA pathways ($DNRA_{FR}$ and $DNRA_{AT}$), and nitrification (NI), since these reactions directly affect NO_3^- loading. To analyze the kinetics of each reaction, we began with the mass of N that is transformed by each reaction across the entire model domain for each time step; these values are directly provided as raw outputs from MIN3P with units of mol N d^{-1}. We then added a spatial dimension to this rate by calculating the transformation rate per square meter of land surface area. For two-dimensional model domains, MIN3P provides transformation and flux rates as if the domain is projected one unit (e.g., m) into the third dimension. Therefore, the land surface of our model is 2 m (x-dimension) by 1 m (projected into y-dimension). Thus, the raw transformation rates were divided by 2 m^2 to determine the riparian hollow N transformation rates per square meter of land (mol N m^{-2} d^{-1})

To compare these transformation rates to the timing of surface flux events, we also calculate when spikes occur in the rates. Here, a spike is defined where a transformation rate increases and crosses a specified threshold value, which was chosen as either ∼50% or ∼75% of the maximum rate. While the number of spikes will always increase or remain the same with lower threshold values, we found that changing the threshold value (when the threshold value is at least above the mean value) does not considerably change the percentage of spikes associated with a specific type of surface flux. Therefore, while there exist more mathematically sophisticated techniques of spike detection, this method is sufficient for the purposes of our analysis.

NO_3^- Mass Balance Definitions and Calculations

For the purposes of mass balance analysis, we provide the following terms and definitions:

NO_3^- sink: more NO_3^- flows into the model domain than flows out; this term is controlled by both transport and reactions.

NO_3^- source: more NO_3^- flows out of the model domain than flows in; this term is controlled by both transport and reactions.

Percent source/sink: the percentage of NO_3^- influx that is gained or lost by the hollow throughout the simulation; 0% source/sink represents a NO_3^- outflux equal to the NO_3^- influx; −50% source/sink represents a NO_3^- outflux equal to one-half of the NO_3^- influx, indicating the hollow is a net NO_3^- sink; +100% source/sink represents a NO_3^- outflux that is double the NO_3^- influx, indicating the hollow is a net NO_3^- source.

Net NO_3^- removing or net consuming: within the model domain, more NO_3^- is removed than is produced by aqueous

reactions; i.e. the total amount of NO_3^- removed by DN and DNRA is greater than the total amount of NO_3^- yielded by NI; this term is controlled only by reaction rates.

Net NO_3^- yielding: within the model domain, more NO_3^- is yielded by aqueous reactions than is consumed; i.e., the total amount of NO_3^- yielded by NI is greater than the total amount of NO_3^- removed by DN and DNRA; this term is controlled only by reaction rates.

The mass influx, mass outflux, change in storage, and net mass removed or net mass yielded across the domain during each time step are directly provided as raw data outputs from the MIN3P simulations. The cumulative values for these parameters are also provided at each time step, so total mass influx, for example, across the entirety of each simulation could be found by evaluating the cumulative mass influx at the final time step of each simulation. As with the N transformation rates, we added a spatial dimension to determine flux rates per square meter of riparian hollow (mol NO_3^- m^{-2} d^{-1}) and cumulative flux per square meter of riparian hollow (mol NO_3^- m^{-2}). The percent source/sink term for each simulation was determined by calculating (total mass outflux–total mass influx)/(total mass influx).

Scaling

To better understand the magnitude of riparian hollow N fluxes relative to the catchment N budget, we estimated the contribution of riparian hollow NO_3^--N outfluxes to in-stream NO_3^--N fluxes near the outlet of the East River catchment. The first step to determine this contribution was to calculate the NO_3^--N outflux from the total area of the catchment covered by riparian hollows. Using an approximation provided by Duncan et al. that riparian hollows cover up to 1% of the total catchment area (Duncan et al., 2013), we multiplied 1% of the catchment area by the cumulative NO_3^--N outflux per square meter of riparian hollow to determine the NO_3^--N outflux from the total area of the catchment covered by riparian hollows. We then divided these fluxes by the corresponding in-stream NO_3^--N fluxes for each model period to approximate the contribution of riparian hollows to the in-stream NO_3^--N budget. The in-stream NO_3^--N fluxes were determined using concentration-discharge relationships gathered near the outlet of the East River catchment (Newcomer M. et al., 2020).

To provide another metric on how riparian hollow N fluxes impact catchment scale N fluxes, we also approximated the in-stream NO_3^--N outflux of a hypothetical watershed lacking riparian hollows. To determine this, we first calculated the NO_3^--N influx into the total area of the catchment covered by riparian hollows, using the same method described in the previous paragraph that was used to determine the total outflux. We then determined the net effect of the riparian hollows by subtracting the total influx from the total outflux; a negative value in this case would mean riparian hollows are removing NO_3^--N before it reaches the stream, while a positive value would mean the presence of riparian hollows results in an increase in stream NO_3^--N.

RESULTS

Model Validation

At depths of 10 cm and 60 cm, the simulated θ generally followed *in situ* θ trends well (**Figure 7**). At 10 cm depth, major and minor peaks and troughs in measured θ can also be seen in simulated θ, albeit frequently at varying magnitudes. The most significant discrepancy occurs during June 2017, during which there is bankfull overflow in the simulated domain. This bankfull overflow likely did not occur in the downstream floodplain, since there are no significant changes in measured θ. Other minor discrepancies can likely be attributed to model sediment parameters being slightly different from downstream *in situ* sediment parameters, as changes in these parameters can affect water retention curves and associated hysteresis (Likos et al., 2014). At 60 cm depth, both simulated and measured θ show an initial trough, followed by a mostly static period, and end with a gradual decline. The simulated θ reaches its maximum soil moisture content (indicating saturation) during the static period due to high groundwater levels. Saturation is not seen in the measured θ, possibly due to (1) higher porosity in the downstream *in situ* domain than in the simulated domain, (2) location relative to the river, or (3) varying thicknesses of topsoil and graded cobble layers.

In general, the simulated concentrations fall within the range of measured concentrations for each species of interest (**Figure 8**). Simulated NO_3^- concentrations are slightly larger than measured NO_3^- concentrations, though they are well within the same order magnitude and follow the same overall trend. Simulated NH_4^+ and $O_{2(aq)}$ concentrations are near the lower and more densely populated end of the range of respective measured concentrations, and they also follow the same general trend as measured concentrations.

Riparian Hollow Surface Flux Periods and N-Cycling Kinetics

Distribution of Surface Flux Events and N Transformation Spikes

Surface flux occurs for 24% of the time simulated; 47% of the surface flux (as determined by duration rather than number of events or magnitude of events) is due to snowmelt, 39% rainfall, and 14% bankfull overflow (**Figure 9**). While each season consists of several surface flux events, there tend to be fewer surface flux events in later months, primarily mid-August through October.

In general, DN rates are higher than NI rates and both DNRA rates. There are several short periods during which the NI rate is greater than the DN rate, though the spikes in NI during these periods generally display a rapid onset and are not usually sustained over long periods of time. Both DNRA rates are consistently lower than DN and NI rates, with $DNRA_{FR}$ rates ∼33% of DN rates and $DNRA_{AT}$ rates negligible (<1%) relative to DN rates.

Each $DNRA_{FR}$ spike coincides with a spike in NI, though the converse is not always true. Eighty one percentage of the spikes

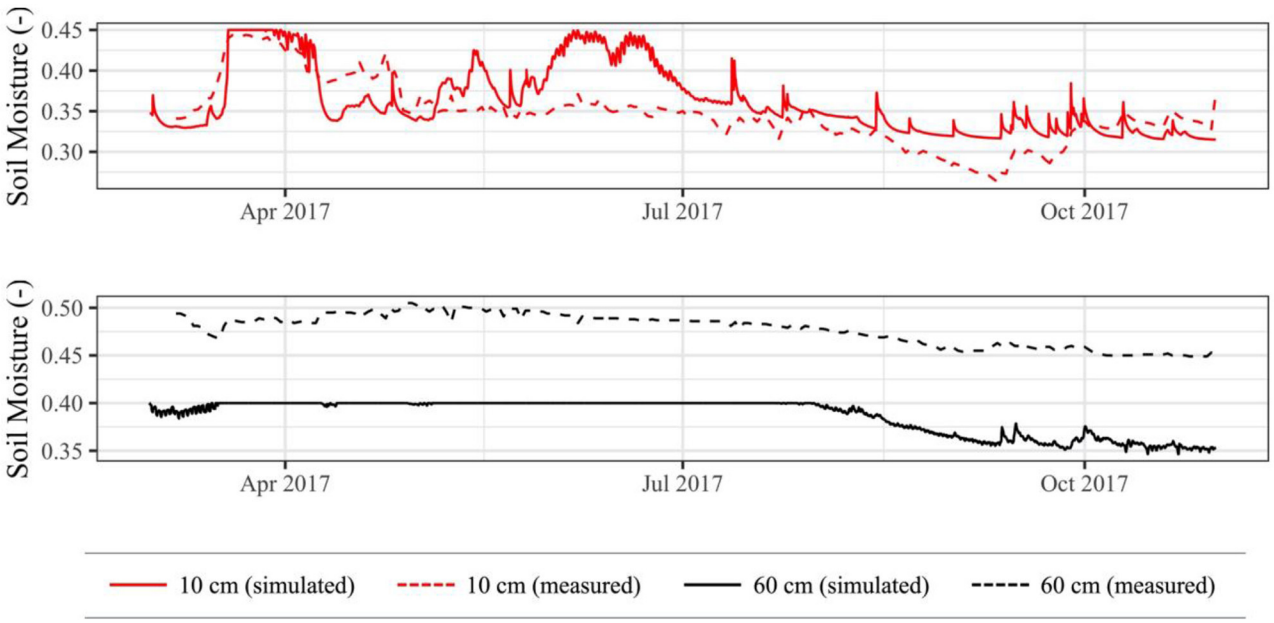

FIGURE 7 | Simulated soil moisture contents compared to *in situ* soil moisture contents across 2017 simulation period.

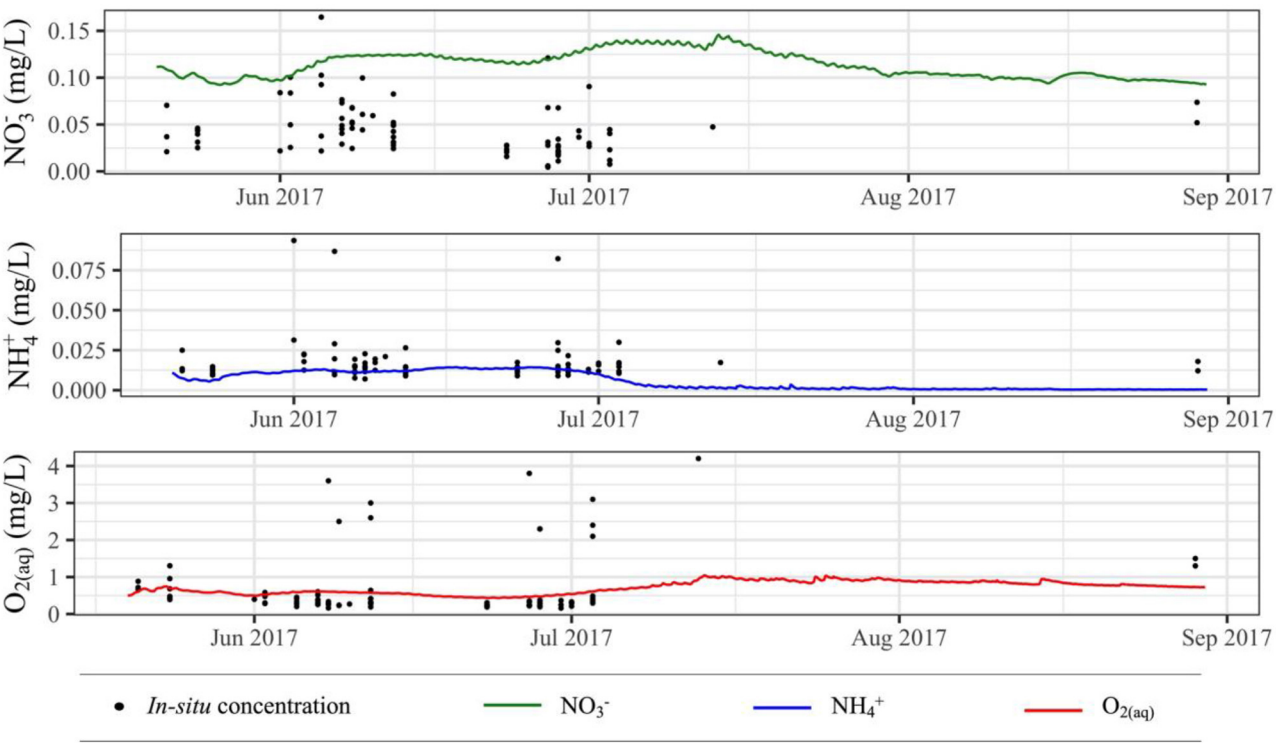

FIGURE 8 | Simulated aqueous species concentrations compared to *in situ* aqueous species concentrations; multiple y-values for a single x-value represent *in situ* measurements at multiple locations and/or depths on a given day.

in $DNRA_{FR}$ occur at the onset of surface flux due to rainfall, 12% occur at the onset of surface flux due to snowmelt, and the remaining 6% are not directly associated with the onset of a surface flux event. Spikes in $DNRA_{FR}$ rates were determined using a threshold value of 0.125 mmol N m^{-2} d^{-1}; similar percentages were obtained using various threshold values.

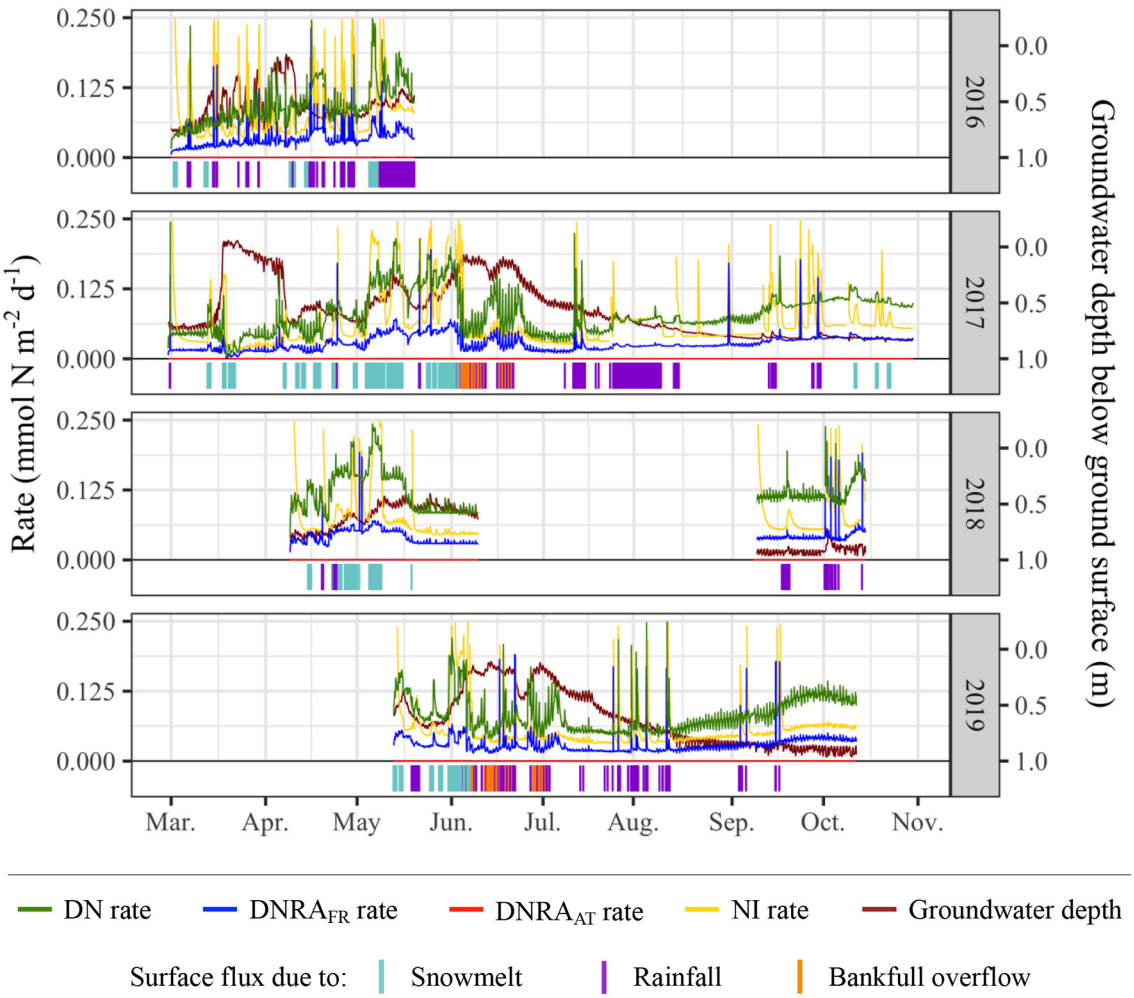

FIGURE 9 | N-transformation rates, groundwater depth, and surface flux periods/sources. In the bottom portion of each plot, the presence of a vertical line indicates surface flux occurring at that time, and the color of the vertical line represents the source of the surface flux. Simulations were only run for periods when sufficient data were available.

Effects of Groundwater on N Transformation Rates

When comparing groundwater table depth to N-transformation rates, a few key trends related to groundwater depth, bankfull overflow, and NI rates appear. The lowest NI rates, occurring during mid-March 2017, are associated with the shallowest groundwater levels across all simulations. A significant decrease in NI rates is also observed throughout June 2017, another period of shallow groundwater levels. This pattern can be identified at several points throughout the simulations, across different types and magnitudes of surface flux. Bankfull overflow events, observed during June-July of 2017 and 2019, can also be related to shallow groundwater events and low NI rates. Shallow groundwater levels, however, do not fully inhibit spikes in NI rates. For example, during early to late June 2019, NI rates are near their lowest and groundwater is at its shallowest for the analyzed portion 2019; however, there are also three spikes in NI during this period, occurring at the onset of rainfall events. These patterns suggest that upwelling of reduced groundwater is an important inhibitor of NI, but also that rainfall events (associated with about 70% of NI spikes, as determined using threshold values of 0.1875 and 0.125 mmol N m^{-2} d^{-1}) and snowmelt events (associated with 24% of NI spikes) can provide brief periods of geochemical conditions favorable for NI metabolisms.

NO_3^- Mass Balance Dynamics

Time-series analysis of NO_3^- mass balance parameters, including mass influx, mass outflux, change in storage, and mass removing/yielding rates, indicates that riparian hollows frequently fluctuate between net removing and net yielding behavior, typically due to the onset of different types of surface flux (**Figure 10**). The percentage of time during which the domain is net removing ranges from 74 to 87% of each simulation, with spikes in NI rates resulting in net NO_3^- yielding behavior occurring, on average, for 20% of each simulation. Of this 20% during which net yielding conditions prevail, 43% occurs during periods of no surface flux, 29% during snowmelt

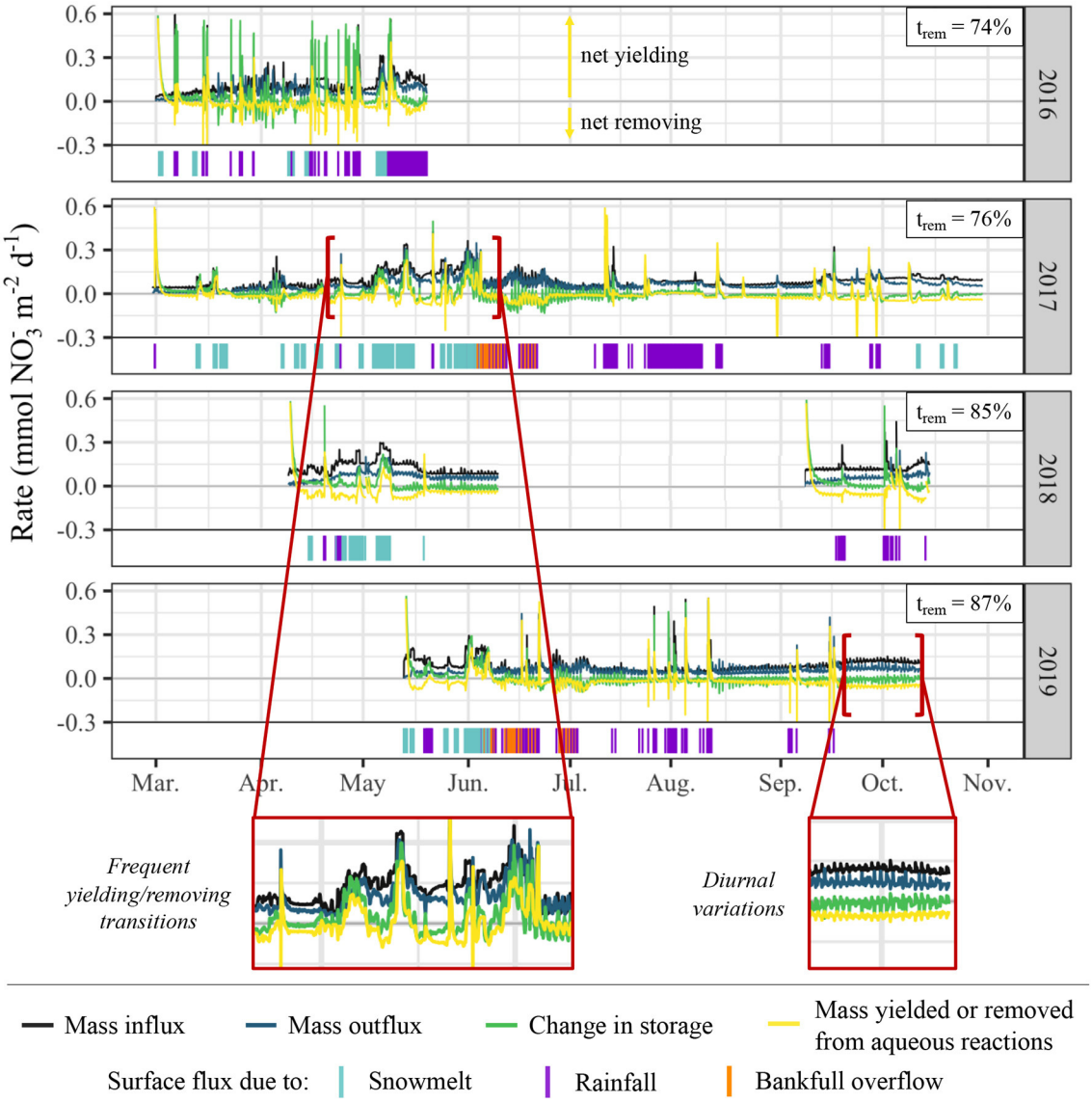

FIGURE 10 | Time-series of NO_3^- mass balance dynamics and surface flux periods/sources. Mass balance parameters are presented in rates of mol NO_3^- d^{-1} and represent dynamics spatially summed across the entire model domain. Positive mass removing/yielding rates from aqueous reactions represent net NO_3^- yield (NI > DN + $DNRA_{FR+AT}$), and negative values represent net NO_3^- removal (NI < DN + $DNRA_{FR+AT}$). The percentage of time during which the domain is net removing (t_{rem}) is denoted at the upper right corner of each plot.

events, 24% during rainfall events, and 4% during bankfull overflow events. Given surface flux only occurs for 24% of the total simulation period but for 57% of the total net yielding period, it appears that surface flux events preferentially result in net yielding behavior.

While the peak magnitude of removing behavior is far less than the peak magnitude of yielding behavior, cumulative NO_3^- mass balance calculations for each model period indicate that the significantly longer durations of removing behavior result in the simulated hollow functioning as a net NO_3^- remover for all model periods (**Table 2**). This behavior translates to each of the model periods operating as net NO_3^- sinks, though the degree of sink-behavior is impacted by variability from meteorological conditions. During the 2019 monsoon season, for example, there was a one-month period (mid-Sep. to mid-Oct.) with minimal surface flux due to rainfall. This resulted in very mild but constant NO_3^- removal behavior. During the same one-month period in 2018, however, there were several rainfall-driven surface flux events, resulting in far more dramatic removal behavior and thus NO_3^- sink functionality.

Riparian Hollows and the Stream N Budget

Aggregating total outfluxes and comparing with stream N exports indicate riparian hollows can be major contributors to stream N budgets (**Table 3**). In-stream exports of NO_3^--N range from 0.14 to 1.7 Mg across the different simulation periods; riparian hollow

TABLE 2 | Cumulative NO_3^- mass balance values separated by year and relevant sub-period for which the model was run.

Year	Model start	Model end	Total influx (mmol m^{-2})	Total outflux (mmol m^{-2})	Percent source/sink	Net change in storage (mmol m^{-2})	Net removed/yielded from aqueous reactions (mmol m^{-2})
2016	3/1/16	5/20/16	9.40	6.07	−35.3%	1.51	−1.56
2017	3/1/17	11/1/17	22.77	16.88	−25.9%	1.91	−3.21
2018	4/10/18	6/11/18	8.20	4.35	−46.9%	0.63	−3.05
2018	9/9/18	10/16/18	4.93	2.18	−55.7%	0.37	−2.33
2019	5/14/19	8/20/19	14.47	9.42	−34.9%	1.08	−3.60

Influx, outflux, and change in storage values are presented as cumulative mass fluxes in millimols per square meter of riparian hollow. Definitions for "Percent source/sink" and "Removed/yielded" are provided in the text.

TABLE 3 | Scaled contribution of the total NO_3^- outflux from riparian hollows across the catchment to the in-stream NO_3^--N outflux for each of the simulation periods.

Year	Model start	Model end	Riparian hollow NO_3^--N mass outflux (Mg)	In-stream NO_3^--N mass outflux (Mg)	Riparian hollow contribution to total in-stream NO_3^--N outflux
2016	3/1/16	5/20/16	0.072	0.998	7%
2017	3/1/17	11/1/17	0.200	0.856	23%
2018	4/10/18	6/11/18	0.052	0.467	11%
2018	9/9/18	10/16/18	0.026	0.144	18%
2019	5/14/19	8/20/19	0.112	1.762	6%

contributions to these in-stream NO_3^--N exports range from 0.026 to 0.2 Mg, assuming that riparian hollows comprise 1% of the total catchment area above the meander where field data was collected (**Figure 9**; Duncan et al., 2013). The total contribution of riparian hollows as a percentage of the total in-stream NO_3^--N outflux ranged from 6 to 23%, with a temporally weighted average of 15%. Out of the five time periods we simulated, the year 2017 had the highest percentage of riparian hollow contributions to stream N exports, accounting for nearly one-quarter of the in-stream NO_3^--N outflux.

Using the mass NO_3^- influx of the model domain and removing any source/sink behavior introduced via riparian hollows, we calculated that in-stream NO_3^--N outfluxes could increase by up to 20% in the complete absence of riparian hollows. Therefore, despite the seemingly large contribution of riparian hollows to in-stream NO_3^--N budgets, our calculations in a hypothetical watershed lacking riparian hollows show that these features can be inhibitors of upland NO_3^- reaching the stream.

DISCUSSION

Hydrologic Controls on N-Cycling

Our results show that groundwater upwelling significantly inhibits NI, which is expected due to the anoxic and reducing properties of the groundwater at this site. This trend aligns well with previous studies conducted at the site, where measured *in situ* NI rates were often minimal (Personal communication, E. Brodie). DN rates were not as limited by groundwater upwelling as NI rates were, though the simulations did still yield lower DN rates during periods of shallow groundwater. This can likely be attributed to the limited concentration of electron acceptors (i.e., NO_3^-) in the highly reduced groundwater. During previous field campaigns conducted at this site, DN was not observed through analysis of genomic samples (Sorenson et al., 2019). However, this does not mean that DN was not occurring at the time of sampling; it likely means that sampling locations, depths, and/or timing were not suited to capture measurable DN rates. This study can help inform future field campaigns both spatially and temporally, as our simulations suggest that (1) DN occurs at higher rates near the surface, rather than in the deeper, highly reduced groundwater, and (2) DN rates more often spike at the onset of rainfall events, rather than during shallow groundwater conditions or snowmelt events.

Shifts in snowmelt timing and magnitude, as well as more precipitation falling as rain than snow, could have substantial impacts on NO_3^--N exports given the controls we observed on N-transformation rates. With anticipated dryer and warmer winters in alpine regions, as predicted by past studies conducted at this site, our results suggest that spikes in DN, $DNRA_{FR}$, NI rates will likely increase in frequency and magnitude due to (1) deeper groundwater levels related to shorter snowmelt periods, and (2) an increase in proportion of surface flux events due to rainfall coupled with a decrease in the proportion of surface flux events due to snowmelt (Hubbard et al., 2018). The net impact of such changes in the partitioning of rainfall and snowfall is the potential shift of riparian hollows to functioning as more significant NO_3^- sinks, further decreasing the net NO_3^--N exports in an already NO_3^--limited watershed. This suggested trend has previously been observed through analysis of a 50-year concentration-discharge time series of the East River during which there are declines in inorganic nitrogen over time and down the watershed network (Newcomer M. E. et al., 2020).

Riparian Hollow Source/Sink Behavior and Scaled Impact

Our simulated riparian hollow functions as a net NO_3^- sink, removing or retaining approximately one-quarter to one-half of the NO_3^- that is transported through the domain. We found the

most significant reaction consuming NO_3^- and removing NO_3^- from the domain was DN; however, NO_3^- was quite sensitive to surface flux events. Only 15% of net removing behavior occurred during periods of surface flux, while a much more significant 57% of net yielding behavior occurred during periods of surface flux.

Our scaling results show that riparian hollows may contribute a significant portion of the in-stream NO_3^--N outflux, emphasizing their role as one of the major ecosystem control points within the riparian corridors. We also calculated that in-stream NO_3^--N outfluxes could increase by up to 20% in the complete absence of riparian hollows. This indicates that the presence of these riparian hollows may inhibit upland NO_3^- from reaching the stream, resulting in decreases in watershed N exports.

We acknowledge many different sources of uncertainty could shift these estimates. These calculations assumed that the groundwater baseflow always travels from the beneath riparian hollow into the stream, implying gaining conditions for the periods analyzed. While this may result in an overestimate of the total contribution of riparian hollows to the in-stream NO_3^--N outflux, groundwater baseflow has been shown to be an important source of streamflow across all seasons at this site, justifying the assumption of gaining conditions.

Among the several types of ecosystem control points proposed by Bernhardt et al. our simulated riparian hollow would be classified as an activated control point that "supports high transformation rates only when the delivery rate of one or more limiting reactants increases and when abiotic conditions required for a particular biogeochemical process are optimized" (Bernhardt et al., 2017). None of the key N-transformation reactions are sustained for the entirety of each simulation due to limited substrate availability and/or unsuitable abiotic conditions, usually related to electron acceptor availability or oxygen levels; i.e., limited NO_3^- and oxic waters prevent consistently high DN and DNRA rates, while limited NH_4^+ and limited dissolved oxygen prevent consistently high NI rates. In watersheds with excess nutrients, such as those containing agricultural catchments, riparian hollows could act as permanent control points, within which there is a "continuous delivery of reactants and nearly constant appropriate environmental conditions all for sustained high rates of biogeochemical activity relative to the surrounding landscape," due to a sustained excess of NO_3^- constantly promoting DN and/or DNRA (Bernhardt et al., 2017). This study shows that transient hydrologic conditions in some watersheds, however, can prevent riparian hollows from functioning as permanent control points. This conclusion is important when considering the behavior of riparian hollows in an eastern U.S. catchment measured by Duncan et al., who found that >99% of all surface DN occurs within riparian hollows (Duncan et al., 2013). Under transient hydrologic conditions, DN within riparian hollows may not be sustained, and since these are essentially the only features promoting DN within the watershed studied by Duncan et al., the overall DN potential of the watershed could dramatically decrease under limited substrate conditions or unsuitable abiotic conditions, as shown in our simulations.

TABLE 4 | Relative contribution of DNRA and DN to total NO_3^- reduction under different settings.

DNRA:DN	Setting	Source
1:3	Alpine riparian floodplain	Rogers et al., 2020 [This study]
1:2	Montane grassland	Chen et al., 2015
3:1	Various riparian floodplains	Wang et al., 2020b
1:13–1:20	Temperate floodplain	Sgouridis et al., 2011
2:1–1:5	Riparian rhizosphere	Wang et al., 2020a

Importance of Dissimilatory Nitrate Reduction to Ammonium

Our results show that DNRA can be an important pathway for NO_3^- reduction. In our simulations, we found DNRA accounted for 25% of NO_3^- reduction during monsoon/snow periods and was most sensitive to long dry conditions. At our site, the primary DNRA pathway was fermentative, since sulfide concentrations were not high enough to induce the autotrophic pathway. The ratio of NO_3^- reduced by DNRA to that of DN for our study falls within previously documented ranges, which are presented for context in **Table 4**. The presence of this alternative pathway is significant because DNRA reduces NO_3^- to a reactive and biologically available form of N, NH_4^+(aq), as opposed to DN, which reduces NO_3^- to relatively inert and biologically unavailable N_2(g). This conservation of biologically available N can have significant impacts on the overall N mass balance by promoting greater NI rates, enhancing the net primary productivity by providing a sustained source of N for primary producers (Marchant et al., 2014; Domangue and Mortazavi, 2018). DNRA is not commonly accounted for in reaction networks of model-based studies, including studies analyzing nitrogen mass balances of systems. Our study and previous studies show that DNRA should, at a minimum, be considered as part of the reaction network based on, but not limited to, C:N ratios, electron-acceptor abundance, and sulfide concentrations in the system (Giblin et al., 2013; Marchant et al., 2014). We suggest inclusion of DNRA could assist in developing model-based studies that are more accurate and more widely applicable.

Recent advances in genome-resolved reactive transport modeling make it possible to better quantify the role of and controls on DNRA. Analyzing metagenomic samples can reveal the presence or absence of DNRA-related organisms and can indicate whether the pathways comprising DNRA are fully, partially, or not represented in a sample (Arkin et al., 2018; Carnevali et al., 2020; Shaffer et al., 2020). Further metabolomic modeling and flux balance analysis can help quantify DNRA kinetics relative to DN and NI kinetics under various conditions, such as different growth media, limited substrates, or the presence of inhibiting species (Kleerebezem and van Loosdrecht, 2010; Arkin et al., 2018; Rawls et al., 2019; Song et al., 2020). Integrating such metagenomic and metabolomic data into reactive transport models is an important next step in both conceptualizing and quantifying the key controls on reach- and watershed-scale N balances, and we suggest future studies will need to explore this frontier to accurately develop relevant reaction networks.

CONCLUSION

In this study, we used numerical modeling informed by an array of *in situ* datasets to quantify the N-cycling kinetics of riparian hollows under transient hydrologic conditions, which included transient surface flux from snowmelt, bankfull overflow, groundwater upwelling, and rainfall. From this study, we concluded that riparian hollows behave as one of the major ecosystem control points within riparian corridors through their primary function as NO_3^- sinks. We observed that periods of groundwater upwelling are a significant inhibitor of N-transformation within riparian hollows, while rainfall events are key activators of the N-retaining function of riparian hollows. Given these observed hydrologic controls, we expect that the NO_3^--sink capacity of riparian hollows will increase in magnitude with future climatic perturbations, such as shorter snowmelt seasons and more frequent rainfall events, within mountainous headwater catchments, further limiting watershed inorganic N exports. We also highlighted the importance of DNRA in the N mass balance of this system, and we encourage future model-based studies to consider this reaction as potentially integral to the N cycle within their system. This study elucidates the significance of riparian hollows as small-scale controls on reach- and watershed-scale N mass balances, and it further emphasizes the importance of using a multi-scale approach when considering aggregated watershed functions.

DATA AVAILABILITY STATEMENT

All data associated with the modeling results of this article are available for free and public use at: https://data.ess-dive.lbl.gov/view/, doi: 10.15485/1734795 (Rogers et al., 2020).

AUTHOR CONTRIBUTIONS

DR, MN, DD, CS, NB, PN, MC, MB, EB, BA, and SH developed the conceptual framework for the study. MN, JR, BF, KW, BD, and PF performed all field work. DR, MN, NB, EB, DD, and PN developed the reaction network and geochemical boundary conditions. DR performed all numerical modeling, data analysis, and developed the manuscript for the study. All authors contributed to revising the manuscript.

FUNDING

This material is based upon work supported as part of the Watershed Function Scientific Focus Area funded by the U.S. Department of Energy, Office of Science, Office of Biological, and Environmental Research under Award Number DE-AC02-05CH11231.

ACKNOWLEDGMENTS

The authors thank Danyang Su for useful software suggestions and Sergi Molins for helpful discussions on the scope of our simulations. The authors would also like to thank the three reviewers for helping to improve the clarity and applicability of this manuscript.

SUPPLEMENTARY MATERIAL

The Supplementary Material for this article can be found online at: https://www.frontiersin.org/articles/10.3389/frwa.2021.590314/full#supplementary-material

REFERENCES

Adam, J. C., Hamlet, A. F., and Lettenmaier, D. P. (2009). Implications of global climate change for snowmelt hydrology in the twenty-first century. *Hydrol. Process* 23, 962–972. doi: 10.1002/hyp.7201

Appelo, C. A. J., and Postma, D. (2005). "Nitrate reduction," in *Geochemistry, Groundwater, and Pollution*, 2nd Edn (Leiden: A. A. Balkema Publishers), 458–488. doi: 10.1201/9781439833544

Appling, A. P., Bernhardt, E. S., and Stanford, J. A. (2014). Floodplain biogeochemical mosaics: a multidimensional view of alluvial soils. *J. Geophys. Res. Biogeosci.* 119, 1538–1553. doi: 10.1002/2013JG002543

Arkin, A. P., Cottingham, R. W., Henry, C. S., Harris, N. L., Stevens, R. L., Maslov, S., et al. (2018). KBase: the united states department of energy systems biology knowledgebase. *Nat. Biotechnol.* 36, 566–569. doi: 10.1038/nbt.4163

Arora, B., Spycher, N. F., Steefel, C. I., Molins, S., Bill, M., Conrad, M. E., et al. (2016). Influence of hydrological, biogeochemical and temperature transients on subsurface carbon fluxes in a flood plain environment. *Biogeochemistry* 127, 367–396. doi: 10.1007/s10533-016-0186-8

Barnhart, T. B., Molotch, N. P., Livneh, B., Harpold, A. A., Knowles, J. F., and Schneider, D. (2016). Snowmelt rate dictates streamflow: snowmelt rate dictates streamflow. *Geophys. Res. Lett.* 43, 8006–8016. doi: 10.1002/2016GL069690

Bernard-Jannin, L., Sun, X., Teissier, S., Sauvage, S., and Sánchez-Pérez, J.-M. (2017). Spatio-temporal analysis of factors controlling nitrate dynamics and potential denitrification hot spots and hot moments in groundwater of an alluvial floodplain. *Ecol. Eng.* 103, 372–384. doi: 10.1016/j.ecoleng.2015.12.031

Bernhardt, E. S., Blaszczak, J. R., Ficken, C. D., Fork, M. L., Kaiser, K. E., and Seybold, E. C. (2017). Control points in ecosystems: moving beyond the hot spot hot moment concept. *Ecosystems* 20, 665–682. doi: 10.1007/s10021-016-0103-y

Blankinship, J. C., Meadows, M. W., Lucas, R. G., and Hart, S. C. (2014). Snowmelt timing alters shallow but not deep soil moisture in the Sierra Nevada. *Water Resour. Res.* 50, 1448–1456. doi: 10.1002/2013WR014541

Carnevali, P. B. M., Lavy, A., Thomas, A. D., Crits-Christoph, A., Diamond, S., Meéheust, R., et al. (2020). Meanders as a scaling motif for understanding of floodplain soil microbiome and biogeochemical potential at the watershed scale. *bioRxiv*. doi: 10.1101/2020.05.14.086363

Carroll, R., Bearup, L. A., Brown, W., Dong, W., Bill, M., and Willlams, K. H. (2018). Factors controlling seasonal groundwater and solute flux from snow-dominated basins. *Hydrol. Process* 32, 2187–2202. doi: 10.1002/hyp.13151

Carroll, R., and Williams, K. H. (2019). Discharge data collected within the East River for the Lawrence Berkeley National Laboratory Watershed Function Science Focus Area (water years 2015-2018). *Environ. Syst. Sci. Data Infrastr. Virt. Ecosyst. Watershed Funct. SFA*. doi: 10.21952/WTR/1495380

Castaldelli, G., Vincenzi, F., Fano, E. A., and Soana, E. (2020). In search for the missing nitrogen: closing the budget to assess the role of denitrification in agricultural watersheds. *Appl. Sci.* 10:2136. doi: 10.3390/app10062136

Chen, Z., Wang, C., Gschwendtner, S., Willibald, G., Unteregelsbacher, S., Lu, H., et al. (2015). Relationships between denitrification gene expression, dissimilatory nitrate reduction to ammonium and nitrous oxide and dinitrogen production in montane grassland soils. *Soil Biol. Biochem.* 87, 67–77. doi: 10.1016/j.soilbio.2015.03.030

Clark, M., and Pitlick, J. (2005). Seasonal cycle shifts in hydroclimatology over the western united states. *J. Clim.* 18, 372–384. doi: 10.1175/JCLI-3272.1

Clow, D. W. (2010). Changes in the timing of snowmelt and streamflow in colorado: a response to recent warming. *J. Clim.* 23, 2293–2306. doi: 10.1175/2009JCLI2951.1

Dafflon, B., Malenda, H., and Dwivedi, D. (2020). Groundwater level elevation and temperature across Meander C at the Lower Montane in the East River Watershed, Colorado. *Environ. Syst. Sci. Data Infrastr. Virt. Ecosyst. Watershed Funct. SFA*. doi: 10.15485/1647041

Domangue, R. J., and Mortazavi, B. (2018). Nitrate reduction pathways in the presence of excess nitrogen in a shallow eutrophic estuary. *Environ. Pollut.* 238, 599–606. doi: 10.1016/j.envpol.2018.03.033

Dudley, R. W., Hodgkins, G. A., McHale, M. R., Kolian, M. J., and Renard, B. (2017). Trends in snowmelt-related streamflow timing in the conterminous United States. *J. Hydrol.* 547, 208–221. doi: 10.1016/j.jhydrol.2017.01.051

Duncan, J. M., Band, L. E., Groffman, P. M., and Bernhardt, E. S. (2015). Mechanisms driving the seasonality of catchment scale nitrate export: evidence for riparian ecohydrologic controls: seasonality of catchment nitrate export. *Water Resour. Res.* 51, 3982–3997. doi: 10.1002/2015WR016937

Duncan, J. M., Groffman, P. M., and Band, L. E. (2013). Towards closing the watershed nitrogen budget: spatial and temporal scaling of denitrification: scaling denitrification. *J. Geophys. Res. Biogeosci.* 118, 1105–1119. doi: 10.1002/jgrg.20090

Dwivedi, D., Arora, B., Steefel, C. I., Dafflon, B., and Versteeg, R. (2018a). Hot spots and hot moments of nitrogen in a riparian corridor. *Water Resour. Res.* 54, 205–222. doi: 10.1002/2017WR022346

Dwivedi, D., Steefel, C. I., Arora, B., Newcomer, M., Moulton, J. D., Dafflon, B., et al. (2018b). Geochemical exports to river from the intrameander hyporheic zone under transient hydrologic conditions: east river mountainous watershed, Colorado. *Water Resour. Res.* 54, 8456–8477. doi: 10.1029/2018WR023377

Falco, N., Wainwright, H., Dafflon, B., Leger, E., Peterson, J., Steltzer, H., et al. (2019). Remote sensing and geophysical characterization of a floodplain-hillslope system in the East River Watershed, Colorado. *Environ. Syst. Sci. Data Infrastr. Virt. Ecosyst. Watershed Funct. SFA*. doi: 10.21952/WTR/1490867

Fassnacht, S., Venable, N., McGrath, D., and Patterson, G. (2018). Sub-seasonal snowpack trends in the rocky mountain national park area, Colorado, USA. *Water* 10:562. doi: 10.3390/w10050562

Faybishenko, B. (2020). Unsaturated and saturated hydraulic parameters of soils at the east River Watershed, Colorado calculated using the pedotransfer function method. *Environ. Syst. Sci. Data Infrastr. Virt. Ecosyst. Watershed Funct. SFA*. doi: 10.15485/1734577

Fetter, C. W. (2001). *Applied Hydrogeology. 4th Edn*. Upper Saddle River, NJ: Prentice-Hall.

Fox, P., Bill, M., Heckman, K., Conrad, M. E., Anderson, C., Keiluweit, M., et al. (2019). Geochemical characterization of floodplain sediments from Meander C and O in the East River Watershed, CO, USA. *Environ. Syst. Sci. Data Infrastr. Virt. Ecosyst. Watershed Funct. SFA*. doi: 10.21952/WTR/1572186

Frei, S., Knorr, K. H., Peiffer, S., and Fleckenstein, J. H. (2012). Surface micro-topography causes hot spots of biogeochemical activity in wetland systems: a virtual modeling experiment. *J. Geophys. Res. Biogeosci.* 117:G00N12. doi: 10.1029/2012JG002012

Fritze, H., Stewart, I. T., and Pebesma, E. (2011). Shifts in Western North American snowmelt runoff regimes for the recent warm decades. *J. Hydrometeorol.* 12, 989–1006. doi: 10.1175/2011JHM1360.1

Geuzaine, C., and Remacle, J. F. (2009). Gmsh: a three-dimensional finite element mesh generator with built-in pre- and post-processing facilities. *Int. J. Num Methods Eng.* 79, 1309–1331. doi: 10.1002/nme.2579

Giblin, A., Tobias, C., Song, B., Weston, N., Banta, G., and Rivera-Monroy, V. (2013). The importance of dissimilatory nitrate reduction to ammonium (DNRA) in the nitrogen cycle of coastal ecosystems. *Oceanography* 26, 124–131. doi: 10.5670/oceanog.2013.54

Harpold, A. A., and Molotch, N. P. (2015). Sensitivity of soil water availability to changing snowmelt timing in the western U.S. *Geophys. Res. Lett.* 42, 8011–8020. doi: 10.1002/2015GL065855

Hettinger, R. D., and Kirschbaum, M. A. (2002). *Stratigraphy of the Upper Cretaceous Mancos Shale (Upper Part) and Mesaverde Group in the Southern Part of the Uinta and Piceance Basins*. Reston, VA: U.S. Department of the Interior, U.S. Geological Survey.

Hubbard, S. S., Williams, K. H., Agarwal, D., Banfield, J., Beller, H., Bouskill, N., et al. (2018). The east river, colorado, watershed: a mountainous community testbed for improving predictive understanding of multiscale hydrological-biogeochemical dynamics. *Vadose Zone J.* 17:180061. doi: 10.2136/vzj2018.03.0061

Kleerebezem, R., and van Loosdrecht, M. C. M. (2010). A generalized method for thermodynamic state analysis of environmental systems. *Crit. Rev. Environ. Sci. Technol.* 40, 1–54. doi: 10.1080/10643380802000974

Knowles, N., Dettinger, M. D., and Cayan, D. R. (2006). Trends in snowfall versus rainfall in the western united states. *J. Clim.* 19, 4545–4559. doi: 10.1175/JCLI3850.1

Kuypers, M. M. M., Marchant, H. K., and Kartal, B. (2018). The microbial nitrogen-cycling network. *Nat. Rev. Microbiol.* 16, 263–276. doi: 10.1038/nrmicro.2018.9

Likos, W. J., Lu, N., and Godt, J. W. (2014). Hysteresis and uncertainty in soil water-retention curve parameters. *J. Geotech. Geoenviron. Eng.* 140:04013050. doi: 10.1061/(ASCE)GT.1943-5606.0001071

Lipnikov, K., Svyatskiy, D., and Vassilevski, Y. (2010). A monotone finite volume method for advection–diffusion equations on unstructured polygonal meshes. *J. Comput. Phys.* 229, 4017–4032. doi: 10.1016/j.jcp.2010.01.035

Lucas, R. W., Sponseller, R. A., Gundale, M. J., Stendahl, J., Fridman, J., Högberg, P., et al. (2016). Long-term declines in stream and river inorganic nitrogen (N) export correspond to forest change. *Ecol. Appl.* 26, 545–556. doi: 10.1890/14-2413

Lutz, S. R., Trauth, N., Musolff, A., Van Breukelen, B. M., Knöller, K., and Fleckenstein, J. H. (2020). How important is denitrification in riparian zones? Combining end-member mixing and isotope modeling to quantify nitrate removal from riparian groundwater. *Water Resourc. Res.* 56:e2019WR025528. doi: 10.1029/2019WR025528

Marchant, H. K., Lavik, G., Holtappels, M., and Kuypers, M. M. M. (2014). The fate of nitrate in intertidal permeable sediments. *PLoS ONE* 9:e104517. doi: 10.1371/journal.pone.0104517

Maurer, G. E., and Bowling, D. R. (2014). Seasonal snowpack characteristics influence soil temperature and water content at multiple scales in interior western U.S. mountain ecosystems. *Water Resourc. Res.* 50, 5216–5234. doi: 10.1002/2013WR014452

Mayer, K. U. (1999). *A Numerical Model for Multicomponent Reactive Transport in Variably Saturated Porous Media.* (Dissertation), Waterloo, ON: University of Waterloo.

Mayer, K. U., Benner, S. G., and Blowes, D. W. (1999). The reactive transport model MIN3P: application to acid mine drainage generation and treatment - nickel rim mine site, Sudbury, Ontario. *Min. Environ.* 1, 145–154.

Mayer, K. U., Frind, E. O., and Blowes, D. W. (2002). Multicomponent reactive transport modeling in variably saturated porous media using a generalized formulation for kinetically controlled reactions. *Water Resour. Res.* 38, 13-1–13-21. doi: 10.1029/2001WR000862

Mayer, K. U., and MacQuarrie, K. T. B. (2010). Solution of the MoMaS reactive transport benchmark with MIN3P—model formulation and simulation results. *Comput. Geosci.* 14, 405–419. doi: 10.1007/s10596-009-9158-6

McCabe, G. J., and Clark, M. P. (2005). Trends and variability in snowmelt runoff in the western united states. *J. Hydrometeorol.* 6, 476–482. doi: 10.1175/JHM428.1

Molins, S., Greskowiak, J., Wanner, C., and Mayer, K. U. (2015). A benchmark for microbially mediated chromium reduction under denitrifying conditions in a biostimulation column experiment. *Comput. Geosci.* 19, 479–496. doi: 10.1007/s10596-014-9432-0

Nakshatrala, K. B., Mudunuru, M. K., and Valocchi, A. J. (2013). A numerical framework for diffusion-controlled bimolecular-reactive systems to enforce maximum principles and non-negative constraint. *J. Comput. Phys.* 253, 278–307. doi: 10.1016/j.jcp.2013.07.010

Newcomer, M. E., Bouskill, N., Maier, U., Dwivedi, D., Steefel, C. I., Williams, K. H., et al. (2019). *Advancing Understanding, Modeling, and Scaling of Ecological Control Points in Mountainous River Corridors (Invited)*. Presented at the American Geophysical Union Fall Meeting 2019, B42A-07. Retrieved from https://agu-do03.confex.com/agu/fm19/meetingapp.cgi/Paper/499462

Newcomer, M. E., Bouskill, N. J., Wainwright, H., Maavara, T., Arora, B., Siirila-Woodburn, E. R., et al. (2020). Hysteresis patterns of watershed nitrogen retention and loss over the past 50 years in United States

Hydrological Basins. (Preprint on ESSOAr). *Global Biogeochem. Cycles.* doi: 10.1002/essoar.10504643.1

Newcomer, M. E., Hubbard, S. S., Fleckenstein, J. H., Maier, U., Schmidt, C., Thullner, M., et al. (2018). Influence of hydrological perturbations and riverbed sediment characteristics on hyporheic zone respiration of CO_2 and N_2. *J. Geophys. Res. Biogeosci.* 123, 902–922. doi: 10.1002/2017JG004090

Newcomer, M. E., Raberg, J., Dwivedi, D., Fox, P., Nico, P., Dong, W., and Steefel, C. (2020). Hyporheic, floodplain, and surface water (on floodplain and river) geochemical datasets, and shapefiles on meander C at the East River, Colorado [Data set]. *Environ. Syst. Sci. Data Infrastr. Virt. Ecosyst. Watershed Funct. SFA.* doi: 10.15485/1647038

Newcomer, M. E., and Rogers, D. B. (2020). Gap-filled meteorological data (2011-2020) and modeled potential evapotranspiration data from the KCOMTCRE2 WeatherUnderground weather station, from the East River Watershed, Colorado [Data set]. *Environ. Syst. Sci. Data Infrastr. Virt. Ecosyst. Watershed Funct. SFA*. doi: 10.15485/1734790

Pederson, G. T., Gray, S. T., Ault, T., Marsh, W., Fagre, D. B., Bunn, A. G., et al. (2011). Climatic controls on the snowmelt hydrology of the northern rocky mountains. *J. Clim.* 24, 1666–1687. doi: 10.1175/2010JCLI3729.1

Pellerin, B. A., Saraceno, J. F., Shanley, J. B., Sebestyen, S. D., Aiken, G. R., Wollheim, W. M., et al. (2012). Taking the pulse of snowmelt: *in situ* sensors reveal seasonal, event and diurnal patterns of nitrate and dissolved organic matter variability in an upland forest stream. *Biogeochemistry* 108, 183–198. doi: 10.1007/s10533-011-9589-8

Peters, A., Durner, W., and Wessolek, G. (2011). Consistent parameter constraints for soil hydraulic functions. *Adv. Water Resour.* 34, 1352–1365. doi: 10.1016/j.advwatres.2011.07.006

Pinay, G., Bernal, S., Abbott, B. W., Lupon, A., Marti, E., Sabater, F., et al. (2018). Riparian corridors: a new conceptual framework for assessing nitrogen buffering across biomes. *Front. Environ. Sci.* 6:47. doi: 10.3389/fenvs.2018.00047

R Core Team. (2020). *R: A Language and Environment for Statistical Computing (Version 3.6.2)*. Vienna: R Core Team. Retrieved from https://www.R-project.org

Rassam, D., Šimunek, J., Mallants, D., and van Genuchten, M. (2018). *The HYDRUS-1D Software Package for Simulating the Movement of Water, Heat, and Multiple Solutes in Variably Saturated Media: Tutorial, Version 1.00*. CSIRO Land and Water.

Rawls, K. D., Dougherty, B. V., Blais, E. M., Stancliffe, E., Kolling, G. L., Vinnakota, K., et al. (2019). A simplified metabolic network reconstruction to promote understanding and development of flux balance analysis tools. *Comput. Biol. Med.* 105, 64–71. doi: 10.1016/j.compbiomed.2018.12.010

Reid, M. A., Reid, M. C., and Thoms, M. C. (2016). Ecological significance of hydrological connectivity for wetland plant communities on a dryland floodplain river, MacIntyre river, Australia. *Aquat. Sci.* 78, 139–158. doi: 10.1007/s00027-015-0414-7

Ridgley, J. L., Condon, S. M., and Hatch, J. R. (2013). *Geology and Oil and Gas Assessment of the Mancos-Menefee Composite Total Petroleum System*. Reston, VA: U.S. Department of the Interior, U.S. Geological Survey. 107.

Rogers, D. B., Newcomer, M. E., Raberg, J., Dwivedi, D., Steefel, C. I., Bouskill, N., et al. (2020). "Modeling the impact of riparian hollows on river corridor nitrogen exports," in *AGU Fall Meeting 2020*. doi: 10.15485/1734795

Sgouridis, F., Heppell, C. M., Wharton, G., Lansdown, K., and Trimmer, M. (2011). Denitrification and dissimilatory nitrate reduction to ammonium (DNRA) in a temperate re-connected floodplain. *Water Res.* 45, 4909–4922. doi: 10.1016/j.watres.2011.06.037

Shaffer, M., Borton, M. A., McGivern, B. B., Zayed, A. A., La Rosa, S. L., Solden, L. M., et al. (2020). DRAM for distilling microbial metabolism to automate the curation of microbiome function. *Microbiology.* 48, 8883–8900. doi: 10.1101/2020.06.29.177501

Song, H.-S., Stegen, J. C., Graham, E. B., Lee, J.-Y., Garayburu-Caruso, V. A., Nelson, W. C., et al. (2020). Representing organic matter thermodynamics in biogeochemical reactions via substrate-explicit modeling. *Syst. Biol.* 11:531756. doi: 10.1101/2020.02.27.968669

Sorenson, P., Brodie, E., Beller, H., Wang, S., Bill, M., and Bouskill, N. J. (2019). Soil nitrogen, water content, microbial biomass, and archaeal, bacterial and fungal communities from the East River Watershed, Colorado collected in 2016-2017. *Environ. Syst. Sci. Data Infrastr. Virt. Ecosyst. Watershed Funct. SFA*. doi: 10.15485/1577267

Stewart, I. T. (2009). Changes in snowpack and snowmelt runoff for key mountain regions. *Hydrol. Process* 23, 78–94. doi: 10.1002/hyp.7128

Su, D., Mayer, K. U., and MacQuarrie, K. T. (2019). MIN3P-HPC: a high performance unstructured grid code for subsurface flow and reactive transport simulation. *Comput. Geosci.* doi: 10.1007/s11004-020-09898-7

Suecker, J. K., Ryan, J. N., Kendall, C., and Jarrett, R. D. (2000). Determination of hydrologic pathways during snowmelt for alpine/subalpine basins, rocky mountain national park, Colorado. *Water Resour. Res.* 36, 63–75. doi: 10.1029/1999WR900296

The Weather Company. (2020). *Gold Link - KCOMTCRE2*. Retrieved from https://www.wunderground.com/dashboard/pws/KCOMTCRE2

Van Meter, K. J., Basu, N. B., and Van Cappellen, P. (2017). Two centuries of nitrogen dynamics: Legacy sources and sinks in the mississippi and susquehanna river basins: two centuries of nitrogen dynamics. *Glob. Biogeochem. Cycles* 31, 2–23. doi: 10.1002/2016GB005498

Wang, S., Pi, Y., Jiang, Y., Pan, H., Wang, X., Wang, X., et al. (2020a). Nitrate reduction in the reed rhizosphere of a riparian zone: from functional genes to activity and contribution. *Environ. Res.* 180:108867. doi: 10.1016/j.envres.2019.108867

Wang, S., Pi, Y., Song, Y., Jiang, Y., Zhou, L., Liu, W., et al. (2020b). Hotspot of dissimilatory nitrate reduction to ammonium (DNRA) process in freshwater sediments of riparian zones. *Water Res.* 173:115539. doi: 10.1016/j.watres.2020.115539

Wolff, R. G. (1982). *Physical Properties of Rocks – Porosity, Permeability, Distribution Coefficients, and Dispersivity (Open-File Report)*. Reston, VA: U.S. Department of Interior Geological Survey, 123.

Wu, Y. (2017). *Soil Moisture Data; YXW_FP_1, YXW_FP_2, YXW_FP_3*. Watershed Function SFA. Retrieved from https://wfsfa-data.lbl.gov/#

Xie, M., Mayer, K. U., Claret, F., Alt-Epping, P., Jacques, D., Steefel, C., et al. (2015). Implementation and evaluation of permeability-porosity and tortuosity-porosity relationships linked to mineral dissolution-precipitation. *Computat. Geosci.* 19, 655–671. doi: 10.1007/s10596-014-9458-3

Yanai, R. D., Vadeboncoeur, M. A., Hamburg, S. P., Arthur, M. A., Fuss, C. B., Groffman, P. M., et al. (2013). From missing source to missing sink: long-term changes in the nitrogen budget of a northern hardwood forest. *Environ. Sci. Technol.* 47, 11440–11448. doi: 10.1021/es4025723

Yano, Y., Qubain, C., Holyman, Z., Jencso, K., and Hu, J. (2019). Snowpack influences spatial and temporal soil nitrogen dynamics in a western U.S. montane forested watershed. *Ecosphere* 10:e02794. doi: 10.1002/ecs2.2794

Yin, G., Hou, L., Liu, M., Li, X., Zheng, Y., Gao, J., et al. (2017). DNRA in intertidal sediments of the yangtze estuary: DNRA in sediments of yangtze estuary. *J. Geophys. Res. Biogeosci.* 122, 1988–1998. doi: 10.1002/2017JG003766

Zilli, F. L., and Paggi, A. C. (2013). Ecological responses to different degrees of hydrologic connectivity: assessing patterns in the bionomy of benthic chironomids in a large river-floodplain system. *Wetlands* 33, 837–845. doi: 10.1007/s13157-013-0440-y

Conflict of Interest: The authors declare that the research was conducted in the absence of any commercial or financial relationships that could be construed as a potential conflict of interest.

The handling editor declared a past co-authorship with one of the authors CS.

frontiers in Water

ORIGINAL RESEARCH
published: 08 April 2021
doi: 10.3389/frwa.2021.574684

Groundwater Inflows to the Columbia River Along the Hanford Reach and Associated Nitrate Concentrations

Abigail Conner[1,2], *Michael N. Gooseff*[1,2]*, *Xingyuan Chen*[3], *Evan Arntzen*[3] and *Vanessa Garayburu-Caruso*[3]

[1] Institute of Arctic and Alpine Research, University of Colorado, Boulder, CO, United States, [2] Department of Civil, Environmental, and Architectural Engineering, University of Colorado, Boulder, CO, United States, [3] Pacific Northwest National Laboratory, Richland, WA, United States

Healthy river ecosystems require the interaction of many physical and biological processes to maintain their status. One physical process supporting biogeochemical cycling is hydrologic exchange (i.e., hydrologic exchange flows, HEFs) between relatively fast-flowing channel waters and slower-flowing surface and subsurface waters (lateral and vertical). Land uses adjacent to rivers have the potential to alter the water quality of off-channel surface and subsurface waters, and HEFs therefore have the potential to deliver solutes associated with river-adjacent land uses to rivers. HEFs can be nonpoint, diffuse sources of pollution, making the ultimate pollution source difficult to identify, especially in large rivers. Here, we seek to identify HEFs in the Columbia River near Richland, WA by looking for anomalies in temperature and electrical conductivity (EC) along the bed of the river in February, June, July, August, and November 2018. These are ultimately the "ends" of HEFs as they are locations of subsurface inflow to the river. We found these anomalies to be a combination of warmer or colder and higher (but not lower) EC than river water. We identified a majority of warm anomalies in February and July 2018, and majority cold anomalies in June, August, and November 2018. High-EC anomalies were found mostly in February, August, and November. Combined, we observe a shift from warm, high EC anomalies dominating in February to equivalent EC, warm anomalies in June, to equivalent EC, cool anomalies dominating July. In August, we also measured dissolved nitrate (NO_3^-) *in-situ* to determine whether anomalies were associated with increased NO_3^- loading to the river, especially along the eastern shoreline, which is dominated by agricultural land use. Inflows along the eastern shoreline have greater concentrations of nitrate than river water (up to 10 mg N–NO_3^-/L). This research demonstrates that HEFs are temporally and spatially dynamic transferring heat and solutes to rivers.

Keywords: stream-groundwater interaction, groundwater inflow, water quality, Columbia River, Hanford Reach, hydrologic exchange flows (HEFs)

OPEN ACCESS

Edited by:
Sarah E. Godsey, Idaho State University, United States

Reviewed by:
Si-Liang Li, Tianjin University, China
Megan J. Klaar, University of Leeds, United Kingdom

***Correspondence:**
Michael N. Gooseff
michael.gooseff@colorado.edu

Specialty section:
This article was submitted to Water and Critical Zone, a section of the journal Frontiers in Water

Received: *20 June 2020*
Accepted: *22 February 2021*
Published: *08 April 2021*

Citation:
Conner A, Gooseff MN, Chen X, Arntzen E and Garayburu-Caruso V (2021) Groundwater Inflows to the Columbia River Along the Hanford Reach and Associated Nitrate Concentrations. Front. Water 3:574684. doi: 10.3389/frwa.2021.574684

INTRODUCTION

Healthy river ecosystems require the interaction of many processes to maintain a high level of water quality, including hydrologic exchange flows (HEFs)—exchanges between channel waters with subsurface and off-channel waters (Harvey and Gooseff, 2015). HEFs include exchanges between channels and water in riverbeds and riverbanks (i.e., hyporheic exchange, bank storage), slow-moving water alongside the main channel, overbank flow into and out of floodplains, gains of water into the river from surface flows, and gains of water from groundwater alongside the river. These complex exchanges may occur repeatedly with variations in source and destination. HEFs may originate at the river channel (i.e., hyporheic exchange) or on the landscape (e.g., irrigation water applied to fields adjacent to rivers) (see conceptual overview in Payn et al., 2009), but their direction and magnitude are determined by spatiotemporal dynamics in water tables and hydraulic conductivity fields of the subsurface (e.g., Woessner, 2000; Shuai et al., 2019). Rivers are the common termination point for HEFs because they typically occupy the lowest point of valley cross-sections. As such, rivers often receive water, solutes, and energy through HEFs. Rivers can also lose water, solutes and energy through HEFs, but these locations are often more difficult to identify than locations of HEF inputs.

Land uses in and adjacent to river corridors have a strong influence on river water quality (e.g., Lenat and Crawford, 1994). Floodplains are often attractive to development because of proximity to rivers and they are often fertile lands for agricultural development. Whereas urbanization often increases impermeable conditions and seeks to channelize overland flows in river corridors, agricultural activity often results in the addition of water and fertilizers to soils (Hodson and Donner, 2011). Excess fertilizer applied to soils can infiltrate to depth and be transported to rivers via groundwater flow paths, i.e., HEFs (Gilmore et al., 2016). Because HEFs are not obvious to the naked eye, the locations of fertilizer-derived solutes, such as nitrate (NO_3^-) entry to the river are difficult to identify, especially in large rivers.

The motivations for this research are to improve the understanding of the dynamic nature of HEF inputs to rivers in space and time. Here we focus on an 82 km segment of the Columbia River in eastern Washington State, USA. The west side of the river corridor is dominated by the Department of Energy's Hanford Site, where land development is sparse, and the east side of the river corridor is dominated by agricultural land use (crops). The river discharge in this segment is controlled by a series of upstream dams for both flood control and power generation. This work aims to investigate the relationship between HEFs and land use by comparing spatially distributed measurements of the locations of subsurface inflow to the Columbia River to nitrate measurements in the river. Specifically, we seek to determine the degree of connectivity between irrigation, HEFs, and rivers by (1) characterizing the water quality of HEFs during irrigation and non-irrigation seasons, and (2) relating nitrate concentrations with associated HEFs to sources of inflows (i.e., by contrasting the east shore and west shore of the river). We identify subsurface inflows to the river by measuring anomalies in temperature and electrical conductivity (EC) compared to river values, and expect that with the exception of the known high-nitrate concentration groundwater plume at one location along the western shore of the river, that nitrate concentrations associated with subsurface inflows to the river are generally higher along the eastern shoreline.

STUDY SITE AND METHODS

Study Site

We conducted this study along a reach of the Columbia River in eastern Washington. The Columbia River is a major river in the Pacific Northwest, originating in the Rocky Mountains of British Columbia, meandering through Washington State, and entering the Pacific Ocean along the border of Washington and Oregon. The Columbia River is highly developed, containing 19 hydroelectric dams and supporting 600,000 acres of farmland (USACE, 2018). Within the Columbia River, the study site for this research is located on the so-called Hanford Reach (e.g., Cardenas and Markowski, 2011) bounded upstream by Priest Rapids Dam and extending downstream to the city of Richland (**Figure 1**) [Northwest Power Conservation Council (NPCC), 2019]. These boundaries also define the only non-tidal, free-flowing section of the Columbia River in the United States (Clinton, 2000). Although the Hanford Reach is free-flowing, not backed up by dams, the river discharge is regulated by the upstream Priest Rapids Dam and others further upstream. River flows are typically high during the spring as snowmelt fills upriver reservoirs and during the summer due to high demands for power (**Figure 2**).

Irrigation east of the Hanford Reach is made possible by the Columbia Basin Project (USBR, 2014). The Columbia Basin Project diverts water from upstream of Grand Coulee Dam, located upstream of the Hanford Reach. The diverted water is routed through canals to local agricultural fields for irrigation. Excess irrigation water may reach constructed canals that divert return flows to specific points in the river or follow subsurface pathways that may end up in the river. Both of these fates contribute to HEFs for this reach.

In contrast to the eastern shoreline, the western shoreline of the Hanford Reach is the location of the Hanford Project, a plutonium development site from the Cold War. The Hanford Site is no longer used for plutonium development, and the current goal of the site is clean-up and remediation of the area. The western shoreline is largely undeveloped and has been generally inaccessible to the public for >80 years. Therefore, the topography and ecosystem of the land near the shoreline remains relatively undisturbed and is dominated by native shrub steppe compared to the western shoreline. The land use contrast between the two sides of the river allows for comparison of the occurrence of HEFs and associated nitrate concentrations on the irrigated eastern shoreline to the non-irrigated western shoreline.

Due to the adjacent location to the Hanford Site, and concern over resulting pollution from the site, the Hanford Reach of the river is well-studied. Previous field studies have identified sites of groundwater inflow into the river on the western shoreline (Lee

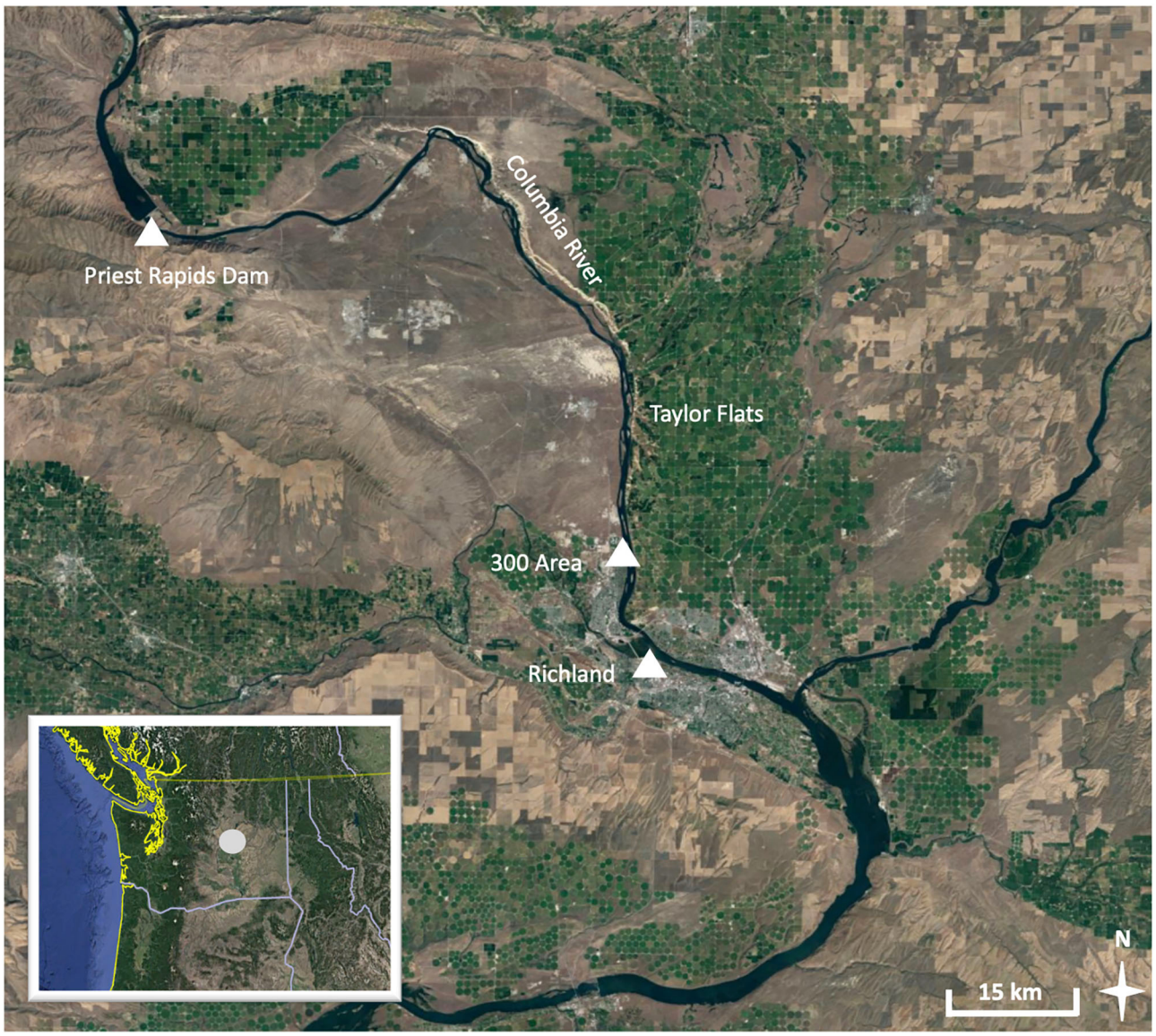

FIGURE 1 | Map of Hanford reach. This map shows the location of the Hanford Reach in Washington State (inset) and a satellite view of Hanford Reach. The Reach begins below the Priest Rapids Dam (46.643578 N, 119.910357 W), and continues until the confluence with the Snake River. Note the green coloring, indicating locations of irrigation, in contrast to the native brown landscape. Map data from Google, Landsat.

et al., 1997). Hydrologic models of the reach predict HEFs along both shorelines but disagree on locations and timing of inflows (Zhou et al., 2018; Shuai et al., 2019), highlighting the need for field research, especially along the eastern shoreline.

Field Data Collection

Measuring HEFs in the field at the reach scale presents time and resource challenges, which, over the last several decades, has led to rapid development of numerical modeling approaches (Kasahara and Wondzell, 2003; Kiel and Cardenas, 2014; Gomez-Velez et al., 2017; Song et al., 2018; Shuai et al., 2019; Zachara et al., 2020). Reach-scale field data of HEFs are needed to validate the predicted exchanges by these models (Lee et al., 1997; Shuai et al., 2019).

The Hanford Reach is no exception to the challenges of measuring HEFs at the reach scale. Traditional tracer methods are impractical for this size of a river [low flows are on the order of 2,000 cm; though see Fernald et al. (2001) for an example], field studies of water exchanges in the reach focus on point-based measurements (Geist, 2000; Arntzen et al., 2006; Song et al., 2018) or transects (Cardenas and Markowski, 2011). However, these studies do not describe HEFs across the reach scale. To measure HEFs in smaller rivers and lakes, thermal probes have been towed along the beds and in the main water column simultaneously

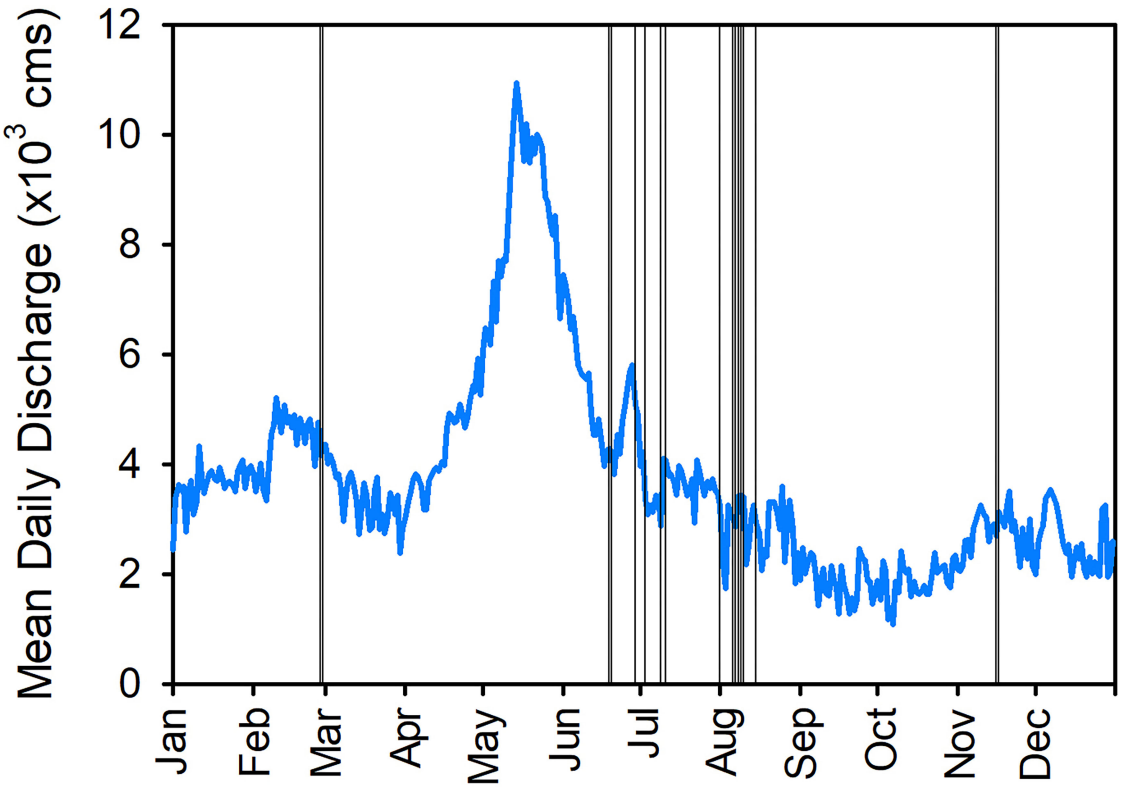

FIGURE 2 | Mean daily discharge on the Columbia River for calendar year 2018, as observed at the Priest Rapids gage (USGS 12472800). Vertical lines indicate days of field data collection along the Hanford reach.

to identify inflows, which have a different temperature signal than river water (Harvey et al., 1997; Vaccaro and Maloy, 2006; Zhou et al., 2017). This approach allows for the collection of data over a large spatial scale. In order to characterize HEFs along the Hanford Reach, we chose to apply this method by towing sensors downstream.

We used both water temperature and electrical conductivity (EC) to identify subsurface inflows to the riverbed (Conner et al., 2020). There are known differences between EC and temperature values of river water and groundwater in the Columbia River (Dirkes et al., 1999; Zachara et al., 2020). Specifically, we used Campbell Scientific sensors: high-sensitivity 109-SS temperature probes (one in the shallow water column, one dragged along the bed), CS547 EC probes (one in the shallow water column, one dragged along the bed), and a GPS receiver. EC measurements are noted to be accurate to ±5% according to manufacturer guidance. All of these sensors were connected to and controlled by a CR1000 datalogger, collecting at a one-second interval. Electrical conductivity data is normalized to a specific conductivity. All data reported here are specific conductance. A Submersible Ultraviolet Nitrate Analyzer (SUNA) Seabird sensor was used to measure nitrate concentrations from August 8–16, 2018 (the only period it was available to our field team). The SUNA sensor collected 15 readings at 2 s intervals, every 2 min from the shallow water column (it was not dragged along the bed). To verify the SUNA measurements, 10 grab samples of river water were collected adjacent to the SUNA unit on August 15. These samples were analyzed for nitrate concentrations using a Dionex ICS-2000 anion chromatograph with AS40 auto sampler using an isocratic method. The nitrate concentration of grab samples ranged from 0 to 4.5 mg $N–NO_3^-$/L. Lab measurements confirmed SUNA measurements within 5% difference.

To compare the temperature and EC along the streambed with the water column, sensors were deployed on two ropes—one to measure along the riverbed, and the other ∼1–2 m above the riverbed, depending on the depth of the water column (**Figure 3**). Several metal fishing weights were affixed to the end of each rope to keep them taught. Sensors were affixed ∼0.3 m from the end of each rope to prevent collision with the weights. For the longer rope (to collect data along the bed), this design also allowed the sensors to skim over the rocks on the riverbed, avoiding sensor damage. The weights likely disturbed the bed in several places, but we expect that our velocity of travel was great enough that any material that was entrained into the flow was not directly reaching the sensors (30 cm above the bed).

Field campaigns were conducted during the summer (June, July, and August) with data collected from a canoe in order to provide navigability along the river shorelines. The canoe, a 4.2 m pointed Radisson model, provided enough stability to

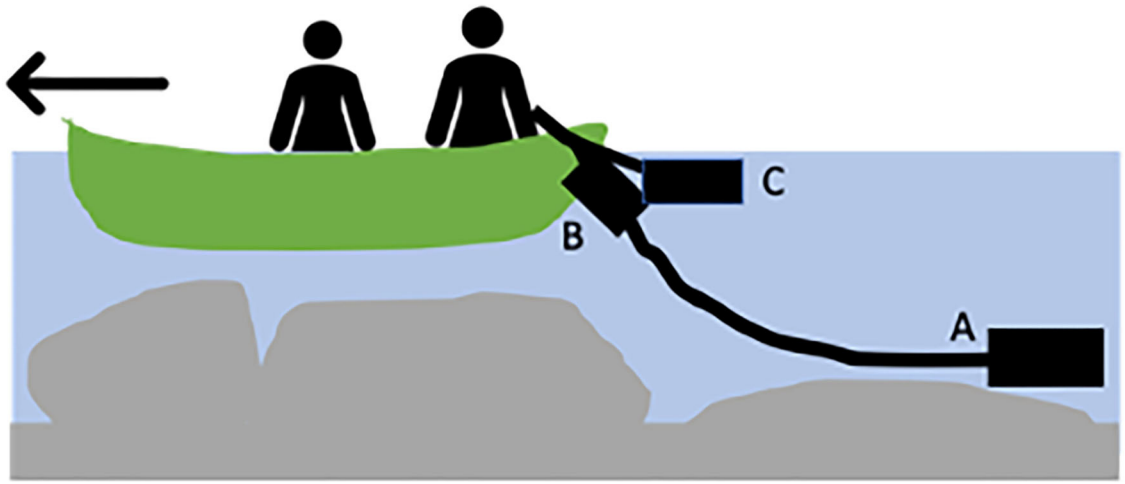

FIGURE 3 | Data collection schematic; **(A)** temperature and EC sensors were deployed on a "long rope" to collect data near the riverbed, **(B)** temperature and EC sensors were also deployed in shallow water, and **(C)** during August 2018, the SUNA sensor was deployed near the shallow sensors.

drag sensors while floating downstream. We used a small trolling electric motor (130 N of thrust) to power and steer the canoe. The motor allowed us to move upstream during low flows with currents around 2–3 kph. During high flows (∼85,000 cm) and fast currents (max 10 kph), we could not travel upstream, but we managed to collect data at a higher spatial density. During the February and November 2018 field campaigns, we collected data from a jet boat in a similar method to the canoe. Like a canoe, a jet boat has the ability to navigate shallow waters, and because the boat can travel faster, it has the added ability to target specific locations.

Measurements were made along the entire length of the Hanford Reach, but we focused most of our data collection on the lower 28 km of the reach from Savage Island to Richland (**Figure 4**). We chose daily study traverses along the Hanford Reach that allowed comparison between irrigated and non-irrigated river shoreline (**Figure 4**). The specific sections of river floated each day depended on discharge, weather conditions, and time of year.

Data Analysis

We developed a system for evaluating anomalies of water temperature and EC as we compared observations from the riverbed to those made in the water column (**Table 1**). We expected that inflow anomalies associated with broader (i.e., distal) groundwater inflows to the river would be warmer than the river water in February and November, and colder than river water June–August. However, we observed both warmer and colder anomalies in all times of the year. In all of our observations, EC was either equivalent between river water column and riverbed, or the bed EC was elevated compared to the river water column. Thus, we characterize the riverbed EC to be "elevated" or "not anomalous" in our characterization of measurements made.

The categories of anomalies (**Table 1**) are interpreted differently in the summer vs. fall/winter months. For example, in summer months, distal groundwater would be expected to be lower in temperature than the river water and therefore its discharge leads to, for example Category 4 anomalies, and shallow HEFs (perhaps hyporheic exchange or surface water inputs) would be warmer than the river water and lead to Category 2 or 3 anomalies. However, these would be reversed in the late fall/winter field campaigns when the river water is relatively colder. During these campaigns, we expect the distal groundwater inflows to be warmer (Categories 2 or 3) and the shallow HEFs to be colder (Categories 1 or 4).

We also hypothesize that anomalies with elevated EC are associated with HEFs near irrigation and have higher concentrations of nitrate than the river. Furthermore, we expect anomalies without variation in EC from the river channel occur away from agriculture and that they would have low/background concentrations of nitrate (similar to those of the river). Nitrate concentrations were not measured in February, June, July, and November.

In order to identify anomalies within the temperature measurements, we developed a model of background temperature trends and calculated anomalies from measurements. Data analysis was completed in R 3.5.2, including R packages stats (loess model), and xts/zoo (time data manipulation). Background trend of river temperature was modeled using a local-smoothing model (loess) for summer data, and a linear model for fall and spring seasons (**Figure 5**). A linear model is better suited for capturing the trend during February and November temperatures than the loess model, due to the fewer days of data. Loess models capture the general trend by smoothing a specified span of the data (1/10). Since the Columbia River carries a large volume of well-mixed water, the spatial temperature fluctuations were minimal within the same day. The temperature values predicted by the chosen model for data, and

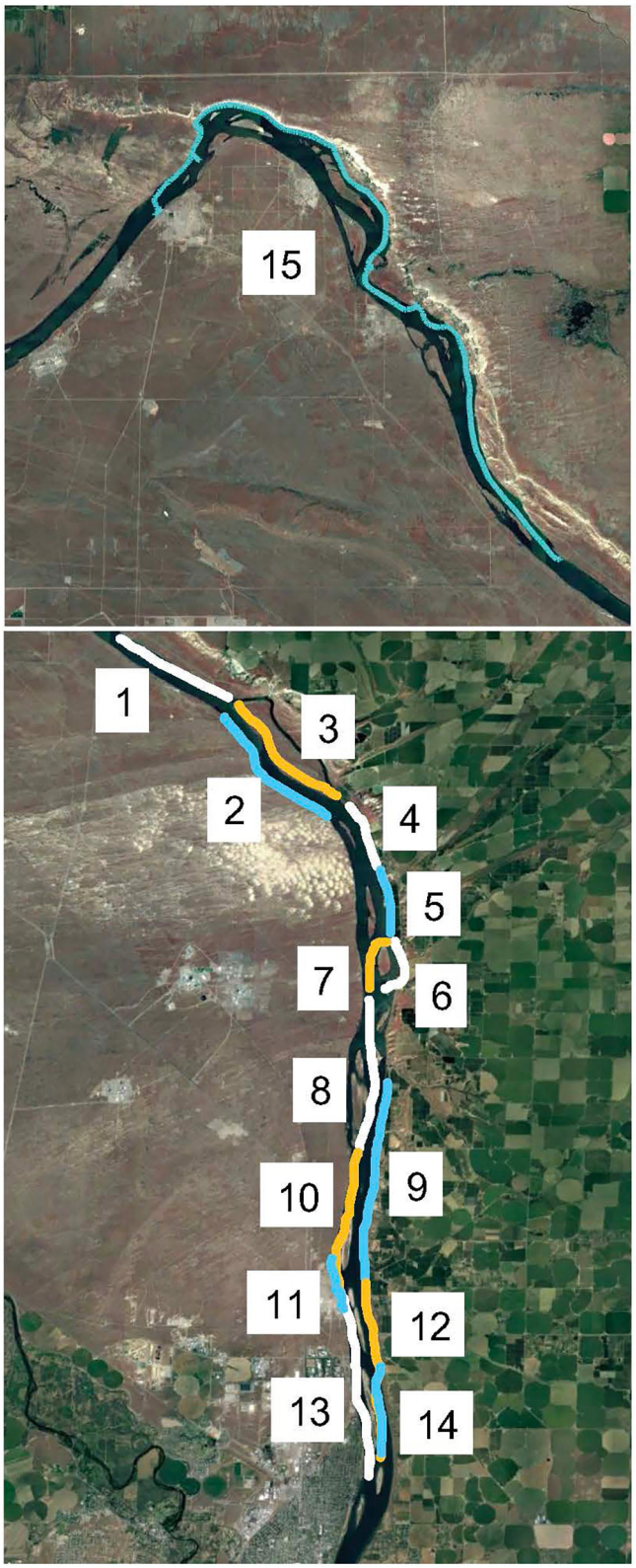

Date	Locations
2/27	9, 11, 12
2/28	15
6/19	1, 3, 4
6/20	11, 13
6/29	1, 3, 4
7/3	12, 14
7/9	1, 2, 4
7/11	15
8/1	1, 2, 4
8/6	1, 2, 4
8/7	5, 7, 8, 10
8/8	5, 6, 9, 11
8/9	9
8/10	11, 13
8/15	1, 2, 3, 4
11/16	9, 10, 11
11/17	1, 2, 5, 6

FIGURE 4 | Sampling locations along the Hanford reach of the Columbia River as indicated by section and date (month/date) of 2018. The locations refer to the sections of river as labeled in the map. Each location is numbered, and colors are used to distinguish between sections. Map data from Google, Landsat.

those within an error range (June–August: ±0.25°C; February and November: ±0.1°C) are assumed to represent background river-water temperatures. A smaller error parameter was used for fall and winter data due to less fluctuation in temperature during these seasons. Measurements that fall outside of the error range are considered to be anomalies.

To identify anomalies in EC, we identified a threshold to separate anomalies from background river-water values for both shallow and deep sensors. We determined the threshold by using the median EC value (123.46 μS/cm) of the main river channel from measurements taken in the center of the river. The position of each measurement on either shoreline or the center was approximated during data processing using GPS coordinates and research notes. Values of EC below this threshold are background values, while measurements above this value are considered anomalies (**Figure 6**).

TABLE 1 | Water quality anomaly categories (4) based on observed electrical conductivity (EC) and water temperature from the sensors on the riverbed, relative to river water column observations.

Comparison to river water	Lower temperature	Higher temperature
Elevated EC	Category 1	Category 2
Not Anomalous EC	Category 4	Category 3

Temperature anomalies are categorized by the associated conductivity anomaly type. The colors of each category correspond with data presented in maps further in this paper.

RESULTS

Seasonal Variation of Anomalies

Water temperature anomalies of the riverbed demonstrated a surprising shift across months/seasons of 2018 (**Figure 7**). In February and July, the majority of anomalies had a higher temperature relative to the river (89 and 60%, respectively). In June, all identified anomalies had low temperatures relative to the river water column. In August, low temperature anomalies composed the majority (53%) of those observed, although only a 6% difference between the frequency of high temperature and low temperature anomalies was identified. Low temperature anomalies also were the majority of identified anomalies in November (60%).

Riverbed EC anomalies, relative to the river water also varied between months (**Figure 7**). In February and November, when irrigation does not occur, the majority of identified anomalies had high EC (68 and 57%, respectively). The majority of anomalies in August were also those with high EC (67%). However, in June

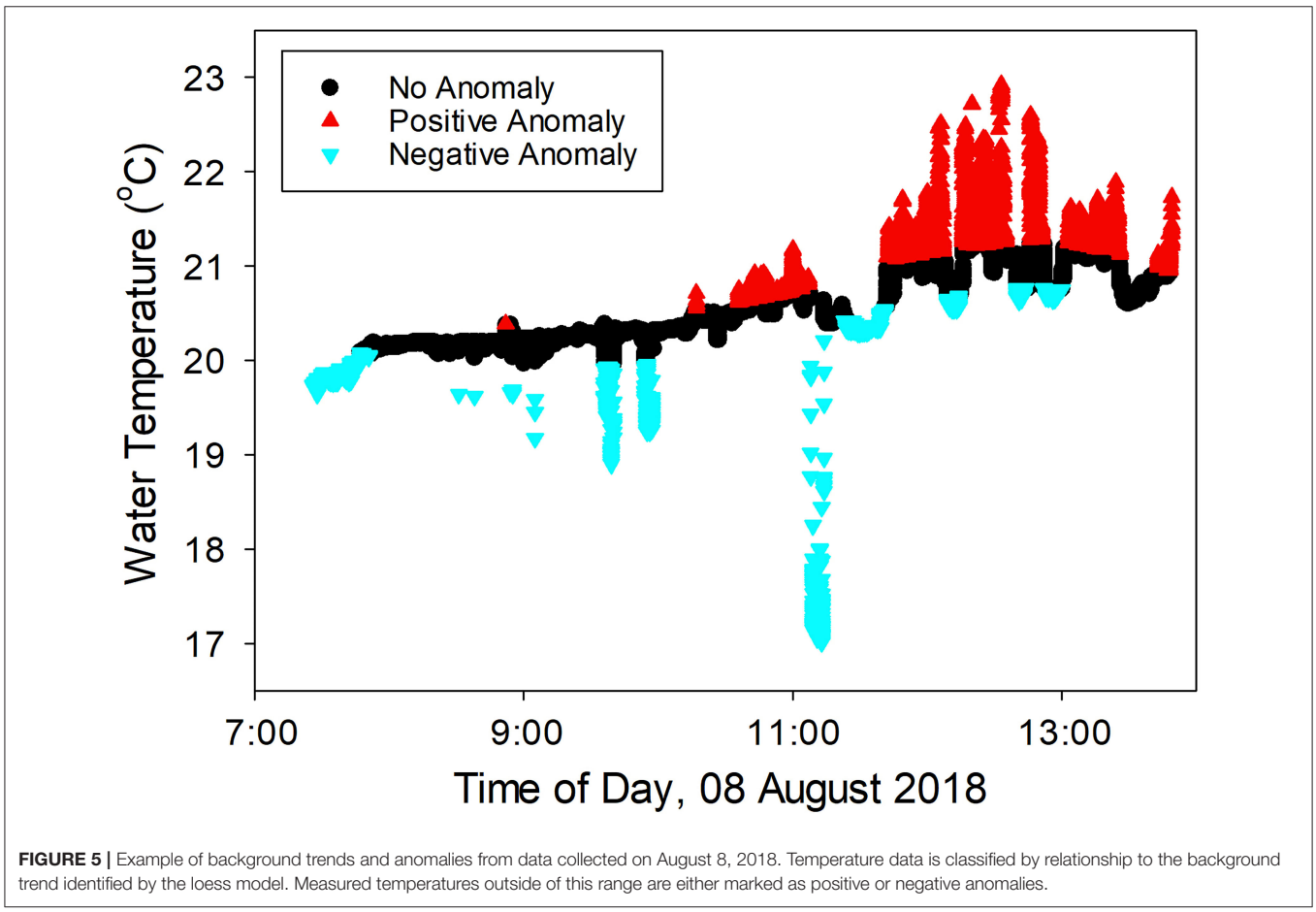

FIGURE 5 | Example of background trends and anomalies from data collected on August 8, 2018. Temperature data is classified by relationship to the background trend identified by the loess model. Measured temperatures outside of this range are either marked as positive or negative anomalies.

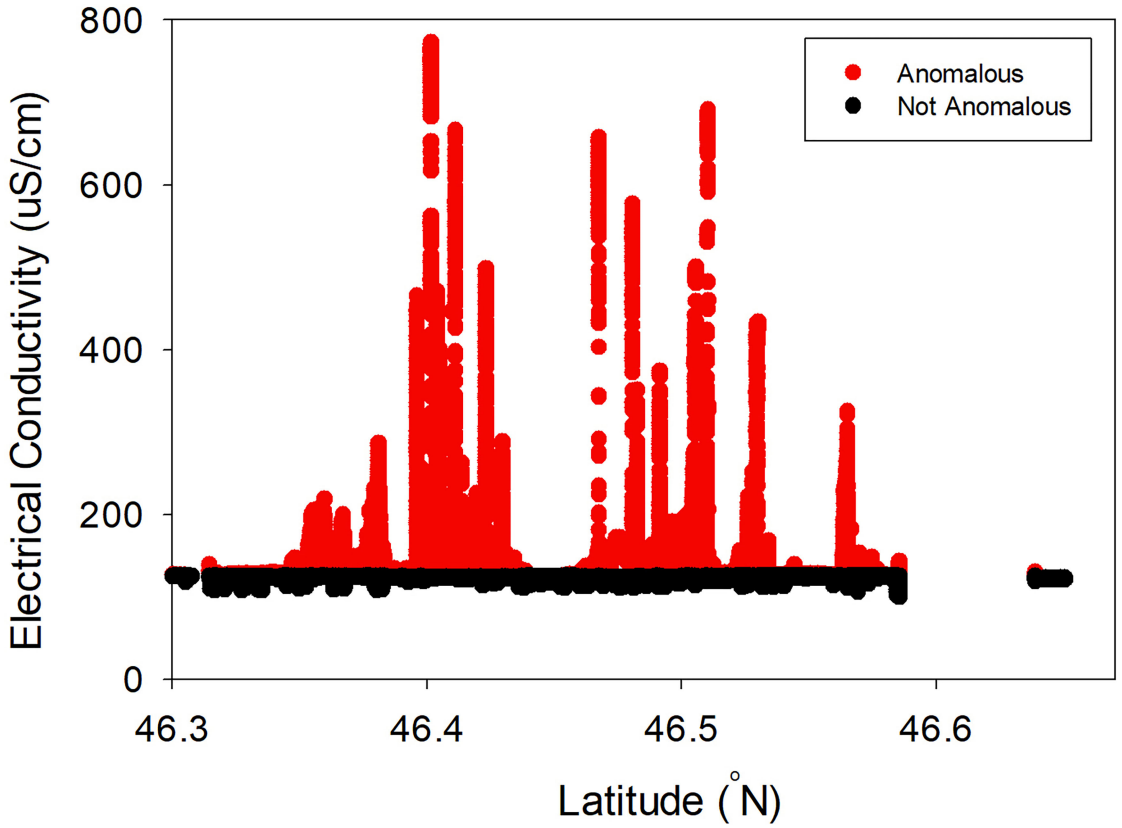

FIGURE 6 | Example of EC anomalies determined from EC values measured during the summer, plotted in space (North to South along the river). Values below the median indicate values similar to river water (Categories 3 and 4), while those above the median indicate comparatively more saline inflows (Categories 1 and 2).

and July, EC measurements that were not anomalous made up the majority of the measurements (55 and 60%, respectively).

After we determined anomalies in temperature and EC, locations were categorized based on the categories determined in **Table 1**. In 2018, the abundance of each category of anomaly changed across the seasons (**Figure 8**), and the category with the largest percentage of anomalies identified in each month varied. In February, Category 2 (high EC; high temperature) was the most commonly identified anomaly type (57%). In June, Category 3 (not anomalous EC; high temperature) was the most commonly identified anomaly (54%). In July, Category 4 (not anomalous EC; low temperature) was the most commonly identified (41%), and in August and November the majority returned to Category 2 (44 and 40%, respectively). At no time was Category 1 (high EC; low temperature) the majority of observed anomaly type. During February and June, Category 4 (not anomalous EC; low temperature) anomalies were identified as 0% of the anomalies identified, as was Category 1 (high EC; low temperature) in June. In February, no category 2 (high EC; low temperature) anomalies were observed, and in June, no Category 1 (high EC; low temperature) or 3 (not anomalous EC; high temperature) anomalies were observed.

Spatial Distribution of Anomalies

Locations of anomalies found along shorelines were more dispersed and smaller in July (**Figure 9**) than in August (**Figure 10**). In particular, Category 1 (high EC; low temperature) and Category 2 (high EC; high temperature) anomalies were clustered in a few locations in early July, whereas in early August, they were distributed along the much more of the length of river between Savage Island and Richland. Category 3 (not anomalous EC; high temperature) and Category 4 (not anomalous EC; low temperature) anomalies showed less of an increase in spatial distribution between early July and early August but did increase in distribution. The increased distribution of Category 3 (not anomalous EC; high temperature) was most evident near the 300-Area and the increase in distribution of Category 4 (not anomalous EC; low temperature) was particularly evident west of Savage Island. Anomalies were also more frequently identified on the eastern shoreline of the river (72% of total) than the western shoreline (28% of total) during July and August.

The US Geological Survey has instrumented an agricultural water return channel (USGS 12473503) on the eastern bank of this segment of the Columbia River. Collected parameters include specific conductance and water temperature, among others. The station initiated data collection in April 2019. For the 2019

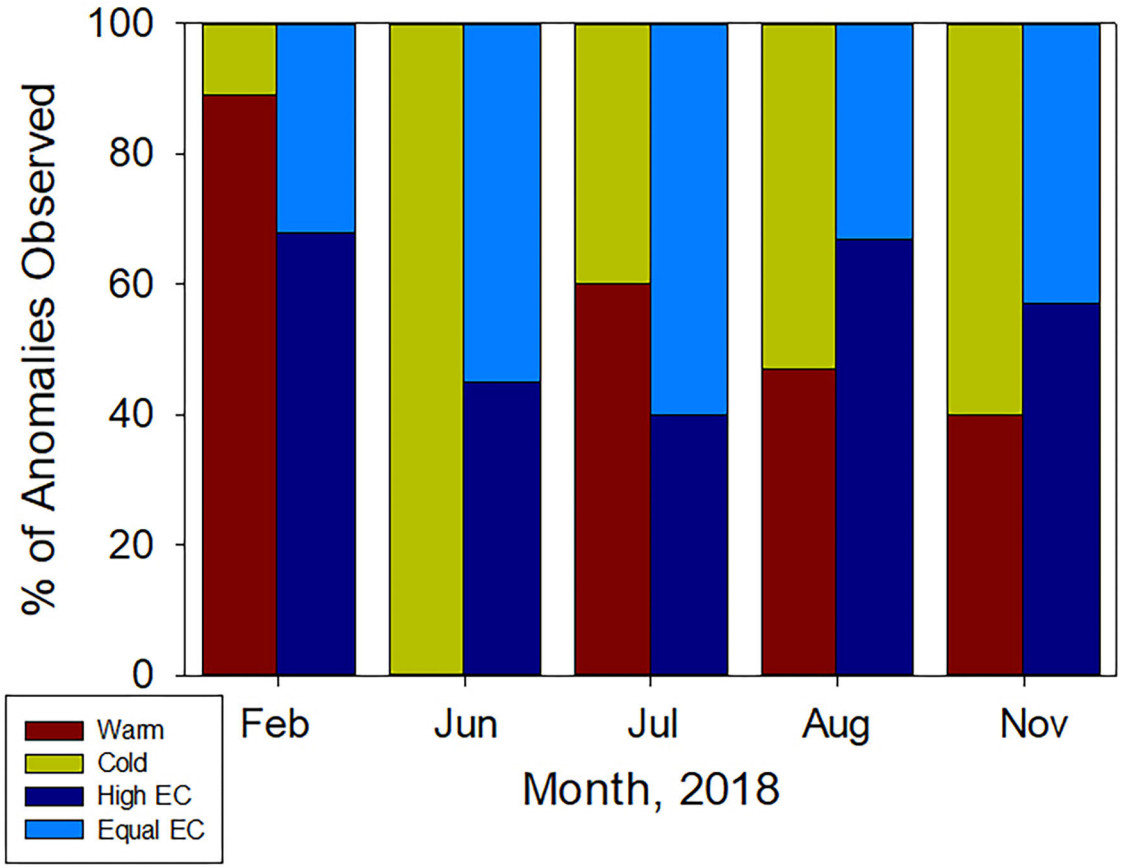

FIGURE 7 | Relative proportion of anomalies by month of field campaigns in 2018.

water year, specific conductance ranged from 369 to 582 μS/cm, temperature ranged from 9.3 to 26.5°C. The peak temperatures observed in this wasteway are higher than we observed in our data collection campaigns, though the conductance is lower than the peak values we observed (in excess of 600 μS/cm; **Figure 6**). It is worth noting that these data collection periods are different—our field campaigns completed in 2018, and the USGS started collecting data in 2019. However, the USGS data suggest that warm, high conductivity water is likely from irrigation sources.

Nitrate Concentration Correlation to Riverbed Anomalies

Dissolved nitrate concentrations observed in the river water column using the SUNA vary from 0 to 9.38 mg $N–NO_3^-$/L. Dissolved nitrate was observed along both shores of the river, though we measured the relatively high nitrate concentrations along the eastern shoreline of the reach. We identified three distributed clusters of nitrate measurements along the eastern shoreline. The most significant cluster of nitrate concentrations along the western shoreline is located near the 300-Area, where we observed the highest nitrate concentrations.

Here we highlight three locations of nitrate observation clusters. The first location is the western shoreline of the river adjacent to the 300-Area (**Figure 11**). Results show a cluster of Category 1 and Category 2 anomalies along this section and substantial nitrate concentrations along the 300 Area shoreline, despite the lack of irrigation on the adjacent shoreline. There is, however, a known plume of high-nitrate concentration groundwater adjacent to the river in this location (USDOE, 2010). While the western part of the river corridor here is not irrigated, it appears that the groundwater plume with high dissolved nitrate concentrations is indeed providing a strong identifiable signal of nitrate along the shoreline.

A second area of interest, also along the western shoreline (where there is no irrigation of the lands) is across from Savage Island (**Figure 12**). Unlike the nitrate observations near the 300 Area, this location has a majority of Category 3 riverbed anomalies and generally low observed nitrate concentrations in August 2018.

Finally, the eastern shoreline adjacent to Taylor Flats is a heavily irrigated area and we observed the largest cluster of riverbed anomalies, suggesting extensive HEFs entering the river, and greatest extent of dissolved nitrate measurements (**Figure 13**). All riverbed anomalies along this shoreline are Categories 1 and 2—i.e., all associated with high EC. Several low-concentration nitrate observations occur in locations where

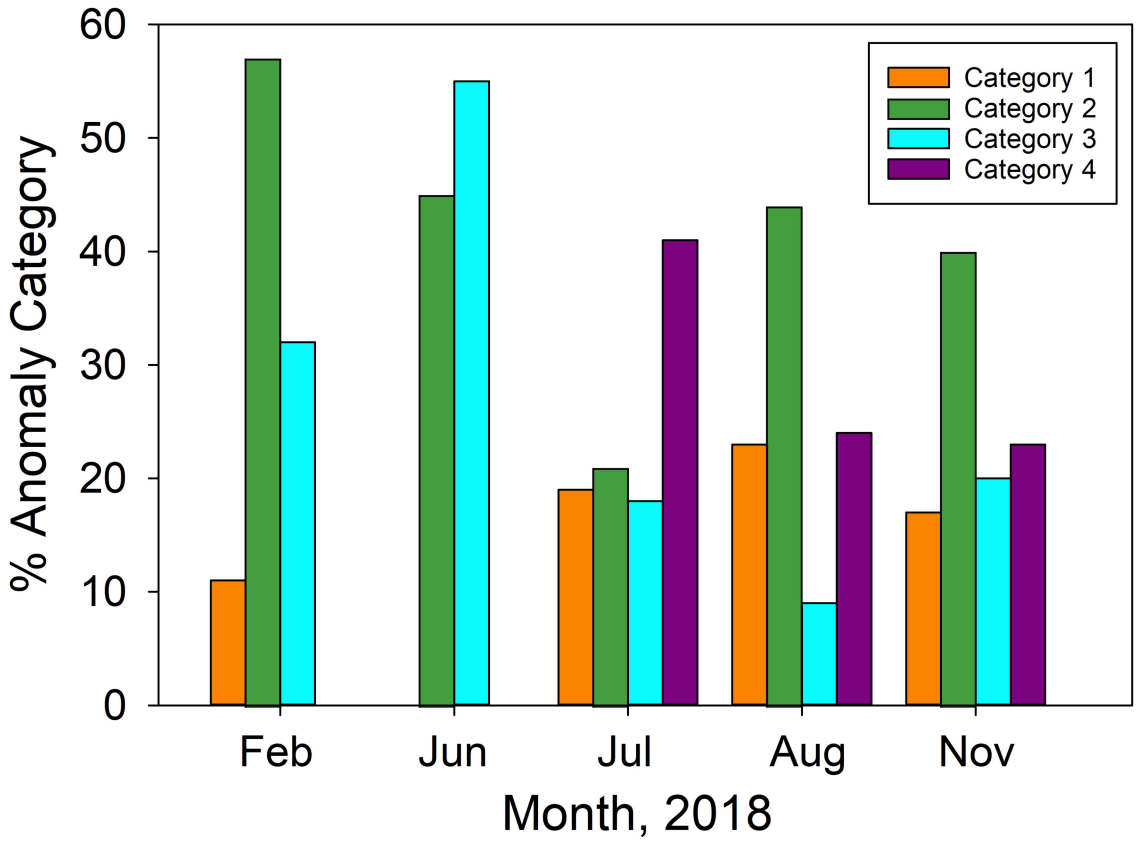

FIGURE 8 | Proportion of each anomaly type identified in each month of field campaigns in 2018.

no riverbed anomalies occur (i.e., no temperature or EC values abnormal from river water conditions). This may be the result of downstream transport from upstream inflows and inefficient mixing along the shoreline, or perhaps other HEFs return to the river here with EC and temperature signatures that are very similar to the river water (lateral hyporheic exchange perhaps). The largest nitrate concentrations along the eastern shore are coincident with riverbed anomalies.

DISCUSSION

Seasonal Variation

The fluctuation in river flow impacts HEFs by changing the gradient between the river and adjacent groundwaters. River flow varies throughout the year, from its highest stage in the summer due to snowmelt, to its lowest stage in the fall at the end of the dry season (**Figure 2**). The annual fluctuation of the river flow creates a variation between conditions where the river is losing water to HEFs and conditions where the river is gaining water from HEFs in September due to hydraulic gradients (Shuai et al., 2019). Models suggest that the river is more frequently under losing conditions around the times of high annual flow, between approximately April and early June, and gaining conditions during the rest of the year (Zhou et al., 2018; Shuai et al., 2019). Diurnal variation in river stage also impacts HEFs, as water moves out of the river during high stages, and into the river during low stages. The identified anomalies agree with increases in the lower stage later in the summer, as many more inflows to the river were identified during early August compared to early July. During data collection in August and November, the stage of the river fluctuates the most dramatically of any time of the year. This fluctuation of up to 3 m at the stage logger below Priest Rapids Dam causes surface water intrusion into the groundwater (Johnson et al., 2012; Song et al., 2018; Shuai et al., 2019). During February data collection, the river is expected to be losing water, although less so than late summer.

Spatial Distribution of Anomalies, Nitrate, and Nearby Land Use

One cluster of anomalies on the west shoreline, adjacent to non-irrigated land, is identified west of Savage Island. Due to its accessibility, data were collected along this shoreline several times throughout the year, and serves as a representation of HEFs without irrigation influence. This shoreline is dominated by a cluster of Category 3 anomalies (not anomalous EC; higher temperature), with occasional Category 4 anomalies (not anomalous EC; lower temperature) and fewer Category 2 anomalies (higher EC; higher temperature). The majority

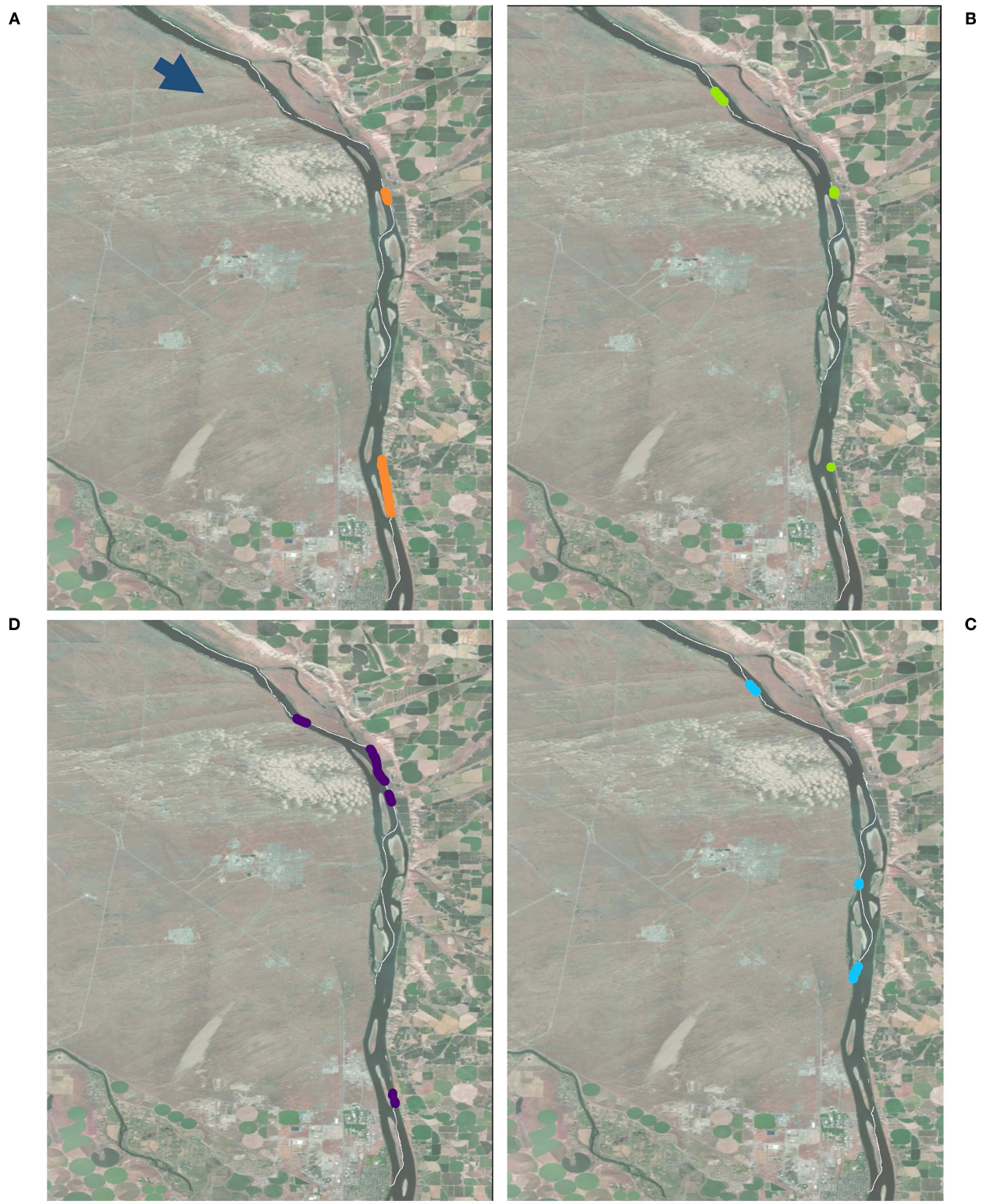

FIGURE 9 | Anomalies found July 3–17 that were **(A)** Category 1 (high EC; low temperature), **(B)** Category 2 (high EC; high temperature), **(C)** Category 3 (not anomalous EC; high temperature), and **(D)** Category 4 (not anomalous EC; low temperature) are all present during this time range, but each category of anomaly is only present in a few locations. The white line shows all the paths traversed during this time period. Map data from Google, Landsat.

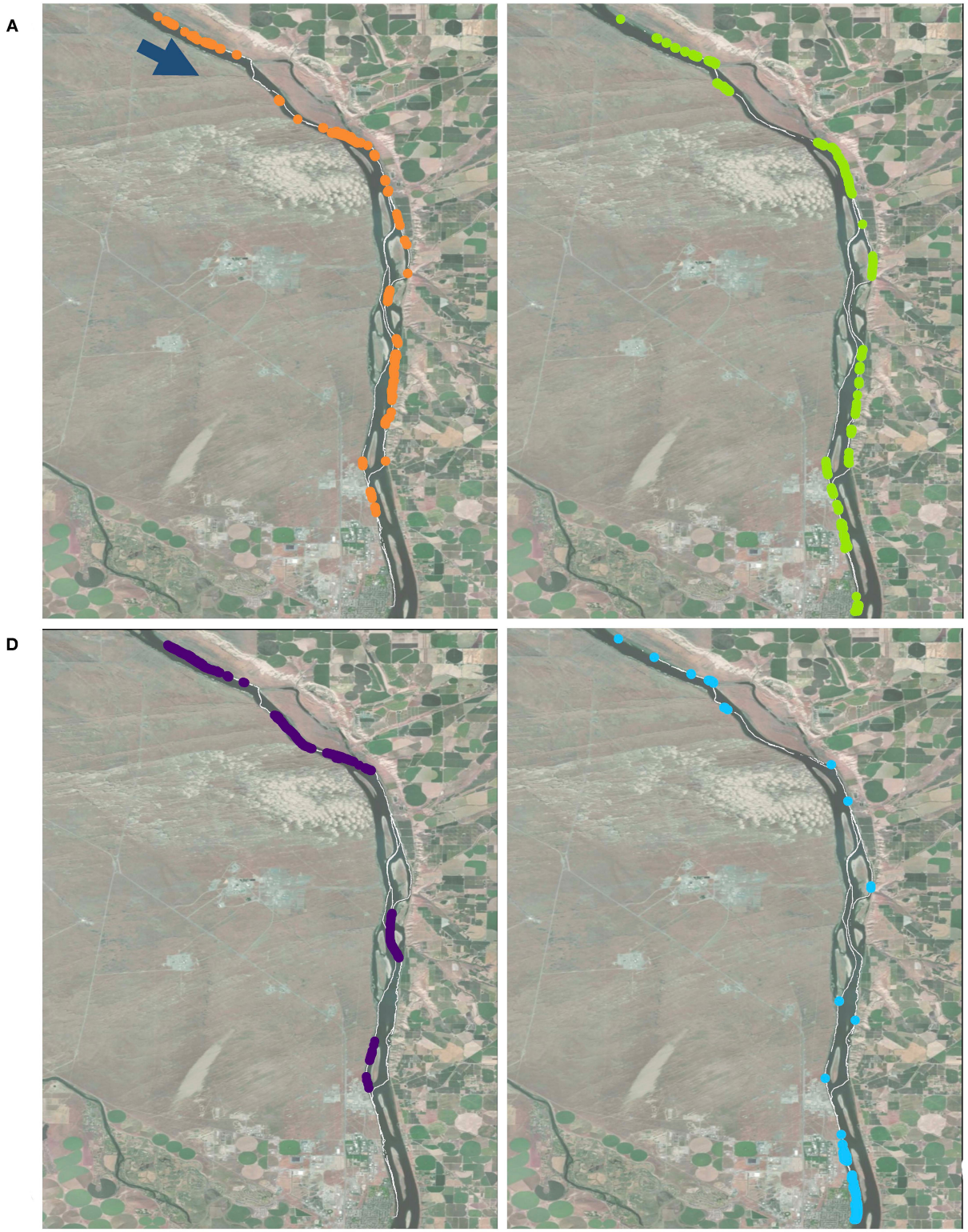

FIGURE 10 | Anomalies observed from August 1–14 that were **(A)** Category 1 (high EC; low temperature), **(B)** Category 2 (high EC; high temperature), **(C)** Category 3 (not anomalous EC; high temperature), and **(D)** Category 4 (not anomalous EC; low temperature) are all present during this time range, but each category of anomaly is only present in a few locations. Category 3 anomalies are clustered near the southern end of the study site, and Category 4 anomalies are clustered near the northern end of the study site. The white line shows all the paths traversed during this time period. Map data from Google, Landsat.

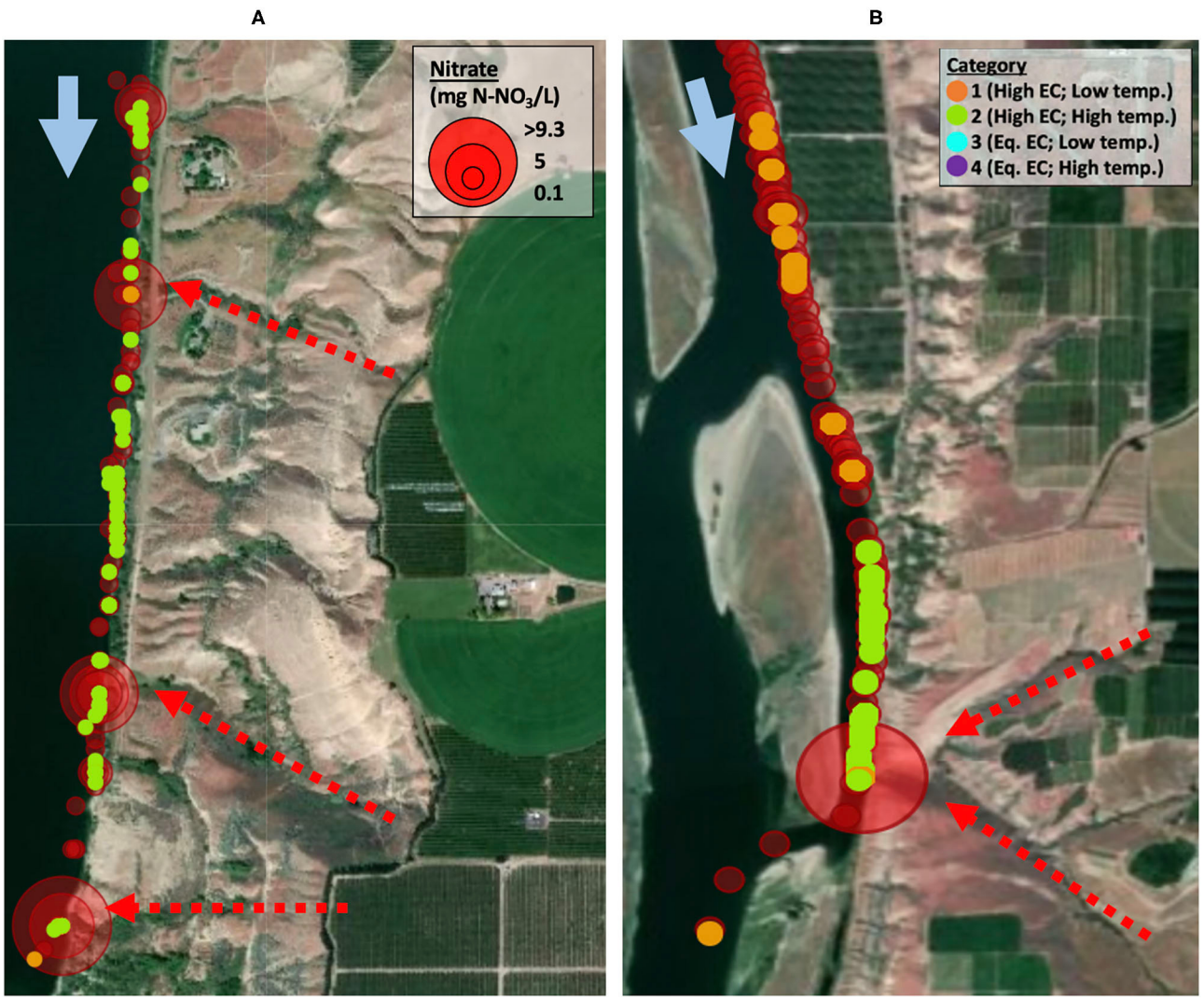

FIGURE 11 | (A) Riverbed anomalies and **(B)** nitrate concentrations along the shoreline adjacent to the 300-Area of the Hanford Reserve. This shoreline is dominated by anomalies with high EC. The river water along the shoreline also has high nitrate concentrations. Map data from Google, Landsat.

of Category 3 and 4 anomalies in this location supports the prediction that these not anomalous EC categories of anomalies are associated with non-irrigated land use. The inflows along this shoreline create habitats with water warmer than river water (Category 2 and 3), and most likely surface-originating inflows. The occasional Category 4 anomalies along the shoreline are likely from groundwater seepage, as the hills lining the river in this location allow for natural pathways of groundwater seepage.

The irrigated eastern shoreline of the river showed a greater frequency of anomalies than the dry landscape of the western shoreline (**Figure 13**). The addition of irrigation water to the landscape, some of which is not used by crops, increases surface runoff and infiltration to groundwater. Of the ∼3 billion cubic meters of water diverted from the Grand Coulee Dam within a year, much returns to the river, although there are no measurements of the total quantity of surface and groundwater return flow (USBR, 2014). In general, we observe high nitrate concentrations when we observe high EC (**Supplementary Figure 1**), however, there are several cases where high EC is not associated with high nitrate concentrations.

Not only is the frequency of identified anomalies greater on the eastern shoreline, the category of anomalies is different than on the western shoreline. On the eastern shoreline, Category 1 (high EC; low temperature) and Category 2 (high EC; high temperature) anomalies dominate the landscape. These anomaly categories are both associated with high EC relative to the river. High EC, indicative of high concentrations of dissolved solids in water, is a common occurrence in surface water and groundwater of irrigated landscapes, due to the influx of nutrients and pesticides from agricultural practices. However, high EC values do not indicate the source of the dissolved solids present

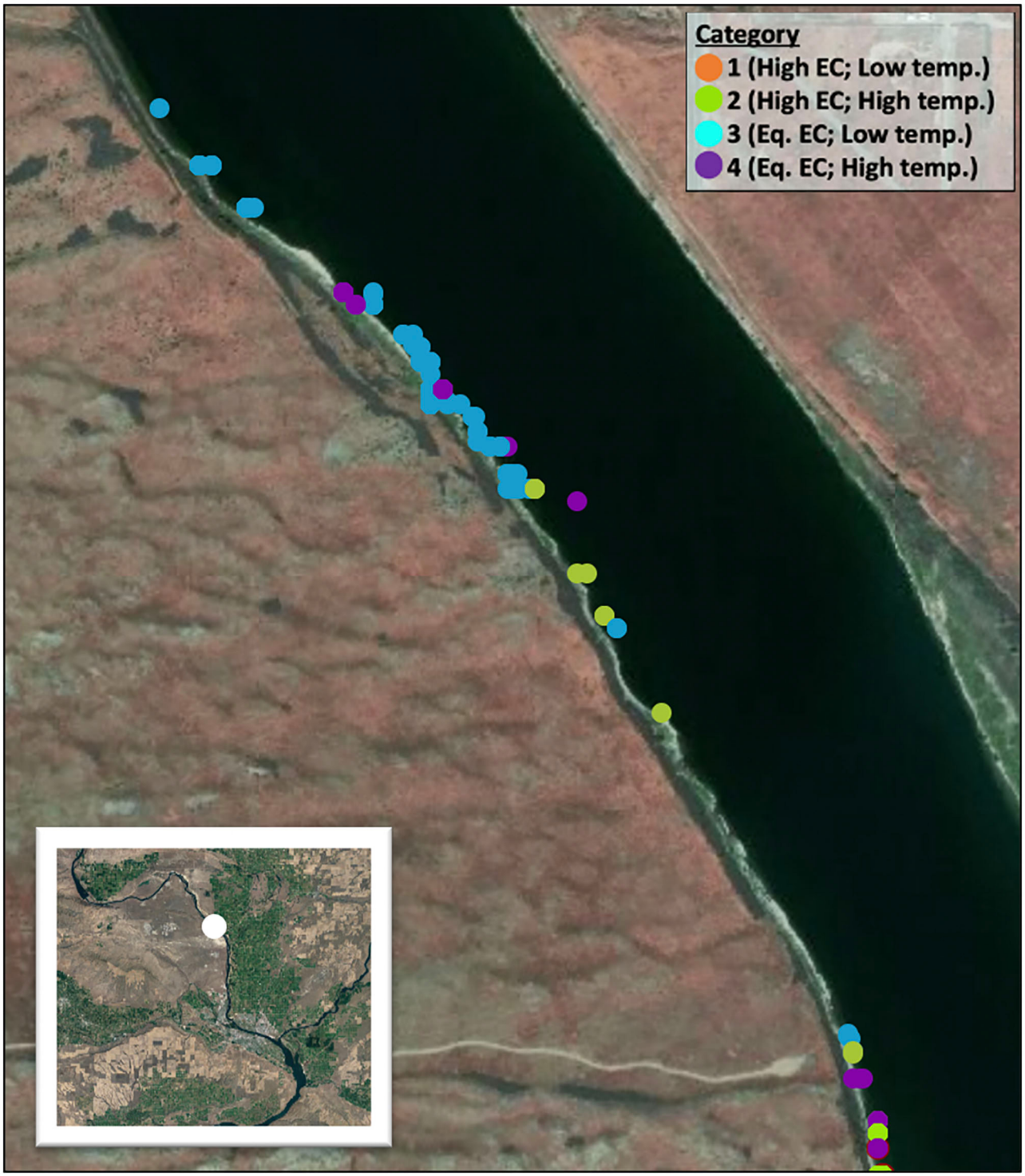

FIGURE 12 | Anomalies along non-irrigated land. The anomalies shown along the western shoreline of the Columbia River next to Savage Island are dominated by Category 3 anomalies. There are also some instances of Category 4 anomalies. Map data from Google, Landsat.

in the water and may originate from soil types. Groundwater in the Hanford Reach is known to have naturally higher EC values than river water (Johnson et al., 2012). The corroboration of coincident nitrate concentrations in the water along the shoreline suggests that the high EC values can be attributed to irrigation runoff or associated seepage.

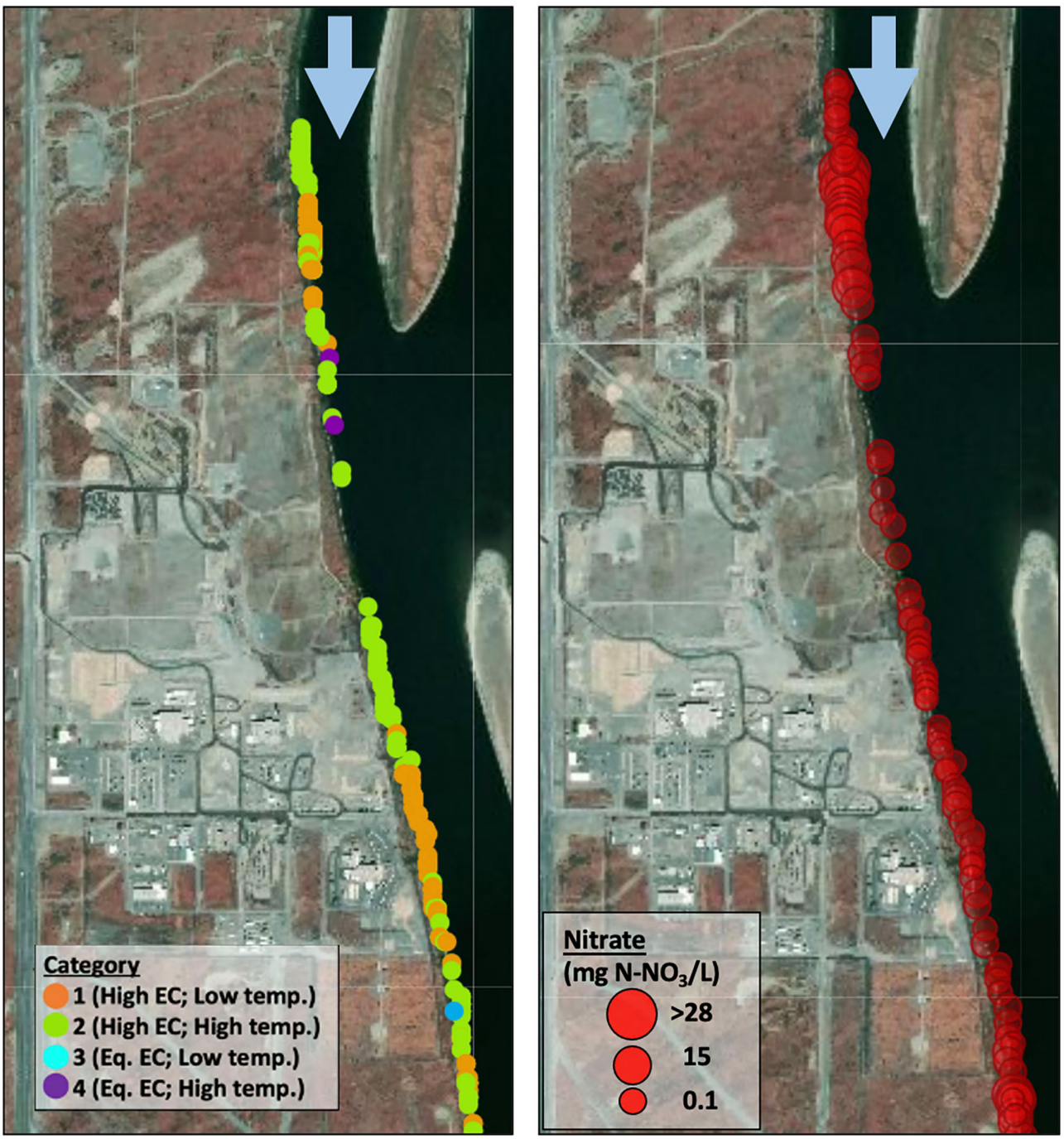

FIGURE 13 | Nitrate concentrations and riverbed anomalies along irrigated eastern shoreline for **(A)** an area just upstream of Johnson Island, and **(B)** an area near Homestead Island. Potential surface flow paths from irrigated fields down to the river are indicated by red arrows. Map data from Google, Landsat.

Although there are few nitrate concentration observations on the western shoreline, there are two clusters. One cluster of nitrate anomalies is located north of Richland, near the "300-Area." The 300-Area was a site of plutonium development and is now the site of a known nitrate plume expanding south and east (USDOE, 2010). This groundwater plume is located in the same area as a cluster of nitrate anomalies along the shoreline, and so it is reasonable to assume this is the source of the nitrate observations clustered along the 300-Area shoreline. The other location of nitrate anomalies on the western shoreline is located

TABLE 2 | Summary of anomaly interpretations.

Comparison to river water	Lower temperature	Higher temperature
Elevated EC	Category 1 • Moderately deep groundwater mixed with irrigation infiltration • Increased NO_3^- concentration	Category 2 • Surface/shallow irrigation water • Increased NO_3^- concentration
Not Anomalous EC	Category 4 • Deep groundwater • Low NO_3^- concentration	Category 3 • Surface/shallow non-irrigation sourced water • Low NO_3^- concentration

Anomalies with high EC are associated with agriculture. Anomalies with high temperature during the summer are surface inflows, and those with low temperature are groundwater. The colors of each category correspond with data presented in maps further in this paper.

west from Savage Island. This cluster is smaller than the one near the 300-Area and classified as Category 4 riverbed anomalies. There are no known contamination sites from Hanford in this area, nor irrigation adjacent to this shoreline. It is possible that contamination from upstream plumes travels through subsurface flow pathways and enters the river at this site.

The highest quantity of nitrate observations is located adjacent to irrigated lands along the eastern shoreline near Taylor Flats. The irrigated shoreline has high frequencies of Category 1 (high EC; low temp) and 2 anomalies, which are associated with high concentrations of nitrate. All nitrate observations are associated with riverbed anomalies categorized as Category 1 and 2.

The association of high-EC anomalies and nitrate near Taylor Flats suggests that part of the measured EC concentrations is a result of dissolved nitrate. The relationship between high-EC and high nitrate concentrations confirms our prediction that anomalies with high-EC originate from irrigation runoff. The presence of high-EC and high nitrate concentration measurements along shorelines that are adjacent to irrigated land suggests that there may be other agricultural-sourced solutes also entering the river through inflows. These may include dissolved phosphorus, pesticides, and insecticides. However, it is important to note that not all high-EC occurrences coincide with high nitrate concentrations (**Supplementary Figure 1**). Elevated nitrate concentrations could have been sourced from nitrification that may be associated with increased chemical weathering causing coincident high-EC conditions (Yue et al., 2015).

The data collected here suggest an interpretation of the riverbed categories identified using water temperature and EC (**Table 2**). In the summer season, when irrigation is occurring, we interpret Category 1 riverbed waters with low temperature and high EC to be associated with moderately deep groundwater that has a substantial irrigation water signature carrying increased solute loads including dissolved nitrate. We interpret Category 2 riverbed anomalies as those indicating very shallow or surface irrigation-sourced water that carry high concentrations of dissolved nitrate. We interpret Category 3 riverbed anomalies, having high temperature and not anomalous EC to the river water as those sourced from shallow or surface non-irrigation derived water, and therefore likely to have low nitrate concentrations. Finally, we interpret Category 4 riverbed anomalies with low temperatures and not anomalous EC to be indicative of relatively deep groundwater and therefore expected to have low dissolved nitrate concentrations.

High concentrations of nitrate measured in this reach are above toxic levels for salmon, but they are also very locally observed. Chinook salmon swim upriver to the Hanford Reach to return to their breeding grounds to spawn. Although adults have low nitrate sensitivity, likely due to the ameliorating effect of water salinity, eggs and young salmon (fry) are much more sensitive (Camargo et al., 2005). Chinook salmon fry experience a significant increase in mortality, known as nitrate toxicity, at 4.5 mg $N–NO_3^-$/L (Kincheloe et al., 1979). The maximum nitrate concentration measured in this study was 37.9 mg $N–NO_3^-$/L, more than nine times the reported lethal concentration. The localized high nitrate concentrations along the shoreline makes that particular habitat unsuitable for salmon fry.

In this study, we focused on the location and characteristics of the termini of HEFs and the expected correlation of the location of these to river-adjacent land use. These data and interpretations are useful for comparing to other groundwater flow modeling activities in the area and not anomalous related research. However, because we were not able to define the sources or entire paths of HEFs, which would have required extensive installation of wells and other subsurface interrogation, we rely on the correlation of nearby surface activities to subsurface conditions. Thus, additional study to better tie activities across the landscape to HEFs of the Columbia River (and other rivers) is warranted.

The goal of this study was to determine the impact of river corridor land use on river water quality. We used measurements of temperature and EC along the streambed to identify locations of water inflows. We demonstrate that along the Hanford reach, irrigation increases the spatial distribution of inflows into the river. The high concentrations of nitrate associated with irrigation-related HEFs indicate that agricultural land use on the east side of the river plays an important role in transferring nitrate to the river, at concentrations high enough to negatively interfere with the shoreline aquatic habitat. Future work could focus on the relative ages of groundwater in HEFs and the nitrate associated with them to evaluate how residence time and transport from source to river may be affecting the observed temporal and spatial patterns along the river shorelines.

Irrigation-influenced inflows were found to be most prevalent during late summer when river flows decrease. The large stage fluctuations from hydropower operations during late summer increase the gradients between groundwater/surface inflows and river water, increasing inflowing water. Since late summer is the driest time of the year, many of these exchanges involve irrigation runoff with high concentrations of nitrate.

DATA AVAILABILITY STATEMENT

The datasets presented in this study can be found in online repositories. The names of the repository/repositories

and accession number(s) can be found in the article/**Supplementary Material**.

AUTHOR CONTRIBUTIONS

AC conducted all field research, conducted analyses, and wrote the first draft of the paper. MG and XC directed this research, performed some field data collection, guided field data collection and analyses, and helped to write the paper. EA provided field support and conducted some of the field data collection. VG-C analyzed samples and contributed to data analyses. All authors contributed to the article and approved the submitted version.

FUNDING

This material is based upon work supported by the Department of Energy, award grant numbers DE-SC0018165 and DE-SC0020339. Any opinions, findings, and conclusions or recommendations expressed in this material are those of the author(s) and do not necessarily reflect the views of the Department of Energy.

ACKNOWLEDGMENTS

This research was supported by the U.S. Department of Energy (DOE), Office of Biological and Environmental Research (BER), as part of BER's Subsurface Biogeochemical Research Program (SBR), grant nos. DE-SC0018165 and DE-SC0020339. Data were collected in collaboration with the SBR Scientific Focus Area (SFA) at the Pacific Northwest National Laboratory (PNNL). This paper describes objective technical results and analysis. Any subjective views or opinions that might be expressed in the paper do not necessarily represent the views of the U.S. Department of Energy or the United States Government. PNNL is operated for the DOE by Battelle Memorial Institute under contract DE-AC05-76RL01830.

SUPPLEMENTARY MATERIAL

The Supplementary Material for this article can be found online at: https://www.frontiersin.org/articles/10.3389/frwa.2021.574684/full#supplementary-material

Supplementary Figure 1 | All nitrate observations compared to the coincident EC values measured in the shallow sensors (i.e., closest to the SUNA unit).

REFERENCES

Arntzen, E. V., Geist, D. R., and Dresel, P. E. (2006). Effects of fluctuating river flow on groundwater-surface water mixing in the hyporheic zone of a regulated, large cobble bed river. *River Res. Appl.* 22, 937–946. doi: 10.1002/rra.947

Camargo, J. A., Alonso, A., and Salamanca, A. (2005). Nitrate toxicity to aquatic animals: a review with new data for freshwater invertebrates. *Chemosphere* 58, 1255–1267. doi: 10.1016/j.chemosphere.2004.10.044

Cardenas, M. B., and Markowski, M. S. (2011). Geoelectrical imaging of hyporheic exchange and mixing of river water and groundwater in a large regulated river. *Env. Sci. Technol.* 45, 1407–1411. doi: 10.1021/es103438a

Clinton, W. J. (2000). *Proclamation 7319-Establishment of the Hanford Reach National Monument*.

Conner, A., Gooseff, M., and Chen, X. (2020). *Boat-Dragged Riverbed and Mid-Column Water Quality along the Hanford Reach in the Columbia River Shorelines*. Quantifying Distributed Exchanges of Groundwater with River Corridors. ESS Digital Repository.

Dirkes, R., Hanf, R., and Poston, T. (1999). *Hanford Site Environmental Report for Calendar Year 1998*. Pacific Northwest National Labs.

Fernald, A. G., Wigington, P. J. Jr., and Landers, D.H. (2001). Transient storage and hyporheic flow along the Willamette River, Oregon: Field measurements and model estimates. *Water Resour. Res.* 37, 1681–1694. doi: 10.1029/2000WR900338

Geist, D. R. (2000). Hyporheic discharge of river water into fall chinook salmon (*Oncorhynchus tshawytscha*) spawning areas in the Hanford Reach, Columbia River. *Can. J. Fish. Aquat. Sci.* 57, 1647–1656. doi: 10.1139/f00-102

Gilmore, T. E., Genereux, D. P., Solomon, D. K., Farrell, K. M., and Mitasova, H. (2016). Quantifying an aquifer nitrate budget and future nitrate discharge using field data from streambeds and well nests. *Water Resour. Res.* 52, 9046–9065. doi: 10.1002/2016WR018976

Gomez-Velez, J. D., Wilson, J. L., Cardenas, M. B., and Harvey, J. W. (2017). Flow and residence times of dynamic river bank storage and sinuosity-driven gyporheic exchange. *Water Resour. Res.* 53, 8572–8595. doi: 10.1002/2017WR021362

Harvey, F. E., Lee, D. R., Rudolph, D. L., and Frape, S. K. (1997). Locating groundwater discharge in large lakes using bottom sediment electrical conductivity mapping. *Water Resour. Res.* 33, 2609–2615. doi: 10.1029/97WR01702

Harvey, J., and Gooseff, M. (2015). River corridor science: hydrologic exchange and ecological consequences from bedforms to basins. *Water Resour. Res.* 51, 6893–6922. doi: 10.1002/2015WR017617

Hodson, M. E., and Donner, E. (2011). "Managing adverse soil chemical environments," in *Russell's Soil Conditions and Plant Growth*, eds. P. J. Gregory and S. Nortcliff (Chichester: Wiley/Blackwell), 195–237.

Johnson, T. C., Slater, L. D., Ntarlagiannis, D., Day-Lewis, F. D., and Elwaseif, M. (2012). Monitoring groundwater-surface water interaction using time-series and time-frequency analysis of transient three-dimensional electrical resistivity changes. *Water Resour. Res.* 48, W07506. doi: 10.1029/2012WR011893

Kasahara, T., and Wondzell, S. M. (2003). Geomorphic controls on hyporheic exchange flow in mountain streams. *Water Resour. Res.* 39, 1005. doi: 10.1029/2002WR001386

Kiel, B. A., and Cardenas, M. B. (2014). Lateral hyporheic exchange throughout the Mississippi River network. *Nat. Geosci.* 7, 413–417. doi: 10.1038/ngeo2157

Kincheloe, J. W., Wedemeyer, G. A., and Koch, D. L. (1979). Tolerance of developing salmonid eggs and fry to nitrate exposure. *Bull. Environ. Contam. Toxicol.* 23, 575–578. doi: 10.1007/BF01770006

Lee, D. R., Geist, D. R., Saldi, K., Hartwig, D., and Cooper, T. (1997). *Locating Ground-Water Discharge in the Hanford Reach of the Columbia River (PNNL-11516)*. United States Department of Energy.

Lenat, D. R., and Crawford, J. K. (1994). Effects of land use on water quality and aquatic biota of three North Carolina Piedmont streams. *Hydrobiologia* 294, 185–199. doi: 10.1007/BF00021291

Northwest Power and Conservation Council (NPCC) (2019). *Hanford Reach*. Retrieved from: https://www.nwcouncil.org/reports/columbia-river-history/hanfordreach

Payn, R. A., Gooseff, M. N., McGlynn, B. L., Bencala, K. E., and Wondzell, S. M. (2009). Channel water balance and exchange with subsurface flow along a mountain headwater stream in Montana, United States. *Water Resour. Res.* 45, W11427. doi: 10.1029/2008WR007644

Shuai, P., Chen, X., Song, X., Hammond, G. E., Zachara, J., Royer, P., et al. (2019). Dam operations and subsurface hydrogeology control dynamics of hydrologic exchange flows in a Regulated River reach. *Water Resour. Res.* 55, 2593–2612. doi: 10.1029/2018WR024193

Song, X., Chen, X., Stegen, J., Hammond, G., Song, H.-S., Dai, H., et al. (2018). Drought conditions maximize the impact of high-frequency flow variations on thermal regimes and biogeochemical function in the hyporheic zone. *Water Resour Res.* 54, 7361–7382. doi: 10.1029/2018WR022586

USACE (2018) *National Inventory of Dams, US Army Corps of Engineers*. Available online at: http://nid.usace.army.mil/cm_apex/f?p=838:4:0::NO (accessed June 19, 2020).

USBR (2014). *The Story of the Columbia Basin Project*. US Bureau of Reclamation. Available online at: https://www.usbr.gov/pn/project/brochures/columbiabasinproject.pdf

USDOE (2010). *Hanford Site Groundwater Monitoring and Performance Report for 2009*. US Department of Energy. Available online at: http://pdw.hanford.gov/arpir/index.cfm/viewDoc?accession=0084237 (accessed June 19, 2020).

Vaccaro, J. J., and Maloy, K. J. (2006). *A Thermal Profile Method to Identify Ground-Water Discharge Areas and Preferred Salmonid Habitats for Long River Reaches*. U.S. Geological Survey Scientific Investigations Report 2006–5136.

Woessner, W. (2000). Stream and fluvial plain ground water interactions: rescaling hydrogeologic thought. *Ground Water* 38, 423–429. doi: 10.1111/j.1745-6584.2000.tb00228.x

Yue, F., Li, S., Liu, C., Lang, Y., and Ding, H. (2015). Sources and transport of nitrate constrained by the isotopic technique in a karst catchment: an example from Southwest China. *Hydrol. Process*. 29, 1883–1893. doi: 10.1002/hyp.10302

Zachara, J. M., Chen, X., Song, X., Shuai, P., Murray, C., and Resch, C. T. (2020). Kilometer-scale hydrologic exchange flows in a gravel bed river corridor and their implications to solute migration. *Water Resour. Res*. 56, e2019WR025258. doi: 10.1029/2019WR025258

Zhou, T., Bao, J., Huang, M., Hou, Z., Arntzen, E., Song, X., et al. (2018). Riverbed hydrologic exchange dynamics in a large regulated river reach. *Water Resour. Res*. 54, 2715–2730. doi: 10.1002/2017WR020508

Zhou, T., Huang, M., Bao, J., Hou, Z., Arntzen, E., Mackley, R., et al. (2017). A new approach to quantify shallow water hydrologic exchanges in a large regulated river reach. *Water* 9, 703. doi: 10.3390/w9090703

Conflict of Interest: The authors declare that the research was conducted in the absence of any commercial or financial relationships that could be construed as a potential conflict of interest.

The handling editor declared a past co-authorship with one of the authors MG.

Advantages of publishing in Frontiers

OPEN ACCESS
Articles are free to read for greatest visibility and readership

FAST PUBLICATION
Around 90 days from submission to decision

HIGH QUALITY PEER-REVIEW
Rigorous, collaborative, and constructive peer-review

TRANSPARENT PEER-REVIEW
Editors and reviewers acknowledged by name on published articles

Frontiers
Avenue du Tribunal-Fédéral 34
1005 Lausanne | Switzerland

Visit us: www.frontiersin.org
Contact us: frontiersin.org/about/contact

REPRODUCIBILITY OF RESEARCH
Support open data and methods to enhance research reproducibility

DIGITAL PUBLISHING
Articles designed for optimal readership across devices

FOLLOW US
@frontiersin

IMPACT METRICS
Advanced article metrics track visibility across digital media

EXTENSIVE PROMOTION
Marketing and promotion of impactful research

LOOP RESEARCH NETWORK
Our network increases your article's readership